Packing Constraint of Octaoxyethylene Octyl Ether Carboxylates in Micelles and Bicelles and Fibrillar Self-Assembly of Glycyrrhizic Acid Ammonium Salt

Dissertation

zur Erlangung des Doktorgrades
der Naturwissenschaften (Dr. rer. nat.)
der Fakultät für Chemie und Pharmazie
der Universität Regensburg

vorgelegt von
Patrick Denk
aus Salzweg
2024

Die Arbeit wurde angeleitet von:	Prof. Dr. Werner Kunz
Promotionsgesuch eingereicht am:	
Kolloquiumstermin:	
Gutachter:	Prof. Dr. Werner Kunz
	Prof. Dr. Thomas Zemb
	Prof. Dr. Hubert Motschmann
Vorsitzender:	Prof. Dr. Oliver Tepner

Artistic depiction of the core-shell micellar phase and the interdigitated micellar phase (bottom right) encountered for the herein studied surfactant $C_8E_8CH_2COOH$. The image was also used in the inside back cover of volume 623 of the Journal of Colloid and Interface Science.

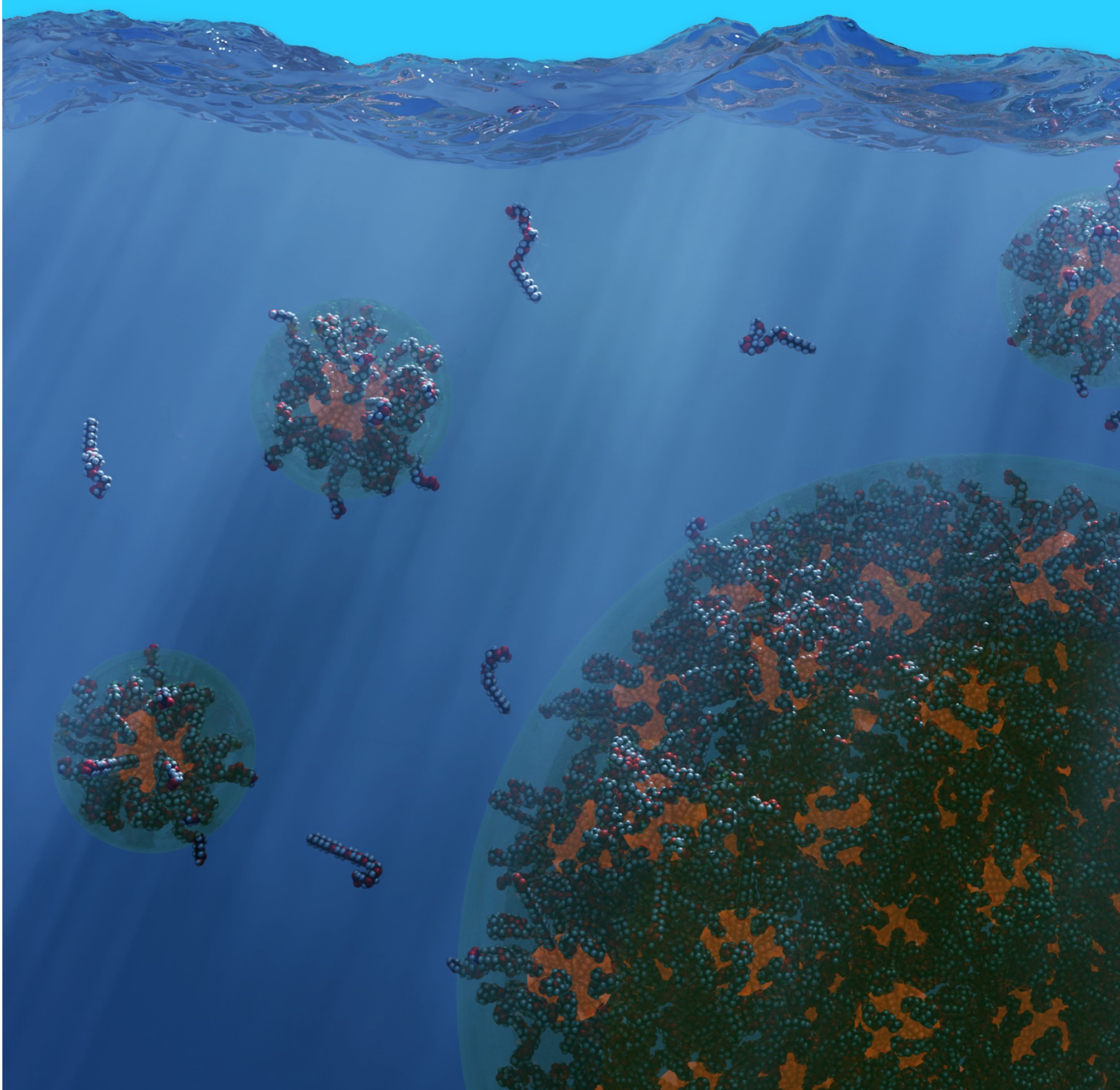

Preface and Acknowledgement

This PhD thesis was carried out at the Institute of Physical and Theoretical Chemistry, Faculty of Chemistry and Pharmacy, University of Regensburg, under the supervision of Prof. Dr. Werner Kunz. With the exceptions of small-angle scattering, cryogenic transmission electron microscopy (cryo-TEM), diffusion-ordered NMR spectroscopy (DOSY-NMR), quantitative ^{13}C-NMR spectroscopy, and rotational rheometry, the experimental work was conducted at the aforementioned institute between November 2020 and December 2023. Some data used in this work, especially in Chapter I., were already collected during experiments for my master thesis (P. Denk, Phase Behavior and Simple Coacervation of Akypo™ LF2 in Aqueous Solutions, [unpublished] master thesis, University of Regensburg, 2020.) between January 2020 and October 2020. Small- and wide-angle X-ray scattering (SWAXS) experiments were performed partly by Dr. Asmae El Maangar at the Institut de Chimie Séparative de Marcoule (ICSM) during her time as a PhD student and partly by Dr. Lauren Matthews and Dr. Sylvain Prévost at the European Synchrotron Radiation Facility (ESRF) in Grenoble. Small-angle neutron scattering (SANS) experiments were carried out by Dr. Sylvain Prévost at the Institut Laue-Langevin – The European Neutron Source (ILL) in Grenoble. Cryo-TEM was performed by Sapir Lifshiz-Simon under supervision by Prof. Dr. Yeshayahu Talmon at the Technion – Israel Institute of Technology in Haifa. DOSY-NMR as well as quantitative ^{13}C-NMR measurements were conducted by Dr. Wagner Menezes da Silva under supervision by Prof. Dr. Ruth Gschwind at the Institute of Organic Chemistry at the University of Regensburg. Rotational rheometry was performed by the author of this thesis at the Institute of Pharmacy at the University of Regensburg.

Since the majority of the results presented in this thesis is already published, all chapters containing original research, i.e., Chapters II., III., IV., V., and VI., are written as a self-contained study in the form of the respective published article(s). The chapters are organized according to following convention: Abstract, Introduction, Experimental Section, Results and Discussion, Conclusion and Outlook, and References. Each of these chapters also has its own Appendix containing supplementary material. At the beginning of each chapter, the respective publications are referenced, and the author contributions are declared. A complete list of publications as well as poster presentations at national and international

conferences is given at the end of the thesis. Chapter I. serves as an introduction, showing how this work, dealing mostly with an alkyl ether carboxylic acid surfactant, complements the literature in the field of surfactant science. Chapter VII. is a brief summary of the most important conclusions to be drawn from this work.

This PhD thesis would not have been possible without the help and support of a multitude of people and institutions, whom I want to thank in the following:

First and foremost, I would like to express my deepest gratitude to my supervisor, Prof. Dr. Werner Kunz, for giving me the opportunity to work independently at the Institute of Physical and Theoretical Chemistry on an interesting subject dealing with the self-assembly of amphiphilic molecules on the nanoscale. I also want to thank him for the fruitful discussions, his guidance, his interest in my work, and of course for his financial support throughout the years.

I would also like to extend my deepest gratitude to Prof. Dr. Thomas Zemb (ICSM), with whom I had the pleasure to work with throughout the years, ever since I started my master thesis. Without his guidance, expertise in small-angle scattering, ingenious scientific input, and his innumerable ideas, this thesis would not be nearly as comprehensive as it turned out to be. I thank him for being a mentor to me, with his everlasting willingness to help and discuss with me.

Special thanks go to Dr. Asmae El Maangar (ICSM), Dr. Lauren Matthews (ESRF), and Dr. Sylvain Prévost (ILL) for providing SAXS and SANS data and being helpful co-workers on various publications. In this regard, I must also thank the ESRF and ILL for providing the equipment and beam time to make most of these experiments possible. I am also grateful to Dr. Jyotsana Lal from the Argonne National Laboratory in Lemont, Illinois, for her help with my first model simulations of SAXS data during her visit at our institute.

Special thanks further go to Sapir Lifshiz-Simon and Prof. Dr. Yeshayahu (Ishi) Talmon from the Technion – Israel Institute of Technology in Haifa for state-of-the-art imaging of soft condensed matter using cryogenic and freeze-fracture transmission electron microscopy.

Many thanks go to Dr. Wagner Menezes da Silva for performing DOSY-NMR, as well as quantitative ^{13}C-NMR spectroscopy, at the Institute of Organic Chemistry at the University

of Regensburg. Likewise, I thank Prof. Dr. Ruth Gschwind for making these experiments possible at her facilities.

I am grateful to Prof. Dr. Achim Göpferich for letting me run rheological experiments in his facilities at the Institute of Pharmacy at the University of Regensburg, and specifically thank his PhD students Johannes Lang and Carsten Damm for their instructions.

For providing all oligoether carboxylate surfactants free of charge, I thank the Kao Chemicals GmbH (Emmerich am Rhein, Germany) in person of Dr. Thomas Myrdek. I am also grateful to him for his support regarding any questions concerning these surfactants.

I would like to acknowledge the effort of all people working for the Central Analytical Services of the Faculty of Chemistry and Pharmacy at the University of Regensburg, who enabled the easy access to nuclear magnetic resonance (NMR) spectroscopy and mass spectrometry.

Further thanks go to all staff members of the Institute of Physical and Theoretical Chemistry for the pleasant working environment and their assistance. I would like to personally thank Dominik Zahnweh, Diana Funkner, and Bastian Rödig, who all shared the laboratory with me for some time throughout the years, for always helping out when help was necessary and making my stay more joyful. In the same way, I would like to thank my colleagues Dr. Alexander Dietz, Dominik Feucht, Florian Kroiß, Philipp Polzer, Vanessa Lustig, and Lukas Moser for the great atmosphere in the office. Additional thanks go to Dominik Feucht for introducing me to various techniques, including rolling-ball viscometry and surface tension measurements. I also thank Dr. Jonas Blahnik for introducing me to the experimental aspects of dynamic light scattering, and Apl. Prof. Dr. Rainer Müller for his helpful information on vapor pressure osmometry. I also wish to thank David Kleber, who sparked the interest in the first surfactant I worked on. I am also grateful to the various interns, who conducted their internship or bachelor thesis under my supervision. I thank Julia Grasenhiller, Julia-Marie Maier, Markus Maier, Lea Sammet, and Dominik Bubak for contributing to my work.

Especially helpful to me during this time were of course all my friends and my whole family, who made all these endeavors possible. Words cannot express my gratitude for their unconditional support and encouragement.

Table of Contents

Chapter I.

Introduction and Strategy

In this thesis, mainly the surfactant octaoxyethylene octyl ether carboxylic acid and its metal salts are examined. **Chapters II. and III.** are concerned with the phase behavior and microstructures in binary mixtures with water. In **Chapters IV. and V.**, this surfactant is mixed with dioxyethylene oleyl ether carboxylic acid, utilizing the vastly different areas per molecule of the two surfactants, to form a special bicellar nematic gel. In **Chapter VI.**, a different topic is presented. The fibrillar structures formed by the natural sweetener and hydrogelator glycyrrhizic acid ammonium salt in water and in water/ethanol mixtures are elucidated.

Each of these chapters is a self-contained study, and the vast majority of the presented results is already published. Therefore, each chapter is written and organized like a research article with the following general organization: Abstract, Introduction, Experimental Section, Results and Discussion, Conclusion and Outlook, and References. In addition, each chapter has its own Appendix containing supplementary material. On the first page of each chapter, the respective publications are referenced , and the contributions of all authors are declared. A complete list of publications as well as poster presentations at national and international conferences is given at the end of this thesis.

The following introduction is written for the main topic of this thesis, the self-assembly of single and mixed surfactant systems containing octaoxyethylene octyl ether carboxylic acid (**Chapters II.** to **V.**). Since **Chapter VI.**, though also concerning self-assembly, is not thematically connected to the other chapters, the introduction given in **Section VI.2.** of said chapter should suffice.

I.1. Scientific Dogmata in Surfactant Self-Assembly

Self-assembly of surfactant molecules into molecular aggregates, called micelles, is a consequence of the surfactant's inner conflict imposed by its amphiphilic molecular structure. A surfactant molecule comprises at least one hydrophilic and at least one hydrophobic part, which would not stay together but separate, were they not covalently bound together. Since the hydrophilic headgroup and the hydrophobic tail are bound together, the only way to resolve the conflict is to self-assemble into micelles to form hydrophobic domains of tails and hydrophilic domains of headgroups to minimize the contact area. In modern physical chemistry, resolving a conflict means minimizing Gibbs free energy within the possibilities set by sterical constraints since molecules cannot overlap. In water, the situation is the same as the hydrophilic headgroups interact with water molecules and form a polar domain, while water is excluded from the nonpolar domain made of the hydrophobic tails.

Though soaps have been used for cleaning purposes by humans for at least 4800 years without understanding the mechanisms behind their functionality [1], the scientific exploration of surfactant self-assembly started in 1913, when McBain [2] first suggested the existence of self-assembled aggregates in aqueous soap solutions. Throughout the more than 100 years long history of surfactant science, many scientists contributed towards the understanding and prediction of surfactant self-assembly, continuously improving models and theories. A clear and extensive overview of the most important milestones was given by Nagarajan in 2014 [3].

Self-assembly of surfactants proves to be a complex phenomenon, governed by a subtle interplay of many different forces, such as hydration, electrostatic, Van der Waals, and entropic forces, and geometric constraints imposed by the molecular structure. The introduction of pseudo-phases by Tanford [4,5] in the 1970s has clarified the situation and allowed explicit calculation. Micelles and bound species and the bulk solvent are considered as non-separated but distinct phases, i.e., the chemical potential of each constituent is equal in each pseudo-phase. When the bulk (solvent) phase does not contain any surfactant monomers, the sterical packing of the molecular surfactant films introduced by Israelachvili *et al.* [6,7] dominates over entropic effects.

Despite the significant progresses made by using free energy minimization within the constraints of packing, the huge variety of surfactants with different structures of more or less

complex headgroups and tails further complicates the development of a unified theory of micellization to predict concentration-dependent self-assembly, still leaving a vast playground for both experimentalists and theoreticians in the future.

When entropy plays no role, a molecular packing model for self-assembly can be quantified at first order in a manner described by Israelachvili *et al.* [6,7], considering not only basic thermodynamics and interaction free energies, but also geometrical packing constraints. This model allows for the prediction of the size and shape of micelles through a simple spontaneous molecular packing parameter p_0.

$$p_0 = \frac{v}{a_0 \cdot l_c} , \tag{I.1.1}$$

where v is the partial molecular volume of the hydrophobic tail, l_c is the critical length limiting the radius or the thickness of the aggregate, and a_0 is the equilibrium surface area per surfactant molecule at the hydrophobic-hydrophilic interface. A more detailed discussion of the packing parameter is given in **Appendix A.3**, where also the difference between the spontaneous packing parameter p_0 and the effective packing parameter p is discussed. Since l_c is given by the effective conformational average length of the hydrophobic tail, the ratio v/l_c is constant for common alkyl chains, independently of their length [8]. As a result, the magnitude of p_0 only depends on a_0, which is not simply a geometrical area of the molecule but depends on intermolecular interactions and is obtained by minimizing the free energy in the surfactant film. a_0 only depends on the headgroup and the influence of the tail length is neglected, leading to p_0 and therefore the aggregation properties being determined by the headgroup exclusively. Nagarajan [9] extended the model by additionally considering the free energy of tail deformation, which explicitly depends on the tail length, in the calculation of a_0. Due to its simplicity combined with its relative success in predicting the preferred shapes of surfactant self-assemblies, the packing parameter is still regularly used in the literature to predict the equilibrium aggregates of surfactants, where $0 \leq p_0 \leq 1/3$ for spheres, $1/3 \leq p_0 \leq 1/2$ for cylinders, and $1/2 \leq p_0 \leq 1$ for bilayers. Note that in this packing model, the surfactant molecule is approximated to have a conical shape, i.e., the hydrophobic tail ends in a point. In reality, the end of the hydrophobic tail is of finite size, in the case of a straight alkyl chain given by the size of the CH_3 group. A direct extension of the initial packing concept, using a truncated cone with a second area per molecule, called the chain splay area, assigned to the hydrophobic tail, was proposed by Kulkarni [10] in 2019. The

consideration of the chain splay area is of importance when the packing parameter adopts higher values, especially when reverse structures are formed. In this thesis, the concept of the packing parameter is used as a convenient approximation by a dimensionless number to distinguish between surfactants with different general properties and behavior.

The purpose of this introduction is not to give an overview of the progressions made in self-assembly theory in general, as for example given in ref. [3], but to give an overview of some important surfactant classes and their self-assembly, identifying the dominant molecular driving forces and citing some of the seminal papers that had a significant contribution towards the understanding of these surfactant classes. Further, the research conducted in this thesis will be assessed for its contribution to the field of surfactant self-assembly. Surfactants can be anionic, cationic, nonionic, or zwitterionic. Common surfactants consist of one headgroup and one tail, where the tail is typically one alkyl chain, but can also consist of two or, in principle, even three chains, as for example in phospholipids or triglycerides. Other types of surfactants, such as gemini surfactants or bola surfactants are not considered here. Gemini surfactants are made of two surfactant molecules that are covalently bound together by a molecular bridge, therefore comprising two tails and two headgroups. Bola surfactants have two headgroups bound to both sides of the same hydrophobic chain.

I.1.1. Membrane Lipids

One of the best studied surfactant families is that of membrane lipids, as they play a crucial role in life by forming bilayer membranes and their physicochemical understanding is an important contribution towards the understanding of biological processes. Membrane lipids comprise two acyl chains as hydrophobic part, and depending on their headgroup they can be zwitterionic, e.g., phosphatidylcholines such as 1-palimitoyl-2-oleoylphosphatidylcholine (POPC) or phosphatidylethanolamines such as 1-palimitoyl-2-oleoylphosphatidylethanolamine (POPE), anionic, e.g., phosphatidyl-L-serines such as dioleoylphosphatidyl-L-serine (DOPS), cationic, e.g., 1,2-dioleoyl-3-trimethylammoniumpropane (DOTAP), or nonionic, e.g., glycero-glycolipids such as digalactosyldi-(9Z,12Z,15Z)-octadecatrienoylglycerol (DGDG). The common feature of all membrane forming lipids in water is that the large double tail hydrophobic part imposes a spontaneous packing parameter p_0 close to 1, which leads to the formation of bilayers, i.e., lamellar phases and vesicles

(liposomes).

When trying to understand the molecular driving forces governing the membrane lipid self-assembly, a variety of different contributions must be considered. Two equations of state are required for a full description. On the one hand, the perpendicular equation of state, which includes the inter-bilayer forces determining the swelling. On the other hand, the lateral equation of state, linking the area per molecule of the lipid in the molecular layer to the free energy [11].

The perpendicular equation of state includes the following forces. Attractive van der Waals forces between bilayers, described by Ninham and Parsegian [12], are opposed by a strong repulsive hydration force, first measured accurately by LeNeveu *et al.* [13], see **Fig. I.1**, and theoretically described by Marčelja and Radić [14]. In the case of charged bilayers (formed by anionic or cationic lipids, or by ion adsorption to zwitterionic lipids), electrostatic repulsion also comes into play. To some surprise, Cowley *et al.* [15] have shown that electrostatic repulsion only dominates at large inter-bilayer distances, whereas the dominant repulsive short-range ($\leq$ 3 nm) force, even in charged systems, is the hydration force. An additional contribution to the bilayer interactions is a steric repulsion caused by thermally excited mechanical undulations, which was first pointed out by Helfrich [16–18]. Counter-intuitively, this is a long-range interaction, acting over similar distances as electrostatic repulsions. In addition to the random Helfrich undulations, electrostatically coupled, correlated undulations can be found in the case of ionic lipids, giving rise to the "oyster shell phase" described by Demé *et al.* [19,20]. The dominant molecular driving force governing self-assembly differs for charged and uncharged lipids. While the hydration force dominates for uncharged lipids (zwitterionic and nonionic), electrostatic forces coupled to undulations dominate the behavior of charged lipids (anionic and cationic). The former was confirmed especially by studies concerning the paradox swelling of multilayered systems when adding salts or nonionic solutes, which lead to a positive swelling mainly due to screening of van der Waals attraction [21,22].

Aspects to consider for the lateral equation of state, which is directly linked to the packing parameter p_0, are conformational packing constraints [23], lateral lipid compressibility, and interfacial free energies of hydrophobic-hydrophilic interfaces [24], as first established by Marcelja and Wolfe [25]. Headgroup interactions, such as hydration or electrostatic interactions, directly influence the equilibrium area per molecule a_0, which is obtained by

minimizing the lateral equation of state. A more detailed lateral equation of state for lipids was established by Marsh [26], see **Fig. I.2**.

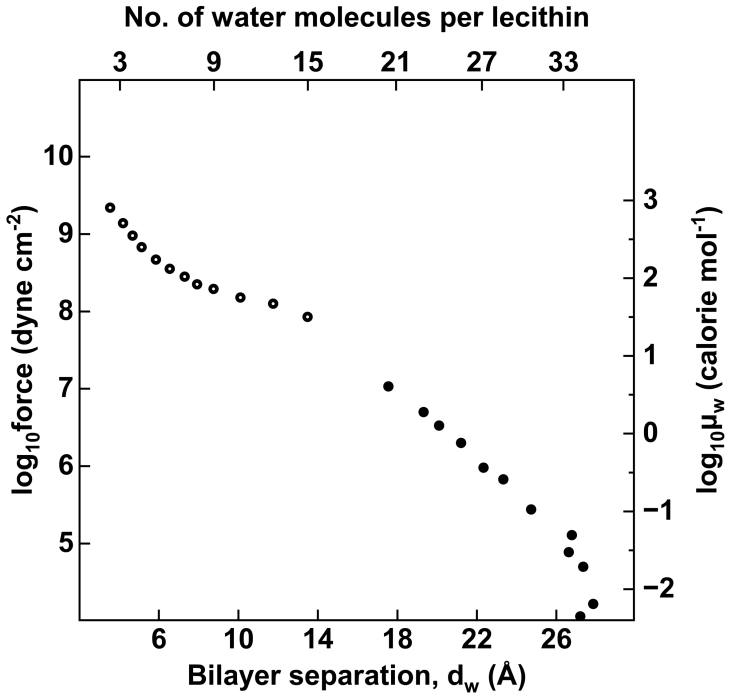

Fig. I.1. First measured perpendicular equation of state for zwitterionic bilayers in units of osmotic pressure and chemical potential of water as a function of the bilayer separation, i.e., the water layer thickness d_w, and the mole ratio of water and lipid. It was also the first proof of the repulsive hydration force between bilayers. Reproduced with permission from [13] (Copyright © 1976 Springer Nature Limited).

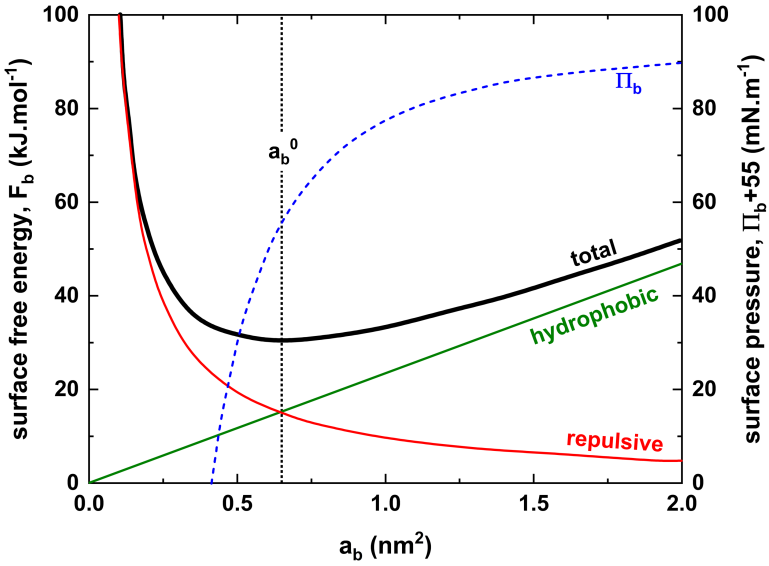

Fig. I.2. Generic lateral equation of state of lipids as established by Marsh [26]. The bilayer surface free energy F_b is given as a function of the area per lipid molecule a_b, indicating the contributions of the hydrophobic and repulsive interactions. The equilibrium area per molecule a_b^0 is obtained at the minimum of the free energy. The surface pressure Π_b in a single monolayer (dashed line) is also given and arbitrarily shifted upward by 55 mN·m^{-1}. The surface pressure $\Pi_b = 0$ at a_b^0. Adapted with permission from [26] (Copyright © 1996 Elsevier B.V.).

The first description of combined lateral and perpendicular equations of state was given by Dubois *et al.* [27] for the lipid-mimicking cationic surfactant didodecyldimethylammonium bromide (DDAB). The same principles can be applied to other surfactant classes, the only significant difference being the respective dominant molecular driving force.

I.1.2. Alkyl Carboxylates

Since fatty acids are the hydrophobic structural units of membrane lipids and have a simple molecular structure comprising only a hydrocarbon chain, in the simplest case an alkyl chain, and a small carboxylic acid headgroup, they attracted some attention as model compounds for lipid membranes even before those were understood in detail [28]. As the acidic form alone is usually insoluble in water, alkyl carboxylate salts, i.e., soaps, or mixtures of fatty acids and alkyl carboxylates, or mixtures of alkyl carboxylates and long-chain alcohol co-surfactants are studied. The smaller volume of the single-chain hydrophobic part compared to double-chain membrane lipids in combination with electrostatically repelling headgroups leads to a spontaneous packing parameter p_0 that is not strictly close to 1 but can be significantly smaller than 1. As a consequence, not only bilayer structures but also different micellar shapes are feasible, the most common phases being cubic, hexagonal, and lamellar phases. Mandell *et al.* [29] extensively studied ternary systems of alkyl carboxylates, fatty acids or long-chain alcohols, and water. Not only did they identify and describe various different (liquid crystalline) phases, but their work was one of the first instances of (ternary) phase diagrams, which were common in metallurgy, being used for surfactant systems. The most important, thoroughly studied system in the process of understanding the self-assembly of alkyl carboxylates is arguably the sodium octanoate – octanoic acid – water system, to which Ekwall and co-workers devoted a series of 14 publications on “Solutions of alkali soaps and water in fatty acids”, published between 1969 and 1989. Instead of citing the whole series, the 1993 overview published by Fontell and Mandell [30] is here referenced. The phase diagram of the ternary system, as represented by Fontell and Mandell, is shown in **Fig. I.3**. Early reviews of the rich phase behavior of alkyl carboxylates in general were given for example by Tiddy [31], Fontell [32], or Ekwall [33].

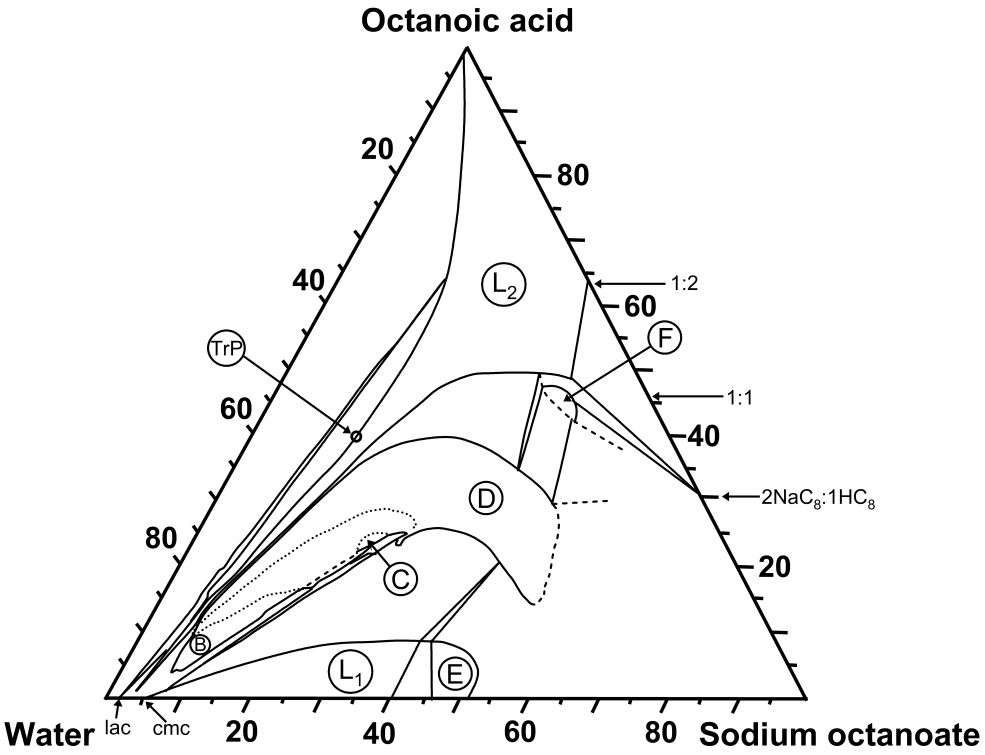

Fig. I.3. Ternary phase diagram of the sodium octanoate (NaC_8) – octanoic acid (HC_8) – water system, in the representation given by Fontell and Mandell [30]. L_1: Aqueous isotropic phase. L_2: Octanoic acid isotropic phase. B, C, and D: Lamellar phases. E: Hexagonal phase (H_1). F: Reverse hexagonal phase (H_2). Phase domains that are not marked with a letter are either biphasic or triphasic, the larger ones typically being biphasic and the very small ones being triphasic. Tie lines are omitted for improved readability. In the sodium octanoate-rich corner, crystals are formed, or crystals coexist with the other phases, see Ekwall and Mandell [34] for more details. Reproduced with permission from [30] (Copyright © 1969 Steinkopff-Verlag).

Naturally, all of the forces governing the self-assembly of lipids, described in **Section I.1.1.**, are also involved in the self-assembly of alkyl carboxylates., and only the main molecular mechanism is different. A recent, very extensive overview of the thermodynamics of micellization, focusing mainly on short-chain alkyl carboxylates, was given by Rosenholm [35]. Surface charge regulation, as initially proposed in 1971 by Ninham and Parsegian [36] for interacting surfaces bearing ionizable groups, turned out to be the dominant mechanism responsible for alterations in aggregation size and shape. Experimental evidence of surface charge regulation was possible by a quantitative deconvolution of charge and structure factor by small-angle neutron and X-ray scattering [37], allowing the determination of charge, hydration, and average aggregation number in a given sample without ambiguity. Results obtained from small-angle scattering can be supported by a complementary dynamic light scattering study, if not only the correlation time but also the Rayleigh ratio of the average static light scattering can be measured in the absence of any dust. One of the first examples was given in 1982 by Hayter and Zemb [38], who studied the structure of sodium octanoate micelles using small-angle neutron scattering. The results of the study were supported by a

complementary light scattering study conducted by Zemb *et al.* [39] one year later. At a time when the aggregation number was still thought to be independent of concentration, they found that globular sodium octanoate micelles grow in size with increasing concentration, while keeping a rather constant surface charge. This is only possible, if the additionally incorporated sodium octanoate molecules are neutral, i.e., associated. In 1984, Evans *et al.* [40] proposed the "dressed micelles" model for ionic micelles with the counterion association as a key parameter, which was later refined and confirmed by Hayter [41], who demonstrated good agreement of model predictions and various experimental results, see **Fig. I.4**. Probably the first study demonstrating charge regulation was given not for an alkyl carboxylate but for the binary system sodium octylphosphate – water at varying pH values by Chevalier *et al.* [42]. The fact alone, that micellar shapes are altered by addition of uncharged fatty acids or alcohols [29] or the addition of salt [43], shows that surface charge regulation is a decisive factor.

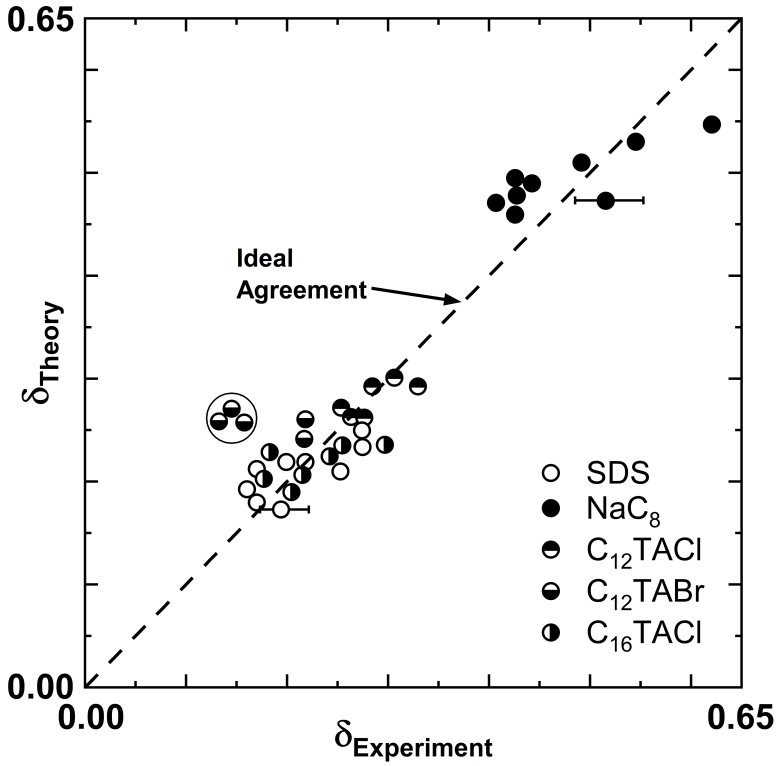

Fig. I.4. A plot of the theoretical (δ_{Theory}), according to the "dressed micelles" model, versus experimental ($\delta_{Experiment}$) degrees of ionization of micelles formed by various surfactants at different ionic strengths, demonstrating the good agreement between experiment and theory. Reproduced with permission from [41] (Copyright © 1992 American Chemical Society).

Another important observation was the isotropic but flow birefringent locally lamellar sponge phase. In 1988, Ekwall and Fontell [44] reported a multitude of small-angle X-ray scattering data, recorded throughout the isotropic L_2 phase of the sodium octanoate –

octanoic acid – water system (**Fig. I.3**). In the same year, Ekwall [45] documented for the first time the "anomalous" linear (one-dimensional) swelling in the L_2 phase along dilution lines towards the water corner, passing the critical point (TrP) of the biphasic domain, see **Fig. I.3**. Since the experimental work for these publications was conducted in the 1960s, this was probably the first documentation of the locally lamellar structure of the "anomalous" phase, which was later called sponge phase or L_3 phase. The locally lamellar structure was also identified by other authors in the same year [46,47]. A more detailed description of the microstructure was given for example by Roux *et al.* [48] a few years later. It should also be noted that such anomalous phases were reported independently by many different authors in various surfactant systems, without knowing the microstructure, including Fontell [49] in 1975 or Lang and Morgan [50] in 1980, who explicitly called the phase "anomalous".

I.1.3. Catanionic Surfactants and Catanionic Mixtures

A catanionic surfactant, as defined by Jokela *et al.* [51] in 1987, is an equimolar mixture of a cationic and an anionic surfactant without any other counterions, i.e., the cationic surfactant is the counterion of the anionic surfactant and *vice versa*. In their second study on the matter, Jokela *et al.* [52] investigated the sodium octanoate – octylammonium octanoate – water system, which is an example of a catanionic mixture since there is no longer equimolarity of anionic and cationic surfactant and sodium ions are present. Notably, Fontell, who had worked a lot on alkyl carboxylates (**Section I.1.2.**), is one of the authors of the second study. The authors found striking similarities between the self-assembly of catanionic surfactants, where both surfactants possess a single hydrocarbon chain of similar length, and zwitterionic lipids, both forming uncharged bilayers, i.e., $p_0 \approx 1$, the spacing of which is dominated by the hydration force. However, when deviating only slightly from equimolarity, the bilayers become charged and the spacing changes dramatically due to inter-bilayer electrostatic repulsion. A similar effect is observed when adding charged species to uncharged lipid bilayers, as pointed out for example by Gulik-Krzywicki *et al.* [53].

Kaler *et al.* [54] studied catanionic mixtures of various different cationic and anionic surfactants in water including their respective counterions, confirming that lamellar phases or stable vesicles are the predominant structure, though other shapes are possible far from

equimolarity. In 1994, Khan *et al.* [55] have shown by comparing the available phase diagrams at the time that this is true if both cationic and anionic surfactant have only one hydrocarbon chain each. Since anionic and cationic headgroups form ion pairs, even in presence of other inorganic counterions, each ion pair essentially behaves like a double-chain surfactant, resembling zwitterionic lipids with a spontaneous packing parameter $p_0 \approx 1$. If, however, at least one of the two ionic surfactants has two hydrocarbon chains, the ion pairs effectively have at least three hydrocarbon chains, which leads to $p_0 > 1$ and the formation of reverse structures. Many different authors published a multitude of studies on different catanionic surfactants or catanionic mixtures, confirming the same principal physicochemical properties. A review of all the available studies and the physicochemical properties was given by Khan and Marques [56] in 1997, yet many studies followed thereafter.

After the presentation of evidence for the formation of thermodynamically stable unilamellar "equilibrium" vesicles in a catanionic mixture by Kaler *et al.* [57] in 1989, various studies thereafter supported this idea. Whether these vesicles are actually thermodynamically stable or just metastable, as most other vesicles prepared from lamellar phases, was an ongoing debate throughout the following decade, see for example Laughlin [58] in 1997. It is now understood that thermodynamically stable vesicles do not exist for nonionic surfactants, but indeed do exist for ionic surfactants. Since electroneutrality must be maintained, the counterion concentration on the inside of the vesicle is significantly increased compared to the outside solution, leading to the average inside concentration exceeding 0.1 M. As a result, the electrostatic repulsions between the headgroups are screened and the equilibrium area per molecule slightly decreases, which leads to a spontaneous curvature towards the inside [20].

Especially in the dilute regime, catanionic surfactants and catanionic mixtures close to equimolarity usually exhibit a strong tendency to precipitate. In catanionic mixtures, the surface charge varies with the mixing ratio of the two surfactants, which not only influences micellar structures in the liquid state, but also crystalline structures. Dubois *et al.* [59,60] identified hollow icosahedra and nanodiscs, for which Meister *et al.* [61] later measured the perpendicular equation of state. A phase prism of the tetradecanoic acid ($C_{13}COOH$) – cetyltrimethylammonium hydroxide (CTAOH) – water system studied by Dubois *et al.* was constructed by Zemb and Dubois [62], and is shown in **Fig. I.5**. Since the hydroxide

counterion of CTAOH and the proton of $C_{13}COOH$ together form a water molecule, the system can be considered a true catanionic surfactant system. Above the chain melting temperature, lamellar phases and stable unilamellar vesicles are formed, as expected for such a catanionic surfactant system. When the vesicle phase is cooled below the chain melting temperature, icosahedra and discs are formed and coexist with crystalline lamellar phases.

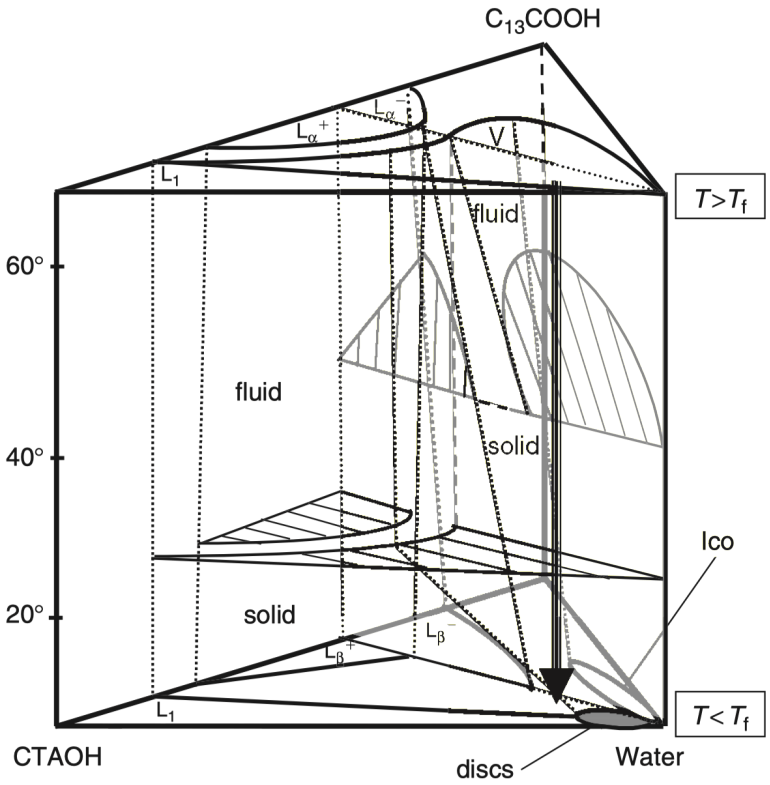

Fig. I.5. Phase prism for the ternary system tetradecanoic acid ($C_{13}COOH$) – cetyltrimethylammonium hydroxide (CTAOH) – water, as given by Zemb and Dubois [62]. The top triangle represents the molten state at temperatures above the chain melting temperature, where around equimolarity of the two surfactants lamellar phases or thermodynamically stable vesicles are formed. The bottom triangle shows the formed crystalline phases, when the mixtures are cooled below the chain melting temperature (cooling is indicated by the arrow). Icosahedra (Ico) or discs coexist with crystalline lamellar phases. L_1: Isotropic micellar phase. L_α^+ and L_α^-: Liquid lamellar phases with excess cationic surfactant or anionic surfactant, respectively. V: Unilamellar vesicles. L_β^+ and L_β^-: Crystalline lamellar phases with excess cationic or anionic surfactant, respectively. Taken with permission from [62] (Copyright © CSIRO Publishing).

As mentioned above, the perpendicular equation of state for (uncharged) bilayer structures of catanionic surfactants is essentially identical to that of uncharged zwitterionic lipid bilayers and dominated by the hydration force, whereas that of non-equimolar catanionic mixtures also includes electrostatic repulsion. An early theoretical model of the latter was given by Jokela *et al.* [63]. A detailed perpendicular equation of state was given by Ricoul *et al.* [64] for a lamellar cationic surfactant – nonionic glycolipid – water system, where surface charge regulation is achieved by varying the fraction of the nonionic glycolipid.

Though this system is not a catanionic mixture, it is thus analogous to non-equimolar catanionic mixtures. However, in catanionic mixtures, where both surfactants initially have another (halide or metal) counterion, the release of these ions into the solution upon mixing of the surfactants leads to a state of significant electrostatic screening due to relatively high salt concentrations.

It is also important to note that the role of the counterions is not independent of the counterion species, i.e., ion effects are specific. The degree of association of the headgroup and the ion and the adsorption of the ion in general depends both on the ion and the chemical structure of the headgroup, which in turn has an influence of the effective surface charge of micelles and influences intermicellar forces. Vlachy *et al.* [65] proposed an ordering of anionic headgroup types and cations based on their tendency to form ion pairs, see **Fig. I.6**, building on the well-known Hofmeister-Collins law of matching water affinities. These effects apply to all ionic surfactant systems, and due to adsorption effects also to uncharged systems in presence of salt, e.g., zwitterionic lipids.

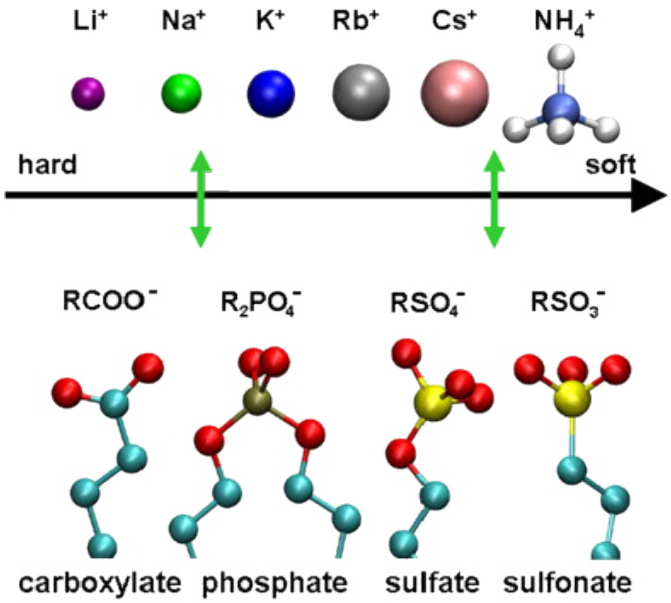

Fig. I.6. Tendency of some anionic surfactant headgroups and their respective counterions to form close ion pairs. The ions and ionic headgroups are ordered based on their polarizability, i.e., their "softness" or "hardness". The figure was taken with permission from [65] (Copyright © 2008 Elsevier B.V.).

I.1.4. Dialkyl Sulfosuccinates, Alkyl Sulfates, and Alkyl Ether Sulfates

All principles described in the previous sections for charged surfactants of course apply to any ionic surfactant. Other examples are alkyl sulfates with the model compound sodium dodecyl sulfate (SDS), alkyl ether sulfates with the model compound sodium lauryl ether sulfate (SLES), and dialkyl sulfosuccinates with the model compound sodium bis(2-ethylhexyl) sulfosuccinate (AOT).

The aqueous phase diagram of AOT with and without sodium chloride was first determined by Fontell [49] and later by Ghosh and Miller [66]. Since the molecular structure of AOT with two lightly branched alkyl chains somewhat resembles that of a short chain anionic lipid, $p_0 \approx 1$ and it is not surprising that lamellar structures are favored. The perpendicular equation of state of AOT in lamellar phases was measured by Antelmi and Kékicheff [67], confirming stabilizing undulation forces, as already mentioned in **Section I.1.1.** for ionic lipids.

Alkyl sulfates, especially SDS, received a lot of attention from fundamental research. One of the most detailed phase diagrams available for any binary mixture of surfactant and water is that constructed for SDS – water (D_2O) by Kékicheff and co-workers [68,69], see **Fig. I.7**. Kékicheff and Cabane [70], a few years later revisited by Kékicheff [71], identified various intermediate structures between the classical hexagonal phase made of "infinite" cylinders and the classical lamellar phase made of extended bilayers, see **Fig. I.7**. These intermediate phases usually extend only over small concentration ranges compared to the classical liquid crystalline phases. They are a consequence of a change in the spontaneous packing parameter p_0 through a change in electrostatic screening or counterion dissociation and hydration. Cylinders first transform into ribbons, i.e., "flattened" cylinders with an ellipsoidal cross-section or a flat inner part and hemispherical edges, which then connect to each other to form a three-dimensional array of rods with various unit cells, until they merge into "infinite" bilayers and form the classical lamellar phase.

Cylindrical micelles can also be flexible, i.e., "worm-like", and branched to form isotropic viscous networks of giant entangled "thread-like" micelles. The first direct experimental evidence of connected thread-like micelles was given by Danino *et al.* [72].These networks are responsible for the viscosity peaks often found in aqueous mixtures of ionic surfactants

as a function of salt concentration. While cylinders require a p_0 around 0.5, the junctions require $p_0 \approx 0.8$ (intermediate between cylinders and bilayers), which can be adjusted by adjusting inter-headgroup interactions. When salt is added to a micellar solution, electrostatics are screened and the repulsion between charged headgroups decreases depending on the salt concentration. Consequently, p_0 also changes with the salt concentration and the formation of a network of entangled worm-like cylinders can be induced. A detailed description and explanation, also including specific ion effects, was recently given by Pleines *et al.* [73].

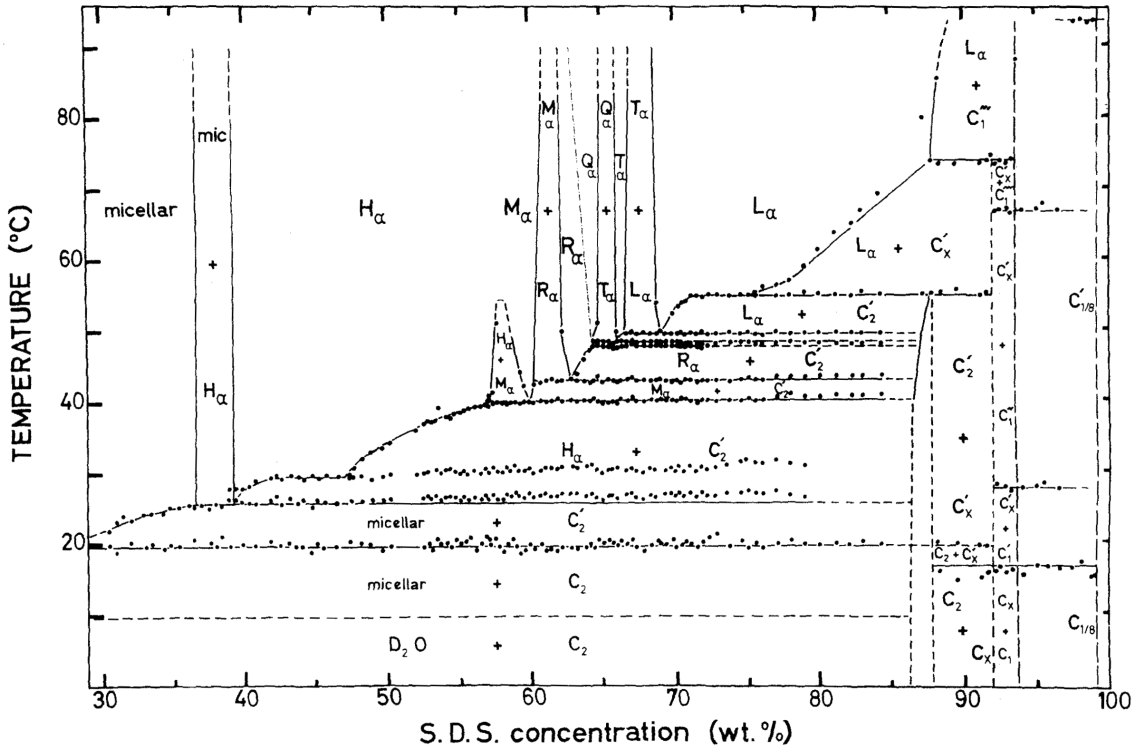

Fig. I.7. Binary phase diagram of the SDS – D_2O system, as constructed by Kékicheff *et al.* [68]. Terminology used by the authors: H_α: Hexagonal phase. M_α: Two-dimensional monoclinic phase. R_α: Rhombohedral phase. Q_α: Cubic phase. T_α: Tetragonal phase. L_α: Lamellar phase. C_x: Crystalline SDS hydrate with x water molecules per SDS molecule. The transition from the hexagonal phase made of long cylinders (H_α) to the lamellar phase made of extended bilayers (L_α) is found to progress via the formation of (connected) ribbons, which are organized in various three-dimensional arrays with different unit cells (M_α, R_α, Q_α, and T_α). Taken with permission from [68] (Copyright © 1989 Elsevier Inc.).

Based on the concept of pseudo-phases, in which the micelle and the monomeric solution are treated as two pseudo-phases, each with a defined surfactant chemical potential, introduced by Tanford already in 1973 [4,5], Missel *et al.* [74,75] developed a so-called "ladder" model for a thermodynamic description of the growth of spherical SDS micelles into worm-like micelles in presence of a 1:1 electrolyte, see **Fig. I.8**.

The cylindrical parts coexist with their hemispherical endcaps, and since the packing

condition is different in those two regions, surfactant molecules can be assigned a different chemical potential in these two “pseudo-phases”. The free energy of the system then depends on the distribution of the surfactant molecules in the two regions, i.e., on the length of the cylinders and the aggregation number. Since the chemical potential difference between the two pseudo-phases is fixed, the free energies of the aggregates as a function of the aggregation number resemble a “ladder”. The expressions for the mean aggregation number and the size distribution of cylindrical micelles obtained from the ladder model are in good agreement with experimental results. Kralchevsky and co-workers worked a lot with alkyl ether sulfates, especially lauryl ether sulfates, which have the advantage of a lower tendency to crystallize compared to SDS due to the additional ethylene oxide units. They extended the ladder model to 2:1 [76] and 3:1 [77] electrolytes, to mixed surfactant systems [78], as well as to disc-like micelles [79,80]. Recently, Danov *et al.* [81–84] published a four papers long series to propose a general molecular-thermodynamic theory for the growth of cylindrical micelles made of ionic surfactants or surfactant mixtures containing ionic surfactants, identifying the “micelle scission” energy, i.e., the excess free energy of the hemispherical endcaps, as the decisive factor for the micellar size.

The existence of a “second critical micelle concentration”, where macroscopic properties of micellar solutions such as viscosity, conductivity, or solubilization change abruptly was already shown in the 1940s and 50s. It is known for a long time that these changes are linked to the transition from globular to worm-like micelles, but it is the ladder model and its extensions that can explain why the transition from globular micelles above the critical micelle concentration to worm-like micelles at a “second critical micelle concentration” is usually relatively sharp. The excess free energy of the endcaps is responsible for very short spherocylinders being energetically unfavorable. Thus, the “initial growth”, i.e., the formation of smaller spherocylinders, is skipped and predominantly longer worm-like micelles are formed. A more detailed description is given by Leermakers *et al.* [85].

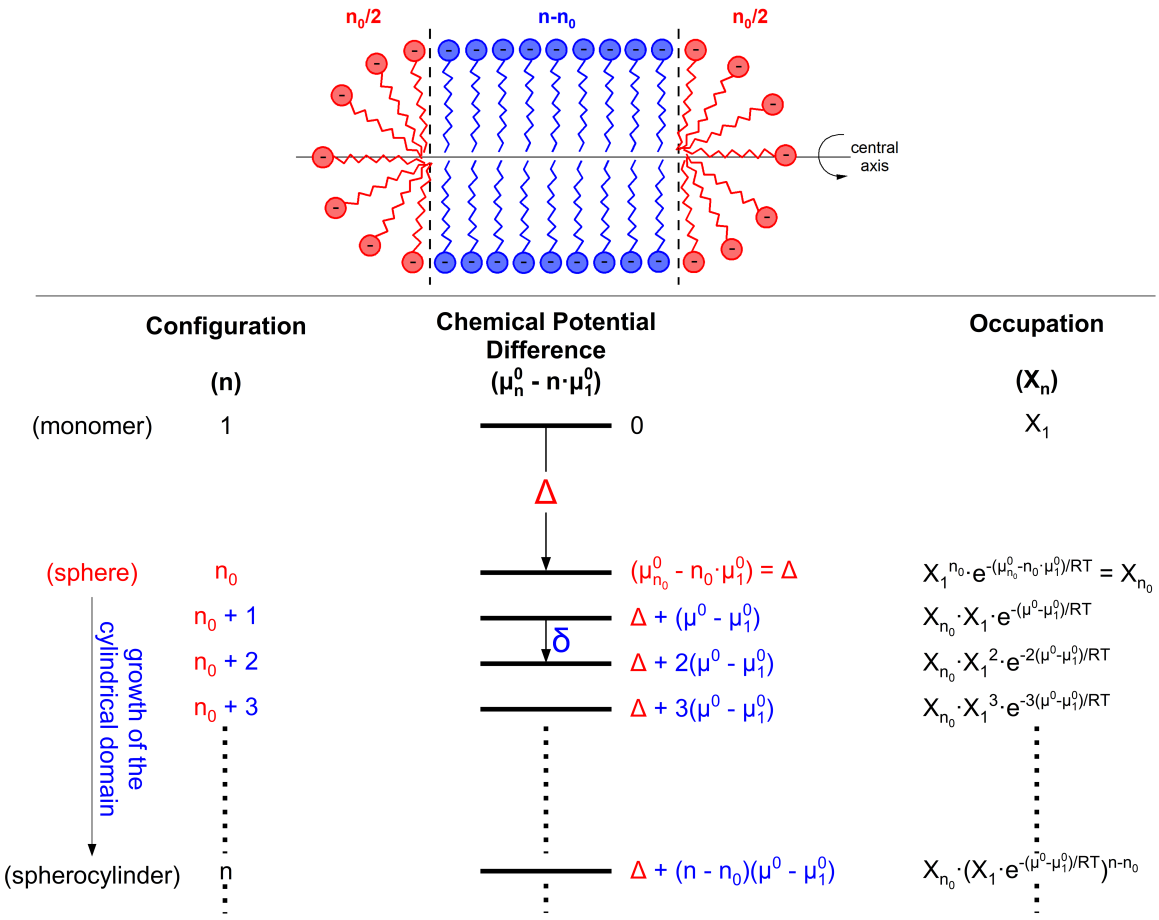

Fig. I.8. The "ladder" model for the chemical potential differences between the three pseudo-phases in a solution of spherocylindrical micelles: 1) The bulk solution, in which the surfactant molecule is dissolved as a monomer. 2) Hemispherical end caps containing $n_0/2$ surfactant molecules each. n_0 is the aggregation number of the minimum sized spherical micelle formed close to the critical micelle concentration. 3) The cylindrical domain of the spherocylinder, containing $n-n_0$ surfactant molecules. μ_1^0 is the chemical potential of a surfactant molecule in the solvent, $\mu_{n_0}^0$ is the chemical potential of n_0 surfactants forming a minimum spherical micelle, and μ^0 is the chemical potential of a surfactant molecule in the cylindrical region of the micelle. The gap spacing Δ is the gain in free energy by forming a minimum spherical micelle out of n_0 surfactant molecules in solution. The ladder spacing δ is the gain in free energy by transferring a surfactant monomer from the bulk solution to the cylindrical region of the micelle. Since δ is constant for each of the $n-n_0$ surfactant molecules added to the cylindric part of the micelle, the chemical potentials form an "infinite ladder" as a function of the aggregation number n. The size distribution of the micelles is given as a Boltzmann distribution over all chemical potential levels, where X_n is the likelihood of a given aggregation number, X_1 being the mole fraction of surfactant monomers in the solution. A schematic drawing of a spherocylindrical micelle is shown at the top, where the hemispherical end caps are colored in red, while the cylindrical part is colored in blue. The figure was adapted with permission from [74] (Copyright © 1980 American Chemical Society).

I.1.5. Nonionic Surfactants – Polyoxyethylene Alkyl Ethers

An early systematic study of the phase behavior of monoglycerides was given by Lutton [86] in 1965, who compared the phase behavior to that of alkyl carboxylates and found similar liquid crystalline phases. However, among the multitude of nonionic surfactant

molecules, polyoxyethylene alkyl ethers, C_iE_j, are the most important and best studied. The equilibrium area per molecule and the spontaneous packing parameter p_0 of course depend both on the alkyl chain length [9] and the number of ethylene oxide groups. Thus, the phase behavior can be varied strongly by adjusting those two molecular features. An extensive study of C_iE_j surfactants with a systematic variation of i and j was given by Mitchell *et al.* [87], also considering previously published data, including those presented for C_8E_4, C_8E_5 by Chakhovskoy [88] as early as 1956. Liquid crystalline phases in these nonionic surfactant systems, i.e., micellar shapes, are found to be much more sensitive to temperature variations compared to those found in systems of ionic surfactants, as is easily seen when comparing the phase diagram of $C_{12}E_5$ [87], see **Fig. I.9**, to the phase diagram of SDS [68], see **Fig. I.7**. In the liquid state, the latter usually exhibits no phase transitions when varying temperature, whereas the former shows various phase transitions when increasing temperature at a constant surfactant concentration. A feature that is usually not observed for ionic surfactants, but is common to all nonionic ethoxylated surfactants, is the "cloud point" at higher temperatures, where a surfactant-rich (micellar) phase separates from a dilute aqueous phase. At temperatures slightly below the cloud point, a single micellar phase is found. This means that intermicellar interactions switch from repulsive to attractive at the cloud point. As shown experimentally in various studies, e.g., Zulauf *et al.* [89], micelles typically also undergo shape transitions as the temperature approaches the clouding temperature. The strong temperature dependence of the micellar shape of C_iE_j surfactants, both in liquid crystalline phases and in micellar phases, was attributed to the hydration of the ethylene oxide headgroups at least since 1978, when Staples and Tiddy [90] proposed that the dominant repulsive force between these micelles is the hydration force, linked to the water molecules bound to the ethylene oxide groups and to the conformational free energy of the headgroups, which is adversely affected by steric hindrance as micelles come closer to each other [87]. This was inspired by the experimental proof of the hydration force between lipid bilayers in the late 1970s [13]. The less water molecules are bound to the ethylene oxide headgroup, the lower is not only the intermicellar repulsive hydration force, but also the volume of the hydrated headgroup. Dehydration of the headgroups is achieved either by increasing the temperature or by increasing the surfactant concentration, leading to a decreasing area per molecule and an increasing p_0, as discussed in ref. [87].

Worm-like micelles, as discussed in the previous section, also exist in solutions of nonionic surfactants. Since nonionic surfactants bear no charge, electrostatic interactions, charge

regulation, and other counterion effects are not responsible for micellar growth. Instead, the ladder model of the chemical potential, initiated by Missel *et al.* [74], was extended to nonionic surfactants accounting for the temperature effects (hydration) by Kato *et al.* [91]. Thomas *et al.* [92] extended the model to mixed nonionic micelles and a general molecular-thermodynamic theory was proposed by Danov *et al.* [93] in 2018.

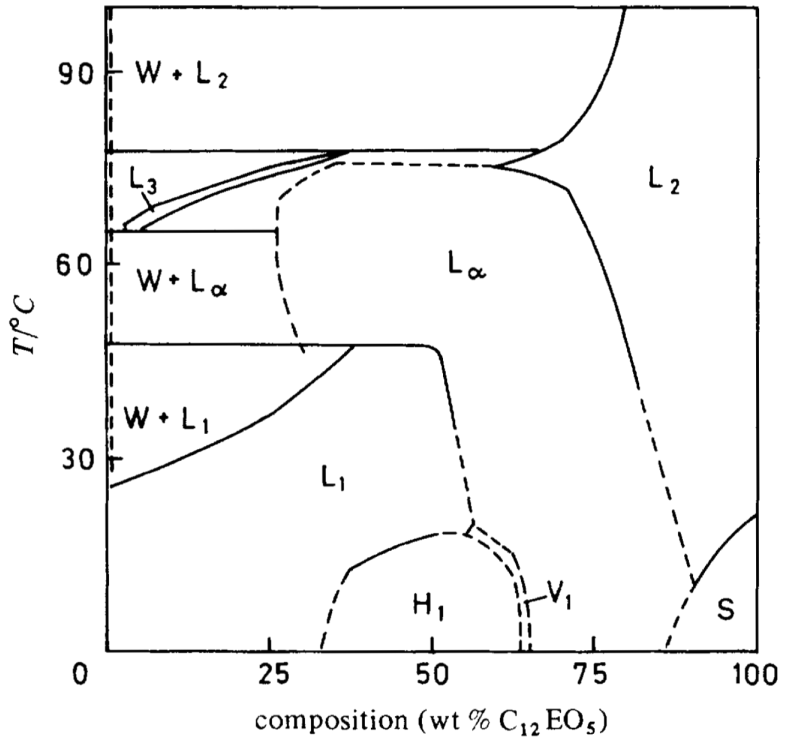

Fig. I.9. Phase diagram of the $C_{12}E_5$ – water system, as reported by Mitchell *et al.* [87]. L_1: Isotropic aqueous micellar phase. L_2: Isotropic surfactant-rich phase. L_3: Isotropic phase, later identified as the locally lamellar sponge phase [48]. H_1: Hexagonal phase. V_1: Bicontinuous cubic phase. L_α: Lamellar phase. S: (Semi-)crystalline phase of neat or hydrated surfactant. Taken with permission from [87] (Copyright © 1983 Royal Society of Chemistry).

I.1.6. Extended Surfactants

Extended surfactants were developed by Salager and co-workers in the process of trying to improve the solubilization of oils in aqueous surfactant solutions. Graciaa *et al.* [94,95] have shown that adding a very hydrophobic amphiphilic compound, which they called "lipophilic linker", to a microemulsion containing classical nonionic surfactants can greatly improve the oil solubilization. By inserting a polyoxypropylene chain as the linker directly into the surfactant molecule, in this case in between the alkyl chain and the headgroup of a SLES molecule, an extended surfactant was obtained and tested by Miñana-Perez *et al.*

[96]. Excellent performance in oil solubilization was confirmed, allowing even the solubilization of triglycerides. A review of the "lipophilic linker effect" was given by Salager *et al.* [97] in 2005. Note that the ethylene oxide groups in the headgroup may be referred to as "hydrophilic linker", the number of which can be adjusted to influence phase behavior.

However, the vast majority of published studies concerning extended surfactants dealt with mixtures of oil and water, not with their aqueous phase behavior. The only binary phase diagram available for an extended surfactant containing both a lipophilic and a hydrophilic linker so far was constructed by Klaus *et al.* [98,99] for an alkyl polyoxypropylene ether sulfate (C_{12-14}–PO_{16}–EO_2–SO_4Na), identifying a lamellar phase, a bicontinuous cubic phase, and inverse phases. The polyoxypropylene chain is rather hydrophobic, though not as hydrophobic as the alkyl chain, and serves as an extension of the hydrophobic tail. The length of the alkyl chain cannot be increased indefinitely as crystallization will be favored. Polyoxypropylene groups on the other hand are much more flexible and do not crystallize as easily, allowing the hydrophobic part of the surfactant to be much larger. Klaus *et al.* have also demonstrated that the polyoxypropylene chain is not extended, making the hydrophobic part bulkier, which in turn increases the equilibrium area per molecule and the spontaneous packing parameter to $p_0 \geq 1$ in most cases. Though, the conformational free energy contribution of the polyoxypropylene chains is expected to be the main additional contribution compared to other ionic or nonionic surfactants, an extension of a molecular-thermodynamic model to extended surfactants is still missing.

I.1.7. Intramicellar Molecular Segregation

In liquid mixed surfactant systems, containing at least two different surfactant species, all surfactant species are usually statistically distributed throughout the micelles. Even though the segregation of surfactant molecules into locations enriched in either one of the species, be it intermicellar or intramicellar, comes with a significant entropic penalty, molecular segregation was evidenced in some cases. Since full random mixing is accompanied by a significant gain in entropy, i.e., the free energy of mixing, molecular segregation is rather rare. Considering packing constraints, one can expect intramicellar segregation in mixtures of surfactants with significantly different spontaneous packing parameters, where one surfactant favors high curvature and the other surfactant favors low curvature, as long as the

gain in free energy by adopting the preferred packing exceeds the loss in free energy due to the entropic penalty of molecular segregation.

Molecular segregation was first evidenced in lipid vesicles, e.g., by Papahadjopoulos *et al.* [100], which can be rationalized by the two different packing conditions on the inside (negative curvature) and outside (positive curvature) layers of the vesicle. Apart from the case of ionic surfactants, where counterion release leads to different electrostatic screening conditions in the vesicle interior and in the bulk, see **Section I.1.3.**, a single surfactant molecule cannot adopt two different packings at the same time, as one of them would be energetically unfavorable. In mixed surfactant systems, the coexistence of these two different packing conditions can be achieved by molecular segregation, where the outer surfactant layer and the inner surfactant layer have different molecular compositions. Such an intra-aggregate segregation also occurs in thermodynamically stable vesicles in catanionic surfactant mixtures, where negative curvature is achieved by alternating anionic and cationic surfactants in the inside layer, and positive curvature is realized by an excess of one of the two species [56]. Intramicellar molecular segregation in a catanionic surfactant system, producing various different shapes, including discs and icosahedra, as a function of the mixing ratio, was also shown by Dubois *et al.* [101].

Another prominent example of intramicellar segregation is that found when mixing two lipids with vastly different spontaneous packing parameters to obtain “bicelles”. Classical “bicelles” are disc-like micelles with molecular segregation into a flat bilayer part and a curved rim, but a multitude of other morphologies were found in such systems. For further information, including synthetic surfactant systems mimicking classical bicelles, the reader is referred to the introduction of **Chapter IV.** (**Section IV.2.**). Notably, the chains are semi-crystalline in the majority of these systems. However, there are also several studies suggesting intramicellar segregation with liquid chains. Early examples are the studies reported by Hendrikx and co-workers [102,103] and Pope and Doane [104] in the case of discs or ribbons, which are surprisingly rarely cited in the literature.

According to theory and practical observation, without molecular segregation of two species disc-like micelles are limited to low aggregation numbers and a small concentration range, i.e., larger discs are energetically unfavorable [79]. The fact that intramicellar molecular segregation can overcome these limitations and enables the coexistence of domains with different packing conditions, in turn giving rise to otherwise instable micellar shapes,

demonstrates the importance of intramicellar segregation.

I.1.8. Overview

An overview of all the mentioned surfactant classes in the previous sections, for which the general phase behavior is well established in the literature, is presented in **Table I.1**. The main molecular driving force governing the self-assembled structures as well as important experimental observations that significantly contributed to the understanding of both the self-assembly of the respective surfactant class and the self-assembly of surfactants in general are stated. Some seminal works, which either presented important new findings or theories or culminated and extended existing knowledge into a generalized theory, are also given.

Table I.1. Overview of surfactant classes, which were studied in detail by many scientists to reveal the molecular driving forces involved in their self-assembly, thus contributing significantly to the general understanding of surfactant self-assembly. Footnotes represent short descriptions of the given seminal papers.

surfactant class	main molecular driving force	important observed shape transitions	key experimental observation	seminal papers
zwitterionic and nonionic lipids	hydration force	restricted to bilayers (lamellae or vesicles)	osmotic equilibrium between multilamellar vesicles and the solvent	LeNeveu *et al.* [13] [a], Marčelja and Wolfe [25] [b], Marsh [26] [c]
ionic lipids	electrostatics and electrostatically coupled undulations	restricted to bilayers – correlated undulations in the oyster shell phase	oyster shell phase	Cowley *et al.* [15] [d], Demé *et al.* [19,20] [e]
alkyl carboxylates	electrostatic charge regulation	shape transitions (globular-cylindrical-lamellar) induced by surface charge variation	locally lamellar structure of the sponge phase	Mandell *et al.* [29] [f], Evans *et al.* [40] [g], Ekwall [45] [h]
catanionic surfactants/mixtures	hydration force/headgroup pairing and release of counterions	mainly bilayers; thermodynamically stable vesicles	osmotic equilibrium between catanionic microcrystallites	Jokela *et al.* [51] [i], Meister *et al.* [61] [j], Kaler *et al.* [57] [k]
alkyl sulfates	electrostatic charge regulation and headgroup packing	ribbon phases and other intermediate phases	continuous transition from cylinders to bilayers via intermediate phases	Kékicheff and Cabane [70] [l], Kékicheff *et al.* [68,69] [m]
alkyl ether sulfates	electrostatic charge regulation and headgroup packing – "ladder" model of the chemical potential	sphere-to-rod transition – micellar growth and branching of worm-like micelles	"second critical micelle concentration" and viscosity maximum as a function of salinity	Danov *et al.* [84] [n], Pleines *et al.* [73] [o]
polyoxyethylene alkyl ethers	headgroup hydration	shape transitions induced due to headgroup dehydration	cloud point and temperature sensitivity of liquid crystalline phases	Mitchell *et al.* [87] [p], Danov *et al.* [93] [q]

[a] First accurate measurement of the hydration force and the perpendicular equation of state.
[b] First established lateral equation of state.
[c] Detailed description of the lateral equation of state.
[d] Measurement of the perpendicular equation of state: Hydration force dominates for small spacings, while electrostatic repulsion dominates for larger spacings.
[e] Identification and description of the oyster shell phase with electrostatically coupled undulations.
[f] Construction of multiple phase diagrams of alkyl carboxylate – fatty acid/long-chain alcohol – water systems and identification of various mesophases.
[g] Formulation of the "dressed micelle" model including counterion binding, i.e., charge regulation, as a parameter.
[h] First documentation of the linear swelling of the sponge phase.
[i] Pioneering work on catanionic surfactants.
[j] Measurement of the perpendicular equation of state for catanionic surfactants/mixtures.
[k] First identification of thermodynamically stable vesicles in a catanionic mixture.
[l] Identification of various intermediate phases between a hexagonal phase made of cylinders and a lamellar phase made of bilayers.
[m] Determination of a detailed binary phase diagram of SDS and water, identifying not only large known phase domains, but also intermediate phases.
[n] Construction of a general molecular-thermodynamic model describing micellar growth of ionic micelles into worm-like micelles, building upon the "ladder" model of the chemical potential initiated by Missel et al. [74] and its various extensions, mainly given by Kralchevsky and co-workers (see text).
[o] Modelling of the viscosity maximum as a function of salt concentration observed in ionic surfactant systems due to worm-like micelle formation, including specific ion effects and branching of worm-like micelles.
[p] Systematic study of polyoxyethylene alkyl ether surfactants, giving a qualitative explanation of the phase behavior with headgroup hydration effects on the packing parameter and other forces involved.
[q] General molecular-thermodynamic model describing the growth of nonionic micelles into worm-like micelles, building upon the "ladder" model of the chemical potential and its extensions, including all known important contributions to the free energy.

I.2. Concept of Melting Point Lowering due to Ethoxylation

The COncept of Melting Point Lowering due to EThoxylation (COMPLET) was established by Kunz and co-workers as an alternative method to obtain room temperature ionic liquids [105–107]. To obtain ionic liquids, i.e., "liquid salts", the melting point must be lowered by increasing the Gibbs free energy of the solid state and/or lowering the Gibbs free energy of the liquid state. In classical ionic liquids, this is achieved by increasing the free energy of the solid state through molecular asymmetry. Typically, bulky cations such as imidazolium, pyrrolidinium, or phosphonium derivatives hinder crystallization [108]. The COMPLET is a different approach, schematically depicted in **Fig. I.10**: Instead of increasing the free energy of the solid state, mainly the free energy of the liquid state is decreased by introducing ethylene oxide groups. Ethylene oxide groups are not only readily hydrated, increasing water solubility, but also bring about a significant conformational entropy contribution even in absence of water. Ethylene oxide groups can be introduced into both anions and cations, making plenty of combinations of anions and cations possible, many of which are more easily accessible and less toxic than classical ionic liquids. It is important to note that finding an adequate number of ethylene oxide groups is a compromise between increasing the conformational entropy and decreasing the free energy of ethylene oxide crystallization, see melting temperature minimum in **Fig. I.10**. Simply increasing the number of ethylene oxide groups also facilitates a crystalline packing of the ethylene oxide chains, which is easily seen by the increasing melting temperatures of polyethylene glycols with increasing number of ethylene oxide groups per molecule [109].

Since the ions are often organic compounds, they can also be surfactants, if there is a large enough hydrophobic group [110–113]. Ionic liquids including a surfactant as cation or anion are often referred to as surface active ionic liquids (SAILs). Polyoxyethylene alkyl ether carboxylates, marketed for example under the tradename Akypo® by Kao Chemicals, are examples of such anionic surfactants. With a sufficient number of ethylene oxide groups, the entropy of the ethylene oxide chain results in low melting points, usually below room temperature, even with trivalent metal cations [110,111]. The surfactant primarily used in this thesis, octaoxyethylene octyl ether carboxylic acid (Akypo® LF2), is such an anion if transformed into a salt, and its ethoxylation explains why the surfactant and its metal salts

are liquid at room temperature. Though the salts of this surfactant may be considered as ionic liquids, the focus of this study is not focused on their properties as ionic liquids but on their properties as surfactants.

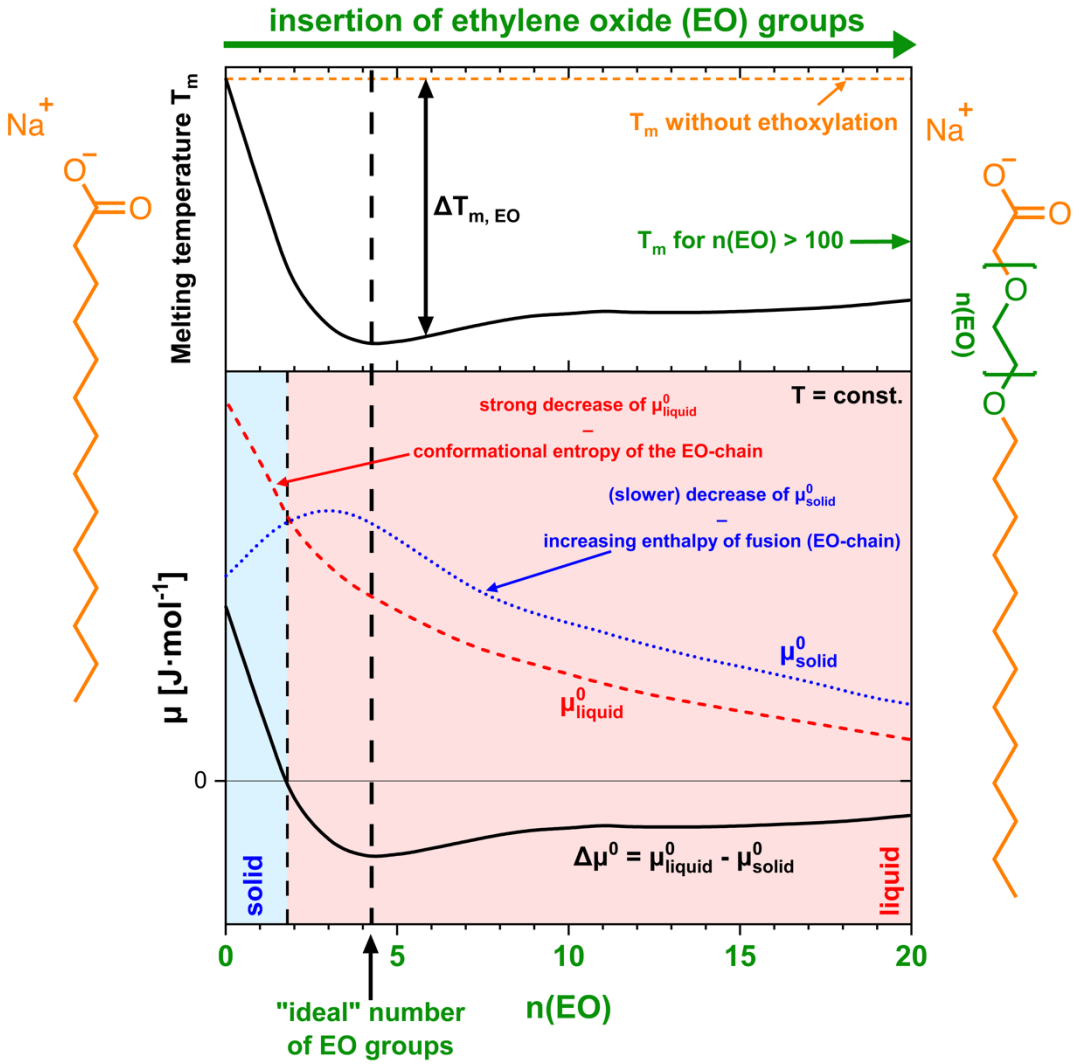

Fig. I.10. Schematic visualization of the COMPLET for an arbitrary surfactant (sodium tetradecanoate; left). Bottom: The chemical potential of the molecule in the liquid state μ^0_{liquid} (dashed red line), the chemical potential of the molecule in the solid state μ^0_{solid} (dotted blue line), and the chemical potential difference $\Delta\mu^0 = \mu^0_{liquid} - \mu^0_{solid}$ (solid black line) are sketched as a function of the number of ethylene oxide (EO) groups inserted into the headgroup, n(EO), at a constant temperature below the melting temperature of the surfactant at n(EO) = 0. As n(EO) is increased, μ^0_{liquid} initially exhibits a strong decrease as a consequence of the conformational entropy of the inserted EO-chains in the liquid state. At the same time, μ^0_{solid} slightly increases initially due to hindrance of molecular packing by the EO groups. When inserting even more EO groups, μ^0_{solid} decreases again because crystalline packing of the EO chains is the easier the higher n(EO) is, i.e., the enthalpy of fusion of the EO chains increases with increasing n(EO). $\Delta\mu^0$ therefore assumes a minimal value at an "ideal" number of EO groups, where the liquid state is favored the most. Consequently, the melting temperature of the (ethoxylated) surfactant, sketched in the top (solid black line) is also minimal for this "ideal" n(EO). Note that, due to a lack of available data on melting points at varying degrees of ethoxylation, the "ideal" n(EO) is arbitrarily chosen roughly based on the few data available to the author. The limiting melting temperature at n(EO) = 0 is given by the melting temperature of the non-ethoxylated surfactant, and the limiting melting temperature for large n(EO) is given by the rather constant melting temperature of polyethylene glycols above a certain number of EO groups (typically ≈63°C for n(EO) > 100). The melting point lowering due to ethoxylation, $\Delta T_{m,EO}$, at an arbitrary n(EO) is also indicated.

It should be noted that the principle of the COMPLET has been used for a long time, a prominent example being SLES as an ethoxylated version of SDS. The ethylene oxide groups of SLES lower the melting temperature of its crystalline state compared to SDS. Another beneficial effect of the ethoxylation is that the ethoxylated surfactants are less prone to precipitation in presence of multivalent cations compared to their non-ethoxylated counterparts. This is easily demonstrated when comparing Akypo® surfactants with classical soaps, the former being liquid at room temperature even with multivalent cations, whereas the latter precipitate in hard water.

These types of surfactants can also be used to overcome a typical problem of catanionic surfactants and mixtures, the high tendency to precipitate around equimolarity of the two ions, see **Section I.1.3**. Using ethoxylated anionic and/or cationic surfactants, liquid catanionic systems can be obtained that would otherwise be crystalline, extending the possibilities for applications [113]. A visual demonstration of this concept is given in **Fig. I.11**.

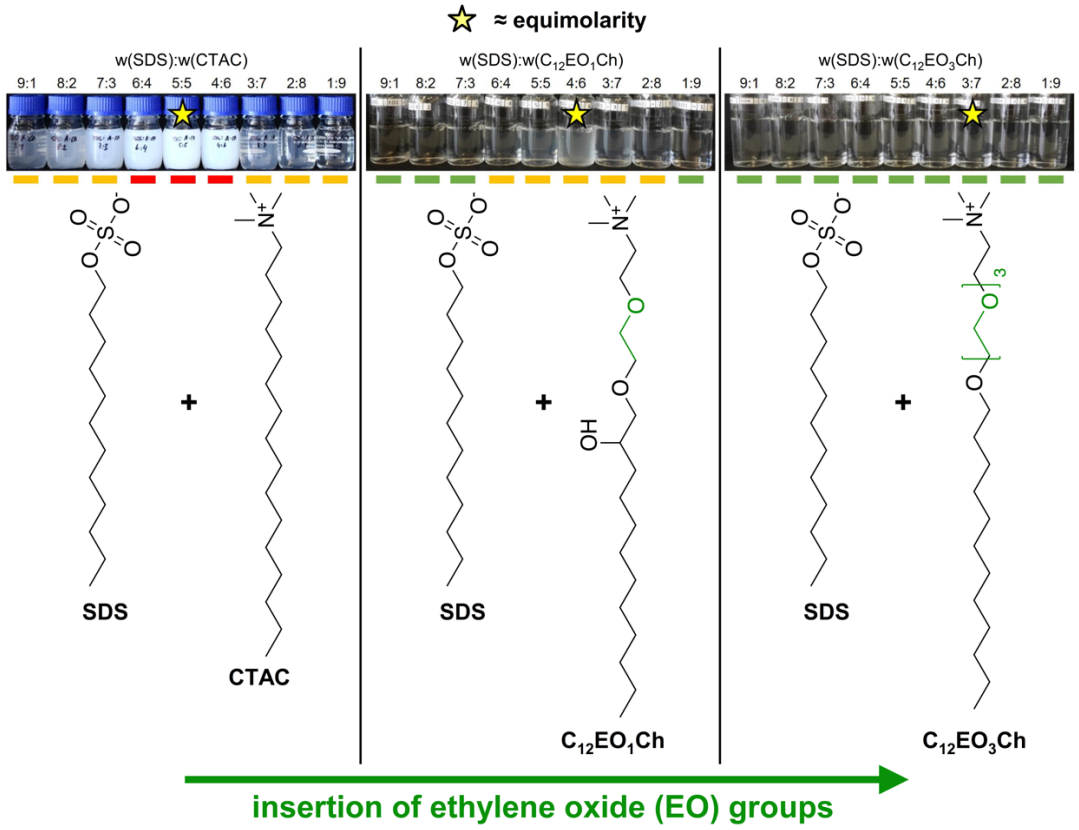

Fig. I.11. Optical appearance of catanionic mixtures with varying degrees of ethoxylation of the cationic surfactant at various mass ratios and a constant total surfactant concentration of 1 $g \cdot L^{-1}$, as reported in [113]. Left: Sodium dodecyl sulfate (SDS) and cetyltrimethylammonium chloride (CTAC). Note that the tendency to precipitate is even more pronounced with dodecyltrimethylammonium chloride (DTAC), not shown here. Middle: SDS and $C_{12}EO_1Ch$. Right: SDS and $C_{12}EO_3Ch$. The photographs and information were taken with permission from [113] (Copyright © 2022 Elsevier B.V.).

I.3. Contributions of This Thesis

The work presented in this thesis deals mainly with octaoxyethylene octyl ether carboxylic acid ($C_8E_8CH_2COOH$) and its mixture with dioxyethylene oleyl ether carboxylic acid ($C_{18:1}E_2CH_2COOH$). Both surfactants can be assigned to the surfactant class of alcohol ether carboxylates (AECs), reviewed several years ago by Chappisi [114], who pointed out that only few studies concerning the behavior of these surfactants are available. Thus, this work expands the knowledge on this neglected surfactant class. Since some neat metal salts of the surfactants are examined (**Chapter III.**), especially concerning their microstructures, this work also gives some insight into the self-assembly of such surfactant ionic liquids.

An important aspect regarding self-assembly science in general, is the fact that $C_8E_8CH_2COOH$ comprises a large headgroup and a significantly smaller hydrophobic tail. Apart from the terminal acetic acid group, the surfactant closely resembles a classical nonionic surfactant with the generic structure C_iE_j. This type of surfactant allows the free variation of the relative volumes of the hydrophobic and hydrophilic parts. As a result of the interest in liquid crystalline phases and shape transitions, usually surfactants with $i \approx 2 \cdot j$ were studied [115]. Remarkably, only in rare cases surfactants with $i \leq j$ were considered [87,116–118]. The interesting aspect is not merely that $i \leq j$, but the ability or inability to undergo micellar shape transitions and to form liquid crystalline phases. The larger i is, the larger j needs to be in order to prevent shape transitions and the formation of liquid crystalline phases. For example, C_8E_8 does not form any liquid crystalline phases [87], whereas $C_{16}E_{20}$ (Brij® 58) forms a multitude of liquid crystalline phases [118], despite $i < j$. As will be shown in this thesis by determination of phase diagrams and small-angle scattering, $C_8E_8CH_2COOH$ does not form any liquid crystalline phases and completely resists a sphere-to-rod transition, i.e., the packing parameter never exceeds 1/3 and the free energy required to change the micellar shape is too high (**Chapters II.** and **III.**). This is due to steric constraints imposed by the large headgroup, which can only be overcome by freezing or similar ordering of the headgroups. Above the freezing point of water, the latter is only possible if the headgroups are only weakly hydrated and is hindered in this case by the large conformational entropy of the headgroup's ethylene oxide chain combined with a low enough number of ethylene oxide groups to avoid favoring their crystallization. To the authors knowledge, so far, the only other surfactant shown to completely resist a sphere-to-rod transition by backing up the binary phase diagram with small-angle scattering data is

$C_{12}E_{23}$ (Brij® 35) [116,117]. Though any surfactant, which exhibits no liquid crystalline phases or only a discontinuous micellar cubic phase in its full binary aqueous phase diagram, is expected to resist a sphere-to-rod transition, only few such phase diagrams are published and usually the microstructures were not elucidated [87].

In addition to giving a detailed study of a surfactant resisting the classical sphere-to-rod transition (and consequently other shape transitions), this property is utilized when mixing $C_8E_8CH_2COOH$ with $C_{18:1}E_2CH_2COOH$ (**Chapter IV.**). In contrast to $C_8E_8CH_2COOH$, the latter favors bilayer formation, i.e., $p_0 \approx 1$. This significant mismatch of preferential curvature leads to intramicellar molecular segregation and the formation of rather large disc-like "bicelles", which is, as mentioned above, a rare form of self-assembly. Nematic alignment of these discs results in a new type of a strongly shear thinning, viscoelastic gel. Even though intramicellar molecular segregation had been identified several times, see **Section I.1.7.**, it is still a phenomenon in self-assembly that is rather rarely considered and still lacks full theoretical explanation. Thus, the extensive study given in this work may aid in completing this task by providing experimental data.

Having the potential of the nematic gels for application in mind, the effects of some additives commonly used in formulation in industry on the microstructures of the mixed surfactant system were also examined (**Chapter V.**). The mechanisms revealed in this study should in principle be applicable to other ethoxylated nonionic surfactants, thus extending the scientific background of the effects of these additives in general.

I.4. References

[1] F.W. Gibbs, The history of the manufacture of soap, Ann Sci 4 (1939) 169–190. https://doi.org/10.1080/00033793900201191.

[2] J.W. McBain, General discussion on colloids and their viscosity, Transactions of the Faraday Society 9 (1913) 99–101. https://doi.org/https://doi.org/10.1039/TF9130900093.

[3] R. Nagarajan, One Hundred Years of Micelles: Evolution of the Theory of Micellization, in: L.S. Romsted (Ed.), Surfactant Science and Technology: Retrospects and Prospects, 1st ed., CRC Press, Boca Raton, 2014: pp. 3–52. https://doi.org/https://doi.org/10.1201/b16802.

[4] C. Tanford, Hydrophobic Effect: Formation of Micelles and Biological Membranes, 1st ed., Wiley, New York, 1973.

[5] C. Tanford, The Hydrophobic Effect and the Organization of Living Matter, Science (1979) 200 (1978) 1012–1018. https://doi.org/10.1126/science.653353.

[6] J.N. Israelachvili, D.J. Mitchell, B.W. Ninham, Theory of self-assembly of hydrocarbon amphiphiles into micelles and bilayers, Journal of the Chemical Society, Faraday Transactions 2: Molecular and Chemical Physics 72 (1976) 1525–1568. https://doi.org/10.1039/F29767201525.

[7] J.N. Israelachvili, D.J. Mitchell, B.W. Ninham, Theory of self-assembly of lipid bilayers and vesicles, Biochimica et Biophysica Acta (BBA) - Biomembranes 470 (1977) 185–201. https://doi.org/10.1016/0005-2736(77)90099-2.

[8] C. Tanford, Micelle shape and size, Journal of Physical Chemistry 76 (1972) 3020–3024. https://doi.org/10.1021/j100665a018.

[9] R. Nagarajan, Molecular packing parameter and surfactant self-assembly: The neglected role of the surfactant tail, Langmuir 18 (2002) 31–38. https://doi.org/10.1021/la010831y.

[10] C. V. Kulkarni, Calculating the 'chain splay' of amphiphilic molecules: Towards quantifying the molecular shapes, Chem Phys Lipids 218 (2019) 16–21. https://doi.org/10.1016/j.chemphyslip.2018.11.004.

[11] P. Bauduin, T. Zemb, Perpendicular and lateral equations of state in layered systems of amphiphiles, Curr Opin Colloid Interface Sci 19 (2014) 9–16. https://doi.org/10.1016/j.cocis.2014.02.002.

[12] B.W. Ninham, V.A. Parsegian, van der Waals Interactions in Multilayer Systems, J Chem Phys 53 (1970) 3398–3402. https://doi.org/10.1063/1.1674507.

[13] D.M. LeNeveu, R.P. Rand, V.A. Parsegian, Measurement of forces between lecithin bilayers, Nature 259 (1976) 601–603. https://doi.org/10.1038/259601a0.

[14] S. Marčelja, N. Radić, Repulsion of interfaces due to boundary water, Chem Phys Lett 42 (1976) 129–130. https://doi.org/10.1016/0009-2614(76)80567-2.

[15] A.C. Cowley, N.L. Fuller, R.P. Rand, V.A. Parsegian, Measurement of repulsive forces between charged phospholipid bilayers, Biochemistry 17 (1978) 3163–3168. https://doi.org/10.1021/bi00608a034.

[16] W. Helfrich, Steric Interaction of Fluid Membranes in Multilayer Systems, Zeitschrift Für Naturforschung A 33 (1978) 305–315. https://doi.org/10.1515/zna-1978-0308.

[17] W. Helfrich, R.M. Servuss, Undulations, steric interaction and cohesion of fluid membranes, Il Nuovo Cimento D 3 (1984) 137–151. https://doi.org/10.1007/BF02452208.

[18] E.A. Evans, V.A. Parsegian, Thermal-mechanical fluctuations enhance repulsion between bimolecular layers., Proceedings of the National Academy of Sciences 83 (1986) 7132–7136. https://doi.org/10.1073/pnas.83.19.7132.

[19] B. Demé, M. Dubois, T. Gulik-Krzywicki, T. Zemb, Giant Collective Fluctuations of Charged Membranes at the Lamellar-to-Vesicle Unbinding Transition. 1. Characterization of a New Lipid Morphology by SANS, SAXS, and Electron Microscopy, Langmuir 18 (2002) 997–1004. https://doi.org/10.1021/la010723b.

[20] B. Demé, M. Dubois, T. Zemb, Giant Collective Fluctuations of Charged Membranes at the Lamellar-to-Vesicle Unbinding Transition. 2. Equation of State in the

Absence of Salt, Langmuir 18 (2002) 1005–1013. https://doi.org/10.1021/la0107244.

[21] B. Demé, M. Dubois, T. Zemb, Swelling of a Lecithin Lamellar Phase Induced by Small Carbohydrate Solutes, Biophys J 82 (2002) 215–225. https://doi.org/10.1016/S0006-3495(02)75388-5.

[22] H.I. Petrache, S. Tristram-Nagle, D. Harries, N. Kučerka, J.F. Nagle, V.A. Parsegian, Swelling of phospholipids by monovalent salt, J Lipid Res 47 (2006) 302–309. https://doi.org/10.1194/jlr.M500401-JLR200.

[23] S. Marčelja, Chain ordering in liquid crystals II. Structure of bilayer membranes, Biochimica et Biophysica Acta (BBA) - Biomembranes 367 (1974) 165–176. https://doi.org/10.1016/0005-2736(74)90040-6.

[24] V.A. Parsegian, N. Fuller, R.P. Rand, Measured work of deformation and repulsion of lecithin bilayers., Proceedings of the National Academy of Sciences 76 (1979) 2750–2754. https://doi.org/10.1073/pnas.76.6.2750.

[25] S. Marčelja, J. Wolfe, Properties of bilayer membranes in the phase transition or phase separation region, Biochimica et Biophysica Acta (BBA) - Biomembranes 557 (1979) 24–31. https://doi.org/10.1016/0005-2736(79)90086-5.

[26] D. Marsh, Lateral pressure in membranes, Biochimica et Biophysica Acta (BBA) - Reviews on Biomembranes 1286 (1996) 183–223. https://doi.org/10.1016/S0304-4157(96)00009-3.

[27] M. Dubois, T. Zemb, N. Fuller, R.P. Rand, V.A. Parsegian, Equation of state of a charged bilayer system: Measure of the entropy of the lamellar–lamellar transition in DDABr, J Chem Phys 108 (1998) 7855–7869. https://doi.org/10.1063/1.476505.

[28] V.A. Parsegian, Theory of liquid-crystal phase transitions in lipid + water systems, Transactions of the Faraday Society 62 (1966) 848. https://doi.org/10.1039/tf9666200848.

[29] L. Mandell, K. Fontell, P. Ekwall, Occurrence of Different Mesomorphous Phases in Ternary Systems of Amphiphilic Substances and Water, in: R.F. Gould (Ed.), Ordered Fluids and Liquid Crystals, ACS, Washington, D.C., 1967: pp. 89–124. https://doi.org/10.1021/ba-1967-0063.ch009.

[30] K. Fontell, L. Mandell, Phase equilibria and phase structure in the ternary systems sodium or potassium octanoate-octanoic acid-water, Colloid Polym Sci 271 (1993) 974–991. https://doi.org/10.1007/BF00654858.

[31] G.J.T. Tiddy, Surfactant-water liquid crystal phases, Phys Rep 57 (1980) 1–46. https://doi.org/10.1016/0370-1573(80)90041-1.

[32] K. Fontell, Liquid Crystallinity in Lipid-Water Systems, Molecular Crystals and Liquid Crystals 63 (1981) 59–82. https://doi.org/10.1080/00268948108071987.

[33] P. Ekwall, Composition, properties and structures of liquid crystalline phases in systems of amphiphilic compounds, in: G.H. Brown (Ed.), Advances in Liquid Crystals, Academic Press Inc., New York, 1975: pp. 1–142.

[34] P. Ekwall, L. Mandell, Solutions of alkali soaps and water in fatty acids, Kolloid-Zeitschrift Und Zeitschrift Für Polymere 233 (1969) 938–944. https://doi.org/10.1007/BF01508019.

[35] J.B. Rosenholm, Critical evaluation of models for self-assembly of short and medium chain-length surfactants in aqueous solutions, Adv Colloid Interface Sci 276 (2020) 102047. https://doi.org/10.1016/j.cis.2019.102047.

[36] B.W. Ninham, V.A.A. Parsegian, Electrostatic potential between surfaces bearing ionizable groups in ionic equilibrium with physiologic saline solution, J Theor Biol 31 (1971) 405–428. https://doi.org/10.1016/0022-5193(71)90019-1.

[37] T. Zemb, P. Charpin, Micellar structure from comparison of X-ray and neutron small-angle scattering, Journal de Physique 46 (1985) 249–256. https://doi.org/10.1051/jphys:01985004602024900.

[38] J.B. Hayter, T. Zemb, Concentration-dependent structure of sodium octanoate micelles, Chem Phys Lett 93 (1982) 91–94. https://doi.org/10.1016/0009-2614(82)85062-8.

[39] T. Zemb, M. Drifford, M. Hayoun, A. Jehanno, Light scattering study of solutions of sodium octanoate micelles, J Phys Chem 87 (1983) 4524–4528. https://doi.org/10.1021/j100245a037.

[40] D.F. Evans, D.J. Mitchell, B.W. Ninham, Ion binding and dressed micelles, J Phys Chem 88 (1984) 6344–6348. https://doi.org/10.1021/j150669a057.

[41] J.B. Hayter, A self-consistent theory of dressed micelles, Langmuir 8 (1992) 2873–2876. https://doi.org/10.1021/la00048a005.

[42] Y. Chevalier, L. Belloni, J.B. Hayter, T. Zemb, Effect of interfacial charge on micellar structure, Journal de Physique 46 (1985) 749–759. https://doi.org/10.1051/jphys:01985004605074900.

[43] P. Ekwall, L. Mandell, K. Fontell, The effect of sodium chloride on the solubilization of decan-1-ol in sodium octanoate solutions and the formation of mesophases, J Colloid Interface Sci 61 (1977) 519–534. https://doi.org/10.1016/0021-9797(77)90470-2.

[44] P. Ekwall, K. Fontell, Solutions of alkali soaps and water in fatty axids VII. X-ray scattering of the isotropic liquid L2-phase, Colloid Polym Sci 266 (1988) 184–191. https://doi.org/10.1007/BF01452817.

[45] P. Ekwall, Solutions of alkali soaps and water in fatty acids VIII. Correlations of X-ray data with other experimental observations, Colloid Polym Sci 266 (1988) 261–278. https://doi.org/10.1007/BF01452589.

[46] C. Cabos, P. Delord, J. Marignan, Local lamellar structure in dense microemulsions, Phys Rev B 37 (1988) 9796–9799. https://doi.org/10.1103/PhysRevB.37.9796.

[47] G. Porte, J. Marignan, P. Bassereau, R. May, Shape transformations of the aggregates in dilute surfactant solutions : a small-angle neutron scattering study, Journal de Physique 49 (1988) 511–519. https://doi.org/10.1051/jphys:01988004903051100.

[48] D. Roux, C. Coulon, M.E. Cates, Sponge phases in surfactant solutions, J Phys Chem 96 (1992) 4174–4187. https://doi.org/10.1021/j100190a017.

[49] K. Fontell, Influence of Electrolyte on Phase Equilibria and Phase Structure in the Binary System of Di-2-Ethylhexyl Sulphosuccinate and Water, in: K.L. Mittal (Ed.), ACS Symposium Series, ACS, Washington, D.C., 1975: pp. 270–277. https://doi.org/10.1021/bk-1975-0009.ch019.

[50] J.C. Lang, R.D. Morgan, Nonionic surfactant mixtures. I. Phase equilibria in C10E4–H2O and closed-loop coexistence, J Chem Phys 73 (1980) 5849–5861. https://doi.org/10.1063/1.440028.

[51] P. Jokela, B. Jönsson, A. Khan, Phase equilibria of catanionic surfactant-water systems, Journal of Physical Chemistry 91 (1987) 3291–3298. https://doi.org/10.1021/j100296a037.

[52] P. Jokela, B. Jönsson, B. Eichmueller, K. Fontell, Phase equilibria in the sodium octanoate-octylammonium octanoate-water system, Langmuir 4 (1988) 187–192. https://doi.org/10.1021/la00079a034.

[53] T. Gulik-Krzywicki, A. Tardieu, V. Luzzati, The Smectic Phase of Lipid-Water Systems: Properties Related to the Nature of the Lipid and to the Presence of Net Electrical Charges, Molecular Crystals 8 (1969) 285–291. https://doi.org/10.1080/15421406908084909.

[54] E.W. Kaler, K.L. Herrington, A.K. Murthy, J.A.N. Zasadzinski, Phase behavior and structures of mixtures of anionic and cationic surfactants, J Phys Chem 96 (1992) 6698–6707. https://doi.org/10.1021/j100195a033.

[55] A. Khan, O. Regev, A. Dumitrescu, A. Caria, Mixed surfactants: Sodium bis(2-ethylhexyl)sulphosuccinate- didodecyldimethyl-ammonium bromide- water system, in: R.H. Ottewill, A.R. Rennie (Eds.), Trends in Colloid and Interface Science VIII. Progress in Colloid & Polymer Science, Vol 97, Steinkopff, Darmstadt, 1994: pp. 146–150. https://doi.org/10.1007/BFb0115153.

[56] A. Khan, E. Marques, Catanionic surfactants, in: I.D. Robb (Ed.), Specialist Surfactants, Springer Netherlands, Dordrecht, 1997: pp. 37–80. https://doi.org/10.1007/978-94-009-1557-2_3.

[57] E.W. Kaler, A.K. Murthy, B.E. Rodriguez, J.A.N. Zasadzinski, Spontaneous Vesicle Formation in Aqueous Mixtures of Single-Tailed Surfactants, Science (1979) 245 (1989) 1371–1374. https://doi.org/10.1126/science.2781283.

[58] R.G. Laughlin, Equilibrium vesicles: fact or fiction?, Colloids Surf A Physicochem Eng Asp 128 (1997) 27–38. https://doi.org/10.1016/S0927-7757(97)03899-5.

[59] M. Dubois, T. Gulik-Krzywicki, B. Demé, T. Zemb, Rigid organic nanodisks of controlled size: A catanionic formulation, Comptes Rendus de l'Académie Des Sciences - Series IIC - Chemistry 1 (1998) 567–575. https://doi.org/10.1016/S1387-1609(98)80012-1.

[60] M. Dubois, B. Demé, T. Gulik-Krzywicki, J.-C. Dedieu, C. Vautrin, S. Désert, E. Perez, T. Zemb, Self-assembly of regular hollow icosahedra in salt-free catanionic solutions, Nature 411 (2001) 672–675. https://doi.org/10.1038/35079541.

[61] A. Meister, M. Dubois, L. Belloni, T. Zemb, Equation of State of Self-Assembled Disklike and Icosahedral Crystallites in the Dilute Range, Langmuir 19 (2003) 7259–7263. https://doi.org/10.1021/la0346806.

[62] T. Zemb, M. Dubois, Catanionic Microcrystals: Organic Platelets, Gigadalton 'Molecules', or Ionic Solids?, Aust J Chem 56 (2003) 971. https://doi.org/10.1071/CH03117.

[63] P. Jokela, B. Jönsson, H. Wennerström, Phase equilibria in systems containing both an anionic and a cationic amphiphile. A thermodynamic model calculation, in: B.

Lindman, G. Olofsson, P. Stenius (Eds.), Surfactants, Adsorption, Surface Spectroscopy and Disperse Systems, Steinkopff, Darmstadt, 1985: pp. 17–22. https://doi.org/10.1007/BFb0114300.

[64] F. Ricoul, M. Dubois, L. Belloni, T. Zemb, C. André-Barrès, I. Rico-Lattes, Phase Equilibria and Equation of State of a Mixed Cationic Surfactant−Glycolipid Lamellar System, Langmuir 14 (1998) 2645–2655. https://doi.org/10.1021/la9711185.

[65] N. Vlachy, B. Jagoda-Cwiklik, R. Vácha, D. Touraud, P. Jungwirth, W. Kunz, Hofmeister series and specific interactions of charged headgroups with aqueous ions, Adv Colloid Interface Sci 146 (2009) 42–47. https://doi.org/10.1016/j.cis.2008.09.010.

[66] O. Ghosh, C.A. Miller, Liquid-crystalline and microemulsion phase behavior in alcohol-free Aerosol-OT/oil/brine systems, J Phys Chem 91 (1987) 4528–4535. https://doi.org/10.1021/j100301a022.

[67] D.A. Antelmi, P. Kékicheff, Measurement of the Compressibility Modulus in a Lyotropic Lamellar Phase Stabilized by Undulation Forces, J Phys Chem B 101 (1997) 8169–8179. https://doi.org/10.1021/jp9715437.

[68] P. Kékicheff, C. Grabielle-Madelmont, M. Ollivon, Phase diagram of sodium dodecyl sulfate-water system, J Colloid Interface Sci 131 (1989) 112–132. https://doi.org/10.1016/0021-9797(89)90151-3.

[69] P. Kékicheff, Phase diagram of sodium dodecyl sulfate-water system, J Colloid Interface Sci 131 (1989) 133–152. https://doi.org/10.1016/0021-9797(89)90152-5.

[70] P. Kékicheff, B. Cabane, Between cylinders and bilayers : structures of intermediate mesophases of the SDS/water system, Journal de Physique 48 (1987) 1571–1583. https://doi.org/10.1051/jphys:019870048090157100.

[71] P. Kékicheff, From Cylinders to Bilayers: A Structural Study of Phase Transformations in a Lyotropic Liquid Crystal, Molecular Crystals and Liquid Crystals 198 (1991) 131–144. https://doi.org/10.1080/00268949108033390.

[72] D. Danino, Y. Talmon, H. Levy, G. Beinert, R. Zana, Branched Threadlike Micelles in an Aqueous Solution of a Trimeric Surfactant, Science (1979) 269 (1995) 1420–1421. https://doi.org/10.1126/science.269.5229.1420.

[73] M. Pleines, W. Kunz, T. Zemb, D. Benczédi, W. Fieber, Molecular factors governing the viscosity peak of giant micelles in the presence of salt and fragrances, J Colloid Interface Sci 537 (2019) 682–693. https://doi.org/10.1016/j.jcis.2018.11.072.

[74] P.J. Missel, N.A. Mazer, G.B. Benedek, C.Y. Young, M.C. Carey, Thermodynamic analysis of the growth of sodium dodecyl sulfate micelles, J Phys Chem 84 (1980) 1044–1057. https://doi.org/10.1021/j100446a021.

[75] P.J. Missel, N.A. Mazer, G.B. Benedek, M.C. Carey, Influence of chain length on the sphere-to-rod transition in alkyl sulfate micelles, J Phys Chem 87 (1983) 1264–1277. https://doi.org/10.1021/j100230a032.

[76] R.G. Alargova, V.P. Ivanova, P.A. Kralchevsky, A. Mehreteab, G. Broze, Growth of rod-like micelles in anionic surfactant solutions in the presence of Ca2+ counterions, Colloids Surf A Physicochem Eng Asp 142 (1998) 201–218. https://doi.org/10.1016/S0927-7757(98)00266-0.

[77] R.G. Alargova, K.D. Danov, P.A. Kralchevsky, G. Broze, A. Mehreteab, Growth of Giant Rodlike Micelles of Ionic Surfactant in the Presence of Al 3+ Counterions, Langmuir 14 (1998) 4036–4049. https://doi.org/10.1021/la970684x.

[78] N.C. Christov, N.D. Denkov, P.A. Kralchevsky, K.P. Ananthapadmanabhan, A. Lips, Synergistic Sphere-to-Rod Micelle Transition in Mixed Solutions of Sodium Dodecyl Sulfate and Cocoamidopropyl Betaine, Langmuir 20 (2004) 565–571. https://doi.org/10.1021/la035717p.

[79] P.A. Kralchevsky, K.D. Danov, S.E. Anachkov, G.S. Georgieva, K.P. Ananthapadmanabhan, Extension of the ladder model of self-assembly from cylindrical to disclike surfactant micelles, Curr Opin Colloid Interface Sci 18 (2013) 524–531. https://doi.org/10.1016/j.cocis.2013.11.002.

[80] S.E. Anachkov, P.A. Kralchevsky, K.D. Danov, G.S. Georgieva, K.P. Ananthapadmanabhan, Disclike vs. cylindrical micelles: Generalized model of micelle growth and data interpretation, J Colloid Interface Sci 416 (2014) 258–273. https://doi.org/10.1016/j.jcis.2013.11.002.

[81] K.D. Danov, P.A. Kralchevsky, S.D. Stoyanov, J.L. Cook, I.P. Stott, Analytical modeling of micelle growth. 1. Chain-conformation free energy of binary mixed spherical, wormlike and lamellar micelles, J Colloid Interface Sci 547 (2019) 245–255. https://doi.org/10.1016/j.jcis.2019.03.105.

[82] K.D. Danov, P.A. Kralchevsky, S.D. Stoyanov, J.L. Cook, I.P. Stott, Analytical modeling of micelle growth. 2. Molecular thermodynamics of mixed aggregates and scission energy in wormlike micelles, J Colloid Interface Sci 551 (2019) 227–241. https://doi.org/10.1016/j.jcis.2019.05.017.

[83] K.D. Danov, P.A. Kralchevsky, S.D. Stoyanov, J.L. Cook, I.P. Stott, Analytical modeling of micelle growth. 3. Electrostatic free energy of ionic wormlike micelles – Effects of activity coefficients and spatially confined electric double layers, J Colloid Interface Sci 581 (2021) 262–275. https://doi.org/10.1016/j.jcis.2020.07.059.

[84] K.D. Danov, P.A. Kralchevsky, R.D. Stanimirova, S.D. Stoyanov, J.L. Cook, I.P. Stott, Analytical modeling of micelle growth. 4. Molecular thermodynamics of wormlike micelles from ionic surfactants: Theory vs. experiment, J Colloid Interface Sci 584 (2021) 561–581. https://doi.org/10.1016/j.jcis.2020.10.004.

[85] F. Leermakers, J.C. Eriksson, H. Lyklema, Association Colloids and their Equilibrium Modelling, in: J. Lyklema (Ed.), Fundamentals of Interface and Colloid Science, Academic Press, 2005: pp. 4.1-4.123. https://doi.org/10.1016/S1874-5679(05)80008-X.

[86] E.S. Lutton, Phase behavior of aqueous systems of monoglycerides, J Am Oil Chem Soc 42 (1965) 1068–1070. https://doi.org/10.1007/BF02636909.

[87] D.J. Mitchell, G.J.T. Tiddy, L. Waring, T. Bostock, M.P. McDonald, Phase behaviour of polyoxyethylene surfactants with water. Mesophase structures and partial miscibility (cloud points), Journal of the Chemical Society, Faraday Transactions 1: Physical Chemistry in Condensed Phases 79 (1983) 975. https://doi.org/10.1039/f19837900975.

[88] N. Chakhovskoy, Contribution à l'étude des éthers monoalcoylés des (poly) éthylène glycols II. Températures critiques de démixtion des systèmes éther monoalcoylé de (poly)éthylène glycol-eau et influence d'un troisième constituant, Bulletin Des

Sociétés Chimiques Belges 65 (1956) 474–493. https://doi.org/10.1002/bscb.19560650506.

[89] M. Zulauf, K. Weckstrom, J.B. Hayter, V. Degiorgio, M. Corti, Neutron scattering study of micelle structure in isotropic aqueous solutions of poly(oxyethylene) amphiphiles, J Phys Chem 89 (1985) 3411–3417. https://doi.org/10.1021/j100261a051.

[90] E.J. Staples, G.J.T. Tiddy, Nuclear magnetic resonance technique to distinguish between micelle size changes and secondary aggregation in anionic and nonionic surfactant solutions, Journal of the Chemical Society, Faraday Transactions 1: Physical Chemistry in Condensed Phases 74 (1978) 2530. https://doi.org/10.1039/f19787402530.

[91] T. Kato, M. Kanada, T. Seimiya, A Thermodynamic Model for Micellar Growth on the Basis of Light Scattering Intensities from Extremely Dilute Solutions of Nonionic Surfactant, J Colloid Interface Sci 181 (1996) 149–158. https://doi.org/10.1006/jcis.1996.0366.

[92] H.G. Thomas, A. Lomakin, D. Blankschtein, G.B. Benedek, Growth of Mixed Nonionic Micelles, Langmuir 13 (1997) 209–218. https://doi.org/10.1021/la9606613.

[93] K.D. Danov, P.A. Kralchevsky, S.D. Stoyanov, J.L. Cook, I.P. Stott, E.G. Pelan, Growth of wormlike micelles in nonionic surfactant solutions: Quantitative theory vs. experiment, Adv Colloid Interface Sci 256 (2018) 1–22. https://doi.org/10.1016/j.cis.2018.05.006.

[94] A. Graciaa, J. Lachaise, C. Cucuphat, M. Bourrel, J.L. Salager, Improving solubilization in microemulsions with additives. 1. The lipophilic linker role, Langmuir 9 (1993) 669–672. https://doi.org/10.1021/la00027a010.

[95] A. Graciaa, J. Lachaise, C. Cucuphat, M. Bourrel, J.L. Salager, Interfacial segregation of an ethyl oleate/hexadecane oil mixture in microemulsion systems, Langmuir 9 (1993) 1473–1478. https://doi.org/10.1021/la00030a008.

[96] M. Miñana-Perez, A. Graciaa, J. Lachaise, J.-L. Salager, Solubilization of polar oils with extended surfactants, Colloids Surf A Physicochem Eng Asp 100 (1995) 217–224. https://doi.org/10.1016/0927-7757(95)03186-H.

[97] J. Salager, R.E. Antón, D.A. Sabatini, J.H. Harwell, E.J. Acosta, L.I. Tolosa, Enhancing solubilization in microemulsions—State of the art and current trends, J Surfactants Deterg 8 (2005) 3–21. https://doi.org/10.1007/s11743-005-0328-4.

[98] A. Klaus, G.J.T. Tiddy, D. Touraud, A. Schramm, G. Stühler, M. Drechsler, W. Kunz, Phase behavior of an extended surfactant in water and a detailed characterization of the dilute and semidilute phases, Langmuir 26 (2010) 5435–5443. https://doi.org/10.1021/la903899w.

[99] A. Klaus, G.J.T. Tiddy, D. Touraud, A. Schramm, G. Stühler, W. Kunz, Phase behavior of an extended surfactant in water and a detailed characterization of the concentrated phases, Langmuir 26 (2010) 16871–16883. https://doi.org/10.1021/la103037q.

[100] D. Papahadjopoulos, G. Poste, B.E. Schaeffer, W.J. Vail, Membrane fusion and molecular segregation in phospholipid vesicles, Biochimica et Biophysica Acta (BBA) - Biomembranes 352 (1974) 10–28. https://doi.org/10.1016/0005-2736(74)90175-8.

[101] M. Dubois, V. Lizunov, A. Meister, T. Gulik-Krzywicki, J.M. Verbavatz, E. Perez, J. Zimmerberg, T. Zemb, Shape control through molecular segregation in giant surfactant aggregates, Proceedings of the National Academy of Sciences 101 (2004) 15082–15087. https://doi.org/10.1073/pnas.0400837101.

[102] Y. Hendrikx, J. Charvolin, M. Rawiso, Segregation of two amphiphilic molecules within nonspherical micelles: A neutron scattering study, J Colloid Interface Sci 100 (1984) 597–600. https://doi.org/10.1016/0021-9797(84)90468-5.

[103] S. Alpérine, Y. Hendrikx, J. Charvolin, Internal structure of aggregates of two amphiphilic species in a lyotropic liquid crystal, Journal de Physique Lettres 46 (1985) 27–31. https://doi.org/10.1051/jphyslet:0198500460102700.

[104] J.M. Pope, J.W. Doane, Curvature-related molecular segregation in lyotropic aggregates of potassium palmitate and benzyl alcohol: A 2H NMR study, J Chem Phys 87 (1987) 3201–3206. https://doi.org/10.1063/1.453007.

[105] R. Klein, O. Zech, E. Maurer, M. Kellermeier, W. Kunz, Oligoether Carboxylates: Task-Specific Room-Temperature Ionic Liquids, J Phys Chem B 115 (2011) 8961–8969. https://doi.org/10.1021/jp200624g.

[106] E. Müller, L. Zahnweh, B. Estrine, O. Zech, C. Allolio, J. Heilmann, W. Kunz, Oligoether carboxylate counterions: An innovative way towards surfactant ionic liquids, J Mol Liq 251 (2018) 61–69. https://doi.org/10.1016/j.molliq.2017.12.037.

[107] O. Zech, M. Kellermeier, S. Thomaier, E. Maurer, R. Klein, C. Schreiner, W. Kunz, Alkali Metal Oligoether Carboxylates—A New Class of Ionic Liquids, Chemistry – A European Journal 15 (2009) 1341–1345. https://doi.org/10.1002/chem.200801806.

[108] M. Petkovic, K.R. Seddon, L.P.N. Rebelo, C. Silva Pereira, Ionic liquids: a pathway to environmental acceptability, Chem. Soc. Rev. 40 (2011) 1383–1403. https://doi.org/10.1039/C004968A.

[109] R. Paberit, E. Rilby, J. Göhl, J. Swenson, Z. Refaa, P. Johansson, H. Jansson, Cycling Stability of Poly(ethylene glycol) of Six Molecular Weights: Influence of Thermal Conditions for Energy Applications, ACS Appl Energy Mater 3 (2020) 10578–10589. https://doi.org/10.1021/acsaem.0c01621.

[110] M. Rothe, E. Müller, P. Denk, W. Kunz, Ionic Liquids Based on the Concept of Melting Point Lowering Due to Ethoxylation, Molecules 26 (2021) 4034. https://doi.org/10.3390/molecules26134034.

[111] M. Rothe, M. Tress, C. Allacher, P. Nuernberger, W. Kunz, Ionic Liquids [M 3+][A −] 3 with Three-Valent Cations and Their Possible Use to Easily Separate Rare Earth Metals, Chemistry – A European Journal 27 (2021) 13052–13058. https://doi.org/10.1002/chem.202101925.

[112] M. Rothe, G. Quintard, M. Kronseder, P. Bauduin, T. Zemb, W. Kunz, Dilution and packing of anionic liquid surfactant in presence of divalent and trivalent counterions, J Mol Liq 384 (2023) 122195. https://doi.org/10.1016/j.molliq.2023.122195.

[113] L. Braun, N. Engelhardt, S.C. Engert, N. Lichterfeld-Weber, G. Oetter, H.-C. Raths, J. Tropsch, W. Kunz, M. Kellermeier, Alkylether derivatives of choline as cationic surfactants for the design of soluble catanionic systems at ambient conditions, J Mol Liq 370 (2023) 121033. https://doi.org/10.1016/j.molliq.2022.121033.

[114] L. Chiappisi, Polyoxyethylene alkyl ether carboxylic acids: An overview of a neglected class of surfactants with multiresponsive properties, Adv Colloid Interface Sci 250 (2017) 79–94. https://doi.org/10.1016/j.cis.2017.10.001.

[115] N.M. Van Os, J.R. Haak, L.A.M. Rupert, K.S. Laboratorium, Physico-Chemical Properties of Selected Anionic, Cationic and Nonionic Surfactants, Elsevier B.V., 1993. https://doi.org/10.1016/c2009-0-09112-0.

[116] M. Tomšič, M. Bešter-Rogač, A. Jamnik, W. Kunz, D. Touraud, A. Bergmann, O. Glatter, Ternary systems of nonionic surfactant Brij 35, water and various simple alcohols: Structural investigations by small-angle X-ray scattering and dynamic light scattering, J Colloid Interface Sci 294 (2006) 194–211. https://doi.org/10.1016/j.jcis.2005.06.088.

[117] R. Schwarzenbacher, M. Kriechbaum, H. Amenitsch, P. Laggner, Characterization of the nanostructures in liquid crystalline mesophases present in the ternary system brij-35/dibutyl ether/H2O by small- and wide-angle X-ray scattering, Journal of Physical Chemistry B 102 (1998) 9161–9167. https://doi.org/10.1021/jp9822889.

[118] S. Fall, B. Pattier, L. Benyayia, A. Gibaud, Binary phase diagram of water/Brij58 studied by SAXS, Acta Phys Pol A 121 (2012) 388–396. https://doi.org/10.12693/APhysPolA.121.388.

Chapter II.

Simple Aqueous Phase Behavior of Octaoxyethylene Octyl Ether Carboxylic Acid ($C_8E_8CH_2COOH$)

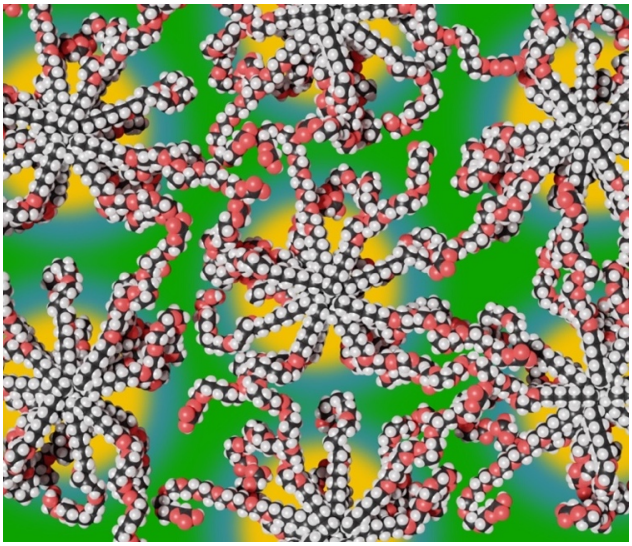

Schematic drawing of the water-poor headgroup interdigitated micellar phase (L_1') with confined hydrocarbon cores (yellow) surrounded by a polar medium of (hydrated) headgroups (green), found at surfactant concentrations above 60 wt%. There is no bulk water, only a hydration layer, which is indicated with a blue color.

Note:

A large portion of this chapter is already included in the author's master thesis (P. Denk, Phase Behavior and Simple Coacervation of Akypo™ LF2 in Aqueous Solutions, [unpublished] master thesis, University of Regensburg, 2020.). The data presented in the master thesis were also published a few months later (P. Denk, A. El Maangar, J. Lal, D. Kleber, T. Zemb, W. Kunz, Phase diagrams and microstructures of aqueous short alkyl chain polyethylene glycol ether carboxylate and carboxylic acid triblock surfactant solutions, J Colloid Interface Sci 590 (2021) 375–386.) [1]. The author of this thesis is the first author of the publication, wrote the original draft, evaluated the data, and conducted most of the experiments. The co-author Dr. Asmae El Maangar performed the SWAXS measurements, the treatment of the raw scattering data, and assisted in editing the original draft. The co-authors Prof. Dr. Thomas Zemb and Prof. Dr. Werner Kunz reviewed the draft and provided scientific input throughout the work. The co-author Dr. Jyotsana Lal assisted in fitting of the SAXS data. The co-author David Kleber conducted preliminary work and prepared the samples used for SWAXS. Some aspects presented in this chapter are also discussed in two other publications (M. Rothe, E. Müller, P. Denk, W. Kunz, Ionic Liquids Based on the Concept of Melting Point Lowering Due to Ethoxylation, Molecules 26 (2021) 4034 and J. Blahnik, E. Müller, L. Braun, P. Denk, W. Kunz, Nanoscopic microheterogeneities or pseudo-phase separations in non-conventional liquids, Curr Opin Colloid Interface Sci 57 (2022) 101535.) [2,3]. The author of this thesis wrote the respective sections of those publications. Presented cryo-TEM images were recorded and evaluated by Sapir Lifshiz-Simon from the group of Prof. Dr. Yeshayahu Talmon at the Technion in Haifa. The intern Lea Sammet assisted in the investigations of the ternary phase behavior with hydrocarbon oils.

II.1. Abstract

The surfactant octaoxyethylene octyl ether carboxylic acid ($C_8E_8CH_2COOH$) is examined in this chapter. Its extraordinarily simple aqueous phase behavior distinguishes this surfactant from the vast majority of surfactants. As a consequence of its small hydrophobic part and significantly larger hydrophilic part, a significant steric constraint is expected during micellization. In addition, fine-tuning via electrostatic interactions should be enabled by the terminal carboxylic acid group of this "essentially nonionic" surfactant.

Phase diagrams of binary mixtures of water and $C_8E_8CH_2COOH$ are established over large concentration and temperature ranges, and in the presence of sodium and calcium ions, as well as hydrocarbon oils. Surface tensions and osmotic pressures are measured to understand the systems. To evaluate the microstructures, also dynamic light scattering (DLS), cryogenic transmission electron microscopy (cryo-TEM), and small-angle X-ray scattering (SAXS) are performed.

Apart from the formation of coacervates at very low surfactant concentrations, spherical micelles persist over the whole concentration and temperature range and do not change in size and shape. At very high surfactant concentrations, above 60 wt%, where the headgroups are no longer fully hydrated, the standard core-shell structure of micelles (L_1 phase) vanishes and highly stabilized aggregates of 8–26 octyl chains are suspended in interdigitated polyoxyethylene layers and form an ''osmotic brush'' (L_1' phase). When the acid is partially transformed into its sodium salt, the repulsion between the micelles increases, whereas bridging between micelles prevails, when calcium cations are available with sufficient electrostatic screening. Remarkably, the negative charges of the headgroups seem to be randomly distributed in the hydrophilic ethylene oxide shell in the case of sodium as counterion. Altogether, a phase diagram without lyotropic liquid crystalline phases, similar to the phase diagram of C_8E_8 already known in the literature, and an extreme shift of the cloud point in temperature and composition is found. The phase properties can be explained by the curvature and packing constraints together with the Lindemann rule applied to short hydrocarbon chains.

II.2. Introduction

Usually, aqueous surfactant solutions show a rich phase behavior as a function of composition and temperature. Beyond spherical micelles, typically other micellar shapes occur and, at higher surfactant concentrations, also various liquid crystalline phases and reversed phases can be found [4]. Further, for nonionic surfactants, also a significant dependence on temperature is observed. This is especially the case for nonionic surfactants containing ethylene oxide (EO) groups as polar heads. Depending on the conditions and the location in the phase diagram, the headgroups can be more or less dehydrated. As a result, the size and the shape of the micelles can significantly vary in the L_1 phase. At higher surfactant concentrations, different liquid crystalline phases, as well as phase separations at higher temperatures, may occur. However, there are some exceptions, for which a remarkably simple phase behavior is found over a large composition and temperature range. This is for example the case for C_8E_8 and C_8E_{12} surfactants, as mentioned by Mitchell *et al.* in 1983 [5], and as early as 1971 for C_8E_6 [6]. Other examples are $C_{12}E_x(CO_2CH_2CH_2)_yOH$ surfactants, as recently found by Spiering *et al.* [7].

In the present chapter, aqueous solutions of a relatively simple and commercially available surfactant, which is liquid at room temperature under ambient pressure, are investigated. It shows a very simple phase behavior over nearly the whole composition range with water and over the whole temperature range, similar to C_8E_8 [5]. The only exception is a small concentration range at surfactant concentrations below the critical micelle concentration (CMC), where a coacervate is formed. Coacervation is termed a special liquid-liquid phase separation of colloidal systems, where the separation is between a concentrated colloid-rich fluid phase that forms in the absence of any precipitation and a very dilute phase. The resulting colloid-rich liquid phase, called coacervate, is more viscous than the supernatant [8]. Coacervation is linked to the counter-intuitive ‘‘concentrating by dilution” phenomena [9]. This has been extensively studied for polymers, lipids, and proteins more than fifty years ago, much less in the case of surfactants [10]. It occurs sometimes in polyelectrolyte solutions, and especially in protein solutions or mixtures of polymers with surfactants [11–15]. Very few and somewhat exotic examples are known, in which more or less complex surfactants can form coacervates under certain conditions, even in the absence of polyelectrolytes [16].

The surfactant octaoxyethylene octyl ether carboxylic acid ($C_8E_8CH_2COOH$), with its commercial name Akypo® LF2 from Kao Chemicals, considered in the present chapter is a triblock, when the acidic proton is exchanged with a counterion, such as sodium. In its acidic form, it resembles nonionic surfactants. Surfactants with three or even four different blocks, consisting of a hydrophobic part, a second, slightly less hydrophobic part (propylene oxide, PO), and a hydrophilic one (either EO or a charged end group or both together) have been known since a long time, for example as phosphoric acid or ester derivatives [17] or as extended surfactants [18–24].

The latter ones, in which the middle part usually consists of hydrophobic PO groups, are particularly interesting, since they (a) allow the miscibility of water and long-chain triglycerides, such as olive oil, and (b) they are liquid at room temperature, because of the high chain flexibility, induced by the large number of PO groups, despite the charged groups at the end of the molecule. This relative insensitivity to the charged head group makes the surfactant thermosensitive and quite insensitive to the presence of even large amounts of divalent cations. In fact, the area per molecule does not vary by more than 5–10%, whether ionized or not. As such, the lateral equation of state (EOS) linking the area per headgroup to the osmotic pressure is poorly dependent on pH and therefore on the degree of ionization of the surfactant [25].

Most nonionic surfactants studied in detail so far, are of the type C_iE_j (polyoxyethylene alkyl ethers) with $i \approx 2 \cdot j$, probably because in this case, the spontaneous packing parameter p_0 is close to 1. A precise definition of the used spontaneous packing parameter p_0 and a comparison with other types of packing parameters appearing in the literature are given in **Appendix A.3**. By contrast, in the case of $C_8E_8CH_2COOH$, the volume of the headgroup ($E_8 + COO^-$ or COOH) is much larger than the volume of the alkyl chain. The important consequences are a) that a sphere-to-rod transition is impossible even at high temperatures, and b) the spontaneous packing parameter p_0 can never be close to 1, even at very high surfactant concentrations and temperatures [26]. Thus, only a spherical core-shell micellar structure is possible. The interesting question is, how such a structure can be maintained over the whole temperature (below the clouding temperature) and concentration range (above the CMC), since there is a complete miscibility of water and surfactant. This is true not only for Na^+, Ca^{2+}, and H^+ as counterions to the $C_8E_8CH_2COO^-$ surfactant, as studied in detail in this thesis, but also for transition metals and rare earth metals.

In this chapter, first the phase diagram of the aqueous surfactant solutions is given and discussed together with results of dynamic light scattering (DLS), then surface tensions and osmotic pressures are discussed. Finally, the underlying structures of the solutions are inferred from small-angle X-ray scattering (SAXS) experiments and confirmed by cryogenic transmission electron microscopy (cryo-TEM). Finally, the consequences of the packing constraints on the phase behavior in presence of hydrocarbon oils are explored. The also observed coacervate region will not be discussed in detail in this chapter, but in **Chapter III**.

II.3. Experimental Section

II.3.1. Materials

The surfactant Akypo® LF2, octaoxyethylene octyl ether carboxylic acid ($C_8E_8CH_2COOH$), was a generous gift from Kao Chemicals (Emmerich am Rhein, Germany). The surfactant is received with 90 wt% actual matter, the main impurities being water (9.0 wt%) and sodium chloride (0.9 wt%). A more detailed analysis of the impurities contained in the used batch is given in **Table A.1**. Note that besides the small carboxylic acid impurities given in **Table A.1**, some impurities are counted as "active matter". Those are carboxymethylated polyethylene glycols as well as nonionic polyoxyethylene alkyl ethers, polyethylene glycols, and various esters of the type $C_8E_xCH_2COOE_yC_8$. $C_8E_8CH_2COOH$ was used as received for the determination of the phase diagrams. For other experiments, $C_8E_8CH_2COOH$ was dehydrated at 90°C up to a concentration of at least 99.5 wt%. In the process, a white precipitate formed, which was removed by simple vacuum filtration. The precipitate is mainly NaCl.

To obtain the sodium salt of $C_8E_8CH_2COOH$, NaOH was added in excess to previously dehydrated $C_8E_8CH_2COOH$ as an aqueous solution containing 1 $mol \cdot L^{-1}$ NaOH. The resulting solution with roughly 30 wt% $C_8E_8CH_2COOH$ was stirred over night to allow a complete reaction of $C_8E_8CH_2COOH$ with NaOH. Subsequent removal of water by vacuum distillation resulted in a liquid of high viscosity and lead to the formation of a white precipitate. In order to remove the precipitate, the liquid was dissolved in acetone and the resulting suspension was filtered using a 0.2 µm PTFE syringe filter. After separation by

distillation of acetone and vacuum drying, a clear, and highly viscous liquid was obtained. ^{1}H-NMR proved that the structure of $C_8E_8CH_2COOH$ was maintained, while the peak of the carboxylic acid hydroxyl group diminished, suggesting the formation of $[Na^+][C_8E_8CH_2COO^-]$, see **Fig. A.1**. Full deprotonation is also suggested by a slightly basic pH of aqueous $[Na^+][C_8E_8CH_2COO^-]$ solutions. $[H^+]_{0.5}[Na^+]_{0.5}[C_8E_8CH_2COO^-]$ was then obtained as a 1:1 mixture of $[Na^+][C_8E_8CH_2COO^-]$ and $C_8E_8CH_2COOH$.

$CaCl_2$ (≥94%), NaCl (p.a., ≥99.5%), and n-dodecane (≥95%) were purchased from Carl Roth (Karlsruhe, Germany). NaOH (p.a., ≥98%) as well as acetone (p.a., ≥99.5%) and n-hexane (p.a., ≥99%) were supplied by Sigma-Aldrich (St. Louis, Missouri, USA). Ultrapure water from a Millipore purification system (resistivity >18 MΩ·cm) was used for all systems containing water.

II.3.2. Phase Diagram Determination

For the determination of the phase diagrams, various samples containing 0.009 wt% to 90 wt% of $C_8E_8CH_2COOH$ in water were heated in a water bath from 0°C to 100°C under continuous stirring. The phase boundaries were determined by visual observation. The accuracy in temperature is ±1°C. Generally, the heating rate was about 15°C per hour. Close to the phase boundary, the samples were equilibrated for at least 30 min per degree Celsius. This rather short equilibration time was chosen because the cloud point transition is very fast and no other phase transitions were observed. Subsequent cooling below the phase boundary showed no noticeable temperature hysteresis of the phase transition. Similarly, two additional phase diagrams of $C_8E_8CH_2COOH$ in water were recorded after addition of $CaCl_2$ and NaOH, respectively. $CaCl_2$ was added in a mole ratio of 0.25 relative to $C_8E_8CH_2COOH$, while NaOH was added in a mole ratio of 0.5. $[H^+]_{0.5}[Na^+]_{0.5}[C_8E_8CH_2COO^-]$ could also be prepared in a concentration of about 99.2 wt% as a clear liquid by a different approach. The phase behavior above 90 wt% was checked using the prepared $[H^+]_{0.5}[Na^+]_{0.5}[C_8E_8CH_2COO^-]$ and vacuum dried $C_8E_8CH_2COOH$.

Ternary phase diagrams of $H_2O/C_8E_8CH_2COOH$/oil were recorded by stepwise addition of oil to binary mixtures of water and surfactant at room temperature (T ≈ 23°C) and visual observation. Other points in the phase diagrams were checked by preparing respective

samples.

II.3.3. Density Measurements

The physical densities were measured using a density meter DMA 5000 M from Anton Paar (Graz, Austria), which operates with the oscillating U-tube method. A condition for each measurement was temperature stability with a maximum deviation of ±0.002°C.

II.3.4. Surface Tension Measurements

A pull-force tensiometer K100MK2 from Krüss (Hamburg, Germany) equipped with a platinum-iridium ring and an automatic dosing system Dosino 800 from Metrohm (Herisau, Switzerland) was used to measure equilibrium surface tension isotherms at 25°C of (a) $C_8E_8CH_2COOH$, (b) $C_8E_8CH_2COOH$ with 10 mM $CaCl_2$ added to the initial solution with the highest concentration, resulting in 0.054 Ca^{2+} ions per $C_8E_8CH_2COOH$ molecule at any given concentration, (c) $C_8E_8CH_2COOH$ with 0.25 $CaCl_2$ per surfactant molecule, and (d) $[H^+]_{0.5}[Na^+]_{0.5}[C_8E_8CH_2COO^-]$. Prior to surface tension measurements, the glassware was soaked in a KOH bath, followed by a HCl bath for at least 24 h and subsequently rinsed thoroughly with water.

To measure the equilibrium surface tensions at 25°C of samples with higher $C_8E_8CH_2COOH$ concentrations, a pendant-drop tensiometer PAT1M from Sinterface (Berlin, Germany) was used. For each sample, at least three separate drops were measured. The densities of the samples are necessary to derive the correct surface tension from the shape of the drop, which is determined by the force balance between gravity and surface tension. Thus, the densities were measured using a density meter DMA 5000 M, see **Section II.3.3**.

II.3.5. Equilibrium Vapor Pressure Measurements to Determine Osmotic Coefficients

Vapor pressure osmometry (VPO) was performed using an Osmomat K-7000 from Knauer (Berlin, Germany) to determine the water activity of several binary mixtures of $C_8E_8CH_2COOH$ and water at a temperature of 25°C. The $C_8E_8CH_2COOH$ content ranged from 20 wt% (mole fraction $x(H_2O) = 0.9917$) up to 99.5 wt% ($x(H_2O) = 0.1311$). The K-7000 is equipped with two thermistors protruding into a thermostated (accuracy ±0.001°C) measurement chamber. A saturated solvent atmosphere is provided inside the chamber, containing a reservoir of water and wetted paper wicks. VPO is an indirect method to measure the vapor pressure of a liquid. To this purpose, a single drop of the sample is attached to one of the thermistors, while a drop of pure water is attached to the second thermistor. Since the water activity and consequently the vapor pressure is lower for the sample drop, water will condensate on the drop, increasing its temperature. The difference in temperature between both drops results in a voltage change between the two thermistors, which is translated into a measurement reading. In order to extract any information from this reading, a calibration is needed. Seven sodium chloride solutions in the concentration range from 0.1 mol·kg^{-1} to 4.0 mol·kg^{-1} were measured to get a calibration curve, relating each measurement value to a specific sodium chloride molality m_{NaCl} possessing the same water activity. A set of equations developed by F. Gibbard and G. Scatchard was used to calculate the osmotic coefficient Φ_{NaCl} for each molality m_{NaCl} [27,28]. The osmotic coefficient of the surfactant solution Φ_S is then given by

$$\Phi_S = \frac{\nu_{NaCl} m_{NaCl} \Phi_{NaCl}}{\nu_S m_S} , \qquad \text{(II.3.1)}$$

where m_{NaCl} is the molality of a sodium chloride solution showing the same measurement reading. The stoichiometric number ν_{NaCl} equals 2, and the stoichiometric number for the surfactant ν_S is assumed to be equal to 1 within the examined concentration range. By definition, Φ_S is related to the water activity a_w as

$$\Phi_S = -\frac{\ln(a_w)}{\nu_S m_S M_w} , \qquad \text{(II.3.2)}$$

where M_w is the molecular weight of water ($M_W = 18.015$ g·mol^{-1}). For each sample, at

least six measurements with individual drops were performed and the mean value was used for further calculations. Overall, the maximum deviation from the mean value was about 2%, usually being about 1%. Preceding each measurement, a zero-point adjustment was done by attaching two drops of pure water and setting the instrument reading to zero after an equilibration time of 5 min. As the temperature change and thus the instrument reading underlies kinetic effects, the measurement value was always taken exactly after 5 min. To ensure equal conditions for each measurement, special care was taken to keep the drop size and shape as constant as possible and, most importantly, equal on both sides.

The obtained water activity can be easily converted to the excess chemical potential of water μ_w^{ex}.

$$\mu_w^{ex} = RT \cdot \ln(a_w) \,, \tag{II.3.3}$$

where R is the ideal gas constant and T is the temperature in K. Further, it can be converted to an osmotic pressure Π_{osm} using the Van't Hoff formula.

$$\Pi_{osm} = -\frac{RT}{V_w} \cdot \ln(a_w) \,, \tag{II.3.4}$$

where V_w is the molar volume of water.

Once the osmotic pressure is determined by vapor pressure osmometry and the corresponding water layer thickness is determined by SAXS, the experimental result is equivalent to a molecular force determination obtained with a surface force apparatus (SFA) [29] or the colloidal probe protocol [30]. To make the conversion from the osmotic pressure to the surface free energy per unit area, the Derjaguin approximation in the case of sphere-sphere is used [31,32]. In a solution containing spherical micelles, the measured osmotic pressure can be interpreted as the osmotic pressure between micelles. Assuming that each micelle is in average surrounded by twelve other micelles, the osmotic pressure between two spheres $\Pi_{S\text{-}S}$ can be calculated by dividing Π_{osm} by a factor of 12 [33]. The radius of the hydrocarbon (HC) core is taken as the radius of the interacting surfaces.

II.3.6. Dynamic Light Scattering

Dynamic light scattering (DLS) experiments were performed at 25°C, using a CGS-3 goniometer system from ALV (Langen, Germany) with a vertically polarized 22 mW HeNe laser (λ = 632.8 nm), as well as the ALV-7004/FAST Multiple Tau digital correlator system. Samples were measured within a cylindrical light-scattering cell with an outer diameter of 10 mm in a temperature-controlled bath of toluene. The homodyne correlation functions $\langle I(0)I(\tau)\rangle$, τ being the correlator delay time, were recorded at an angle of 90° for 120 s. Due to the high dilution of the samples, the refractive index and viscosity of pure water at 25°C were used as solvent properties. Dust was excluded from the sample vial by exhaustive rinsing with acetone, utilizing an acetone washing apparatus and filtration of all samples with 0.2 μm PTFE-membrane filters.

II.3.7. Small- and Wide-Angle X-Ray Scattering

Small- and wide-angle X-ray scattering experiments were carried out on a bench built by Xenocs (Grenoble, France), using X-ray radiation from a molybdenum source (λ = 0.71 Å), delivering a 1 mm large circular beam of energy 17.4 keV. The scattered beam was recorded by a large on-line scanner detector MAR Research 345 from marXperts (Norderstedt, Germany), which was located 750 mm from the sample stage. Off-center detection was used to cover a large q-range simultaneously ($0.2\ nm^{-1} < q < 30\ nm^{-1}$), where $q = \sin(\theta/2)\cdot 4\pi/\lambda$.

Collimation was applied using a 12:∞ multilayer Xenocs mirror (for Mo radiation), coupled to two sets of Forvis Technologies (Santa Barbara, California, USA) scatterless slits, which provides a 0.8 mm × 0.8 mm X-ray beam at the sample position. A high-density polyethylene sample from Goodfellow (Huntingdon, UK) was used as a calibration standard to obtain absolute intensities. Silver behenate in a sealed capillary was used as scattering vector calibration standard. Integration of the 2D spectra was performed using the software FIT2D. Data were normalized taking into account the electronic background of the detector, transmission measurements, and empty cell subtraction.

Fitting of the spectra was done with the SasView package (version 5.0.2) [34], assuming two different models. On the one hand, a core-shell-sphere model with a Hayter-Penfold

RMSA structure factor [35,36] and a Schulz polydispersity distribution was used to fit mainly the spectra of lower concentrated samples, on the other hand, a simple sphere model with a Hayter-Penfold RMSA structure factor was used to fit the spectra of higher concentrated samples without applying any polydispersity. More detailed information on the models can be found in the SasView manual [34].

II.3.8. Cryogenic Transmission Electron Microscopy

Specimens for cryogenic transmission electron microscopy (cryo-TEM) imaging were prepared in a controlled environment vitrification system (CEVS), at 25°C and 100% relative humidity. These controlled conditions are essential for the preservation of the native state of the specimen during its preparation. Before specimen preparation, a carbon-coated perforated polymer film supported on a 200 mesh TEM grid was plasma-etched in a PELCO easiGlow glow-discharger (Ted Pella Inc., Redding, California, USA) to increase its hydrophilicity. Inside the CEVS, the etched grid was held by tweezers. A small drop of the sample was applied onto the grid, and the excess solution was blotted with a filter paper supported on a metal strip, to form a thin film of the solution suitable for cryo-TEM imaging. All the specimens were prepared by blotting the grid twice from the back and then touching a clean area of the filter paper. After blotting, the grid was quickly plunged into liquid ethane at its freezing point. That provided a high cooling rate needed for the vitrification of water. The specimens were kept in liquid nitrogen until transferred into the TEM for imaging.

The specimens were imaged by a FEI (Hillsboro, Oregon, USA) Tecnai T12 G^2 TEM, equipped with a LaB_6 electron gun and operating at 120 kV, and a Thermo-Fisher Scientific (Waltham, Massachusetts, USA) Talos 200C, FEG-equipped, 200 kV, high-resolution TEM. To enhance image contrast, the Volta "phase-plate" (VPP) system of the Talos was used.

II.4. Results and Discussion

II.4.1. Phase Diagrams

The recorded binary phase diagrams of $C_8E_8CH_2COOH$ in water and $[H^+]_{0.5}[Na^+]_{0.5}[C_8E_8CH_2COO^-]$ in water, as well as the pseudo-binary phase diagram of $C_8E_8CH_2COOH$ in water in presence of 0.25 $CaCl_2$ per $C_8E_8CH_2COOH$ molecule, are given as a function of the surfactant concentration in wt% in **Fig. II.1**, as a function of the surfactant mole fraction in **Fig. A.2**, and as function of the molar surfactant concentration in **Fig. A.3**. It is important to note that $C_8E_8CH_2COOH$ was used as received, i.e., including 0.9 wt% NaCl and 9.0 wt% H_2O, for recording the phase diagrams up to 90 wt% $C_8E_8CH_2COOH$. While no concentrations above 90 wt% were considered for $C_8E_8CH_2COOH$ with 0.25 $CaCl_2$ per $C_8E_8CH_2COOH$, higher concentrations were checked using vacuum dried $C_8E_8CH_2COOH$, where most of the NaCl is removed as a precipitate, and neat $[H^+]_{0.5}[Na^+]_{0.5}[C_8E_8CH_2COO^-]$. $C_8E_8CH_2COOH$ is sometimes denoted as $[H^+][C_8E_8CH_2COO^-]$. The green dashed line at higher concentrations indicates the solubility limit of $CaCl_2$. Mixtures with concentrations above this limit were suspensions of solid salt particles. Phase behavior reported above the dashed line applies to the otherwise clear liquids in which the salt particles were suspended. Thus, the mole ratios of $CaCl_2$ and $C_8E_8CH_2COOH$ differ beyond the dashed line.

All three phase diagrams are remarkably simple, showing a large monophasic domain over nearly the whole concentration range up to 90 wt% $C_8E_8CH_2COOH$ and over a wide temperature range. Macroscopically, the monophasic samples are colorless, clear, and isotropic liquids of relatively low viscosity. The only exceptions are the clouding phenomenon at higher temperatures, typical for nonionic surfactants, and the liquid-liquid-phase separation in a small concentration range at very low $C_8E_8CH_2COOH$ concentrations. Clouding is observed for the pure acid $C_8E_8CH_2COOH$ with and without 0.25 $CaCl_2$ but is almost completely suppressed after half neutralization of $C_8E_8CH_2COOH$ with NaOH. The disappearance of clouding can be explained by the transformation of the pseudo-nonionic surfactant $C_8E_8CH_2COOH$ to a more ionic one, giving rise to repulsive electrostatic forces between the charged carboxylate moieties that counteract the aggregation of micelles. $C_8E_8CH_2COOH$ exhibits a lower critical solution temperature (LCST) of 66°C between 16–24 wt% ($0.006 \leq x(C_8E_8CH_2COOH) \leq 0.009$) of surfactant. The addition of $CaCl_2$

lowers the LCST to a temperature of 49°C. The lowering of the cloud point is especially significant at higher concentrations, shifting the LCST to a one order of magnitude larger $C_8E_8CH_2COOH$ mole fraction of 0.09 (72 wt%). On the one hand the cloud point is lowered due to a salting out effect induced by the addition of $CaCl_2$, which dehydrates the surfactant headgroups, and on the other hand Ca^{2+} ions can induce attractive bridging between adjacent micelles.

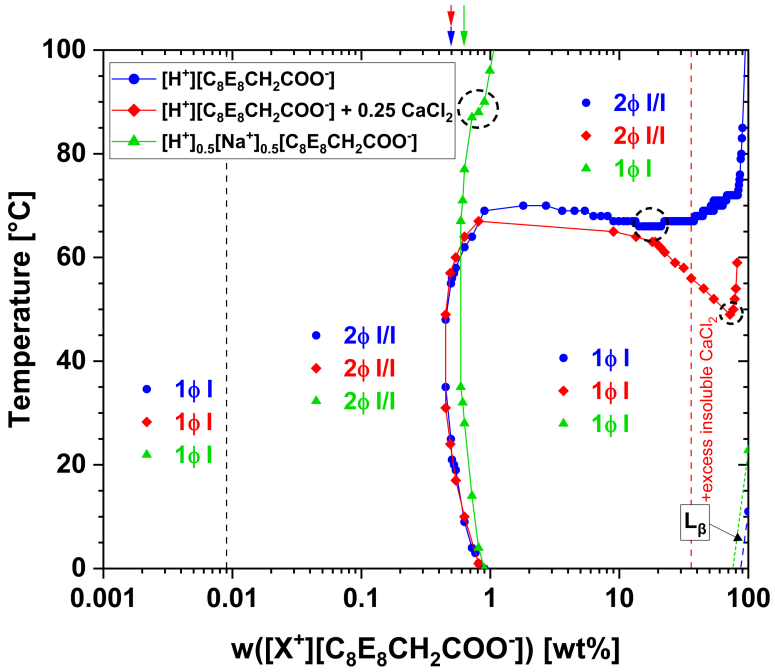

Fig. II.1. Binary phase diagrams of $C_8E_8CH_2COOH$ (here denoted as $[H^+][C_8E_8CH_2COO^-]$), $C_8E_8CH_2COOH$ with 0.25 $CaCl_2$ per $C_8E_8CH_2COOH$ molecule, and $[H^+]_{0.5}[Na^+]_{0.5}[C_8E_8CH_2COO^-]$ in water. The $C_8E_8CH_2COOH$ concentration is given in wt% on a logarithmic scale. Compositions between 0.009 wt% and 90 wt% surfactant in water were visually investigated from 0 to 100°C in all three cases. For $C_8E_8CH_2COOH$ and $[H^+]_{0.5}[Na^+]_{0.5}[C_8E_8CH_2COO^-]$, higher concentrations up to almost 100 wt% surfactant were also investigated. The precision of the phase boundaries in temperature is ±1°C. The red dashed line at a higher concentration indicates the solubility limit of $CaCl_2$, above which the mole ratio of $CaCl_2$ and surfactant in the examined liquid deviates from 0.25. Black dashed circles indicate the lower critical solution temperatures. The colored arrows at the top x-axis indicate the respective critical micelle concentrations at 25°C. 1ϕ I: Single isotropic phase. 2ϕ I/I: Two isotropic phases in equilibrium. L_β: Semi-crystalline lamellar phase. The same phase diagrams are shown as a function of the surfactant mole fraction in **Fig. A.2** and as a function of the surfactant concentration in mol·L^{-1} in **Fig. A.3**.

Yet, in all cases, the extremely broad range of the monophasic low-viscous domain is remarkable. Apart from a small semi-crystalline L_β phase at low temperatures and high surfactant concentrations (≥ 90 wt%), which will be further described in **Chapter III.**, no liquid crystalline (LC) phases can be detected. This is similar to the phase diagram of C_8E_6, where only a small hexagonal domain at around 60 wt% of surfactant and below 20°C has been detected [6], and even more similar to C_8E_8 and C_8E_{12}, for which no LC formation is reported [5].

If $C_8E_8CH_2COOH$ is compared to the well-studied nonionic $C_{12}E_5$ [5,37], the differences are striking:

(i) Unlike $C_{12}E_5$, $C_8E_8CH_2COOH$ cannot form lyotropic liquid crystals at any temperature or composition (with the exception of a semi-crystalline L_β phase at very high surfactant concentrations and low temperatures).
(ii) Moreover, the LCST that is usually observed at a few wt% surfactant concentration, and in the case of $C_{12}E_5$ at a temperature around 30°C, is found at 66°C at a ten times higher surfactant concentration (≈20 wt%) for $C_8E_8CH_2COOH$.
(iii) Finally, there is a seldom described miscibility gap occurring at low $C_8E_8CH_2COOH$ concentrations without any additive, which is insensitive to temperature. A rare example of a similarly shaped biphasic region at very low surfactant concentrations of a single surfactant was reported by Yan *et al.* [38] for the perfluorinated tetrabutylammonium perfluorooctanoate.

The absence of zones with hexagonal or cubic phases is a strong hint towards the absence of sphere-to-cylinder growth, and therefore also towards interdigitation of headgroups between neighboring micelles. Indeed, the alkyl chain length is small: C_8 carboxylate solutions have been studied by SAXS/SANS combinations: The hydrocarbon core is always small (with a radius of around 1 nm), its size depends on concentration, and the aggregation number cannot go outside the range of 30–40 because of steric hindrances and since there cannot be a void in the center and, at the same time, the cross-sectional area per hydrocarbon chain cannot be less than 0.6 nm^2 in the absence of crystallization [39].

In all three cases (i.e., with and without the presence of Na^+ or Ca^{2+}), there is a special liquid-liquid phase separation at very low $C_8E_8CH_2COOH$ concentrations, yielding colloidal droplets. At room temperature, this coacervation domain ranges from 0.009 wt% to 0.52 wt% ($3.00 \cdot 10^{-6} \leq x(C_8E_8CH_2COOH) \leq 1.69 \cdot 10^{-4}$) of surfactant in the acid form. Within that regime, the turbidity decreases with decreasing surfactant concentration, until it can be seen only as a very light blueish haze. Note that the given lower limit corresponds to the limit of visual observability of any turbidity, and thus is somewhat arbitrary. The actual limit is even lower than that, but was not determined. Dynamic light scattering experiments at 25°C, see **Fig. A.4**, confirm the presence of aggregates with an average hydrodynamic radius in the order of 120–140 nm after an equilibration time of 17 h throughout the biphasic domain. As can be seen in **Fig. A.4**A, these droplets are also detectable at

0.0009 wt% $C_8E_8CH_2COOH$, below the limit of visual observability. With increasing equilibration time, the average size of the droplets increases through coalescence or Ostwald ripening, as demonstrated in **Fig. A.4**B. Adding $CaCl_2$ does not influence the phase boundaries of this biphasic regime, whereas the addition of NaOH slightly broadens the biphasic regime. In presence of 0.5 NaOH per surfactant molecule, the upper limit increases to 0.63 wt% ($x([C_8E_8CH_2COO^-]) = 2.11 \cdot 10^{-4}$) at room temperature. Note that the notation $[C_8E_8CH_2COO^-]$ includes all surfactant species, i.e., those with H^+ as "counterion" as well as those with Na^+ as counterion. This indicates a pH-dependence of the phase boundaries of the biphasic regime, which will be explained in **Chapter III**.

From the phase diagrams, it is evident that the miscibility gap, i. e., the liquid-liquid phase separation at very low $C_8E_8CH_2COOH$ concentrations, is not linked to the cloud point phenomenon that occurs at higher concentrations and temperatures with a critical point around 20 wt% and 66°C. The latter is well known and understood in the case of numerous nonionic surfactants of generic formula $C_{2j}E_j$, for which a sphere-to-rod transition can be obtained without molecular packing constraints [40–42]. As will be confirmed in **Chapter III.**, the miscibility gap is caused by surfactant auto-coacervation with a mechanism differing from the classical clouding phenomenon. The appearance of coacervates in simple binary surfactant systems is very unusual, usually only appearing in the case of gemini, i.e., double chain, surfactants [16,43,44]. This phenomenon occurring with a simple, commercially available, cheap surfactant is of particular interest. Therefore, it will be considered in detail in **Chapter III**. The present chapter is instead focused on the structures in the large monophasic region of the phase diagrams.

II.4.2. Surface Tension

The equilibrium surface tensions of aqueous surfactant solutions at 25°C are shown as a function of the mole fraction of $C_8E_8CH_2COOH$ in **Fig. II.2**A. From the initial slope, assuming a dissociation factor of 2, an area per headgroup of about 0.97 nm^2 can be inferred by the Gibbs adsorption isotherm. According to literature [45] on alkyl-EO_8-polyoxyethylene glycol ethers, the area per headgroup is between 0.5 nm^2 and 0.8 nm^2 at 25°C. This is in rough agreement with the value measured here. However, the value depends on the film geometry (curved versus planar), volume conservation, and film flexibility [26,46] so

that it is difficult to infer more precise information from this value. Surprisingly, the surface tension increases again after the minimum related to the CMC, see also **Fig. II.2**B. Usually, this increase is the consequence of surface-active impurities. In this case, remaining non-ethoxylated or only lightly ethoxylated surfactant molecules or esters of the type $C_8E_xCH_2COOE_yC_8$ would be possible candidates for "impurities" that are more surface active than the average surfactant. Using purification procedures such as suggested by Lunkenheimer *et al.* [47] with a fully automated apparatus, no significant differences in the surface tension minimum were observed. Since there is no reason for the dissociation of the carboxylic acid group to increase on increasing the surfactant concentration beyond the CMC, this phenomenon is rather ascribed to some excess surfactant beyond the monolayer, including an ''interphase", where the monolayer is completed by some adsorbed vesicles or hemi-micelles. A review of such effects has been published by Thomas and Penfold [48]. Interestingly, the interphase, which is thicker than a simple dense monolayer, does not evolve at higher concentrations, as can be inferred from the pendant drop tensiometry results, also shown in **Fig. II.2**A. The best description of the air water ''interphase" for $C_8E_8CH_2COOH$ is the Gibbs monolayer plus a significant number of micelles, adsorbed on the monolayer with interdigitation of the micelles and the headgroup in the monolayer. The increase of surface tension with increasing concentration is possible only if something adsorbs below the monolayer condensing it. This has been demonstrated by Langevin and coworkers in the case of added polyelectrolytes [49]. In the present case, there is no other possibility than adsorbing micelles that are present in the bulk.

From additional surface tension measurements, see **Fig. II.2**B and **II.2**C, it can be deduced that neither the CMC values, i.e., the free energy of micelle formation, nor the subsequent increase in surface tension above the CMC linked to interphase formation, is significantly affected after titration with sodium hydroxide or calcium chloride. That the increase in surface tension is roughly independent of counterions, has been shown and explained by Bergeron *et al.* [50]. The rather small effect of sodium and calcium on the CMC was also expected, since the terminal carboxylic head group is only a very minor part of the whole hydrophilic part of the surfactant. Its charge influence on the solubility of the monomers is negligible, as it is on the area per headgroup. In fact, the triblock copolymer behaves more like a nonionic surfactant rather than an ionic one, at least, as far as the CMC is concerned.

The correlation of the CMC and the upper limit of the coacervate regime is striking, see

Fig. II.2C, suggesting that the coacervation only occurs below the CMC. The CMC found for $C_8E_8CH_2COOH$ is 9.4 mmol·L^{-1} (0.51 wt%), which is close to the CMC reported for nonionic C_8E_8 [51,52], while the CMC of $[H^+]_{0.5}[Na^+]_{0.5}[C_8E_8CH_2COO^-]$ is measured to be only slightly higher at 11.3 mmol·L^{-1} (0.62 wt%), as expected for introducing charge. An explanation of this correlation will be given in **Chapter III**.

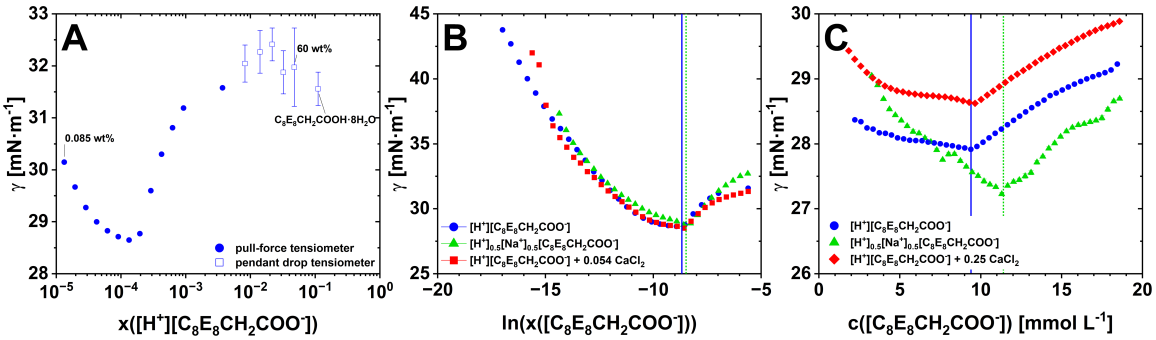

Fig. II.2. (A) Equilibrium surface tension γ as a function of the $C_8E_8CH_2COOH$ (here also denoted as $[H^+][C_8E_8CH_2COO^-]$) mole fraction x($[H^+][C_8E_8CH_2COO^-]$). Data points were obtained by pull-force or pendant drop tensiometry at 25°C in a concentration range from 0.085 wt% (x($C_8E_8CH_2COOH$) = $2.9\cdot10^{-5}$) to 78.95 wt% (x($C_8E_8CH_2COOH$) = 0.11111), where eight water molecules are available for each surfactant molecule. (B) Equilibrium surface tension γ obtained by pull-force tensiometry at a temperature of 25°C as a function of the natural logarithm of the surfactant mole fraction. Isotherms are shown for $C_8E_8CH_2COOH$, $C_8E_8CH_2COOH$ in presence of 0.054 $CaCl_2$ per surfactant molecule, and $C_8E_8CH_2COOH$ after half neutralization with NaOH. The vertical solid blue line indicates the upper limit of the coacervate regime for $C_8E_8CH_2COOH$ with and without $CaCl_2$, while the dotted green line indicates the upper limit for $[H^+]_{0.5}[Na^+]_{0.5}[C_8E_8CH_2COO^-]$. (C) Equilibrium surface tension γ isotherms at 25°C of $C_8E_8CH_2COOH$, $C_8E_8CH_2COOH$ in presence of 0.25 $CaCl_2$ per surfactant molecule, and $[H^+]_{0.5}[Na^+]_{0.5}[C_8E_8CH_2COO^-]$ around the minimum corresponding to the CMC. The obtained CMCs are c($[H^+][C_8E_8CH_2COO^-]$) = 9.4 mmol·L^{-1} (0.51 wt%), c($[H^+][C_8E_8CH_2COO^-]$ + 0.25 $CaCl_2$) = 9.7 mmol·L^{-1} (0.52 wt%), and c($[H^+]_{0.5}[Na^+]_{0.5}[C_8E_8CH_2COO^-]$) = 11.3 mmol·L^{-1} (0.62 wt%). Note that in (C) $[H^+]_{0.5}[Na^+]_{0.5}[C_8E_8CH_2COO^-]$ was used as obtained by mixing $[Na^+][C_8E_8CH_2COO^-]$, obtained by the approach described in **Section II.3.1.**, and $C_8E_8CH_2COOH$, whereas in (B) NaOH was added to the initial aqueous solution of $C_8E_8CH_2COOH$.

II.4.3. Osmotic Pressure

The osmotic pressure as well as the excess chemical potential of water in mixtures of $C_8E_8CH_2COOH$ and water at 25°C are shown as a function of the mole fraction of water in **Fig. II.3**. This representation is equivalent to the equilibrium relative humidity [53]. If applicable, the micellar repeat distance D*, as obtained from SAXS data given in **Section II.4.4.**, is also given. Surprisingly, the osmotic pressure of the "dry", i.e., nearly hydration-water-free $C_8E_8CH_2COOH$ in its acidic form is so high that this surfactant would easily dry potassium chloride or potassium sulfate, but not calcium chloride. This is very peculiar for a large, uncharged molecule (0.85 nm^3), and can only be explained, once the microstructure

is known, see **Section II.4.4**. As seen in **Fig. II.3**, two different regimes can be distinguished. The osmotic pressure increases more rapidly as a function of $x(H_2O)$ below 60 wt% $C_8E_8CH_2COOH$ than it does at higher surfactant concentrations. If **Fig. II.3** is replotted as a function of the mole ratio of water and $C_8E_8CH_2COOH$, see **Fig. A.5**, it can be easily seen that the osmotic pressure increase is much stronger for lower ratios than it is for higher ratios. A transition from a small increase to a rather sharp increase can be located around 10 to 30 water molecules per surfactant molecule (containing eight EO groups), which is in good agreement with the typical number of three hydrating water molecules per EO group, with a first hydration layer of 1–2 water molecules per EO group [54–57]. If there are only eight water molecules available per surfactant molecule, there is no longer any bulk water and only hydration water remains.

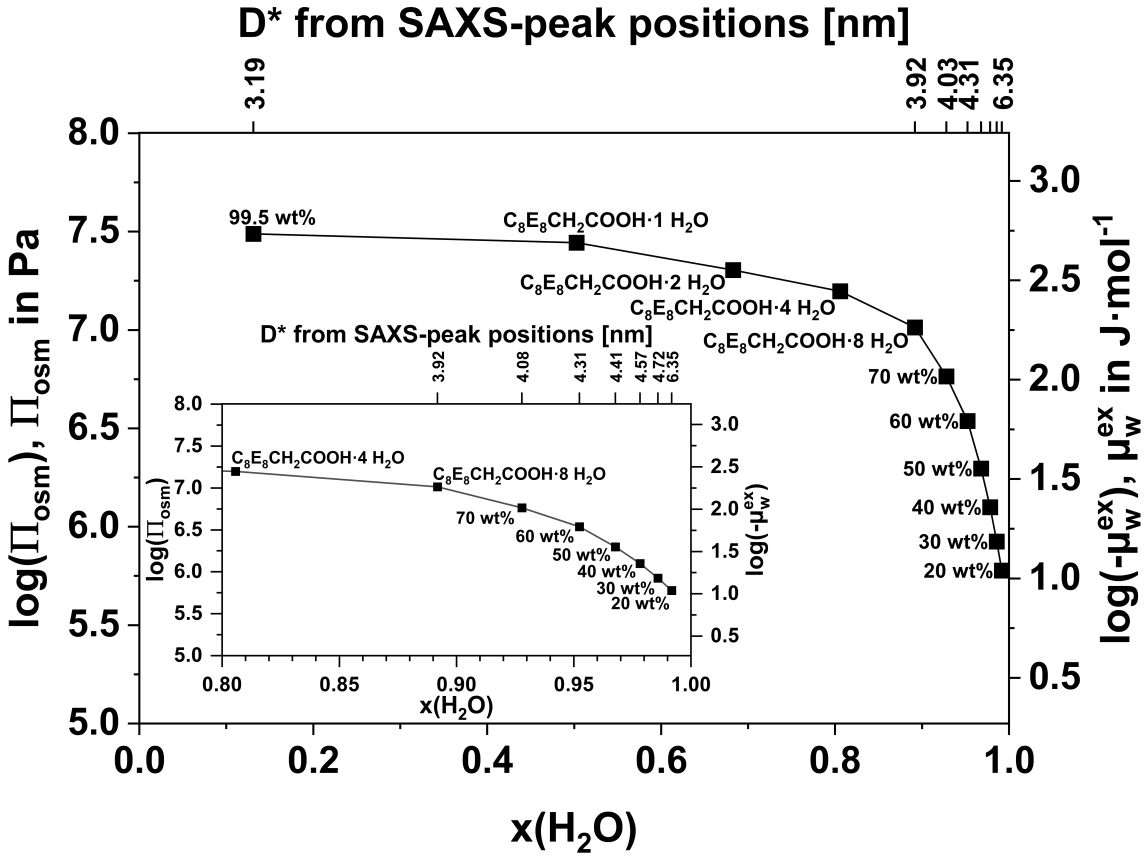

Fig. II.3. The decadic logarithm of the osmotic pressure Π_{osm}, as well as the decadic logarithm of the negative excess chemical potential of water μ_w^{ex}, are plotted as a function of the mole fraction of water $x(H_2O)$ of several binary mixtures of $C_8E_8CH_2COOH$ and water. If known, the correlation length D* for the sample, calculated from the respective peak position in the SAXS spectrum ($D^* = 2\pi \cdot q^{-1}$), is shown on the non-linear top-axis. Note that D* values for samples containing 20 wt% or 30 wt% surfactant were calculated from the structure factors S(q) obtained from model fits, see **Section II.4.4.**, because no pronounced structure factor peaks are visible in the spectra. Π_{osm} was calculated from the water activity a_w , obtained by vapor pressure osmometry, according to eq. (II.3.4). The segment with $0.8 \leq x(H_2O) \leq 1.0$ is magnified in the insert. The excess chemical potential of water μ_w^{ex} is given by eq. (II.3.3). See **Fig. A.5** for the x-axis showing the mole ratio of water and $C_8E_8CH_2COOH$.

The excess chemical potential of water reflects the repulsive force between micellar cores, which have an average contact distance t_w.

$$t_w = D^* - 2R_c \,, \qquad \text{(II.4.1)}$$

where D* is the center-to-center distance of two micelles, as obtained from the SAXS peak position in **Section II.4.4.**, and R_c is the radius of the hydrophobic hydrocarbon core. To get a deeper insight into the structure, the same data can be replotted with another x-scale. Similar to the data representation used to present atomic force microscopy (AFM) or surface force apparatus (SFA) data, one can use as x-axis the value t_w, i.e., the minimum distance between two hydrocarbon cores of two adjacent micelles or, in other words, the thickness of the hydrophilic pseudo-"interphase", see **Fig. II.4**.

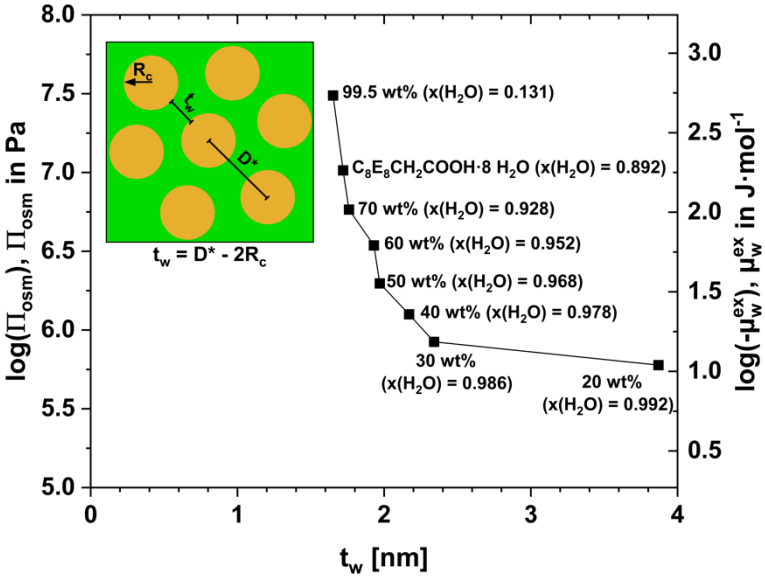

Fig. II.4. Decadic logarithm of the osmotic pressure and of the negative excess chemical potential of water μ_w^{ex} as a function of the respective thickness between hydrocarbon chain-head group interfaces of adjacent micelles $t_w = D^* - 2R_c$ for different mixtures of $C_8E_8CH_2COOH$ and water. A graphical illustration of t_w is shown as a schematic drawing, where orange spheres represent hydrocarbon cores dispersed in a hydrophilic medium (green). D* was obtained from the peak positions in the SAXS spectra ($D^* = 2\pi \cdot q^{-1}$). D* values for samples containing 20 wt% or 30 wt% surfactant were calculated from the structure factors S(q) obtained from model fits, see **Section II.4.4.**, because no pronounced structure factor peaks are visible in the spectra. R_c was derived from the core-shell-sphere model and sphere model fits of the SAXS data, respectively, as will be shown in **Section II.4.4**. Π_{osm} was calculated from the water activity a_w, obtained by vapor pressure osmometry, according to eq. (II.3.4). The excess chemical potential of water μ_w^{ex} is given by eq. (II.3.3).

Note that below 20 wt% $C_8E_8CH_2COOH$, which is not shown in **Fig. II.4** due to a lack of osmometry data, the minimum distance t_w between one micellar sphere and the surrounding 12 micellar spheres (in average) first increases as a result of an interplay between aggregation number and changes in the headgroup conformation, reflecting also the electrostatic

repulsion of the partially charged micelles. This has been discussed by Hayter and Pynn [58] and calculated by Sow-Hsin Chen in the form of a decoupling approximation [59,60]. Surprisingly, above 20 wt% of $C_8E_8CH_2COOH$, the osmotic pressure goes up with increasing concentration, but the distance t_w significantly goes down. This is a first hint at interdigitation, related to the low cost in free energy of interdigitation and consequently to a structure that may be called ‘‘osmotic brush”. For short polymers grafted at surfaces, the ‘‘mushroom”, ‘‘osmotic brush” and ‘‘dense layer” regimes are commonly found [61,62]. Considering the EO_8 headgroup as a short polymer, the interdigitation regime corresponds to the case of an “osmotic brush”. In $C_8E_8CH_2COOH$, the transfer of a free water molecule to the first hydration layer of the ethoxy group costs about 1.5 $k_B \cdot T$, which is the rotational entropy of a water molecule.

Interdigitation is known to occur in liquid crystalline L_β gel phases made of lipids [63], but is here evidenced, to our knowledge for the first time, for micellar solutions. This situation is also common for interdigitated polyelectrolytes [64], but in the present case of $C_8E_8CH_2COOH$, interdigitation is encountered with a relatively simple triblock surfactant, comprising one COOH group and 8 EO groups.

The increase of the osmotic pressure relative to t_w is especially sharp above 50 wt% $C_8E_8CH_2COOH$, suggesting that a significant degree of interdigitation starts to occur around this concentration. Note that the typical hydration layer of 3 H_2O molecules per EO group is exceeded only at surfactant concentrations below 55 wt%, which is why significant interdigitation is to be expected at higher surfactant concentrations. Above roughly 70 wt% $C_8E_8CH_2COOH$, where 13 H_2O molecules are available per surfactant molecule, the osmotic pressure increases sharply, whereas the distance t_w remains roughly constant. Beyond this surfactant concentration, there is not enough water present to fully form the first hydration layer of the EO groups (1.5 H_2O/EO, i.e., 12 $H_2O/C_8E_8CH_2COOH$). This is also reflected by the deviation from the linear relation between physical density and concentration above 60 wt%, see **Fig. A.6** and **Table A.2**.

II.4.4. Small- and Wide-Angle X-Ray Scattering – Inference of Microstructures

Naive fitting of SAXS spectra with adjustable radii of micelles and taking the repulsive contact potential as parameters always produces excellent fits of the scattering patterns, however, with scattering length densities (SLDs) and radii that are not consistent with any realistic packing [65]. This danger of producing excellent fits via unphysical packings disappears when spectra are fitted over large concentration ranges and with self-consistent values of scattering length densities and micellar radii, since molecular volumes and electronic densities are known and cannot be freely varied. In this example of constrained fitting, the only free fitting parameters are the aggregation numbers for the form factor, so the number of molecules per micelle, and the hydration of the headgroups, i.e., the number of water molecules bound by more than 1 $k_B \cdot T$ of free energy to a headgroup. Consequently, here this approach is used, as initiated by Hayter [66] to infer quantitative information over a large q-range and in absolute scale (cm^{-1}), along the whole dilution line.

In **Figs. II.5** and **A.7**, the SWAXS spectra obtained for salt-free $C_8E_8CH_2COOH$ solutions are plotted in linear and logarithmic scale, respectively. Note that broad peaks in the WAXS region ($q \geq 8\ nm^{-1}$) are linked to intermolecular distances, i.e., to packings of water, hydrocarbon chains, and headgroups, as well as their conformations, in the liquid state. The WAXS regime is not further considered here, but shows that there is no crystallization involved. In the SAXS regime, only a broad peak of the form factor P(q), produced by the sensitivity of SAXS to the internal core-shell contrast, is observed at 10 wt% and 20 wt% $C_8E_8CH_2COOH$. At 30 wt%, a peak of the structure factor S(q) emerges, which becomes more pronounced with increasing surfactant concentration. Up to 60 wt% $C_8E_8CH_2COOH$, the underlying form factor peak is clearly visible, before it starts to vanish at around 70 wt% of surfactant. The form factor also presents a characteristic shoulder at lower surfactant concentrations with a local minimum around $q = 0.6\ nm^{-1}$ at 50 wt% $C_8E_8CH_2COOH$, which vanishes at higher surfactant concentrations (≥60 wt%). This oscillating behavior within the low q-range is characteristic of a classical core-shell structure in an aqueous medium (L_1 phase), i.e., here, a compact hydrocarbon core surrounded by hydrated headgroups [67]. The absence of these oscillations at higher surfactant concentrations is characteristic of a two-component system: All hydrocarbon chains are confined in small compact hydrocarbon droplets that are surrounded by more or less hydrated headgroups. There

is no more bulk solvent surrounding the micelles and the headgroups must interdigitate. The micelles are no longer present as separated entities, and the microstructure rather consists of small confined liquid C_8 hydrocarbon cores, separated by incompressible films containing the EO chains, the COOH groups and at most a number of water molecules necessary to fully hydrate the headgroups. This solvent-free phase will be denoted as L_1'. The transition from a classical aqueous core-shell phase to an interdigitated phase without bulk solvent also explains the vanishing of the form factor peak due to the change in contrast, i.e., only smaller hydrocarbon cores remain dispersed in a hydrophilic medium, instead of a core-shell structure in a solvent. It is also important to note that the decrease of the intensity observed at very low q is often an artifact from the subtraction of the empty capillary.

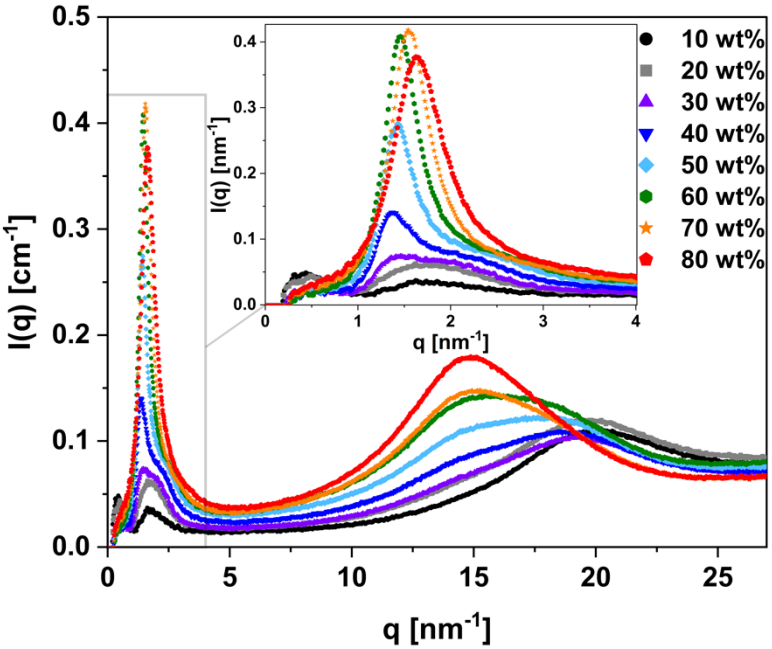

Fig. II.5. SWAXS data of binary mixtures of 10 wt% to 80 wt% $C_8E_8CH_2COOH$ and water in linear scale. The inset is a magnification of the the SAXS q-range of the same data, where a peak occurs. The same data are presented in logarithmic scale in **Fig. A.7**.

Extending the data to even higher concentrations, the SWAXS spectra of neat $C_8E_8CH_2COOH$ (≥99.5 wt%, ≤0.15 H_2O molecules per surfactant molecule) and neat half-neutralized $[H^+]_{0.5}[Na^+]_{0.5}[C_8E_8CH_2COO^-]$ (≥99.2 wt%, ≤0.30 H_2O molecules per surfactant molecule) are given in linear scale in **Fig. II.6** and in logarithmic scale in **Fig. A.8**. For comparison, the spectra of the same surfactants in presence of 8 H_2O molecules per surfactant molecule, i.e., in presence of one hydrating water molecule per EO group, forming the inner hydration layer, are also shown. 8 H_2O molecules per surfactant molecule are available at a concentration of 79 wt% $C_8E_8CH_2COOH$, thus the spectrum is almost identical to

the spectrum of 80 wt% $C_8E_8CH_2COOH$ given in **Figs. II.5** and **A.7**. In all four cases it is evident that the structure is not core-shell but resembles the interdigitated L_1' phase. If half of the carboxylic acid groups are deprotonated and have Na^+ as their counterion, the shape of the peak remains identical. The scattering intensity increases due to an increase in scattering contrast. A slight shift of the peak position to lower q, which is more pronounced in presence of water, suggests that aggregates are slightly bigger with sodium as counterion. Nevertheless, no significant structural change is induced by transforming half of the surfactant molecules to their sodium salt. Another important consequence of the identical peak shape is that the sodium ions are not bound to an interface but are dispersed in the hydrophilic headgroup layer, i.e., the carboxylate groups with their sodium counterions can move freely. Note that Rothe *et al.* [68] suggested that di- and trivalent metal cations are confined to linear channels within the interdigitated headgroup medium in the case of a similar surfactant with a slightly smaller headgroup, $C_8E_5CH_2COOH$. While this cannot be fully excluded without further investigations in the present case, there is no direct indication of such a confinement.

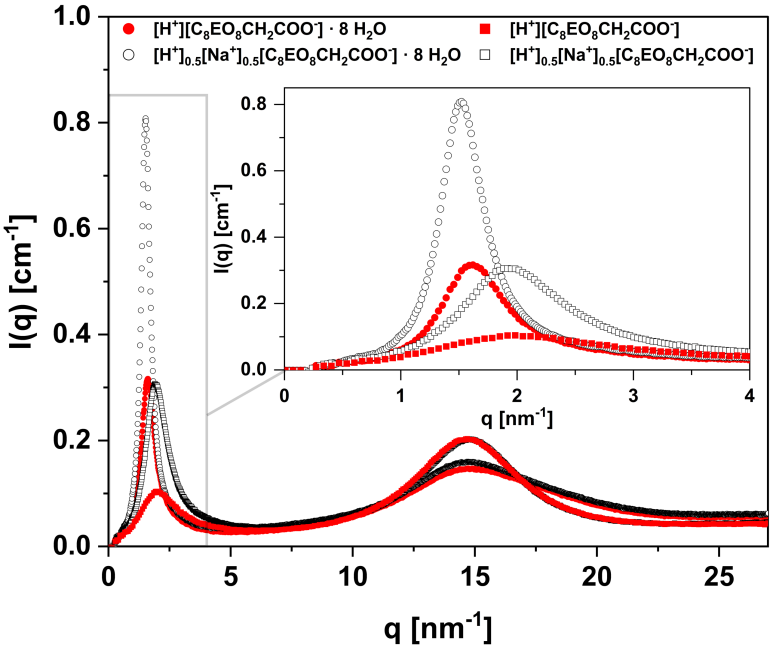

Fig. II.6. SWAXS data of the neat surfactants $C_8E_8CH_2COOH$ (≥99.5 wt%, ≤0.15 H_2O per surfactant molecule), here denoted as $[H^+][C_8E_8CH_2COO^-]$, and $[H^+]_{0.5}[Na^+]_{0.5}[C_8E_8CH_2COO^-]$ (≥99.2 wt%, ≤0.30 H_2O per surfactant molecule), as well as of both surfactants in presence of 8 H_2O molecules per surfactant molecule in linear scale. The inset is a magnification of the SAXS q-range of the same data, where a peak occurs. The same data are presented in logarithmic scale in **Fig. A.8**.

Following the fitting strategy with constrained values, keeping only hydration and aggregation numbers as adjustable quantities, allows for a description of the spectra of the

dilution line shown in **Figs. II.5** and **A.7**, as well as of the spectra shown in **Figs. II.6** and **A.8**. Using the SasView package (version 5.0.2) [34], two different models were used for the two different regimes. For the L_1 phase, a core-shell sphere form factor with a Schulz polydispersity distribution of the core radius and the shell thickness and a Hayter-Penfold RMSA structure factor [35,36] was used. This model could be quite successfully applied for surfactant concentrations of up to 70 wt%, even though there should no longer be a core-shell structure due to the absence of bulk water above 60 wt%. Instead, for the L_1' phase (above 60 wt%) a simple sphere form factor and an effective Hayter-Penfold RMSA structure factor [35,36] was used. The whole RMSA structure factor used for the sphere model can be understood as an effective RMSA structure factor, because there are no freely moving spheres interacting with each other, but spheres separated by more or less compressible, hydrated headgroup layers. The volume fraction of the spheres is in this case also fitted and corresponds to the effective volume fraction of the cores.

In **Fig. II.7**, the sensitivity of the sphere model fit to the sphere radius, i.e., to the hydrocarbon core radius R_c, is visualized exemplary for the data of the concentrated samples given in **Figs. II.6** and **A.8**. The solid lines represent the best fits, while the dashed lines represent a change of the radius by ±30%. It is clearly evident that the precision is better than 30%, which corresponds to a precision in the aggregation number N_{agg} better than 10%.

The rest of the fits to the simple sphere model is shown in **Fig. II.8**A. All best fits to the core-shell sphere model of samples containing 10 wt% to 80 wt% $C_8E_8CH_2COOH$ are presented in **Fig. II.8**B. The parameters of the sphere model fits are given in **Table A.3**, while the parameters of the core-shell sphere model fits are given in **Table A.4**. As can be seen in **Fig. II.8**B, the core-shell sphere model allows a good description of the peak up to 70 wt% $C_8E_8CH_2COOH$ but deviations become more significant at 80 wt%. From **Figs. II.7** and **II.8A** it is evident that the simple sphere model can reproduce the peak positions but not the exact peak shapes, which is to be expected due to oversimplification. The simple sphere model works best at the highest concentrations, see **Fig. II.7**C and **II.7**D. The transition from the core-shell L_1 phase to the interdigitated L_1' phase is not sharp, but continuous with a transition state expected between 50 wt% (30 H_2O molecules per surfactant molecule) and 70 wt% $C_8E_8CH_2COOH$ (13 H_2O molecules per surfactant molecule) due to hydration of the headgroups. Indeed, both models yield similar radii and aggregation numbers in this

range. Since the scattering length density of the shell, sld_shell, is a fitted parameter in the core-shell sphere model, it is important to check if the value is reasonable. The two possible limiting values are known as the scattering length density of the water-free headgroups, sld_head = $10.84 \cdot 10^{-4}$ nm^{-2}, and the scattering length density of water, sld_solvent = $9.41 \cdot 10^{-4}$ nm^{-2}. The scattering length density of the shell can be in between those two values, scaling with the volume fraction of headgroups in the shell ν_{head} according to

$$\text{sld\_shell} = \nu_{head} \cdot \text{sld\_head} + (1-\nu_{head}) \cdot \text{sld\_solvent} . \qquad \text{(II.4.2)}$$

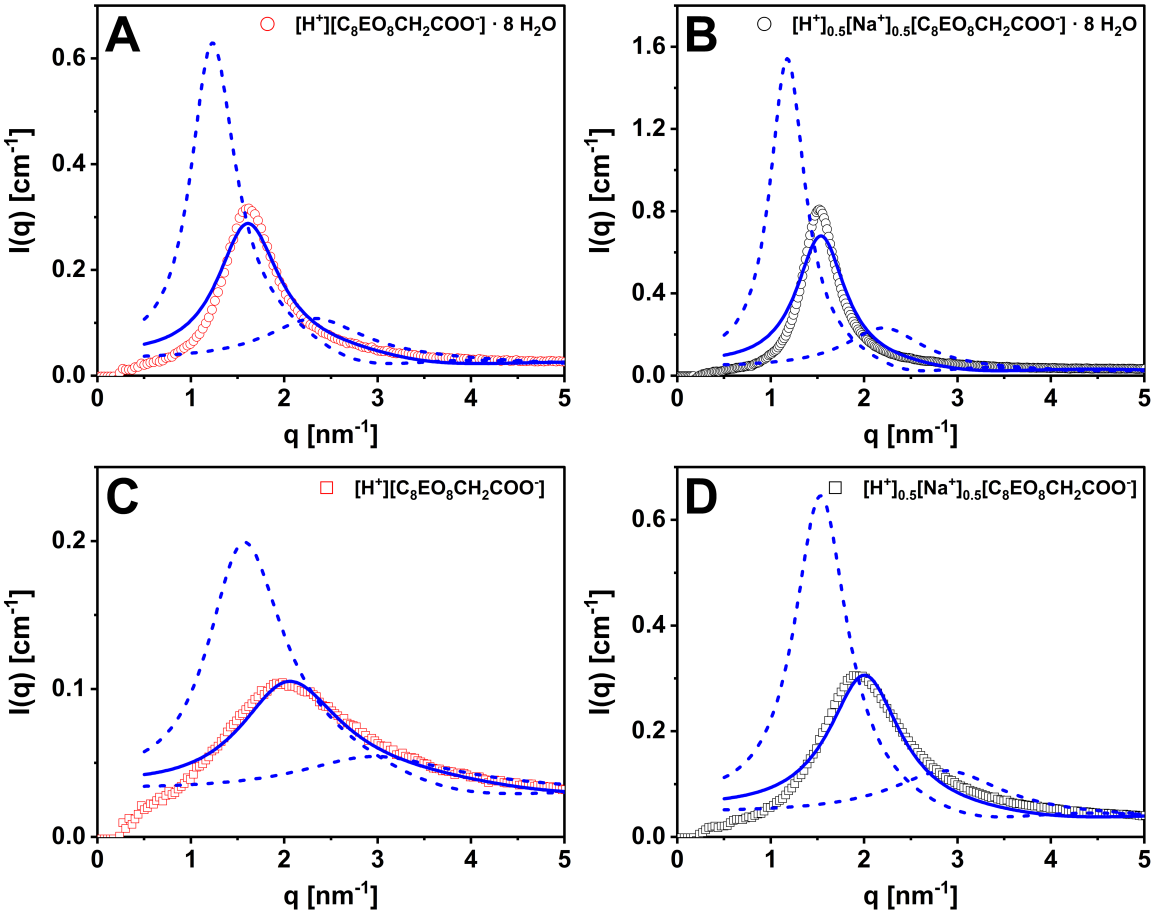

Fig. II.7. The data points correspond to the SAXS peaks of the spectra shown in **Figs. II.6** and **A.8**: (A) $C_8E_8CH_2COOH \cdot 8\ H_2O$, (B) $[H^+]_{0.5}[Na^+]_{0.5}[C_8E_8CH_2COO^-] \cdot 8\ H_2O$, (C) $C_8E_8CH_2COOH$ (≥99.5 wt%, ≤0.15 H_2O per surfactant molecule), and (D) $[H^+]_{0.5}[Na^+]_{0.5}[C_8E_8CH_2COO^-]$ (≥99.2 wt%, ≤0.30 H_2O per surfactant molecule). The solid lines represent the best fits to a sphere form factor with the radius R_c and an effective Hayter-Penfold RMSA structure factor. Changes in the fits by variation of R_c by ±30% are indicated as dashed lines. The fitting parameters and results can be inferred from **Table A.3**.

The obtained ν_{head} can be used to approximate the mole ratio of water and surfactant (headgroups) in the shell, r_{shell}. Comparing r_{shell} to the actual mole ratio given by the sample composition, see **Table A.4**, it is clear that r_{shell} exceeds the actually available mole ratio above 50 wt% $C_8E_8CH_2COOH$. Therefore, the sphere model is considered to be more

suitable above 50 wt%, despite the core-shell sphere model producing seemingly better fits. The obtained hydrocarbon core radius is close to the Tanford length, i.e., the maximum length of the hydrocarbon C_8 chain in the liquid state, of 1.16 nm [69] in all cases up to 70 wt%. At 80 wt%, the radius starts to decrease and reaches a minimum value of around 0.8 nm in the nearly water-free state, indicating that headgroup interdigitation is accompanied by a certain degree of hydrocarbon chain interdigitation. Accordingly, the aggregation number is constant around $N_{agg} \approx 30$ up to around 70 wt%, before it decreases at higher concentrations and reaches a minimum of $N_{agg} = 8$ in the nearly water-free state. The area per molecule can be determined without ambiguity to be $a \approx 0.60$ nm^2 in the non-interdigitated state, which is reasonable compared to typical values reported for C_iEO_j surfactants [45]. Headgroup interdigitation at higher surfactant concentrations results in a significant increase of the area per molecule, which is especially sharp below a mole ratio $n(H_2O)/n(C_8E_8CH_2COOH) < 8$, i.e., when there is an insufficient number of water molecules available to fill the inner hydration layer of the headgroups. In the nearly water-free state, an area per molecule close to 1 nm^2 is found. Since the aggregation number does not increase over the whole concentration range, a significant steric constraint, hindering any micellar growth through a decrease of the area per molecule, is indicated. Therefore, a sphere-to-rod transition or a shape inversion, common for classical $C_{2j}E_j$ surfactants, is impossible. Deprotonation of half of the carboxylic acid groups with NaOH leads to an increase of the aggregation number, i.e., to a decrease of the area per molecule, compared to the acidic state. In presence of 8 H_2O molecules, where a certain degree of interdigitation occurs, the aggregation number increases from 23 to 38 and the area per molecule decreases from 0.67 nm^2 to 0.57 nm^2. The hydrocarbon radius of 1.31 nm suggested by the best fit to the sphere model is slightly larger than the maximum length of C_8 in the liquid state (1.16 nm). Since there is no sign of a semi-crystalline state of the chains in WAXS, and since in the liquid state the spherical radius cannot exceed the Tanford length of the C_8 chain, probably a slightly ellipsoidal shape is adopted. In the almost water free state, the aggregation number is increased from 8 to 17 and the area per molecule is decreased from 0.96 nm^2 to 0.74 nm^2 in the presence of sodium as counterion. This significant difference indicates that sodium could partially inhibit interdigitation, which should also lead to a more distorted, e.g., ellipsoidal, shape.

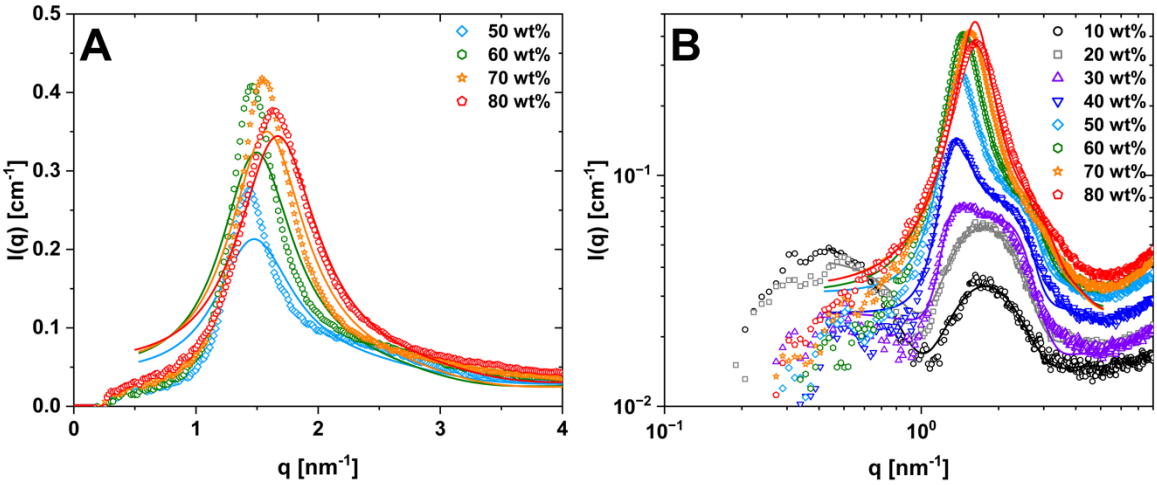

Fig. II.8. (A) The data points correspond to the SAXS peaks in linear scale of the spectra of samples containing 50 wt%, 60 wt%, 70 wt%, or 80 wt% $C_8E_8CH_2COOH$ shown in **Figs. II.5** and **A.7**. Solid lines represent the best fits to a sphere form factor and an effective Hayter-Penfold RMSA structure factor. The fitting parameters and results can be inferred from **Table A.3**. (B) The data points correspond to the SAXS peaks in logarithmic scale of the spectra of samples containing 10 wt% to 80 wt% $C_8E_8CH_2COOH$ shown in **Figs. II.5** and **A.7**. Solid lines represent the best fits to a core-shell sphere form factor and a Hayter-Penfold RMSA structure factor. The fitting parameters and results can be inferred from **Table A.4**.

The dependence of the main quantity governing self-assembly, i.e., of the area per molecule, on the surfactant concentration, as directly obtained from SAXS fits, is visualized in **Fig. II.9**. The area per molecule remains constant in the classical core-shell L_1 regime and starts to increase above 60 wt% due to headgroup interdigitation in the confined hydrocarbon droplet L_1' regime, which confirms the general rule of 2–3 H_2O molecules hydrating each EO group. It is evident that the transition between L_1 and L_1' is progressive, and the scattering can be fitted with both models in the surfactant concentration range from 60 wt% to 70 wt%. Above 70 wt%, however, the interdigitation is strong enough to increase the area per molecule. This increase becomes most significant above 80 wt%, i.e., once there is less than one water molecule available to hydrate each EO group, conforming to the general idea of an innermost hydration layer of one water molecule per EO group.

A scaled sketch of the microstructures corresponding to the two regimes, the core-shell L_1 phase and the interdigitated L_1' phase, confirmed by SAXS is shown in **Fig. II.10**. In most cases, the hydrocarbon cores contain around 30 octyl chains and the spherical shape is conserved due to steric constraints. Only at very high surfactant concentrations, where only water bound to the headgroups is left, interdigitation of the headgroups occurs and leads to a decrease of the aggregation number. A minimum aggregation number of 8 is found in absence of water.

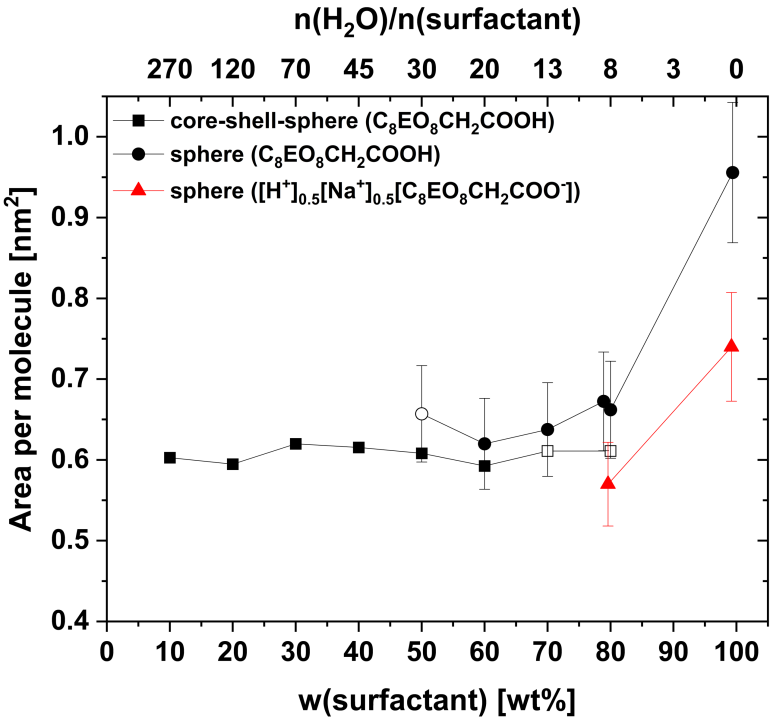

Fig. II.9. Area per molecule as a function of the surfactant concentration derived from SAXS spectra of various binary mixtures of $C_8EO_8CH_2COOH$ or $[H^+]_{0.5}[Na^+]_{0.5}[C_8E_8CH_2COO^-]$ and water by fitting the peaks to a core-shell sphere model or a sphere model, see **Figs. II.7** and **II.8** and **Tables A.3** and **A.4**. Empty symbols indicate that the results of the respective model are unfavored compared to the other model at the given concentrations, e.g., the core-shell model does not reflect the real situations at 70 wt% and 80 wt% due to the absence of bulk water. The error bars shown for the sphere model indicate the effect of an error in the hydrocarbon core radius R_c of ±10%. The mole ratio of water and surfactant is given on the non-linear top axis.

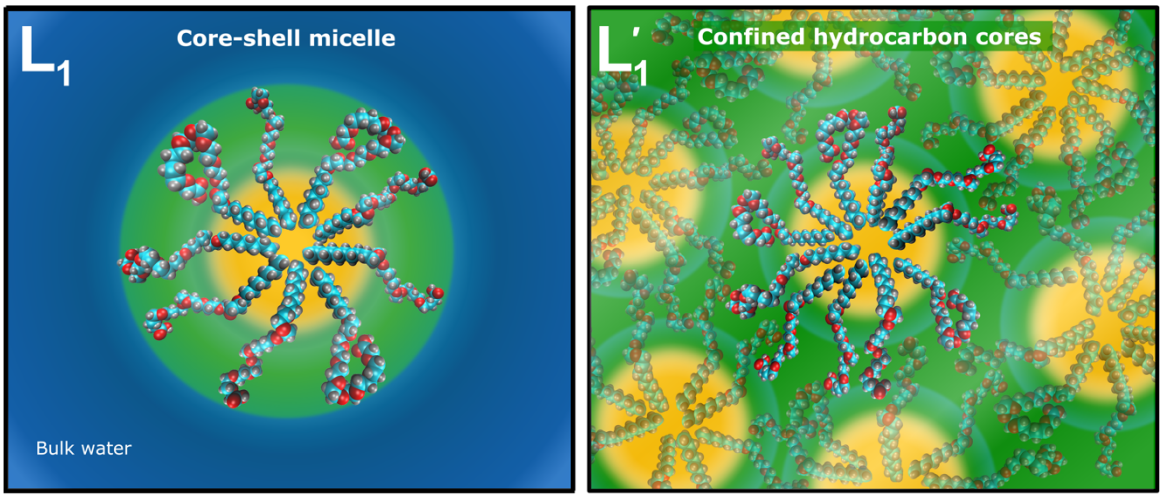

Fig. II.10. Scaled sketch of the two regimes observed in binary mixtures of $C_8E_8CH_2COOH$ and water. Left: The common core-shell structuring of micelles in the L_1 phase. A hydrocarbon core (R_c = 1.2 nm, shown in yellow) is surrounded by a hydrated ethoxy shell (shown in green). The micelles are dispersed in the aqueous bulk medium containing surfactant monomers at CMC (shown in blue). Right: The confined hydrocarbon core regime in the L_1' phase observed in water-poor mixtures is implies interdigitated headgroups and the absence of bulk water. As can be inferred from the osmotic pressure measurements, the compression of the water-poor ethoxy layers is responsible for the stability of the structure.

It is also noteworthy that the spherical shape and approximate size in the L_1 phase could be

confirmed by cryo-TEM imaging, both for $C_8E_8CH_2COOH$ at 2 wt% and 20 wt%, see **Fig. A.9**, and $[H^+]_{0.5}[Na^+]_{0.5}[C_8E_8CH_2COO^-]$ at 20 wt%, see **Fig. A.10**. The typical mean diameter obtained from cryo-TEM images by manual size distribution analysis using ImageJ (version 1.53m) [70] is around 3.3 ± 0.7 nm in all cases, which is reasonable compared to a diameter of around 4.4 nm obtained from SAXS fits (**Table A.4**), given the weak contrast.

Assuming that the micelles or hydrocarbon cores are in average surrounded by 12 other micelles or hydrocarbon cores as in a face-centered cubic lattice, the combined results of SAXS and vapor pressure osmometry, already given in **Fig. II.4**, can be represented in a representation initially proposed by Parsegian and co-workers [71] in the case of phospholipid bilayers. For this purpose, the osmotic pressure between two spheres $\Pi_{S\text{-}S}$, calculated from the measured osmotic pressure Π_{osm} between each micelle and its 12 neighbors according to

$$\Pi_{S\text{-}S} = \frac{\Pi_{osm}}{12}, \tag{II.4.3}$$

is plotted as a function of t_w, see **Fig. II.11**A. $\Pi_{S\text{-}S}$ is typically an exponentially decaying function of the distance t_w, with a decay length δ and a contact pressure $\Pi_{S\text{-}S}(0)$.

$$\Pi_{S\text{-}S}(t_w) = \Pi_{S\text{-}S}(0)\cdot\exp\left(-\frac{t_w}{\delta}\right) \tag{II.4.4}$$

A fit to this equation with a contact pressure $\Pi_{S\text{-}S}(0) = 2.3\cdot10^9$ N·m^{-2} and a decay length δ = 0.21 nm is also shown in **Fig. II.11**A. The contact pressure found here for $C_8E_8CH_2COOH$ is in the same order of magnitude as the contact pressure found for various nonionic glycolipid or zwitterionic phospholipid bilayers [72]. The decay length of 0.21 nm is about 2/3 of the decay length of pure water, which can be understood as the thickness of a water layer, and is typical for sugar, protein, and other polymer solutions [73].

Using this decay length and the Derjaguin approximation in the case of sphere-sphere [31,32], $\Pi_{S\text{-}S}$ between two micelles or hydrocarbon cores can be converted to the surface free energy W(h) between two planes at distance h. The relation of the force between the two spheres at distance h, $F_{S\text{-}S}(h)$, for two spheres of equal radius R and the surface free energy between two planes W(h) is given by

$$F_{S\text{-}S}(h) = \pi \cdot R \cdot W(h) \; . \qquad \text{(II.4.5)}$$

The force $F_{S\text{-}S}(h)$ is given by

$$F_{S\text{-}S}(h) = \pi \cdot R \cdot \int_h^\infty \Pi_{S\text{-}S}(0) \cdot \exp\left(-\frac{x}{\delta}\right) dx = \pi \cdot R \cdot \delta \cdot \Pi_{S\text{-}S}(h) \; . \qquad \text{(II.4.6)}$$

Combination of eqs. (II.4.5) and (II.4.6) yields a simple relation between the osmotic pressure between two spheres and the surface free energy between two planes.

$$W(h) = \delta \cdot \Pi_{S\text{-}S}(h) \qquad \text{(II.4.7)}$$

The resulting surface free energy W(h) for $C_8E_8CH_2COOH$ is given in $J \cdot m^{-2}$ and in $k_BT \cdot nm^{-2}$ as a function of the distance h between the two planes, which is here identical to the hydrophilic layer thickness t_w, in **Fig. II.11**B. This representation resembles data obtained by AFM with colloidal probes or SFA. The same exponential decay as in **Fig. II.11**A is also indicated. It can be seen that the measured surface free energies are well below 1 $k_BT \cdot nm^{-2}$ around h = 1.5 nm, resulting in surface free energies per molecule much smaller than 1 k_BT, obtained by multiplication with the respective area per molecule. Extrapolation to h = 0 suggests that $W(h) >> 1\ k_BT$, showing that the liquid hydrocarbon cores surprisingly behave like hard spheres.

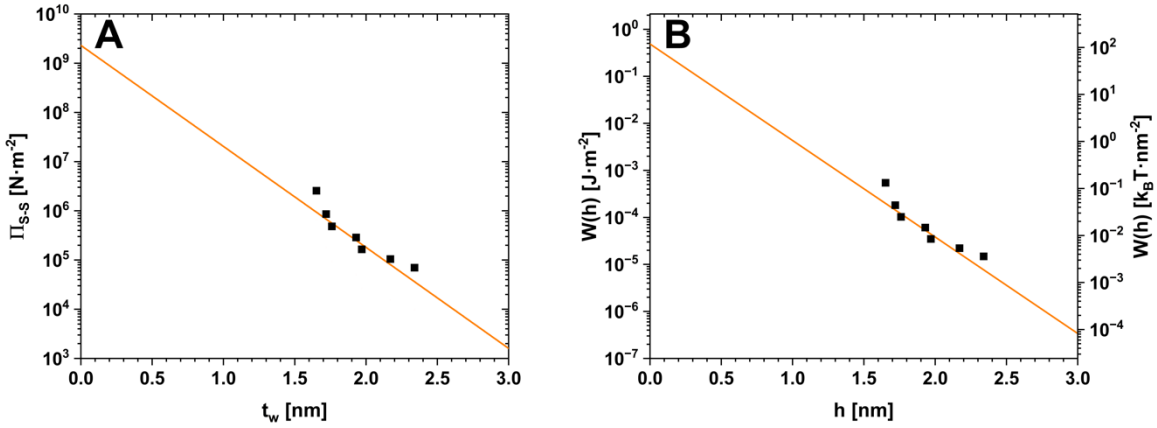

Fig. II.11. (A) Osmotic pressure between two spheres $\Pi_{S\text{-}S}$ at 25°C as a function of the thickness of the hydrophilic layer separating hydrocarbon cores of two adjacent micelles t_w. The data are identical to those shown in **Fig. II.4**, with the exception of the data for 20 wt% $C_8E_8CH_2COOH$ not being shown here. $\Pi_{S\text{-}S}$ is calculated from the measured osmotic pressure Π_{osm} using eq. (II.4.3). The solid line indicates an exponential decay with a decay length of 0.21 nm, described by the equation $\Pi_{S\text{-}S}(t_w) = 2.3 \cdot 10^9\ N \cdot m^{-2} \cdot \exp(-t_w/0.21163\ nm)$. (B) The surface free energy between two equivalent planes W(h), calculated from $\Pi_{S\text{-}S}$ using the Derjaguin approximation, see eqs. (II.4.5)–(II.4.7), as a function of the distance h between the two planes. The distance h is equivalent to the thickness t_w. The solid line indicates the same exponential decay as in (A), where $W(h) = 0.21163\ nm \cdot \Pi_{S\text{-}S}(h = t_w)$.

II.4.5. Ternary Phase Behavior with Hydrocarbon Oils

The steric constraint of $C_8E_8CH_2COOH$, resisting any sphere-to-rod shape transition, is so strong that the surfactant resists forming reverse structures in presence of hydrocarbon oils. This leads to unusual ternary phase diagrams of $H_2O/C_8E_8CH_2COOH$/oil, where mixtures of oil and surfactant form two phases even in absence of water. Exemplary, ternary phase diagrams of $H_2O/C_8E_8CH_2COOH$/n-dodecane and $H_2O/[H^+]_{0.5}[Na^+]_{0.5}[C_8E_8CH_2COO^-]$/n-dodecane at 23°C are shown in **Fig. II.12**. In absence of water, $C_8E_8CH_2COOH$ can uptake about 10 wt% of n-dodecane and any excess n-dodecane is expelled and phase separates. This behavior is unusual, as nonionic surfactants usually fully mix with the oil in absence of water, as for example shown for C_8E_6 and n-dodecane by Marland and Mulley [6]. The more water is added to the system, the less n-dodecane can be solubilized relative to the amount of surfactant present. As shown in **Section II.4.4.**, the area per molecule cannot exceed or drop below a value of around 0.6 nm^2 in the aqueous L_1 phase. As a result, only a small amount of oil can be incorporated into the hydrocarbon core, as incorporation of oil imposes an increase of the area per molecule. This restriction is weakened in the L_1' phase, as headgroup interdigitation leads to an increase of the area per molecule. When half of the surfactant is transformed to the ionic sodium salt, the difference in oil uptake between the L_1 and the L_1' phase is more pronounced. Compared to the acidic state, less oil is solubilized in the L_1 phase up to around 50:50 w(C_8E_8CH2COOH):w(H_2O), but more oil is solubilized in the L_1' phase at higher surfactant concentrations, 13 wt% n-dodecane in absence of water. The increased oil uptake in the interdigitated state in presence of sodium counterions is probably linked to the partial inhibition of interdigitation by the sodium counterions, leading to an ellipsoidal shape and a lower area per molecule compared to the acidic state, as described in **Section II.4.4**.

It should be noted that the same behavior is found for any hydrophobic oil that cannot act as a co-surfactant. As expected, for hydrocarbon oils, the solubilization is better for shorter chains that can be incorporated into the hydrocarbon cores more easily. A ternary phase diagram of $H_2O/C_8E_8CH_2COOH$/n-hexane, where 22 wt% of n-hexane can be incorporated in absence of water, is given in **Fig. A.11**.

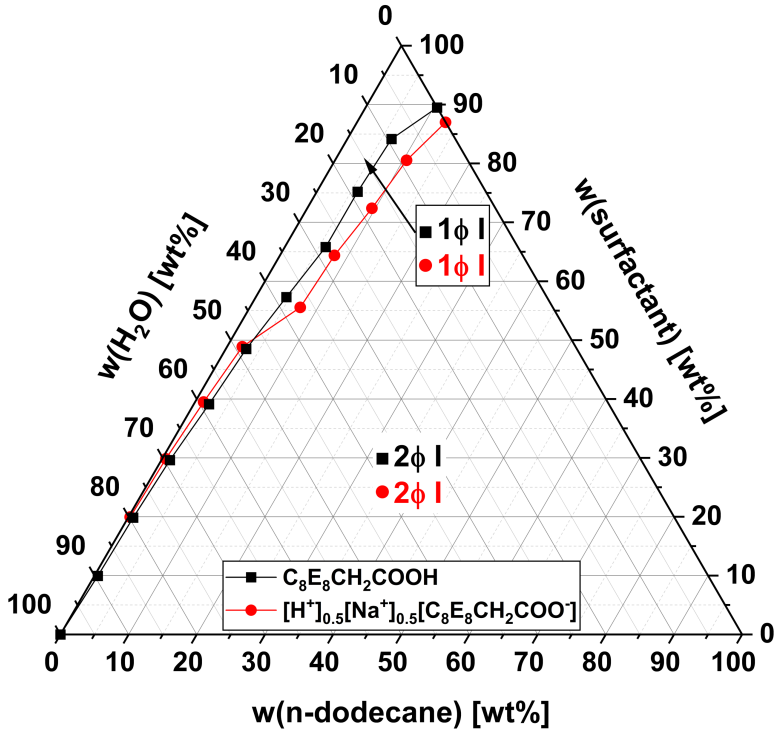

Fig. II.12. Ternary phase diagrams of $H_2O/C_8E_8CH_2COOH$/n-dodecane and $H_2O/[Na^+]_{0.5}[C_8E_8CH_2COO^-]$/n-dodecane at a temperature of 23°C. The precision in w(n-dodecane) is at least ±0.5 wt%. 1ϕ I: Single isotropic phase. 2ϕ I/I: Two isotropic phases in equilibrium.

II.5. Conclusion and Outlook

The surfactant $C_8E_8CH_2COOH$ in its acidic form, as well as half-neutralized by sodium hydroxide and in presence of calcium chloride, has remarkable properties. Due to the presence of eight ethylene oxide groups, it behaves much like a nonionic surfactant, and it is liquid at room temperature. Its behavior is very similar to what was found for C_8E_8 without the carboxylate group [5]. However, the additional charge at the end of the hydrophilic tail allows fine-tuning of its behavior via additional, although not dominating, electrostatic interactions.

Since the hydrophilic tail is long and the hydrophobic part is short, there are opposing constraints for the packing parameter, both the spontaneous and the effective one, as defined in **Appendix A.3.**, and the only compromise is a spherical micelle with a constant size and aggregation number, once the surfactant is mixed with water, i.e., in the L_1 phase. This is in sharp contrast both to conventional non-ionic surfactants with longer hydrocarbon chains [5] and to ionic surfactants [74].

Above a certain surfactant concentration, corresponding to an insufficient hydration of the hydrophilic part, the direct micelles interdigitate and form an ‘‘osmotic brush” in the L_1’ phase. In parallel, the area per headgroup increases significantly. It is noteworthy that here the strong steric constraint is not a consequence of covalent bonds holding the chains together, like in Pluronics™ [75], or of covalent cross-linking, like in gemini-type surfactants [76].

It is striking, how profound the differences are between a surfactant of generic formula C_jE_j with j = 8, compared to the classical, well studied $C_{2j}E_j$ that is described in hundreds of papers [40]. A new regime, for which the classical core-shell picture is not valid anymore, has been detected in the concentrated region above 60 wt%. The steric constraints cause spherical micelles with cores consisting of tightly confined hydrocarbon nanodroplets that are however relatively monodisperse and do not change shape.

Further, in classical $C_{2j}E_j$ surfactants, the cloud point is always related to a shape transition [40–42]. By contrast, in the case of $C_8E_8CH_2COOH$, shape transitions are sterically hindered. All cloud points reflect the competition between entropy and attractive interactions. Therefore, it is concluded that in the case of $C_8E_8CH_2COOH$ the interdigitation free energy is of the right order of magnitude to compete with entropy and produce the cloud point observed at very high concentrations, since attraction is only felt at short distances, when chains are interdigitated. The clouding phenomenon in $C_8E_8CH_2COOH$ systems will be discussed in more detail in **Chapter III**. The same is probably true for the C_8E_8 surfactant, as mentioned (but not further discussed) in [5]. A large monophasic, low viscous region without any birefringence both over wide temperature and concentration ranges is typical for hydrotropes, but exceptional for surfactants. In light of the results inferred from the present thermodynamical and structural study, there are probably two reasons responsible for the particular behavior of $C_8E_8CH_2COOH$, and probably also of C_8E_8:

(a) The hydrophilic part of the surfactant is so big compared to the hydrophobic part that the spontaneous packing parameter is far below 1/3 and even the effective packing parameter can never grow to values above 1/3 (see **Appendix A.3** for the distinction of the two parameters). As a consequence, only spherical micelles are possible. No elongation towards rodlike micelles is possible. As a further consequence, no depletion forces between the spherical micelles exist to induce a phase separation, as it was discussed in the case of rodlike micelles [77–79]. And of course, no hexagonal

or even lamellar phases or reversed ones can form.

(b) Nevertheless, even with spherical micelles, in principle, the formation of a cubic I_1 liquid crystalline phase would be possible. However, in the present case, this is not possible either. Since the hydrocarbon chain is short, the radius of the hydrocarbon core is so small that the thermal excitations of the fluctuations do not meet the Lindemann rule, known from molecular crystals, but also valid at colloidal scale [80]. This is different for surfactants like $C_{12}E_{12}$ that indeed show liquid crystals at high concentrations in water. In other words, this means that there is insufficient attraction between the micelles. Van der Waals attractions scale with the sixth power of the volume and are inversely proportional to the distance between micelles. In the case of C_8, these interactions are much less pronounced (more than a factor of 7) than with C_{12} chains, and, as a consequence, the interactions are too weak to form an I_1 phase.

These constraints also affect the phase behavior when the surfactant is mixed with oil. In contrast to classical nonionic surfactants, there is no full miscibility of surfactant and hydrocarbon oil in absence of water. Instead, only a certain amount of oil can be incorporated into the (interdigitated) direct micellar structure without inducing a structural change.

With the addition of NaOH, the headgroups get partially charged and as a result, the repulsion between the micelles can increase. By contrast, when adding $CaCl_2$ to the acidic surfactant, i.e., charges are screened, the double-charged cations can bridge the micelles and strengthen the osmotic brush. This is reflected in the cloud point that disappears in the charged case with sodium as counterion, whereas the lower critical solution temperature shifts to very high surfactant concentrations (≈72 wt%), i.e., to the interdigitated L_1' phase, when adding $CaCl_2$. The charged carboxylate groups seem to be free to move in the more or less hydrated headgroup volume, which has a thickness of about 1–2 nm. This has been deduced from SAXS experiments. Since the SAXS spectra with and without Na^+ are homothetic, the sodium ions are distributed evenly in the volume provided by hydrated headgroups (shown in green in **Fig. II.10**). This implies a significant configurational entropy. Both the carboxylate headgroups and the counterions are randomly distributed in a polar, yet widely water-free three-dimensional medium around a sharply separated hydrophobic core pseudo-phase.

These peculiar findings specific to $C_8E_8CH_2COOH$ may be used in the future for improved

chemical reaction processes, e.g., to optimize organocatalyzed reactions in structured, water-free media, or even micro- or nanoscaled crystal growth. Further applications may be conceivable in the framework of extraction, separation and purification processes. In classical liquid-liquid separation, there is always a water-rich phase and a solvent-rich phase in thermodynamic equilibrium, and ions, which are originally solubilized in the aqueous phase, partition between those two phases through liquid-liquid phase transfer [81,82]. In some cases, the solvent-rich phase splits into two phases: A light diluent-rich phase and a heavy and viscous extractant-rich phase [83,84]. This phenomenon occurs when processes are intensified by increasing solute and/or extractant concentration. This splitting represents a significant drawback for industrial liquid-liquid extraction processes. In the case of surfactants with general formula $[X^+][C_8E_8CH_2A^-]$, some of the liquid-liquid coexistence domains could be used to implement new processes for analysis or recycling [85]. These would be based on a dynamic equilibrium. A water-poor fluid forms one phase that is present as a coacervate-in-water nanoemulsion, whereas the supernatant forms the aqueous phase. If the metal affinities are different for these two phases, solvent-free – and maybe even extractant-free – extraction can be considered, which would significantly simplify some important processes in hydrometallurgy. Of course, the process maps would need be optimized to obtain the coacervate formation with higher volume fractions. Moreover, temperature-driven processes currently performed in ternary systems based on ultra-flexible microemulsions (UFME) [86–88] could become possible in simpler chemical formulations, avoiding the usage of large amounts of solvo-surfactants [89,90].

In this context, it is important to note that all metal salts of $C_8E_8CH_2COOH$ or $C_8E_5CH_2COOH$ [2,68,91] investigated so far are liquid at room temperature, or slightly above room temperature, even in absence of water. This is true even for trivalent rare earth metals. The phase behavior of the sodium and calcium salt of $C_8E_8CH_2COOH$ will be discussed in detail in **Chapter III.**, which will allow for the construction of a complete generic phase diagram of this surfactant.

II.6. References

[1] P. Denk, A. El Maangar, J. Lal, D. Kleber, T. Zemb, W. Kunz, Phase diagrams and microstructures of aqueous short alkyl chain polyethylene glycol ether carboxylate and carboxylic acid triblock surfactant solutions, J Colloid Interface Sci 590 (2021) 375–386. https://doi.org/10.1016/j.jcis.2021.01.061.

[2] M. Rothe, E. Müller, P. Denk, W. Kunz, Ionic Liquids Based on the Concept of Melting Point Lowering Due to Ethoxylation, Molecules 26 (2021) 4034. https://doi.org/10.3390/molecules26134034.

[3] J. Blahnik, E. Müller, L. Braun, P. Denk, W. Kunz, Nanoscopic microheterogeneities or pseudo-phase separations in non-conventional liquids, Curr Opin Colloid Interface Sci 57 (2022) 101535. https://doi.org/10.1016/j.cocis.2021.101535.

[4] P. Ekwall, L. Mandell, K. Fontell, Solubilization in Micelles and Mesophases and the Transition from Normal to Reversed Structures, Molecular Crystals 8 (1969) 157–213. https://doi.org/10.1080/15421406908084903.

[5] D.J. Mitchell, G.J.T. Tiddy, L. Waring, T. Bostock, M.P. McDonald, Phase behaviour of polyoxyethylene surfactants with water. Mesophase structures and partial miscibility (cloud points), Journal of the Chemical Society, Faraday Transactions 1: Physical Chemistry in Condensed Phases 79 (1983) 975. https://doi.org/10.1039/f19837900975.

[6] J.S. Marland, B.A. Mulley, A phase-rule study of multiple-phase formation in a model emulsion system containing water, n-octanol, n-dodecane and/a non-ionic surface-active agent at 10 and 25°, Journal of Pharmacy and Pharmacology 23 (1971) 561–572. https://doi.org/10.1111/j.2042-7158.1971.tb08718.x.

[7] V.J. Spiering, A. Ciapetti, M.T. Lima, D.W. Hayward, L. Noirez, M. Appavou, R. Schomäcker, M. Gradzielski, Changes in Phase Behavior from the Substitution of Ethylene Oxide with Carbon Dioxide in the Head Group of Nonionic Surfactants, ChemSusChem 13 (2020) 601–607. https://doi.org/10.1002/cssc.201902855.

[8] H.G.B. Jong, H.R. Kruyt, Koazervation, Kolloid-Zeitschrift 50 (1930) 39–48. https://doi.org/10.1007/BF01422833.

[9] P. Ilekti, L. Piculell, F. Tournilhac, B. Cabane, How To Concentrate an Aqueous Polyelectrolyte/Surfactant Mixture by Adding Water, J Phys Chem B 102 (1998) 344–351. https://doi.org/10.1021/jp972575x.

[10] H.R. Kruyt, ed., Colloid Science, Volume II: Reversible Systems, Elsevier Publishing Co., Amsterdam, 1949.

[11] W. Zhao, Y. Wang, Coacervation with surfactants: From single-chain surfactants to gemini surfactants, Adv Colloid Interface Sci 239 (2017) 199–212. https://doi.org/10.1016/j.cis.2016.04.005.

[12] G. Ben Messaoud, L. Promeneur, M. Brennich, S.L.K.W. Roelants, P. Le Griel, N. Baccile, Complex coacervation of natural sophorolipid bolaamphiphile micelles with cationic polyelectrolytes, Green Chemistry 20 (2018) 3371–3385. https://doi.org/10.1039/c8gc01531g.

[13] E. Kizilay, D. Seeman, Y. Yan, X. Du, P.L. Dubin, L. Donato-Capel, L. Bovetto, C. Schmitt, Structure of bovine β-lactoglobulin-lactoferrin coacervates, Soft Matter 10 (2014) 7262–7268. https://doi.org/10.1039/c4sm01333f.

[14] Y. Xu, M. Liu, M. Faisal, Y. Si, Y. Guo, Selective protein complexation and coacervation by polyelectrolytes, Adv Colloid Interface Sci 239 (2017) 158–167. https://doi.org/10.1016/j.cis.2016.06.004.

[15] K.Y. Huang, H.Y. Yoo, Y. Jho, S. Han, D.S. Hwang, Bicontinuous Fluid Structure with Low Cohesive Energy: Molecular Basis for Exceptionally Low Interfacial Tension of Complex Coacervate Fluids, ACS Nano 10 (2016) 5051–5062. https://doi.org/10.1021/acsnano.5b07787.

[16] E. Romera-García, A. Ballesteros-Gómez, S. Rubio, Supramolecular biosolvents made up of self-assembled rhamnolipids: synthesis and characterization, Green Chemistry (2020). https://doi.org/10.1039/d0gc02078h.

[17] X. Cheng, Y. Jin, B. Fan, R. Qi, H. Li, W. Fan, Self-Assembly of Polyurethane Phosphate Ester with Phospholipid-Like Structures: Spherical, Worm-Like Micelles, Vesicles, and Large Compound Vesicles, ACS Macro Lett 5 (2016) 238–243. https://doi.org/10.1021/acsmacrolett.5b00789.

[18] A. Klaus, G.J.T. Tiddy, D. Touraud, A. Schramm, G. Stühler, M. Drechsler, W. Kunz, Phase behavior of an extended surfactant in water and a detailed characterization of the dilute and semidilute phases, Langmuir 26 (2010) 5435–5443. https://doi.org/10.1021/la903899w.

[19] A. Klaus, G.J.T. Tiddy, D. Touraud, A. Schramm, G. Stühler, W. Kunz, Phase behavior of an extended surfactant in water and a detailed characterization of the concentrated phases, Langmuir 26 (2010) 16871–16883. https://doi.org/10.1021/la103037q.

[20] A. Klaus, G.J.T. Tiddy, R. Rachel, A.P. Trinh, E. Maurer, D. Touraud, W. Kunz, Hydrotrope-induced inversion of salt effects on the cloud point of an extended surfactant, Langmuir 27 (2011) 4403–4411. https://doi.org/10.1021/la104744e.

[21] A. Klaus, G.J.T. Tiddy, C. Solans, A. Harrar, D. Touraud, W. Kunz, Effect of salts on the phase behavior and the stability of nano-emulsions with rapeseed oil and an extended surfactant, Langmuir 28 (2012) 8318–8328. https://doi.org/10.1021/la300435t.

[22] A. Graciaa, J. Lachaise, C. Cucuphat, M. Bourrel, J.L. Salager, Improving solubilization in microemulsions with additives. 1. The lipophilic linker role, Langmuir 9 (1993) 669–672. https://doi.org/10.1021/la00027a010.

[23] M. Miñana-Perez, A. Graciaa, J. Lachaise, J.-L. Salager, Solubilization of polar oils with extended surfactants, Colloids Surf A Physicochem Eng Asp 100 (1995) 217–224. https://doi.org/10.1016/0927-7757(95)03186-H.

[24] L.D. Do, A. Withayyapayanon, J.H. Harwell, D.A. Sabatini, Environmentally Friendly Vegetable Oil Microemulsions Using Extended Surfactants and Linkers, J Surfactants Deterg 12 (2009) 91–99. https://doi.org/10.1007/s11743-008-1096-0.

[25] P. Bauduin, T. Zemb, Perpendicular and lateral equations of state in layered systems of amphiphiles, Curr Opin Colloid Interface Sci 19 (2014) 9–16. https://doi.org/10.1016/j.cocis.2014.02.002.

[26] J.-F. Dufrêche, T. Zemb, Bending: from thin interfaces to molecular films in microemulsions, Curr Opin Colloid Interface Sci (2020). https://doi.org/10.1016/j.cocis.2020.06.001.

[27] B. Widera, R. Neueder, W. Kunz, Vapor pressures and osmotic coefficients of aqueous solutions of SDS, C6TAB, and C8TAB at 25°C, Langmuir 19 (2003) 8226–8229. https://doi.org/https://doi.org/10.1021/la034714+.

[28] H.F. Gibbard, G. Scatchard, R.A. Rousseau, J.L. Creek, Liquid-vapor equilibrium of aqueous sodium chloride, from 298 to 373.deg.K and from 1 to 6 mol kg-1, and related properties, J Chem Eng Data 19 (1974) 281–288. https://doi.org/10.1021/je60062a023.

[29] D. Leckband, J. Israelachvili, Intermolecular forces in biology, Q Rev Biophys 34 (2001) 105–267. https://doi.org/10.1017/S0033583501003687.

[30] W.A. Ducker, T.J. Senden, R.M. Pashley, Direct measurement of colloidal forces using an atomic force microscope, Nature 353 (1991) 239–241. https://doi.org/10.1038/353239a0.

[31] J.N. Israelachvili, Intermolecular and Surface Forces, 3rd ed., Academic Press, Waltham, MA, 2011.

[32] B. Derjaguin, Untersuchungen über die Reibung und Adhäsion, IV - Theorie des Anhaftens kleiner Teilchen, Kolloid-Zeitschrift 69 (1934) 155–164. https://doi.org/10.1007/BF01433225.

[33] E.L. Thomas, D.J. Kinning, D.B. Alward, C.S. Henkee, Ordered Packing Arrangements of Spherical Micelles of Diblock Copolymers in Two and Three Dimensions, Macromolecules 20 (1987) 2934–2939. https://doi.org/10.1021/ma00177a049.

[34] M. Doucet, J.H. Cho, G. Alina, J. Bakker, W. Bouwman, P. Butler, K. Campbell, M. Gonzales, R. Heenan, A. Jackson, SasView, (2020). https://doi.org/10.5281/zenodo.3752443.

[35] J. Hansen, J.B. Hayter, A rescaled MSA structure factor for dilute charged colloidal dispersions, Mol Phys 46 (1982) 651–656. https://doi.org/10.1080/00268978200101471.

[36] J.B. Hayter, J. Penfold, An analytic structure factor for macroion solutions, Mol Phys 42 (1981) 109–118. https://doi.org/10.1080/00268978100100091.

[37] R. Strey, R. Schomäcker, D. Roux, F. Nallet, U. Olsson, Dilute lamellar and L3 phases in the binary water–C12E5 system, J. Chem. Soc., Faraday Trans. 86 (1990) 2253–2261. https://doi.org/10.1039/FT9908602253.

[38] P. Yan, J. Huang, R.C. Lu, C. Jin, J.X. Xiao, Y.M. Chen, Two cloud-point phenomena in tetrabutylammonium perfluorooctanoate aqueous solutions: Anomalous temperature-induced phase and structure transitions, Journal of Physical Chemistry B 109 (2005) 5237–5242. https://doi.org/10.1021/jp045283m.

[39] J.B. Hayter, T. Zemb, Concentration-dependent structure of sodium octanoate micelles, Chem Phys Lett 93 (1982) 91–94. https://doi.org/10.1016/0009-2614(82)85062-8.

[40] M. Zulauf, K. Weckstrom, J.B. Hayter, V. Degiorgio, M. Corti, Neutron scattering study of micelle structure in isotropic aqueous solutions of poly(oxyethylene) amphiphiles, J Phys Chem 89 (1985) 3411–3417. https://doi.org/10.1021/j100261a051.

[41] P.A. Kralchevsky, K.D. Danov, S.E. Anachkov, G.S. Georgieva, K.P. Ananthapadmanabhan, Extension of the ladder model of self-assembly from cylindrical to disclike surfactant micelles, Curr Opin Colloid Interface Sci 18 (2013) 524–531. https://doi.org/10.1016/j.cocis.2013.11.002.

[42] K. Imanishi, Y. Einaga, Effects of Hydrophilic Chain Length on the Characteristics of the Micelles of Pentaoxyethylene n-Decyl C10E5 and Hexaoxyethylene n-Decyl C10E6 Ethers, J Phys Chem B 109 (2005) 7574–7581. https://doi.org/10.1021/jp044226q.

[43] A. V. Peresypkin, F.M. Menger, Zwitterionic geminis. Coacervate formation from a single organic compound, Org Lett 1 (1999) 1347–1350. https://doi.org/10.1021/ol990205g.

[44] F.M. Menger, V.A. Seredyuk, R.P. Apkarian, E.R. Wright, Colloidal Assemblies of Branched Geminis Studied by Cryo-etch-HRSEM, J Am Chem Soc 124 (2002) 12408–12409. https://doi.org/10.1021/ja021025w.

[45] N.M. Van Os, J.R. Haak, L.A.M. Rupert, K.S. Laboratorium, Physico-Chemical Properties of Selected Anionic, Cationic and Nonionic Surfactants, Elsevier B.V., 1993. https://doi.org/10.1016/c2009-0-09112-0.

[46] I. Szleifer, D. Kramer, A. Ben-Shaul, W.M. Gelbart, S.A. Safran, Molecular theory of curvature elasticity in surfactant films, J Chem Phys 92 (1990) 6800–6817. https://doi.org/10.1063/1.458267.

[47] K. Lunkenheimer, H.-J. Pergande, H. Krüger, Apparatus for programmed high-performance purification of surfactant solutions, Review of Scientific Instruments 58 (1987) 2313–2316. https://doi.org/10.1063/1.1139343.

[48] R.K. Thomas, J. Penfold, Multilayering of Surfactant Systems at the Air-Dilute Aqueous Solution Interface, Langmuir 31 (2015) 7440–7456. https://doi.org/10.1021/la504952k.

[49] D. Langevin, Polyelectrolyte and surfactant mixed solutions. Behavior at surfaces and in thin films, Adv Colloid Interface Sci 89–90 (2001) 467–484. https://doi.org/10.1016/S0001-8686(00)00068-3.

[50] V. Bergeron, D. Langevin, A. Asnacios, Thin-Film Forces in Foam Films Containing Anionic Polyelectrolyte and Charged Surfactants, Langmuir 12 (1996) 1550–1556. https://doi.org/10.1021/la950654z.

[51] A. Berthod, S. Tomer, J.G. Dorsey, Polyoxyethylene alkyl ether nonionic surfactants: Physicochemical properties and use for cholesterol determination in food, Talanta 55 (2001) 69–83. https://doi.org/10.1016/S0039-9140(01)00395-2.

[52] M. Frindi, B. Michels, R. Zana, Ultrasonic absorption studies of surfactant exchange between micelles and bulk phase in aqueous micellar solutions of nonionic surfactants with a short alkyl chain. 2. C6E3, C6E5, C8E4, and C8E8, Journal of Physical Chemistry 96 (1992) 6095–6102. https://doi.org/10.1021/j100193a082.

[53] J. Wolfe, G. Bryant, Physical Principles of Membrane Damage due to Dehydration and Freezing, in: T.K. Karalis (Ed.), Mechanics of Swelling, Springer Berlin Heidelberg, Berlin, Heidelberg, 1992: pp. 205–224.

[54] S. Lüsse, K. Arnold, The interaction of poly(ethylene glycol) with water studied by 1H and 2H NMR relaxation time measurements, Macromolecules 29 (1996) 4251–4257. https://doi.org/10.1021/ma9508616.

[55] C. Branca, S. Magazù, G. Maisano, F. Migliardo, P. Migliardo, G. Romeo, Hydration Study of PEG/Water Mixtures by Quasi Elastic Light Scattering, Acoustic and Rheological Measurements, J Phys Chem B 106 (2002) 10272–10276. https://doi.org/10.1021/jp014345v.

[56] P.G. Nilsson, B. Lindman, Water self-diffusion in nonionic surfactant solutions. Hydration and obstruction effects, J Phys Chem 87 (1983) 4756–4761. https://doi.org/10.1021/j100246a041.

[57] O. Tirosh, Y. Barenholz, J. Katzhendler, A. Priev, Hydration of polyethylene glycol-grafted liposomes, Biophys J 74 (1998) 1371–1379. https://doi.org/10.1016/S0006-3495(98)77849-X.

[58] J.B. Hayter, R. Pynn, Structure Factor of a Magnetically Saturated Ferrofluid, Phys Rev Lett 49 (1982) 1103–1106. https://doi.org/10.1103/PhysRevLett.49.1103.

[59] S.H. Chen, Small Angle Neutron Scattering Studies of the Structure and Interaction in Micellar and Microemulsion Systems, Annu Rev Phys Chem 37 (1986) 351–399. https://doi.org/10.1146/annurev.pc.37.100186.002031.

[60] M. Kotlarchyk, S. Chen, Analysis of small angle neutron scattering spectra from polydisperse interacting colloids, J Chem Phys 79 (1983) 2461–2469. https://doi.org/10.1063/1.446055.

[61] T. Wu, P. Gong, I. Szleifer, P. Vlček, V. Šubr, J. Genzer, Behavior of Surface-Anchored Poly(acrylic acid) Brushes with Grafting Density Gradients on Solid Substrates: 1. Experiment, Macromolecules 40 (2007) 8756–8764. https://doi.org/10.1021/ma0710176.

[62] A. Naji, R.R. Netz, C. Seidel, Non-linear osmotic brush regime: Simulations and mean-field theory, The European Physical Journal E 12 (2003) 223–237. https://doi.org/10.1140/epje/i2002-10163-4.

[63] G. Pabst, S. Danner, S. Karmakar, G. Deutsch, V.A. Raghunathan, On the Propensity of Phosphatidylglycerols to Form Interdigitated Phases, Biophys J 93 (2007) 513–525. https://doi.org/10.1529/biophysj.106.101592.

[64] R. Israels, F.A.M. Leermakers, G.J. Fleer, E.B. Zhulina, Charged Polymeric Brushes: Structure and Scaling Relations, Macromolecules 27 (1994) 3249–3261. https://doi.org/10.1021/ma00090a018.

[65] V. Degiorgio, M. Corti, Physics of Amphiphiles: Micelles, Vesicles and Microemulsions: Proceedings of the International School of Physics, Enrico Fermi, Course XC, Elsevier Science Pub. Co., Amsterdam, New York, 1985.

[66] J.B. Hayter, J. Penfold, Self-consistent structural and dynamic study of concentrated micelle solutions, Journal of the Chemical Society, Faraday Transactions 1: Physical Chemistry in Condensed Phases 77 (1981) 1851–1863. https://doi.org/10.1039/F19817701851.

[67] T. Zemb, P. Charpin, Micellar structure from comparison of X-ray and neutron small-angle scattering, Journal de Physique 46 (1985) 249–256. https://doi.org/10.1051/jphys:01985004602024900.

[68] M. Rothe, G. Quintard, M. Kronseder, P. Bauduin, T. Zemb, W. Kunz, Dilution and packing of anionic liquid surfactant in presence of divalent and trivalent counterions, J Mol Liq 384 (2023) 122195. https://doi.org/10.1016/j.molliq.2023.122195.

[69] C. Tanford, Micelle shape and size, Journal of Physical Chemistry 76 (1972) 3020–3024. https://doi.org/10.1021/j100665a018.

[70] C.A. Schneider, W.S. Rasband, K.W. Eliceiri, NIH Image to ImageJ: 25 years of image analysis, Nat Methods 9 (2012) 671–675. https://doi.org/10.1038/nmeth.2089.

[71] D.M. LeNeveu, R.P. Rand, V.A. Parsegian, Measurement of forces between lecithin bilayers, Nature 259 (1976) 601–603. https://doi.org/10.1038/259601a0.

[72] R.P. Rand, V.A. Parsegian, Hydration forces between phospholipid bilayers, Biochimica et Biophysica Acta (BBA) - Reviews on Biomembranes 988 (1989) 351–376. https://doi.org/10.1016/0304-4157(89)90010-5.

[73] V.A. Parsegian, T. Zemb, Hydration forces: Observations, explanations, expectations, questions, Curr Opin Colloid Interface Sci 16 (2011) 618–624. https://doi.org/10.1016/j.cocis.2011.06.010.

[74] P. Kékicheff, C. Grabielle-Madelmont, M. Ollivon, Phase diagram of sodium dodecyl sulfate-water system, J Colloid Interface Sci 131 (1989) 112–132. https://doi.org/10.1016/0021-9797(89)90151-3.

[75] N.J. Jain, V.K. Aswal, P.S. Goyal, P. Bahadur, Salt induced micellization and micelle structures of' PEO/PPO/PEO block copolymers in aqueous solution, Colloids Surf A Physicochem Eng Asp 173 (2000) 85–94. https://doi.org/10.1016/S0927-7757(99)00514-2.

[76] A. Bernheim-Groswasser, R. Zana, Y. Talmon, Sphere-to-Cylinder Transition in Aqueous Micellar Solution of a Dimeric (Gemini) Surfactant, J Phys Chem B 104 (2000) 4005–4009. https://doi.org/10.1021/jp994301a.

[77] H.N.W. Lekkerkerker, R. Tuinier, Colloids and the Depletion Interaction, Springer Netherlands, Dordrecht, 2011. https://doi.org/10.1007/978-94-007-1223-2.

[78] H.N.W. Lekkerkerker, A. Stroobants, Phase behaviour of rod-like colloid+flexible polymer mixtures, Il Nuovo Cimento D 16 (1994) 949–962. https://doi.org/10.1007/BF02458781.

[79] S.M. Oversteegen, H.N.W. Lekkerkerker, Testing the Derjaguin approximation for colloidal mixtures of spheres and disks, Phys Rev E 68 (2003) 021404. https://doi.org/10.1103/PhysRevE.68.021404.

[80] T. Okubo, H. Ishiki, H. Kimura, M. Chiyoda, K. Yoshinaga, Rigidity of colloidal crystals of silica spheres modified with polymers on their surfaces in organic solvents, Colloid Polym Sci 280 (2002) 446–453. https://doi.org/10.1007/s00396-001-0631-6.

[81] D. Bourgeois, A. El Maangar, S. Dourdain, Importance of weak interactions in the formulation of organic phases for efficient liquid/liquid extraction of metals, Curr Opin Colloid Interface Sci 46 (2020) 36–51. https://doi.org/10.1016/j.cocis.2020.03.004.

[82] M. Špadina, K. Bohinc, Multiscale modeling of solvent extraction and the choice of reference state: Mesoscopic modeling as a bridge between nanoscale and chemical

engineering, Curr Opin Colloid Interface Sci 46 (2020) 94–113. https://doi.org/10.1016/j.cocis.2020.03.011.

[83] R. Chiarizia, A. Briand, Third Phase Formation in the Extraction of Inorganic Acids by TBP in n -Octane, Solvent Extraction and Ion Exchange 25 (2007) 351–371. https://doi.org/10.1080/07366290701285397.

[84] P. Bauduin, F. Testard, L. Berthon, T. Zemb, Relation between the hydrophile/hydrophobe ratio of malonamide extractants and the stability of the organic phase: investigation at high extractant concentrations, Physical Chemistry Chemical Physics 9 (2007) 3776. https://doi.org/10.1039/b701479a.

[85] T. Zemb, T.A. Hatton, N.L. Abbott, Editorial overview: Colloidal and interfacial challenges related to separations, analysis and recycling, Curr Opin Colloid Interface Sci 46 (2020) A1–A3. https://doi.org/10.1016/j.cocis.2020.08.007.

[86] T.N. Zemb, M. Klossek, T. Lopian, J. Marcus, S. Schöettl, D. Horinek, S.F. Prevost, D. Touraud, O. Diat, S. Marčelja, W. Kunz, How to explain microemulsions formed by solvent mixtures without conventional surfactants, Proceedings of the National Academy of Sciences 113 (2016) 4260–4265. https://doi.org/10.1073/pnas.1515708113.

[87] A. Ullmann, Z. Ludmer, R. Shinnar, Phase transition extraction using solvent mixtures with critical point of miscibility, AIChE Journal 41 (1995) 488–500. https://doi.org/10.1002/aic.690410307.

[88] T. Golan, G. Dahan, Z. Ludmer, N. Brauner, A. Ullmann, Heavy metals extraction with the SRPTE process from two matrices – Industrial sludge and river sediments, Chemical Engineering Journal 236 (2014) 47–58. https://doi.org/10.1016/j.cej.2013.09.062.

[89] F. Nakonechny, D. Avisar, Z. Ludmer, N. Brauner, A. Ullmann, Application of Partially Miscible Solvent System for an Efficient Extraction of Organic Pollutants from Contaminated Sludge, Water Air Soil Pollut 230 (2019) 86. https://doi.org/10.1007/s11270-019-4132-y.

[90] M. Rezaee, Y. Yamini, M. Faraji, Evolution of dispersive liquid–liquid microextraction method, J Chromatogr A 1217 (2010) 2342–2357. https://doi.org/10.1016/j.chroma.2009.11.088.

[91] M. Rothe, M. Tress, C. Allacher, P. Nuernberger, W. Kunz, Ionic Liquids [M3+][A−]3 with Three-Valent Cations and Their Possible Use to Easily Separate Rare Earth Metals, Chemistry – A European Journal 27 (2021) 13052–13058. https://doi.org/10.1002/chem.202101925.

Chapter III.

Phase Behavior of Metal Octaoxyethylene Octyl Ether Carboxylates ($[X^+][C_8E_8CH_2COO^-]$) – Constructing a Complete Generic Phase Diagram

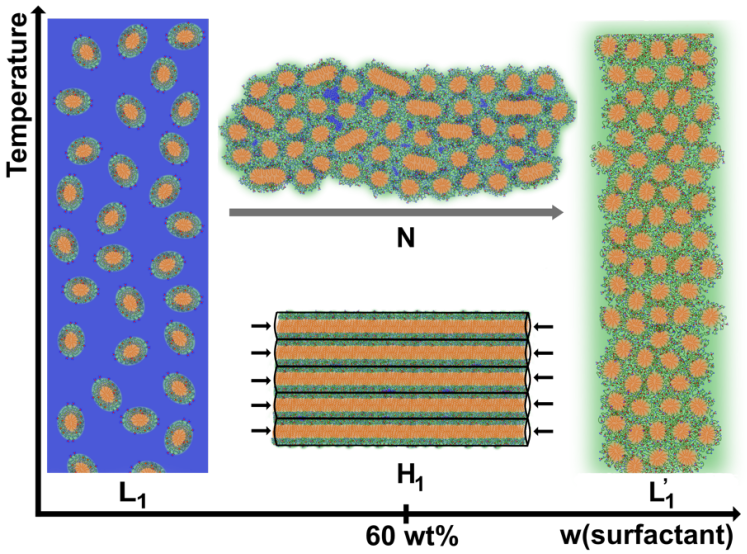

The micellar shape of $[H^+][C_8E_8CH_2COO^-]$ is restricted to spheres. Classical core-shell micelles (L_1) transition into headgroup interdigitated micelles (L_1') at higher concentrations. Transforming the surfactant to its sodium or calcium salt, the micelles are deformed to slightly prolate spheroidal. A hexagonal (H_1) phase within the transition regime between L_1 and L_1' is made possible by a reduction of the area per molecule by counterion-bridging. At higher temperature, the H_1 phase "melts" into a nematic phase (N) consisting of shorter chains of prolate micelles with a preferential orientation (grey arrow).

Note:
Most of this chapter is already published (P. Denk, A. El Maangar, S. Prévost, W. Silva, R. Gschwind, T. Zemb, W. Kunz, Cloud point, auto-coacervation, and nematic ordering of micelles formed by ethylene oxide containing carboxylate surfactants, J Colloid Interface Sci 621 (2022) 470–488.) [1]. The author of this thesis is the first author of the publication, wrote the original draft, evaluated the data, and conducted most of the experiments. The co-authors Dr. Asmae El Maangar and Dr. Sylvain Prévost performed, respectively, the SWAXS and SANS measurements, the treatment of the raw scattering data, and gave some scientific input. The co-authors Dr. Wagner Menezes da Silva and Prof. Dr. Ruth Gschwind performed the DOSY-NMR experiments. The co-authors Prof. Dr. Thomas Zemb and Prof. Dr. Werner Kunz reviewed the manuscript and provided scientific input throughout the work. ESI-MS was conducted by Josef Kiermaier (Central Analytical Services, University of Regensburg). Presented cryo-TEM images were recorded and evaluated by Sapir Lifshiz-Simon from the group of Prof. Dr. Yeshayahu Talmon at the Technion in Haifa. The interns Lea Sammet and Dominik Bubak assisted in preliminary measurements, not presented in this chapter.

III.1. Abstract

In **Chapter II.**, the aqueous phase behavior of octaoxyethylene octyl ether carboxylic acid ($C_8E_8CH_2COOH$), in this chapter denoted as $[H^+][C_8E_8CH_2COO^-]$, and with partial replacement of H^+ by Na^+ and in presence of $CaCl_2$ was determined. It was found that even the neat surfactants are liquid at room temperature and that they form only direct micelles for any water content and over large temperature ranges. The aim of the present chapter was to find an explanation for the clouding in these systems as well as for the coacervation observed at very low surfactant content. It was expected that very similar phase diagrams would be found for a full replacement of H^+ by Na^+ or Ca^{2+} ions.

The phase diagrams of the above-mentioned salts in water are established and the structures of the occurring phases are determined in detail with small- and wide-angle X-ray scattering, small-angle neutron scattering, dynamic light scattering, heat flux differential scanning calorimetry, as well as surface tension, ESI-MS, and NMR experiments.

Surprisingly, a new type of nematic phase was discovered between an isotropic and a hexagonal phase. Based on the complete description of all occurring phases, both in the acidic and the charged surfactant systems, a coherent and unified picture of all these phases could be designed, including the auto-coacervation at low surfactant concentration, the non-conventional clouding at high temperatures, the unusual liquid crystalline phases in a small domain at high surfactant concentrations, and the L_β phase at low temperatures and at very low water content. It turned out that all phenomena are a consequence of the subtle interplay between a) the packing constraint due to the very large headgroup, b) the relatively small hydrocarbon chain, and c) the tunable electrostatic interactions versus entropy.

III.2. Introduction

In **Chapter II.**, the peculiar aqueous phase behavior of octaoxyethylene octyl ether carboxylic acid ($C_8E_8CH_2COOH$), marketed as Akypo® LF2 by Kao Chemicals, was reported. In this chapter, the notation $[H^+][C_8E_8CH_2COO^-]$ is used for the acid to emphasize the counterion of the surfactant, even though the surfactant is mostly nonionic in this case. Its structure closely resembles that of a typical nonionic C_8E_8 surfactant, but is terminated by an additional acetic acid group that can introduce some charge. $[H^+][C_8E_8CH_2COO^-]$ belongs to the not too well studied class of alcohol ethoxycarboxylates or alkyl ether carboxylates (AECs). Chiappisi [2] reviewed AECs seven years ago, remarking the negligence of this surfactant class in the literature. Despite their lack of attention in the literature, AECs are appreciated in various applications owing to their good foaming and emulsification properties combined with their excellent resistance to hard water, high temperatures, acidic and alkaline conditions, and oxidizing agents [3,4]. Nonionic surfactants of the type C_iE_j on the other hand are well studied and described in the literature. Surprisingly, most of the detailed studies deal with surfactants where $i \approx 2j$ ($C_{2j}E_j$), while less attention was paid to those where $i \leq j$ [5,6]. The reason is probably that the spontaneous packing parameter p_0 of $C_{2j}E_j$ is either close to 1, favoring the formation of the lamellar L_α phase, or slightly smaller than 1, allowing the formation of a multitude of lyotropic liquid crystalline phases. Since most liquid crystalline phases are linked to non-spherical micellar shapes, a small p_0 is unfavorable for the formation of liquid crystals. The definition of p_0 and its distinction from other, often ill-defined, packing parameters used in the literature is given in **Appendix A.3**. p_0 is linked to the equilibrium area per molecule [7], which in the case of C_iE_j surfactants is linked to the ratio φ_{head} of the headgroup volume V_{head} and the total surfactant volume V_{tot}. It is, however, important to note that the equilibrium area per molecule cannot be inferred directly from the molecular geometry, see **Appendix A.3**. φ_{head} was successfully used to rationalize the phase behavior of C_iE_j surfactants in the past [8–10]. If φ_{head} is large, as in $C_{2j}E_j$, p_0 is small and spherical micelles are favored, which in turn impedes liquid crystal formation. The smaller φ_{head} is, the larger is p_0 and the easier a micellar shape transition can occur and the more favored is typically liquid crystal formation. However, simply trying to rationalize the phase behavior based on φ_{head} or p_0 completely neglects the influence of the alkyl chain length on packing. It was already pointed out by Nagarajan [11] that the influence of the alkyl chain length cannot be neglected for an adequate prediction of

packing. Indeed, a close comparison of the phase behaviors of the various C_iE_j surfactants reported in the literature reveals that, in order to impede the formation of liquid crystals, φ_{head} needs to be larger for longer alkyl chains [5,6,12–18]. In other words, longer alkyl chains favor the formation of liquid crystals. For example, C_8E_8 [6] ($\varphi_{head} = 0.68$) does not form liquid crystalline phases at all, while $C_{12}E_{12}$ [6] ($\varphi_{head} = 0.69$) and $C_{16}E_{20}$ [13] (Brij® 58, $\varphi_{head} = 0.74$) can still form a cubic I_1 phase and a hexagonal H_1 phase, despite having a slightly larger φ_{head}. While an I_1 phase consists of close-packed spherical micelles and is feasible without a change in micellar shape, the classical H_1 phase is made from hexagonally packed long rods and requires a micellar sphere-to-rod transition [6,19]. Indeed, the headgroup of $C_{12}E_{23}$ [17,18] (Brij® 35, $\varphi_{head} = 0.81$) is large enough to restrict its micellar shape to spheres, leaving the I_1 phase the only liquid crystalline phase to be formed. $[H^+][C_8E_8CH_2COO^-]$ ($\varphi_{head} = 0.71$), similar to C_8E_8, is restricted to spherical micelles and does not form any liquid crystalline phase. The reason for the absence of an I_1 phase is the short alkyl chain length, which may be explained in two equivalent ways. Owing to the short alkyl chain, the radius of the micellar core is too small for the thermal excitations of fluctuations to meet the Lindemann rule. The Lindemann rule was derived for molecular crystals but is also valid at the colloidal scale [20]. An equivalent explanation is that the Van der Waals attractions between the small hydrophobic cores are insufficient to stabilize a cubic packing of the micelles. With increasing radius, the attractive forces increase, thus the C_8 surfactants cannot form an I_1 phase, whereas C_{12} surfactants can.

The restriction to the spherical shape not only affects the liquid crystal formation, but also the effects involved in the clouding phenomenon. As a pseudo-nonionic ethoxylated surfactant, $[H^+][C_8E_8CH_2COO^-]$ exhibits a lower critical solution temperature (LCST), which is well known for classical C_iE_j surfactants. However, the clouding phenomenon of typical $C_{2j}E_j$ surfactants is linked to a micellar shape transition with increasing temperature, accompanied by increased intermicellar attraction due to decreasing headgroup hydration [6,21–24]. The peculiarity of $[H^+][C_8E_8CH_2COO^-]$ is that a sphere-to-rod transition is impossible at any concentration and, as will be shown in this chapter, at any temperature, owing to the large φ_{head} and short C_8 chain. As a result, its clouding behavior should solely be induced by intermicellar attraction due to headgroup dehydration.

An additional feature observed for $[H^+][C_8E_8CH_2COO^-]$ is auto-coacervation below its critical micelle concentration (CMC). Coacervation is a liquid-liquid phase separation from a

colloidal solution triggered by aggregation of the colloids. A colloid-rich coacervate separates from a dilute equilibrium phase. The term was coined about 95 years ago by Bungenberg de Jong and Kruyt [25], who extensively investigated the phenomenon in systems containing macromolecules, such as sugars or proteins. Coacervation can be subdivided into two main categories. Complex coacervation on the one hand and simple coacervation on the other hand. While simple coacervation involves only one colloidal species, complex coacervation involves at least two different colloidal species. Both regularly occur for polymers and proteins and are often triggered by salt addition, temperature, changes in concentration, pH, or addition of other soluble compounds [25–28]. All of these stimuli influence the subtle balance of weak interactions between colloids leading to their coacervation. If simple coacervation occurs without the addition of salt or another compound, it can be referred to as auto-coacervation. Instead of macromolecules, the colloids can also be micelles. If the coacervation process involves colloids made of surfactants exclusively, the coacervation is often called surfactant coacervation, which was reviewed by Wang and Wang [29] in 2014. Surfactant coacervation is less widespread than classical macromolecule coacervation, and if it occurs, the process is usually simple coacervation induced by salt or other organic compounds or complex coacervation [30–36]. Auto-coacervation has been reported for gemini surfactants comprising two alkyl chains [37–39], but is very rare for simple surfactants, unless clouding is considered as such. Clouding of C_iE_j surfactants, where a surfactant-rich phase separates from a dilute micellar solution, is, by definition, auto-coacervation.

It was demonstrated in **Chapter II.** that the spherical micelles of $[H^+][C_8E_8CH_2COO^-]$ exist only in two states. As small classical core-shell micelles dispersed in an aqueous medium in the L_1 phase or as small headgroup interdigitated micelles in the L_1' phase. In the latter, there is no longer any free bulk water and the entire liquid consists of hydrated, interdigitated micelles. The same microstructures are expected for C_8E_8 and C_8E_{12}. In the latter case, molecular dynamics simulations up to surfactant concentrations of 70 wt% are in agreement with a persisting spherical shape [40]. However, $[H^+][C_8E_8CH_2COO^-]$ possesses an additional carboxylic acid moiety, which allows the introduction of charge and counterion effects. Due to the large E_8-part, the counterion X^+ of $[X^+][C_8E_8CH_2COO^-]$ can be chosen at will and the surfactant is even liquid with polyvalent metal counterions [41–43]. In the present chapter, the research reported in **Chapter II.** is expanded with a detailed analysis of the aqueous phase behavior of the surfactant's sodium ($[Na^+][C_8E_8CH_2COO^-]$) and

calcium ($[Ca^{2+}][C_8E_8CH_2COO^-]_2$) salts, allowing for the construction of a full generic phase diagram of $[X^+][C_8E_8CH_2COO^-]$, explaining its entire aqueous phase behavior, which is determined by the restriction to a spherical micellar shape. Features of the phase behavior are auto-coacervation, clouding, a semi-crystalline lamellar L_β phase in absence of water, and a small domain of an optically anisotropic liquid crystalline gel, all of which are counterion sensitive. The liquid crystalline phase is a hexagonal phase that "melts" into a calamitic nematic phase made of oriented prolate micelles at higher temperatures. Calamitic nematic phases have been found near hexagonal phases in ternary systems of an ionic surfactant with n-decanol as co-surfactant [44,45], but have never been described in other binary surfactant systems. The hexagonal phase is the only exception, where a sphere-to-rod transition is observed. This exception is a consequence of a significant counterion effect on the area per molecule through bridging of carboxylate moieties.

III.3. Experimental Section

III.3.1. Materials

Akypo® LS-F2, the salt-free form of Akypo® LF2 (≈0.9 wt% NaCl), was a generous gift from Kao Chemicals GmbH (Emmerich am Rhein, Germany). In this chapter, the surfactant is denoted as $[H^+][C_8E_8CH_2COO^-]$ instead of $C_8E_8CH_2COOH$ (mostly used in the other chapters), as the focus lies on the counterion. Note, however, that in the case of H^+ at natural pH, the surfactant is pseudo-nonionic. Prior to use, $[H^+][C_8E_8CH_2COO^-]$ was vacuum dried at a maximum temperature of 80°C to reduce the water content to at least 0.5 wt%. Known impurities of Akypo® LS-F2 are small amounts of glycolic acid and formic acid, which are expected to be removed by vacuum drying, diglycolic acid, polyethylene glycol, carboxymethylated polyethylene glycol, and various esters. Most of the esters are expected to be hydrolyzed on salt formation with the respective metal hydroxide. As Akypo® LS-F2 is a technical product, the exact composition may slightly vary in different batches. However, no significant differences in the phase behavior were observed using different batches of the surfactant.

Sodium and calcium salts, $[Na^+][C_8E_8CH_2COO^-]$ and $[Ca^{2+}][C_8E_8CH_2COO^-]_2$, were prepared by a simple neutralization reaction of $[H^+][C_8E_8CH_2COO^-]$ with the respective metal

hydroxide in an aqueous mixture. Full conversion was ensured by adding the hydroxide in slight excess. The mixture was vacuum dried, and any excess hydroxide was removed by centrifugation and subsequent filtration with 0.20 µm PTFE membrane filters. Prior to centrifugation and filtration, the mixture was diluted with acetone to decrease the viscosity. Acetone was eventually removed by vacuum distillation to obtain the pure surfactant salt. The remaining water content was checked using the Karl Fischer titration method and was typically less than 0.5 wt%. $[H^+]_{0.5}[Na^+]_{0.5}[C_8E_8CH_2COO^-]$ was obtained by equimolar mixing of $[Na^+][C_8E_8CH_2COO^-]$ and $[H^+][C_8E_8CH_2COO^-]$.

Acetone (p.a., ≥99.5%), NaOH (p.a., ≥98%), and toluene (p.a., ≥99.5%) were purchased from Sigma-Aldrich (St. Louis, Missouri, USA). NaCl (p.a., ≥99.5%) and n-dodecane (≥95%) were purchased from Carl Roth (Karlsruhe, Germany). $Ca(OH)_2$ (p.a., ≥96%) was supplied by Merck Millipore (Burlington, MA, USA). Acetonitrile-D3 (99.80% D, HDO + D_2O less than 0.05%) for ^{1}H-NMR was purchased from Eurisotop (Saint-Aubin, France). The water used for all experiments had a resistivity >18 MΩ·cm and was obtained from distilled water, using a Millipore purification system.

III.3.2. Phase Diagram Determination

For the determination of the binary phase diagrams of $[H^+][C_8E_8CH_2COO^-]$ and $[H^+]_{0.5}[Na^+]_{0.5}[C_8E_8CH_2COO^-]$, as well as the pseudo-binary phase diagram of $[H^+][C_8E_8CH_2COO^-]$ in presence of 0.25 mol $CaCl_2$ per mol of surfactant, the reader is referred to **Chapter II**.

For the other binary phase diagrams, samples were prepared by mixing $[Na^+][C_8E_8CH_2COO^-]$ or $[Ca^{2+}][C_8E_8CH_2COO^-]_2$ with water in various ratios. To facilitate mixing in the case of liquid crystal formation, the sample was heated to about 60°C and subsequently agitated until a homogeneous solution was obtained. Typically, samples were left equilibrated at 20°C for one day prior to investigation of their phase behaviors. The phase behavior was thoroughly determined between 20°C and 100°C with an accuracy of ±1°C by both visual observation and polarization microscopy. Polarization microscopy was performed using a Leitz Orthoplan (Wetzlar, Germany) polarizing microscope equipped with a JVC (Yokohama, Japan) digital camera (TK-C1380) and a Linkam (Epsom, UK)

LTS350 heating/freezing stage comprising a TMS90 temperature controller (±0.5°C) and a CS196 cooling system. Samples were heated from 20°C to 100°C with a heating rate of 5°C·min^{-1}. However, in case of birefringence, the temperature was increased in steps of 1°C. Equilibration times at different temperatures were consistently observed to be fast. Thus, samples were left equilibrated for a few minutes at each temperature and for at least 10 min close to phase transitions. In some cases, phase transitions were determined below 20°C to allow for a better indication of the birefringent regions in the phase diagrams. Melting points of crystalline phases were determined by heat flux differential scanning calorimetry. Endothermal peak maxima were used as melting points, as they are in agreement with visual observation.

III.3.3. Heat Flux Differential Scanning Calorimetry

Heat flux differential scanning calorimetry was conducted using a DSC 8000 heat-flux calorimeter from Perkin Elmer (Waltham, MA, USA). Samples were put in an aluminum pan, which was subsequently sealed by cold welding an aluminum lid onto it. Sample loaded sealed crucibles were measured against an empty reference crucible. Prior to measurement, samples were cooled to -70°C and held at -70°C for 60 min. One heating and cooling cycle consisted of the following steps: Heating from -70°C to 50°C with a heating rate of 3°C·min^{-1}, holding 50°C for 10 min, cooling from 50°C to -70°C with a cooling rate of 3°C·min^{-1}, and holding -70°C for 60 min. For all samples except $[H^+][C_8E_8CH_2COO^-]$, two heating and cooling cycles were run. Six cycles were run for $[H^+][C_8E_8CH_2COO^-]$, showing that two cycles are sufficient for this system.

III.3.4. Surface Tension Measurements

Equilibrium surface tension isotherms at 25°C were measured using a pull-force tensiometer K100MK2 from Krüss (Hamburg, Germany) equipped with a platinum-iridium-ring and an automatic dosing system Dosino 800 from Metrohm (Herisau, Switzerland). Respective solutions were prepared with the highest surfactant concentration to be measured. Subsequently, the surfactant concentration was automatically reduced stepwise by dilution

with water. Prior to measurement, the glass vessel was soaked first in a KOH bath, followed by a HCl bath for at least 24 h. Subsequently, both the glass vessel and the ring were thoroughly rinsed with water and dried.

III.3.5. ^{1}H-NMR Spectroscopy

^{1}H-NMR spectra of neat $[H^+][C_8E_8CH_2COO^-]$ as well as the coacervate separated from a mixture of 0.45 wt% $[H^+][C_8E_8CH_2COO^-]$ and water by centrifugation were recorded at 25°C using a Bruker (Billerica, MA, USA) Avance 400 spectrometer operating at 400 MHz. Both substances were dissolved in acetonitrile-D3 and 16 scans were performed respectively to obtain the ^{1}H-NMR spectra.

Diffusion-ordered nuclear magnetic resonance spectroscopy (DOSY-NMR) experiments were performed using a Bruker Avance III 600 MHz operating at 600.03 MHz for protons, equipped with a 5 mm high-resolution TBIF probe and with pulsed gradient units, capable of producing magnetic field pulsed gradients in the z-direction of 0.54 $T \cdot m^{-1}$. Temperature was certified by internal NMR calibration samples from Bruker. In all measurements (heating and cooling cycles), the samples were equilibrated at each temperature for 10 min before acquisition.

Diffusion measurements were performed using the stimulated echo sequence using bipolar SMSQ10.100 gradient pulses and eddy current delay before the detection with a convection compensation pulse program (Pulsed Field Gradient Spin Echo – PFGSE) [46,47]. Typically, in each experiment, 32 spectra of 32,768 data points were collected, with values for the duration of the magnetic field pulsed gradients (δ) of 3.0 ms to 5.0 ms, diffusion delay (Δ) of 50 ms to 300 ms. An eddy current delay was set to 5 ms, and the gradient recovery time was 200 ms. The square shaped pulsed gradient was incremented from 10% to 95% of the maximum gradient strength in a linear ramp. To determine the diffusion coefficients, the spectra were first processed in the F2 dimension by standard Fourier transform and baseline correction with the Bruker Topspin software package (version 4.1.3). The diffusion coefficients are calculated by exponential fitting of the data belonging to individual columns of the 2D matrix using the Origin 9.8 data software program. The NMR signal intensity (I) is related to the experimental conditions and the diffusion coefficient (D) according

to the Stejskal-Tanner equation [48]

$$I = I_0 \cdot \exp\left[-q^2 \cdot D \cdot \left(\Delta - \frac{\delta}{3}\right)\right] , \qquad \text{(III.3.1)}$$

where I_0 is the NMR signal in the absence of applied field gradient, Δ is the diffusion time, q is the gradient used in the spatial encoding and decoding of the spin. The gradient q is given by

$$q = \gamma \cdot g \cdot \delta , \qquad \text{(III.3.2)}$$

where γ is the gyromagnetic ratio of the observed nucleus, g is the gradient strength, and δ is the duration over which gradient is applied. By plotting I versus $q^2 \cdot [\Delta - (\delta/3)]$ and fitting the decay curves, the diffusion coefficient is determined [49].

III.3.6. Electrospray Ionization Mass Spectrometry

Electrospray ionization mass spectrometry (ESI-MS) data were obtained from the central analytics mass spectrometry facilities of the Faculty of Chemistry and Pharmacy, University of Regensburg. ESI-MS of neat $[H^+][C_8E_8CH_2COO^-]$ as well as the coacervate separated from a mixture of 0.45 wt% $[H^+][C_8E_8CH_2COO^-]$ and water by centrifugation was performed on an Agilent (Santa Clara, California, USA) Q-TOF 6540 UHD.

III.3.7. Karl-Fischer Titration

Water contents were measured with the aid of volumetric or coulometric Karl-Fischer titration. Volumetric Karl-Fischer titration was performed using a KF titrator 870 KF Titrino plus from Metrohm, while coulometric Karl-Fischer titration was performed using an 899 Coulometer from Metrohm, equipped with a platinum indicator and a platinum generator electrode without a diaphragm. Generally, water contents were measured at least six times and averaged.

III.3.8. Small- and Wide-Angle X-Ray Scattering

Small- and wide-angle X-ray scattering (SWAXS) experiments were carried out on a bench, built by Xenocs (Grenoble, France) using X-ray radiation from a molybdenum source ($\lambda = 0.71$ Å), delivering a 1 mm large circular beam of energy 17.4 keV. The scattered beam was recorded by a large on-line scanner detector MAR Research 345 from marXperts (Norderstedt, Germany) which was located 750 mm from the sample stage. Off-center detection was used to cover a large q-range simultaneously ($0.2\ nm^{-1} < q < 30\ nm^{-1}$), where $q = \sin(\theta/2)\cdot 4\pi/\lambda$, θ being the scattering angle.

Collimation was applied using a 12:∞ multilayer Xenocs mirror (for Mo radiation), coupled to two sets of Forvis (Santa Barbara, CA, USA) scatterless slits, which provides a 0.8 mm × 0.8 mm X-ray beam at the sample position. A high-density polyethylene sample from Goodfellow (Huntingdon, UK)was used as a calibration standard to obtain absolute intensities. Silver behenate in a sealed capillary was used as scattering vector calibration standard. Integration of the 2D spectra was performed using the software FIT2D. Data were normalized taking into account the electronic background of the detector, transmission measurements, and empty cell subtraction.

III.3.9. Small-Angle Neutron Scattering

Small-angle neutron scattering (SANS) data were acquired on the instrument D11 at the Institut Laue-Langevin, Grenoble, France. Samples prepared with D_2O as a solvent to increase contrast and reduce incoherent background were contained in Hellma (Müllheim, Germany) quartz cuvettes type 120-QS of 1 mm pathway. Measurements were carried out for 1 min per sample and per temperature, with a new multi-tube detector, at a wavelength $\lambda = 6.0$ Å (relative FWHM 9 %) and a sample-to-detector distance of 2.5 m, to cover a q-range of 0.02–0.37 $Å^{-1}$, where q is the magnitude of the wavevector ($q = \sin(\theta/2)\cdot 4\pi/\lambda$, θ being the scattering angle). Cuvettes were placed in a prototype Peltier sample-changer from Quantum Northwest (Liberty Lake, Washington, USA), at measured temperatures typically within ±0.02°C of the set-point. Temperature was increased by steps of 10°C. Once the set-temperature was reached, a delay of ≈4 min was implemented. Data reduction was performed with Grasp 9.25b, accounting for detector background (measured with

$^{10}B_4C$), transmission, sample pathway, parralax, scattering by D_2O, and dividing by the scattering of 1 mm H_2O as a flat field correction. The intensity of 1 mm H_2O was used as a secondary standard to obtain absolute scale. A constant (independent on temperature, linearly dependent on volume fraction) was further subtracted to account for incoherent background due to hydrogen. Data are available on demand (https://doi.org/10. 5291/ILL-DATA.EASY-963) [50].

III.3.10. Cryogenic Transmission Electron Microscopy

Specimens for cryogenic transmission electron microscopy (cryo-TEM) imaging were prepared in a controlled environment vitrification system (CEVS), at 25°C and 100% relative humidity. These controlled conditions are essential for the preservation of the native state of the specimen during its preparation. Before specimen preparation, a carbon-coated perforated polymer film supported on a 200 mesh TEM grid was plasma-etched in a PELCO easiGlow glow-discharger (Ted Pella Inc., Redding, California, USA) to increase its hydrophilicity. Inside the CEVS, the etched grid was held by tweezers. A small drop of the sample was applied onto the grid, and the excess solution was blotted with a filter paper supported on a metal strip, to form a thin film of the solution suitable for cryo-TEM imaging. All the specimens were prepared by blotting the grid twice from the back and then touching a clean area of the filter paper. After blotting, the grid was quickly plunged into liquid ethane at its freezing point. That provided a high cooling rate needed for the vitrification of water. The specimens were kept in liquid nitrogen until transferred into the TEM for imaging.

The specimens were imaged by a FEI (Hillsboro, Oregon, USA) Tecnai T12 G^2 TEM, equipped with a LaB_6 electron gun and operating at 120 kV, and a Thermo-Fisher Scientific (Waltham, Massachusetts, USA) Talos 200C, FEG-equipped, 200 kV, high-resolution TEM. To enhance image contrast, the Volta "phase-plate" (VPP) system of the Talos was used.

III.4. Results and Discussion

III.4.1. Phase Diagrams

The carboxylic acid group of $[H^+][C_8E_8CH_2COO^-]$ has an apparent pK_a around 4.0 and solutions of the acid in water have a pH in the range of 2.1 to 2.6, depending on the surfactant concentration. The pH decreases with increasing surfactant concentration in the aqueous regime before it starts to slightly increase in the concentrated regime (>60 wt%). E.g., the pH is 2.1 at 50 wt% and 2.3 at 70 wt% $[H^+][C_8E_8CH_2COO^-]$. Binary phase diagrams of the acid form $[H^+][C_8E_8CH_2COO^-]$ and the half-neutralized form with sodium as counterion $[H^+]_{0.5}[Na^+]_{0.5}[C_8E_8CH_2COO^-]$ are given in **Fig. III.1**A and **III.1**B. A pseudo-binary phase diagram of $[H^+][C_8E_8CH_2COO^-]$ in presence of 0.25 mol $CaCl_2$ per mol of surfactant is shown in **Fig. III.1**C. Addition of $CaCl_2$ was chosen to study the effect of Ca^{2+} ions at acidic pH, i.e., if electrostatics are screened. Note that the indicated precipitate is not the surfactant's calcium salt but insoluble excess $CaCl_2$. The three phase diagrams have already been discussed in detail and were complemented with a detailed study of the microstructures in **Chapter II**. In all three cases, the phase behavior is remarkably simple. No liquid crystalline phases are formed and only a monophasic isotropic liquid phase is observed over the whole concentration and temperature range. The only exceptions are the clouding phenomenon at higher temperatures and an auto-coacervation below the CMC, where two isotropic liquids coexist in equilibrium. Both phenomena are influenced by the counterion through electrostatic interactions, which will be explained later in this chapter. One crucial conclusion from the previous chapter is the microstructuring in the monophasic domain of $[H^+][C_8E_8CH_2COO^-]$ (**Fig. III.1**A), as derived from small-angle X-ray scattering (SAXS). Compared to the volume of the octyl chain, the volume of the headgroup is so large that there is a significant packing constraint, only allowing spherical structures. At 25°C, up to around 60 wt% $[H^+][C_8E_8CH_2COO^-]$, spherical core-shell micelles of constant size (aggregation number $N_{agg} \approx 30$, core radius $R_c \approx 1.2$ nm) and shape are formed (L_1 phase). The core radius and the aggregation number are in good agreement with the theoretical conformation-averaged length of a C_8 chain (1.16 nm) and the resulting maximum theoretical aggregation number for spherical micelles [51]. Above about 60 wt% of surfactant, there is no longer any bulk water, but only hydration water, which leads to the partial interdigitation of the hydrated ethoxylated headgroups. As a result, a polar medium of interdigitated headgroups is formed, in which small hydrocarbon cores are confined (L_1' phase). The size of

these cores decreases gradually with increasing surfactant concentration and reaches its minimum in the complete absence of water (≈100 wt% $[H^+][C_8E_8CH_2COO^-]$), where $N_{agg} \approx 8$ and $R_c \approx 0.8$ nm. Another interesting feature is that the carboxylate groups are not confined but can move freely in the polar interdigitated phase with a thickness of 1–2 nm, as suggested by homothety of the scattering of concentrated $[H^+][C_8E_8CH_2COO^-]$ and $[H^+]_{0.5}[Na^+]_{0.5}[C_8E_8CH_2COO^-]$. Note that the concentration range around 60 wt% should be understood as a transition zone between the L_1 phase and the L_1' phase, where headgroup interdigitation is just about to start. This transition state is here denoted as the L_1/L_1' phase.

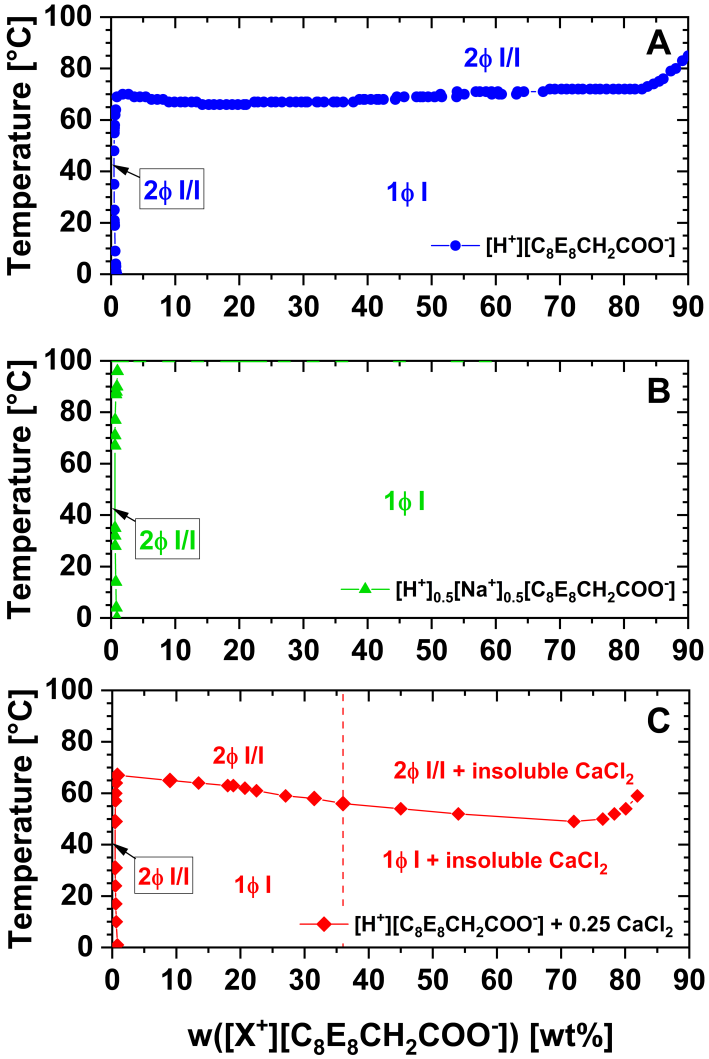

Fig. III.1. (A) Binary phase diagram of $[H^+][C_8E_8CH_2COO^-]$ in water from 0 wt% to 90 wt% of surfactant in a temperature range from 0°C to 100°C. (B) Binary phase diagram of $[H^+]_{0.5}[Na^+]_{0.5}[C_8E_8CH_2COO^-]$ in water from 0 wt% to 82 wt% of surfactant in a temperature range from 0°C to 100°C. (C) Pseudo-binary phase diagram of $[H^+][C_8E_8CH_2COO^-]$ in water in presence of 0.25 mol $CaCl_2$ per mol of surfactant from 0 wt% to 90 wt% of surfactant in a temperature range from 0°C to 100°C. The dashed line indicates the limit of complete solubility of $CaCl_2$ in the mixture. Points beyond this line refer to the mixture in which the solid particles are dispersed. 1ϕ I: Single isotropic phase. 2ϕ I/I: Two isotropic phases in equilibrium. The phase diagrams are redrawn from **Chapter II**.

In **Chapter II.**, full salts, where all of the carboxylate moieties have a counterion other than H^+, were not investigated. Thus, binary phase diagrams of $[Na^+][C_8E_8CH_2COO^-]$ and $[Ca^{2+}][C_8E_8CH_2COO^-]_2$ in water were recorded over the full composition range for temperatures ranging from 20°C to 100°C and are given in **Fig. III.2**A and **III.2**B, respectively. The pH of solutions of $[Na^+][C_8E_8CH_2COO^-]$ and $[Ca^{2+}][C_8E_8CH_2COO^-]_2$ corresponds to the pH of the equivalence point of a respective titration of the acid $[H^+][C_8E_8CH_2COO^-]$ and is typically around 9.3. It should be noted that the region below 2 wt% of surfactant is not shown, because the temperature dependence of the boundaries of the potential auto-coacervation regime was not determined. Auto-coacervation is either found to be less pronounced or completely absent for the salts. In both cases, there is no longer any lower critical solution temperature (LCST). Since the suppression of clouding is already observed for $[H^+]_{0.5}[Na^+]_{0.5}[C_8E_8CH_2COO^-]$ (**Fig. III.1**B), the absence of a LCST is expected for the full salts. Similar to the previously reported phase diagrams (**Fig. III.1**), the vast majority of the aqueous phase diagrams of $[Na^+][C_8E_8CH_2COO^-]$ and $[Ca^{2+}][C_8E_8CH_2COO^-]_2$ is occupied by an isotropic micellar phase, either L_1 or L_1'. However, at 20°C, samples are birefringent between 54 wt% and 67.5 wt% in the case of $[Na^+][C_8E_8CH_2COO^-]$ and between about 60 wt% and 68 wt% in the case of $[Ca^{2+}][C_8E_8CH_2COO^-]_2$ (full symbols, solid lines). In the region from 56 wt% to 67 wt% for the sodium salt and from about 62 wt% to 68 wt% for the calcium salt (empty symbols, dashed lines), a gel is observed. In the region between the solid and the dashed lines, where a birefringent liquid crystalline phase is in equilibrium with an isotropic L_1/L_1' phase, samples are liquids with a slightly increased viscosity. When the temperature is increased, the liquid crystal starts to "melt" above a certain temperature (empty symbols, dashed lines) and is then in equilibrium with an isotropic L_1/L_1' phase, until it completely melts into an isotropic L_1/L_1' phase at slightly higher temperatures (full symbols, solid lines). The maximum temperatures, for which birefringence is observed are 47°C for $[Na^+][C_8E_8CH_2COO^-]$ and 31°C for $[Ca^{2+}][C_8E_8CH_2COO^-]_2$, respectively. For the purpose of neutron scattering experiments, the phase boundaries of the liquid crystalline phases of $[Na^+][C_8E_8CH_2COO^-]$ were also determined in D_2O instead of H_2O. As can be inferred from **Fig. B.1**, the phase diagram is almost identical in both cases. Only a slight shift of the liquid crystalline region to lower concentrations is observed when H_2O is replaced by D_2O.

Another observed feature is a paste-like (waxy) semi-crystalline phase of neat $[Na^+][C_8E_8CH_2COO^-]$ (in absence of water) below 28°C. The crystallization at room

temperature is typically very slow. Thus, heat flux differential scanning calorimetry (DSC) was performed to determine the phase transition temperatures. Since the commercial surfactant is not a "pure" compound, but there is a distribution of the number of ethylene oxide (EO) groups in the headgroup centered around eight, the crystalline phase should have a melting range rather than a melting point. Here, the peak maximum during heating is reported as phase transition temperature, as it is also in agreement with visual observations. DSC measurements of $[Na^+][C_8E_8CH_2COO^-]$, $[H^+]_{0.5}[Na^+]_{0.5}[C_8E_8CH_2COO^-]$, $[Ca^{2+}][C_8E_8CH_2COO^-]_2$, and $[H^+][C_8E_8CH_2COO^-]$ are given in **Fig. B.2**. A similar endothermal peak is observed in all cases at varying temperatures. While water-free $[Na^+][C_8E_8CH_2COO^-]$ and $[H^+]_{0.5}[Na^+]_{0.5}[C_8E_8CH_2COO^-]$ are liquid only above 27°C and 23°C, respectively, $[Ca^{2+}][C_8E_8CH_2COO^-]_2$ and $[H^+][C_8E_8CH_2COO^-]$ are already liquid above 19°C and 11°C, respectively. Addition of water gradually decreases the melting temperature, as can be seen in **Fig. III.2**A and in DSC heating curves given in **Fig. B.3**. The structure of the crystalline phase will be discussed later.

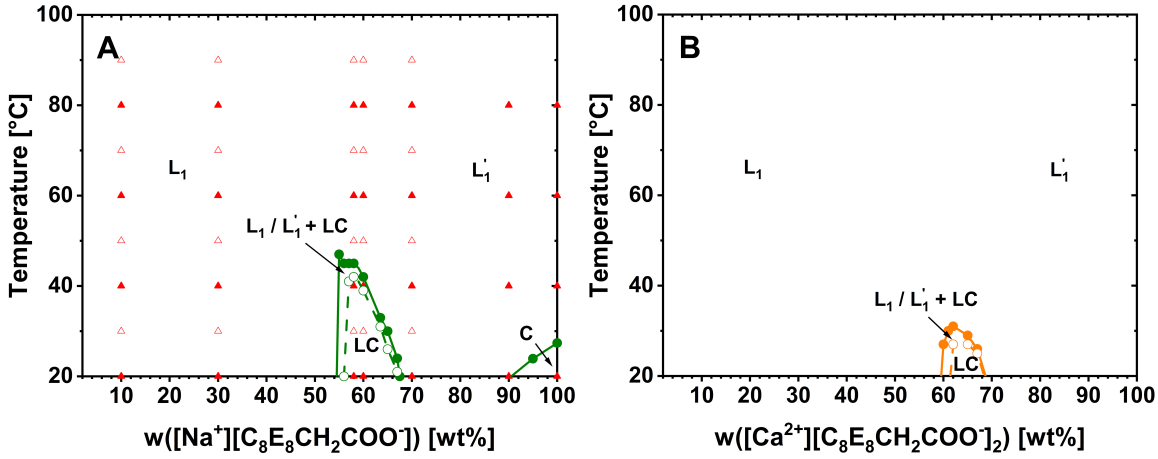

Fig. III.2. (A) Binary phase diagram of $[Na^+][C_8E_8CH_2COO^-]$ in water from 2 wt% to 100 wt% of surfactant in a temperature range from 20°C to 100°C. (B) Binary phase diagram of $[Ca^{2+}][C_8E_8CH_2COO^-]_2$ in water from 2 wt% to 100 wt% of surfactant in a temperature range from 20°C to 100°C. L_1: Solution of core-shell micelles. L_1': Headgroup-interdigitated micellar regime. L_1/L_1': Transition zone between L_1 and L_1'. LC: Liquid crystalline phase. C: Semi-crystalline phase. Phase boundaries of the liquid crystalline regions were determined by visual observation combined with polarized optical microscopy with an accuracy in temperature of ±1°C. Melting temperatures of the semi-crystalline phase were deduced from heat flux differential scanning calorimetry, see **Fig. B.3**. Full circles indicate boundaries between regions where liquid crystals are observed and completely isotropic regions, while empty circles indicate the boundaries between regions where only a liquid crystalline phase is observed and regions where a liquid crystalline phase coexists with an isotropic liquid. Full triangles indicate points, where both SAXS (in H_2O) and SANS (in D_2O) were measured. Empty triangles indicate points where only SANS was measured. The phase diagram of $[Na^+][C_8E_8CH_2COO^-]$ is also given in D_2O instead of H_2O up to a maximum surfactant concentration of 90 wt% in **Fig. B.1**.

III.4.2. Hexagonal and Nematic Phases

In **Chapter II.**, the argument was made that the packing constraint of $[X^+][C_8E_8CH_2COO^-]$ due to its large headgroup is so strong that a sphere-to-rod transition is impossible and thus no liquid crystals are formed. While this seems to be true for the surfactant's acid and partially deprotonated forms, the observation of a birefringent liquid crystalline phase in the case of its full sodium and calcium salts (**Fig. III.2**) suggests that the packing constraint can be overcome under certain conditions.

As described above, there is a transition between a core-shell micellar phase (L_1) and a headgroup interdigitated micellar phase (L_1') in the binary system of $[H^+][C_8E_8CH_2COO^-]$ and water. While the SAXS study in **Chapter II.** was limited to 25°C, the same microstructuring can be assumed for higher temperatures, based on the phase diagrams and the constrained structuring along the studied dilution line. In this chapter, SAXS and SANS experiments were performed on various mixtures of $[Na^+][C_8E_8CH_2COO^-]$ and water (H_2O for SAXS and D_2O for SANS) at different temperatures, ranging from 20°C to 90°C. Note that the phase diagram of $[Na^+][C_8E_8CH_2COO^-]$, see **Fig. III.2**A, was also recorded in D_2O instead of H_2O to make sure that the same structures are investigated in SAXS and SANS, see **Fig. B.1**. The phase diagrams in H_2O and D_2O were found to be almost identical. SAXS and SANS spectra of binary mixtures of 10, 30, 58, 60, and 70 wt% of $[Na^+][C_8E_8CH_2COO^-]$ and water are given in a linear scale in **Fig. III.3**. The same spectra in logarithmic scale are given in **Fig. B.4**. At any given temperature, the scattering evolves as a function of surfactant concentration, apart from the occurrence of liquid crystalline phases at lower temperatures, in the same way as described in detail for $[H^+][C_8E_8CH_2COO^-]$ at 25°C in **Chapter II**. This can be exemplarily seen in the SAXS spectra of a dilution line from 10 wt% to 90 wt% $[Na^+][C_8E_8CH_2COO^-]$ at 60°C, as shown in **Fig. B.5**, both in linear and in logarithmic scale. This result suggests that the surfactant generally is restricted to a spheroidal shape, independent of concentration, temperature, and ionic character. Due to the ionic headgroup, a slight distortion of the shape to either an oblate or a prolate ellipsoidal shape is expected. However, the ellipticity, i.e., the ratio of the axial radius and the equatorial radius, is too small to have a significant effect on scattering. This is also confirmed by cryo-TEM imaging of a sample containing 20 wt% $[Na^+][C_8E_8CH_2COO^-]$, see **Fig. B.6**, where small spheroidal micelles with a diameter of 3.2 ± 0.8 nm are observed. Note that the same structures are observed for

$[H^+][C_8E_8CH_2COO^-]$, see **Fig. A.9** (**Chapter II.**). The ellipticity is too small to make an identification of an ellipsoidal shape possible. The presence of a hexagonal phase implies a slightly prolate shape. While scattering does not allow to exclude an oblate shape, an oblate shape is usually less favored than a prolate one, as a larger portion of the surfactants is located in areas of unfavorable curvature [7]. Due to the prolate shape, surfactant molecules at the tips of the micelles (axial positions) possess a larger area per molecule than those on the sides (equatorial positions). As known from the literature, the area per molecule is connected to the dissociation of ions from carboxylate moieties [52], i.e., a larger area per molecule indicates dissociation of the ions. Thus, it can be assumed that sodium ions are more or less dissociated at the tips of the micelles, which in turn renders the tips of the micelles charged. On the other hand, the sides are apparently uncharged because the charges are balanced by bound ions. For any investigated $[Na^+][C_8E_8CH_2COO^-]$ concentration, the position of the structure factor peak remains almost constant upon increasing temperature, as can be seen in a plot of D* as a function of temperature in **Fig. B.7**. The only exception is a weak (variation of less than 0.2 nm between 20°C and 80°C), but gradual shift of the structure factor peak to lower q-values at 30 wt% $[Na^+][C_8E_8CH_2COO^-]$, also observed to a lesser extent at 10 wt% in SANS and above the melting temperature of the hexagonal phase at 58 wt% and 60 wt%, meaning that the average distance between micelles increases with increasing temperature. Due to the conservation of total volume, an increase in micellar distance at a given concentration corresponds to an increase in micellar size, i.e., an increase in aggregation number. This behavior is expected for ethoxylated headgroups owing to conformational changes and dehydration of ethoxy groups and is well described in the literature for nonionic C_iE_j surfactants [21,53,54]. The absence of a shift at higher concentrations, where headgroups are interdigitated, is a consequence of only hydration water being left, which results in a smaller influence of temperature on the area per molecule.

It should be noted that the SAXS data for binary mixtures of $[H^+][C_8E_8CH_2COO^-]$ were fitted to a model of spherical micelles in **Chapter II.**, while the micelles in reality may be slightly prolate spheroidal as well. However, the ellipticity is most certainly very low ($\leq$1.3), as can already be inferred from the absence of any liquid crystalline phases. Thus, the spherical model is still suitable for $[H^+][C_8E_8CH_2COO^-]$. In the case of $[Na^+][C_8E_8CH_2COO^-]$, the ellipticity is still expected to be quite low ($\leq$1.6).

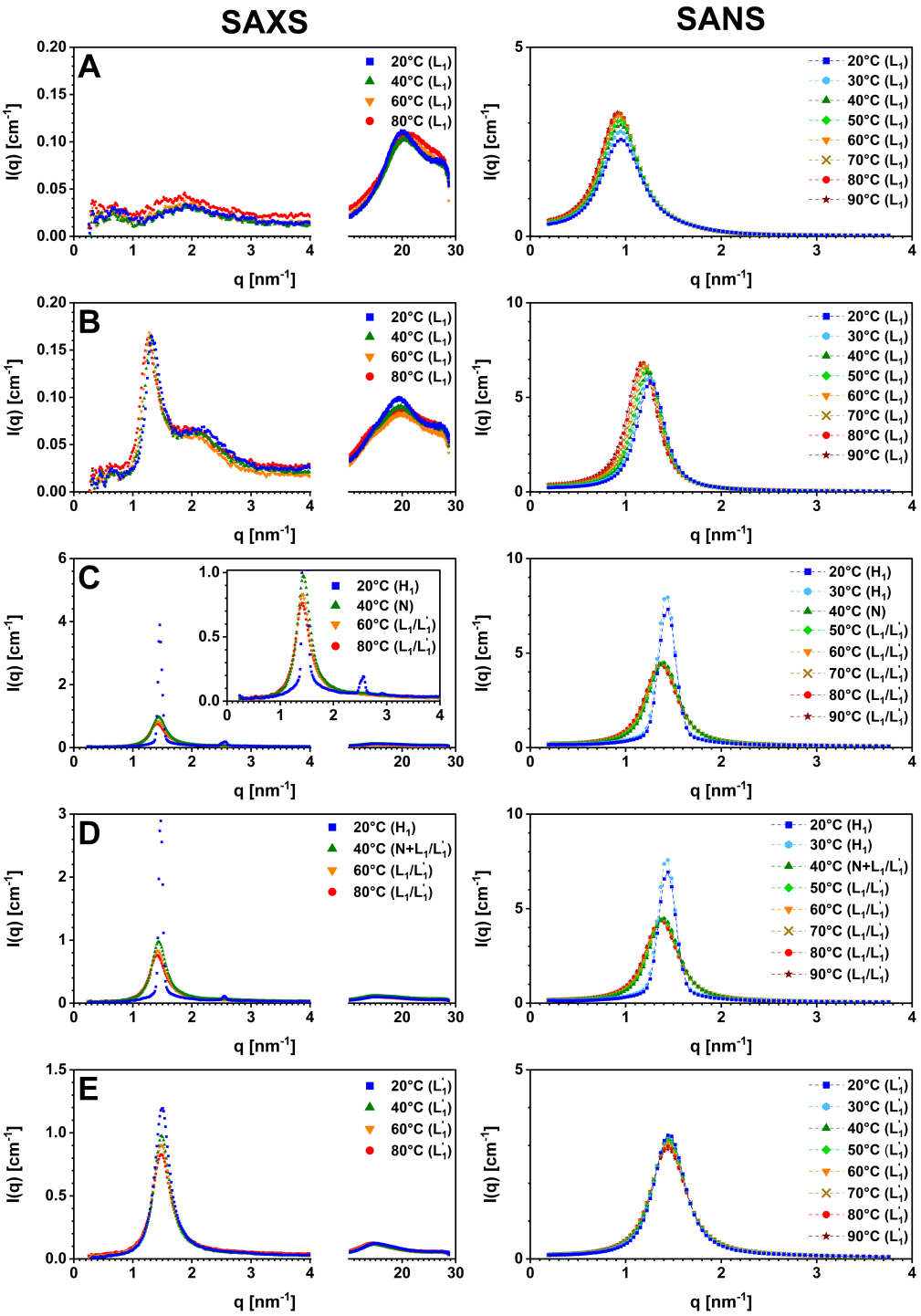

Fig. III.3. SAXS (left column) and SANS (right column) along a dilution line of $[Na^+][C_8E_8CH_2COO^-]$ at different temperatures in linear scale. (A) 10 wt% of $[Na^+][C_8E_8CH_2COO^-]$ in water (H_2O for SAXS and D_2O for SANS). The L_1 core-shell microstructure is found at any temperature. (B) 30 wt% of $[Na^+][C_8E_8CH_2COO^-]$ in water (H_2O for SAXS and D_2O for SANS). The L_1 core-shell microstructure is found at any temperature. (C) 58 wt% of $[Na^+][C_8E_8CH_2COO^-]$ in water (H_2O for SAXS and D_2O for SANS). At 20°C and 30°C, the hexagonal phase (H_1) is observed. At 40°C the H_1 phase is molten into an optically birefringent nematic phase (N). For higher temperatures, the flocculated micellar regime (transition between L_1 and L_1') is observed. (D) 60 wt% of $[Na^+][C_8E_8CH_2COO^-]$ in water (H_2O for SAXS and D_2O for SANS). At 20°C and 30°C, the hexagonal phase (H_1) is observed. At 40°C the H_1 phase is molten into an optically birefringent nematic phase in equilibrium with a flocculated micellar phase ($N+L_1/L_1$'). For higher temperatures, the flocculated micellar regime is observed. (E) 70 wt% of $[Na^+][C_8E_8CH_2COO^-]$ in water (H_2O for SAXS and D_2O for SANS). The headgroup interdigitated micellar regime (L_1') is observed at any temperature. The same spectra in logarithmic scale are given in **Fig. B.4**.

In analogy to its acidic form, the transition zone between the L_1 and the L_1' phase for $[Na^+][C_8E_8CH_2COO^-]$ can be located around 60 wt% of surfactant. In contrast to the acidic form, however, $[Na^+][C_8E_8CH_2COO^-]$ forms a liquid crystalline phase within the transition zone at lower temperatures (≤47°C), see **Fig. III.2**A. At 20°C and 30°C, SAXS and SANS reveal a hexagonal phase for the 58 wt% and 60 wt% samples, see **Fig. III.3**C and **III.3**D. This is especially evident in the SAXS spectra at 20°C, where the contrast is increased compared to SANS due to the sodium ions. In **Fig. III.4**, the SAXS and SANS spectra of the 58 wt% and 60 wt% samples are shown in semi-logarithmic (log-lin) scale. At 58 wt%, a first order Bragg peak is located at $q_1 = 1.454\ nm^{-1}$ ($D_1^* = 4.32$ nm), a much weaker second order Bragg peak is located at $q_2 = 2.554\ nm^{-1}$ ($D_2^* = 2.46$ nm), and a very weak third order Bragg peak is located at $q_3 = 2.922\ nm^{-1}$ ($D_3^* = 2.15$ nm), where $D_i^* = 2\pi \cdot q_i^{-1}$. At 60 wt%, $q_1 = 1.471\ nm^{-1}$ ($D_1^* = 4.27$ nm), $q_2 = 2.544\ nm^{-1}$ ($D_2^* = 2.47$ nm), and $q_3 = 2.964\ nm^{-1}$ ($D_3^* = 2.12$ nm). Those positions follow the typical series for a hexagonal packing, where $q_2 = \sqrt{3} \cdot q_1$ and $q_3 = \sqrt{4} \cdot q_1$ [55]. Thus, the birefringent gels at 58 wt% and 60 wt% are hexagonal phases (H_1). Note that the peaks are quite sharp, suggesting that either the alkyl chains or the ethylene oxide chains are weakly semi-crystalline to produce a well-ordered liquid crystal, but not crystalline enough to produce peaks of a crystal lattice in the WAXS regime. In the case of classical C_iE_j surfactants, a hexagonal phase consists of hexagonally ordered long rod-like micelles [6,19,56]. Hence, the occurrence of a hexagonal phase for $[Na^+][C_8E_8CH_2COO^-]$ indicates that the strong packing constraint of $[X^+][C_8E_8CH_2COO^-]$, usually allowing only the formation of spherical to slightly prolate spheroidal micelles, can be overcome in a small concentration and temperature range in presence of sodium counterions. At higher temperatures, the hexagonal phase is molten first into a nematic phase (N) and then into the flocculated micellar regime (transition of the L_1 to the L_1' phase, L_1/L_1') made of prolate micelles with partially interdigitated headgroups.

Due to the conservation of volume, the diameter of the hydrophobic cores must be smaller in the cylindrical shape compared to the prolate spheroidal shape, which, in turn, reduces the distance between the cores upon merging the cores into cylinders. A smaller distance corresponds to a shift of the peak maximum to higher q-values. Thus, if cylinders are formed, usually a significant shift of the peak maximum to higher q is observed. Comparing > 40°C spectra (L_1/L_1') to 20°C and 30°C spectra (H_1) in **Figs. III.3**C, **III.3**D, and **III.**4, it can be clearly seen that there is no significant shift to higher q upon formation of the hexagonal phase. Only a very small shift can be observed in SANS, which is not sufficient to

directly deduce a transition to a cylindrical state from it. Given the absence of a peak shift and the strong packing constraint of the surfactant, one could also imagine a hexagonal packing of chains made of connected (ion-bridged) prolate micelles. Surprisingly, the expected shift of the peak if the prolate hydrocarbon cores merged into “infinite” cylinders, see **Appendix B.2.** for the calculation, is insignificant in the present case. The absence of a peak shift can also be seen when comparing the peak position for 58 wt% $[Na^+][C_8E_8CH_2COO^-]$ at 20°C, giving D* = 4.32 nm, to the peak position at room temperature for an isotropic micellar solution of 60 wt% $[H^+][C_8E_8CH_2COO^-]$, giving D* = 4.30 nm, see **Chapter II**. As mentioned above and shown in **Chapter II.**, $[H^+][C_8E_8CH_2COO^-]$ does not form liquid crystalline phases and forms spherical micelles. Thus, scattering alone does not allow us to make a definite statement, whether a sphere-to-rod transition is undergone or not. The expected hydrocarbon core radius of infinite cylinders in a hexagonal packing, calculated from D* = 4.32 nm, would be close to 1.1 nm. Since this radius is slightly lower than the conformation-averaged length of 1.16 nm, the hydrocarbon cores could be tilted from the perpendicular direction to the hydrophobic/hydrophilic interface: Chain tilts in order to reduce area mismatch are well-known in smectic C phases and lipids, but the existence of tilt in a hexagonal phase has rarely been observed.

To find out whether the H_1 phase is made of cylinders or prolate micelles, the H_1-to-L_1/L_1’ transition was followed by diffusion-ordered NMR spectroscopy (DOSY-NMR). Usually, the surfactant self-diffusion significantly increases, when smaller micelles (disconnected cores) transition into long (“infinite”) cylinders, because the surfactant molecules can move along the axis of the cylinders [57,58]. The self-diffusion of the surfactant molecules was examined by DOSY-NMR in a temperature range between 5°C and 60°C for samples containing 30 wt% and 65 wt% $[Na^+][C_8E_8CH_2COO^-]$. The measured surfactant self-diffusion coefficients are given as a function of temperature in **Fig. B.8**. Prior to measurement, each sample was left equilibrated for 10 min at each temperature. Note that the observed self-diffusion always represents the self-diffusion of surfactant molecules in a liquid phase, and not in the H_1/N-gel-phase, since the self-diffusion is too slow in the gel. Though not shown in **Fig. B.8**, it was not possible to measure surfactant self-diffusion below the melting temperature of the liquid crystalline phase at 58 wt% $[Na^+][C_8E_8CH_2COO^-]$ during heating. On re-cooling the sample, self-diffusion could be measured even below the melting temperature, which is linked to the kinetics of the reformation of the liquid crystalline phase. As the self-diffusion on re-cooling can still be measured after the macroscopical reformation

of the gel, the phase transition must be locally incomplete at the time of the measurement. At 65 wt% $[Na^+][C_8E_8CH_2COO^-]$ it was possible to measure self-diffusion even during heating in the temperature range of the liquid crystalline phase, which indicates the presence of a liquid portion. In the isotropic liquid phase (L_1/L_1') above the melting temperature of the liquid crystalline phase, the surfactant self-diffusion is virtually identical for samples containing 58 wt% and 65 wt% of surfactant. On heating the 65 wt% sample, the transition from the H_1 phase to the N phase or to the isotropic liquid is not seen in surfactant self-diffusion. On re-cooling, however, the self-diffusion coefficient jumps from $7.53 \cdot 10^{-12}$ $m^2 \cdot s^{-1}$ at 24°C to $15.58 \cdot 10^{-12}$ $m^2 \cdot s^{-1}$ at 22°C. A transition at 24°C can also be identified in the ^{1}H-spectra, see **Fig. B.9**, which is slightly lower than the transition temperature of 26°C observed macroscopically and with polarized optical microscopy. The observed sharp doubling of the surfactant self-diffusion coefficient is similar to the jump in self-diffusion reported by Constantin *et al.* [58] for a fluorescent dye in the isotropic liquid-to-hexagonal phase transition of $C_{12}E_6$, who found an increase in self-diffusion by a factor of approximately 2.5 at a surfactant concentration of 60 wt%. Since $C_{12}E_6$ forms a classical hexagonal phase made of "infinite" cylinders, the increase in self-diffusion indicates a spheroid-to-rod transition in the case of $[Na^+][C_8E_8CH_2COO^-]$. Note that the cylinders could also be an intermediate state between a perfect cylinder and separated prolate micelles, i.e., partially merged prolate micelles, as the diffusion only proves that hydrocarbon cores are merged. Moreover, the diffusion behavior in the nematic phase and the L_1/L_1' phases are similar, confirming that hydrocarbon cores are disconnected in the nematic phase. Micelles must be prolate and/or start to coalesce in the nematic region.

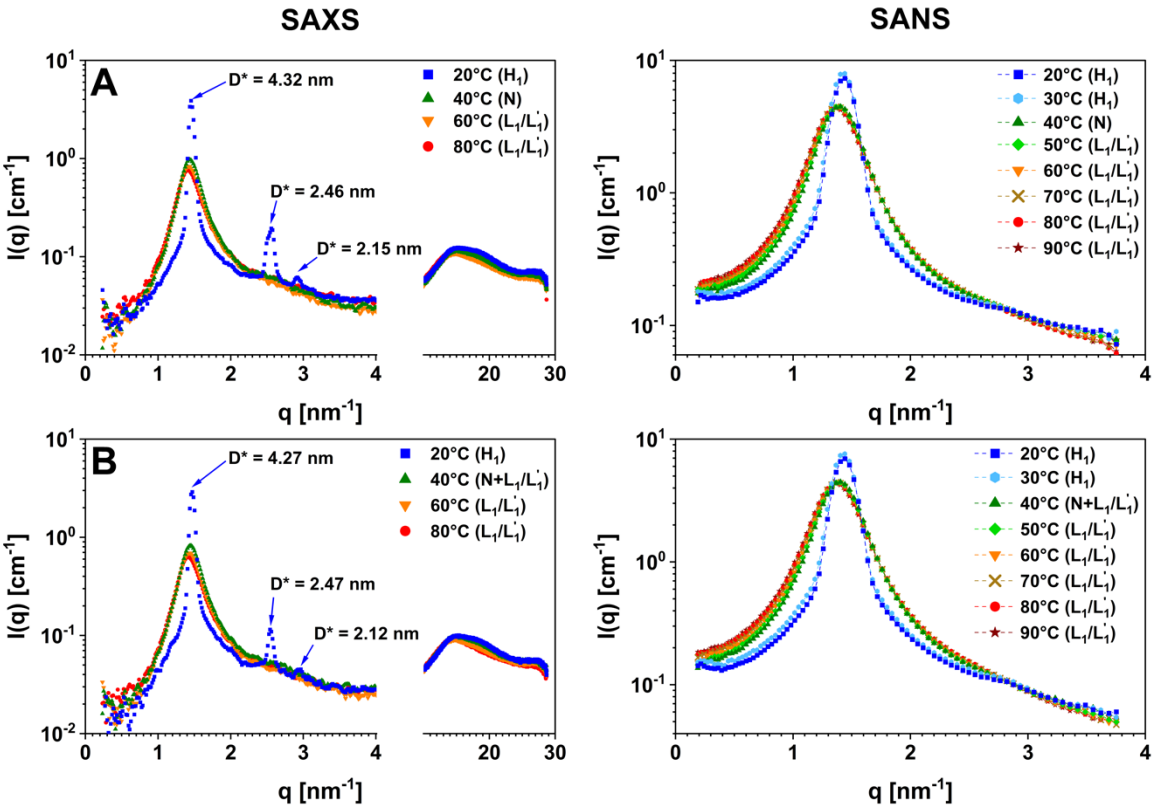

Fig. III.4. Proof of the transition from a hexagonal phase to a nematic phase made of prolate micelles via SAXS (left column) and SANS (right column). (A) 58 wt% [Na^+][$C_8E_8CH_2COO^-$] in water (H_2O for SAXS and D_2O for SANS) at temperatures ranging from 20°C to 90°C. A hexagonal phase (H_1) at low temperatures transitions into a nematic phase (N) and eventually into an isotropic flocculated micellar phase (L_1/L_1') at higher temperatures. (B) 60 wt% [Na^+][$C_8E_8CH_2COO^-$] in water (H_2O for SAXS and D_2O for SANS) at temperatures ranging from 20°C to 90°C. At lower temperatures, a H_1 phase is observed that also melts into a nematic phase and into an isotropic L_1/L_1' phase at higher temperatures. At 40°C, the nematic phase is in coexistence with the L_1/L_1' phase ($N+L_1/L_1$'). SAXS spectra are given in log-lin scale in the left column and corresponding SANS spectra are given in log-lin scale in the right column. The same spectra are given in linear scale in **Fig. III.3**C and **III.3**D and in logarithmic scale in **Fig. B.4**C and **B.4**D. Peak positions are indicated as $D^* = 2\pi/q_{max}$.

If, apart from the hexagonal phase, a sphere-to-rod transition is impossible due to packing constraints and the number of surfactant molecules present per micelle is larger than the maximal number that can be packed in a spherical aggregate, a significant stress on the area per molecule and the equatorial radius of micellar cores arises. Because of this stress, the equilibrium area per molecule must decrease and the averaged molecular chain length must increase [59,60]. In the case of spherical micelles, e.g., in the case of sodium octanoate [61], the conformation-averaged length at room temperature l_0, which equals the Tanford length (1.16 nm in the case of an octyl chain), has been verified by SAXS and SANS. In the case of stress exerted on the area per molecule due to a large aggregation number, resulting in axial elongation, that imposes to reduce the area below the equilibrium area given by the lateral equation of state [62], linking the molar Gibbs energy to the packing parameter, the entropic cost of extending the chain from l_0 to the maximum all-*trans* extended

length l_{max} is only 1–2 k_BT per molecule [63]. As proposed by Dill [64], Dill and Flory [65], as well as Fromherz [66], the effective length approaches the fully extended length l_{max}, in our case estimated as 1.45 ± 0.05 nm on the basis of bond lengths and angles as in crystallographic tables, since gauche conformations are forbidden by the constraint of packing more molecules together than would be possible in a sphere. Assuming a local face-centered-cubic-like closed packing of prolate micelles in the isotropic L_1/L_1' phase at 58 wt% $[Na^+][C_8E_8CH_2COO^-]$ at 60°C (above the hexagonal and the nematic phase), the aggregation number is derived from D* = 4.42 nm as N_{agg} = 76. Further assuming an equatorial radius, including protrusion effects, between 1.4 nm and 1.5 nm, an ellipticity ranging from 1.3 to 1.6 is obtained, see **Appendix B.2**. The corresponding area per molecule ranges from 0.455 nm^2 to 0.470 nm^2. The ellipticity is also reasonable compared to the result obtained by the same calculation for 30 wt% $[Na^+][C_8E_8CH_2COO^-]$ at 20°C, where the micelles can be safely assumed not to form cylinders, using the conformation-averaged length l_0 = 1.16 nm. From D* = 4.80 nm, an aggregation number of 44, an ellipticity of 1.675, and an area per molecule of 0.588 nm^2 are derived, see **Appendix B.2**. At 30 wt%, the stress on the area per molecule is much lower, justifying the use of l_0. However, the equatorial radius could also extend from l_0 towards l_{max} even at 30 wt%. Note that in these calculations it is neglected that the observed peak position is not identical to the peak position of the structure factor, which would strictly speaking be used for the calculation. The SANS spectrum of 30 wt% $[Na^+][C_8E_8CH_2COO^-]$ at 20°C on absolute scale can be fitted quite well with a prolate core-shell ellipsoid form factor and a Hayter-Penfold RMSA structure factor, as can be seen in **Fig. B.10** (details are given in the caption of **Fig. B.10**). It is important to note that different combinations of radii and ellipticity produce the same fit, as long as the volume remains constant. Thus, no statement can be made about the actual ellipticity. One possible fit in this case is obtained with a core radius of 1.10 nm, an ellipticity of 1.27, and a shell thickness of 1.01 nm. This would correspond to an aggregation number of 29 and an area per molecule of 0.627 nm^2, which is fairly close to what was obtained for a 30 wt% $[H^+][C_8E_8CH_2COO^-]$ solution using a core-shell sphere form factor in **Chapter II**.

The observed transition from an isotropic micellar (L_1/L_1') phase to the H_1 phase through a nematic phase is linked to hydrocarbon core coalescence during the nematic-to-hexagonal transition. The coalescence of cores is also well-known for micelles of surfactants with polar headgroups of much smaller volume, such as C_8E_5 and C_8E_6, for which the coalescence and shape transition going from an isotropic phase to the hexagonal phase are well

documented: They exhibit a similarly shaped hexagonal domain below 20°C at around 60 wt% of surfactant. Molecular dynamics simulations and SANS clearly evidence a sphere-to-rod transition and suggest a classical H_1 phase comprising long cylindrical micelles in those cases [21,40]. Since $[Na^+][C_8E_8CH_2COO^-]$ seems to be able to form cylinders, despite the packing constraint of $[H^+][C_8E_8CH_2COO^-]$ being too strong to allow a sphere-to-rod transition, the effective area per molecule must decrease in the ionic form. Note that the sphere-to-rod transition could also be incomplete, resulting in necklace of prolate micelles with merged hydrocarbon cores. The reason for the decrease of the area per molecule is attractive intra- and intermicellar bridging of the headgroups' carboxylate moieties via sodium ions that exceeds electrostatic repulsions of the charged headgroups. Rosenlehner *et al.* [67] reported that sodium ions form ion triplets with carboxylates ($RCOO^-\cdots Na^+\cdots RCOO^-$), leading to a stronger binding of the carboxylates than in carboxylic acid dimers. The bridging has the strongest effect within the L_1/L_1' regime, where the hexagonal phase is observed, since the micelles are in close proximity and almost no bulk-water is left, i.e., not all water molecules are bound to the hydration layer of the headgroups, but there is not enough free water to separate the micelles.

At higher temperatures, but still within the birefringent gel region, the H_1 phase "melts" into a nematic phase (N). SAXS and SANS of the nematic phase can be seen in **Figs. III.3**C and **III.4**A at 40°C. The scattering is very similar to the scattering of the L_1/L_1' phase. Such similarities in scattering are common for nematic phases, as there is only a weak ordering with restrictions in rotational movement. The proof that there is a nematic ordering is the birefringence of the sample, see **Fig. III.5**. In fact, the nematic phase is still a gel until coexistence of the N phase and the L_1/L_1' phase is reached at slightly higher temperatures (region between solid and dashed line in **Figs. III.2**A and **III.5**), where the samples start to become liquid. Scattering in the coexistence regime can be seen in **Figs. III.3**D and **III.4**B at 40°C. Since scattering of the N phase and the L_1/L_1' phase is similar, scattering in the coexistence regime is also similar. Coexistence of an isotropic phase and a birefringent phase is clearly evident in polarized optical microscopy, see **Fig. B.11**. In **Fig. B.11**, the transition from the H_1 phase to the N phase and eventually to the isotropic L_1/L_1' phase is shown as observed with polarization microscopy for a 58 wt% $[Na^+][C_8E_8CH_2COO^-]$ sample. In contrast to the H_1 phase, the formation of a nematic phase with only local orientational order is impossible with "infinite" cylinders. There are no indications in scattering that cylinders or ellipsoids with an ellipticity ≥2 are formed in the L_1 phase at lower

concentrations. Thus, the nematic phase (at 40°C) must be made of micelles of similar ellipticity as in the isotropic phase at higher temperature (60°C), some of them probably starting to merge to form longer prolate micelles. In the nematic phase, only a direction of the long axis along the nematic axis is favored, without a peak shift perpendicular to the nematic axis. The above mentioned higher counterion dissociation at the axial positions of the micelles probably enables bridging of carboxylates of adjacent micelles via sodium ions preferentially at the axial positions of the micelles. In addition to the bridging of the carboxylates via sodium ions, the headgroup interdigitation is enhanced at axial positions of the micelles to sufficiently hydrate/coordinate the ions. Thus, the nematic ordering is achieved by the preferential orientation of (a) chains of a few smaller slightly prolate micelles and (b) elongated micelles originating from the merging of the smaller micelles. This is a rare report of a nematic phase in a binary surfactant system, the only example known to the authors being the cesium pentadecafluorooctanoate/water system [68,69].

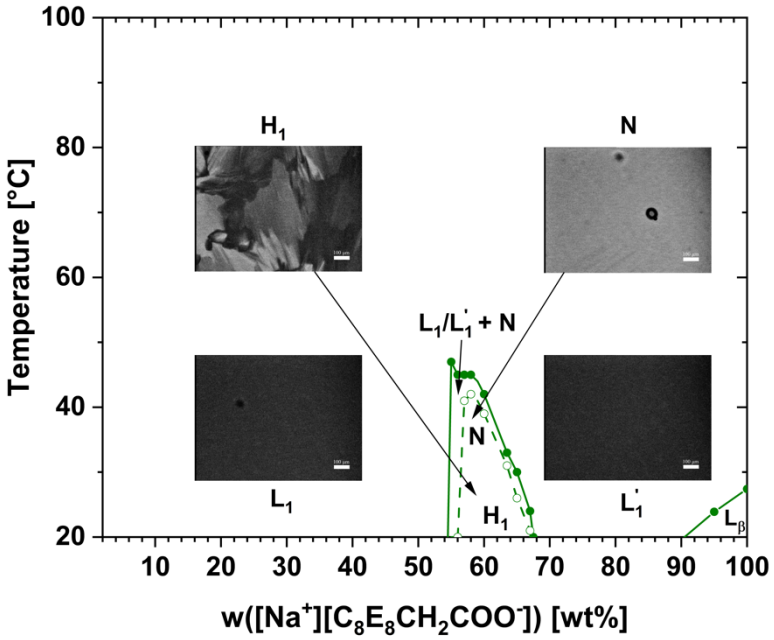

Fig. III.5. Confirmation of the liquid crystals by polarized optical microscopy. Micrographs (x100 magnification) of the four different regimes appearing in binary solutions of $[Na^+][C_8E_8CH_2COO^-]$ taken across crossed polarizing filters. Scale bars indicate a length of 100 µm. Their positions in the phase diagram are indicated by arrows, if necessary. L_1: Core-shell micellar solution. L_1': Headgroup-interdigitated micellar regime. L_1/L_1': "Flocculated" micellar regime (transition from L_1 to L_1'). H_1: Hexagonal phase. N: Nematic phase. L_β: Semi-crystalline lamellar phase.

The transition from the H_1 phase to the N phase can be rationalized as a "melting" of the "infinite" cylinders. With increasing temperature, thermal energy more and more overcomes the ion-bridging of the carboxylates, increasing the effective area per molecule and inducing a cylinder-to-spheroid transition. In the intermediate state, where some prolate

micelles are still merged and ions can still sufficiently bridge some of the micelles, a preferential orientation can be induced, and a nematic phase can form. Once the transition into the smaller prolate micelles is complete and thermal fluctuations exceed the effect of ion-bridging, there is an isotropic L_1/L_1' phase of randomly oriented micelles. With that knowledge, the binary phase diagram of $[Na^+][C_8E_8CH_2COO^-]$, as shown in **Fig. III.2**A, can be redrawn in **Fig. III.5** with superposed polarization microscopy images to confirm the structures deduced from small-angle scattering. The balance between ion-bridging and thermal energy is also influenced by electrostatic repulsion. Screening electrostatics of a 58 wt% $[Na^+][C_8E_8CH_2COO^-]$ sample by equimolar addition of NaCl increases the onset of the liquid crystal "melting" from 43°C to 57°C. It is also important to note that the formation of a H_1 or a N phase is only observed if the acid is (almost) fully transformed into the respective salt, i.e., if x is close to 1 in $[H^+]_{1-x}[Na^+]_x[C_8E_8CH_2COO^-]$. It remains unknown, whether this is merely due to ion-bridging being just strong enough to overcome the strong packing constraint for $x \approx 1$, or if the esters present in $[H^+][C_8E_8CH_2COO^-]$ significantly destabilize the hexagonal phase even in low quantities. The latter are hydrolyzed during synthesis of $[Na^+][C_8E_8CH_2COO^-]$ and are reintroduced by mixing $[Na^+][C_8E_8CH_2COO^-]$ and $[H^+][C_8E_8CH_2COO^-]$ to produce $[H^+]_{1-x}[Na^+]_x[C_8E_8CH_2COO^-]$ with varying x. It is, however, important to note that no hexagonal phase is formed by $[H^+][C_8E_8CH_2COO^-]$ in absence of ester impurities, see **Chapter IV.** (**Appendix C.2.**), showing that ion-bridging is indeed required to overcome the packing constraint.

It is also noteworthy that the area per molecule can be influenced by the addition of oil as a solute. If around 10 wt% n-dodecane are solubilized in an aqueous mixture initially containing 58 wt% $[Na^+][C_8E_8CH_2COO^-]$, the hexagonal phase is stabilized, and the "melting" temperature is increased to above 90°C. However, outside of the concentration range of hexagonal phase formation, no structural influence of n-dodecane is observed macroscopically. As shown for $[H^+][C_8E_8CH_2COO^-]$ in **Chapter II.**, only a certain amount of oil can be incorporated into the spheroidal micelles of $[Na^+][C_8E_8CH_2COO^-]$, and any excess oil phase separates. This is also true for a binary mixture of $[Na^+][C_8E_8CH_2COO^-]$ and n-dodecane. Therefore, the effect of the purely hydrophobic oil on the area per molecule of the surfactant alone is insufficient to overcome the strong packing constraint of the surfactant. Though it was not tested, it can be expected that the addition of n-dodecane lowers the minimum required x of $[H^+]_{1-x}[Na^+]_x[C_8E_8CH_2COO^-]$ for hexagonal phase formation.

For $[Ca^{2+}][C_8E_8CH_2COO^-]_2$ instead of $[Na^+][C_8E_8CH_2COO^-]$, the macroscopic phase behavior, see **Fig. III.2**B, and appearance in polarization microscopy is basically identical. Thus, the microstructures are expected to be identical as well. Surprisingly, the liquid crystalline phases formed by $[Ca^{2+}][C_8E_8CH_2COO^-]_2$ "melt" at lower temperatures than those formed by $[Na^+][C_8E_8CH_2COO^-]$. This indicates that the decrease of the area per molecule is more pronounced with sodium counterions than with calcium counterions.

III.4.3. Lower Critical Solution Temperature

For further discussions regarding the lower critical solution temperature (LCST) and auto-coacervation, the phase diagrams of $[H^+][C_8E_8CH_2COO^-]$, $[H^+]_{0.5}[Na^+]_{0.5}[C_8E_8CH_2COO^-]$, $[H^+][C_8E_8CH_2COO^-]$ in presence of 0.25 mol $CaCl_2$ per mol of surfactant (**Fig. III.1**), as well as $[Ca^{2+}][C_8E_8CH_2COO^-]_2$ (**Fig. III.2**B) are replotted in **Fig. III.6**A in a semi-logarithmic scale (lin-log). An enlargement of the auto-coacervation regime is also given in linear scale in **Fig. III.6**B. Clouding, i.e., a LCST (dashed circles in **Fig. III.6**A), is observed for $[H^+][C_8E_8CH_2COO^-]$ and $[H^+][C_8E_8CH_2COO^-]$ in presence of 0.25 mol $CaCl_2$ per mol of surfactant, only rudimentarily for $[H^+]_{0.5}[Na^+]_{0.5}[C_8E_8CH_2COO^-]$, but not for $[Ca^{2+}][C_8E_8CH_2COO^-]_2$ and $[Na^+][C_8E_8CH_2COO^-]$. The LCST is 66°C around 14 wt% to 21 wt% of surfactant in the case of $[H^+][C_8E_8CH_2COO^-]$, which is about 30°C lower than the LCST reported by Mitchell *et al.* [6] for the nonionic counterpart C_8E_8. As already demonstrated by Corti *et al.* [70] in 1984, the cloud point for short-chain ($i \leq 8$) nonionic surfactants C_iE_j can be described by flocculation of small globular micelles through attractive temperature dependent interactions. In the case of more classical $C_{2j}E_j$ surfactants ($j > 4$), the cloud point is well known to be accompanied by a change in micellar shape, i.e., a sphere-to-cylinder growth [22–24]. Even for C_8E_4 and C_8E_5, Glatter *et al.* [21] stated that a transition in micellar shape is involved in the micellar flocculation approaching the LCST. Since neither $[H^+][C_8E_8CH_2COO^-]$ nor $[Na^+][C_8E_8CH_2COO^-]$ show a transition in shape or a strong increase in size with increasing concentration or temperature (see sections above), the mechanism of clouding can be safely assumed to be aggregation of small globular or slightly prolate micelles. This is also supported by comparing the critical point of $[H^+][C_8E_8CH_2COO^-]$ to the theoretical model described by Kjellander [71]. Kjellander used various models based on hard spheres with an attractive potential to determine theoretically

the critical point of aqueous solutions of C_iE_j. For various potentials, he determined that the critical volume fraction φ_c must be in the range of 7.4% to 17.4%. He used his findings to demonstrate that most C_iE_j (of the regular type close to $C_{2j}E_j$) have a far too low critical volume fraction to be compatible with a spherical model, and deduced that elongation into flexible wormlike micelles was necessary.

However, for the case of $[H^+][C_8E_8CH_2COO^-]$, the critical point is between 13% and 20%, in full agreement with Kjellander's model of sticky hard spheres with an energy well of the order of around -0.75 k_BT. Using the Flory-Huggins theory (which should in principle only be applied for large aggregation numbers), $\varphi_c = 0.155$ leads to an aggregation number of $N_{agg} = [(1-\varphi_c)/\varphi_c]^2 = 30$, in good agreement with the experimental findings (**Chapter II.**). Thus, the lower LCST for $[H^+][C_8E_8CH_2COO^-]$ compared to C_8E_8 can be ascribed to stronger attractive forces between spherical micelles of $[H^+][C_8E_8CH_2COO^-]$. Headgroup termination by a carboxylic acid moiety could explain enhancement of intermicellar interactions through COOH-COOH bridging [72]. If all carboxylic acid moieties are deprotonated, as in $[Na^+][C_8E_8CH_2COO^-]$ and $[Ca^{2+}][C_8E_8CH_2COO^-]_2$, the micelles are charged and electrostatic repulsions between micelles inhibit micelle flocculation. Thus, clouding is inhibited and no LCST is observed (up to 100°C). While bridging of the carboxylate moieties via sodium or calcium ions is imaginable, as described in the previous section, electrostatic repulsions seem to be predominant at higher temperatures. Only at lower temperatures and if micelles are in close proximity (in the L_1/L_1' phase), sufficient bridging via ions is conceivable to form the hexagonal and nematic phase described above. If only half of the carboxylic acid moieties are deprotonated, as is the case for $[H^+]_{0.5}[Na^+]_{0.5}[C_8E_8CH_2COO^-]$, electrostatic repulsion already exceeds intermicellar attraction. As a result, there is no longer any clouding. Only at very low concentrations of about 0.7 wt% to 1.0 wt% $[H^+]_{0.5}[Na^+]_{0.5}[C_8E_8CH_2COO^-]$, close to the auto-coacervation regime, a residual of the clouding curve may be located. The LCST would then be around 87°C. If electrostatics are screened, the presence of Ca^{2+} ions shifts the LCST to a lower temperature and higher concentration. The LCST of $[H^+][C_8E_8CH_2COO^-]$ in water upon addition of $CaCl_2$ is shifted from 66°C to 49°C and from about 20 wt% of surfactant to 72 wt% of surfactant. This shift can be explained by attractive intermicellar bridging via calcium ions which, due to electrostatic screening, is no longer surpassed by electrostatic repulsions. In these systems, clouding is very likely a separation of a concentrated headgroup interdigitated L_1' phase from a more dilute micellar L_1 phase. A dynamic equilibrium of L_1 and L_1'

means that the win in binding enthalpy and the increase of entropy through water release upon interdigitation is compensated by hydration energy and translational energy in the core-shell regime. Seemingly, the increase in binding enthalpy through ion cross-linking is strongest in the L_1/L_1' regime (transition between core-shell and headgroup interdigitated micelles), as the LCST is located in this regime if Ca^{2+} ions are present and electrostatics are screened.

To estimate the tie-lines in the clouding regime, the two phases separating at 90°C from aqueous solutions containing 20 wt% and 40 wt% $[H^+][C_8E_8CH_2COO^-]$, respectively, were separated and their surfactant concentrations were determined gravimetrically and by measuring their water content with the Karl Fischer titration method. In both cases, a L_1/L_1' phase containing 65 wt% to 70 wt% $[H^+][C_8E_8CH_2COO^-]$ separates from a dilute L_1 phase containing less than 2 wt% of surfactant. The observation of clouding above 70 wt% of surfactant gives rise to the question, which phases form in equilibrium. As the tie-lines at lower concentrations end in the L_1/L_1' phase around 65 wt% of surfactant, the tie-lines at higher concentrations could be expected to start around 65 wt% of surfactant and end at higher concentrations. E.g., at 80 wt% of surfactant and 90°C, a rather small amount of one phase separates from another. Both phases have similar densities and cannot be adequately separated without heated centrifugation. However, water content measurements indeed indicate the separation of a L_1/L_1' phase of similar concentration from a more concentrated L_1' phase. Thus, tie-lines always seem to be connected to the L_1/L_1' phase, which fittingly may be understood as a phase of "flocculated" micelles.

In this regard it is important to note that the surfactant Akypo® LF2 ($[H^+][C_8E_8CH_2COO^-]$) was used as received for recording these phase diagrams, see **Chapter II.**, which means that 0.01 g NaCl are present per 1 g of surfactant. If all the salt is removed by cloud point extraction, see **Fig. IV.1** in **Chapter IV.**, a cloud point is only observed up to 70 wt% $[H^+][C_8E_8CH_2COO^-]$. If NaCl is then added in the same amount as initially present, the clouding curve changes to what is observed here (**Fig. III.6**A). Thus, the liquid-liquid phase separation above 70 wt% $[H^+][C_8E_8CH_2COO^-]$ only occurs in presence of salt, and as can be seen in the case of 0.25 mol $CaCl_2$ present per mol of surfactant, the LCST can even shift to around 70 wt% of surfactant as a result of ion-bridging.

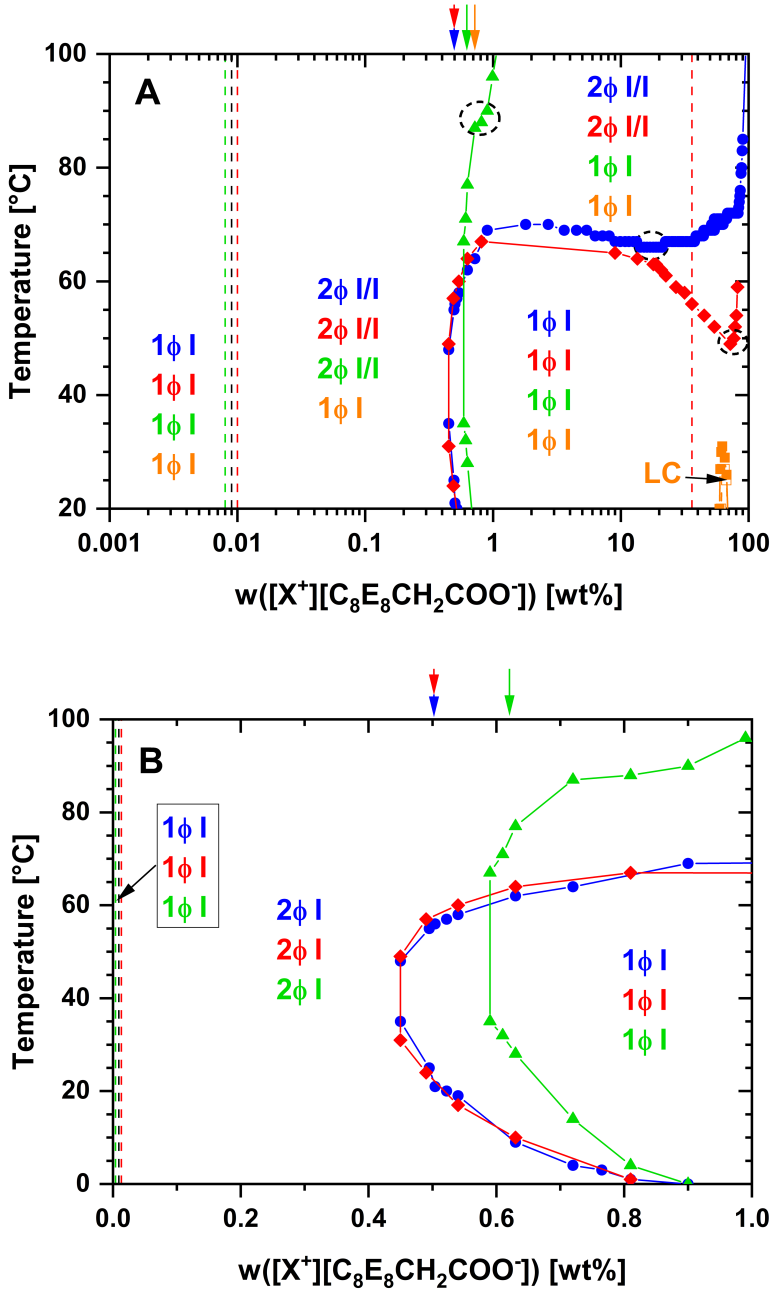

Fig. III.6. (A) Binary phase diagrams of $[H^+][C_8E_8CH_2COO^-]$, $[H^+]_{0.5}[Na^+]_{0.5}[C_8E_8CH_2COO^-]$, and $[Ca^{2+}][C_8E_8CH_2COO^-]_2$, as well as a pseudo-binary phase diagram of $[H^+][C_8E_8CH_2COO^-]$ in presence of 0.25 mol $CaCl_2$ per mol of surfactant in water. Weight fractions are given in a logarithmic scale. The red dashed line indicates the limit of full solubility of $CaCl_2$ in the mixture (pseudo-binary diagram). Points beyond this line refer to the mixture in which the solid particles are dispersed. The dashed lines at very low concentration indicate the visual lower limit of the biphasic region (not precise). (B) Enlargement of the coacervate regime at low concentrations in linear scale. Symbols and colors are identical to those in (A). 1ϕ I: Single isotropic phase. 2ϕ I/I: Two isotropic phases in equilibrium. LC: Liquid crystalline phase (H_1 or N). Arrows indicate the respective critical micelle concentrations at room temperature as derived from surface tension measurements. Dashed circles mark the respective lower critical solution temperatures (LCSTs). The phase diagrams are redrawn from **Chapter II.** with added data.

III.4.4. Auto-Coacervation

As can be seen in **Fig. III.6**, there is a rather temperature independent biphasic region at very low surfactant concentrations in most cases, the only studied exceptions being the full salts $[Na^+][C_8E_8CH_2COO^-]$ and $[Ca^{2+}][C_8E_8CH_2COO^-]_2$. Measurements of the CMC with the surface tension dependence method at 25°C, see **Fig. B.12**, suggest that the biphasic regime is only observed below the CMC determined for the surfactant that is a mixture of $[X^+][C_8E_jCH_2COO^-]$ with different numbers j of ethylene oxide groups and an average of slightly above 8 ethylene oxide groups per headgroup, see **Fig. III.7**. The respective CMCs are indicated by arrows in the phase diagrams in **Fig. III.6**, highlighting the correlation of the phase boundary and the CMC. The CMC of $[H^+][C_8E_8CH_2COO^-]$ is indicated at a concentration of 0.51 wt% (9.4 mmol·L^{-1}). It remains (almost) unchanged upon addition of $CaCl_2$, as the pH remains acidic. However, if electrostatic repulsions are introduced, the CMC slightly increases. The CMC of $[H^+]_{0.5}[Na^+]_{0.5}[C_8E_8CH_2COO^-]$ is determined to be 0.62 wt% (11.3 mmol·L^{-1}), while the CMCs of $[Na^+][C_8E_8CH_2COO^-]$ and $[Ca^{2+}][C_8E_8CH_2COO^-]_2$ are evidenced at a concentration of around 0.71 wt% (12.5 mmol·L^{-1}). This increase can be explained by the introduction of electrostatic repulsions on transforming the pseudo-nonionic surfactant $[H^+][C_8E_8CH_2COO^-]$ to an ionic one. It is well known in literature that ionic surfactants generally exhibit higher CMCs than nonionic surfactants [73]. The increase is relatively small and no significant effect of the nature of the counterion on the CMC is observed, showing that the surfactant, even in its ionic form, behaves more like a nonionic surfactant with only a rather small influence of the ionic group. This is to be expected, since the nonionic E_8-part is much larger than the ionic carboxylate group. If the surfactant is mixed with water in a concentration below the CMC, small liquid droplets (~100 nm) are spontaneously formed, and a slightly turbid mixture is obtained. Over time, the droplets grow and eventually sediment under gravity. The growth and overall droplet sizes were examined using dynamic light scattering (DLS), as presented in **Section II.4.1.** of **Chapter II**. The main conclusions are that both the initial size and the speed of growth of the droplets increases with increasing concentration, i.e., the closer the surfactant concentration is to the CMC, the larger are the formed droplets.

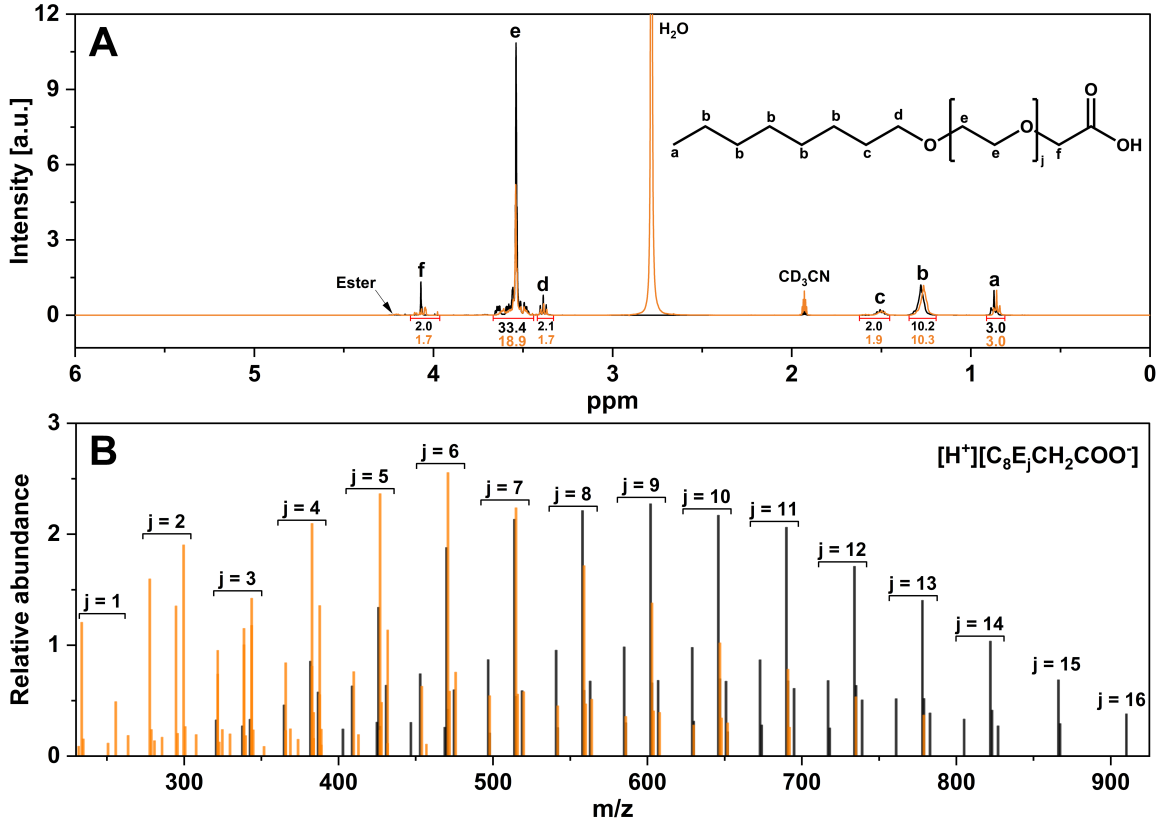

Fig. III.7. ^{1}H-NMR and ESI-MS – enrichment of $[H^+][C_8E_jCH_2COO^-]$ surfactants with a lower degree of ethoxylation in the coacervate. (A) 400 MHz ^{1}H-NMR (NS 64) of the coacervate separated from an aqueous 0.45 wt% $[H^+][C_8E_8CH_2COO^-]$ solution in CD_3CN (orange) superposed to 400 MHz ^{1}H-NMR (NS 64) of the "initial" surfactant $[H^+][C_8E_8CH_2COO^-]$ with polydisperse headgroups (marketed as Akypo® LF2 by Kao Chemicals) in CD_3CN (black). Peaks are integrated and assigned to the respective ^{1}H-atoms, see structure and letters. Integration is normalized to the integral of the terminal CH_3 group (a), which is set to 3. The integral of the hydrogens of the ethylene oxide groups (e) suggests that $j \approx 8.4$ ($\approx [H^+][C_8E_8CH_2COO^-]$) in the "initial" surfactant, and $j \approx 4.7$ ($\approx [H^+][C_8E_5CH_2COO^-]$) in the coacervate. Note that j found for the coacervate can vary from $4 \leq j \leq 5$. The signal of the CH_2 group of the terminal acetic acid moiety (f) is split in the coacervate. Reasons could be the higher abundancy of $[H^+][C_8E_jCH_2COO^-]$ with a low degree of ethoxylation, where the CH_2 group has a slightly different chemical shift and the partial deprotonation of the carboxylic acid moiety. A small amount of esters is indicated by a multiplet located around 4.245 ppm. (B) Qualitative ESI-MS in the positive ion mode of the coacervate separated from a 0.45 wt% $[H^+][C_8E_8CH_2COO^-]$ (orange) superposed to a qualitative ESI-MS in the positive ion mode of "initial" surfactant $[H^+][C_8E_8CH_2COO^-]$ (black). While the degree of ethoxylation is centered around j = 9 in the "initial" surfactant, the coacervate is enriched in surfactant molecules with a lower degree of ethoxylation, the most prominent signal originating from j = 6. Generally, each $[H^+][C_8E_jCH_2COO^-]$ molecule exhibits signals at m/z values of (189+44j) and (190+44j) for the $(M+H)^+$ ion, (206+44j) and (207+44j) for the $(M+NH_4)^+$ ion, and (211+44j) and (212+44j) for the $(M+Na)^+$ ion. Some smaller signals can be assigned to C_8E_j molecules. Note that smaller amounts of $C_8E_xCH_2COOE_yC_8$ esters can also be detected, despite not being seen in the figure.

Further, an increase in pH leads to smaller droplets and a slower growth, partially because the CMC shifts to a slightly higher concentration, and partially because electrostatic repulsions between droplets reduce coalescence. Typically, fully deprotonated species, such as $[Na^+][C_8E_8CH_2COO^-]$ and $[Ca^{2+}][C_8E_8CH_2COO^-]_2$, do not form coacervate droplets at all. However, if Ca^{2+} is added to $[H^+][C_8E_8CH_2COO^-]$ as $CaCl_2$, i.e., if electrostatics are screened, a strong increase in the droplets' growth speed can be observed. This is typical

for coacervation from mixtures, and different from a "normal" two-phase region, where two phases of different compositions of the same molecules are separated by a tie-line between phase boundaries. This situation has already been encountered for the pseudo-binary system of didodecyldimethylammonium bromide (DDAB), for which neutral and ionic forms coexist differently in coacervates [37].

At first glance, the origin of the coacervate droplet formation could be simply assigned to hydrophobic "impurities" that are solubilized by the surfactant above the CMC and phase separate below the CMC. Akypo® LF2 ($[H^+][C_8E_8CH_2COO^-]$) is a technical grade product with a relatively broad distribution of $[H^+][C_8E_jCH_2COO^-]$ molecules around j = 8, where $0 \leq j \leq 20$, see **Fig. III.7**B. The small amounts of other known impurities, see **Section III.3.1.**, are not expected to phase separate below the CMC. Of the distribution of different headgroup sizes, those surfactants with $j < 4$ can be expected to be insoluble in water below the CMC [6]. If there would be a simple phase separation of those surfactants, the droplets would show a distribution of $[H^+][C_8E_jCH_2COO^-]$, where j would be well below 4 (equal to the average of the water-insoluble $[H^+][C_8E_jCH_2COO^-]$ molecules). However, ^{1}H-NMR suggests that $j \approx 4–5$, see **Fig. III.7**A. A decrease of the integral of the $–CH_2$ signals of the ethylene oxide groups relative to the integral of the signal of the terminal $–CH_3$ group is observed when comparing ^{1}H-NMR of the separated coacervate to ^{1}H-NMR of the "initial" surfactant, see **Fig. III.7**A. This is confirmed by qualitative ESI-MS, see **Fig. III.7**B, where the center of the headgroup distribution is shifted from j = 9 in the "initial" surfactant to j = 6 in the separated coacervate. A smaller amount of esters of the type $C_8E_xCH_2COOE_yC_8$ is also indicated in both cases. These esters must play an important role in the auto-coacervation, as a removal of the esters by ion exchange, see **Chapter IV.** (**Appendix C.2.**), leads to vanishing of the auto-coacervation regime. This also explains why there is no coacervation for $[Na^+][C_8E_8CH_2COO^-]$ and $[Ca^{2+}][C_8E_8CH_2COO^-]_2$. During the reaction of $[H^+][C_8E_8CH_2COO^-]$ with excess NaOH or $Ca(OH)_2$, the esters are hydrolyzed, which are then missing for the auto-coacervation. Note that depending on the synthesis, esters may not be fully hydrolyzed. In the case of remaining esters, weak auto-coacervation is still observed.

Simple phase separation would not meet the criteria for coacervation, since coacervation is a liquid-liquid phase separation from a colloidal solution by aggregation of the colloids. However, as will be explained below, the described phase separation is in fact auto-

coacervation. Both, ^{1}H-NMR and ESI-MS show an enrichment of surfactants with shorter headgroups in the coacervate. To measure^{1}H-NMR and ESI-MS, the coacervate was separated as a more viscous clear liquid phase by centrifugation (20,000 g for 30 min). The separated coacervate's water content was determined to be about 40 wt% by the Karl Fischer titration method. Further, it shows clouding behavior just above room temperature, which is reasonable for a mixture of 60 wt% $[H^+][C_8E_{4\text{-}5}CH_2COO^-]$ and water. A rough approximation of the separated volumes from samples containing 0.36 wt% $[H^+][C_8E_8CH_2COO^-]$, $[H^+][C_8E_8CH_2COO^-]$+0.25 $CaCl_2$, or $[H^+]_{0.5}[Na^+]_{0.5}[C_8E_8CH_2COO^-]$ suggests that less than 10 wt% (approximately 8 wt%) of the initial surfactant are contained in the coacervate. SAXS of the coacervate reveals scattering that conforms to the phase of "flocculated" micelles (L_1/L_1'), i.e., a concentrated phase of partially headgroup interdigitated spherical micelles. X-ray scattering of the coacervate, as separated twice from two different samples, is shown superposed to scattering of $[H^+][C_8E_8CH_2COO^-]$ at concentrations ranging from 10 wt% to 70 wt% (taken from **Chapter II.**) in **Fig. III.8**. Considering the invariant Q* of the scattering, see **Figs. B.13 and B.14**, a surfactant concentration of around 70 wt% in the coacervate is suggested. However, it is shown in **Fig. III.7** that the coacervate is enriched in surfactant molecules with a lower degree of ethoxylation to give in average $[H^+][C_8E_5CH_2COO^-]$. As a result, the volume fraction of the hydrocarbon cores increases from 0.175 in the "initial" surfactant to 0.202 in the coacervate, and the invariant has to be rescaled to take into account this increase. By rescaling the invariant, a surfactant content in the coacervate close to 60 wt% is found, which is in agreement with the direct measurement of the water content of 40 wt%. The enrichment in shorter headgroups in the coacervate also explains the change in the scattering shape and the peak position, as the coacervate does not represent the "initial" $[H^+][C_8E_8CH_2COO^-]$ anymore.

Combining all results, the auto-coacervation can be confirmed and explained. Below the "collective" CMC of $[H^+][C_8E_8CH_2COO^-]$, the more hydrophobic ester molecules (with two C_8-chains) induce the formation of micelles together with predominantly the surfactant molecules with a lower degree of ethoxylation. As a result, those micelles are enriched in surfactant molecules with a low degree of ethoxylation. Since the headgroups are shorter, the spontaneous packing parameter is larger, the micelles have a larger aggregation number, and the intermicellar repulsion is lower. Subsequently, the micelles aggregate through intermicellar attraction, and their headgroups partially interdigitate. Through the aggregation of the micelles, a concentrated micellar L_1/L_1' phase (60–70 wt% of surfactant with an

average number of 4–5 EO groups) is separated from a sub-CMC aqueous solution, which meets the criteria for auto-coacervation. Thus, the tie-line of the auto-coacervation regime does not start or end at the phase boundaries but within phases, i.e., the tie-line starts inside the auto-coacervation regime (below the CMC) and ends in the L_1/L_1' phase above 60 wt% of surfactant. The volume of the coacervate is limited by the amount of the esters and possibly also by the amount of the most hydrophobic surfactants in the mixture. In principle, this observation could be used to remove the least hydrophilic surfactant portion from the surfactant mixture by simple dilution and centrifugation, though a small amount of the esters would need to be added. While concentration by evaporation of water under vacuum may be energy consuming, it would also be a suitable and reliable way to remove the ester impurities from the surfactant to prepare a surfactant that has a large L_1 domain and does not coacervate in practice.

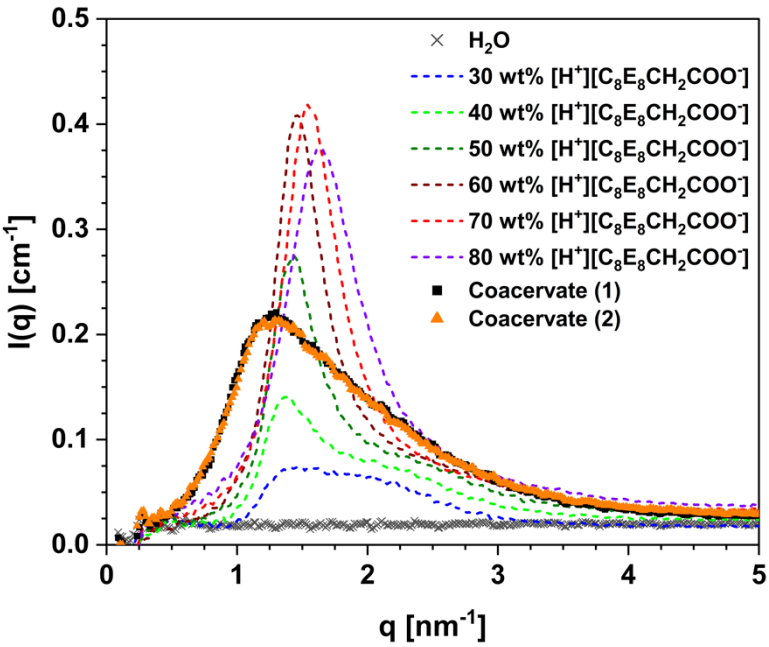

Fig. III.8. The small-angle X-ray scattering obtained from the coacervate separated from two individual 0.36 wt% $[H^+][C_8E_8CH_2COO^-]$ samples is intermediate between the core-shell micellar L_1 (30 wt% to 40 wt%) and the interdigitated water-poor L_1' regime (50 wt% to 80 wt%). The peak shape and position of the coacervate are not equivalent to the case of $[H^+][C_8E_8CH_2COO^-]$, because the surfactant composition is different in the coacervate. The exact surfactant content in the coacervate can be deduced directly by considering the invariant, see **Figs. B.13** and **B.14**.

As far as the counterion effects are concerned, analogies to the LCST behavior can be drawn. If electrostatics are screened, Ca^{2+} ions enhance intermicellar attraction through intermicellar bridging and as a result enhance the speed of the coacervate droplet growth. On the other hand, if charge is introduced and electrostatics are not screened, as in the case of $[H^+]_{0.5}[Na^+]_{0.5}[C_8E_8CH_2COO^-]$, electrostatic repulsion reduces intermicellar attraction,

leading to a decrease in the growth speed of the coacervate droplets. No auto-coacervation is observed for $[Na^+][C_8E_8CH_2COO^-]$ and $[Ca^{2+}][C_8E_8CH_2COO^-]_2$ (even with DLS), meaning that even the surfactants with a low degree of ethoxylation are dissolved in water. The reason for the absence of auto-coacervation is the absence of esters. In any case, the amount of formed coacervate is determined and limited by the amount of present esters and $[H^+][C_8E_jCH_2COO^-]$ molecules with $j < 4$ (at room temperature). This was confirmed by extracting the rest of the surfactant from the supernatant (after separating the coacervate) and preparing an equally concentrated sample (0.36 wt%) using the surfactant from the supernatant. No auto-coacervation is observed. Another peculiarity is observed for a batch of $[Na^+][C_8E_8CH_2COO^-]$, in which not all esters were hydrolyzed. While this batch of $[Na^+][C_8E_8CH_2COO^-]$ (used also for surface tension measurements) exhibits auto-coacervation mainly up to the CMC (0.71 wt%), auto-coacervation is also observed to a lesser extent above the CMC, up to approximately 1.60 wt%. This behavior is also reflected in the surface tension measurement (**Fig. B.12**), where the increase in surface tension above the CMC shows a pronounced change of slope around 1.53 wt%. The knowledge of the coacervation phenomenon also explains the counter-intuitive increase in surface tension above the CMC. Since coacervation separates the most hydrophobic surfactants from the mixture, a variation of the surface tension can be explained by at least two mechanisms: Removal of the most hydrophobic surfactant molecules from the surface, and/or adsorption of micelles under the water-air-interface, as observed in several cases by Penfold and co-workers [74].

III.4.5. L_β Phase

As described above, there is a semi-crystalline phase at very high surfactant concentrations in any case. The melting temperature for $[H^+][C_8E_8CH_2COO^-]$ was determined to be 11°C. With increasing ionicity, the melting temperature increases. $[H^+]_{0.5}[Na^+]_{0.5}[C_8E_8CH_2COO^-]$ melts around 23°C and $[Na^+][C_8E_8CH_2COO^-]$ melts above 27°C. Since $[Ca^{2+}][C_8E_8CH_2COO^-]_2$ already melts around 19°C, sodium seems to favor the semi-crystalline state more than calcium does. Small- and wide-angle X-ray scattering (SWAXS) spectra of $[H^+][C_8E_8CH_2COO^-]$ and $[Na^+][C_8E_8CH_2COO^-]$ (no added water) at temperatures ranging from 20°C to 80°C are shown in logarithmic scale in **Fig. B.15**. Scattering of

$[Na^+][C_8E_8CH_2COO^-]$ at 20°C, shown in semi-logarithmic (log-lin) scale in **Fig. III.9**, clearly evidences a semi-crystalline lamellar phase (L_β) in equilibrium with small amounts of L_1' phase. A first order Bragg peak is located in the SAXS region at $q_1 = 0.908$ nm^{-1} ($D_1^* = 6.92$ nm). Second order, third order, fourth order, and fifth order Bragg peaks are located at $q_2 = 1.806$ nm^{-1} ($D_2^* = 3.48$ nm), $q_3 = 2.685$ nm^{-1} ($D_3^* = 2.34$ nm), $q_4 = 3.632$ nm^{-1} ($D_4^* = 1.73$ nm), and $q_5 = 4.553$ nm^{-1} ($D_5^* = 1.38$ nm), respectively. The peak positions follow the characteristic series for lamellar phases, where $q_2 = 2 \cdot q_1$, $q_3 = 3 \cdot q_1$, $q_4 = 4 \cdot q_1$, and $q_5 = 5 \cdot q_1$ [55]. First order and second order peaks are pronounced, while third order, fourth order, and fifth order peaks are only weakly visible. The third order peak is only seen as a shoulder of the second order peak. The wide-angle X-ray scattering (WAXS) regime reveals Bragg peaks at q = 13.5 nm^{-1}, 15.6 nm^{-1}, 16.4 nm^{-1}, 18.4 nm^{-1}, and 25.2 nm^{-1} superposed to the WAXS pattern of the liquid L_1' phase. As these peak positions are very similar to those found for crystalline PEG 400 (9–10 EO-groups) by Lind et al. [75], and none of them seems to be assigned to hydrocarbon chain crystallization [76,77], it is assumed that the headgroups of $[Na^+][C_8E_8CH_2COO^-]$ are crystallized at 20°C, while the hydrocarbon chains retain their liquid state. As pointed out by Takahashi and Tadokoro [78], this scattering pattern corresponds to a primitive monoclinic structure $P2_1/a\text{-}C_{2h}^5$ ($a = 0.805$ nm, $b = 1.304$ nm, $c = 1.948$ nm, and $\beta = 125.4°$), where the ethylene oxide chains are suggested to form 7/2 helical turns per unit cell. Above the melting temperature, the scattering corresponds to the expected L_1' phase. While the formation of a hydrocarbon chain crystallized lamellar phase is commonly observed for fatty acids and their salts, where also liquid crystalline lamellar phases are commonly found [79], the formation of a lamellar phase for $[X^+][C_8E_8CH_2COO^-]$ is significantly less favored. To form the L_β phase, the free energy of crystallization must overcome the entropy of a large headgroup, i.e., of a large area per headgroup. With this, the observation of the L_β phase exclusively at very high surfactant concentrations can be explained. The more water molecules are present, the larger the area per headgroup becomes due to headgroup hydration. As a result, entropy increases with increasing water content and a lower temperature is required for the head-group crystallization energy to overcome entropy. At a water content of 11 wt% (3.5 water molecules per headgroup), the melting temperature of the L_β phase of $[Na^+][C_8E_8CH_2COO^-]$ is already below 20°C, see **Fig. B.3**. From the first order peak, a repeat distance of 6.92 nm is deduced for $[Na^+][C_8E_8CH_2COO^-]$. The theoretical extended length (zigzag conformation) of the headgroup (approximated as E_9, i.e., the $-CH_2COO^-$ is

approximated as an additional ethylene oxide unit) is about 3.3 nm, while the length is about 2.5 nm in the helix conformation and 1.9 nm in the meander conformation [80]. Owing to the crystalline state of the headgroup's EO-groups, the helix conformation is the best guess. The cross-sectional area of the headgroup is significantly decreased upon crystallization, while the cross-sectional area of the liquid-like alkyl chain remains more or less constant [75], which enables a lamellar packing. As a result, the hydrocarbon chains are not expected to significantly interdigitate, if the headgroups do not interdigitate. With a thickness of the headgroup layer of 2·2.5 nm if the surfactant molecules are not tilted, the thickness of the liquid-like hydrocarbon layer would be about 1.92 nm. 1.92 nm is significantly longer than the theoretical conformation-averaged alkyl chain length of 1.16 nm [51], and slightly shorter than twice the conformation-averaged length (2.32 nm). However, a repeat distance of 6.92 nm would be met if the surfactant molecules were tilted by an angle of 19° with a non-interdigitated headgroup layer of 2·23.6 Å thickness and a liquid-like alkyl chain layer of 2.19 nm thickness. Hence, one plausible structure would consist of non-interdigitated layers of crystalline headgroups in their usual helical conformation and liquid-like layers of non-interdigitated hydrocarbon chains, where the surfactant molecules are tilted by an angle of 19°. $[H^+][C_8E_8CH_2COO^-]$ (**Fig. B.15**A), as expected with a melting temperature of 11°C, shows only the L_1' phase at the examined temperatures.

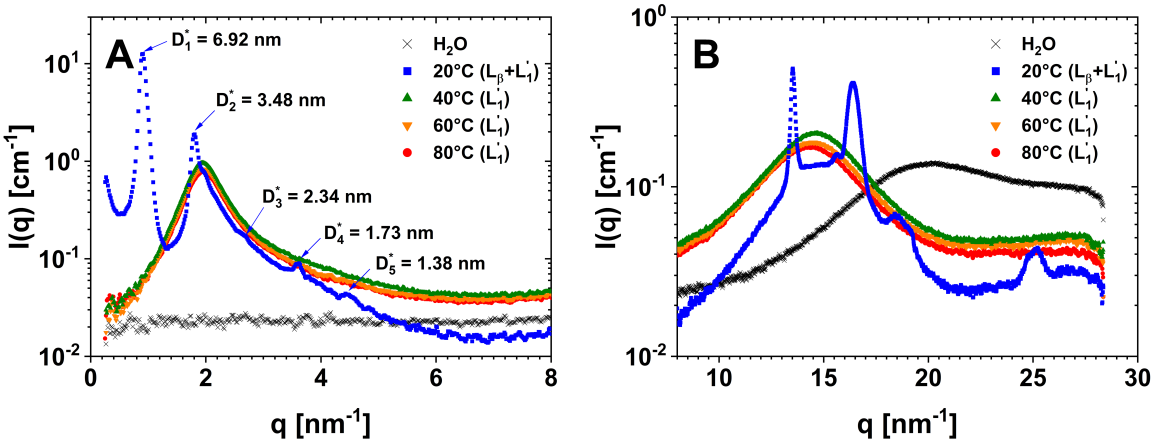

Fig. III.9. (A) SAXS spectra of neat (no added water) $[Na^+][C_8E_8CH_2COO^-]$ at 20, 40, 60, and 80°C in semi-logarithmic (log-lin) scale. (B) Respective WAXS spectra of neat $[Na^+][C_8E_8CH_2COO^-]$ at 20, 40, 60, and 80°C. At 20°C, a lamellar L_β phase with crystalline headgroups is observed, whereas the headgroup interdigitated micellar L_1' phase is observed at higher temperatures. The whole spectrum is given in log-log scale in **Fig. B.15**B.

III.5. Conclusion and Outlook

The surfactant $[X^+][C_8E_8CH_2COO^-]$, where X^+ can be H^+ or any other (polyvalent) cation such as Na^+ or Ca^{2+}, has a rather short hydrophobic part and a much larger hydrophilic part. This results in a significant packing constraint, generally making a sphere-to-rod transition impossible. As a result, only spherical to slightly prolate spheroidal micelles are observed in binary mixtures with water at most compositions and temperatures. The only exception is a small domain of a hexagonal (H_1) phase, where "infinite" cylinders form. The H_1 phase is only formed by the fully ionic form of the surfactant, i.e., if all counterions are metal cations. This is a result of the reduction of the area per molecule by ion-bridging of the carboxylate moieties. Otherwise, the only exception, where a deviation from the spheroidal shape is possible, is a semi-crystalline lamellar L_β phase at very high surfactant concentrations and low temperature. Formation of a lamellar phase despite the strong packing constraint is only possible upon headgroup crystallization. For the formation of the L_β phase, the gain in free energy by headgroup crystallization has to overcome the entropy of the headgroups with a large area per molecule. Apart from that, the restriction in micellar shape has various consequences on the aqueous phase behavior:

(a) The lower critical solution temperature (LCST), and clouding as a whole, are resulting from the flocculation of small spherical micelles, driven by intermicellar attraction. Owing to the large area per molecule, the micelles cannot significantly grow in size or undergo a transition in shape, as it is usually the case upon clouding of classical $C_{2j}E_j$ surfactants [22–24]. Attractive forces, i.e., (ion-)bridging via carboxylic acid or carboxylate moieties and Van der Waals interactions are opposed by electrostatic repulsion. An increase in temperature enhances attractive forces by dehydration of the head-groups.

(b) Formation of classical liquid crystalline phases is impossible for $[H^+][C_8E_8CH_2COO^-]$ and only possible for its salts in a small domain around 60 wt% of surfactant, where the effect of counterion-bridging is strong enough to sufficiently decrease the area per molecule. The only conceivable liquid crystalline phase with spherical micelles would be a cubic I_1 phase. However, the formation of an I_1 phase is not possible with $[X^+][C_8E_8CH_2COO^-]$, because the Lindemann rule is not met with a short C_8 chain. The Lindemann rule is known from molecular crystals but is also

valid at colloidal scale [20]. Owing to the short C_8 chain, the radius of the hydrocarbon cores is too small for the thermal excitations of the fluctuations to meet the Lindemann rule. In other words, the intermicellar attraction is too weak. Since Van der Waals attraction scales with the sixth power of volume and is inversely proportional to the distance between micelles, attraction is >7 times stronger for C_{12} than it is for C_8. As a result, $C_{12}E_j$ surfactants with large headgroups can indeed form an I_1 phase, while $[X^+][C_8E_8CH_2COO^-]$ cannot. A good example is Brij® 35 ($C_{12}E_{23}$), which has a higher headgroup volume to total surfactant volume ratio than $[X^+][C_8E_8CH_2COO^-]$, thus being restricted to spherical micelles, but still forms an I_1 phase [17,18].

(c) A nematic phase (N) is formed by prolate micelles. The restriction to a spherical shape is softened when H^+ is exchanged by Na^+ or Ca^{2+}, i.e., if the acid form of the surfactant is transformed to its ionic form, and the spherical shape is deformed into a slightly prolate spheroid. In the prolate shape, the counterions at the axial positions of the micelles are dissociated to a larger extent than those at the equatorial positions [52]. As a result, the ions can bridge micelles preferentially via carboxylate moieties at the axial positions, leading to the formation of short chains made of a few (≤ 3) prolate micelles. In addition, the intra- and intermicellar counterion-bridging of headgroups reduces the area per molecule, which leads to a merging of some of the smaller prolate micelles into larger, more prolate ones. Both the chains of smaller prolate micelles and some merged micelles are preferentially oriented to result in a nematic ordering. Upon further cooling of the nematic phase, the effect of counterion-bridging increases and the area per molecule is sufficiently decreased to form a hexagonal (H_1) phase made of "infinite" cylinders. The H_1 phase exclusively forms within the transition regime between the core-shell micellar L_1 phase and the headgroup interdigitated micellar L_1' phase, where micelles are already in close proximity to each other to enable sufficient ion-bridging. Here, opposing forces are thermal fluctuations and electrostatic repulsions. An increase in temperature leads to a decreasing effect of ion-bridging on the area per molecule, "melting" the hexagonal phase into a nematic phase (N) and eventually into an isotropic micellar phase. In the L_1' phase, the extent of interdigitation is too large, increasing the area per molecule to favor spheroidal aggregates. The absence of a significant peak shift in SAXS and SANS in the nematic-to-hexagonal transition would in principle leave open the possibility that the

hexagonal phase is not made of "infinite" cylinders but of chains made of prolate micelles (similar to the nematic phase). However, surfactant self-diffusion suggests that the hydrocarbon cores are merged and not entities separated by interdigitated headgroup layers. The hexagonal phase of $[X^+][C_8E_8CH_2COO^-]$ could still share some characteristics with a transition from a classical hexagonal phase of "infinite" cylinders (H_1) to a cubic Im3m phase, proposed by Sakya *et al.* [81] in binary mixtures of $C_{12}E_{12}$ and water. Sakya *et al.* proposed that undulations form in the hexagonally packed cylinders with the cylinders subsequently being "pinched" at regular intervals to form the isotropic cubic phase made of spherical micelles. There are some examples of calamitic as well as discotic nematic phases made of prolate or oblate micelles with charged surfactants and a co-surfactant in literature [44,45] that always involve a micellar shape transition through the right ratio between surfactant and cosurfactant. Thus, they are intermediate states between an isotropic micellar phase and lamellar or H_1 phases.

(d) Auto-coacervation, unusual for simple surfactant systems [29], is observed below the critical micelle concentration (CMC) and is triggered by ester impurities of the type $C_8E_xCH_2COOE_yC_8$ that aggregate with surfactants with a lower degree of ethoxylation ($[X^+][C_8E_8CH_2COO^-]$ is a distribution of $[X^+][C_8E_jCH_2COO^-]$ with $0 \leq j \leq 20$). Intermicellar attraction enhanced by dimerization of carboxylic acid moieties or ion-bridging of carboxylate moieties leads to the formation and separation of a concentrated "flocculated" micellar L_1/L_1' phase from a sub-CMC solution. Attraction is opposed by electrostatic repulsions.

A complete generic phase diagram of the $[X^+][C_8E_8CH_2COO^-]$ system with schematic drawings of the proposed structures is shown in **Fig. III.10**. The different features of the phase behavior will now be briefly discussed with respect to the effects of ionicity and the type of counterion. In its acidic form, $[H^+][C_8E_8CH_2COO^-]$ behaves much like a nonionic surfactant, showing a LCST of 66°C around 20 wt% of surfactant. Compared to the truly nonionic counterpart C_8E_8, having a LCST around 96°C at very low surfactant concentrations [6], the carboxylic acid moiety enhances intermicellar attraction through carboxylic acid dimerization [72]. An increase in ionicity with monovalent sodium ions ($[H^+]_{0.5}[Na^+]_{0.5}[C_8E_8CH_2COO^-]$ and $[Na^+][C_8E_8CH_2COO^-]$) or divalent calcium ions ($[Ca^{2+}][C_8E_8CH_2COO^-]_2$) increases electrostatic repulsions, thus inhibiting a LCST. If

electrostatic repulsions are screened, e.g., in the case of $[H^+][C_8E_8CH_2COO^-]$ + 0.25 $CaCl_2$, ions can bridge intermicellarly and shift the LCST to lower temperatures and into the L_1/L_1' phase, where the effect of ion-bridging is most pronounced. The L_1/L_1' phase also plays a role above the clouding curve at high temperatures. One of the separating phases always seems to be a L_1/L_1' phase, even if the initial mixture is a L_1' phase. The mechanism of auto-coacervation is similar to the mechanism responsible for clouding with the difference that it is triggered below the CMC by the hydrophobic esters and involves the more hydrophobic portion of the surfactant's distribution of different degrees of ethoxylation. It is observed in all cases, where esters are present. Increasing ionicity increases the CMC, thus extending the auto-coacervation regime, while at the same time electrostatic repulsions are increased. Despite the growth of the coacervate droplets being slowed down, $[Na^+][C_8E_8CH_2COO^-]$ still undergoes auto-coacervation if esters are present, showing that electrostatic repulsion alone is not sufficient to inhibit auto-coacervation. Formation of a H_1 or N phase is only possible in fully ionic forms such as $[Ca^{2+}][C_8E_8CH_2COO^-]_2$ and $[Na^+][C_8E_8CH_2COO^-]$, and only within the L_1/L_1' regime, where ion-bridging is strong enough to induce the formation of chains made of prolate micelles and to induce a sufficient decrease in the area per molecule to enable a spheroid-to-rod transition. The effect of Na^+ ions seems to be stronger than the effect of Ca^{2+} ions, since the H_1 and N phase are stable up to higher temperatures for $[Na^+][C_8E_8CH_2COO^-]$ (47°C) than for $[Ca^{2+}][C_8E_8CH_2COO^-]_2$ (31°C). Forces opposing the liquid crystal formation are thermal fluctuations and electrostatic repulsions. Thus, the "melting" temperature of the H_1 phase can be further increased by reducing electrostatic repulsions by addition of salt. The semi-crystalline L_β phase is observed at low water content and low temperatures in any case. The effects of ionicity and the counterion on its melting temperature seem to be similar to the effects on the "melting" of the H_1 phase. Ionicity increases the melting temperature, and the increase is more pronounced with Na^+ than with Ca^{2+}. Thus, the melting temperature is highest for $[Na^+][C_8E_8CH_2COO^-]$ (27°C), followed by $[Ca^{2+}][C_8E_8CH_2COO^-]_2$ (19°C) and $[H^+][C_8E_8CH_2COO^-]$ (11°C).

A controlled transition from micellar core-shell to more compact nanostructures was shown to exist in aqueous mixtures of $[X^+][C_8E_8CH_2COO^-]$, where X^+ can be virtually any (polyvalent) metal cation [41–43]. In this case, the more compact structures can be understood as constrained hydrocarbon cores surrounded by a medium of partially interdigitated, more or less hydrated headgroups. In the headgroup interdigitated micellar regime, which can

also be achieved by sub-CMC auto-coacervation and clouding, the chemical potential of water is high, and the water concentration is low. Since water is bound as hydration water to the ethylene oxide headgroups, chemical reactions may be conceivable in a controlled way. A recent example of a constrained micellar core was given by Lyu *et al.* [82], using the micelle to achieve confined metal reduction.

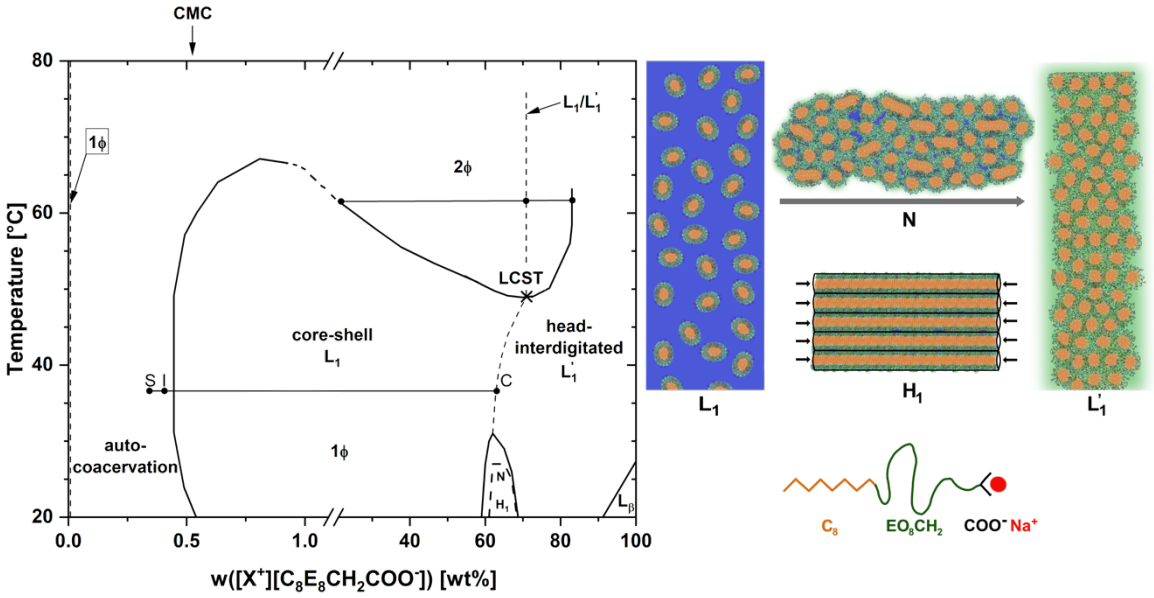

Fig. III.10. A generic phase diagram of $[X^+][C_8E_8CH_2COO^-]$ in water. The phase diagram was drawn based on the diagrams shown in this chapter. The vertical dashed line around 60 wt% to 70 wt% $[X^+][C_8E_8CH_2COO^-]$ marks the transition from a core-shell micellar L_1 phase and a headgroup interdigitated L_1' phase, here termed L_1/L_1' phase. One tie-line (lower solid horizontal line) indicates the compositions of the coacervate (C) and the supernatant (S) originating from an initial solution of composition (I) through auto-coacervation. Tie-lines shown within the biphasic regime above the lower critical solution temperature (LCST) indicate the separation of a L_1/L_1' phase from either a dilute L_1 phase (if the initial concentration is below the L_1/L_1' phase) or a more concentrated L_1' phase (if the initial concentration is above the L_1/L_1' phase). 1ϕ: Single isotropic phase. 2ϕ: Two isotropic phases in equilibrium. L_1: Solution of core-shell micelles. L_1': Headgroup-interdigitated micellar regime. L_1/L_1': Transition state between L_1 and L_1' ("flocculated" micellar regime). N: Nematic phase. H_1: Hexagonal phase. L_β: Semi-crystalline lamellar phase. Schematic drawings of the proposed phases for $[Na^+][C_8E_8CH_2COO^-]$ are shown on the right-hand side. Color code: Blue: water, orange: alkyl chains, green: (hydrated) headgroups, black: carboxylate groups, and red: sodium ions. Drawings are not to scale.

In contrast to complex coacervation, simple auto-coacervation, apart from clouding, is quite uncommon for single-chain surfactant systems without additives. A rare example for simple coacervation in single-chain surfactant systems was reported by Cohen *et al.* [30–32] for rather complex quaternary ammonium salts. Other examples of simple surfactant coacervation without additives are usually reported for gemini-type surfactants with two hydrophobic chains [37–39,83]. The surfactant-rich coacervate is sometimes termed supramolecular solvent (SUPRA), which are nanostructured liquids and promising alternatives for conventional organic solvents in extraction processes [83]. In the case of

didodecyldimethylammonium bromide (DDAB), and probably other gemini surfactants, the coacervate is made from a lamellar phase [37]. In the case of $[X^+][C_8E_8CH_2COO^-]$, the corresponding SUPRA is the L_1/L_1' phase, which is not only accessible in a controlled way by sub-CMC auto-coacervation but also by clouding. It should be noted that the esters, required to trigger the auto-coacervation, are similar to gemini surfactants as they possess two alkyl chains. However, the main components of the coacervate are $[X^+][C_8E_jCH_2COO^-]$ surfactant molecules. The carboxylate moiety of $[X^+][C_8E_8CH_2COO^-]$ is potentially beneficial in extraction processes including metal ions.

III.6. References

[1] P. Denk, A. El Maangar, S. Prévost, W. Silva, R. Gschwind, T. Zemb, W. Kunz, Cloud point, auto-coacervation, and nematic ordering of micelles formed by ethylene oxide containing carboxylate surfactants, J Colloid Interface Sci 621 (2022) 470–488. https://doi.org/10.1016/j.jcis.2022.04.046.

[2] L. Chiappisi, Polyoxyethylene alkyl ether carboxylic acids: An overview of a neglected class of surfactants with multiresponsive properties, Adv Colloid Interface Sci 250 (2017) 79–94. https://doi.org/10.1016/j.cis.2017.10.001.

[3] W.W. Schmidt, D.R. Durante, R. Gingell, J.W. Harbell, Alcohol ethoxycarboxylates - Mild, high-foaming surfactants for personal-care products, JAOCS, Journal of the American Oil Chemists' Society 74 (1997) 25–31. https://doi.org/10.1007/s11746-997-0114-0.

[4] H. Meijer, J.K. Smid, Polyether Carboxylates, in: H.W. Stache (Ed.), Anionic Surfactants - Organic Chemistry, Marcel Dekker Inc, New York, 1996: pp. 313–352.

[5] N.M. Van Os, J.R. Haak, L.A.M. Rupert, K.S. Laboratorium, Physico-Chemical Properties of Selected Anionic, Cationic and Nonionic Surfactants, Elsevier B.V., 1993. https://doi.org/10.1016/c2009-0-09112-0.

[6] D.J. Mitchell, G.J.T. Tiddy, L. Waring, T. Bostock, M.P. McDonald, Phase behaviour of polyoxyethylene surfactants with water. Mesophase structures and partial miscibility (cloud points), Journal of the Chemical Society, Faraday Transactions 1: Physical Chemistry in Condensed Phases 79 (1983) 975. https://doi.org/10.1039/f19837900975.

[7] J.N. Israelachvili, D.J. Mitchell, B.W. Ninham, Theory of self-assembly of hydrocarbon amphiphiles into micelles and bilayers, Journal of the Chemical Society, Faraday Transactions 2: Molecular and Chemical Physics 72 (1976) 1525–1568. https://doi.org/10.1039/F29767201525.

[8] Y. Nibu, T. Inoue, Phase behavior of aqueous mixtures of some polyethylene glycol decyl ethers revealed by DSC and FT-IR measurements, J Colloid Interface Sci 205 (1998) 305–315. https://doi.org/10.1006/jcis.1998.5621.

[9] H. Kunieda, K. Shigeta, K. Ozawa, M. Suzuki, Self-Organizing Structures in Poly(oxyethylene) Oleyl Ether - Water System, 5647 (1997) 7952–7957.

[10] K.L. Huang, K. Shigeta, H. Kunieda, Phase behavior of polyoxyethylene dodecyl ether-water systems, Prog Colloid Polym Sci 110 (1998) 171–174. https://doi.org/10.1007/bfb0118071.

[11] R. Nagarajan, Molecular packing parameter and surfactant self-assembly: The neglected role of the surfactant tail, Langmuir 18 (2002) 31–38. https://doi.org/10.1021/la010831y.

[12] A.A. Ali, B.A. Mulley, Formation of liquid crystal and other non-fluid phases in emulsions containing non-ionic surfactants, Journal of Pharmacy and Pharmacology 30 (1978) 205–213. https://doi.org/10.1111/j.2042-7158.1978.tb13206.x.

[13] S. Fall, B. Pattier, L. Benyayia, A. Gibaud, Binary phase diagram of water/Brij58 studied by SAXS, Acta Phys Pol A 121 (2012) 388–396. https://doi.org/10.12693/APhysPolA.121.388.

[14] W. Zhuang, X. Chen, J. Cai, G. Zhang, H. Qiu, Characterization of lamellar phases fabricated from Brij-30/water/1-butyl-3-methylimidazolium salts ternary systems by small-angle X-ray scattering, Colloids Surf A Physicochem Eng Asp 318 (2008) 175–183. https://doi.org/10.1016/j.colsurfa.2007.12.034.

[15] N.R.B. Coleman, G.S. Attard, Ordered mesoporous silicas prepared from both micellar solutions and liquid crystal phases, Microporous and Mesoporous Materials 44–45 (2001) 73–80. https://doi.org/10.1016/S1387-1811(01)00170-6.

[16] Z. Wang, F. Liu, Y. Gao, W. Zhuang, L. Xu, B. Han, G. Li, G. Zhang, Hexagonal liquid crystalline phases formed in ternary systems of Brij 97-water-ionic liquids, Langmuir 21 (2005) 4931–4937. https://doi.org/10.1021/la050266p.

[17] R. Schwarzenbacher, M. Kriechbaum, H. Amenitsch, P. Laggner, Characterization of the nanostructures in liquid crystalline mesophases present in the ternary system brij-35/dibutyl ether/H2O by small- and wide-angle X-ray scattering, Journal of Physical Chemistry B 102 (1998) 9161–9167. https://doi.org/10.1021/jp9822889.

[18] M. Tomšič, M. Bešter-Rogač, A. Jamnik, W. Kunz, D. Touraud, A. Bergmann, O. Glatter, Ternary systems of nonionic surfactant Brij 35, water and various simple alcohols: Structural investigations by small-angle X-ray scattering and dynamic light scattering, J Colloid Interface Sci 294 (2006) 194–211. https://doi.org/10.1016/j.jcis.2005.06.088.

[19] G.J.T. Tiddy, Surfactant-water liquid crystal phases, Phys Rep 57 (1980) 1–46. https://doi.org/10.1016/0370-1573(80)90041-1.

[20] T. Okubo, H. Ishiki, H. Kimura, M. Chiyoda, K. Yoshinaga, Rigidity of colloidal crystals of silica spheres modified with polymers on their surfaces in organic solvents, Colloid Polym Sci 280 (2002) 446–453. https://doi.org/10.1007/s00396-001-0631-6.

[21] O. Glatter, G. Fritz, H. Lindner, J. Brunner-Popela, R. Mittelbach, R. Strey, S.U. Egelhaaf, Nonionic micelles near the critical point: Micellar growth and attractive interaction, Langmuir 16 (2000) 8692–8701. https://doi.org/10.1021/la000315s.

[22] M. Zulauf, K. Weckstrom, J.B. Hayter, V. Degiorgio, M. Corti, Neutron scattering study of micelle structure in isotropic aqueous solutions of poly(oxyethylene) amphiphiles, J Phys Chem 89 (1985) 3411–3417. https://doi.org/10.1021/j100261a051.

[23] P.A. Kralchevsky, K.D. Danov, S.E. Anachkov, G.S. Georgieva, K.P. Ananthapadmanabhan, Extension of the ladder model of self-assembly from cylindrical to disclike surfactant micelles, Curr Opin Colloid Interface Sci 18 (2013) 524–531. https://doi.org/10.1016/j.cocis.2013.11.002.

[24] K. Imanishi, Y. Einaga, Effects of Hydrophilic Chain Length on the Characteristics of the Micelles of Pentaoxyethylene n-Decyl C10E5 and Hexaoxyethylene n-Decyl C10E6 Ethers, J Phys Chem B 109 (2005) 7574–7581. https://doi.org/10.1021/jp044226q.

[25] H.G. Bungenberg de Jong, H.R. Kruyt, Chemistry. - Coacervation (Partial miscibility in colloid systems). (Preliminary Communication)., 131 (1929).

[26] B. Mohanty, H.B. Bohidar, Systematic of Alcohol-Induced Simple Coacervation in Aqueous Gelatin Solutions, Biomacromolecules 4 (2003) 1080–1086. https://doi.org/10.1021/bm034080l.

[27] C.J. van Oss, Coacervation, Complex-Coacervation and Flocculation, J Dispers Sci Technol 9 (1988) 561–573. https://doi.org/10.1080/01932698808944011.

[28] J.K. Sorensen, T. Richardson, D.B. Lund, Using Some Physicochemical Properties of Proteins in Coacervate Systems, in: 1979: pp. 173–190. https://doi.org/10.1021/bk-1979-0092.ch009.

[29] M. Wang, Y. Wang, Development of surfactant coacervation in aqueous solution, Soft Matter 10 (2014) 7909–7919. https://doi.org/10.1039/C4SM01386G.

[30] I. Cohen, T. Vassiliades, Critical phenomena in aqueous solutions of long chain quaternary ammonium salts. II. Specificity and light scattering properties, J Phys Chem 65 (1961) 1774–1781. https://doi.org/10.1021/j100827a021.

[31] I. Cohen, T. Vassiliades, Coacervation in aqueous cationic soap solutions, J Am Oil Chem Soc 39 (1962) 246–250. https://doi.org/10.1007/BF02631703.

[32] I. Cohen, P. Economou, A. Libackyj, Critical phenomenon in aqueous solutions of long chain quaternary ammonium salts. IV. Hyamine 1622-iodine complex systems, J Phys Chem 66 (1962) 1829–1834. https://doi.org/10.1021/j100816a013.

[33] B.W. Barry, G.M.T. Gray, Micelle formation and coacervation in mixtures of alkyltrimethylammonium bromides with di and trihydroxy bile salts, J Colloid Interface Sci 52 (1975) 327–339. https://doi.org/10.1016/0021-9797(75)90207-6.

[34] J. Bhattacharjee, V.K. Aswal, P.A. Hassan, R. Pamu, J. Narayanan, J. Bellare, Structural evolution in catanionic mixtures of cetylpyridinium chloride and sodium deoxycholate, Soft Matter 8 (2012) 10130. https://doi.org/10.1039/c2sm25460c.

[35] L.X. Jiang, J. Bin Huang, A. Bahramian, P.X. Li, R.K. Thomas, J. Penfold, Surface Behavior, Aggregation and Phase Separation of Aqueous Mixtures of Dodecyl Trimethylammonium Bromide and Sodium Oligoarene Sulfonates: the Transition to Polyelectrolyte/Surfactant Behavior, Langmuir 28 (2012) 327–338. https://doi.org/10.1021/la2040938.

[36] G.I. Mukhayer, S.S. Davis, Interactions between large organic ions of opposite charge, J Colloid Interface Sci 66 (1978) 110–117. https://doi.org/10.1016/0021-9797(78)90190-X.

[37] M. Dubois, T. Zemb, Phase Behavior and Scattering of Double-Chain Surfactants in Diluted Aqueous Solutions, Langmuir 7 (1991) 1352–1360. https://doi.org/10.1021/la00055a011.

[38] F.M. Menger, V.A. Seredyuk, R.P. Apkarian, E.R. Wright, Colloidal Assemblies of Branched Geminis Studied by Cryo-etch-HRSEM, J Am Chem Soc 124 (2002) 12408–12409. https://doi.org/10.1021/ja021025w.

[39] A. V. Peresypkin, F.M. Menger, Zwitterionic geminis. Coacervate formation from a single organic compound, Org Lett 1 (1999) 1347–1350. https://doi.org/10.1021/ol990205g.

[40] E.A. Crespo, L.F. Vega, G. Pérez-Sánchez, J.A.P. Coutinho, Unveiling the phase behavior of CiEj non-ionic surfactants in water through coarse-grained molecular dynamics simulations, Soft Matter 17 (2021) 5183–5196. https://doi.org/10.1039/d1sm00362c.

[41] M. Rothe, E. Müller, P. Denk, W. Kunz, Ionic Liquids Based on the Concept of Melting Point Lowering Due to Ethoxylation, Molecules 26 (2021) 4034. https://doi.org/10.3390/molecules26134034.

[42] M. Rothe, M. Tress, C. Allacher, P. Nuernberger, W. Kunz, Ionic Liquids [M 3+][A −] 3 with Three-Valent Cations and Their Possible Use to Easily Separate Rare Earth Metals, Chemistry – A European Journal 27 (2021) 13052–13058. https://doi.org/10.1002/chem.202101925.

[43] M. Rothe, G. Quintard, M. Kronseder, P. Bauduin, T. Zemb, W. Kunz, Dilution and packing of anionic liquid surfactant in presence of divalent and trivalent counterions, J Mol Liq 384 (2023) 122195. https://doi.org/10.1016/j.molliq.2023.122195.

[44] Y. Hendrikx, J. Charvolin, Structural relations between lyotropic phases in the vicinity of the nematic phases, Journal de Physique 42 (1981) 1427–1440. https://doi.org/10.1051/jphys:0198100420100142700.

[45] V. Hendrikx, J. Charvolin, M. Rawiso, L. Liebert, M.C. Holmes, Anisotropic aggregates of amphiphilic molecules in lyotropic nematic phases, J Phys Chem 87 (1983) 3991–3999. https://doi.org/10.1021/j100243a039.

[46] D.H. Wu, A.D. Chen, C.S. Johnson, An Improved Diffusion-Ordered Spectroscopy Experiment Incorporating Bipolar-Gradient Pulses, J Magn Reson A 115 (1995) 260–264. https://doi.org/10.1006/jmra.1995.1176.

[47] A. Jerschow, N. Müller, Suppression of Convection Artifacts in Stimulated-Echo Diffusion Experiments. Double-Stimulated-Echo Experiments, Journal of Magnetic Resonance 125 (1997) 372–375. https://doi.org/10.1006/jmre.1997.1123.

[48] E.O. Stejskal, J.E. Tanner, Spin Diffusion Measurements: Spin Echoes in the Presence of a Time-Dependent Field Gradient, J Chem Phys 42 (1965) 288–292. https://doi.org/10.1063/1.1695690.

[49] C.S. Johnson, Diffusion ordered nuclear magnetic resonance spectroscopy: principles and applications, Prog Nucl Magn Reson Spectrosc 34 (1999) 203–256. https://doi.org/10.1016/S0079-6565(99)00003-5.

[50] T. Zemb, S. Prévost, Testing the existence of micellar necklace hexagonal lyotropic liquid crystal. Institut Laue-Langevin (ILL), (2021). https://doi.org/https://dx.doi.org/10.5291/ILL-DATA.EASY-963.

[51] C. Tanford, Micelle shape and size, Journal of Physical Chemistry 76 (1972) 3020–3024. https://doi.org/10.1021/j100665a018.

[52] B.W. Ninham, V.A.A. Parsegian, Electrostatic potential between surfaces bearing ionizable groups in ionic equilibrium with physiologic saline solution, J Theor Biol 31 (1971) 405–428. https://doi.org/10.1016/0022-5193(71)90019-1.

[53] H. Matsuura, K. Fukuhara, Conformational analysis of poly(oxyethylene) chain in aqueous solution as a hydrophilic moiety of nonionic surfactants, J Mol Struct 126 (1985) 251–260. https://doi.org/10.1016/0022-2860(85)80118-6.

[54] G. Karlstroem, A new model for upper and lower critical solution temperatures in poly(ethylene oxide) solutions, J Phys Chem 89 (1985) 4962–4964. https://doi.org/10.1021/j100269a015.

[55] O. Glatter, Scattering Methods and their Application in Colloid and Interface Science, 1st ed., Elsevier, Amsterdam, 2018. https://doi.org/10.1016/C2016-0-04640-5.

[56] P. Van Der Schoot, The hexagonal phase of wormlike micelles, Journal of Chemical Physics 104 (1996) 1130–1139. https://doi.org/10.1063/1.470768.

[57] L. Sallen, P. Oswald, P. Sotta, Diffusion in the Micellar and Hexagonal Phases of the C12EO6/H2O Mixture: A Directional-Growth Study, Journal de Physique II 7 (1997) 107–138. https://doi.org/10.1051/jp2:1997117.

[58] D. Constantin, P. Oswald, M. Impéror-Clerc, P. Davidson, P. Sotta, Connectivity of the Hexagonal, Cubic, and Isotropic Phases of the C12EO6/H2O Lyotropic Mixture Investigated by Tracer Diffusion and X-ray Scattering, J Phys Chem B 105 (2001) 668–673. https://doi.org/10.1021/jp002672h.

[59] S. Marčelja, Molecular Model for Phase Transition in Biological Membranes, Nature 241 (1973) 451–453. https://doi.org/10.1038/241451a0.

[60] S. Marčelja, Chain ordering in liquid crystals II. Structure of bilayer membranes, Biochimica et Biophysica Acta (BBA) - Biomembranes 367 (1974) 165–176. https://doi.org/10.1016/0005-2736(74)90040-6.

[61] J.B. Hayter, T. Zemb, Concentration-dependent structure of sodium octanoate micelles, Chem Phys Lett 93 (1982) 91–94. https://doi.org/10.1016/0009-2614(82)85062-8.

[62] P. Bauduin, T. Zemb, Perpendicular and lateral equations of state in layered systems of amphiphiles, Curr Opin Colloid Interface Sci 19 (2014) 9–16. https://doi.org/10.1016/j.cocis.2014.02.002.

[63] T. Zemb, C. Chachaty, Alkyl chain conformations in a micellar system from the nuclear spin relaxation enhanced by paramagnetic ions, Chem Phys Lett 88 (1982) 68–73. https://doi.org/10.1016/0009-2614(82)80072-9.

[64] K.A. Dill, Configurations of the amphiphilic molecules in micelles, J Phys Chem 86 (1982) 1498–1500. https://doi.org/10.1021/j100206a006.

[65] K.A. Dill, P.J. Flory, Molecular organization in micelles and vesicles, Proceedings of the National Academy of Sciences 78 (1981) 676–680. https://doi.org/10.1073/pnas.78.2.676.

[66] P. Fromherz, The Surfactant-Block Structure of Micelles, Synthesis of the Droplet and of the Bilayer Concept, Berichte Der Bunsengesellschaft Für Physikalische Chemie 85 (1981) 891–899. https://doi.org/10.1002/bbpc.19810851015.

[67] K. Rosenlehner, B. Schade, C. Böttcher, C.M. Jäger, T. Clark, F.W. Heinemann, A. Hirsch, Sodium Effect on Self-Organization of Amphiphilic Carboxylates: Formation of Structured Micelles and Superlattices, Chemistry - A European Journal 16 (2010) 9544–9554. https://doi.org/10.1002/chem.201001150.

[68] N. Boden, S.A. Corne, K.W. Jolley, Lyotropic mesomorphism of the cesium pentadecafluorooctanoate/water system: high-resolution phase diagram, J Phys Chem 91 (1987) 4092–4105. https://doi.org/10.1021/j100299a031.

[69] M.C. Holmes, D.J. Reynolds, N. Boden, Concentration-temperature dependence of the size and shape of the micelles in the cesium pentadecafluorooctanoate/water system, J Phys Chem 91 (1987) 5257–5262. https://doi.org/10.1021/j100304a025.

[70] M. Corti, C. Minero, V. Degiorgio, Cloud point transition in nonionic micellar solutions, J Phys Chem 88 (1984) 309–317. https://doi.org/10.1021/j150646a029.

[71] R. Kjellander, Phase separation of non-ionic surfactant solutions. A treatment of the micellar interaction and form, Journal of the Chemical Society, Faraday Transactions 2 78 (1982) 2025. https://doi.org/10.1039/f29827802025.

[72] J. Chen, C.L. Brooks, H.A. Scheraga, Revisiting the carboxylic acid dimers in aqueous solution: Interplay of hydrogen bonding, hydrophobic interactions and entropy, Journal of Physical Chemistry B 112 (2008) 242–249. https://doi.org/10.1021/jp074355h.

[73] J.H. Clint, Surfactant Aggregation, 1st ed., Springer Science+Business Media New York, New York, 1992. https://doi.org/10.1007/978-94-011-2272-6.

[74] R.K. Thomas, J. Penfold, Multilayering of Surfactant Systems at the Air-Dilute Aqueous Solution Interface, Langmuir 31 (2015) 7440–7456. https://doi.org/10.1021/la504952k.

[75] T.K. Lind, E.J. Nilsson, B. Wyler, D. Scherer, T. Skansberger, M. Morin, V. Kocherbitov, J. Engblom, Effects of ethylene oxide chain length on crystallization of polysorbate 80 and its related compounds, J Colloid Interface Sci 592 (2021) 468–484. https://doi.org/10.1016/j.jcis.2021.01.065.

[76] G. Förster, A. Meister, A. Blume, Chain packing modes in crystalline surfactant and lipid bilayers, Curr Opin Colloid Interface Sci 6 (2001) 294–302. https://doi.org/10.1016/S1359-0294(01)00091-7.

[77] G. Förster, A. Meister, A. Blume, Van der Waals energy contour map describing the orthorhombic hydrocarbon chain packing of symmetry Pbnm, Physical Chemistry Chemical Physics 2 (2000) 4503–4508. https://doi.org/10.1039/b003278f.

[78] Y. Takahashi, H. Tadokoro, Structural Studies of Polyethers, (-(CH2)m-O-)n . X. Crystal Structure of Poly(ethylene oxide), Macromolecules 6 (1973) 672–675. https://doi.org/10.1021/ma60035a005.

[79] D.M. Small, The Physical Chemistry of Lipids. In: Handbook of lipid research, 4, Plenum Press New York, New York, 1986.

[80] P. Alexandridis, U. Olsson, B. Lindman, Self-Assembly of Amphiphilic Block Copolymers, Macromolecules 28 (1995) 7700–7710.

[81] P. Sakya, J.M. Seddon, R.H. Templer, R.J. Mirkin, G.J.T. Tiddy, Micellar Cubic Phases and Their Structural Relationships: The Nonionic Surfactant System C12EO12 /Water, Langmuir 13 (1997) 3706–3714. https://doi.org/10.1021/la9701844.

[82] Y. Lyu, Y. Guo, R. Cai, R. Peng, C. Hong, X. Chen, W. Hou, X. Li, J. Tan, Y. Zou, X. Zhang, Q. Liu, W. Tan, Spherically Directed Synthesis and Enhanced Cellular Internalization of Metal-Crosslinked DNA Micelles, Chem 5 (2019) 913–928. https://doi.org/10.1016/j.chempr.2019.02.004.

[83] E. Romera-García, A. Ballesteros-Gómez, S. Rubio, Supramolecular biosolvents made up of self-assembled rhamnolipids: synthesis and characterization, Green Chemistry (2020). https://doi.org/10.1039/d0gc02078h.

Chapter IV.

A Self-Thickening Discotic Lyotropic Nematic Phase – Mixing Two Polyoxyethylene Alkyl Ether Carboxylic Acids

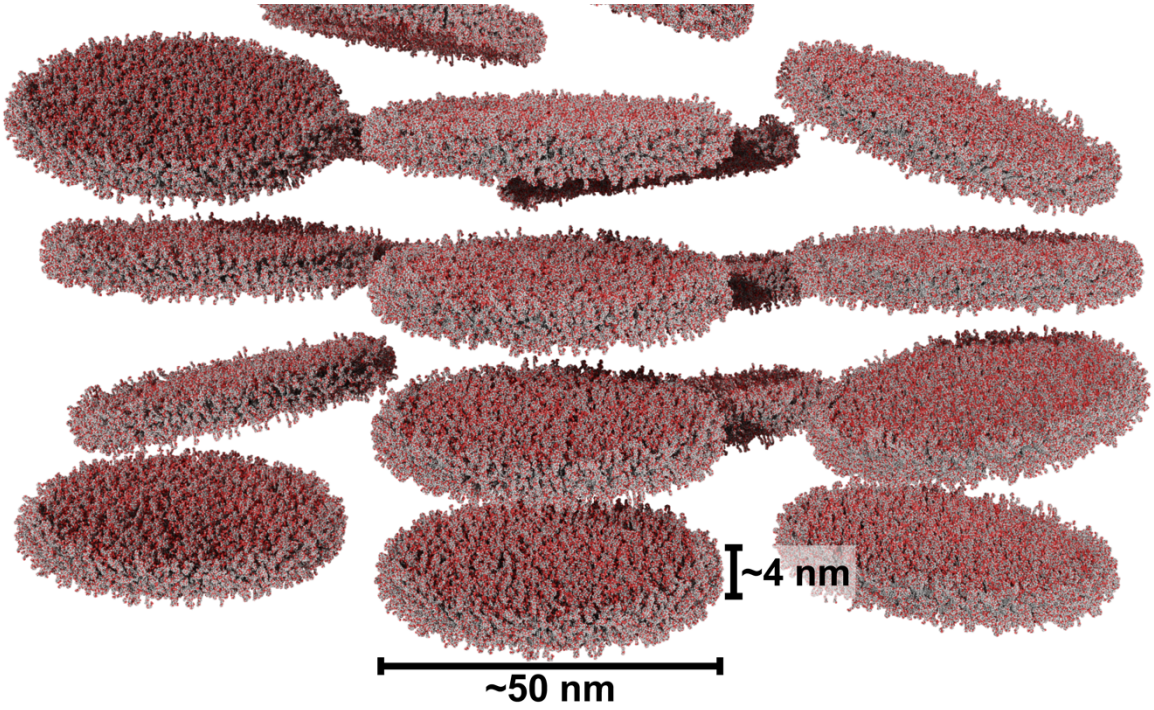

Scaled sketch of a discotic lyotropic nematic phase made of bicelles, formed when mixing octaoxyethylene octyl ether carboxylic acid, $C_8E_8CH_2COOH$, and dioxyethylene oleyl ether carboxylic acid, $C_{18:1}E_2CH_2COOH$, in water.

Note:
The majority of this chapter is already published (P. Denk, L. Matthews, S. Prévost, T. Zemb, W. Kunz, A dilute nematic gel produced by intramicellar segregation of two polyoxyethylene alkyl ether carboxylic acids, J Colloid Interface Sci 659 (2024) 833–848.) [1]. The author of this thesis is the first author of the publication, wrote the original draft, evaluated the data, and conducted most of the experiments. The co-authors Prof. Dr. Thomas Zemb and Prof. Dr. Werner Kunz assisted by reviewing the draft and giving scientific input throughout the work. The co-authors Dr. Lauren Matthews and Dr. Sylvain Prévost performed the small-angle scattering measurements and the treatment of raw scattering data. The interns Julia Grasenhiller, Markus Maier, and Julia-Marie Maier were involved in performing preliminary experiments on this subject, but did not contribute to the data presented in this chapter.

IV.1. Abstract

As described in **Chapters II.** and **III.**, the surfactant octaoxyethylene octyl ether carboxylic acid, $C_8E_8CH_2COOH$, has such a bulky headgroup and short alkyl chain that the common sphere-to-cylinder transition cannot occur. The surfactant dioxyethylene oleyl ether carboxylic acid, $C_{18:1}E_2CH_2COOH$, on the other hand is mimicking lipids and forms only bilayers. If the two surfactants are mixed, intramicellar molecular segregation is imposed due to the different packing constraints. Since the curvature constraints are temperature dependent due to hydration of ethylene oxide groups, temperature is expected to influence the degree of intramicellar segregation and consequently the formed microstructures.

In this chapter, phase diagrams as a function of temperature, surfactant mole ratio, and active matter content are established. The isotropic liquid-liquid phase separation common to all nonionic surfactants, i.e., the clouding phenomenon, as well as discotic nematic phases and lamellar phases are found. The focus lies on the nematic phase and its stability. Texture determination by polarizing microscopy is used to distinguish between the different phases. Small-angle X-ray scattering (SAXS) and small-angle neutron scattering (SANS) are applied to elucidate the microstructures at various points in the phase diagrams. Further, the rheology of the nematic phase as well as the influences of adding salt and increasing the surfactants' ionic character are investigated.

In a defined mole ratio of the two surfactants, intramicellar segregation is sufficient to produce a viscoelastic discotic nematic phase at low temperature, which is capable of entrapping air bubbles or other objects of any size. The disc-like aggregates are bicelles consisting of a flat bilayer part and a high-curvature rim that limits the diameter of the bicelles. Heating induces partial intramicellar mixing, reducing the fraction of the limiting rim. This results in a growth of the bicellar diameter until eventually a pseudo-lamellar phase is formed. A further increase in temperature leads to the transition into an isotropic phase of fully randomly mixed micelles, showing the common liquid-liquid miscibility gap at higher temperatures. This uncommon phase sequence, bicelles, lamellar phase, micelles, and water-poor packed micelles, is a consequence of intramicellar segregation of two surfactants with a significant mismatch between their headgroup and tail lengths, opposed by temperature induced intramicellar mixing. The same sequence can be induced by dehydrating the headgroups with the addition of salt instead of an increase in temperature.

IV.2. Introduction

"Bilayer micelles", abbreviated as "bicelles", made of bilayers of defined size limited by an outer rim, were first identified by Sanders and Schwonek in 1992 [2]. Classical bicelles are formed when mixing a long-chain lipid, such as dimyristoylphosphatidylcholine (DMPC), and a short-chain lipid, such as dihexanoylphosphatidylcholine (DHCP), in water in adequate mixing ratios. Typically, bicelles are formed if the lipid mixture contains around 65–85% of the long-chain lipid [3–5]. The packing conditions can be rationalized using the geometrical chain packing model introduced by Israelachvili *et al.* [6]. The long-chain lipid has a spontaneous packing parameter $p_0 \approx 1$ and favors low curvature in a bilayer packing, while the short-chain lipid has a lower p_0 and favors higher curvature. The packing parameter is defined and discussed in **Appendix A.3**. Due to this mismatch, intramicellar molecular segregation occurs and results in the formation of disc-like bicelles consisting of a bilayer disc that is limited by an outer half-toroidal rim. Since their discovery, bicelles have gained significant interest in biochemical and biophysical chemistry, because they mimic biological membranes and are often orientable in magnetic fields, making them attractive vessels for NMR studies of membrane proteins [2,5,7–11]. Various different morphologies are found in systems containing disc-like bicelles, such as perforated or unperforated uni- and multilamellar vesicles, "infinite" lamellae and perforated lamellae, branched and unbranched worm-like micelles, and ribbons [4,5,8,9,12,13]. Apart from worm-like micelles, all these structures are related as the curvature for the long-chain lipid approaches zero, the difference being the degree of intramicellar segregation of the two lipids. If the rim-forming short-chain surfactant is completely mixed into the bilayer, i.e., if there is full intramicellar random mixing, vesicles or "infinite" lamellae are formed. Ribbons and perforated lamellae can be rationalized as intermediate states between disc-like bicelles and "infinite" lamellae. If disc-like bicelles start to merge due to a reduction in intramicellar segregation, the remaining high curvature rims either form holes in an extended lamella or limit the bilayers into ribbons. In fact, disc-like bicelles are usually found only below the chain melting temperature of the long chain surfactant, above which other morphologies emerge [4,9]. Due to this rich phase behavior, the term "bicelle" is often used to refer to systems made of a hydrophobic and a more hydrophilic lipid, independent of the structures' morphologies. In this thesis, the term "bicelle" is used in its original meaning only for the disc-like morphology. Typical diameters of such disc-like bicelles are in the range of 15–50 nm, the thickness

typically being around 4–6 nm [9]. Nematic or smectic phases of bicelles are often induced by bicellar orientation in strong magnetic fields [3,5,8,9,14].

Bicelles can not only be formed with lipids, but also with other, synthetic surfactants, see for example ref. [15,16]. An early example of synthetic (lipid-free) bicelles with a diameter of around 50 nm, made of sodium decyl sulfate, decanol, and sodium sulfate in water, that can be magnetically oriented into a discotic nematic phase was given by Lawson *et al.* [17] in 1967 and later verified by others [18,19]. In fact, these synthetic bicelles, though not termed "bicelles", were found even before the classical bicelles were described. Although disc-like micelles are relatively rare, several examples are known [20–27], many of which may be considered as synthetic bicelles. Synthetic bicelles can also be formed in catanionic mixtures, for which intramicellar molecular segregation into a bilayer and a rim was shown [28–30]. If the number density of discs is sufficiently high, a discotic nematic phase is formed [21–24,26,31–33]. Usually, discotic lyotropic nematic phases are found as a transition state between an isotropic micellar phase and an "infinite" lamellar phase, whereas calamitic lyotropic nematic phases are found between an isotropic micellar phase and a hexagonal phase made of "infinite" rods [32,34]. The isotropic-nematic-lamellar/hexagonal transition then involves micellar growth to increase anisotropy until the smaller micelles merge into "infinite" lamellae or cylinders. For the system cesium pentadecafluorooctanoate/D_2O it was shown that all three phases, the isotropic phase, the discotic nematic phase, and the lamellar phase, are made of the same small disc-like micelles (diameter ≤10 nm) [35]. In this case, the isotropic-nematic-lamellar transition is rather an isotropic-nematic-smectic transition, where the lamellar phase is a smectic phase made of layered discs. Discotic lyotropic nematic phases made of discoidal micelles or bicelles are usually of low viscosity, slightly shear thinning, and only slightly viscoelastic [36–39]. Packed onion-like multilamellar vesicles (MLVs) on the other hand are known to form shear thinning viscoelastic gels that are capable of entrapping air bubbles [40–42].

Long lasting entrapment of objects between 1 μm and 1 mm in size is still a problem with classical micelles or microemulsions. Polymeric formulations have either no threshold, below which an elastic gel allows for quasi-infinite entrapment, or long relaxation times, making mixing difficult. In this chapter, it is shown that a new viscoelastic water-swollen nematic phase of synthetic bicelles is obtained upon mixing two commercially available extended carboxylic acid surfactants, namely Akypo® LF2 ($C_8E_8CH_2COOH$) and Akypo®

RO 20 VG ($C_{18:1}E_2CH_2COOH$), in the right concentration and temperature range. The underlying mechanism is molecular segregation inside of each bicelle. A possible advantage of the nematic phase over packed MLVs is its continuous aqueous phase. The defects in the nematic order are spaced by at least a three to five times the size of the bicelles, which are the fundamental structural units. Any object larger than the spacing between defects is efficiently entrapped, since displacement of the entrapped object requires displacement of the defects, which requires much more than 1 $k_B \cdot T$ [43]. Efficient entrapment that can be used in applications could even be experimentally proved using visible air bubbles under soft centrifugation. A nematic phase with similar properties, obtained by mixing lauric acid, Neodol® 91-8 ($C_{9\text{-}11}E_8$), and a fragrance oil, was recently reported by Tchakalova *et al.* [44].

In this chapter, phase diagrams are determined as a function of temperature, surfactant composition, and active matter concentration, covering a wide range of temperatures, the whole range of possible surfactant compositions at a fixed active matter concentration, and the whole range of active matter concentrations at a fixed surfactant composition. The microstructures are identified by means of small-angle X-ray scattering (SAXS), small-angle neutron scattering (SANS), and optical birefringence. Further, the rheology of the nematic phase and the effects of salts (NaCl and $CaCl_2$) and bases (NaOH and $Ca(OH)_2$) on the nematic phase formation are examined.

IV.3. Experimental Section

IV.3.1. Materials

The surfactants octaoxyethylene octyl ether carboxylic acid, $C_8E_8CH_2COOH$ ($M = 541\ g \cdot mol^{-1}$), commercialized under the name Akypo® LF2 (90.0 wt% active matter, 0.9 wt% NaCl, 9.1 wt% water), and dioxyethylene oleyl ether carboxylic acid, $C_{18:1}E_2CH_2COOH$ ($M = 415\ g \cdot mol^{-1}$), commercialized under the name Akypo® RO 20 VG (95.8 wt% active matter, 0.1 wt% NaCl, 4.1 wt% water), as well as their ethoxylated alcohol precursors C_8E_8 and $C_{18:1}E_2$, were a generous gift by Kao Chemicals GmbH (Emmerich am Rhein, Germany). The hydrophobic chain of $C_{18:1}E_2CH_2COOH$ is a mixture of various hydrocarbon chains. $C_{18:1}$ denotes an oleyl ((Z)-octadec-9-enyl) chain and is the most abundant chain with a fraction of at least 75%. While the proportion of the (E)-isomer is

unknown, the (Z)-isomer is expected to be the predominant species. Saturated myristyl, cetyl, and stearyl, as well as other unsaturated species, mainly $C_{18:x}$, make up for the other 25% of the chains, the cetyl group being the most abundant after $C_{18:1}$ with a fraction of around 10%. Both surfactants are technical products with a broad distribution of the degree of ethoxylation, typically containing small amounts of glycolic acid, formic acid, diglycolic acid, polyethylene glycol, carboxymethylated polyethylene glycol, nonionic polyoxyethylene alkyl ethers, and various esters of the type $C_8E_xCH_2COOE_yC_8$ or $C_{18:1}E_xCH_2COOE_yC_{18:1}$, respectively, as impurities. No differences in phase behavior were observed if using different batches of the surfactants.

Traces of remaining impurities, such as NaCl, as well as hydrophilic impurities, can be removed by cloud point extraction. Experimental details and problems arising for $C_{18:1}E_2CH_2COOH$ after vacuum drying can be inferred from **Appendix C.2**. If not stated otherwise, $C_8E_8CH_2COOH$ was used after purification by cloud point extraction and $C_{18:1}E_2CH_2COOH$ was used as received. This decision was made to reduce the amount of hydrophilic non-surfactant impurities and NaCl, while at the same time ensuring reproducibility. The water content was accounted for in any calculations.

A further way to purify the surfactants is to remove nonionic impurities by ion exchange. The method used and adapted in this work was described and evaluated by Cattelaens *et al.* [45], who have demonstrated the effectiveness of the process for the removal of nonionic impurities from ethoxylated and non-ethoxylated carboxymethylated fatty alcohols. Experimental details are given in **Appendix C.2**. Potentiometric pH titrations of $C_8E_8CH_2COOH$ before and after ion exchange, see **Fig. C.1**, also clearly indicate an increase of the carboxylic acid fraction. If a constant average molar mass of 541 $g \cdot mol^{-1}$ is assumed for $C_8E_8CH_2COOH$, an increase in the acid fraction from 82 mol% to 95 mol% is obtained. Note, however, that the molar mass and its possible change during purification are not known precisely, and more analytical data would be necessary to deduce precise acid fractions. An increase of the physical density after the purification process, see **Section IV.3.5.**, is also in agreement with the removal of the less dense nonionic impurities.

2-propanol (p.a., ≥99.8%) was purchased from Fisher Scientific (Pittsburgh, Pennsylvania, USA). KOH (p.a., ≥85.0%), 1 M hydrochloric acid, $Ca(OH)_2$ (p.a., ≥96.0%), lauric acid (≥99.0%), and squalane (for gas chromatography) were purchased from Merck (Darmstadt, Germany). 1 M NaOH solution, NaCl (p.a., ≥99.5%), $CaCl_2 \cdot 2\,H_2O$ (p.a., ≥99%),

n-dodecane (≥95%), and the linear polydimethylsiloxane silicon oil M20 were supplied by Carl Roth (Karlsruhe, Germany). (R)-(+)-Limonene (≥97%) was purchased from Sigma-Aldrich (St. Louis, Missouri, USA). D_2O (99% D) was supplied by Eurisotop (Saint-Aubin, France). Extra virgin olive oil (PDO Chania IGP) was purchased from Edeka (Hamburg, Germany). Akypo® RO 90 VG and Akypo® TEC-AM VG were generous gifts by Kao Chemicals GmbH. Ultrapure water from a Millipore purification system (resistivity >18 MΩ·cm) was used for all systems containing water.

IV.3.2. Phase Diagram Determination

All phase diagrams were determined in a temperature range of 10°C to 95°C using a Julabo (Seelbach, Germany) F32-HD refrigerated and heating circulator. Occasionally, phase transitions were evaluated below 10°C for a better determination of phase boundaries. Samples were prepared in 16×100 mm test tubes with sealed polypropylene screw caps. Prior to the recording of phase diagrams, samples were usually heated to 50°C and mixed with a vortex mixer during re-cooling. Phase boundaries were determined by visual observation with an accuracy in temperature of ±1°C during heating. The temperature was adjusted in steps of 1°C and samples were left to equilibrate for at least 10 min. An equilibration time of 10 min was found to be more than sufficient for all observed phase transitions and the same phase boundaries were found during cooling. In case of inhomogeneity, samples were agitated using a vortex mixer and left equilibrated again before evaluation of the equilibrium phase. To allow full macroscopic phase separation, some samples were left equilibrated for up to 72 h. To distinguish different liquid crystalline and isotropic phases, samples were observed between crossed polarizers. In addition, polarizing microscopy was performed using a Leitz (Wetzlar, Germany) Orthoplan polarizing microscope equipped with a JVC (Yokohama, Japan) digital camera (TK-C1380) and a Linkam (Epsom, UK) LTS350 heating/freezing stage comprising a TMS90 temperature controller (±0.5°C) and a CS196 cooling system. To be able to investigate both phases of biphasic samples at room temperature, complete phase separation was facilitated by centrifugation with a 3-18KS centrifuge from Sigma Laborzentrifugen (Osterode am Harz, Germany).

IV.3.3. Small-Angle X-Ray Scattering

Small-angle X-ray scattering (SAXS) data were performed on the ID02, TRUSAXS, beamline at the European Synchrotron Radiation Facility (ESRF, Grenoble, France). The X-ray energy used was 12.23 keV, corresponding to a wavelength, $\lambda = 0.101$ nm. A single sample-to-detector distance of 0.8 m was used, covering a q-range of 0.072–7.5 nm^{-1}, where q is the magnitude of the scattering vector and is given by $q = \sin(\theta/2)\cdot 4\pi/\lambda$. All measurements were carried out in quartz capillaries of diameter ø = 1.5 mm, with the exception of sample 20M*, for which a capillary with ø = 2 mm was used. 2D SAXS patterns were recorded by a Dectris (Baden-Daettwil, Switzerland) Eiger2 4M pixel array detector, and the sample transmission was simultaneously measured. To obtain sufficient statistics for good data quality, 12 frames of 1 s exposure time were averaged, and samples underwent a radiation damage test to ensure this did not cause damage to the sample. The resulting 2D images were normalized to an absolute intensity scale and azimuthally averaged to obtain the 1D profiles. The 1D SAXS patterns were then subtracted using a capillary of water adjusted by a factor to account for the temperature. Scattering was isotropic in all cases.

IV.3.4. Small-Angle Neutron Scattering

Small-angle neutron scattering (SANS) data were collected on instrument D33 at the Institut Laue-Langevin – The European Neutron Source (ILL, Grenoble, France). Samples were poured in 1 mm pathway quartz cuvettes of type 120 from Hellma GmbH (Müllheim, Germany), kept on a thermalized sample-changer. A single configuration with a wavelength of 4.62 Å (relative FWHM 10%) was used. The beam was entirely collimated, and the rear detector was placed at a distance of 13.3 m from the sample, the four front panels being at distances of 1.7 m (top and bottom) and 1.9 m (left and right). Data were processed with GRASP 10.16b [46], using the monitor as normalizer, correcting for the flat field, transmission, background noise as measured with sintered $^{10}B_4C$ at the sample position, and subtracting the contribution from a cuvette filled with D_2O. Absolute scale was obtained from the measurement of the attenuated direct beam on the detector, with a known attenuation coefficient. If not stated otherwise, given data are radially averaged. Some samples exhibit anisotropic scattering, but only the scattering intensity, not the features of the

scattering curve, were found to depend on the azimuthal angle.

IV.3.5. Density Measurements

The physical densities of $C_8E_8CH_2COOH$ after cloud point extraction, vacuum dried $C_{18:1}E_2CH_2COOH$, $C_8E_8CH_2COOH$ and $C_{18:1}E_2CH_2COOH$ after purification by ion exchange and cloud point extraction, as well as various other mixtures, were measured using a density meter DMA 5000 M from Anton Paar (Graz, Austria), which operates with the oscillating U-tube method. To be able to extrapolate the surfactants' densities for any temperature, the densities were measured in steps of 5°C between 20°C and 50°C. A condition for each measurement was temperature stability with a maximum deviation of ±0.002°C. The data and their linear relations are given in **Fig. C.2**.

IV.3.6. Molecular Volumes and Scattering Length Densities

The molecular volumes and scattering length densities (SLDs) of the surfactants, also split into a hydrophobic and hydrophilic moiety, and water (H_2O) and (D_2O) are given in **Appendix C.3.**, including details on their calculation.

IV.3.7. Conductivity and Potentiometric pH Measurements

Potentiometric pH measurements and automated titrations were performed using a 905 Titrando high-end titrator for potentiometric titration equipped with a flat membrane pH glass electrode and an 800 Dosino dosing unit from Metrohm (Herisau, Switzerland). Conductivity measurements were performed using a conductivity measuring cell (cell constant $c = 0.8\ cm^{-1}$) with an integrated Pt1000 temperature sensor from Metrohm. To be able to calculate the reduced molar conductivity for a titration of a sample containing 20 wt% surfactant mixture with NaCl solution, the same titration was performed with pure water as analyte. To allow for sufficient mixing during titrations involving the nematic phase, a slow titration speed, typically $0.06\ mL \cdot min^{-1}$, was chosen.

IV.3.8. Karl-Fischer Titration

Volumetric or coulometric Karl-Fischer titration was used to check water contents of the surfactants and separated phases. Volumetric Karl-Fischer titration was performed for higher water contents using a KF titrator 870 KF Titrino plus from Metrohm, while coulometric Karl-Fischer titration was performed for lower water contents using an 899 Coulometer from Metrohm, equipped with a platinum indicator and a platinum generator electrode without a diaphragm. Water contents were measured at least five times and averaged.

IV.3.9. Threshold of Bubble Rising

Air bubbles of different sizes were introduced into a nematic gel containing 20 wt% surfactant mixture with R($C_{18:1}E_2CH_2COOH$) = 0.655 by simple shaking by hand. At rest, air bubbles are infinitely entrapped, i.e., they do not rise. If buoyancy is increased by centrifugation, bubbles start to rise above a certain threshold. A 3-18KS centrifuge from Sigma Laborzentrifugen, equipped with a swing-out rotor 11180 and round buckets 13190, was used to increase the centrifugal force step by step. In total, four centrifuge tubes with conical bottom (15 mL) were filled with 10 mL of nematic gel each and various bubbles were monitored by taking photographs after each centrifugation step. The rotation of the rotor was increased in steps of 100 RPM at 25°C, starting at 100 RPM. The threshold for a given bubble is then narrowed down to a range between the centrifugation step where the bubble starts to rise and the preceding step. The threshold can be used to calculate the pressure exerted by the nematic gel on the air bubble. Further details are given in **Appendix C.4**.

IV.3.10. Rheology

All rheological measurements were performed at 25°C with a Kinexus lab+ rotational rheometer with Peltier plate temperature control from Malvern Panalytical (Malvern, UK). Prior to sample loading, the sample was shaken by hand and air bubbles were avoided on sample loading.

A cone-plate setup consisting of an upper 40 mm stainless steel cone with an inclination

angle of 4° and a stationary lower 70 mm stainless steel plate was used for recording flow curves. The gap size was set to 200 µm and shear ramps were applied with shear rates in the range of $1 \cdot 10^{-4}\ s^{-1} \leq \dot{\gamma} \leq 1000\ s^{-1}$. Typically, the shear ramp was performed within 40 min and 20 points were recorded per decade. No thixotropic or rheopectic behavior was found when first increasing the shear rate, and subsequently decreasing it.

Oscillatory rheology was performed with a parallel plate setup consisting of an upper 40 mm stainless steel plate and a stationary lower 70 mm stainless steel plate. Measurements were performed with two different gap sizes of 500 µm and 1000 µm. Strain controlled amplitude sweeps were performed to determine the linear viscoelastic region at constant angular frequencies of $\omega = 6.28$, 10, 62.8, and 100 $rad \cdot s^{-1}$. Frequency sweeps were performed at constant complex strains of $\gamma^* = 0.1$, 0.2, 0.5, and 1.0%.

IV.4. Results and Discussion

IV.4.1. Phase Diagrams

The focus of this chapter is a mixture of two commercial ethoxylated alkyl ether carboxylate surfactants, namely, Akypo® LF2 ($C_8E_8CH_2COOH$) and Akypo® RO 20 VG ($C_{18:1}E_2CH_2COOH$). In binary mixtures with water, both surfactants individually exhibit remarkably simple phase behaviors. The only feature in the phase diagram of purified $C_{18:1}E_2CH_2COOH$ in water, see **Fig. IV.1**A, is the formation of a semi-crystalline lamellar L_β phase at lower temperatures up to around 90 wt% of surfactant (2.5 water molecules per headgroup). First, increasing the water content leads to an increase of the melting temperature of the L_β phase, until a maximum of around 48°C is reached around 80 wt% of surfactant (6 water molecules per headgroup). Further addition of water does not influence the melting temperature of the L_β phase, and a dilute aqueous phase separates from the L_β phase. This indicates that the L_β phase is most stable at a certain degree of headgroup hydration, and any excess water is expelled from the L_β phase. Depending on the hydration of the carboxylic acid group, the available number of water molecules per ethylene oxide (EO) group at 80 wt% surfactant is between 2 and 3, which is in good agreement with the most common hydration number for the inner hydration shell of EO reported in the literature [47–49]. Beyond basic hydration of the headgroups, $C_{18:1}E_2CH_2COOH$ and water are

not miscible. It is important to note that in most cases throughout this chapter, $C_{18:1}E_2CH_2COOH$ was used as received, and no L_β phase is observed without purification in the examined temperature range. The phase diagram is identical, only that the surfactant-rich phase is an isotropic liquid over the whole temperature range. Probably, the ester impurities, see **Section IV.3.1.**, destabilize the L_β phase.

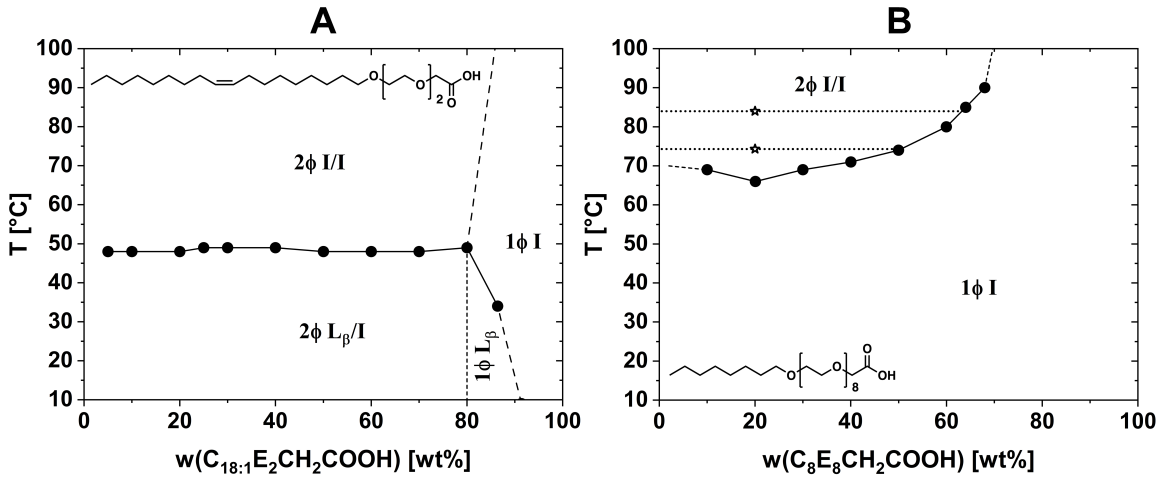

Fig. IV.1. (A) Binary phase diagram of Akypo® RO 20 VG ($C_{18:1}E_2CH_2COOH$) in water after purification by ion exchange and cloud point extraction. Without purification, the L_β phase is not formed within the observed temperature range, and an isotropic liquid phase is observed instead. (B) Binary phase diagram of Akypo® LF2 ($C_8E_8CH_2COOH$) in water after cloud point extraction. The two empty stars indicate points, where tie lines (horizontal dotted lines) were determined. 1ϕ I: Monophasic isotropic liquid. 2ϕ I/I: Two isotropic liquids in equilibrium. In the notation 2ϕ I/I, the former "I" regards the top phase, whereas the latter "I" regards the bottom phase. L_β: Semi-crystalline lamellar phase. Dashed lines indicate extrapolations of the phase boundaries based on the data, but are not connecting two data points.

The binary phase diagram of the more hydrophilic $C_8E_8CH_2COOH$ is shown in **Fig. IV.1**B. As discussed in detail in **Chapters II.** and **III.** and the respective papers [50,51], $C_8E_8CH_2COOH$ does not form any liquid crystalline phases and the only observed feature is a lower critical solution temperature (clouding). The indicated tie lines (dotted horizontal lines) in the biphasic region were determined by measuring the water contents of the two separated phases. Note, however, that in previous chapters $C_8E_8CH_2COOH$ was mostly used as received, whereas $C_8E_8CH_2COOH$ used in this chapter was purified by cloud point extraction, see **Section IV.3.1**. The different shape of the clouding curve is mainly caused by the removal of NaCl (initial NaCl content of 0.01 g NaCl per 1 g of surfactant) during cloud point extraction. Note that both surfactants are used in their acidic form with a pH around 2.2 at 20 wt% of surfactant.

As will be elucidated in this chapter, the phase behavior becomes more diverse as a function of the surfactant ratio, when both surfactants are mixed. Most interestingly, a self-

thickening, shear-thinning nematic gel with fast relaxation time can be obtained. In the following, the surfactant composition will be given as R($C_{18:1}E_2CH_2COOH$), where n is the amount of the respective surfactant in mol, which is calculated using the average molecular mass given in **Section IV.3.1**.

$$R(C_{18:1}E_2CH_2COOH) = \frac{n(C_{18:1}E_2CH_2COOH)}{n(C_{18:1}E_2CH_2COOH) + n(C_8E_8CH_2COOH)} \qquad (IV.4.1)$$

The recorded phase diagram of the $C_8E_8CH_2COOH$/$C_{18:1}E_2CH_2COOH$ surfactant mixture as a function of the surfactant composition R($C_{18:1}E_2CH_2COOH$) at a constant total surfactant content of 20 wt% is shown in **Fig. IV.2**. Both surfactants are used in their acidic form, resulting in a pH around 2.2 at 20 wt% of surfactant. The apparent pK_a of $C_8E_8CH_2COOH$ at 5 wt% of surfactant is around 3.9 (see **Fig. C.1**), the apparent pK_a of $C_{18:1}E_2CH_2COOH$ is unknown, and the apparent pK_a of the mixture with R($C_{18:1}E_2CH_2COOH$) = 0.655 at 20 wt% is around 4.6 (see **Section IV.4.5.**). Given the apparent pK_a of 4.6, the expected degree of acid dissociation is less than 0.5%, rendering the surfactants with a surface charge density of less than $-1.9 \cdot 10^{-3}$ C·m^{-2} pseudo-nonionic. In order to be able to assess possible influences of the nonionic impurities, especially esters, the same phase diagram was recorded using both surfactants after purification by ion exchange (see **Section IV.3.1.**) and is shown in **Fig. C.3**. The principal phase behavior is found to be similar in both cases, the main differences being a shift of the phase boundaries to slightly higher values of R($C_{18:1}E_2CH_2COOH$) and higher temperatures after purification. As mentioned above, $C_{18:1}E_2CH_2COOH$ purified by ion exchange can form a L_β phase in presence of water, whereas unpurified $C_{18:1}E_2CH_2COOH$ cannot. The same is true for mixtures with R($C_{18:1}E_2CH_2COOH$) $\geq$ 0.9, which can form a L_β phase if the surfactants are used after purification by ion exchange.

Apart from a small biphasic isotropic domain at low temperatures around R($C_{18:1}E_2CH_2COOH$) = 0.2, which only appears in presence of the more hydrophobic ester impurities, the mixture is a single isotropic micellar phase below the critical clouding temperature up to approximately R($C_{18:1}E_2CH_2COOH$) = 0.5. At R($C_{18:1}E_2CH_2COOH$) = 0, $C_8E_8CH_2COOH$ forms small spherical micelles (aggregation number $N_{agg} \approx 30$, radius $r \approx 2.5$ nm [50,51]) and the lower critical solution temperature (LCST) is reached at 66°C around 20 wt% of surfactant. With increasing fraction of the hydrophobic $C_{18:1}E_2CH_2COOH$, the critical temperature decreases to 48°C at

$R(C_{18:1}E_2CH_2COOH) \approx 0.5$. It is to be expected that the two surfactants form mixed micelles, progressively deviating from the initially spherical shape. Applying the geometrical chain packing model introduced by Israelachvili *et al.* [6], $C_8E_8CH_2COOH$ with its short C_8 chain and large headgroup has a spontaneous packing parameter $p_0 \leq 1/3$, thus packing into a spherical shape, and $C_{18:1}E_2CH_2COOH$ with its long $C_{18:1}$ chain and relatively small headgroup has a p_0 close to 1, thus favoring lamellar packing. Therefore, a progression towards an (oblate) ellipsoidal shape can be expected.

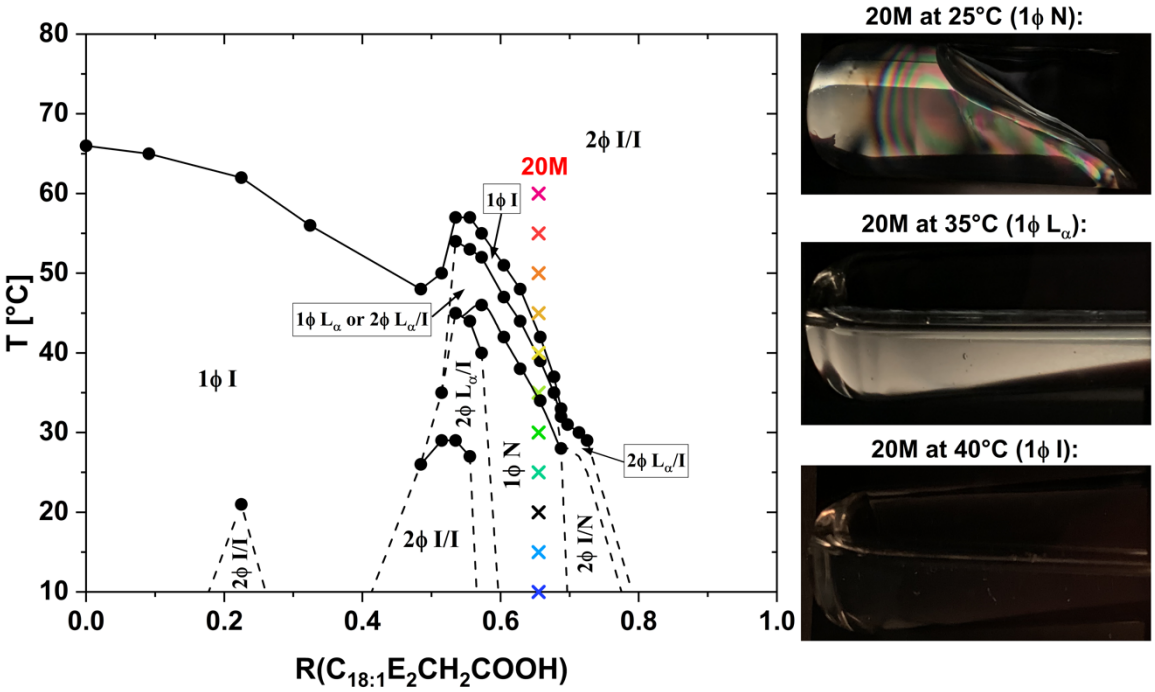

Fig. IV.2. Phase diagram of the $C_8E_8CH_2COOH/C_{18:1}E_2CH_2COOH$ surfactant mixture in water at a fixed total surfactant content of 20 wt%. The mixing ratio of the two surfactants, given as $R(C_{18:1}E_2CH_2COOH)$, is varied. 1ϕ I: Monophasic isotropic liquid. 2ϕ I/I: Two isotropic liquids in equilibrium. In the notation 2ϕ I/I, the former "I" regards the top phase, whereas the latter "I" regards the bottom phase. L_α: Lyotropic lamellar phase. N: Lyotropic nematic phase. The colored crosses indicate samples measured with SAXS. The three images depict sample 20M (20 wt% surfactant, $R(C_{18:1}E_2CH_2COOH) = 0.655$) between crossed polarizers at 25°C (1ϕ N), 35°C (1ϕ L_α), and 40°C (1ϕ I). Pictures were taken during heating of the sample from 10°C. After 30 min of equilibration at the respective temperature, the cylindrical glass tube (diameter ≈ 1.6 cm) containing the sample was placed horizontally (perpendicular to the direction of gravity) between crossed polarizers. The same phase diagram with both surfactants purified by ion exchange is shown in **Fig. C.3**.

Following the transition 1ϕ I → 2ϕ I/I around $R(C_{18:1}E_2CH_2COOH) \approx 0.5$, the complete phase sequence on increasing $R(C_{18:1}E_2CH_2COOH)$ at room temperature is 2ϕ I/I → 2ϕ L_α/I → 1ϕ N → 2ϕ I/N → 2ϕ L_α/I → 2ϕ I/I, where "I" denotes an isotropic L_1 phase, "L_α" a lamellar, and "N" a nematic phase. In the used notation, the first letter refers to the top phase, while the second letter refers to the denser bottom phase. In absence of ester impurities, see **Fig. C.3**, the 2ϕ I/N domain does not appear, suggesting that the small

isotropic phase contains hydrophobic ester impurities that are not solubilized in the nematic phase. Further, the nematic phase usually transitions into two isotropic phases via 1ϕ N → 1ϕ L_α → 1ϕ I → 2ϕ I/I, where 2ϕ L_α/I may appear as a coexistence domain in a narrow concentration or temperature range during the transition 1ϕ L_α → 1ϕ I. The appearance of an excess phase containing hydrophobic ester impurities in the 2ϕ I/N domain slightly alters this phase sequence. A surfactant partitioning seems to occur in the 2ϕ I/I domain above R($C_{18:1}E_2CH_2COOH$) = 0.5, where a smaller, turbid, less dense upper phase separates from a larger (≥ 80 vol%) bottom phase. The bottom phase at R($C_{18:1}E_2CH_2COOH$) = 0.524 contains 17 wt% of surfactant, while the top phase is richer in surfactant, suggesting that micelles in the bottom phase contain a larger fraction of the hydrophilic $C_8E_8CH_2COOH$, while the top phase is a dispersion of hydrated insoluble $C_{18:1}E_2CH_2COOH$. On heating, the mixing of the two surfactants is expected to be facilitated, explaining the transition to the 2ϕ L_α/I domain by incorporation of enough $C_8E_8CH_2COOH$ into the $C_{18:1}E_2CH_2COOH$-rich upper phase to achieve a water-soluble lamellar phase. The subsequent transition to a nematic phase can also be explained by further mixing of the two surfactants until the two separate phases, i.e., the $C_{18:1}E_2CH_2COOH$-rich lamellar top phase and the $C_8E_8CH_2COOH$-rich isotropic micellar bottom phase, merge into a single phase of mixed aggregates. At sufficient R($C_{18:1}E_2CH_2COOH$), an increase in temperature and an increase in R($C_{18:1}E_2CH_2COOH$) have similar effects.

This complex phase sequence can be rationalized by considering partial molecular segregation of the two surfactant species. Whereas there is no segregation in the isotropic mixed micellar phase for R($C_{18:1}E_2CH_2COOH$) < 0.5, on increasing R($C_{18:1}E_2CH_2COOH$) there is first intermicellar segregation into two different phases, i.e., two different microstructures, because intramicellar segregation is impossible for small spheroidal aggregates due to the cost in entropy being too high, and eventually, around R($C_{18:1}E_2CH_2COOH$) = 0.6, the two different microstructures mix to form a single species of larger aggregates, where intramicellar segregation occurs. $C_{18:1}E_2CH_2COOH$, favoring lamellar packing, is preferably populating regions of low curvature, while $C_8E_8CH_2COOH$, favoring spherical packing, preferably populates regions of high curvature. Thus, packing considerations suggest disc-like structures, also referred to as bicelles in literature. Intramicellar molecular segregation was shown for catanionics [28–30], and is also the reason for the formation of bicelles when mixing a lipid with another (lipid) surfactant, which favor different curvatures [5,8–11,16]. When starting in the nematic phase, e.g., at R($C_{18:1}E_2CH_2COOH$) = 0.66 (sample 20M

indicated in the phase diagram), the observed phase sequence with increasing temperature is similar to the sequence observed at constant temperature with increasing R($C_{18:1}E_2CH_2COOH$): 1ϕ N → 1ϕ L_α → 1ϕ I → 2ϕ I/I with a narrow transition zone during the transition 1ϕ L_α → 1ϕ I, where both phases are in equilibrium. This sequence can also be explained by an increase in intramicellar surfactant mixing, i.e., a decrease in intramicellar segregation, on increasing temperature or R($C_{18:1}E_2CH_2COOH$). A sufficient degree of mixing leads to merging of the bicelles into soft, highly undulating pseudo-lamellar structures, which then finally transform into mixed micelles in the isotropic phase. The eventual phase separation into two isotropic phases at a critical temperature is in most cases a classical cloud point. However, at high values of R($C_{18:1}E_2CH_2COOH$) and lower temperatures, the two surfactants possibly partition between the two phases, with an aqueous phase containing $C_8E_8CH_2COOH$-rich aggregates on the one hand and a hydrated $C_{18:1}E_2CH_2COOH$ phase on the other hand. A separation into a dilute aqueous phase and a surfactant-rich phase containing both surfactants fully mixed would then be expected at higher temperatures.

Interestingly, the clouding temperature shows re-entrant behavior: It increases from 48°C around R($C_{18:1}E_2CH_2COOH$) = 0.5 to 57°C at R($C_{18:1}E_2CH_2COOH$) = 0.56, before decreasing again with increasing R($C_{18:1}E_2CH_2COOH$). In absence of ester impurities, this local maximum of the critical temperature is shifted to 67°C at R($C_{18:1}E_2CH_2COOH$) = 0.62 and almost matches the critical temperature at R($C_{18:1}E_2CH_2COOH$) = 0. The increase of the critical temperature coincides with the appearance of lyotropic liquid crystalline (LC) phases and the position of the local maximum in R($C_{18:1}E_2CH_2COOH$) matches the first appearance of the nematic phase. Critical temperatures are related to dehydration of headgroups and significantly differ for the two surfactants. In absence of intramicellar segregation, the critical temperature shows a sigmoidal shape, decreasing with increasing fraction of the hydrophobic surfactant. The intramicellar segregation present in the bicellar nematic domain is the origin of the re-entrant behavior that is clearly shown in **Fig. IV.2**.

The nematic phase is viscoelastic, capable of entrapping air bubbles, and strongly shear thinning, see rheology data in **Figs. C.4** and **C.5**. As can be seen in **Fig. C.4** and **Table C.1**, the obtained flow curves of a nematic gel containing 20 wt% of surfactant mixture with R($C_{18:1}E_2CH_2COOH$) = 0.655 show two shear thinning domains that can both be fitted with

the Herschel-Bulkley model [52], giving two different yield stresses, one being slightly above 1 Pa and the other one being around 10 Pa. A possible explanation for this behavior is that first larger nematic domains start to move above the first yield stress, before microscopic domains or individual discs start to move relative to each other above the second yield stress. Macroscopic viscoelasticity and air bubble entrapment can be seen in **Video C.1**. Due to the shear thinning character, the gel-like mixture can be easily pipetted or mixed. After shaking of a nematic gel, bubbles are fixated instantaneously, suggesting that the viscoelastic structure is restored in less than 1 s. The macroscopic appearance of a nematic gel with $R(C_{18:1}E_2CH_2COOH) = 0.655$ between crossed polarizers at 25°C can be seen in the first image in **Fig. IV.2**. When going to the pseudo-lamellar phase above 34°C, the viscosity decreases, gel-like viscoelastic behavior is lost, and the optical appearance changes (see second image in **Fig. IV.2**). In the isotropic phase above 39°C (see third image in **Fig. IV.2**), a low viscosity is maintained. A full sequence of images taken between crossed polarizers between 10°C and 40°C is shown in **Fig. C.6**. Within the nematic domain, both birefringence and viscosity increase with increasing temperature.

A nematic phase is found in a range of $0.55 \leq R(C_{18:1}E_2CH_2COOH) \leq 0.73$, where for $R(C_{18:1}E_2CH_2COOH) \geq 0.688$ a small isotropic excess phase coexists with the nematic phase due to the presence of ester impurities, see **Fig. IV.2**. A reference mixing ratio of $R(C_{18:1}E_2CH_2COOH) = 0.655$, well inside the nematic domain, was chosen so that the mixture is monophasic and nematic already at low temperatures (≥ 5°C). In absence of impurities, a monophasic nematic region is observed for $0.60 \leq R(C_{18:1}E_2CH_2COOH) \leq 0.90$ and the reference mixing ratio was increased to $R(C_{18:1}E_2CH_2COOH) = 0.706$, due to the shift of the phase boundaries to higher values of $R(C_{18:1}E_2CH_2COOH)$, see **Fig. C.3**. Pseudo-binary phase diagrams of the surfactant mixtures in water at a constant $R(C_{18:1}E_2CH_2COOH) = 0.655$ with impurities and at a constant $R(C_{18:1}E_2CH_2COOH) = 0.706$ without impurities are given in **Figs. IV.3** and **C.7**, respectively. The principal phase behavior is the same in both cases. The nematic phase is stable in an exceptionally large concentration and temperature range, extending from 8 wt% surfactant up to around 55 wt% surfactant. Below 8 wt% (and above the critical micelle concentration), permanent birefringence and viscoelasticity are lost and the mixture is of low viscosity and flow birefringent. In presence of the hydrophobic ester impurities (**Fig. IV.3**), the flow birefringent phase is in equilibrium with a small volume of an isotropic phase, whereas in absence of the impurities (**Fig. C.7**), only the flow birefringent phase is

observed. Thus, the small isotropic phase found in presence of impurities is probably an excess phase, containing mainly hydrophobic ester impurities. Over the whole nematic domain, the same phase sequence as described above is found on increasing temperature: 1ϕ N → 1ϕ L_α → 1ϕ I → 2ϕ I/I with a small 2ϕ L_α/I domain during the transition between the lamellar to the isotropic phase. The lamellar phase is confirmed by polarizing microscopy, see first image in **Fig. IV.3**, where typical Maltese crosses are observed.

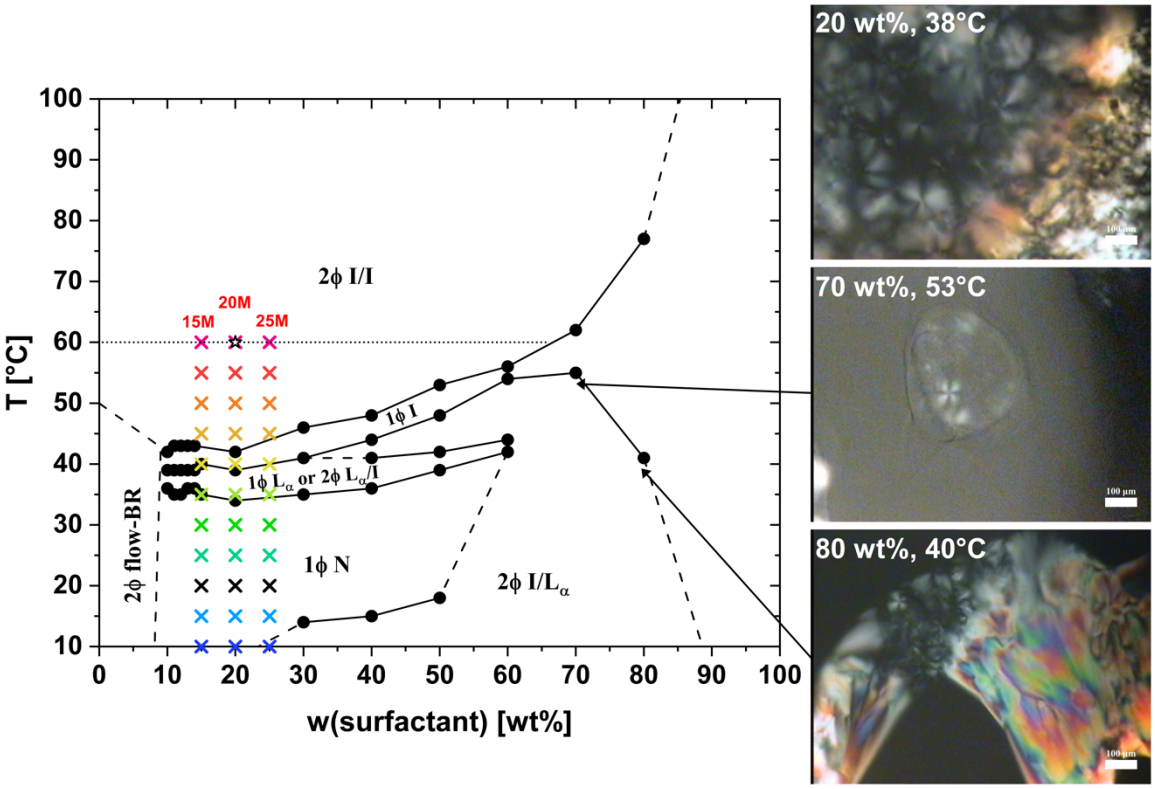

Fig. IV.3. Pseudo-binary phase diagram of a $C_8E_8CH_2COOH/C_{18:1}E_2CH_2COOH$ surfactant mixture with a fixed surfactant composition R($C_{18:1}E_2CH_2COOH$) = 0.655 in water as a function of the surfactant concentration. 1ϕ I: Monophasic isotropic liquid. 2ϕ I/I: Two isotropic liquids in equilibrium. In the notation 2ϕ I/I, the former "I" regards the top phase, whereas the latter "I" regards the bottom phase. L_α: Lyotropic lamellar phase. N: Lyotropic nematic phase. Flow-BR denotes flow birefringence. The colored crosses indicate samples measured with SAXS using a color code related to temperature increase. The empty star indicates a point, where a tie line (horizontal dotted line) was determined. The shown polarizing microscope images were taken between crossed polarizers at a 100x magnification and sample thicknesses of 0.48 mm (70 wt%) and 0.96 mm (20 wt% and 80 wt%). The scale bars indicate a length of 100 µm. A similar phase diagram with both surfactants purified by ion exchange is shown in **Fig. C.7**.

The phase sequence is modified above 30 wt% of surfactant, where the additional formation of a different lamellar phase prior to reaching the isotropic phase is observed at higher temperatures. The same lamellar L_α phase in equilibrium with a smaller isotropic phase is formed at room temperature on increasing the surfactant concentration beyond 55 wt%. The lamellar (smectic) nature of this phase is confirmed by polarizing microscopy, see second and third image in **Fig. IV.3**, where typical Maltese crosses can be seen before

its complete melting into an isotropic phase at higher temperatures. In contrast to the lamellar phase found at lower surfactant mixing ratios, see **Figs. IV.2** and **C.3**, which is less dense than the coexisting isotropic micellar phase, the lamellar phase following the nematic phase at high weight fractions is denser than the coexisting isotropic phase. Since the surfactant mixture is only slightly denser than water if most of the $C_8E_8CH_2COOH$ is mixed with $C_{18:1}E_2CH_2COOH$, this observation suggests that the lamellar phase contains a large fraction of both surfactants. Even further increasing the surfactant concentration, a single isotropic, hydrated surfactant phase is obtained above 85 wt% of surfactant. The eventual phase separation into two isotropic phases at higher temperatures, observed up to 85 wt% of surfactant, corresponds to the classical clouding phenomenon found for nonionic ethoxylated surfactants [53], where a surfactant-rich phase separates from a dilute aqueous phase. This is confirmed by the determination of a tie-line at 20 wt% of surfactant and 60°C, see dotted horizontal line in **Fig. IV.3**.

Note that similar phase diagrams can be obtained by mixing the surfactants' alcohol precursors C_8E_8 and $C_{18:1}E_2$ in similar mole ratios. Though this system was not investigated in detail, the similar macroscopic appearance and similar birefringence texture of the nematic phase suggest that the microstructures are also similar. For example at $R(C_{18:1}E_2) = 0.655$ and 20 wt% of surfactant ($pH \approx 6.3$), the same phase sequence, 1ϕ N (16–52°C) $\rightarrow$ 1ϕ L_α (53–55°C) $\rightarrow$ 1ϕ I (56–61°C) $\rightarrow$ 2ϕ I/I (≥62°C), is observed. This proves that the carboxylic acid group does not play an important role in the formation of the nematic phase.

IV.4.2. Dilution of Bicelles to an Isotropic Fluid

On dilution of the nematic phase to below 8 wt% of surfactant, the nematic phase transitions into an optically isotropic fluid that is easily identified between crossed polarizers to be a flow birefringent phase. The nematic order is lost upon dilution as soon as rotational freedom is gained by an increase of the average spacing between the bicelles beyond the average diameter of the bicelles present. At rest, the mixture appears isotropic because the bicelles can freely rotate, but when applying shear, the bicelles can be momentarily oriented in the direction of the applied shear, resulting in flow birefringence. The dilute flow birefringent state can be used to analyze the form factor of the microstructures by small-angle

scattering. Since the flow birefringent state is only monophasic in absence of ester impurities, samples containing 5 wt% of surfactant purified by ion exchange are used. Since the physical density of the surfactant mixture is close to 1 $g \cdot cm^{-3}$, the volume fraction equals the weight fraction in H_2O.

For investigation by SAXS versus temperature, sample 5M_a_0.706 was used, where "5M" stands for 5 vol% surfactant mixture in H_2O, "a" indicates that only the carboxylic acid surfactants after purification by ion exchange were used, and $R(C_{18:1}E_2CH_2COOH) = 0.706$. Scattering was recorded at various temperatures between 5°C and 60°C. The resulting scattering curves are shown in **Fig. IV.4**A. The respective points in the phase diagram are indicated in **Fig. C.7**. As can be seen in the phase diagram, the critical clouding temperature is reached at 62°C and sample 5M_a_0.706 is monophasic and flow birefringent over the whole temperature range covered by SAXS.

The scattering curves represent a form factor oscillation with a constant position of the maximum around $q = 1.1\ nm^{-1}$ over the whole temperature range. At 5°C, there is a sharp local minimum around $q = 0.30\ nm^{-1}$, and probably a sharp second local minimum around $q = 4\ nm^{-1}$ that is not resolved. Up to 20°C, the minima stay sharp, while the first one slightly shifts to approximately $q = 0.23\ nm^{-1}$. Further increasing the temperature leads to an increasingly less pronounced form factor oscillation with increasingly flat minima. At 40°C, only a weak first local minimum is observed at $q = 0.20\ nm^{-1}$ and a still sharp second local minimum is resolved for the first time around $q = 4\ nm^{-1}$. For the highest measured temperature 60°C, which is close to the critical solution temperature, the minima are still at a similar position but are much weaker compared to lower temperatures. The flattening of the minima suggests an increasing variation in aggregate thickness with increasing temperature. The oscillation in the form factor and the exact positions of the minima originate from the core-shell structure of the aggregates [54]. Changes of the structure factor can be excluded as the reason for the flattening of the minima, since the region sensitive to the structure factor is at lower q ($<0.1\ nm^{-1}$). This can be seen in **Fig. IV.4**B, where deviations from the form factor fits occur only at low q. The increasing variation in apparent aggregate thickness is a result of a decreasing intramicellar molecular segregation of the two surfactant species $C_8E_8CH_2COOH$ and $C_{18:1}E_2CH_2COOH$ with increasing temperature. In the case of bicelles, i.e., discs with a $C_{18:1}E_2CH_2COOH$-rich flat bilayer part and a $C_8E_8CH_2COOH$-rich curved rim, decreasing segregation leads to an increasing bicelle

radius because less relative volume of rims results in larger discs. However, despite being partially mixed into the flat bilayer part, $C_8E_8CH_2COOH$ with its much larger headgroup still is the main component of the rims. Thus, mixing of the two surfactants with big and small headgroups may be the origin of strong fluctuations, i.e., undulations, in the bilayer part.

The overall scattering contrast is quite low for X-rays, but several orders of magnitude higher for neutrons. Additionally, SAXS is highly sensitive to the internal core-shell structure, whereas SANS better probes the overall structure. Therefore, SANS of sample d-5M_a_0.706, a sample in D_2O equivalent to sample 5M_a_0.706 in H_2O, was recorded at 20°C. "d-5M" denotes that 5 vol% of surfactant mixture are dissolved in D_2O. The phase behavior in D_2O was found to be identical with a significant general decrease of the critical temperature and all other phase transition temperatures. In **Fig. C.8**, a partial phase diagram covering different mixing ratios of the surfactants at a constant surfactant content of 20 vol% (≈18.4 wt%) in D_2O, using surfactants purified by ion exchange, is compared to the same phase diagram at 20 vol% (≈20 wt%) of surfactant in H_2O. It is important to note that the difference is caused by a solvent effect and not by a pH effect, as the equivalent pH in D_2O is only slightly increased from around 2.2 to around 2.4. The reading of the electrode calibrated in H_2O, pH^*, was converted to the equivalent pH using ref. [55]. For sample d-5M_a_0.706, the critical temperature is only 50°C, compared to 62°C for 5M_a_0.706. The neutron scattering is shown in a Kratky-plot in **Fig. IV.4**B and is directly compared in log-scale to the X-ray scattering of the equivalent sample in H_2O in **Fig. IV.4**C. The SANS curve follows a q^{-2} slope in the mid-q range (0.06–1.5 nm^{-1}). In the absence of long-range interference effects, such as Ornstein-Zernike [56], this demonstrates the presence of large two-dimensional aggregates: Finite discs, large sheets, or ribbons. With the background knowledge of the phase diagrams of the two surfactants and their mixture in water, this is only compatible with the presence of disc-like bicelles. The Kratky-representation allows for a more detailed look and is used to compare the SANS data of d-5M_a_0.706 at 20°C to the data obtained for two additional samples with different surfactant mixing ratios, see **Fig. IV.4**B. The samples d-5M_a_0.677 and d-5M_a_0.750 contain 5 vol% of surfactant mixture in D_2O, where $R(C_{18:1}E_2CH_2COOH)$ = 0.677 and 0.750, respectively. Solid lines represent best fits to an oblate core-shell ellipsoid form factor using the SasView package (version 5.0.4) [57]. Details about fitting and obtained parameters are given in **Figs. IV.5** and **C.9** and **Table C.2**. To avoid producing excellent fits with

unphysical packings by freely varying too many parameters [58], a constrained fitting approach, as initiated by Hayter [59], is adopted. Constraints are imposed by SLDs and micellar radii that must be self-consistent with known molecular volumes and electronic densities, see **Appendix C.3**. In all three cases, the best fit suggests a polar hydrophobic core radius close to 2 nm, corresponding to the length of an oleyl $C_{18:1}$ chain [60,61]. It is worth noting that the fit is sensitive to the polar core radius, which is visualized by the simulation (dashed line) in **Fig. IV.5**A. The hydrophilic shell thickness is similar in all cases and varies from 2.3 nm along the equatorial half-axis to 0.9 nm along the polar half-axis, in good agreement with, respectively, the lengths of the -E_8CH_2COOH and -E_2CH_2COOH headgroups. The length of the EO-chain in the liquid state is intermediate between the fully extended length (zigzag conformation), which is about 3.3 nm for -E_8CH_2COOH and 1.1 nm for -E_2CH_2COOH, and the meander conformation, which is about 1.9 nm for -E_8CH_2COOH and 0.6 nm for -E_2CH_2COOH [62]. The only parameter that changes between the three surfactant mixing ratios is the equatorial core radius. For $R(C_{18:1}E_2CH_2COOH) = 0.677$, an equatorial core radius of 23.8 nm is found, which increases to 24.6 nm at $R(C_{18:1}E_2CH_2COOH) = 0.706$, and to 27.1 nm at $R(C_{18:1}E_2CH_2COOH) = 0.750$. Since the obtained micellar dimensions reflect the molecular dimensions of the two surfactants, these results are fully consistent with intramicellar segregation of $C_8E_8CH_2COOH$ and $C_{18:1}E_2CH_2COOH$, where $C_{18:1}E_2CH_2COOH$ favors the polar positions of low curvature and $C_8E_8CH_2COOH$ favors the equatorial positions of high curvature. The increase of the equatorial radius with increasing fraction of $C_{18:1}E_2CH_2COOH$ can also be explained by molecular segregation, because additional $C_{18:1}E_2CH_2COOH$ favors the flat inner part of the oblate ellipsoid, consequently increasing its size. Due to the large aspect ratio (≥ 12), these oblate ellipsoids resemble discs. However, the actual structure of the discs may also differ from an oblate ellipsoid. Instead of an oblate ellipsoid, where the hydrophobic core thickness, i.e., the polar radius, gradually decreases towards the equatorial half-axis, a flat cylindrical disc of constant thickness with an elliptical rim, i.e., a bicelle, would also be feasible. Both geometries are ideal cases and, in reality, the structure might be intermediate between the two ideal geometries. Further deviations from a perfectly uniform structure can be expected due to local variations in thickness of the flat disc part as a result of local molecular segregation. Local molecular segregation leads to the formation of regions of higher curvature, which can either be bumps protruding from the discs, or small holes perforating the disc. The latter can be rationalized as a rim of higher curvature, forming not only on the edge of the disc but also

inside the disc.

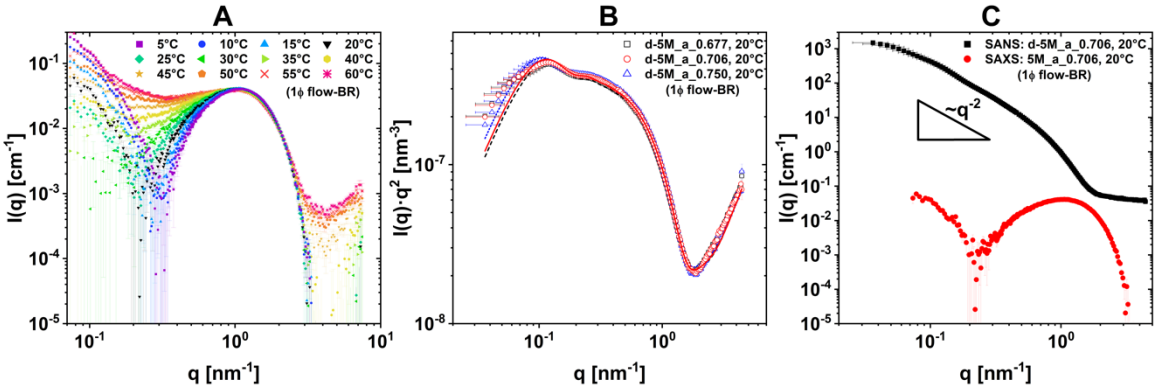

Fig. IV.4. (A) SAXS data of sample 5M_a_0.706, containing 5 vol% surfactant mixture purified by ion exchange with R($C_{18:1}E_2CH_2COOH$) = 0.706 in H_2O, at different temperatures between 5°C and 60°C. (B) SANS data of samples d-5M_a_0.677 (black), d-5M_a_0.706 (red), and d-5M_a_0.750 (blue) at 20°C represented in a Kratky plot. All three samples contain 5 vol% of surfactant mixture purified by ion exchange in D_2O. The composition of the surfactant mixture is varied so that R($C_{18:1}E_2CH_2COOH$) equals 0.677, 0.706, and 0.750, respectively. The lines represent best fits to an oblate core-shell ellipsoid form factor for d-5M_a_0.677 (dashed line), d-5M_a_0.706 (solid line), and d-5M_a_0.750 (dotted line). For details, see **Figs. IV.5** and **C.9** and **Table C.2**. (C) Comparison of SANS of sample d-5M_a_0.706 (black) and SAXS of sample 5M_a_0.706 (red).

Perforated lamellar (also named "mesh" phases) and disc-like structures have been reported in literature as intermediate states in phase sequences involving discs [63–67]. As suggested by SAXS, see above, these variations increase with increasing temperature, leading to variations in the layer thickness, i.e., undulations. It remains unknown, whether the formation of possible perforations is favored or disfavored with increasing temperature, though a decrease in segregation with increasing temperature should destabilize the internal rims and therefore the perforations. Despite the possible deviations from a perfect bicellar structure, the discs are formed due to the two opposing curvature contributions of the two surfactants, fully justifying the use of the term "bicelle" in this work.

As can be seen in **Fig. IV.5**B, the basic shape of the SANS form factor can also be described with an inhomogeneous lamella form factor, which, however, fails to fit all the features of the data, including the minimum in the Kratky-plot. The best fit, reproducing at least the correct position of the kink in scattering around q = 1.8 nm^{-1}, i.e., the minimum in the Kratky-plot, gives a bilayer half-thickness of 1.2 nm. Such a small half-thickness compared to the usual length of 2 nm for a $C_{18:1}$ chain is only possible if the alkyl chains are interdigitated. Interestingly, 1.2 nm is almost precisely the length of a C_8 chain [68], reducing chain packing constraints for mixing the two surfactants in a microstructure. A non-interdigitated half-thickness of 2 nm would shift the position of the minimum to lower q, as visualized

by the simulation given as a dashed line in **Fig. IV.5**B. In fact, alkyl chain interdigitation is also required in the proposed oblate ellipsoid, because only the polar half-axis matches the $C_{18:1}$ chain length of 2 nm, but the thickness of the core decreases towards the equator of the ellipsoid. Thus, the $C_{18:1}$ chains can be safely considered to be nearly fully interdigitated. A tendency towards interdigitation of the oleyl chain can also be inferred from the polymorphism of oleic acid crystallization close to the melting point. The crystalline α and γ phases comprise stacks of oleic acid bilayers with separated carboxylic acid and methyl group planes, whereas the β phase comprises a layered structure of fully interdigitated oleic acid molecules. In the latter, carboxylic acid groups and methyl groups are alternating in the same plane instead of forming two separate planes [69,70].

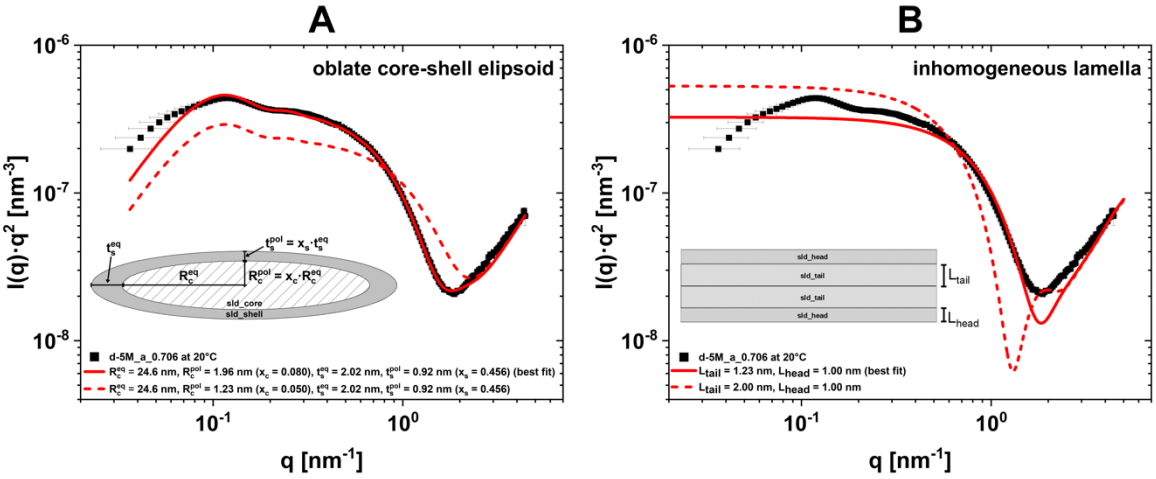

Fig. IV.5. (A) SANS data (black squares) of sample d-5M_a_0.706 at 20°C, containing 5.0 vol% (4.5 wt%) surfactant mixture with $R(C_{18:1}E_2CH_2COOH) = 0.706$ in D_2O, fitted to the form factor of an oblate core-shell ellipsoid. (B) SANS data (black squares) of sample d-5M_a_0.706 at 20°C, fitted to an inhomogeneous lamellar form factor.
Data and fits are shown in a Kratky plot. The solid red lines represent the best fits, while the dashed red lines visualize the influence of a change in R_c^{pol} or L_{tail}, respectively. If R_c^{pol} or L_{tail} equal 2.0 nm, they correspond to the length of a $C_{18:1}$ chain. The lamellar model clearly suggests interdigitation of the hydrocarbon chains with $L_{tail} = 1.23$ nm and the oblate ellipsoidal model suggests an equatorial core radius close to 2 nm. The latter case is also in agreement with hydrocarbon chain interdigitation, as the cross-sectional polar radius decreases towards the equator of the oblate ellipsoid. Fitting parameters are given in detail in **Table C.2**. The same fits are plotted in linear scale in **Fig. C.9**.

IV.4.3. Effect of Temperature on the Nematic Gel

After the identification of the form factor in the previous **Section IV.4.2.**, in this section the effect of temperature on the nematic gel is elucidated. A viscoelastic, gel-like nematic phase with permanent birefringence is formed above 8 wt% and up to about 55 wt% of

surfactant, see **Fig. IV.3**. SAXS data of sample 20M, recorded during a temperature scan from 5°C to 60°C, are shown in **Fig. IV.6**. Sample 20M contains 20 vol% (= 20 wt%) of surfactant mixture with the "reference" surfactant composition $R(C_{18:1}E_2CH_2COOH) = 0.655$ in H_2O and has a pH of 2.24. The measured points are indicated as colored crosses in the phase diagrams in **Figs. IV.2** and **IV.3**. From 5°C to 30°C, the mixture is a nematic phase, and a structure factor peak is seen in SAXS. The structure factor peak is barely visible at 5°C and becomes more pronounced with increasing temperature, suggesting that the ordering of the bicelles increases with increasing temperature. This finding is in agreement with the macroscopic observation of increasing birefringence and increasing viscoelasticity with increasing temperature and corresponds to an increase of the average bicelle diameter with temperature. When the disc diameter increases, the rotation of the bicelles is progressively more hindered as the diameter grows in relation to the average spacing of the bicelles. The increase in size on the other hand can be explained by a decrease in molecular segregation of the two surfactants. With increasing temperature, more $C_8E_8CH_2COOH$ molecules are incorporated into the flat part of the bicelle, which decreases the volume fraction of the rim and leads to a growth of the bicellar diameter. Up to 25°C, the peak position is rather constant at $q = 0.280$ nm^{-1}, corresponding to a repeat distance of $D^* = 22.4$ nm, which is smaller than the outer radius of around 26 nm obtained from the form factor in SANS at 20°C. Therefore, bicelles with an equatorial radius of 26 nm seem to be a reasonable assumption even at higher concentrations and in H_2O. However, it should be noted that the total surfactant concentration and the change of solvent from H_2O to D_2O can influence the size of the bicelles. In surfactant systems, the average size of aggregates tends to increase with increasing surfactant concentration [35]. On the other hand, a decrease in diameter of classical lipid bicelles with increasing lipid concentration was reported. The influence of concentration on bicellar size is, however, small compared to the effect of the lipid composition [9,13]. An increase of the average diameter beyond 26 nm with increasing surfactant concentration is to be expected in the presented system, as the nematic phase exhibits significant viscoelastic gel-like behavior (**Fig. C.5**), suggesting that the disc radius is considerably larger than the repeat distance of 22.4 nm. A further hint at disc growth with increasing surfactant concentration may be the transition of the nematic phase to a lamellar phase around 55 wt% of surfactant, see **Figs. IV.3** and **C.7**, which can be interpreted either as "infinite" growth of the discs to lamellae, or as a dense lamellar packing of large discs [71]. An effect of D_2O is to be expected, because D_2O shifts all phase transitions to lower temperatures, and therefore, at the same temperature, the

degree of molecular segregation should vary in D_2O compared to H_2O.

Before transitioning into a pseudo-lamellar phase at 35°C, the structure factor peak of the nematic phase becomes even sharper and its position shifts to slightly lower $q_1 = 0.257$ nm^{-1} ($D_1^* = 24.4$ nm) at 30°C. Even a weak second order peak around $q_2 = 2 \cdot q_1$, typical for lamellar ordering [72], appears, indicating an increase in long-range order. Before intramicellar segregation into a rim and a flat part disappears completely, discs grow much larger, i.e., smaller discs merge into larger ones, resulting in a quasi-lamellar organization of large discs. When reaching the lamellar phase at 35°C, the structure factor peak is shifted to lower $q = 0.221$ nm^{-1} ($D^* = 28.5$ nm), broadened, and no second order peak is visible. Hence, the formed lamellae are not "infinite" but finite undulating pseudo-lamellae with a low degree of long-range order. Undulations lead to a higher consumption of surfactant material for the same average thickness, resulting in a larger average spacing. A first evaluation to estimate the long-range order in smectics can be made by using the Scherrer relation [73]: The ratio $q_{max}/\Delta q$(FWHM), i.e., the ratio of the position of the structure factor peak maximum to the full width at half maximum (FWHM). This ratio gives the coherence length in number of layers before a defect occurs. The ratio is plotted as a function of temperature in **Fig. C.10**A. The higher the ratio is, the higher is the long-range order. From 15°C to 25°C, the ratio is about 4 in the nematic phase, meaning that on average four bicelles are stacked before a defect occurs, increases to 7 at 30°C, and eventually decreases to 2 when the pseudo-lamellar phase is reached at 35°C. This progression reflects the conclusions drawn above.

It is also worth noting that the bicelles in the nematic phase can be oriented by shear. While usually no anisotropic scattering was observed in SAXS, SANS measurements of corresponding samples in D_2O, see **Section IV.4.4.**, at 20°C showed significant anisotropy in scattering along the direction of applied shear during cuvette filling. For SANS, cuvettes with a thickness of 1 mm were used and cuvettes were not shaken after capillary filling, whereas for SAXS, capillaries with a thickness of 1.5 mm were used and capillaries were shaken after filling. A 2D SANS pattern of sample d-20M, containing 20 vol% of surfactant mixture with $R(C_{18:1}E_2CH_2COOH) = 0.655$, at 20°C is shown in **Fig. C.10**B. As can be inferred from the scattering pattern, the scattered intensity is higher along the direction of cuvette filling, the highest intensity being observed in an azimuthal angle sector of 30°. This implies that the bicelles are oriented along the direction of applied shear and are mostly

tilted by an angle $\varphi \leq 15°$ relative to the direction of shear, showing that the rotation of the bicelles is sufficiently hindered to retain the shear-induced orientation.

When further heating the sample to 40°C, the pseudo-lamellar phase transforms into an isotropic phase, before at 45°C phase separation occurs above the critical solution temperature. Within the isotropic phase, the structure factor peak flattens even more and is only weak and broad, which is a result of the loss of long-range order. The peak position is shifted to higher q = 0.322 nm^{-1} (D* = 19.5 nm). As can also be seen in SANS data of sample d-20M at 20°C (1ϕ N) and 33°C (1ϕ I), given in **Fig. C.11**, the form factor does not significantly change in the isotropic phase. As mentioned above, all phase boundaries are shifted to lower temperatures in D_2O, see **Fig. C.8**. The SANS data at 33°C can be fitted with a core-shell ellipsoid form factor and a simple Hayter-Penfold RMSA structure factor [59,74], see dashed line in **Fig. C.11** and **Table C.2**. The obtained parameters for the polar shell thickness (0.8 nm), the equatorial shell thickness (2.3 nm), and the polar core radius (2.2 nm) are similar to those obtained for the form factors of 5 vol% samples and are in agreement with the molecular dimensions, see **Section IV.4.2**. The only significant difference is the equatorial core radius, which is 11.8 nm in the isotropic phase at 20 vol% surfactant at 33°C, and therefore considerably smaller than a radius around 24 nm found in the flow-birefringent phase at 5 vol%. Note that the surfactant ratio is slightly different ($R(C_{18:1}E_2CH_2COOH)$ = 0.655 compared to 0.677) and the potential effect of the surfactant concentration on the disc size is unknown. For sample d-20M (D_2O), the peak of the isotropic phase at 33°C is located at q = 0.211 nm^{-1} (D* = 29.8 nm), while the peak position in the nematic phase at 20°C is located at slightly higher q = 0.259 nm^{-1} (D* = 24.2 nm). Since a repeat distance of 24.2 nm is only slightly smaller than the outer radius, including the shell, of the disc observed at 5 vol% (≈26 nm), while the sample is viscoelastic, the average disc radius must be larger than 26 nm. An outer radius, including the shell, close to 14 nm in the isotropic phase is considerably smaller than the average spacing of 29.8 nm. As a result, the discs can freely rotate, which is in agreement with the phase being isotropic. It is important to note that the peak position of the isotropic phase in SANS of sample d-20M (D_2O) is at slightly lower q than that of the nematic phase at 20°C (**Fig. C.11**), while in SAXS the peak of sample 20M (H_2O) is at slightly higher q in the isotropic phase than in the nematic phase (**Fig. IV.6**). At 33°C, sample d-20M is very close to the phase transition from a pseudo-lamellar phase to the isotropic phase (less than 1°C), while at 40°C, sample 20-M is at least 1°C further above the phase transition temperature. The same phase

transitions and the same changes in SAXS were also seen for samples 15-M and 25-M, containing, respectively, 15 vol% and 25 vol% of surfactant in H_2O, see **Fig. C.12**. In all cases, the peak position in the isotropic phase varies relative to the peak position of the nematic phase, and of the pseudo-lamellar phase. The peak in the isotropic phase shifts to higher q, the farther away the temperature is to the transition to a pseudo-lamellar phase. A shift to higher q corresponds to a decreasing repeat distance as a result of a decrease in average size of the micelles. The general progression of the repeat distance D*, i.e., of the structure factor peak position is identical at all three concentrations, 15, 20, and 25 vol%, and is depicted in **Fig. C.13** for SAXS samples in H_2O.

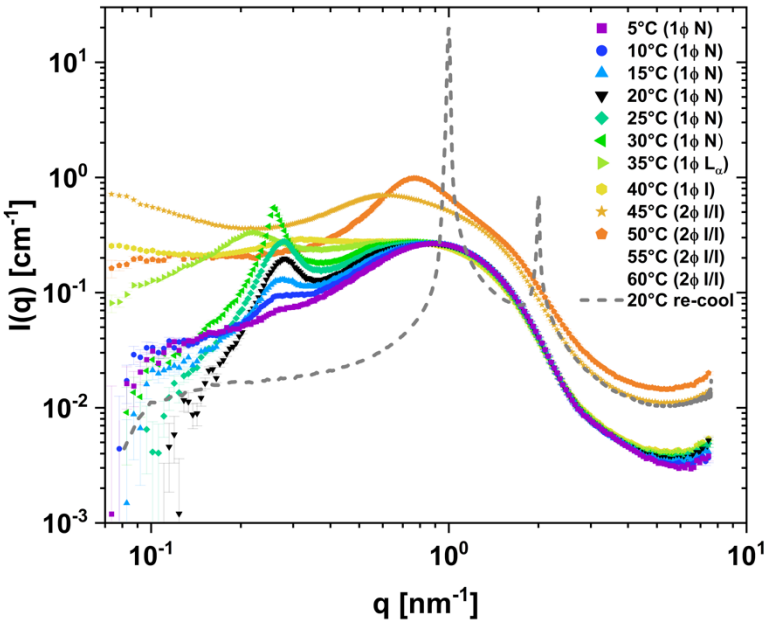

Fig. IV.6. SAXS data of sample 20M, containing 20 vol% surfactant mixture with $R(C_{18:1}E_2CH_2COOH) = 0.655$ in H_2O, at various temperatures, taken during heating from 5°C to 60°C and after re-cooling to 20°C (gray dashed line). The measured points are indicated in the phase diagrams in **Figs. IV.2** and **IV.3**. At 5°C to 30°C, the sample is a nematic phase (1ϕ N). At 35°C, a pseudo-lamellar phase (1ϕ L_α) is formed, which transitions into an isotropic phase (1ϕ I) at 40°C. At 45°C and above, phase separation into a dilute bottom phase and a surfactant-rich top phase (2ϕ I) occurs. Note that data for 55°C and 60°C are missing because the beam did not hit the surfactant-rich phase during phase separation. The same temperature scans are given in **Fig. C.12** for samples 15M and 25M, containing 15 vol% and 25 vol% of the surfactant mixture, respectively.

At 45°C and above, after reaching the critical clouding temperature, micelles attract each other and a surfactant-rich isotropic phase separates from an aqueous phase. With increasing temperature, the surfactant-rich phase becomes increasingly dense by expelling more and more water, which is indicated by a shift of the structure factor peak to higher q. After re-cooling the separated phases to 20°C (dashed line in **Fig. IV.6**), the surfactant-rich top phase, containing about 65 wt% of surfactant, forms a lamellar phase made of "infinite"

sheets, much larger than the observed spacing, which is sufficiently well ordered to produce sharp first- and second-order Bragg-peaks. A comparison of SAXS of the nematic phase at 20°C and of the metastable lamellar phase after re-cooling is also given in semi-logarithmic scale in **Fig. C.14**. If the two phases are re-mixed at 20°C by shaking, the nematic phase is formed. Note that the scattering curves of sample 20M are missing for 55°C and 60°C, because the beam did not hit the surfactant-rich phase. A similar series of measurements for a similar sample (20M*, see figure caption), recorded on another occasion, is given in **Fig. C.15**, showing the same phase behavior, including the two higher temperatures.

IV.4.4. Effect of Nematic Gel Dilution at Room Temperature

In **Fig. IV.7**, the effect of dilution on the small-angle scattering of the nematic gel is depicted. SAXS of three samples 15M, 20M, and 25M, containing 15 vol%, 20 vol%, and 25 vol% of surfactant mixture with R($C_{18:1}E_2CH_2COOH$) = 0.655 in H_2O, is shown in **Fig. IV.7**A. SANS of the corresponding samples in D_2O, d-15M, d-20M, and d-25M, containing the same volume fractions of surfactant, is shown in **Fig. IV.7**B. The repeat distance D*, extracted directly from the scattering curve, increases from 18.2 nm at 25 vol% surfactant to 22.4 nm at 20 vol% to 31.1 nm at 15 vol% in SAXS, and from 19.1 nm to 24.2 nm to 32.9 nm in SANS. As can be seen in a plot of D* versus the number density of surfactant molecules in **Fig. IV.7**C, the swelling of the structures upon dilution is close to one-dimensional swelling (slopes of -1.04 and -1.05). This is in agreement with two-dimensional structures, such as the proposed stacks of large discs or lamellar structures. Due the swelling relation and since scattering curves do not significantly change apart from the structure factor, the basic structural units remain unchanged on dilution. The swelling is expected to persist to a minimum of 8 wt% of surfactant, below which the mixture loses permanent birefringence. Thus, the maximum spacing is around 60 nm, the water layer thickness being in the same order of magnitude as the bicelle diameter. The expected minimum spacing before forming a lamellar phase around 55 wt% of surfactant is close to 9 nm. Macroscopically, dilution leads to a decrease in viscosity, viscoelasticity, and eventually in birefringence. This is a result of the average spacing significantly exceeding the bicellar radius, leading to free rotation of bicelles and a loss of preferential order. To the best of our knowledge, such a behavior is here found by combining two single chain surfactants for

the first time. This peculiar nematic phase is only present because alkyl chains are interdigitated to produce stiffer discs, as could be demonstrated by SANS/SAXS, and because intramicellar segregation of the two surfactants is efficient. These properties probably allow for a series of formulations of low active matter content, polymer-free, self-thickening hydrogels.

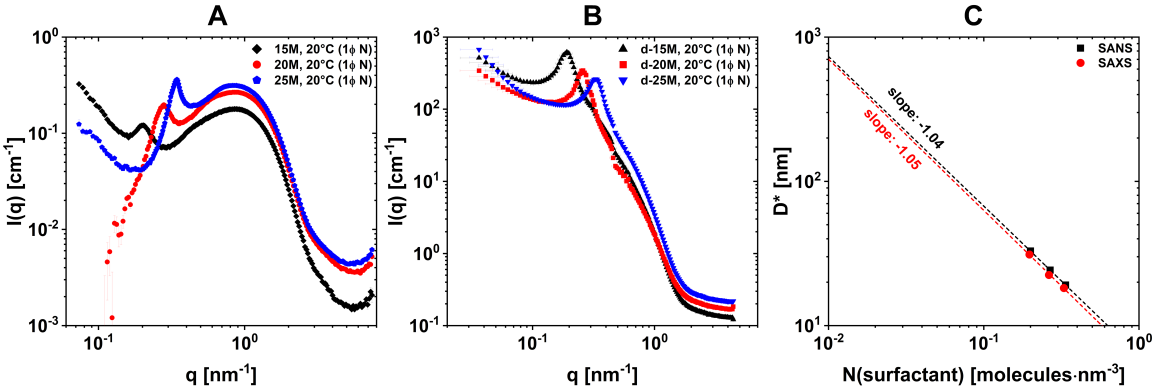

Fig. IV.7. (A) SAXS data of nematic gel samples 15M, 20M, and 25M at 20°C, containing, respectively, 15 vol%, 20 vol%, and 25 vol% surfactant mixture with R($C_{18:1}E_2CH_2COOH$) = 0.655 in H_2O. The same data can be seen in the temperature series given in **Figs. IV.6** and **C.12**. (B) SANS data of corresponding nematic gel samples d-15M, d-20M, and d-25M at 20°C, containing the same volume fractions of surfactant in D_2O with R($C_{18:1}E_2CH_2COOH$) = 0.655. (C) Repeat distance $D^* = 2\pi/q_{max}$, obtained from the peak maxima in (A) and (B), as a function of the number of surfactant molecules per unit volume N(surfactant). Dashed lines represent linear fits of the data obtained by SAXS (red points) and SANS (black squares) with slopes of -1.04 and -1.05, respectively.

As can be seen in **Fig. C.16**, the magnitude of the slope of the swelling law increases with increasing temperature, which is in agreement with increasing fluctuations in bilayer thickness due to increasing intramicellar mixing, as discussed in **Section IV.4.3**. The most negative slope of -1.33 is observed in the undulating pseudo-lamellar phase, indicating the "loss" of material due to undulations, according to the Helfrich model [75]. In the isotropic phase, the slope increases to -0.89 as a result of smaller discs no longer swelling in one dimension only, since the distance between neighboring discs in their equatorial plane can no longer be neglected. Note that the slope in the isotropic phase is also influenced by the change in micellar size, depending on the exact position in the isotropic domain of the phase diagram, see **Section IV.4.3**.

IV.4.5. Effect of NaOH/$Ca(OH)_2$ and NaCl/$CaCl_2$ on the Nematic Gel

In **Fig. IV.8**A, the pH and specific conductivity measured during titration of a sample containing 20 wt% surfactant (R($C_{18:1}E_2CH_2COOH$) = 0.655) with 1 M NaOH solution at 25°C are given. A phase diagram versus temperature and the degree of ionization at a constant surfactant content of 20 wt% with R($C_{18:1}E_2CH_2COOH$) = 0.655 is shown in **Fig. IV.8**B. As can be seen in both **Fig. IV.8**A and **IV.8**B, introducing electrostatics by deprotonation of the surfactants' carboxylic acid moieties destabilizes the nematic phase. Despite the total surfactant concentration decreasing to 13.3 wt% over the course of the titration in **Fig. IV.8**A, the phase transitions are almost identical compared to a constant surfactant concentration in **Fig. IV.8**B. At 25°C, deprotonating only 5% of the surfactants leads to the disappearance of the nematic phase. First, a biphasic region with an isotropic top phase and a lamellar bottom phase occurs, before two isotropic phases are formed above 8% of deprotonation. When reaching a deprotonation of around 70%, the mixture becomes a single isotropic phase of low viscosity. This phase sequence suggests that making the headgroups increasingly ionic results in a structural transition towards increasingly globular micelles, as electrostatic repulsion between adjacent headgroups leads to an increase in area per headgroup, and therefore to a decrease of the spontaneous packing parameter. Up to around 15% of deprotonation, the introduced electrostatic repulsion can be compensated by headgroup dehydration on increasing temperature. Around 15% of deprotonation a temperature of at least 90°C is required to form the nematic phase. Despite the high temperature, the mixtures appear to be strongly viscoelastic. Note that the obtained apparent acid fraction of 74.7 mol% of the surfactant mixture, calculated using the average molar masses of the surfactants, is lower than the apparent acid fraction of around 82 mol% found for $C_8E_8CH_2COOH$ (**Fig. C.1**). This is in agreement with the higher content of nonionic ester impurities expected for $C_{18:1}E_2CH_2COOH$, see **Section IV.3.1.** and **Appendix C.2**.

The pH and reduced molar conductivity of a mixture initially containing 20 wt% of surfactant with R($C_{18:1}E_2CH_2COOH$) = 0.655 measured at 27°C during titration with a 5 M NaCl solution is given in **Fig. IV.8**C. A phase diagram as a function of temperature and NaCl concentration, obtained by addition of NaCl to a mixture with an initial surfactant concentration of 20 wt% with R($C_{18:1}E_2CH_2COOH$) = 0.655, is given in **Fig. IV.8**D. NaCl has a salting-out effect on the surfactant mixture, decreasing the phase transition temperatures by

dehydrating the surfactant headgroups without altering the phase sequence. The nematic phase is stable up to at least 0.6 M NaCl at room temperature, and thus should be formed even in sea water [76]. The initial decrease of the pH by around 0.3 pH units is partially a result of H^+ release as Na^+ partially replaces H^+ as a counterion of the carboxylate groups. At higher NaCl concentrations, the pH electrode reading is influenced by the salt, resulting in up to 0.2 pH units lower readings [77]. The reduced molar conductivity, i.e., the ratio of the molar conductivity of the mixture and the molar conductivity of brine containing the same salt concentration, is below 0.1 in the viscous nematic gel, and sharply increases in the pseudo-lamellar phase until it reaches a value of around 0.4 in the isotropic phase. A relative water self-diffusion of around 0.5 [78] and a reduced conductivity of around 0.5 [79] were reported for 10 vol% to 20 vol% of a L_3 sponge phase formed by $C_{12}E_5$. The relative water self-diffusion typically found in a micellar L_1 phase of globular nonionic micelles of similar volume fraction is between 0.7 and 0.8 [80]. However, as pointed out by Photinos and Saupe [81], a slightly perforated lamellar structure and a layered structure of discs are not easily distinguishable in terms of conductivity. Thus, it can be expected that conductivities of an isotropic phase containing relatively large discs and an isotropic sponge phase are similar as well.

The important conclusions to be drawn from this investigation are the limiting salt concentrations for a possible viscosity control strategy using salt, as commonly applied for sodium dodecyl sulfate (SDS) or sodium dodecylbenzenesulfonate (SDBS), and that the nematic gel can be transformed into standard globular micelles by adding 0.5 NaOH per surfactant molecule.

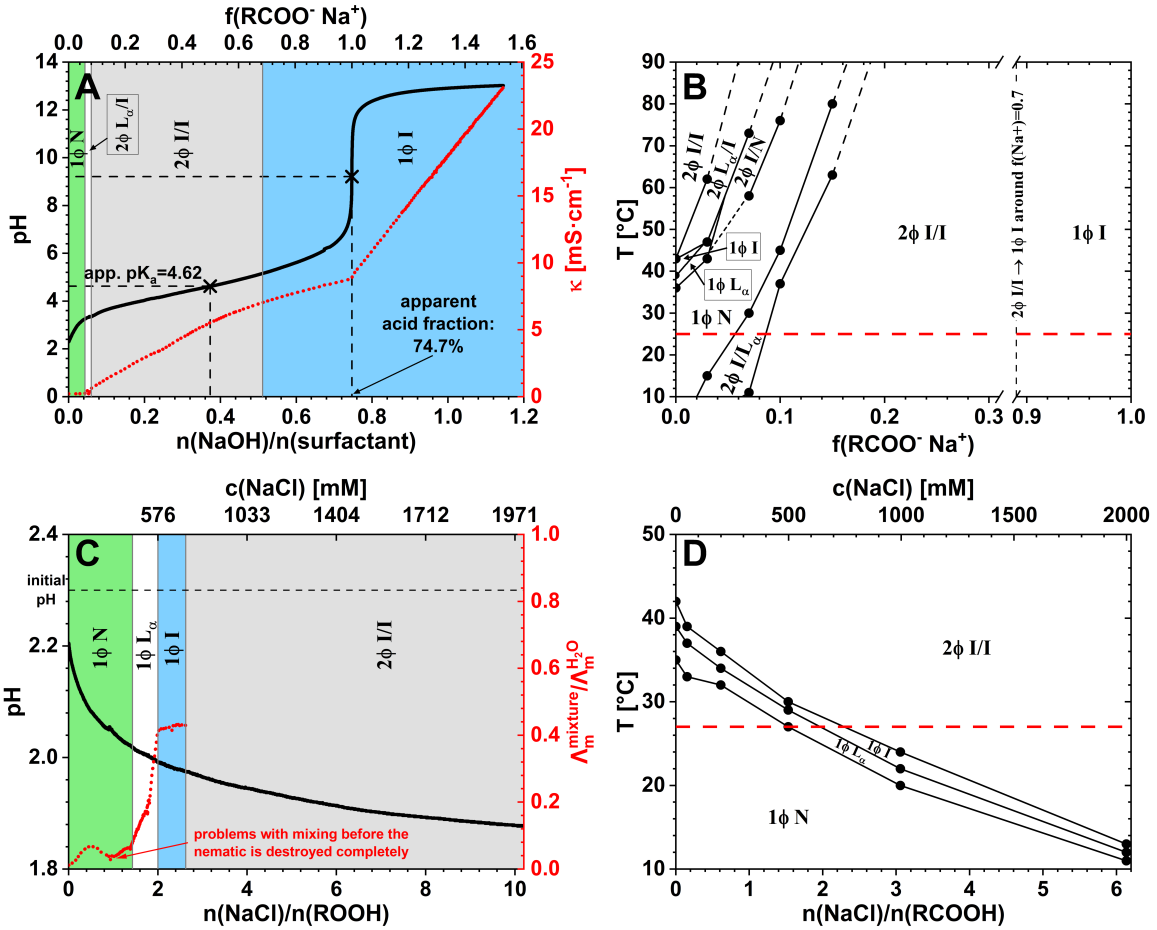

Fig. IV.8. (A) pH (solid black line) and specific conductivity (dotted red line) measured during titration of a 20 wt% nematic gel ($R(C_{18:1}E_2CH_2COOH)$ = 0.655) with 1 M NaOH solution at 25°C. Dilution due to titration leads to a progressive decrease of the surfactant content to 13.3 wt%. $f(RCOO^- Na^+)$ = $n(RCOO^- Na^+)/[n(ROOH)+n(RCOO^- Na^+)]$ is the fraction of ionic surfactants with sodium as counterion in the surfactant mixture and was corrected by the obtained apparent acid fraction of 74.7%. (B) Phase diagram at a constant surfactant concentration of 20 wt% with $R(C_{18:1}E_2CH_2COOH)$ = 0.655 as a function of the degree of ionization. $f(RCOO^- Na^+)$ was varied by addition of NaOH. The dashed red line is probed in the titration in (A), with the difference of a gradually decreasing surfactant concentration in (A). (C) pH (solid black line) and reduced molar conductivity (dotted red line) measured during titration of a 20 wt% nematic gel ($R(C_{18:1}E_2CH_2COOH)$ = 0.655) with 5 M NaCl solution at 27°C. Dilution due to titration leads to a progressive decrease of the surfactant content to 12.1 wt%. The linear bottom x-axis was calculated with an apparent acid fraction of 74.7%, while the non-linear top x-axis gives the molar concentration of NaCl at various points. (D) Phase diagram as a function of the NaCl concentration, recorded by adding NaCl to a mixture with an initial surfactant concentration of 20 wt% with $R(C_{18:1}E_2CH_2COOH)$ = 0.655. The bottom x-axis gives the mole ratio of NaCl and carboxylic acid surfactants, considering an apparent acid fraction of 74.7%, while the top x-axis gives the molar concentration of NaCl. The dashed red line is probed in the titration in (C), with the difference of a gradually decreasing surfactant concentration in (C). For the phase notations, see previous phase diagrams.

It should also be noted that NaOH and NaCl have opposing effects on curvature, the former increasing it by introducing electrostatic repulsion, and the latter decreasing it by dehydrating headgroups and screening electrostatics. Thus, the nematic phase can also be tweaked by combining the additions of NaOH and NaCl. As can be seen in **Fig. IV.8**A and **IV.8**B, a nematic phase cannot be obtained in the whole temperature range if 30% of the carboxylic

acid groups are deprotonated with NaOH, i.e., if f(RCOO$^-$ Na$^+$) = 0.3. When NaCl is added to a mixture with an initial surfactant content of 20 wt% with R($C_{18:1}E_2CH_2COOH$) = 0.655 and f(RCOO$^-$ Na$^+$) = 0.3, see **Fig. IV.9**, a nematic phase can be obtained. With increasing NaCl concentration, the phase transition temperatures decrease. In this case, a shift of the nematic phase to room temperature is not quite reached. A very high NaCl concentration of around 2.5 mol·L^{-1}, approaching saturation, is required, which corresponds to about 7 NaCl per carboxylate surfactant, to obtain a nematic phase at 26°C. For lower initial values of f(RCOO$^-$ Na$^+$), lower temperatures can be reached with less added NaCl. Another example is given in **Fig. C.17**, where NaCl is added at an initial surfactant content of 20 wt% with R($C_{18:1}E_2CH_2COOH$) = 0.655 and f(RCOO$^-$ Na$^+$) = 0.1. In this case, only around 0.3 mol·L^{-1} NaCl, i.e., around 1 equivalent of NaCl per carboxylate surfactant, are required to reduce the minimum temperature of the nematic phase from 45°C to room temperature.

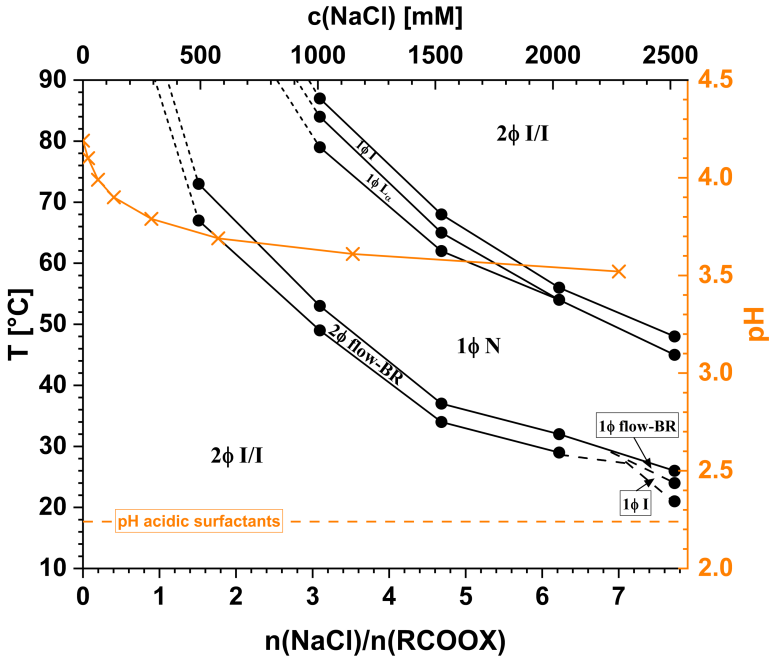

Fig. IV.9. Phase diagram recorded by addition of NaCl to a mixture with an initial surfactant concentration of 20 wt% with R($C_{18:1}E_2CH_2COOH$) = 0.655 and an initial f(RCOO$^-$ Na$^+$) = n(RCOO$^-$ Na$^+$)/[n(ROOH)+n(RCOO$^-$ Na$^+$)] = 0.3, corrected for an apparent acid fraction of 74.7 mol% (see **Fig. IV.8**A), as a function of the NaCl concentration. The bottom x-axis gives the mole ratio of NaCl and carboxylate surfactants (RCOOX = RCOOH + RCOO$^-$ Na$^+$), considering an apparent acid fraction of 74.7%, while the top x-axis gives the molar concentration of NaCl. The right y-axis gives the measured pH (orange crosses). The horizontal orange dashed line indicates the pH of a respective mixture of the two acidic surfactants, i.e., at f(RCOO$^-$ Na$^+$) = 0, in absence of salt. The phase notations can be inferred from previous phase diagrams.

In principle, the above-mentioned behavior is similar with calcium as divalent counterion, using $Ca(OH)_2$ and $CaCl_2$ instead of NaOH and NaCl. In analogy to **Fig. IV.8**B, a phase diagram recorded at a constant surfactant content of 20 wt% with

$R(C_{18:1}E_2CH_2COOH) = 0.655$ as a function of the fraction of ionic surfactant species with calcium as counterion is shown in **Fig. C.18**. As with sodium, the minimal temperature required for nematic phase formation increases with increasing ionization. However, within the covered temperature range, a nematic phase is found at high temperatures up to around 60% of deprotonated carboxylic acid groups, i.e., $f[RCOO^- (Ca^{2+})_{0.5}] \approx 0.6$, which is a much higher limiting fraction than $f(RCOO^- Na^+) \approx 0.15$ found for sodium. Another difference is that the isotropic monophasic domain found in the case of sodium above $f(RCOO^- Na^+) \approx 0.7$ is not observed for calcium, where two isotropic phases are in equilibrium up to full ionization. These findings can be explained with intramicellar bridging of adjacent surfactant anions by calcium, which opposes the effect of electrostatic repulsion between the surfactant anions. While the electrostatic repulsion leads to a reduction of the spontaneous packing parameter, in favor of globular aggregates, the ion bridging increases the packing parameter. As a result, the transition into globular micelles is faster with sodium than with calcium. In analogy to **Fig. IV.9**, when $CaCl_2$ is added to a mixture with an initial surfactant content of 20 wt% with $R(C_{18:1}E_2CH_2COOH) = 0.655$ and $f[RCOO^- (Ca^{2+})_{0.5}] = 0.3$, see **Fig. C.19**, the temperature required for the nematic phase to be formed can be reduced. Interpretation is further complicated by the fact that $CaCl_2$ is not only screening electrostatics but is also pH active, making the mixture more acidic, as can also be seen in **Fig. C.19**. However, a nematic phase is also not obtained at room temperature with this approach.

Without the addition of salt for electrostatic screening, the accessible metal counterion fraction to obtain a nematic phase at room temperature is limited to less than 10%. In an attempt to increase the metal fraction, mixtures of the surfactant alcohols $C_{18:1}E_2$ and C_8E_8 and the calcium salt $(C_{18:1}E_2CH_2COO^-)_2\ Ca^{2+}$ or $(C_8E_8CH_2COO^-)_2\ Ca^{2+}$ were tested. The observed phase behavior as a function of the fraction of ionic surfactant with calcium as counterion is similar to that shown in **Fig. C.18** for the mixtures of carboxylic acid surfactants. The fraction of ionic surfactant for which a nematic phase is obtained at room temperature cannot be increased by spacing the ionic species with purely nonionic species.

IV.5. Molecular Segregation Controlling Bicellar Size

As discussed in **Section IV.4.**, intramicellar molecular segregation is the reason for bicelle formation. $C_{18:1}E_2CH_2COOH$ favors a low curvature, adopting lamellar packing, while $C_8E_8CH_2COOH$ favors a high curvature, adopting spherical packing, see **Chapters II.** and **III**. The former tendency is expressed in the formation of a L_β phase in binary mixtures of $C_{18:1}E_2CH_2COOH$ and water, see **Fig. IV.1**A. On mixing of the two surfactants, $C_8E_8CH_2COOH$ forms curved rims, limiting the size of the $C_{18:1}E_2CH_2COOH$ bilayers. The resulting shape is a bicelle, as sketched in **Fig. IV.10**, in which the two surfactants are segregated. To quantify segregation, one can introduce separate surfactant mole fractions for the bilayer disc and the spheroidal rim.

$x_{disc}(C_8E_8CH_2COOH) = n_{disc}(C_8E_8CH_2COOH)/[n_{disc}(C_8E_8CH_2COOH) + n_{disc}(C_{18:1}E_2CH_2COOH)]$ is the mole fraction of $C_8E_8CH_2COOH$ in the flat disc part, while $x_{rim}(C_{18:1}E_2CH_2COOH)$ is the mole fraction of $C_{18:1}E_2CH_2COOH$ in the spheroidal rim. For complete intramicellar segregation, $x_{disc}(C_8E_8CH_2COOH) = 0$ and $x_{rim}(C_{18:1}E_2CH_2COOH) = 0$, while for full intramicellar mixing the mole fractions are given by $R(C_{18:1}E_2CH_2COOH)$, where $x_{disc}(C_8E_8CH_2COOH) = 1 - R(C_{18:1}E_2CH_2COOH)$ and $x_{rim}(C_{18:1}E_2CH_2COOH) = R(C_{18:1}E_2CH_2COOH)$. For a given composition of the surfactant mixture, the bicellar dimensions can be calculated as a function of $x_{disc}(C_8E_8CH_2COOH)$ and $x_{rim}(C_{18:1}E_2CH_2COOH)$, see **Appendix C.5**. For $R(C_{18:1}E_2CH_2COOH) = 0.706$, the calculated values of the bicellar hydrophobic core radius R_{core} are given as a function of $x_{disc}(C_8E_8CH_2COOH)$ and $x_{rim}(C_{18:1}E_2CH_2COOH)$ in **Fig. IV.10**. In the case of full intramicellar mixing, indicated as a green line in **Fig. IV.10**, the core radius diverges and cannot be predicted. The opposite case of complete intramicellar segregation would produce bicelles with $R_{core} = 10.3$ nm, significantly smaller than $R_{core} \approx 24$ nm obtained from SANS fits, see **Fig. IV.5**. Complete intramicellar segregation is only a hypothetical state, as a certain degree of mixing of the two surfactants is to be expected due to the entropy of mixing. For a core radius of 24 nm at 20°C, indicated as a blue plane in **Fig. IV.10**A, a variety of disc and rim compositions would be feasible, as can be derived by considering the intersection of the plane with the possible values for R_{core} (black surface in **Fig. IV.10**A). The possible combinations of the two compositions can be seen in the graph as a projection of the intersection to the $x_{disc}(C_8E_8CH_2COOH)$-$x_{rim}(C_{18:1}E_2CH_2COOH)$-plane (blue line). High values of $x_{rim}(C_{18:1}E_2CH_2COOH)$ are unrealistic, as that would imply a

preference of $C_{18:1}E_2CH_2COOH$ for high curvature. Thus, the most probable combinations of $x_{disc}(C_8E_8CH_2COOH)$ and $x_{rim}(C_{18:1}E_2CH_2COOH)$ are those with low values of $x_{rim}(C_{18:1}E_2CH_2COOH)$, which is indicated by a more intense color of the blue line. If the rims are made predominantly of $C_8E_8CH_2COOH$, i.e., if $x_{rim}(C_{18:1}E_2CH_2COOH) \approx 0$, the predicted disc composition for a core radius of 24 nm would be $x_{disc}(C_{18:1}E_2CH_2COOH) \approx 0.8 > R(C_{18:1}E_2CH_2COOH)$.

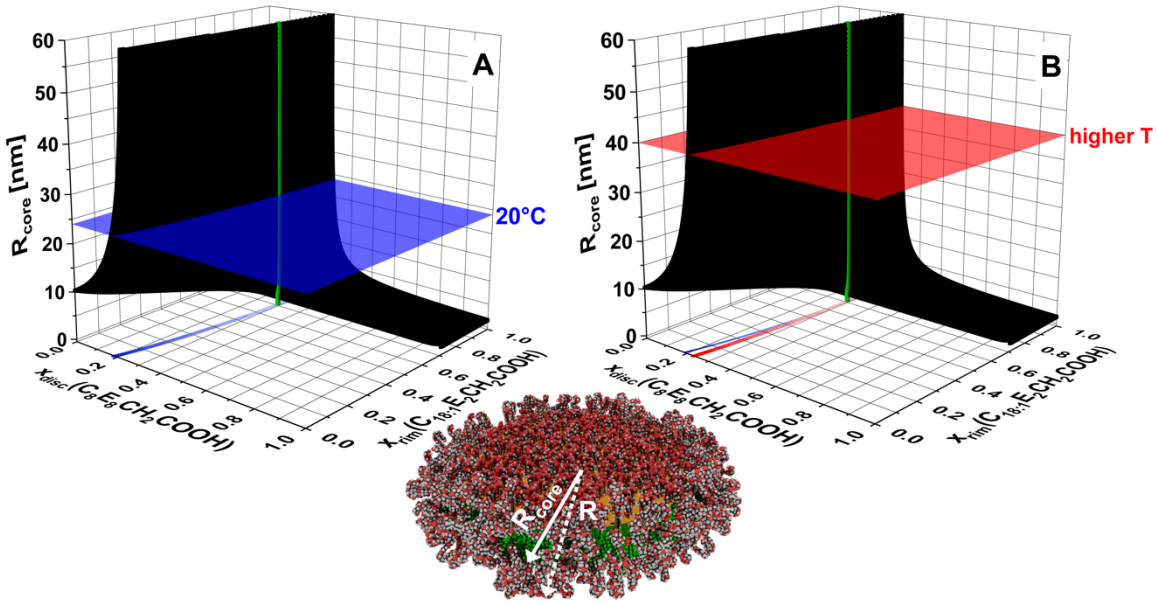

Fig. IV.10. Calculated hydrocarbon core radius R_{core} of a bicelle consisting of a flat cylindrical disc and a spheroidal rim as a function of the surfactant mole fractions $x_{disc}(C_8E_8CH_2COOH)$ and $x_{rim}(C_{18:1}E_2CH_2COOH)$. $x_{disc}(C_8E_8CH_2COOH) = 1 - x_{disc}(C_{18:1}E_2CH_2COOH)$ describes the mole fraction of $C_8E_8CH_2COOH$ in the flat disc, and $x_{rim}(C_{18:1}E_2CH_2COOH) = 1 - x_{rim}(C_8E_8CH_2COOH)$ describes the mole fraction of $C_{18:1}E_2CH_2COOH$ in the spheroidal rim. In the calculations, see **Appendix C.5.**, the solvent-free hydrophobic core is considered. Thus, both mole fractions only take into account the two surfactants. A total surfactant composition as in samples 5M_a_0.706 and d-5M_a_0.706 is assumed ($R(C_{18:1}E_2CH_2COOH) = 0.706$). The vertical green line indicates where $x_{disc}(C_8E_8CH_2COOH) = 1 - R(C_{18:1}E_2CH_2COOH)$ and $x_{rim}(C_{18:1}E_2CH_2COOH) = R(C_{18:1}E_2CH_2COOH) = 0.706$, i.e., where the two surfactants fully mix. At these points, the calculation of R_{core} diverges and R_{core} cannot be predicted. A scaled model of a bicelle with full intramicellar segregation is also shown.
(A) The blue plane indicates R_{core} at 20°C, as obtained from a fit of the SANS data of sample d-5M_a to a core-shell ellipsoid form factor, see **Fig. IV.5**A. The intersection of the blue plane and the black surface (R_{core}) is shown as a projection to the $x_{disc}(C_8E_8CH_2COOH)$-$x_{rim}(C_{18:1}E_2CH_2COOH)$-plane (blue line) and yields the possible combinations of $x_{disc}(C_8E_8CH_2COOH)$ and $x_{rim}(C_{18:1}E_2CH_2COOH)$ to obtain a bicelle with R_{core} = 24 nm. The darker color of the blue line at lower values of $x_{rim}(C_{18:1}E_2CH_2COOH)$ indicates that larger values for $x_{rim}(C_{18:1}E_2CH_2COOH)$ are unlikely. (B) The red plane indicates R_{core} at a higher temperature, where R_{core} was arbitrarily chosen to be 40 nm. In addition to the blue the $x_{disc}(C_8E_8CH_2COOH)$-$x_{rim}(C_{18:1}E_2CH_2COOH)$ projection from (A), the intersection of the red plane and the black surface (R_{core}) is shown as a projection to the the $x_{disc}(C_8E_8CH_2COOH)$-$x_{rim}(C_{18:1}E_2CH_2COOH)$-plane (red line) and yields the possible combinations of $x_{disc}(C_8E_8CH_2COOH)$ and $x_{rim}(C_{18:1}E_2CH_2COOH)$ to obtain a bicelle with R_{core} = 40 nm.

An increase in temperature facilitates intramicellar mixing, reducing the volume fraction of rims limiting the bicellar size, thus increasing its core radius. This is visualized in **Fig.**

IV.10B, where the red plane indicates an arbitrarily chosen core radius of 40 nm at elevated temperature. The possible rim and disc compositions for R_{core} = 40 nm are given as a red line in **Fig. IV.10**B, where the blue line for R_{core} = 24 nm is also shown for comparison. To increase R_{core}, $x_{disc}(C_8E_8CH_2COOH)$ has to increase, i.e., more $C_8E_8CH_2COOH$ has to be removed from the rim and mixed into the disc. For $x_{rim}(C_{18:1}E_2CH_2COOH) \approx 0$, $x_{disc}(C_{18:1}E_2CH_2COOH)$ would decrease from around 0.8 at 20°C to around 0.75. Note that the required change of $x_{disc}(C_8E_8CH_2COOH)$ to increase R_{core} would decrease with increasing $x_{rim}(C_{18:1}E_2CH_2COOH)$, as a state of full intramicellar mixing would be approached.

IV.6. Conclusion and Outlook

Synthetic (lipid-free), almost uncharged bicelles are formed by mixing $C_8E_8CH_2COOH$ and $C_{18:1}E_2CH_2COOH$ in appropriate ratios $R(C_{18:1}E_2CH_2COOH)$. The bicelles are formed due to intramicellar segregation of the two surfactants into a high curvature rim, favored by $C_8E_8CH_2COOH$, and a flat disc, favored by $C_{18:1}E_2CH_2COOH$. The bicellar size at a given surfactant composition is controlled by the degree of intramicellar segregation, which is influenced by temperature. For the compositions investigated by small-angle scattering at room temperature, typical bicelle diameters are around 50 nm. In sufficient number, above 8 wt% of surfactant, the bicelles form a discotic viscoelastic nematic phase with a maximum swelling of 60 nm. The nematic phase is surrounded by various lamellar phases. Above 55 wt% of surfactant, bicelles either fully merge into “infinite” lamellae or only partially merge to form a lamellar-like stack of large discs [71]. On decreasing $R(C_{18:1}E_2CH_2COOH)$ below the limit of the nematic phase, molecular segregation is intermicellar, resulting in phase separation of a $C_{18:1}E_2CH_2COOH$-rich lamellar phase and a $C_8E_8CH_2COOH$-rich isotropic phase. On increasing $R(C_{18:1}E_2CH_2COOH)$ or temperature, the nematic phase transitions into a pseudo-lamellar phase of large undulating discs, followed by an isotropic phase of smaller disc-like micelles, and eventually phase separation occurs on reaching the critical solution temperature. The latter is the classical clouding phenomenon observed for ethoxylated nonionic surfactants [53]. After phase separation above the critical temperature, there is a metastable state of a concentrated lamellar top phase and a dilute isotropic bottom phase after re-cooling, which returns to the nematic equilibrium state on mixing the two phases. This should allow for a formulation of a

concentrated lamellar phase as a precursor to the viscoelastic nematic phase, achievable by simple dilution.

Two possible applications of nematic phases of swollen bicelles were tested:

(a) Incorporation of droplets of apolar hydrocarbon oils by dispersion in the nematic phase. However, even when adding very apolar oils (high oil/water partition coefficient logP value) such as squalane, the nematic phase disappears. Phase maps obtained by successive addition of squalane to nematic gels containing 20 wt% surfactant with varying R($C_{18:1}E_2CH_2COOH$) are given in **Fig. C.20**. A small amount of squalane is solubilized in the nematic phase, before a transition to a lamellar phase, followed by a transition to a microemulsion, is induced. The solubilization performance tends to increase with increasing R($C_{18:1}E_2CH_2COOH$). At R($C_{18:1}E_2CH_2COOH$) = 0.615 and room temperature, the nematic phase and the microemulsion persist up to 2 wt% and 10 wt% squalane, respectively. At R($C_{18:1}E_2CH_2COOH$) = 0.688, the nematic phase persists up to 7 wt% squalane, while the microemulsion is stable up to 20 wt% squalane. When using the surfactants purified by ion exchange, the solubilized amount of oil in a nematic phase can be further increased, because higher values of R($C_{18:1}E_2CH_2COOH$) are accessible, see **Fig. C.3**. However, no dispersion of excess oil droplets in the nematic phase could be achieved with hydrocarbon oils. The only tested oil that is dispersible in the nematic phase for several weeks without destroying the gel-like nature of the mixture is a linear polydimethylsiloxane oil (Huber M20). Further details on tests aiming for the dispersion of different oils in the nematic phase are described in **Appendix C.6**.

(b) The threshold between infinite entrapment and floating of air bubbles introduced by simple shaking by hand was evaluated as described in **Section IV.3.9.** and **Appendix C.4**. Considering the dynamic range of radii of air bubbles that could be tracked between 190 µm and 1070 µm, a slope of -1 is evidenced in **Fig. IV.11**. This shows that the floating is driven by defects in the nematic phase. To the best of our knowledge, the nematic phase is the first fully open structure that shows a threshold without closed microcapsules, thus enabling capsule-free encapsulation. A nematic phase with similar properties but made of sheets consisting of small prolate micelles linked by carboxylic acid dimerization [82] instead of large discs, thus requiring fatty acids as linkers, was recently reported by Tchakalova *et al.* [44]. A short comment on this

nematic phase is given in **Appendix C.7**. Since the disc radius is typically 25 nm, air bubbles with a diameter of 1 mm have a threshold linked to the number of defects in 1 mm^3 of sample. The number of defects is also linked to the color bands seen in the polarized image of a nematic gel shown in **Fig. IV.2**A. By extrapolation of the data in **Fig. IV.11**, a threshold for floating of an object of 8 μm radius is expected to be of the order of 300 Pa. Transposing this to typical capsules in this size range and a conservative value of fragrance density of 0.8 $g \cdot cm^{-3}$, suggests that entrapment of such capsules would persist up to typical ultracentrifugation. These values show that the threshold in Pa is sufficient to encapsulate objects for a very long time, until shaking or temperature increase releases objects from the shear thinning nematic phase that is stable up to 34°C in the examined case.

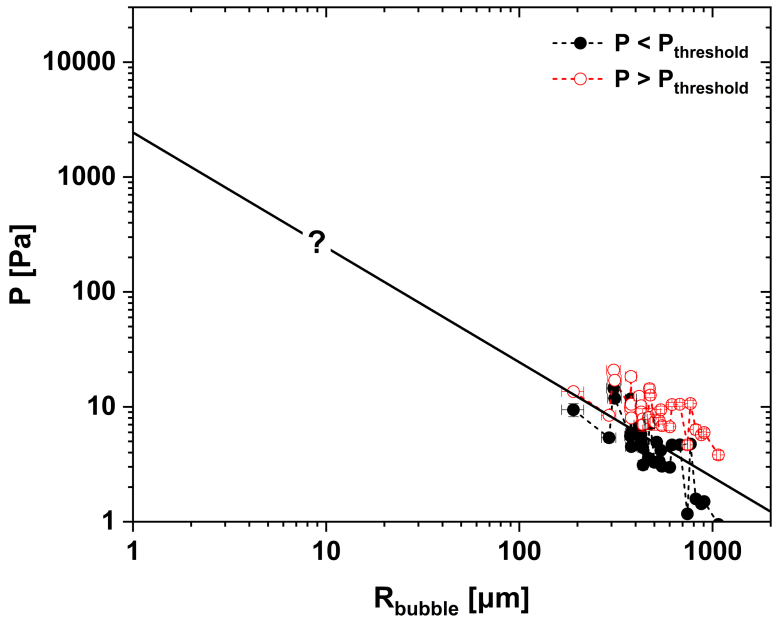

Fig. IV.11. Testing entrapment of air bubbles in a nematic gel containing 20 wt% surfactant mixture with $R(C_{18:1}E_2CH_2COOH) = 0.655$ at 25°C. It reveals the size dependence of the threshold between full entrapment and floating, determined by progressive soft centrifugation (**Appendix C.4.**).

The investigated nematic gels can be loaded with oils, but have a relatively low performance in solubilization of oils compared to other microemulsions [83,84]. They are good for encapsulating air bubbles as well as any micron sized objects other than liquids that influence phase behavior. Note that the low pH (≈2.2) of the presented nematic gels can be limiting for the selection of dispersible materials. However, the same nematic gel can be achieved without carboxylic acid groups, i.e., with $C_{18:1}E_2$ and C_8E_8, in which case the pH can be freely varied. On the other hand, the presence of the carboxylic acid groups allows for the implementation of at least a few percent of counterions, which could

potentially extend the field of application, e.g., to magnetic properties and catalysis. The nematic gel is easy to handle since the viscosity is low when shear is applied. At zero shear, on the other hand, viscosity is "infinite", and the relaxation time for structure restoration after applied shear is negligible (<1 s), see also **Video C.1**. This should make mixing with high pressure homogenizers very easy. In addition, any solute released from an entrapped capsule is free to move by diffusion in a totally continuous aqueous phase and does not have to cross multiple bilayers in an uncontrolled way.

A somewhat similar mixture of surfactants, comprising $C_{18:1}E_9CH_2COOH$, $C_8E_8CH_2COOH$, and $C_6E_3CH_2COOH$, is commercialized by Kao Chemicals under the name Akypo® TEC-AM VG. However, this mixture cannot form a bicellar nematic phase because the long-chain surfactant, $C_{18:1}E_9CH_2COOH$, is too hydrophilic and has a lower spontaneous packing parameter.

IV.7. References

[1] P. Denk, L. Matthews, S. Prévost, T. Zemb, W. Kunz, A dilute nematic gel produced by intramicellar segregation of two polyoxyethylene alkyl ether carboxylic acids, J Colloid Interface Sci 659 (2024) 833–848. https://doi.org/10.1016/j.jcis.2024.01.014.

[2] C.R. Sanders, J.P. Schwonek, Characterization of magnetically orientable bilayers in mixtures of dihexanoylphosphatidylcholine and dimyristoylphosphatidylcholine by solid-state NMR, Biochemistry 31 (1992) 8898–8905. https://doi.org/10.1021/bi00152a029.

[3] G. Raffard, S. Steinbruckner, A. Arnold, J.H. Davis, E.J. Dufourc, Temperature−Composition Diagram of Dimyristoylphosphatidylcholine−Dicaproylphosphatidylcholine "Bicelles" Self-Orienting in the Magnetic Field. A Solid State 2 H and 31 P NMR Study, Langmuir 16 (2000) 7655–7662. https://doi.org/10.1021/la000564g.

[4] M.-P. Nieh, C.J. Glinka, S. Krueger, R.S. Prosser, J. Katsaras, SANS Study of the Structural Phases of Magnetically Alignable Lanthanide-Doped Phospholipid Mixtures, Langmuir 17 (2001) 2629–2638. https://doi.org/10.1021/la001567w.

[5] J. Katsaras, T.A. Harroun, J. Pencer, M.-P. Nieh, "Bicellar" Lipid Mixtures as used in Biochemical and Biophysical Studies, Naturwissenschaften 92 (2005) 355–366. https://doi.org/10.1007/s00114-005-0641-1.

[6] J.N. Israelachvili, D.J. Mitchell, B.W. Ninham, Theory of self-assembly of hydrocarbon amphiphiles into micelles and bilayers, Journal of the Chemical Society, Faraday Transactions 2: Molecular and Chemical Physics 72 (1976) 1525–1568. https://doi.org/10.1039/F29767201525.

[7] R.R. Vold, R.S. Prosser, A.J. Deese, Isotropic solutions of phospholipid bicelles: A new membrane mimetic for high-resolution NMR studies of polypeptides, J Biomol NMR 9 (1997) 329–335. https://doi.org/10.1023/a:1018643312309.

[8] E.J. Dufourc, Bicelles and nanodiscs for biophysical chemistry, Biochimica et Biophysica Acta (BBA) - Biomembranes 1863 (2021) 183478. https://doi.org/10.1016/j.bbamem.2020.183478.

[9] L. Barbosa-Barros, G. Rodríguez, C. Barba, M. Cócera, L. Rubio, J. Estelrich, C. López-Iglesias, A. de la Maza, O. López, Bicelles: Lipid Nanostructured Platforms with Potential Dermal Applications, Small 8 (2012) 807–818. https://doi.org/10.1002/smll.201101545.

[10] K.S. Mineev, K.D. Nadezhdin, S.A. Goncharuk, A.S. Arseniev, Characterization of Small Isotropic Bicelles with Various Compositions, Langmuir 32 (2016) 6624–6637. https://doi.org/10.1021/acs.langmuir.6b00867.

[11] P.M. Macdonald, R. Soong, Diffusion NMR and bicelle morphology, Can J Chem 89 (2011) 1021–1035. https://doi.org/10.1139/v11-038.

[12] R. Soong, M.-P. Nieh, E. Nicholson, J. Katsaras, P.M. Macdonald, Bicellar Mixtures Containing Pluronic F68: Morphology and Lateral Diffusion from Combined SANS and PFG NMR Studies, Langmuir 26 (2010) 2630–2638. https://doi.org/10.1021/la902795h.

[13] L. van Dam, G. Karlsson, K. Edwards, Direct observation and characterization of DMPC/DHPC aggregates under conditions relevant for biological solution NMR, Biochimica et Biophysica Acta (BBA) - Biomembranes 1664 (2004) 241–256. https://doi.org/10.1016/j.bbamem.2004.06.005.

[14] C. Loudet-Courreges, F. Nallet, E.J. Dufourc, R. Oda, Unprecedented Observation of Days-Long Remnant Orientation of Phospholipid Bicelles: A Small-Angle X-ray Scattering and Theoretical Study, Langmuir 27 (2011) 9122–9130. https://doi.org/10.1021/la1050817.

[15] S.H. Park, S.J. Opella, Triton X-100 as the “Short-Chain Lipid” Improves the Magnetic Alignment and Stability of Membrane Proteins in Phosphatidylcholine Bilayers for Oriented-Sample Solid-State NMR Spectroscopy, J Am Chem Soc 132 (2010) 12552–12553. https://doi.org/10.1021/ja1055565.

[16] S. Taguchi, Y. Kimura, Y. Akiyama, Y. Tachibana, T. Yamamoto, Fluorescent Anisotropy Evaluation of Bicelle Formation Employing Carboxyl BODIPY and Pyrromethene, J Oleo Sci 71 (2022) ess21295. https://doi.org/10.5650/jos.ess21295.

[17] K.D. Lawson, T.J. Flautt, Magnetically oriented lyotropic luquid crystalline phases, J Am Chem Soc 89 (1967) 5489–5491. https://doi.org/10.1021/ja00997a054.

[18] L.Q. Amaral, C.A. Pimentel, M.R. Tavares, J.A. Vanin, Study of a magnetically oriented lyotropic mesophase, J Chem Phys 71 (1979) 2940–2945. https://doi.org/10.1063/1.438696.

[19] B.J. Forrest, F.Y. Fujiwara, L.W. Reeves, Order profiles of host decyl sulfate and decylammonium chains and guest carboxylic acids and carboxylates in aligned type II DM lyomesophases, J Phys Chem 84 (1980) 662–670. https://doi.org/10.1021/j100443a019.

[20] E.Y. Sheu, P. Lo Nostro, G. Capuzzi, P. Baglioni, Micelle and Microemulsion Properties of Cesium Di-Dodecyl-Dimethylsulfosuccinate, Cs-AOT, Langmuir 15 (1999) 6671–6676. https://doi.org/10.1021/la990059n.

[21] H.-D. Dörfler, C. Görgens, Mizellpolymorphie lyotroper Mesophasen, Tenside Surfactants Detergents 36 (1999) 314–321. https://doi.org/10.1515/tsd-1999-360509.

[22] C.F. Dietrich, P. Rudquist, K. Lorenz, F. Giesselmann, Chiral Structures from Achiral Micellar Lyotropic Liquid Crystals under Capillary Confinement, Langmuir 33 (2017) 5852–5862. https://doi.org/10.1021/acs.langmuir.7b01074.

[23] G. Colafemmina, R. Recchia, A.S. Ferrante, S. Amin, G. Palazzo, Lauric Acid-Induced Formation of a Lyotropic Nematic Phase of Disk-Shaped Micelles, J Phys Chem B 114 (2010) 7250–7260. https://doi.org/10.1021/jp1020774.

[24] L.J. Yu, A. Saupe, Observation of a Biaxial Nematic Phase in Potassium Laurate-1-Decanol-Water Mixtures, Phys Rev Lett 45 (1980) 1000–1003. https://doi.org/10.1103/PhysRevLett.45.1000.

[25] S.E. Anachkov, P.A. Kralchevsky, K.D. Danov, G.S. Georgieva, K.P. Ananthapadmanabhan, Disclike vs. cylindrical micelles: Generalized model of micelle growth and data interpretation, J Colloid Interface Sci 416 (2014) 258–273. https://doi.org/10.1016/j.jcis.2013.11.002.

[26] N. Boden, S.A. Corne, K.W. Jolley, Lyotropic mesomorphism of the cesium pentadecafluorooctanoate/water system: high-resolution phase diagram, J Phys Chem 91 (1987) 4092–4105. https://doi.org/10.1021/j100299a031.

[27] D. Danino, Cryo-TEM of soft molecular assemblies, Curr Opin Colloid Interface Sci 17 (2012) 316–329. https://doi.org/10.1016/j.cocis.2012.10.003.

[28] M. Dubois, V. Lizunov, A. Meister, T. Gulik-Krzywicki, J.M. Verbavatz, E. Perez, J. Zimmerberg, T. Zemb, Shape control through molecular segregation in giant surfactant aggregates, Proceedings of the National Academy of Sciences 101 (2004) 15082–15087. https://doi.org/10.1073/pnas.0400837101.

[29] M. Dubois, L. Belloni, Th. Zemb, B. Demé, Th. Gulik-Krzywicki, Formation of rigid nanodiscs: edge formation and molecular separation, in: Trends in Colloid and Interface Science XIV. Progress in Colloid and Polymer Science, Springer Berlin Heidelberg, Berlin, Heidelberg, 2000: pp. 238–242. https://doi.org/10.1007/3-540-46545-6_47.

[30] A. Meister, M. Dubois, L. Belloni, T. Zemb, Equation of State of Self-Assembled Disklike and Icosahedral Crystallites in the Dilute Range, Langmuir 19 (2003) 7259–7263. https://doi.org/10.1021/la0346806.

[31] M. Dubois, T. Gulik-Krzywicki, B. Demé, T. Zemb, Rigid organic nanodisks of controlled size: A catanionic formulation, Comptes Rendus de l'Académie Des Sciences - Series IIC - Chemistry 1 (1998) 567–575. https://doi.org/10.1016/S1387-1609(98)80012-1.

[32] B.J. Forrest, L.W. Reeves, New lyotropic liquid crystals composed of finite nonspherical micelles, Chem Rev 81 (1981) 1–14. https://doi.org/10.1021/cr00041a001.

[33] V. Hendrikx, J. Charvolin, M. Rawiso, L. Liebert, M.C. Holmes, Anisotropic aggregates of amphiphilic molecules in lyotropic nematic phases, J Phys Chem 87 (1983) 3991–3999. https://doi.org/10.1021/j100243a039.

[34] Y. Hendrikx, J. Charvolin, Structural relations between lyotropic phases in the vicinity of the nematic phases, Journal de Physique 42 (1981) 1427–1440. https://doi.org/10.1051/jphys:0198100420100142700.

[35] M.C. Holmes, D.J. Reynolds, N. Boden, Concentration-temperature dependence of the size and shape of the micelles in the cesium pentadecafluorooctanoate/water system, J Phys Chem 91 (1987) 5257–5262. https://doi.org/10.1021/j100304a025.

[36] D. Venkata Sai, G. Mirri, P.H.J. Kouwer, R. Sahoo, I. Musevic, S. Dhara, Unusual temperature dependence of elastic constants of an ambient-temperature discotic nematic liquid crystal, Soft Matter 12 (2016) 2960–2964. https://doi.org/10.1039/C6SM00065G.

[37] L.R.P. de Andrade Lima, A.D. Rey, Linear viscoelasticity of discotic mesophases, Chem Eng Sci 59 (2004) 3891–3905. https://doi.org/10.1016/j.ces.2004.06.016.

[38] A. Nikzad, A. Akbari, D. Grecov, Rheological properties of discotic nematic liquid crystals: graphene oxide dispersions study, Liq Cryst 48 (2021) 1685–1698. https://doi.org/10.1080/02678292.2021.1897890.

[39] C.L.S. Risi, A.M. Figueiredo Neto, P.R.G. Fernandes, A.R. Sampaio, E. Akpinar, M.B.L. Santos, Shear viscosity and rheology of ternary and quaternary lyotropic liquid crystals in discotic and calamitic nematic phases, Rheol Acta 54 (2015) 529–543. https://doi.org/10.1007/s00397-015-0850-2.

[40] R. Abdel-Rahem, M. Gradzielski, H. Hoffmann, A novel viscoelastic system from a cationic surfactant and a hydrophobic counterion, J Colloid Interface Sci 288 (2005) 570–582. https://doi.org/10.1016/j.jcis.2005.03.040.

[41] H. Hoffmann, C. Thunig, P. Schmiedel, U. Munkert, Surfactant Systems with Charged Multilamellar Vesicles and Their Rheological Properties, Langmuir 10 (1994) 3972–3981. https://doi.org/10.1021/la00023a013.

[42] M. Gradzielski, The rheology of vesicle and disk systems — Relations between macroscopic behaviour and microstructure, Curr Opin Colloid Interface Sci 16 (2011) 13–17. https://doi.org/10.1016/j.cocis.2010.07.005.

[43] P.-G. de Gennes, J. Prost, The Physics of Liquid Crystals, 2nd ed., Clarendon Press, Oxford, 1993.

[44] V. Tchakalova, C.L.P. Oliveira, A.M. Figueiredo Neto, New Lyotropic Complex Fluid Structured in Sheets of Ellipsoidal Micelles Solubilizing Fragrance Oils, ACS Omega (2023). https://doi.org/10.1021/acsomega.3c03500.

[45] F. Cattelaens, M. Jäger, T. Myrdek, Purification of carboxymethylated fatty alcohol derivates using ion exchange resins, J Surfactants Deterg 26 (2023) 111–117. https://doi.org/10.1002/jsde.12641.

[46] C.D. Dewhurst, Graphical reduction and analysis small-angle neutron scattering program: GRASP, J Appl Crystallogr 56 (2023) 1595–1609. https://doi.org/10.1107/S1600576723007379.

[47] R. Kjellander, E. Florin, Water structure and changes in thermal stability of the system poly(ethylene oxide)–water, Journal of the Chemical Society, Faraday

Transactions 1: Physical Chemistry in Condensed Phases 77 (1981) 2053. https://doi.org/10.1039/f19817702053.

[48] O. Tirosh, Y. Barenholz, J. Katzhendler, A. Priev, Hydration of polyethylene glycol-grafted liposomes, Biophys J 74 (1998) 1371–1379. https://doi.org/10.1016/S0006-3495(98)77849-X.

[49] C. Branca, S. Magazù, G. Maisano, F. Migliardo, P. Migliardo, G. Romeo, Hydration Study of PEG/Water Mixtures by Quasi Elastic Light Scattering, Acoustic and Rheological Measurements, J Phys Chem B 106 (2002) 10272–10276. https://doi.org/10.1021/jp014345v.

[50] P. Denk, A. El Maangar, J. Lal, D. Kleber, T. Zemb, W. Kunz, Phase diagrams and microstructures of aqueous short alkyl chain polyethylene glycol ether carboxylate and carboxylic acid triblock surfactant solutions, J Colloid Interface Sci 590 (2021) 375–386. https://doi.org/10.1016/j.jcis.2021.01.061.

[51] P. Denk, A. El Maangar, S. Prévost, W. Silva, R. Gschwind, T. Zemb, W. Kunz, Cloud point, auto-coacervation, and nematic ordering of micelles formed by ethylene oxide containing carboxylate surfactants, J Colloid Interface Sci 621 (2022) 470–488. https://doi.org/10.1016/j.jcis.2022.04.046.

[52] W.H. Herschel, R. Bulkley, Konsistenzmessungen von Gummi-Benzollösungen, Kolloid-Zeitschrift 39 (1926) 291–300. https://doi.org/10.1007/BF01432034.

[53] D.J. Mitchell, G.J.T. Tiddy, L. Waring, T. Bostock, M.P. McDonald, Phase behaviour of polyoxyethylene surfactants with water. Mesophase structures and partial miscibility (cloud points), Journal of the Chemical Society, Faraday Transactions 1: Physical Chemistry in Condensed Phases 79 (1983) 975. https://doi.org/10.1039/f19837900975.

[54] T. Zemb, P. Charpin, Micellar structure from comparison of X-ray and neutron small-angle scattering, Journal de Physique 46 (1985) 249–256. https://doi.org/10.1051/jphys:01985004602024900.

[55] A. Krężel, W. Bal, A formula for correlating pKa values determined in D2O and H2O, J Inorg Biochem 98 (2004) 161–166. https://doi.org/10.1016/j.jinorgbio.2003.10.001.

[56] L.S. Ornstein, F. Zernike, Accidental deviations of density and opalescence at the critical point of a single substance, Proc. Akad. Sci.(Amsterdam) XVII (1914) 793–806. http://www.dwc.knaw.nl/DL/publications/PU00012727.pdf.

[57] M. Doucet, J.H. Cho, G. Alina, Z. Attala, J. Bakker, W. Bouwman, P. Butler, K. Campbell, T. Cooper-Benun, C. Durniak, L. Forster, M. Gonzalez, R. Heenan, A. Jackson, S. King, P. Kienzle, J. Krzywon, R. Murphy, T. Nielsen, L. O'Driscoll, W. Potrzebowski, S. Prescott, R. Ferraz Leal, P. Rozyczko, T. Snow, A. Washington, SasView, (2021). https://doi.org/10.5281/zenodo.4467703.

[58] V. Degiorgio, M. Corti, Physics of Amphiphiles: Micelles, Vesicles and Microemulsions: Proceedings of the International School of Physics, Enrico Fermi, Course XC, Elsevier Science Pub. Co., Amsterdam, New York, 1985.

[59] J. Hansen, J.B. Hayter, A rescaled MSA structure factor for dilute charged colloidal dispersions, Mol Phys 46 (1982) 651–656. https://doi.org/10.1080/00268978200101471.

[60] L. Chiappisi, S. David Leach, M. Gradzielski, Precipitating polyelectrolyte–surfactant systems by admixing a nonionic surfactant – a case of cononsurfactancy, Soft Matter 13 (2017) 4988–4996. https://doi.org/10.1039/C7SM00747G.

[61] M. Schwarze, L. Chiappisi, S. Prévost, M. Gradzielski, Oleylethoxycarboxylate – An efficient surfactant for copper extraction and surfactant recycling via micellar enhanced ultrafiltration, J Colloid Interface Sci 421 (2014) 184–190. https://doi.org/10.1016/j.jcis.2014.01.037.

[62] P. Alexandridis, U. Olsson, B. Lindman, Self-Assembly of Amphiphilic Block Copolymers, Macromolecules 28 (1995) 7700–7710.

[63] L.M. Bergström, S. Skoglund, K. Edwards, J. Eriksson, I. Grillo, Spontaneous Transformations between Surfactant Bilayers of Different Topologies Observed in Mixtures of Sodium Octyl Sulfate and Hexadecyltrimethylammonium Bromide, Langmuir 30 (2014) 3928–3938. https://doi.org/10.1021/la4042259.

[64] K. Emelyanova, I. Gotlib, A. Shishkina, M. Voznesenskiy, A. Victorov, Molecular Thermodynamic Modeling of Self-Assembly into Branches and Spatial Networks in Solution, J Chem Eng Data 61 (2016) 4013–4022. https://doi.org/10.1021/acs.jced.6b00531.

[65] K.A. Emelyanova, A.I. Victorov, Driving Force for Spontaneous Perforation of Bilayers Formed by Ionic Amphiphiles in Aqueous Salt, Langmuir 33 (2017) 13438–13443. https://doi.org/10.1021/acs.langmuir.7b02885.

[66] K.A. Emelyanova, A.I. Victorov, Molecular thermodynamic modeling of a bilayer perforation in mixed catanionic surfactant systems, Physical Chemistry Chemical Physics 20 (2018) 27924–27929. https://doi.org/10.1039/C8CP04593C.

[67] M. Almgren, Stomatosomes: perforated bilayer structures, Soft Matter 6 (2010) 1383. https://doi.org/10.1039/b922707e.

[68] C. Tanford, Micelle shape and size, Journal of Physical Chemistry 76 (1972) 3020–3024. https://doi.org/10.1021/j100665a018.

[69] S. Abrahamsson, I. Ryderstedt-Nahringbauer, The crystal structure of the low-melting form of oleic acid, Acta Crystallogr 15 (1962) 1261–1268. https://doi.org/10.1107/S0365110X62003321.

[70] F. Kaneko, K. Yamazaki, K. Kitagawa, T. Kikyo, M. Kobayashi, Y. Kitagawa, Y. Matsuura, K. Sato, M. Suzuki, Structure and Crystallization Behavior of the β Phase of Oleic Acid, J Phys Chem B 101 (1997) 1803–1809. https://doi.org/10.1021/jp963400a.

[71] M. Dubois, D. Carrière, R. Iyer, M.A. Arunagirinathan, J. Bellare, J.M. Verbavatz, T. Zemb, From dispersed nanodiscs to thin films of layered organic material via reversible swelling, Colloids Surf A Physicochem Eng Asp 319 (2008) 90–97. https://doi.org/10.1016/j.colsurfa.2007.05.051.

[72] O. Glatter, Scattering Methods and their Application in Colloid and Interface Science, 1st ed., Elsevier, Amsterdam, 2018. https://doi.org/10.1016/C2016-0-04640-5.

[73] P. Scherrer, Bestimmung der Größe und der inneren Struktur von Kolloidteilchen mittels Röntgenstrahlen, Nachrichten von Der Gesellschaft Der Wissenschaften Zu Göttingen, Mathematisch-Physikalische Klasse 1918 (1918) 98–100. http://eudml.org/doc/59018.

[74] J.B. Hayter, J. Penfold, An analytic structure factor for macroion solutions, Mol Phys 42 (1981) 109–118. https://doi.org/10.1080/00268978100100091.

[75] F. Campelo, C. Arnarez, S.J. Marrink, M.M. Kozlov, Helfrich model of membrane bending: From Gibbs theory of liquid interfaces to membranes as thick anisotropic elastic layers, Adv Colloid Interface Sci 208 (2014) 25–33. https://doi.org/10.1016/j.cis.2014.01.018.

[76] F.J. Millero, R. Feistel, D.G. Wright, T.J. McDougall, The composition of Standard Seawater and the definition of the Reference-Composition Salinity Scale, Deep Sea Research Part I: Oceanographic Research Papers 55 (2008) 50–72. https://doi.org/10.1016/j.dsr.2007.10.001.

[77] G. Hinds, P. Cooling, A. Wain, S. Zhou, A. Turnbull, Technical Note: Measurement of pH in Concentrated Brines, CORROSION 65 (2009) 635–638. https://doi.org/10.5006/1.3319089.

[78] B. Balinov, U. Olsson, O. Soederman, Structural similarities between the L3 and bicontinuous cubic phases in the AOT-brine system, J Phys Chem 95 (1991) 5931–5936. https://doi.org/10.1021/j100168a041.

[79] R. Strey, R. Schomäcker, D. Roux, F. Nallet, U. Olsson, Dilute lamellar and L3 phases in the binary water–C12E5 system, J. Chem. Soc., Faraday Trans. 86 (1990) 2253–2261. https://doi.org/10.1039/FT9908602253.

[80] P.G. Nilsson, B. Lindman, Water self-diffusion in nonionic surfactant solutions. Hydration and obstruction effects, J Phys Chem 87 (1983) 4756–4761. https://doi.org/10.1021/j100246a041.

[81] P.J. Photinos, A. Saupe, Calculations on the electric conductivity of a lyotropic mesophase with perforated lamellae, J Chem Phys 81 (1984) 563–566. https://doi.org/10.1063/1.447338.

[82] J. Chen, C.L. Brooks, H.A. Scheraga, Revisiting the carboxylic acid dimers in aqueous solution: Interplay of hydrogen bonding, hydrophobic interactions and entropy, Journal of Physical Chemistry B 112 (2008) 242–249. https://doi.org/10.1021/jp074355h.

[83] M.L. Klossek, D. Touraud, W. Kunz, Microemulsions with renewable feedstock oils, Green Chemistry 14 (2012) 2017. https://doi.org/10.1039/c2gc35035a.

[84] K. Ozawa, U. Olsson, H. Kunieda, Oil-Induced Structural Change in Nonionic Microemulsions, J Dispers Sci Technol 22 (2001) 119–124. https://doi.org/10.1081/DIS-100102687.

Chapter V.

The Effect of Common Additives on Nematic Gels Formed by Mixtures of Polyoxyethylene Alkyl Ether Carboxylic Acids

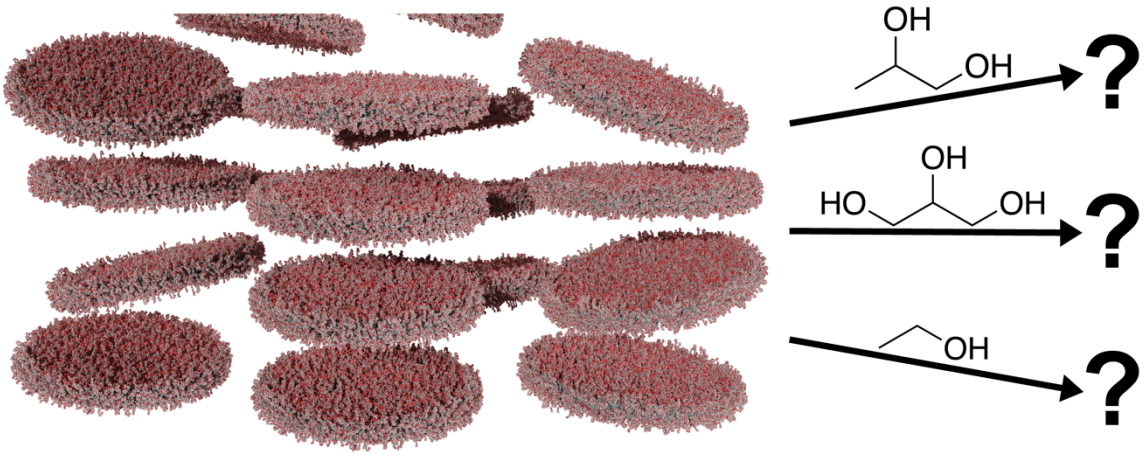

What happens to the nematic gel described in the previous chapter when three of the most common additives in health- and home-care formulation, namely propylene glycol (top), glycerol (center), and ethanol (bottom), are added?

Note:
Most of this chapter is already published (P. Denk, L. Matthews, T. Zemb, W. Kunz, Formulating additives in thermoresponsive surfactant-based nematic liquid crystals, Tenside Surfactants Detergents 61 (2024) 228–239 [1]. The author of this thesis is the first author of the publication, wrote the original draft, evaluated the data, and conducted most of the experiments. The co-authors Prof. Dr. Thomas Zemb and Prof. Dr. Werner Kunz assisted by reviewing the draft and giving scientific input throughout the work. The co-author Dr. Lauren Matthews performed the small-angle scattering measurements and the treatment of raw scattering data. The interns Julia Grasenhiller and Markus Maier were involved in performing preliminary experiments on this subject, but did not contribute to the data presented in this chapter.

V.1. Abstract

It was shown in **Chapter IV.** that bicelles can be formed by mixing in given mole fractions two ethoxylated alkyl ether carboxylic acid surfactants of very different hydrophilic-lipophilic balance (HLB) in water. Since the viscoelastic nematic gel has potential application in encapsulation, for example of fragrances or microcapsules, its stability towards additives often used in formulation is of interest.

In the present chapter, the effect of adding three of the most used additives in formulation in health- and home care, propylene glycol, glycerol, and ethanol, is determined. The effects of the additives are determined and compared in a concentrated isotropic phase above the lower-critical solution temperature (LCST), a pseudo-lamellar phase, and a discotic nematic phase. The two latter are birefringent, and the nematic phase is viscoelastic. Propylene glycol acts as a co-solvent, improving the temperature stability of the nematic phase up to 20 wt% propylene glycol. Further addition of propylene glycol reduces the phase transition temperatures, inducing microstructural changes due to headgroup dehydration and preferential solubilization of the hydrophilic short chain surfactant. Glycerol acts as an anti-solvent, progressively decreasing phase transition temperatures by dehydration of headgroups. Ethanol is a good co-solvent for the surfactant-mixture. Adding up to 5 wt% ethanol increases the temperature stability of the nematic phase. Higher concentrations of ethanol lead to a single isotropic phase with increasingly molecular dissolution of the surfactants. The effect of the considered additives on molecular packing is followed by high resolution X-Ray scattering.

V.2. Introduction

Lyotropic nematic phases can be divided into two major subclasses, the calamitic and the discotic nematic phases. While calamitic nematic phases are made of finite elongated prolate ellipsoidal or rod-like micelles with a preferential orientation, discotic nematic phases consist of disc-like micelles. A well-known class of disc-like micelles are bilayer micelles, abbreviated as bicelles, classically formed by mixing a long-chain lipid, e.g., dimyristoylphosphatidylcholine (DMPC), with a short-chain lipid, e.g., dihexanoylphosphatidylcholine (DHCP) [2–6], in water. The basic mechanism governing bicelle formation is intramicellar molecular segregation of the two lipid species, which can be easily rationalized using the geometrical chain packing model introduced by Israelachvili *et al.* [7]. The hydrophobic long-chain lipid has a spontaneous packing parameter $p_0 \approx 1$, thus favoring low curvature in a bilayer packing, whereas the hydrophilic short-chain lipid has a $p_0 \approx 1/3$, thus favoring high curvature in a spherical packing. The definition of the packing parameter can be inferred from **Appendix A.3**. The resulting structure is a disc-like bicelle, consisting of a flat bilayer part and a spheroidal rim. Bicelles are typically formed if the lipid mixture contains 65–85% of the long-chain lipid [2–4]. The diameter of a bicelle, typically in the range of 15-50 nm, mainly depends on the mixing ratio of the two lipids and on the degree of intramicellar segregation [8–11], both influencing the volume fraction of rims available to limit bilayer growth. Instead of lipids, various other surfactants can be used to form disc-like micelles, following the same principle. As in **Chapter IV.**, all disc-like micelles formed by intramicellar segregation are referred to as bicelles in this chapter. Examples are mixtures of lipids and synthetic surfactants [12,13], catanionics [9–11,14], mixtures of two ionic or nonionic surfactants or mixtures of ionic surfactants with a co-surfactant and a salt [15–22], or in rare cases even binary mixtures of a surfactant and water [23–25]. It should be noted that classical lipid mixtures typically form disc-like bicelles only below the chain melting temperature of the long-chain surfactant [3,5]. While disc-like bicelles can form nematic phases in absence of a magnetic field if the number density of bicelles is sufficiently high [14,18–21,24,26,27], mixtures containing bicelles are often isotropic and a nematic order is only induced by applying a strong external magnetic field [2,4,5,28,29]. Even in the former case, nematic phases are usually of low viscosity and not or only slightly viscoelastic [30–33].

In **Chapter IV.**, a new discotic lyotropic nematic phase made of bicelles formed by mixing

octaoxyethylene octyl ether carboxylic acid ($C_8E_8CH_2COOH$) and dioxyethylene oleyl ether carboxylic acid ($C_{18:1}E_2CH_2COOH$) in water is described. At rest, the bicellar nematic phase exhibits viscoelastic gel-like behavior with peculiar entrapment properties. Large air bubbles or other objects that do not alter the surfactant aggregation can be entrapped for a long time, as the buoyancy or gravitational force must exceed a certain threshold to induce floating, creaming, or sedimentation. At the same time, its strong shear-thinning behavior and almost instantaneous relaxation after destroying the structure by shear make the nematic gel easy to handle and easy to mix with other components.

In this chapter, the effects of three common alcohol additives, propylene glycol (PG), glycerol (G), and ethanol (EtOH), on the phase behavior of this system are explored. Phase diagrams are constructed as a function of temperature and additive concentration and the effects of the additive concentration and the temperature on the microstructures are examined via high-resolution small-angle X-ray scattering.

V.3. Experimental Section

V.3.1. Materials

The liquid surfactants octaoxyethylene octyl ether carboxylic acid, $C_8E_8CH_2COOH$ ($M = 541\ g \cdot mol^{-1}$, HLB = 16), commercialized under the name Akypo® LF2 (90.0 wt% active matter, 0.9 wt% NaCl, 9.1 wt% water), and dioxyethylene oleyl ether carboxylic acid, $C_{18:1}E_2CH_2COOH$ ($M = 415\ g \cdot mol^{-1}$, HLB = 8), commercialized under the name Akypo® RO 20 VG (95.8 wt% active matter, 0.1 wt% NaCl, 4.1 wt% water), as well as their ethoxylated alcohol precursors, were a generous gift by Kao Chemicals GmbH (Emmerich am Rhein, Germany). Both surfactants are technical products with a broad distribution of the degree of ethoxylation. Typical impurities are small amounts of glycolic acid, formic acid, diglycolic acid, polyethylene glycol, carboxymethylated polyethylene glycol, nonionic polyoxyethylene alkyl ethers and various esters of the type $C_8E_xCH_2COOE_yC_8$ or $C_{18:1}E_xCH_2COOE_yC_{18:1}$, respectively. Though different batches of the surfactants may not be identical, no differences in phase behavior were observed using different batches.

To remove hydrophilic impurities and NaCl, cloud point (CP) extraction was performed.

After thorough mixing of the surfactant with excess water (≈70 vol%), phase separation was induced by equilibration at 90°C. Once phase separation was complete, the aqueous phase was removed, and the procedure was repeated two additional times. As a last step, the surfactant was vacuum dried.

It was observed that phase boundaries of aqueous $C_8E_8CH_2COOH$/$C_{18:1}E_2CH_2COOH$ mixtures shift if $C_{18:1}E_2CH_2COOH$ is dried prior to use. The extent of the shift depends on the resting time of $C_{18:1}E_2CH_2COOH$ in absence of water. The reason for the changes is most likely the slow formation of more esters between carboxylic acid surfactant molecules and nonionic alcohol surfactant impurities, as the removal of water shifts the equilibrium towards the esters. For $C_8E_8CH_2COOH$, which has a higher degree of ethoxylation and contains less nonionic impurities, no effect on phase behavior is observed.

Propylene glycol (p.a., ≥99.5%) and ethanol (p.a., ≥99.8%) were purchased from Sigma-Aldrich (St. Louis, Missouri, USA). Glycerol (p.a., ≥99%) was purchased from Fisher Scientific (Pittsburgh, Pennsylvania, USA). Ultrapure water from a Millipore purification system (resistivity >18 MΩ cm) was used for all experiments.

For the determination of phase diagrams, $C_{18:1}E_2CH_2COOH$ was used as received, while $C_8E_8CH_2COOH$ was used after CP extraction. Samples for small-angle X-ray scattering (SAXS) experiments were prepared using both surfactants after CP extraction, explaining the occasional mismatch between the expected phase at a given temperature from the phase diagram and the actually observed phase in SAXS.

V.3.2. Phase Diagram Determination

A Julabo (Seelbach, Germany) F32-HD refrigerated and heating circulator was used to determine phase diagrams in a temperature range of 10°C to 95°C. Samples were prepared in 16×100 mm test tubes with sealed polypropylene screw caps. During sample preparation, mixing was usually facilitated by heating to 50°C. Phase boundaries were determined during heating by visual observation with the help of crossed polarizers. The accuracy in temperature is ±1°C, as temperature was adjusted in steps of 1°C with a minimum equilibration time of 10 min. Phase transitions were found to be much faster than 10 min and the same phase boundaries are found during cooling. Inhomogeneous samples were agitated using a

vortex mixer and equilibrated again to ensure the observation of the equilibrium phase. To examine the separating phases, biphasic samples were sometimes left equilibrated for up to 72 h to allow complete macroscopic phase separation. At room temperature, phase separation was facilitated using a 3-18KS centrifuge from Sigma Laborzentrifugen (Osterode am Harz, Germany).

V.3.3. Small-Angle X-Ray Scattering

Small-angle X-ray scattering (SAXS) data were performed on the ID02, TRUSAXS, beamline at the European Synchrotron Radiation Facility (ESRF, Grenoble, France). The X-ray energy used was 12.23 keV, corresponding to a wavelength, $\lambda = 0.101$ nm. A single sample-to-detector distance of 0.8 m was used, covering a q-range of 0.072–7.5 nm^{-1}, where q is the magnitude of the scattering vector and is given by $q = \sin(\theta/2)\cdot 4\pi/\lambda$. Measurements were carried out in quartz capillaries of diameter ø = 2 mm. 2D SAXS patterns were recorded by a Dectris (Baden-Daettwil, Switzerland) Eiger2 4M pixel array detector and the sample transmission was simultaneously measured. To obtain sufficient statistics for good data quality, 12 frames of 1 s exposure time were averaged, and samples underwent a radiation damage test to ensure this did not cause damage to the sample. The resulting 2D images were normalized to an absolute intensity scale and azimuthally averaged to obtain the 1D profiles. The 1D SAXS patterns were then subtracted using a capillary of water adjusted by a factor to account for the respective additive and the temperature. All samples, except M-20PG, are radially averaged. For sample “M-20PG”, the 2D SAXS pattern is anisotropic due to microstructure orientation in the sample, and to avoid artifacts in the 1D profiles, the averaging was restricted to an azimuthal angle range of 50–80°.

V.3.4. NMR Spectroscopy

Quantitative ^{13}C-NMR was measured at a temperature of 25°C using a 600 MHz spectrometer equipped with a TCI cryoprobe. To ensure accurate quantification, a pulse sequence incorporating inverse gated decoupling was employed. The experiment was performed at a frequency of 150.94 MHz and comprised 128 scans with an FID resolution of 0.50 Hz and

a relaxation delay of 10 seconds. The sample containing H_2O was measured without dissolution in a solvent. D_2O was set as solvent for the measurement, despite not being present in the sample.

V.4. Results and Discussion

A detailed study of the phase behavior of $C_8E_8CH_2COOH/C_{18:1}E_2CH_2COOH$ mixtures in water is given in **Chapter IV**. A nematic gel made of disc-like bicelles can be achieved in a large range of surfactant mixing ratios and total surfactant concentrations. A monophasic nematic gel in water is formed at room temperature for $0.60 \leq R(C_{18:1}E_2CH_2COOH) \leq 0.69$, where

$$R(C_{18:1}E_2CH_2COOH) = \frac{n(C_{18:1}E_2CH_2COOH)}{n(C_{18:1}E_2CH_2COOH) + n(C_8E_8CH_2COOH)}, \qquad (V.4.1)$$

in a concentration range from 8 wt% to 55 wt% of surfactant. As demonstrated in **Chapter IV.**, the clear nematic domain can be extended to a larger range of $R(C_{18:1}E_2CH_2COOH)$ by removal of the hydrophobic ester impurities. Throughout this chapter, the total surfactant concentration is fixed at 20 wt% and the mixing ratio is fixed at $R(C_{18:1}E_2CH_2COOH) = 0.655$. The pH of the mixture in absence of additives is around 2.2. The effect of three alcohols as additives, namely propylene glycol (PG), glycerol (G), and ethanol (EtOH), is examined. Findings are interpreted assuming intramicellar molecular segregation of the two surfactants, for details the reader is referred to **Chapter IV**. $C_{18:1}E_2CH_2COOH$ (HLB = 8, spontaneous packing parameter $p_0 \approx 1$) favors lamellar packing, whereas $C_8E_8CH_2COOH$ (HLB = 16, $p_0 < 1/3$) favors high curvature spherical packing. The compromise is a disc-like bicelle with intramicellar segregation, where $C_8E_8CH_2COOH$ favors the curved rim and $C_{18:1}E_2CH_2COOH$ favors the flat bilayer part.

The phase observed for samples in SAXS at a given temperature does not always correspond to the phase suggested by the given phase diagrams. The reason for the difference is the usage of vacuum dried $C_{18:1}E_2CH_2COOH$ for SAXS samples, instead of $C_{18:1}E_2CH_2COOH$ as received for the phase diagrams, leading to a slight shift of the phase boundaries, see **Section V.3.1**.

It is also worth noting that the carboxylic acid surfactants may react with alcohols to form esters. This is indicated by a shift of the phase boundaries over time, see **Fig. D.1**. Generally, the formation of these esters seems to have a stabilizing effect on the nematic phase. The reaction was not quantified, but the reaction appears to be facilitated at high temperatures during the determination of the phase boundaries, while being slow when stored at room temperature. As already mentioned in **Section IV.4.1.**, it was observed that the same nematic gels are formed using the surfactants' alcohol precursors, C_8E_8OH and $C_{18:1}E_2OH$. This way, side reactions with the alcohol additives can be prevented.

V.4.1. Effect of Propylene Glycol

In absence of additives, see **Chapter IV.**, the viscoelastic nematic phase (1ϕ N) transitions into an isotropic fluid (1ϕ I) at 39°C via a pseudo-lamellar phase (1ϕ L_α), before the critical temperature is reached at 42°C and a concentrated surfactant-rich phase separates from a dilute aqueous phase. The latter is the typical clouding phenomenon observed for ethoxylated nonionic surfactants. The transition of the nematic phase made of disc-like bicelles into a pseudo-lamellar phase is observed at 34°C. For the sake of clarity, a small temperature-range, in which the pseudo-lamellar phase and the isotropic phase coexist, is not shown in the phase diagrams. The bicelles with a diameter of around 50 nm at room temperature tend to grow with increasing temperature due to a decrease of intramicellar segregation. The pseudo-lamellar phase appears close to full intramicellar mixing, leading to the growth of bicelles to giant undulating discs that organize in a quasi-lamellar arrangement. The isotropic state at even higher temperature contains smaller disc-like mixed micelles, after "melting" the pseudo-lamellar phase.

The effect of adding propylene glycol (PG) on the phase behavior can be inferred from the phase diagram shown in **Fig. V.1**. The phase sequence remains the same as without additive. The nematic phase persists up to almost 30 wt% PG. Up to 20 wt% PG, PG has a stabilizing effect versus temperature, leading to a shift of the phase boundaries to slightly higher temperatures. The phase sequence observed on increasing the PG content is similar to the phase sequence observed on increasing temperature. Beyond 30 wt% PG, the nematic phase is instable. First, a lamellar phase forms in equilibrium with an isotropic phase. This domain is similar to the small 2ϕ L_α/I domain observed during heating. Further increasing the PG

content leads to the transition to an isotropic phase and eventually to the phase separation into a concentrated isotropic and a dilute isotropic phase.

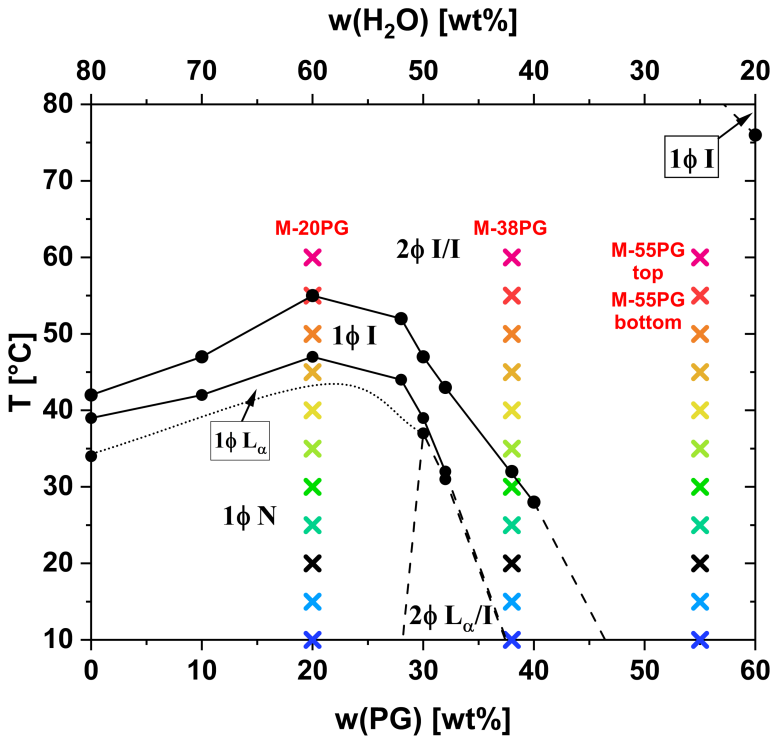

Fig. V.1. Phase diagram of 20 wt% of surfactant mixture with R($C_{18:1}E_2CH_2COOH$) = 0.655 in propylene glycol (PG)/water mixtures as a function of the PG weight fraction. Colored crosses indicate the points where SAXS was measured. 1ϕ I: Monophasic isotropic liquid. 2ϕ I/I: Two isotropic liquids in equilibrium. In the notation 2ϕ I/I, the former I regards the top phase, whereas the latter I regards the bottom phase. L_α: Lyotropic lamellar phase. N: Lyotropic nematic phase. The transition 1ϕ N → 1ϕ L_α is shown as a dotted line and is not accurate, because it is hard to determine macroscopically.

Points measured by SAXS are indicated as colored crosses in **Fig. V.1**, though the phase diagram does not directly reflect the phases for the SAXS samples (see **Section V.3.1.**). The 1D scattering curves are given in **Fig. V.2**. A temperature scan of a sample containing 20 wt% PG, see **Figure V.2**A, reveals the same scattering progression on heating of the nematic phase as in absence of PG, see **Section IV.4.3**. This suggests that PG does not alter the general microstructures and thus does not have a significant influence on intramicellar segregation. As shown by Shigeta *et al.* [34], the addition of PG increases the cloud point of $C_{18:1}E_j$ with $j \geq 10.7$ by progressively dissolving the surfactant. Further, the critical micelle concentration (CMC) is slightly increased when adding PG [35,36], suggesting that PG rather acts as a co-solvent than as a co-surfactant. The increased solubility of the surfactants in the mixed solvent could explain the increase of the cloud point up to 20 wt% PG in the present system. A second stabilizing effect could be the increase of the repulsive hydration force between the structures, opposing intermicellar attraction involved in

clouding. As can be inferred from **Fig. D.2**, the shift of the peak position with increasing temperature, i.e., the progression of the repeat distance $D^* = 2\pi/q_{max}$, is also similar with and without PG. Compared to no added additive, D* is slightly increased by approximately 2 nm from close to 23 nm to around 25 nm, suggesting either a decrease of the total volume fraction of aggregates due to dissolution of surfactant in the solvent, or a growth of discs in presence of PG. The surfactant dissolution is expected to be more significant for $C_8E_8CH_2COOH$, which is miscible with PG, than for the more hydrophobic $C_{18:1}E_2CH_2COOH$, which is barely soluble in PG. Predominant dissolution of $C_8E_8CH_2COOH$ would effectively increase the $C_{18:1}E_2CH_2COOH$ fraction in the bicelles, which would additionally lead to a slight growth of their average size. Even though the role of PG is mainly that of a co-solvent, the bicelle size may also be slightly influenced by PG acting as a co-surfactant. In analogy to the additive-free system (**Section IV.4.3.**), when cooling down after phase separation at 60°C, a concentrated lamellar phase in equilibrium with a dilute isotropic phase is obtained that is metastable at room temperature. It can be easily transformed to a nematic phase by shaking and remixing the two phases.

Scattering of the isotropic phase at 38 wt% PG, see **Figure V.2**B, is similar to scattering of the isotropic phase at elevated temperature in absence of PG, see **Section IV.4.3**. SAXS at 55 wt% PG reveals scattering of worm-like aggregates in the surfactant-rich top phase, typical of concentrated phases of many nonionic surfactants [37,38], see **Figure V.2**C. The average spacing, as derived from the peak maximum in a Holtzer-plot (I(q)·q versus q), is 10 nm. The bottom phase on the other hand, see **Figure V.2**D, exhibits almost no scattering. An analysis of the two phases at 55 wt% PG, separated at 25°C, reveals that $C_{18:1}E_2CH_2COOH$ is almost entirely in the top phase (≈ 59 wt% solvent), while 1/3 of $C_8E_8CH_2COOH$ remains in the bottom phase (≈ 94.5 wt% solvent), see **Table D.1** and **Figure D.3**. This confirms the assumption made above that preferentially $C_8E_8CH_2COOH$ is monomerically dissolved in the solvent. Since PG does not significantly enhance the solubility of $C_{18:1}E_2CH_2COOH$, the decrease of the clouding temperature above 20 wt% PG is explainable by PG dehydrating the surfactant headgroups, and, to a smaller extent, by dissolution of $C_8E_8CH_2COOH$ leading to a higher fraction of $C_{18:1}E_2CH_2COOH$ in the structures. Note that the situation changes over time as the surfactants form esters with PG, increasing their solubility in the solvent.

In conclusion, moderate amounts of PG can be used as an additive to a bicellar nematic

phase formulation, while higher amounts of PG can be used to induce a bicelle-to-worm-like micelle transition. High amounts of PG could be used if separation of hydrophilic and hydrophobic ethoxylated alkyl ether (carboxylic acid) surfactants is required, for instance in closed-loop process charts, implying circular use of surfactants.

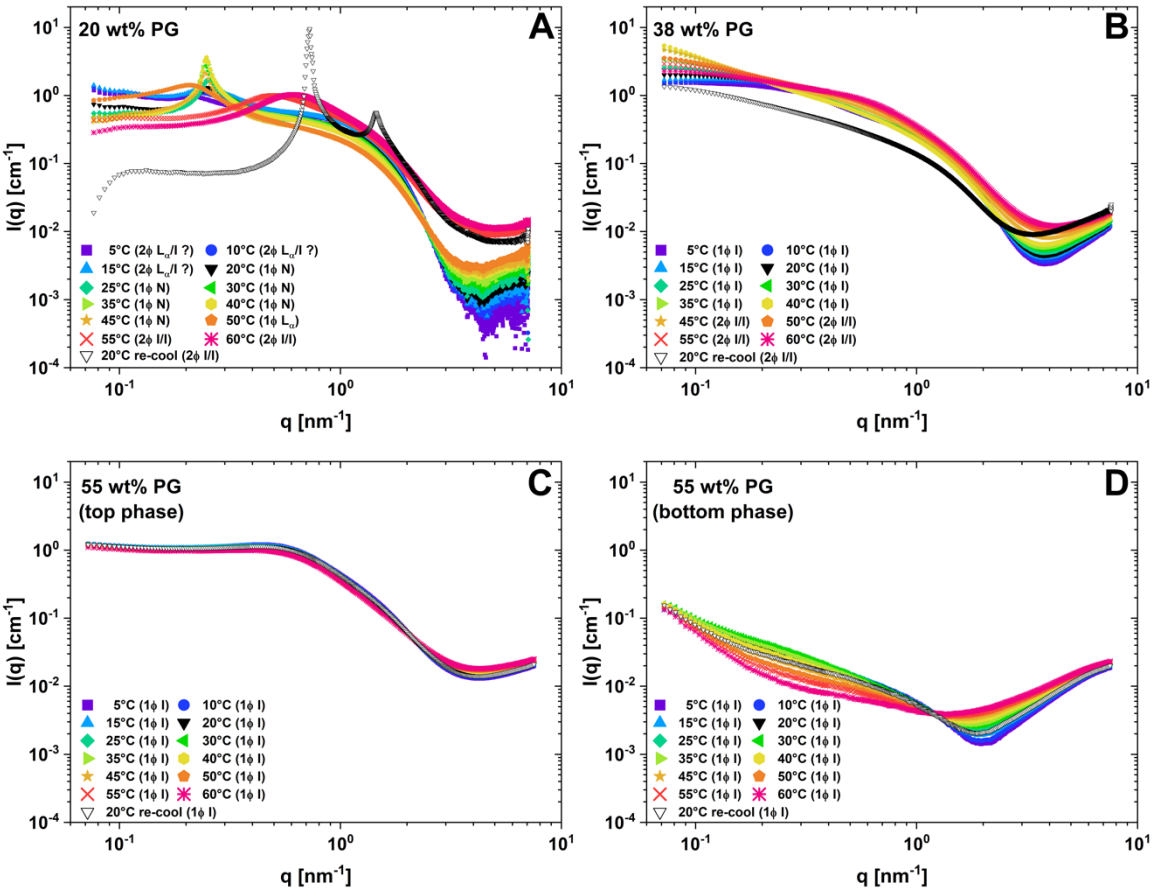

Fig. V.2. SAXS data obtained at different temperatures and propylene glycol (PG) concentrations. The temperature scan was performed during heating from 5°C to 60°C, and in addition, scattering was recorded after re-cooling from 60°C to 20°C. For the explanation of phase notations and the approximate locations of the measured samples in the phase diagram, see **Fig. V.1**. (A) Sample "M-20PG", containing 20 wt% PG. The present phase at 5°C to 15°C is not known for sure. Either the pseudo-lamellar phase of the 2ϕ L_α/I domain or a weakly birefringent nematic phase is seen. In the 2ϕ I/I domain, the scattering of the surfactant-rich phase is seen. (B) Sample "M-38PG", containing 38 wt% PG. (C) Sample "M-55PG top", i.e., the top phase separated at 25°C from the biphasic system containing 55 wt% PG. (D) Sample "M-55PG bottom", i.e., the bottom phase separated at 25°C from the biphasic system containing 55 wt% PG.

V.4.2. Effect of Glycerol

Addition of glycerol (G) does not change the general phase behavior and the observed phase sequence, see **Fig. V.3**. The addition of G leads only to a continuous decrease of the phase transition temperatures, in contrast to PG, for which the phase transition temperatures

go through a maximum around 20 wt% PG. G is not able to dissolve either of the two surfactants. Thus, G has an anti-solvent effect, i.e., a "salting-out" effect, on the surfactants by effectively dehydrating their polar headgroups. G has no direct influence on the micelles by acting as a co-surfactant or accumulating in the poly(oxyethylene) shell. This was also pointed out in ref. [34,39,40] for various other nonionic surfactants, for which the addition of G generally decreases the clouding temperature. As a result, the addition of G is virtually equivalent to increasing the temperature. At room temperature, the nematic phase is stable up to about 20 wt% G.

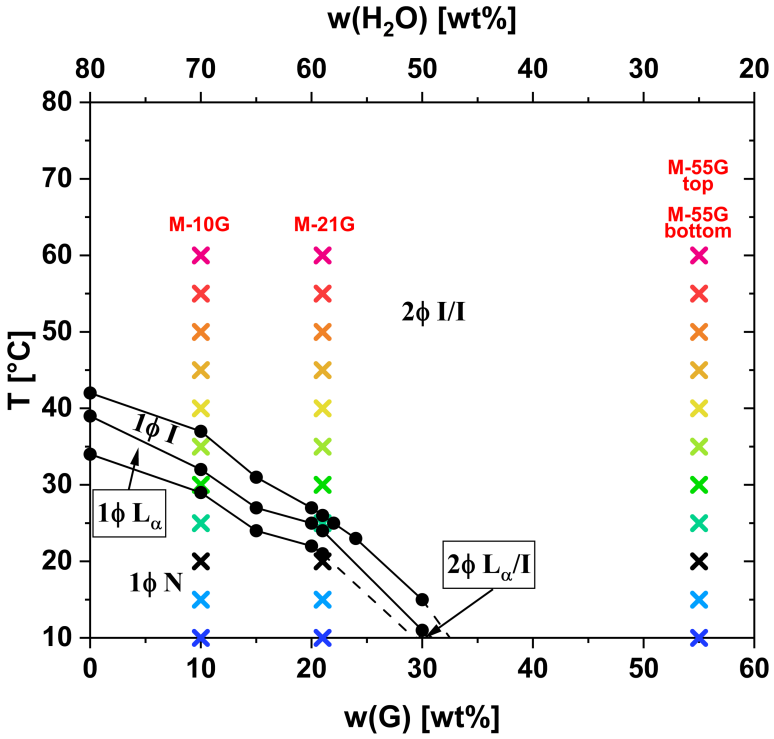

Fig. V.3. Phase diagram of 20 wt% of surfactant mixture with R($C_{18:1}E_2CH_2COOH$) = 0.655 in glycerol (G)/water mixtures as a function of the G weight fraction. Colored crosses indicate the points where SAXS was measured. 1ϕ I: Monophasic isotropic liquid. 2ϕ I/I: Two isotropic liquids in equilibrium. In the notation 2ϕ I/I, the former I regards the top phase, whereas the latter I regards the bottom phase. L_α: Lyotropic lamellar phase. N: Lyotropic nematic phase.

Points measured by SAXS are indicated as colored crosses in **Fig. V.3**. Note, however, that the phase diagram does not directly reflect the phases of the SAXS samples (see **Section V.3.1.**). The 1D scattering curves are given in **Fig. V.4**. The data of a sample containing 10 wt% G, see **Fig. V.4**A, and of a sample containing 21 wt% G, see **Fig. V.4**B, confirm that G does not alter the principal phase behavior, only shifting the phase transitions to lower temperatures. This can also be seen in the similar progression of the repeat distance D*, see **Fig. D.2**. In both cases, the correlation peaks in the nematic phase are sharp, and the closer the temperature is to the transition from the nematic phase to a pseudo-lamellar

phase, the sharper the peak becomes. Even a weak second order correlation peak at $q_{max,2} = 2 \cdot q_{max,1}$ is visible, indicating well-ordered stacks of the quasi-two-dimensional very large discs, approaching the structure of a pseudo-lamellar phase. The same effect is observed without additive because an increase in temperature favors intramicellar mixing, leading to an increase of the average disc size, see **Chapter IV**. The fact that peaks are sharper at lower temperatures in presence of G shows that the presence of G favors intramicellar mixing. Thus, the addition of G is equivalent to an increase in temperature. Consequently, addition of G decreases the stability of the nematic gel towards higher temperatures. As in absence of additive or with PG, when cooling down after phase separation at 60°C, a concentrated lamellar phase in equilibrium with a dilute isotropic phase is obtained that is metastable at room temperature and can be safely transformed into a nematic phase upon gentle shaking. The air bubble encapsulating nematic phase can be observed by customers similar to the Triphasic™ shampoo.

At 55 wt% G and a temperature of 25°C, phase separation into two isotropic phases occurs. The more viscous top phase takes up around 25 vol% of the sample, while the bottom phase takes up around 75 vol%. The physical densities at 25°C are 1.0012 $g \cdot cm^{-3}$ and 1.1725 $g \cdot cm^{-3}$ for the top and bottom phase, respectively, while the water contents are around 7 wt% and 32 wt%. Since the physical density of the bottom phase is almost identical to the value of 1.1724 $g \cdot cm^{-3}$ expected for a G/water mixture containing 32 wt% of water [41], it can be inferred that the bottom phase is the mixed solvent and does not contain a significant amount of surfactant. Note that the sample composition suggests a mixed solvent containing close to 33 wt% of water. The physical density of the more viscous top phase, containing mainly the surfactant mixture, on the other hand, is close to the physical density 0.9984 $g \cdot cm^{-3}$ of the neat surfactant mixture. Thus, G results in significant dehydration of the surfactants. These findings are in agreement with SAXS, suggesting densely packed worm-like micelles in the top phase, see **Fig. V.4**C, and no aggregates in the bottom phase, see **Fig. V.4**D. The repeat distance between the axes of cylinders found in the top phase at 55 wt% G is $D^* \approx 5$ nm (derived from a Holtzer plot), compared to $D^* \approx 10$ nm at 55 wt% PG, where the solvent content in the phase is significantly higher (59 wt%).

All these findings are in agreement with the idea that G is an anti-solvent for the surfactants, whereas PG is, at least up to a certain concentration, a co-solvent for the surfactants.

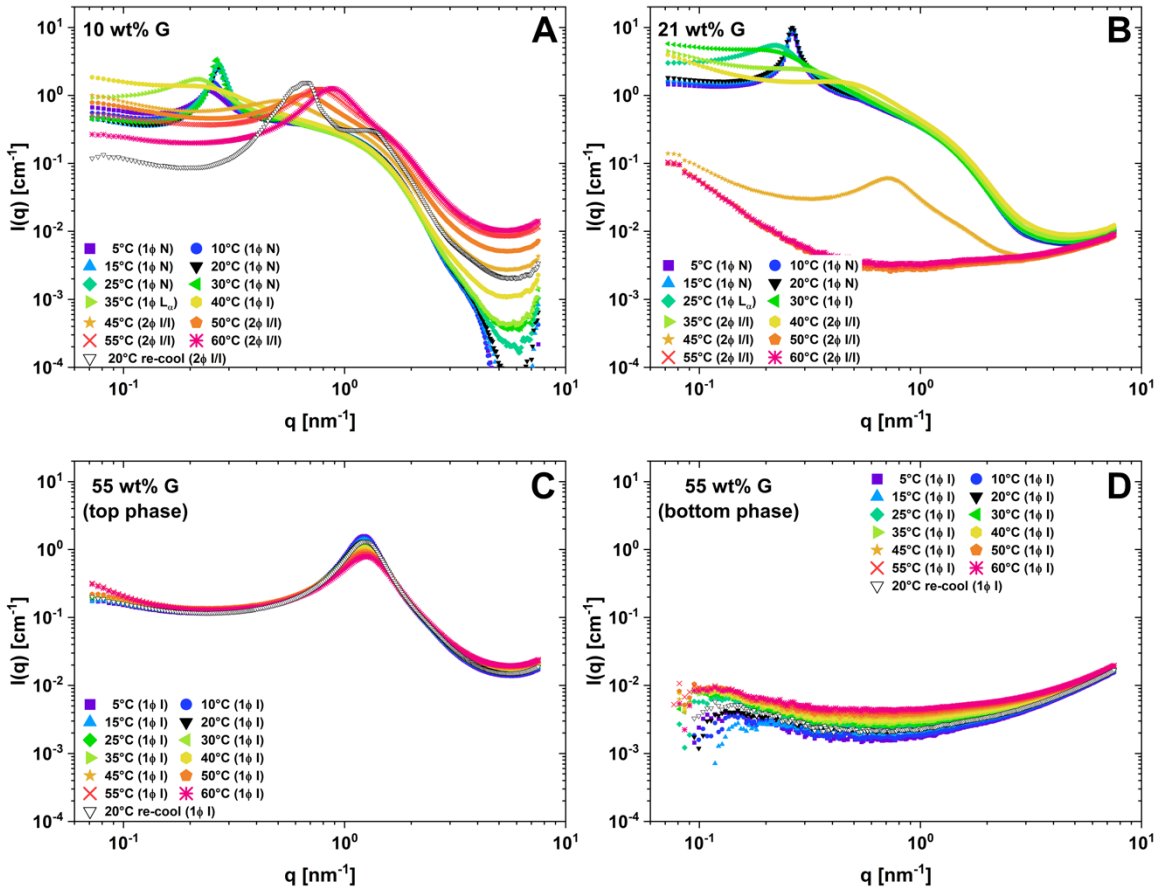

Fig. V.4. SAXS data obtained at different temperatures and glycerol (G) concentrations. The temperature scan was performed during heating from 5°C to 60°C, and in addition, scattering was recorded after re-cooling from 60°C to 20°C. For the explanation of phase notations and the approximate locations of the measured samples in the phase diagram, see **Fig. V.3**: (A) Sample "M-10G", containing 10 wt% G. (B) Sample "M-21G", containing 21 wt% G. (C) Sample "M-55G top", i.e., the top phase separated at 25°C from the biphasic system containing 55 wt% G. (D) Sample "M-55G bottom", i.e., the bottom phase separated at 25°C from the biphasic system containing 55 wt% G.

V.4.3. Effect of Ethanol

The influence of ethanol (EtOH) on the phase behavior of the system is shown in **Fig. V.5**. Up to 5 wt%, EtOH has a similar effect as PG has up to 20 wt%, stabilizing the nematic gel towards higher temperatures. The nematic phase is only stable up to less than 10 wt% EtOH. Up to about 20 wt% EtOH, the general phase behavior is similar to the phase behavior in absence of additives. Above 20 wt% EtOH, a single isotropic phase is formed, and the only remaining feature is a cloud point. The cloud point sharply increases above 20 wt% EtOH and completely disappears close to 30 wt% EtOH. The formation of a single isotropic mixture over the whole temperature range is not observed for G and PG as additives, suggesting that ethanol is a good co-solvent for both surfactants, in turn leading to

gradual dissolution of surfactant. Indeed, ethanol is miscible with both $C_8E_8CH_2COOH$ and $C_{18:1}E_2CH_2COOH$, while PG is a good solvent only for $C_8E_8CH_2COOH$ and G is a bad solvent for both. The co-solvent effect of ethanol is also known to increase the cloud point of other ethoxylated nonionic surfactants [42]. Since the surfactants are both soluble in ethanol, it is peculiar that phase separation occurs even at low temperatures above around 45 wt% EtOH. Within this biphasic domain, only a small volume (≈ 3 vol%) of an isotropic phase containing around 5 wt% of water separates from the rest of the isotropic mixture. At 55 wt% EtOH, the small phase is the denser bottom phase, whereas at 50 wt% EtOH the small phase is the less dense top phase. Since the top phase at 55 wt% EtOH has a density of 0.8878 $g \cdot cm^{-3}$ and adding more EtOH decreases the density, the density of the smaller phase should be slightly above 0.8878 $g \cdot cm^{-3}$. Due to the small volume, much less than the total surfactant volume of approximately 20 vol%, it was expected that this phase contains mainly the insoluble ester impurities (see **Section V.3.1.**). This was confirmed by using purified surfactants without ester impurities, in which case the whole biphasic domain at higher EtOH contents disappears. For details on the purification, the reader is referred to **Appendix C.2.** and ref. [43].

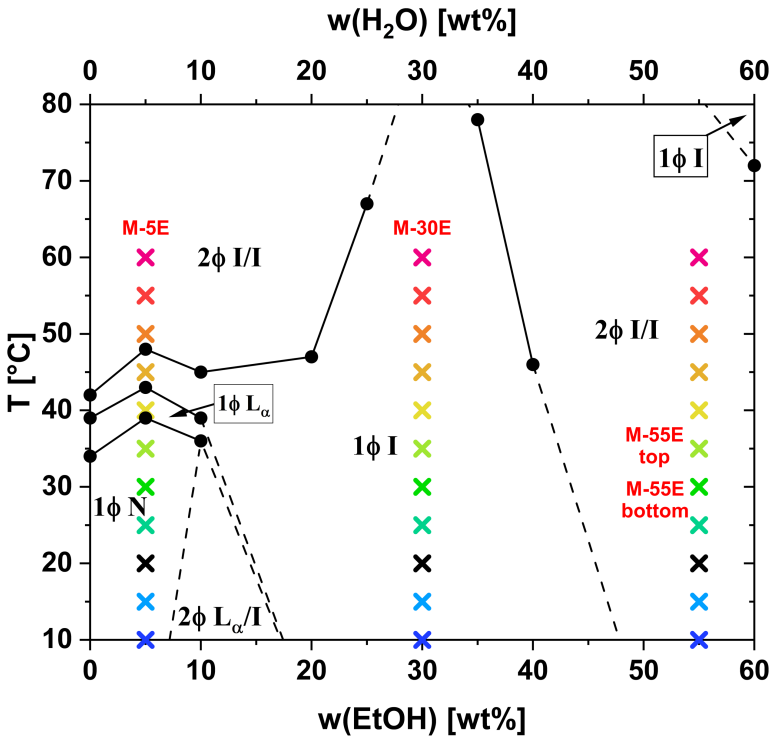

Fig. V.5. Phase diagram of 20 wt% of surfactant mixture with $R(C_{18:1}E_2CH_2COOH) = 0.655$ in ethanol (EtOH)/water mixtures as a function of the EtOH weight fraction. Colored crosses indicate the points where SAXS was measured. 1ϕ I: Monophasic isotropic liquid. 2ϕ I/I: Two isotropic liquids in equilibrium. In the notation 2ϕ I/I, the former I regards the top phase, whereas the latter I regards the bottom phase. L_α: Lyotropic lamellar phase. N: Lyotropic nematic phase.

SAXS data recorded at 5 wt% EtOH, see **Fig. V.6**A, confirm that small amounts of EtOH do not alter the principal phase behavior. This is also reflected in the progression of the correlation peak position, as can be seen in **Fig. D.2**. The typical observation that within the nematic phase an increase in temperature leads to an increasingly pronounced correlation peak is also observed. The structural reason for this phenomenon is an increase in bicellar diameter with increasing temperature due to enhanced intramicellar mixing of the two surfactants, effectively decreasing the fraction of high curvature rims limiting the discs. Macroscopically, the increasing correlation peak, i.e., the growing discs, manifest as increasing birefringence and viscosity. In presence of 5 wt% EtOH, the discs at 5°C and 10°C are too small to impose any long-range order, thus there is no correlation peak, and the sample is less viscous and only flow birefringent. In addition to the co-solvent effect of EtOH, slightly reducing the volume fraction of bicelles by dissolving some of the surfactant, EtOH could also have an effect as a co-surfactant, as EtOH is known to affect surfactant aggregation [44–47]. As for PG, see **Section V.4.1.**, the co-solvent effect, i.e., the decrease of the aggregating surfactant volume fraction, is also indicated by an increase of the spacing D* between discs by at least 2 nm compared to the sample without additive. As with the other two additives described or without any additive, a metastable lamellar phase is formed after re-cooling from 60°C to 20°C. Note that the scattering of the lamellar phase is not shown, because only scattering of the dilute phase was recorded.

Scattering in the isotropic phase at 30 wt% EtOH, see **Fig. V.6**B, reflects either worm-like or more or less globular micelles. As typical for high ethanol contents, the aggregates are expected to be less defined and pervaded by ethanol [44–47]. With increasing EtOH content, the pervaded aggregates are expected to be increasingly globular. A globular state is certainly reached at 55 wt% EtOH, see **Fig. V.6**C, where barely any scattering from small aggregates remains, i.e., where most of the micelles are dissolved. As mentioned above, the small bottom phase at 55 wt% EtOH probably contains a large fraction of ester impurities. Since the water content is only around 5 wt%, the SAXS curves, see **Fig. V.6**D, resemble scattering of hydrocarbon cores in a medium of hydrated headgroups, similar to what was found for sub-CMC auto-coacervation of $C_8E_8CH_2COOH$, see **Chapter IV**. A spacing of 3.2 nm ($q_{max} \approx 1.98\ nm^{-1}$) is in good agreement with the dimensions of a $C_{18:1}E_2CH_2COOE_2C_{18:1}$ ester, where the length of a $C_{18:1}$ chain is 2 nm and the length of the hydrophilic linker is around 2 nm, which would result in a center-to-center distance of around 3 nm between hydrocarbon cores.

Similar to PG, EtOH acts mainly as a co-solvent. Compared to PG, EtOH is a better co-solvent for both surfactants, capable of dissolving both surfactants completely. Despite not being a nematic gel, it is interesting to note that the mixture containing 20 wt% to 40 wt% EtOH is a four-component specific formulation that should be able to solubilize hydrophobic molecules as well as electrolytes such as sodium salicylate.

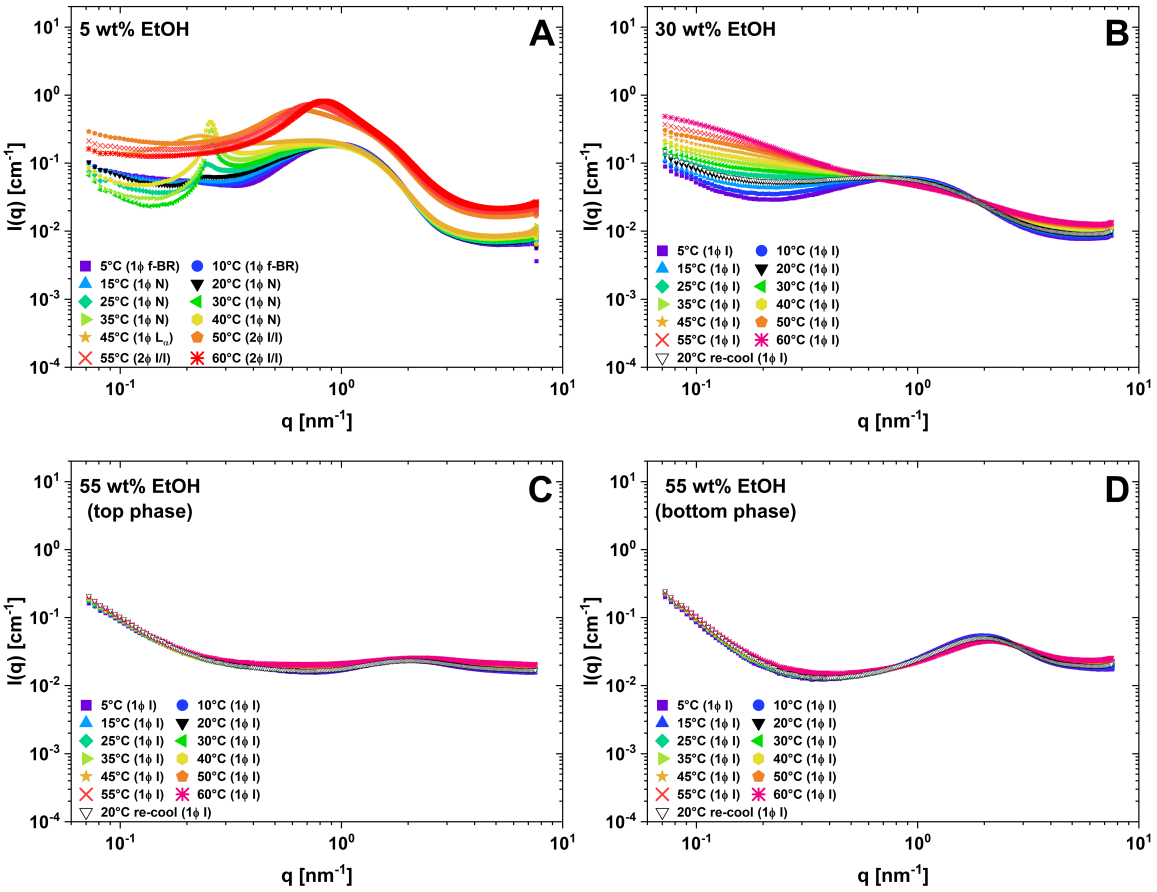

Fig. V.6. SAXS data obtained at different temperatures and ethanol (EtOH) concentrations. The temperature scan was performed during heating from 5°C to 60°C, and in addition, scattering was recorded after re-cooling from 60°C to 20°C. For the explanation of phase notations and the approximate locations of the measured samples in the phase diagram, see **Fig. V.5**: (A) Sample "M-5E", containing 5 wt% of EtOH. (B) Sample "M-30E", containing 30 wt% EtOH. (C) Sample "M-55E top", i.e., the top phase separated at 25°C from the biphasic system containing 55 wt% EtOH. (D) Sample "M-55E bottom", i.e., the bottom phase separated at 25°C from the biphasic system containing 55 wt% EtOH.

V.5. Conclusion and Outlook

The effect of propylene glycol (PG), glycerol (G), and ethanol (EtOH) on a bicellar lyotropic nematic gel formed by a mixture of $C_8E_8CH_2COOH$ and $C_{18:1}E_2CH_2COOH$, described in detail in **Chapter IV.**, was tested. The nematic gel has a peculiar entrapment property, capable of entrapping even large air bubbles or particles at rest, while being easy to handle due to strong shear-thinning. PG and EtOH act as co-solvents, whereas G acts as an anti-solvent. EtOH is a good solvent for both surfactants and is effective in destroying the nematic phase by dissolution of the micelles. The nematic gel is stable up to less than 10 wt% of EtOH. Up to 5 wt% of additive, however, EtOH slightly stabilizes the nematic gel at higher temperatures. PG is a worse co-solvent because it is not able to dissolve $C_{18:1}E_2CH_2COOH$ in significant amounts and the nematic gel persists up to almost 30 wt% PG. PG stabilizes the nematic gel up to 20 wt% PG. G on the other hand is not leading to dissolution of surfactant and only dehydrates the surfactant headgroups. This is equivalent to a salting-out effect, decreasing the temperature stability of the nematic gel. Due to this effect, however, the gel is more viscoelastic at lower temperatures in presence of G. At room temperature, the nematic gel is stable up to around 20 wt% G.

These effects can also be seen in **Fig. V.7**, in which the SAXS data of the nematic gel without additive at 25°C, with 5 wt% EtOH at 30°C, with 10 wt% G at 25°C, with 21 wt% G at 15°C, and with 20 wt% PG at 30°C are superposed. The temperatures were chosen so that the sample is well inside the nematic domain. The scattering is similar in all cases and only differs in shape due to variations in scattering contrast with different (mixed) solvents. At 10 wt% G, the correlation peak is not shifted compared to the additive-free sample because no additional surfactant is monomerically dissolved in the mixed solvent. The slight shift to lower q at 21 wt% G, also observed in absence of additives close to the transition into a pseudo-lamellar phase at higher temperature, is a result of disc growth due to headgroup dehydration, which leads to increased intramicellar mixing of the two surfactants. At 20 wt% PG on the other hand, the peak is slightly shifted to lower q because some surfactant is dissolved in the mixed solvent and the preferential dissolution of $C_8E_8CH_2COOH$ leads to bicellar growth. The shift is more pronounced with only 5 wt% EtOH, as EtOH is a better co-solvent for both surfactants.

The formation of a single isotropic phase above 15 wt% EtOH due to surfactant

solubilization allows for a formulation of an isotropic phase that becomes nematic (or lamellar) on evaporation of EtOH first and water later. Since the metastable state of coexistence of a surfactant-rich lamellar phase and a dilute solvent phase after phase separation above the critical temperature and subsequent re-cooling can be easily transformed back into a nematic phase by simple mixing, a formulation of a concentrated lamellar phase as precursor to a viscoelastic nematic phase would be feasible.

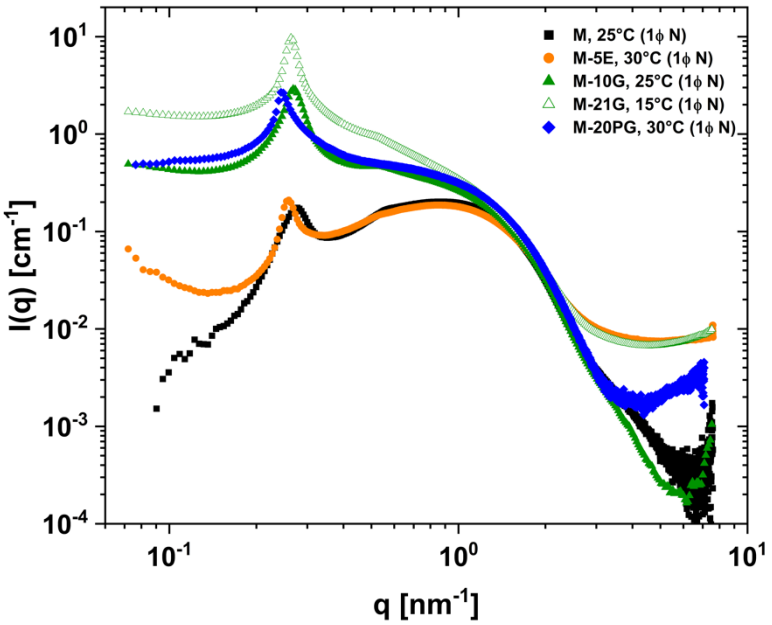

Fig. V.7. SAXS data of samples "M", identical to sample "20M*" in **Chapter IV.**, containing no additive, at 25°C, "M-5E", containing 5 wt% EtOH, at 30°C, "M-10G", containing 10 wt% G, at 25°C, "M-21G", containing 21 wt% G, at 15°C, and "M-20PG", containing 20 wt% PG, at 30°C. All samples contain 20 wt% of a $C_8E_8CH_2COOH/C_{18:1}E_2CH_2COOH$ surfactant mixture with $R(C_{18:1}E_2CH_2COOH) = 0.655$, and are nematic gels (1ϕ N) at the given temperatures.

V.6. References

[1] P. Denk, L. Matthews, T. Zemb, W. Kunz, Formulating additives in thermoresponsive surfactant-based nematic liquid crystals, Tenside Surfactants Detergents 61 (2024) 228–239. https://doi.org/10.1515/tsd-2023-2579.

[2] G. Raffard, S. Steinbruckner, A. Arnold, J.H. Davis, E.J. Dufourc, Temperature−Composition Diagram of Dimyristoylphosphatidylcholine−Dicaproylphosphatidylcholine "Bicelles" Self-Orienting in the Magnetic Field. A Solid State 2 H and 31 P NMR Study, Langmuir 16 (2000) 7655–7662. https://doi.org/10.1021/la000564g.

[3] M.-P. Nieh, C.J. Glinka, S. Krueger, R.S. Prosser, J. Katsaras, SANS Study of the Structural Phases of Magnetically Alignable Lanthanide-Doped Phospholipid Mixtures, Langmuir 17 (2001) 2629–2638. https://doi.org/10.1021/la001567w.

[4] J. Katsaras, T.A. Harroun, J. Pencer, M.-P. Nieh, “Bicellar” Lipid Mixtures as used in Biochemical and Biophysical Studies, Naturwissenschaften 92 (2005) 355–366. https://doi.org/10.1007/s00114-005-0641-1.

[5] L. Barbosa-Barros, G. Rodríguez, C. Barba, M. Cócera, L. Rubio, J. Estelrich, C. López-Iglesias, A. de la Maza, O. López, Bicelles: Lipid Nanostructured Platforms with Potential Dermal Applications, Small 8 (2012) 807–818. https://doi.org/10.1002/smll.201101545.

[6] C.R. Sanders, J.P. Schwonek, Characterization of magnetically orientable bilayers in mixtures of dihexanoylphosphatidylcholine and dimyristoylphosphatidylcholine by solid-state NMR, Biochemistry 31 (1992) 8898–8905. https://doi.org/10.1021/bi00152a029.

[7] J.N. Israelachvili, D.J. Mitchell, B.W. Ninham, Theory of self-assembly of hydrocarbon amphiphiles into micelles and bilayers, Journal of the Chemical Society, Faraday Transactions 2: Molecular and Chemical Physics 72 (1976) 1525–1568. https://doi.org/10.1039/F29767201525.

[8] L. van Dam, G. Karlsson, K. Edwards, Direct observation and characterization of DMPC/DHPC aggregates under conditions relevant for biological solution NMR, Biochimica et Biophysica Acta (BBA) - Biomembranes 1664 (2004) 241–256. https://doi.org/10.1016/j.bbamem.2004.06.005.

[9] A. Meister, M. Dubois, L. Belloni, T. Zemb, Equation of State of Self-Assembled Disklike and Icosahedral Crystallites in the Dilute Range, Langmuir 19 (2003) 7259–7263. https://doi.org/10.1021/la0346806.

[10] M. Dubois, L. Belloni, Th. Zemb, B. Demé, Th. Gulik-Krzywicki, Formation of rigid nanodiscs: edge formation and molecular separation, in: Trends in Colloid and Interface Science XIV. Progress in Colloid and Polymer Science, Springer Berlin Heidelberg, Berlin, Heidelberg, 2000: pp. 238–242. https://doi.org/10.1007/3-540-46545-6_47.

[11] M. Dubois, V. Lizunov, A. Meister, T. Gulik-Krzywicki, J.M. Verbavatz, E. Perez, J. Zimmerberg, T. Zemb, Shape control through molecular segregation in giant surfactant aggregates, Proceedings of the National Academy of Sciences 101 (2004) 15082–15087. https://doi.org/10.1073/pnas.0400837101.

[12] S.H. Park, S.J. Opella, Triton X-100 as the “Short-Chain Lipid” Improves the Magnetic Alignment and Stability of Membrane Proteins in Phosphatidylcholine Bilayers for Oriented-Sample Solid-State NMR Spectroscopy, J Am Chem Soc 132 (2010) 12552–12553. https://doi.org/10.1021/ja1055565.

[13] S. Taguchi, Y. Kimura, Y. Akiyama, Y. Tachibana, T. Yamamoto, Fluorescent Anisotropy Evaluation of Bicelle Formation Employing Carboxyl BODIPY and Pyrromethene, J Oleo Sci 71 (2022) ess21295. https://doi.org/10.5650/jos.ess21295.

[14] M. Dubois, T. Gulik-Krzywicki, B. Demé, T. Zemb, Rigid organic nanodisks of controlled size: A catanionic formulation, Comptes Rendus de l’Académie Des Sciences - Series IIC - Chemistry 1 (1998) 567–575. https://doi.org/10.1016/S1387-1609(98)80012-1.

[15] K.D. Lawson, T.J. Flautt, Magnetically oriented lyotropic luquid crystalline phases, J Am Chem Soc 89 (1967) 5489–5491. https://doi.org/10.1021/ja00997a054.

[16] L.Q. Amaral, C.A. Pimentel, M.R. Tavares, J.A. Vanin, Study of a magnetically oriented lyotropic mesophase, J Chem Phys 71 (1979) 2940–2945. https://doi.org/10.1063/1.438696.

[17] B.J. Forrest, F.Y. Fujiwara, L.W. Reeves, Order profiles of host decyl sulfate and decylammonium chains and guest carboxylic acids and carboxylates in aligned type II DM lyomesophases, J Phys Chem 84 (1980) 662–670. https://doi.org/10.1021/j100443a019.

[18] H.-D. Dörfler, C. Görgens, Mizellpolymorphie lyotroper Mesophasen, Tenside Surfactants Detergents 36 (1999) 314–321. https://doi.org/10.1515/tsd-1999-360509.

[19] C.F. Dietrich, P. Rudquist, K. Lorenz, F. Giesselmann, Chiral Structures from Achiral Micellar Lyotropic Liquid Crystals under Capillary Confinement, Langmuir 33 (2017) 5852–5862. https://doi.org/10.1021/acs.langmuir.7b01074.

[20] G. Colafemmina, R. Recchia, A.S. Ferrante, S. Amin, G. Palazzo, Lauric Acid-Induced Formation of a Lyotropic Nematic Phase of Disk-Shaped Micelles, J Phys Chem B 114 (2010) 7250–7260. https://doi.org/10.1021/jp1020774.

[21] L.J. Yu, A. Saupe, Observation of a Biaxial Nematic Phase in Potassium Laurate-1-Decanol-Water Mixtures, Phys Rev Lett 45 (1980) 1000–1003. https://doi.org/10.1103/PhysRevLett.45.1000.

[22] S.E. Anachkov, P.A. Kralchevsky, K.D. Danov, G.S. Georgieva, K.P. Ananthapadmanabhan, Disclike vs. cylindrical micelles: Generalized model of micelle growth and data interpretation, J Colloid Interface Sci 416 (2014) 258–273. https://doi.org/10.1016/j.jcis.2013.11.002.

[23] E.Y. Sheu, P. Lo Nostro, G. Capuzzi, P. Baglioni, Micelle and Microemulsion Properties of Cesium Di-Dodecyl-Dimethylsulfosuccinate, Cs-AOT, Langmuir 15 (1999) 6671–6676. https://doi.org/10.1021/la990059n.

[24] N. Boden, S.A. Corne, K.W. Jolley, Lyotropic mesomorphism of the cesium pentadecafluorooctanoate/water system: high-resolution phase diagram, J Phys Chem 91 (1987) 4092–4105. https://doi.org/10.1021/j100299a031.

[25] M.C. Holmes, D.J. Reynolds, N. Boden, Concentration-temperature dependence of the size and shape of the micelles in the cesium pentadecafluorooctanoate/water system, J Phys Chem 91 (1987) 5257–5262. https://doi.org/10.1021/j100304a025.

[26] B.J. Forrest, L.W. Reeves, New lyotropic liquid crystals composed of finite nonspherical micelles, Chem Rev 81 (1981) 1–14. https://doi.org/10.1021/cr00041a001.

[27] V. Hendrikx, J. Charvolin, M. Rawiso, L. Liebert, M.C. Holmes, Anisotropic aggregates of amphiphilic molecules in lyotropic nematic phases, J Phys Chem 87 (1983) 3991–3999. https://doi.org/10.1021/j100243a039.

[28] E.J. Dufourc, Bicelles and nanodiscs for biophysical chemistry, Biochimica et Biophysica Acta (BBA) - Biomembranes 1863 (2021) 183478. https://doi.org/10.1016/j.bbamem.2020.183478.

[29] C. Loudet-Courreges, F. Nallet, E.J. Dufourc, R. Oda, Unprecedented Observation of Days-Long Remnant Orientation of Phospholipid Bicelles: A Small-Angle X-ray Scattering and Theoretical Study, Langmuir 27 (2011) 9122–9130. https://doi.org/10.1021/la1050817.

[30] D. Venkata Sai, G. Mirri, P.H.J. Kouwer, R. Sahoo, I. Musevic, S. Dhara, Unusual temperature dependence of elastic constants of an ambient-temperature discotic nematic liquid crystal, Soft Matter 12 (2016) 2960–2964. https://doi.org/10.1039/C6SM00065G.

[31] L.R.P. de Andrade Lima, A.D. Rey, Linear viscoelasticity of discotic mesophases, Chem Eng Sci 59 (2004) 3891–3905. https://doi.org/10.1016/j.ces.2004.06.016.

[32] A. Nikzad, A. Akbari, D. Grecov, Rheological properties of discotic nematic liquid crystals: graphene oxide dispersions study, Liq Cryst 48 (2021) 1685–1698. https://doi.org/10.1080/02678292.2021.1897890.

[33] C.L.S. Risi, A.M. Figueiredo Neto, P.R.G. Fernandes, A.R. Sampaio, E. Akpinar, M.B.L. Santos, Shear viscosity and rheology of ternary and quaternary lyotropic liquid crystals in discotic and calamitic nematic phases, Rheol Acta 54 (2015) 529–543. https://doi.org/10.1007/s00397-015-0850-2.

[34] K. Shigeta, U. Olsson, H. Kunieda, Effect of Alcohols (Propanol, Propylene Glycol, and Glycerol) on Cloud Point and Micellar Structure in Long-Poly(oxyethylene)n Oleyl Ethers Systems, in: Stud Surf Sci Catal, Elsevier Inc., 2001: pp. 93–96. https://doi.org/10.1016/S0167-2991(01)82042-5.

[35] C.M. Romero, A.P. Escamilla, A.C.F. Ribeiro, M.A. Esteso, Effect of 1,2-propanediol on the Critical Micelle Concentration of Decyltrimethylammonium Bromide at Temperatures from 293.15 K to 308.15 K, Int J Mol Sci 23 (2022) 15884. https://doi.org/10.3390/ijms232415884.

[36] L. Marszall, J.W. Van Valkenburg, The effect of glycols on the hydrophile-lipophile balance and the micelle formation of nonionic surfactants, J Am Oil Chem Soc 59 (1982) 84–87. https://doi.org/10.1007/BF02678718.

[37] C.A. Dreiss, Wormlike micelles: where do we stand? Recent developments, linear rheology and scattering techniques, Soft Matter 3 (2007) 956. https://doi.org/10.1039/b705775j.

[38] K.D. Danov, P.A. Kralchevsky, S.D. Stoyanov, J.L. Cook, I.P. Stott, E.G. Pelan, Growth of wormlike micelles in nonionic surfactant solutions: Quantitative theory vs. experiment, Adv Colloid Interface Sci 256 (2018) 1–22. https://doi.org/10.1016/j.cis.2018.05.006.

[39] G. D'Errico, D. Ciccarelli, O. Ortona, Effect of glycerol on micelle formation by ionic and nonionic surfactants at 25 °C, J Colloid Interface Sci 286 (2005) 747–754. https://doi.org/10.1016/j.jcis.2005.01.030.

[40] L. Cantù, M. Corti, V. Degiorgio, H. Hoffmann, W. Ulbricht, Nonionic micelles in mixed water-glycerol solvent, J Colloid Interface Sci 116 (1987) 384–389. https://doi.org/10.1016/0021-9797(87)90134-2.

[41] A. Volk, C.J. Kähler, Density model for aqueous glycerol solutions, Exp Fluids 59 (2018) 75. https://doi.org/10.1007/s00348-018-2527-y.

[42] M. Alauddin, T. Parvin, T. Begum, Effect of Organic Additives on the Cloud Point of Triton X-100 Micelles, Journal of Applied Sciences 9 (2009) 2301–2306. https://doi.org/10.3923/jas.2009.2301.2306.

[43] F. Cattelaens, M. Jäger, T. Myrdek, Purification of carboxymethylated fatty alcohol derivates using ion exchange resins, J Surfactants Deterg 26 (2023) 111–117. https://doi.org/10.1002/jsde.12641.

[44] R. Zana, Aqueous surfactant-alcohol systems: A review, Adv Colloid Interface Sci 57 (1995) 1–64. https://doi.org/10.1016/0001-8686(95)00235-I.

[45] P. Denk, S. Prévost, L. Matthews, Q. Prasser, T. Zemb, W. Kunz, The effect of ethanol on fibrillar hydrogels formed by glycyrrhizic acid monoammonium salt, J Colloid Interface Sci 630 (2023) 762–775. https://doi.org/10.1016/j.jcis.2022.10.138.

[46] H. Suzuki, Studies of the Effect of Ethanol and Sodium Chloride on the Micellization of Sodium Dodecyl Sulfate by Gel Filtration, Bull Chem Soc Jpn 49 (1976) 1470–1474. https://doi.org/10.1246/bcsj.49.1470.

[47] P. Becher, Nonionic surface-active compounds. X. Effect of solvent on micellar properties, J Colloid Sci 20 (1965) 728–731. https://doi.org/10.1016/0095-8522(65)90046-2.

Chapter VI.

Microstructure of Fibrillar Hydrogels Formed by Glycyrrhizic Acid Monoammonium Salt – Effects of Ethanol, Temperature, pH, and Salt

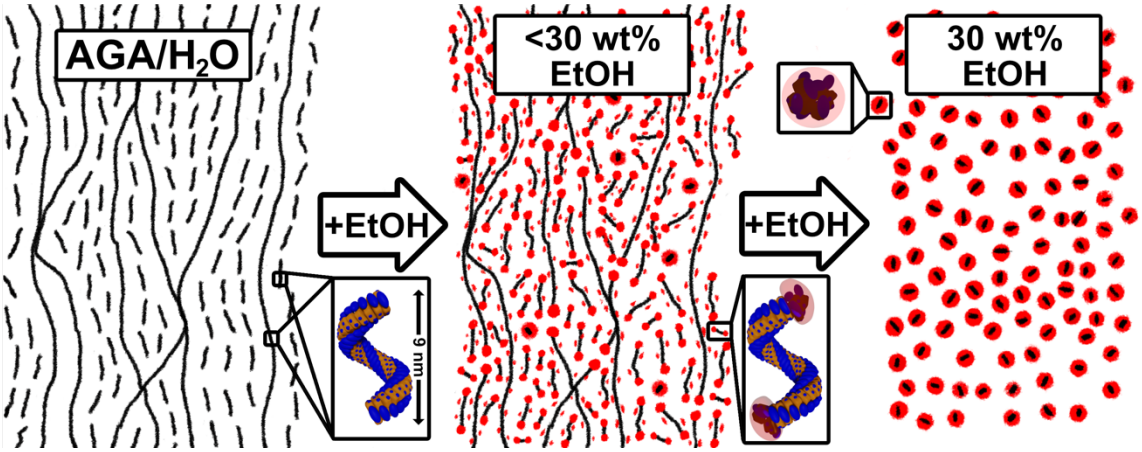

Left: In the binary system glycyrrhizic acid monoammonium salt (AGA)/H_2O, "infinite" rigid helical fibrils coexist with shorter fibrils. Middle: Ethanol (EtOH, red) as a co-solvent facilitates the formation of end caps, thus reducing the length of short fibrils; the "infinite" ones stay initially intact as they do not have unstable ends. Right: As EtOH reaches a threshold concentration (≈30 wt%), only end caps remain, meaning that all fibrils have been transformed into micelle-like aggregates pervaded by an EtOH-enriched solvent.

Note:

The content presented in this chapter is already published (P. Denk, S. Prévost, L. Matthews, Q. Prasser, T. Zemb, W. Kunz, The effect of ethanol on fibrillar hydrogels formed by glycyrrhizic acid monoammonium salt, J Colloid Interface Sci 630 (2023) 762–775.) [1]. The author of this thesis is the first author of the publication, wrote the original draft, evaluated the data, and conducted most of the experiments. The co-authors Dr. Sylvain Prévost, Prof. Dr. Thomas Zemb, and Prof. Dr. Werner Kunz assisted by reviewing the draft and giving scientific input throughout the work. Small-angle scattering measurements and the treatment of raw scattering data were performed by the co-authors Dr. Lauren Matthews (SAXS) and Dr. Sylvain Prévost (SAXS and SANS). The simulations given in Figs. E.17 and E.18, as well as the calculation given in Appendix E.4., were done by Dr. Sylvain Prévost. The co-author Dr. Quirin Prasser recorded parts of the presented phase map during his time as an intern at our institute. He was supervised by Christiane Beate Jung, Dr. Didier Touraud, and Dr. Eva Müller, without whose groundwork the publication and this chapter would not have come to existence.

VI.1. Abstract

While **Chapters II. to V.** are thematically related and build upon each other, a different topic is discussed in this chapter. In contrast to all previous chapters, this chapter does not deal with polyoxyethylene alkyl ether carboxylic acid surfactants, but with an amphiphilic natural sweetener, the monoammonium salt of glycyrrhizic acid (AGA). Despite being amphiphilic, AGA is different from classical surfactants due to its molecular shape. AGA is known to form fibrillar hydrogels and few studies regarding self-assembly of AGA have been published. Yet, the understanding of the fibrillar microstructures and the gelation remains vague. Thus, an attempt is made in this chapter to achieve a deeper understanding of the microstructures and the gelation process of binary solutions of AGA in water. Further, the effect of ethanol on the microstructures is examined to pave the way for potential enhancement of drug loading in AGA hydrogels.

A partial room temperature phase map of the ternary system AGA/ethanol/water was recorded. Small-angle X-ray and neutron scattering experiments were performed over wide ranges of compositions in both binary AGA/water and ternary AGA/ethanol/water mixtures to get access to the micro-structuring.

Binary aqueous solutions of AGA form birefringent gels consisting of a network of long helical fibrils. “Infinitely” long negatively charged fibrils are in equilibrium with shorter fibrils (≈25 nm), both of which have a diameter of about 3 nm and are made of around 30 stacks of AGA per helical period (≈9 nm), with each stack consisting of two AGA molecules. The interaxial distance (order of magnitude ≈20 nm) varies with an almost two-dimensional swelling. Addition of ethanol reduces electrostatic repulsion and favors the formation of fibrillar end caps, reducing the average length of shorter fibrils, as well as the formation of small, swollen aggregates. While the gel network built by the long fibrils is resilient to a significant amount of ethanol, all fibrils are finally dissolved into small aggregates above a certain threshold concentration of ethanol (≈30 wt%).

VI.2. Introduction

Glycyrrhizic acid (or glycyrrhizin) is an edible natural sweetener obtained from the licorice root (glycyrrhiza glabra) and is at least 30 times sweeter than sucrose. Currently, glycyrrhizic acid (GA) and its ammonium salt (AGA) are listed in the register of flavoring substances, allowing their unrestricted use in food. GA is contained in licorice confectionery, and both GA and AGA are added not only to a wide range of food products, but also to health products and personal care products such as toothpaste. Only if ingested in large quantities, various studies indicate negative effects such as hypertension [2–4]. For regular ingestion, the Scientific Committee on Food of the European Commission recommends a maximum ingestion of 100 mg/day [5]. Chemically, GA is a monodesmosidic saponin consisting of a pentacyclic triterpenoid aglycone part (18β-glycyrrhetenic acid) and a glycone part made of a disaccharide (β-(1,2)-diglucuronic acid). After ingestion, GA is hydrolyzed to give 18β-glycyrrhetenic acid, which is the biologically active metabolite. It is known to possess a multitude of beneficial pharmaceutical properties. For an overview, the reader is referred to Asl *et al.* [4] and Graebin [6]. Thus, it is still subject of great interest in pharmaceutics. Among others, anti-inflammatory, antimicrobial and antiviral, antiprotozoal, and antitumor activities are reported. GA was shown to inhibit SARS coronaviruses in vitro almost 20 years ago [7]. Recently, GA was shown to also effectively inhibit SARS-CoV-2 replication in vitro [8]. In addition to its own biological activity, GA is interesting for drug delivery in pharmaceutical applications [9,10]. GA is slightly amphiphilic and, at intermediate pH (4–6), capable of forming aggregates and supramolecular hydrogels [11]. The intermediate pH is inherent for AGA, which is known to form fibrillar hydrogels [12,13]. Due to its ability to form supramolecular hydrogels, AGA ($M = 840\ g \cdot mol^{-1}$) is considered a natural low molecular weight (LMW) hydrogelator. Most of the commonly used LMW hydrogelators are synthetic derivatives [14–21], but some natural molecules have also been used to form supramolecular hydrogels [21,22]. Since hydrogel formation by AGA is a result of self-assembly, i.e., of weak interactions, and not of covalent crosslinking (as in polymeric hydrogels), other (hydrophobic) compounds can be incorporated to a certain extent and easily released later. Thus, AGA is both a solubilizer and a hydrogelator, two properties that render AGA a promising drug delivery agent. In addition, AGA hydrogels are birefringent, i.e., the natural compound alone forms a liquid crystalline hydrogel.

A potential to incorporate various solutes in gels and solutions of AGA was already

predicted by Tykarska *et al.* [23] in 2013, who investigated the unusual solid state isomorphism of GA and its salts. In the solid state, GA is arranged in a layered structure, in which the diglucuronic acid moieties form sugar platforms separated by hydrophobic layers of aglycone moieties. The arrangement leaves rather hydrophilic channels (≈42 % of the crystal volume), where solvent molecules and ions can be incorporated. These channels are the origin of the isomorphism, because cations like NH_4^+ can replace hydrogen bonded water molecules within the channels without changing the molecular arrangement. In solution, the degree of ionization is much more important. The fully protonated form (GA) is not sufficiently soluble in water to allow any self-assembly. While mono- or di-deprotonated forms are required to enable self-assembly in water, a too high degree of ionization inhibits self-assembly and leads to a monomeric (or dimeric) solution. As a consequence, self-assembly of GA is observed in a rather narrow pH range from pH ≈ 4 to pH ≈ 7 [11]. Binary solutions of AGA always have a natural pH in this range and thus AGA can self-assemble. Opposed to the solid state, AGA does not form layered, but fibrillar aggregates in solution [11–13]. As will also be shown in this chapter, the fibrils are rather of a core-shell-like nature and too thin to have an internal structure similar to that in the solid state. Saha *et al.* [12] have recently shown that the fibrils are right-handed helices.

Though there is already a principal understanding of the aggregation and gelation of AGA in water in the literature, the system is far from being fully understood. The aim of this chapter is to give a more complete description of the microstructuring of AGA in water, and further to examine the effect of ethanol as a hydrotrope or cosolvent on the microstructures and gelation. In the scope of solute solubilization and drug delivery, adding a hydrotrope like ethanol should further increase the solubility of hydrophobic solutes in the gel. This important aspect will be investigated in another paper, currently in preparation by Kunz and co-workers [24]. In this chapter, a partial ternary phase map of the system AGA/ethanol/water at room temperature will be given. With the aid of mainly small- and wide-angle X-ray scattering (SWAXS) as well as small-angle neutron scattering (SANS) over large ranges of compositions with and without ethanol, and additionally considering already published studies [11–13], a detailed description of the formed microstructures and their impact on gelation is offered. The effects of temperature, salt (NaCl) addition, and pH help getting a better understanding of the forces involved in microstructuring and gelation.

VI.3. Experimental Section

VI.3.1. Materials

Glycyrrhizic acid monoammonium salt (≥95%), herein abbreviated as AGA (ammonium glycyrrhizic acid), and ethanol (≥98.8%) were purchased from Sigma-Aldrich (St. Louis, Missouri, USA). Note that, according to the supplier, the main impurity in AGA is water. D_2O (99% D) and d6-ethanol (99% D) were supplied by Eurisotop (Saint-Aubin, France). Sodium hydroxide solution (1 $mol \cdot L^{-1}$) and sodium chloride (≥99.5 %) were purchased from Carl Roth (Karlsruhe, Germany). Hydrochloric acid solution (1 $mol \cdot L^{-1}$) was purchased from Supelco (Bellefonte, PA, USA). Ultrapure water from a Millipore purification system (resistivity > 18 MΩ·cm) was used for all systems containing water.

VI.3.2. Phase Map Determination

As will be shown below, prepared gels and sols are not always in the thermodynamic equilibrium state and the observed viscosity depends on the preparation history. The microstructures in the sub-nm to hundreds of nm range are accessible by investigating series of dilutions with small-angle scattering. While the general microstructures and the close-range ordering are found to be much less dependent on preparation history, not a real thermodynamic phase diagram is determined, but a ‘‘phase map”. The phase map captures some of the features of true phase diagrams, but not all. The term phase map will be used throughout this chapter. The partial ternary phase map of the system glycyrrhizic acid monoammonium salt (AGA)/H_2O/ethanol (EtOH) was determined at room temperature (≈23°C) by preparing various samples with different AGA and ethanol contents. Generally, the AGA content was varied at a fixed ethanol content to find the critical gel concentration (CGC) or the solubility limit. Typically, the appropriate amount of AGA was weighed in a glass vial (4 cm length × 1.9 cm diameter) and the desired amounts of EtOH and water were added. A vortex mixer was used to homogenize the mixture, which was further stirred for several minutes. Except for some samples containing larger amounts of AGA, samples were not heated to facilitate mixing. This is important to note because the optical appearance is found to be influenced by heating and the subsequent cooling rate. Thus, the reported optical

appearance of a sample corresponds to its appearance after mixing at room temperature without heating. A sample is considered a gel if no gravitational flow is observed after inversion of the vial at room temperature.

VI.3.3. Small- and Wide-Angle X-Ray Scattering

Small- and wide-angle X-ray scattering (SWAXS) data were all acquired on the beam line ID02 at the European Synchrotron Radiation Facility (ESRF, Grenoble, France), in four occasions. Samples were always contained in quartz capillaries, but depending on the experiment and the viscosity of the sample set, they were either in individual quartz capillaries (10 μm quartz thickness, WJM-Glas / Müller GmbH, Berlin, Germany) or in a flow-through capillary (50 μm quartz thickness, Hilgenberg GmbH, Malsfeld, Germany).

SWAXS of samples containing 3.0 wt% AGA and a varying amount of ethanol, as well as samples containing no ethanol and a varying concentration of AGA, were measured on the beamline ID02 [25] at ESRF. The detector was a CCD Rayonix MX170-HS from Rayonix, L.L.C. (Evanston, Illinois, USA), placed at the sample-to-detector distances of 0.77, 5, and 30.69 m, thus covering a total q-range of 0.002–10 nm^{-1}, where q is the magnitude of the wavevector: $q = \sin(\theta/2)\cdot 4\pi/\lambda$, θ being the scattering angle. A fixed wavelength of 0.099 nm was chosen ($\Delta E/E \approx 10^{-4}$). Samples were poured in individual quartz capillaries of 10 μm quartz walls and a diameter of around 1.55 ± 0.15 mm. Typically, eleven successive acquisitions at different positions in the capillaries were averaged, also providing the standard deviation and corresponding error-bars. A water capillary was used as a background subtracted from all data files. SWAXS data of all other samples containing 30 wt% ethanol and a varying amount of AGA were also measured on the beamline ID02 [26] at ESRF, but in a flow through setup with an inner capillary diameter of 2 mm. For these measurements an Eiger2 4 M pixel array detector from Dectris (Baden-Daettwil, Switzerland) was used, and the sample transmission was measured simultaneously. 2D SAXS patterns were measured at three sample-to-detector distances: 1, 10, and 31 m, covering a total q-range of 0.001–7 nm^{-1}. 2D WAXS patterns were measured simultaneously using a CCD Rayonix LX170-HS detector at a sample-to-detector distance of 0.145 m, covering a q-range of 5.26–36.8 nm^{-1}. To improve data statistics, 20 acquisitions were made at each distance and averaged, using an exposure time of 1 s for the WAXS and 1 m measurements, and 0.1 s

for the 10 m and 31 m measurements. Scattering of the solvent (30 wt% EtOH/70 wt% H_2O or D_2O) was subtracted as background from all data files. Further, small-angle X-ray scattering of samples containing 3.0 wt% AGA, with or without 30 wt% ethanol, and a varying amount of NaCl was measured analogously, but samples were measured in individual quartz capillaries. Scattering of the solvent (including ethanol and NaCl) was subtracted as background from all data files. SAXS of samples containing 3.0 wt% AGA in H_2O at pH 3.99, 4.65, 5.10, 6.00, and 6.99, respectively, was also measured on the beamline ID02 [26] at ESRF. The pH of the mixtures was adjusted using a NaOH solution (1 $mol \cdot L^{-1}$) or HCl solution (1 $mol \cdot L^{-1}$), respectively. Gel samples (pH 3.99 and 4.65) were measured in individual quartz capillaries with a typical diameter of around 1.8 mm, while liquid samples were measured in a flow through setup with an inner capillary diameter of 2 mm. Data were acquired at two detector distances of 1.0 m and 9.7 m, at a wavelength of 0.099 nm, using an Eiger2 4 M pixel array detector from Dectris. Data were corrected for flat field, spatial distortion, electronic and dark noise, and transmitted flux. If not stated otherwise, 1D data are radially averaged. 1D data were normalized using the level of water as a standard ($d\sigma/d\Omega = 0.0163\ cm^{-1}$) and dividing by the corresponding path lengths. The temperature was kept constant at 25°C using a Peltier stage LFI3751 from Wavelength Electronics (Bozeman, Montana, USA). For a sample containing 3.0 wt% AGA in H_2O, temperature was varied using the same Peltier stage, and samples were left for equilibration for at least 30 min prior to data acquisition.

VI.3.4. Small-Angle Neutron Scattering

Small-angle neutron scattering (SANS) data were measured at the Institut Laue-Langevin – The European Neutron Source (ILL, Grenoble, France) on instrument D33 [27] for AGA in D_2O and on D11 [28] for AGA in D_2O/ethanol mixtures (with either perdeuterated d6-ethanol, or hydrogenated d0-ethanol). For both instruments, three sample-to-detector distances were used. On D11, the wavelength was 0.46 nm (FWHM 9%) and the distances were 1.4, 8, and 39 m. On D33, the wavelength was 0.60 nm (FWHM 10%) at sample-to-detector distances of 2 m and 5 m, and 1.30 nm (FWHM 10%) at a sample-to-detector distance of 12.8 m. Data were corrected with the program LAMP, accounting for deadtime, transmission, detector background (using measurements with $^{10}B_4C$ as absorber), and

normalizing with monitor, using a flat field obtained from H_2O (1 mm) measurement. The contribution from the empty container was subtracted. Absolute scale was determined from the flux by acquisition of the attenuated direct beams.

Note that as opposed to all other samples, for SANS, samples were not only prepared with D_2O, but (due to the viscosity of the gel) also directly quartz cuvettes with 1.25 mm quartz walls and a sample pathway of 2 mm (model 120-QS from Hellma GmbH, Müllheim, Germany) were used, and to dissolve AGA a heat gun was used to warm up and homogenize the solution. However, the resulting spectra are similar to those obtained by SAXS, i.e., the preparation does not have a significant effect on the structure at the nanoscale.

VI.3.5. Density Measurements

The physical density of AGA was calculated from the densities of solutions containing AGA. The first solution contained 0.5 wt% AGA in water, while the second solution contained 1.0 wt% AGA and 30 wt% ethanol in water. Densities of the two solutions and their respective solvents were measured at 25°C multiple times using a density meter DMA 5000 M from Anton Paar (Graz, Austria), which operates with the oscillating U-tube method. Assuming a linear dependence of the reciprocal density on the mass fraction, the apparent density of AGA was obtained by linear extrapolation, leading to a value of $\rho = 1.339\ g \cdot cm^{-3}$ (apparent volume $V = 1.042\ nm^3$). Measured densities are given in **Table E.1**.

VI.3.6. Molecular Volumes and Scattering Length Densities

The experimentally measured apparent molecular volume of AGA (see **Section VI.3.5.**) was split into two groups: (a) The ammonium diglucuronate moiety and (b) the aglycone moiety. The molecular volume of the aglycone part was estimated using ChemSketch, and the density value obtained for the sugar-based headgroup is close to the classical value of $\approx 1.6\ g \cdot cm^{-3}$ for polysaccharides. The molecular volumes as well as the scattering length densities (SLDs) used for the AGA molecule and the solvents, H_2O, D_2O, ethanol, and d6-ethanol, are summarized in **Table VI.1**.

Table VI.1. Scattering length densities for X-rays (SLD_X) and neutrons (SLD_N), as well as molecular volumes V, physical densities ρ (at 25°C), and molar masses M of the compounds used in this study. Labile hydrogens will exchange with the solvent, and the number of hydrogens concerned is marked as (H/D) in the molecular formula. SLD_N is strongly affected, which is reflected by its dependence on the fraction of exchangeable deuterium in the solvent d (d = 0 in H_2O and d = 1 in D_2O). Note that all other values are given for the compound without any H/D exchange.

compound	formula	M [g·mol^{-1}]	ρ [g·cm^{-3}]	V [nm^{-3}]	SLD_X [10^{-4} nm^{-2}]	SLD_N [10^{-4} nm^{-2}]
water	H_2O	18.015	0.997	0.030	9.41	-0.56
heavy water	D_2O	20.028	1.109	0.030	9.41	6.38
ethanol	C_2H_6O	46.068	0.789	0.097	7.57	-0.34
d6-ethanol	C_2D_6O	52.105	0.892	0.097	7.57	6.10
AGA	$C_{42}H_{55}(H/D)_{10}NO_{16}$	839.963	1.339	1.042	12.24	1.33+1.00d
aglycone	$C_{30}H_{44}(H/D)O_3$	453.677	1.138	0.662	10.61	0.73+0.16d
ammonium diglucuronate	$C_{12}H_{11}(H/D)_9NO_{13}$	386.286	1.688	0.380	15.09	2.36+2.47d

The intensity recorded in small-angle scattering is proportional to the square of the difference in scattering length densities, called contrast. For X-rays, the main contrast is that between solvent and diglucuronate moiety, which is 4.7 times higher than that between solvent and aglycone. For neutrons, the main contrast is between the solvent and the aglycone moiety. Taking into account H/D exchange of labile hydrogens (only 1 for the aglycone part, but 6 for the glucuronate part and 3 for the ammonium ion), the aglycone/D_2O contrast is 3.5 times higher than that of diglucuronate/D_2O.

VI.3.7. Potentiometric pH Titration

The potentiometric titration of a sample containing 3.0 wt% AGA in water and pH measurements were performed at room temperature (≈23°C) using a 905 Titrando high-end titrator for potentiometric titration equipped with a flat membrane pH glass electrode and an 800 Dosino dosing unit from Metrohm (Herisau, Switzerland).

VI.4. Results and Discussion

VI.4.1. Phase Map

The recorded partial ternary phase map of the glycyrrhizic acid monoammonium salt (AGA)/ethanol (EtOH)/H_2O system at room temperature is shown in **Fig. VI.1**. **Fig. VI.1**A is a triangular representation, in which the different macroscopic states are schematically indicated based on the actually investigated points. **Fig. VI.1**B is the same phase map in a rectangular representation, showing only the investigated points. The same rectangular phase map is given in mole fractions instead of weight percent in **Fig. E.1**.

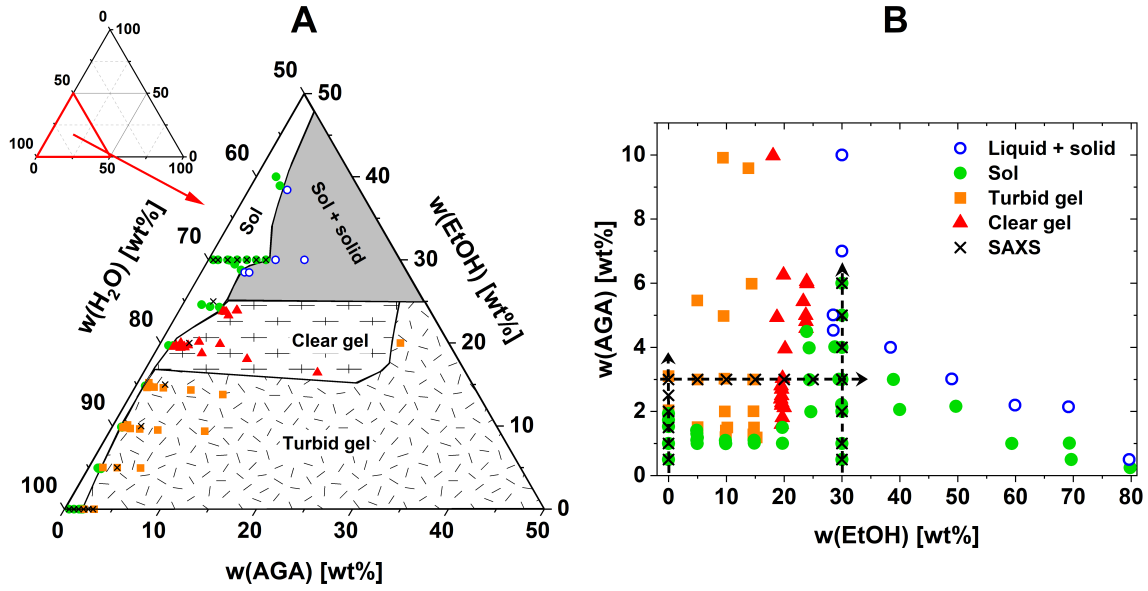

Fig. VI.1. (A) Partial ternary phase map of the AGA/EtOH/H_2O-system at room temperature (≈23°C) in wt%. Investigated compositions are indicated. (B) Rectangular representation of the determined phase map at room temperature. Empty blue points indicate a saturated sol of AGA in equilibrium with excess solid AGA, green points indicate a monophasic sol, orange squares a turbid gel, and red triangles a clear gel. Black crosses mark the compositions of samples used for small-angle X-ray scattering (SAXS). Black dashed arrows signal the three dilution lines examined by SAXS. Note that the turbidity of the gel does not originate from insoluble residues of AGA, but from inhomogeneities within the gel. The same rectangular phase map (B) is given in mole fractions in **Fig. E.1**.

It is important to note that the reported macroscopic properties in **Fig. VI.1** and **Fig. E.1** are valid for samples that were prepared without heating, see **Section VI.3.2**. The effect of heating can be quite different in different systems of LMW gelators, as discussed for example by Draper and Adams [29]. In this case, heating during homogenization of the sample can affect the gelation process, leading to either a turbid or a clear gel. The turbidity of the gels is not assigned to a macroscopic phase separation, but to inhomogeneities in the gel network. Note that for all gels in this work a shear-thinning behavior and self-healing

properties are observed. Vigorous shaking of a sample leads to a transition from a gel to a fluid state. At rest, the gel can reform after a while. In absence of EtOH, binary mixtures of AGA and water are liquid sols at AGA contents below 2.0 wt% and a turbid gel at an AGA content of at least 2.0 wt%.

In the following, the lowest concentration of AGA, where gelation occurs, will be referred to as the critical gel concentration (CGC). However, the CGC in this system is also influenced by the method of sample preparation. If samples are heated during sample preparation, and then re-cooled to room temperature without agitation, a (weak) gel can already form at 0.5 wt% of AGA, compared to 2.0 wt% without heating. In both cases, not only the gel samples, but also the sol samples can appear birefringent between crossed polarizers. The sols can either appear isotropic or birefringent, depending on sample preparation, i.e., samples are birefringent if they are liquid, but exhibit increased viscosity, whereas they are isotropic if the viscosity is seemingly close to that of pure water. The increased viscosity indicates the presence of gel-like domains, which should be responsible for birefringence. Without heating, the addition of EtOH gradually reduces the CGC to 1.2 wt% AGA at 15 wt% EtOH, while the formed gels still appear turbid. A further increase of the EtOH content on the other hand significantly increases the CGC to about 4.5 wt% AGA at 25 wt% EtOH and results in the formation of clear gels. At even higher EtOH concentrations, gel formation is no longer observed. Instead, only isotropic colloidal sols with a maximum solubility of AGA are formed. An overall maximum solubility is found at 30 wt% EtOH, where around 6.0 wt% AGA are solubilized. Above 30 wt% EtOH, the solubility of AGA gradually decreases until AGA is barely soluble in pure EtOH.

The fundamental features of the phase behavior are that addition of ethanol induces first a) a vanishing of the turbidity indicating large domains of heterogeneities, then b) with higher ethanol content, a sudden gel-sol transition, and c) with even more added ethanol, phase separation with excess solid, identified as mainly solid AGA microcrystallites, induced by anti-solvent effects dominant at high EtOH concentration.

Before coming to the molecular mechanisms in the ternary fluid, the focus first lies on the microstructures formed in binary mixtures of AGA and water, followed by the modifications observed in ternary mixtures of AGA/EtOH/H_2O. Small-angle X-ray scattering (SAXS) measurements along three dilution lines (black crosses in **Fig. VI.1**) are discussed. The binary dilution line does not involve EtOH and covers 0.5 wt% to 3 wt% AGA in water.

The second dilution line concerns the effect of EtOH on the microstructuring of samples containing 3 wt% AGA. Thus, the EtOH content is varied between 0 wt% and 30 wt% EtOH. A third dilution line at a constant EtOH content of 30 wt%, where a gel can no longer form, covers the sol state of the mixtures over the whole solubility range of AGA up to 6 wt%. The three dilution lines are signaled in the phase map (**Fig. VI.1**B) by three black dashed arrows with black crosses identifying the explored points.

VI.4.2. Revisiting the Glycyrrhizic Acid Ammonium Salt Self-Assembly in Water

Before heading to ternary systems of AGA/EtOH/H_2O, the purpose of this section is to describe the AGA molecule with respect to its dimensions and to identify the microstructures formed in binary mixtures of AGA and water. The micro-structuring in binary mixtures of AGA and water was initially explored in two seminal papers by Saha *et al.* [12], who focused on the elucidation of the microstructures formed in binary mixtures of AGA and water by means of atomic force microscopy (AFM) of dried samples, and by Matsuoka *et al.* [11], who described the effect of pH on the aggregation of glycyrrhizic acid (GA) at lower GA concentrations (≤1 wt%). Recently, Tucker *et al.* [13] examined the self-assembly of lower concentrations of AGA (<0.5 wt%) in D_2O by means of small-angle neutron scattering (SANS). Note that samples were heated to 45°C and ultrasonicated for 30 min, and samples measured by SANS had not gelled. All of the investigations agree on the formation of rod-like aggregates and suggest that formed gels are fibrillar networks. However, the understanding of the microstructuring of AGA is still quite limited in the literature. Adding SAXS information on a large q-range and a large concentration-range, complemented by SANS, a complete picture of the aggregation of AGA in water is proposed in this work.

Glycyrrhizic acid (GA) is a monodesmosidic saponin consisting of a hydrophopic pentacyclic triterpenoid aglycone part (18β-glycyrrhetenic acid) and a hydrophilic glycone part made of a disaccharide (β-(1,2)-diglucuronic acid), see **Fig. VI.2**A. AGA, as used in this work, is the monoammonium salt of GA. As a result, AGA is slightly amphiphilic. The molecule contains three carboxylic acid groups, two in the hydrophilic part (pK_{a1} and pK_{a2}) and one in the hydrophobic part (pK_{a3}). Zeng and Hu [30] reported the dissociation

constants of glycyrrhizic acid to be 3.98 (pK_{a1}), 4.62 (pK_{a2}), and 5.17 (pK_{a3}). Our potentiometric titration of an aqueous 3 wt% AGA sample, see **Fig. E.2**, suggests equal apparent dissociation constants for the remaining two carboxylic acid groups of 5.01 (apK_{a2} and apK_{a3}). The pH of a binary mixture of 3 wt% AGA and water is around 4.6, suggesting that at least 85% of the GA molecules are at least singly deprotonated in solution, if pK_{a1} is assumed to be 3.98. Note that Tucker *et al.* [13] reported similar pH values for their AGA solutions, but, based on their data on the surface adsorption of AGA with and without added electrolyte, assumed that GA molecules are mainly protonated and thus nonionic, in contrast to what is expected for the given pH and pK_a values. A plot of the expected fractions of all protonated GA species in solution as a function of pH is shown in **Fig. E.3**, assuming either the pK_a values reported by Zeng and Hu [30] or $apK_{a2} = apK_{a3} = 5.01$, as measured in this study (**Fig. E.2**), and $pK_{a1} = 3.98$, as reported by Zeng and Hu. Matsuoka *et al.* [11] have shown that the pH strongly affects the self-assembly of GA. They found that rod-like aggregates form above the critical micelle concentration (CMC) at pH 5–6, whereas they no longer observed any self-assembly at pH 7 by means of light scattering, suggesting that mono- and di-deprotonated forms of GA are required for self-assembly.

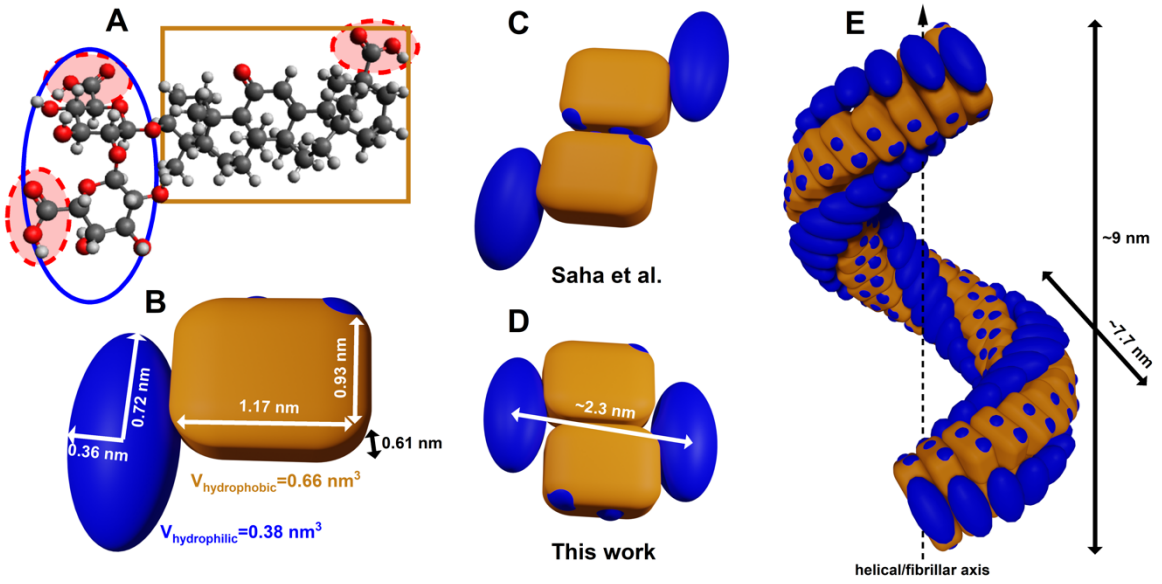

Fig. VI.2. (A) Ball-and-stick model of the glycyrrhizic acid (GA) molecule. The blue ellipse illustrates the modelling of the hydrophilic diglucuronic acid part as a blue ellipsoid and the orange rectangle illustrates the modelling of the hydrophobic aglycone part as an orange cuboid. Red ellipses underline the positions of negative charges in the case of dissociation. (B) Scaled block model of the GA molecule. The assumed dimensions as well as the volumes of the hydrophilic and the hydrophobic parts, see main text, are indicated. Blue dots on the orange cuboid represent the hydrophilic carboxylic acid and carbonyl groups of the aglycone part. It should be noted that those two groups are not included in the given hydrophilic volume, but in the hydrophobic volume. (C) Dimeric GA subunit of fibrillar stacks of GA as proposed by Saha *et al.* [12]. (D) Dimeric GA subunit of fibrillar stacks of GA proposed in this work. The indicated length of 2.3 nm is inferred from the first peak of the form factor oscillation in SAXS, see **Fig. VI.4**B. (E) Scaled right-handed helix comprising stacks of GA-dimers.

The GA molecule has a L-shaped structure, which can be coarse-grained into a double block model similar to the one proposed by Saha *et al.* [12], see **Fig. VI.2**B. The hydrophobic aglycone part (orange) is modelled as a cuboid and the hydrophilic glycone part (blue) as an ellipsoid. Blue dots drawn on one side of the slightly flat orange cuboid reflect the local polarity induced by the presence of carboxylic acid and carbonyl groups of the aglycone part. However, the aglycone part as a whole is considered as the hydrophobic part of the molecule in the following. As shown in **Table VI.1**, molecular volumes of $V = 1.04\ nm^3$, $V_{hydrophobic} = 0.66\ nm^3$, and $V_{hydrophilic} = 0.38\ nm^3$ are deduced for AGA, the aglycone part, and the glycone part, respectively. Since Saha *et al.* [12] inferred a stacking distance of 0.61 nm between AGA molecules within fibrils, we use 0.61 nm as the height of the cuboid and hence as the vertical stacking distance in the helical stacks. The length of the cuboid is estimated to be 1.17 nm, leaving a width of 0.93 nm to get the correct $V_{hydrophobic}$. The glycone part is approximated as a prolate ellipsoid with an ellipticity (ratio of axial radius and equatorial radius) of 2. The equatorial radius and the axial radius are then given as 0.36 nm and 0.72 nm, respectively. The combined length of the whole molecule is then $2 \cdot 0.36\ nm + 1.17\ nm = 1.89\ nm$, which is close to the energy minimized length of glycyrrhizic acid of 1.86 nm [12].

It was already shown that AGA forms long helical fibrils leading to hydrogel formation in aqueous solution. In this work, a dimeric building block similar to the one suggested by Saha *et al.* [12] is assumed, which is also supported by the fibrillar diameter they deduced from wide-angle X-ray scattering (WAXS) and AFM. They suggested that aglycone moieties interact laterally, leaving the hydrophilic glycone units exposed to water on opposite sides. In their depiction, adapted in **Fig. VI.2**C, the glycone units maximize the distance to each other, resulting in the hydrophilic groups of the aglycone parts to point towards each other, thus not being exposed to water. In this work, more compact dimers are suggested, as depicted in **Fig. VI.2**D, with the hydrophilic groups of the aglycone parts being exposed to water. Note that, though they are referred to as dimers, these subunits are not actually dimers in water, but stacking units within larger aggregates. Structures of actual dimers of GA in water were examined by means of molecular dynamics simulations by Zelikman *et al.* [31]. Saha *et al.* [12] reported that the fibrils formed by AGA have a right-handed twist with a periodicity of 9 nm. Both WAXS data presented by Saha *et al.* and our small-angle scattering data are in agreement with a fibrillar diameter of around 3 nm. It should be noted that, though Saha *et al.* deduced a fibrillar diameter of 2.5 nm from the height-profile of

their AFM measurements, the lateral thickness of the fibrils in their AFM images seems to be close to 10 nm. The full width at half maximum of the fibrils' transversal height profile, i.e., the height profile perpendicular to the fibrillar axis, they give is around 7.7 nm. Thus, in this work it is proposed that AGA fibrils with a diameter of around 3 nm form right-handed helices with an outer diameter of 7.7 nm and a periodicity of 9 nm. A scaled representation of one period (≈9 nm) of a right-handed helix made of our proposed dimeric GA subunits is shown in **Fig. VI.2**E. A periodicity of 9 nm with a stacking distance of 0.61 nm is obtained for 30 stacks of GA dimers with an intra-stack local rotation of the dimers around their own axis by approximately 25° per stack. This means about 30 stacks induce one helical turn. The periodicity in the z-plane (parallel to the fibrillar axis) would correspond to a weak broad band expected around 0.7 nm^{-1} in SAXS. The illustration given in **Fig. VI.2**E is also in good agreement with forward scattering and fits to a simplified model, as will be shown in **Section VI.4.5**. Note, however, that the given dimensions of the helical structure (i.e., helical diameter and period) are likely polydisperse in solution, as distinct features in the scattering patterns would be expected for monodisperse helices.

The small-angle scattering analysis is started by a comparison of radially averaged SAXS and SANS of a gel containing 3 wt% AGA in H_2O or D_2O, respectively, see **Fig. VI.3**. Samples were measured at their natural pH or pH*, respectively. The pH of 3 wt% AGA in H_2O is around 4.6, while the pH*, i.e., the direct reading of the H_2O-calibrated pH electrode in D_2O, of 3 wt% AGA in D_2O is around 4.8, which is equivalent to a pH of around 4.9 [32]. Note that the same phase behavior is found for D_2O instead of H_2O. Due to different scattering contrasts (see **Sections VI.3.3.** and **VI.3.4.** for details), SAXS is mostly sensitive to the hydrophilic diglucuronic acid moiety, while SANS is mostly sensitive to the hydrophobic aglycone moiety. While the low- (<0.06 nm^{-1}) and mid-q (0.06 nm^{-1} to 1.5 nm^{-1}) ranges of the scattering curves are similar, the high-q (>1.5 nm^{-1}) range exhibits characteristic form factor oscillations in SAXS, the first one ranging from q = 2 nm^{-1} to 5 nm^{-1}, but not in SANS, where the intensity falls off only at q ≈ 5 nm^{-1}. From this it can be concluded that the form factor oscillations in SAXS are originating from repeat distances of hydrophilic diglucuronic acid moieties, i.e., that the structure is core-shell-like, where mostly the shell is seen in SAXS and mostly the core is seen in SANS. Note that the repeat distance of the hydrophobic aglycone part, as expected from the structure illustrated in **Fig. VI.2**E, should be reflected in the neutron scattering at higher q-values than measured (a repeat distance of $D^* = 0.61$ nm would appear at $q = 2\pi/D^* = 10.3$ nm^{-1}). In fact, the first

minimum of the form factor oscillations in SANS is seen just within the measured q-range. The low-q intensity is assigned to the gel-network formed by "infinite" fibrils. Comparing SAXS and SANS of a liquid sample containing 1 wt% AGA, see **Fig. E.4**, the same observations are made. Coexistence of shorter fibrils and "infinite" fibrils is suggested by the scattering patterns (see end of **Section VI.4.2.** and fits in **Section VI.4.5.**) and is in agreement with macroscopic observations, as will be discussed throughout this work. Radial anisotropy of scattering is observed for all gel samples, see **Fig. E.5**. The 2D SAXS pattern of the gel containing 1.5 wt% AGA in H_2O is exemplarily shown in **Fig. E.6**A. Anisotropy is almost exclusively seen in the mid-q range and is mostly induced by shear in the process of filling capillaries with the gel samples, i.e., radial scattering of heated samples gelling inside the capillary upon re-cooling is rather isotropic. However, the anisotropy only concerns the scattering intensity, while the scattering pattern itself is independent of the azimuthal angle. This is clearly seen comparing the 1D spectra of the sample containing 1.5 wt% AGA at different azimuthal angles Ψ, see **Fig. E.6**B. As shown in **Fig. E.6**C, the scattering intensity can be explained by the sum of two contributions: (a) An isotropic (Ψ-independent) power law $I_{iso}(q)$ and (b) an anisotropic (Ψ-dependent) peaked profile $C(\Psi)\cdot I_{aniso}(q)$, where $C(\Psi)$ only depends on Ψ and $I_{aniso}(q)$ only depends on q (i.e., the scattering angle and not the azimuthal angle). The periodicity of $C(\Psi)$ is displayed in **Fig. E.6**B, from which a period of about 180° can be inferred. The dependence of the scattering intensity on the azimuthal angle indicates (shear-induced) alignment of scatterers along particular directions. In this case, the preferential direction corresponds to the direction of capillary filling. Since the peak position as well as the peak width is, however, independent of the azimuthal angle, i.e., an isotropic periodicity of uniform distribution is observed, the repeat distance between scatterers is not influenced by the alignment. This observed heterogeneity in orientation means that local alignment is imposed by the presence of long fibrils, and only larger domains are oriented by shear. Thus, liquid crystalline domains with inherent preferential orientation of the fibrils are suggested. A preferential orientation of shorter fibrils is expected to be imposed by the surrounding "infinite" fibrils. The ordering of the shorter fibrils may be described as a nematic ordering. Note that others have successfully created lyotropic nematic gels by inducing gel formation in a nematic phase formed by a surfactant system by adding low-molecular-weight gelators, which form a fibrillar gel network [33]. We note that these systems are rather complex and contain multiple components, whereas a simple binary system of AGA and water can form a similar structure. Shear-induced alignment of domains of pre-oriented shorter fibrils within a network of "infinite"

fibrils can also explain the observation of one anisotropic and one isotropic scattering contribution. On capillary filling, a portion of the domains is aligned in the direction of capillary filling, while another portion remains isotropically oriented. Scattering of the aligned domains is anisotropic, whereas scattering of the isotropically oriented domains is isotropic. In principle, both contributions should have the same scattering pattern, i.e., a peaked profile with identical peak position, with the difference of a Ψ-independent intensity in the isotropic case and a Ψ-dependent intensity in the anisotropic case. However, since the intensity is much more pronounced in the anisotropic contribution, the peaked profile is included in the anisotropic contribution during principal component analysis (PCA) and thus subtracted from the isotropic contribution. The remaining isotropic scattering is the observed power law.

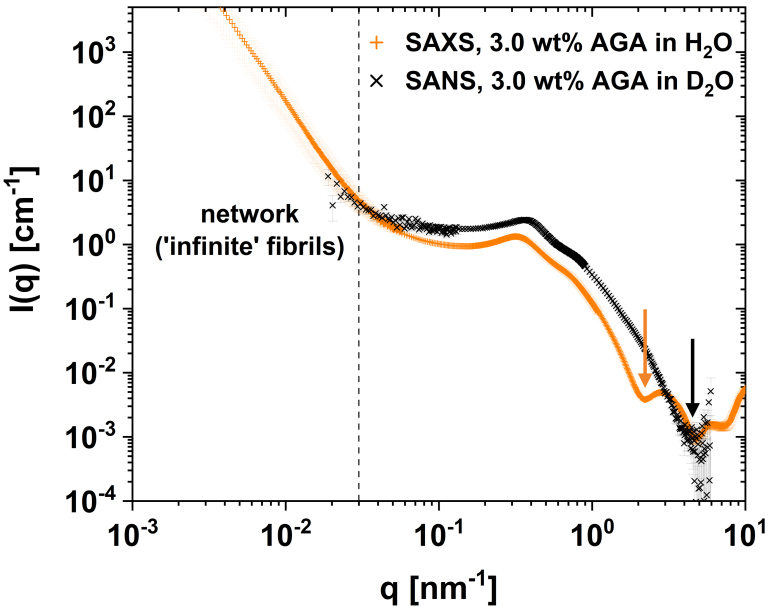

Fig. VI.3. Comparison of the SAXS (orange) and SANS (black) data obtained for two samples containing 3.0 wt% of AGA in H_2O or D_2O, respectively. The low-q scattering intensity to the left of the vertical dashed line reflects the scattering of the gel network formed by "infinite" fibrils. Orange and black arrows indicate the first minimum of the form factor oscillations seen in SAXS and SANS, respectively.

Anisotropy of the gel samples is also seen macroscopically between crossed polarizers. Birefringence of a gel made of 3.0 wt % AGA in H_2O observed between crossed polarizers is shown in **Fig. E.6D**.

SAXS spectra measured along the binary dilution line in the phase map (**Fig. VI.1**), covering mixtures of 0.5 wt% to 3.0 wt% AGA in H_2O, are shown in a logarithmic scale in **Fig. VI.4**A. To highlight the form factor oscillations, the high-q data are also plotted in a linear scale in **Fig. VI.4**B. A green color indicates that the samples containing 0.5 wt% to 1.5 wt%

AGA were still able to flow under gravity, while an orange color indicates the gel-like nature of the samples containing 2.0 wt% to 3.0 wt% AGA. It is important to note that the liquid-like samples can also be birefringent and are also capable of forming gels, if they are heated and re-cooled with sufficiently low agitation. Further, the cooling rate can certainly influence the gelation process. Lower cooling rates are expected to favor the growth of longer fibrils, thus favoring gel formation. The spectra in **Fig. VI.4** suggest that similar microstructures form in all samples. Except for the intensity, form factor oscillations are almost identical in all cases with peak positions around $q = 2.74\ nm^{-1}$, corresponding to a length of $D^* = 2\pi/q = 2.3$ nm, and $q = 6.16\ nm^{-1}$, corresponding to $D^* = 1.0$ nm. This proves that the close-range ordering of the AGA molecules is identical in the examined concentration-range for both liquid-like and gel-like samples. The length of 2.3 nm reflects the spacing between centers of the hydrophilic diglucuronic acid moieties perpendicular to the helical fibril's long axis, i.e., the diameter of the fibril. The second peak ($q = 6.16\ nm^{-1}$) is either a second order peak of the first peak ($q = 2.74\ nm^{-1}$) or reflects the average repeat distance of the hydrophilic groups along the fibril. If the latter is the case, a rotation of each stack around its own local axis by approximately 25° relative to its neighboring stacks, as illustrated in **Fig. VI.2**E, is implied. Saha *et al.* [12] deduced a comparable diameter for AGA fibrils from AFM (2.5 nm) of dried samples and WAXS (2.8 nm) of a lyophilized gel. Small changes of the diameter could be induced upon solvent removal. Further, the scattering of the liquid 0.5 wt% AGA sample exhibits a q^{-1} decay in the mid-q range, in agreement with a rod-like or fibrillar scatterer. As can be seen in SANS of samples containing 0.1 wt% to 3.0 wt% AGA, see **Fig. E.7**, similar scatterers are formed even at 0.1 wt% AGA, indicating that the critical aggregation concentration (CAC) is below 0.1 wt% (1.2 mM) AGA. In addition to the underlying slope of approximately -1, a second contribution to the mid-q scattering emerges in the form of a structure factor peak with increasing AGA concentration. To extract the correct structure factor peak positions, the structure factor S(q) is approximated by dividing the data shown in **Fig. VI.4** by the data obtained for the sample containing 0.5 wt% AGA, see **Fig. E.8**A. The peak position is indicative of a typical interaxial distance that is the 2D analogue of a mesh size observed in isotropic gels. Hence, the interaxial distance $\xi_{exp} = 2\pi/q_{peak}$ is derived. Note that the peak does not reflect a 2D mesh size of the network formed by the "infinite" fibrils, but the interaxial distance between both "infinite" fibrils and shorter fibrils and is caused by electrostatic repulsions between the fibrils. A second oscillation is visible at higher AGA concentrations, showing a repeat distance in the directions perpendicular to the helical fibrils that is a few times the interaxial

distance ξ_{exp}. The obtained values for ξ_{exp} are 24.2 nm (1.5 wt% AGA), 20.8 nm (2.0 wt% AGA), 19.5 nm (2.5 wt % AGA), and 17.1 nm (3.0 wt% AGA) and are plotted as a function of the volume fraction of AGA φ(AGA) in a logarithmic scale in **Fig. E.8**B. Note that only the volume fraction of the AGA molecules participating in aggregate formation should be used, but since the actual CAC is not known and relatively low (<0.1 wt%), the total volume fraction of AGA is used. The slope of -0.48 indicates a 2D dilution law, in which all present molecules participate. This is to be expected for charged repulsive helical fibrils with an average length larger than the interaxial distance. Note that, the slope of the low-q scattering is typical for gels, but also measured for the solvent due to parasitic scattering and reflections at interfaces (see **Fig. E.9** for a comparison of the solvent subtracted scattering to scattering of only H_2O). However, the low-q scattering intensity is significantly higher for all samples containing AGA than for just water. This conforms to the formation of "infinite" fibrils by AGA, which is consistent with the formation of a gel, but is also influenced by microheterogeneities of the quartz capillaries and the gel.

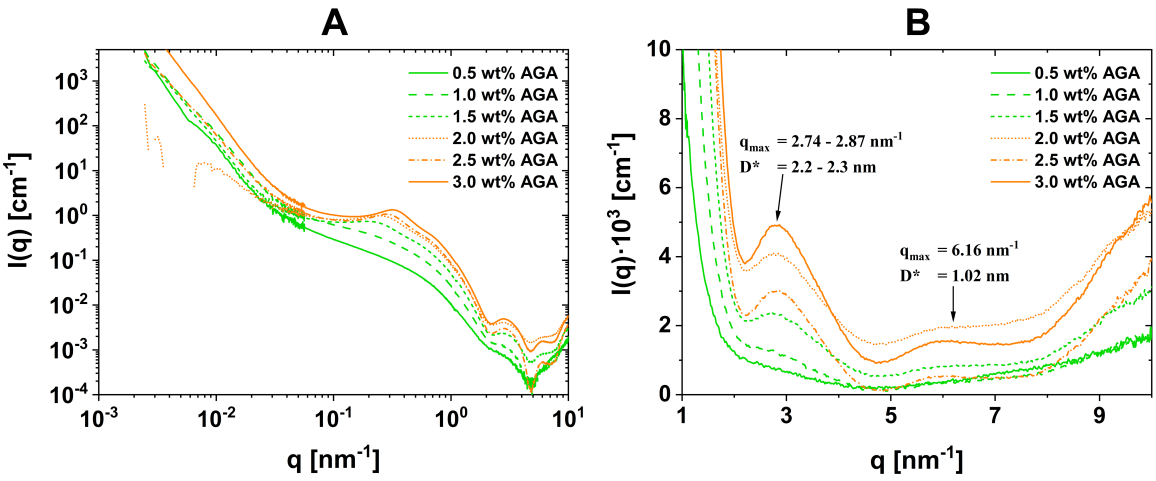

Fig. VI.4. (A) SAXS spectra of binary mixtures of AGA and water with AGA concentrations ranging from 0.5 wt% to 3.0 wt% in logarithmic scale. Sol samples are shown in green, while samples that formed a turbid gel are shown in orange. Solvent scattering (H_2O) is subtracted. (B) The form factor oscillations seen in the higher q-range are given in a linear scale. The maxima of the form factor oscillations are indicated.

Since the average length of the helical fibrils is around 25 nm (see **Section VI.4.5.**), and the number of AGA stacks per helical period of 9 nm is around 30, we can evaluate the overlap volume fraction φ*, see **Appendix E.2**. Assuming that the average length is roughly independent of the AGA concentration (*vide infra*) and not taking into account additional space required due to electrostatic repulsion, φ* is around 1.00 at a concentration of 2.8 wt% AGA and increases to 1.06 at 3.0 wt% AGA, meaning that the semi-dilute regime is reached at around 2.8 wt% AGA. Taking into account a few nanometers of repulsion

between negative charges, the samples showing an interaction peak in SAXS (≥1.5 wt% AGA) are well above the semi-dilute regime and the electrostatic repulsion between fibrils justifies the swelling relation that is nearly two-dimensional. As discussed above, the data and macroscopic appearance suggest that a portion of the AGA molecules forms "infinite" fibrils responsible for the gel-like network, while the other portion of AGA molecules forms shorter bits of fibrils that are slightly longer than their interaxial distance. The orientation of the latter is imposed by the orientation of the longer fibrils. For the sake of completeness, the possibility of a gel made of only "infinite" fibrils without any shorter fibrils is briefly discussed. Due to the fibrillar structure and the birefringence (anisotropy) of the gels, the gel can be modelled as "infinite" fibrils made of dimeric stacks of AGA (**Fig. VI.2**E) oriented in a hexagonal lattice to calculate the expected 2D mesh size ξ_{calc}. To this purpose, on the one hand the fraction of AGA molecules participating in the fibril formation and on the other hand the helicity of the fibrils, i.e., the average number of individual fibrils forming a superhelical fibril, are varied to match ξ_{calc} and the experimentally found ξ_{exp}. For each combination of the two parameters, the total available length of fibrils is given by the AGA concentration. The calculation is given in **Appendix E.3.** and a plot of ξ_{exp} versus ξ_{calc} is shown in **Fig. E.10**. It can be seen that ξ_{exp} and ξ_{calc} perfectly match for two borderline cases: (a) Only 90% of the AGA molecules form fibrils that do not form any superhelices (helicity of 1), or (b) all AGA molecules form fibrils that form superhelices in average consisting of 1.1 fibrils (helicity of 1.1). Case (a) would mean that 10% of the AGA molecules are dissolved as monomers (or dimers), which is unlikely because fibrils already form at much lower concentrations. Case (b) does in principle conform to the AFM images presented by Saha *et al.* [12], where few entanglements of fibrils are seen. Of course, any intermediate case between (a) and (b) would be possible, and an intermediate case also seems reasonable. Saha *et al.* also reported only long ("infinite") fibrils and no shorter ones, opposing what we suggest. Probably the shorter fibrils grow into larger ones during the process of solvent evaporation prior to AFM imaging. However, our data suggest the coexistence of "infinite" and shorter fibrils (see further discussion and especially the fits in **Section VI.4.5.**). Note that, since the dilution law is almost 2D, shorter fibrils are expected to be in average quite close to each other in the direction of the fibrillar axis. This could result in a relatively small error, when assuming only "infinite" fibrils, if the shorter fibrils have the same local orientation. While the orientation of the short fibrils is in principle expected to follow that of the "infinite" fibrils, the assumption of a perfect local orientation in a hexagonal lattice remains an approximation.

Note that also the gel's shear-thinning and self-healing properties may be explained by co-existence of "infinite" and shorter fibrils. On applying shear, "infinite" fibrils are broken down into shorter fibrils, in turn leading to the destruction of the gel network and the transition to a fluid state. The self-healing of the gel can be explained by regrowth of the "infinite" fibrils by both diffusion of AGA monomers/dimers and interconnection of shorter fibrils. It is to be expected that the self-healing properties are the better the higher the AGA concentration is, because more shorter fibrils are in close proximity to each other with increasing AGA concentration. This is most likely the reason why, in contrast to higher concentrations, no stable gel is formed below 2.0 wt% AGA if the sample is continuously agitated at room temperature during sample preparation, even though a gel can be formed if the sample is mixed at elevated temperature and re-cooled at rest.

The proposed structures are in good agreement with the data presented by Matsuoka *et al.* [11] for 5 mM GA (≈0.4 wt%) at pH 5 and Tucker *et al.* [13] for AGA in a concentration range from 1 mM to 5 mM (≈0.08 wt% to 0.4 wt%). It needs to be emphasized that measurements of both Matsuoka *et al.* and Tucker *et al.* were performed at significantly lower concentrations than the majority of the measurements presented in this study. However, as mentioned before, the here presented data suggest that for all investigated concentrations the same microstructures are formed. Matsuoka *et al.* attempted to fit their SAXS data to the form factor of a rod-like scatterer and derived a radius of 1.5 nm and an average length of 21 nm, whereas Tucker *et al.* attempted to fit their SANS data to a model of a prolate core-shell ellipsoid and derived an outer radius of 1.6 nm and an ellipticity around 17, corresponding to a length of 27 nm. As can be expected, both models yield similar results. Note that their results are in favor of the assumption of a roughly constant average fibrillar length, as three independent studies suggest fairly similar values for different concentrations. A diameter of 3 nm is in good agreement with our proposed fibrillar structure, where the center-to-center distance between two hydrophilic diglucuronic acid moieties is 2.3 nm, giving an outer diameter of approximately 3 nm if two times the radius of the hydrophilic moiety (0.36 nm) is added. Tucker *et al.* suggested that gel formation originates from a 3D network of the long prolate ellipsoids, because they found no indications of a detectable number of longer ("infinite") fibrils. We emphasize that the sample preparation has a strong influence on fibrillar growth and that the "infinite" fibrils cannot be distinguished from shorter ones in the mid-q range, and suggest that the shorter (≈25 nm) elongated aggregates are indeed shorter fibrils with no structural difference compared to the "infinite" fibrils.

The observation that gelation is enhanced by pre-heating the sample and letting it re-cool at rest, is in agreement with that idea, because (slow) cooling from a dissolved monomeric (or dimeric) state, see **Section VI.4.4.**, is expected to favor longer growth of the fibrils due to a smaller number of "nucleation" sites. In fact, Tucker *et al.* heated their samples to 45°C and ultrasonicated them for 30 min, which likely prevents the formation of longer fibrils. Further, Tucker *et al.* did not measure the low-q range <0.06 nm^{-1}, where scattering of "infinite" fibrils is detected in this study.

VI.4.3. Modification of the Microstructures by the Addition of Ethanol

To study the effect of ethanol (EtOH) on the microstructures of AGA, SAXS spectra of samples containing 3 wt% AGA and a varying amount of EtOH in H_2O were recorded and are shown in a logarithmic scale in **Fig. VI.5**. Samples containing 0 wt% to 20 wt% EtOH are birefringent gels, whereas samples containing 25 wt% or 30 wt% EtOH are isotropic liquids. The scattering patterns and the fact that a gel still forms, prove that the fibrillar structure persists up to 20 wt%. Also, the positions of the high-q form factor oscillations remain virtually unchanged upon addition of EtOH, suggesting unchanged close-range ordering of the AGA molecules, at least as far as the cross-section perpendicular to the fibrillar axis, i.e., the diameter of the fibril, is concerned. At 20 wt% EtOH, the form factor oscillations start to vanish, until they are completely gone at 30 wt % EtOH. This suggests that the close-range ordering of the AGA molecules changes, which is clearly visible at 30 wt% EtOH, where only an interaction peak originating from repulsive aggregates much smaller than the fibrils remains. The smaller aggregates at 30 wt% EtOH are expected to contain a significant amount of EtOH and are a result of EtOH acting as a co-solvent to make the water/EtOH mixture a better solvent for AGA, breaking down the fibrillar stacking of AGA, and will be discussed in more detail in **Section VI.4.4**. Since a gel still forms at 20 wt% EtOH, "infinite" fibrils must still form, and the vanishing of the form factor oscillations suggests that two different close-range orderings of the AGA molecules coexist: (a) Fibrillar stacks of AGA molecules and (b) smaller, less-ordered aggregates of AGA containing EtOH. A slope of -0.92 in the mid-q range suggests that there are still fibrils in the liquid sample at 25 wt% EtOH, which are insufficient in number or length to enable gel

formation (similar to the liquid samples in the binary mixtures of AGA and water, see **Section VI.4.2.**, with the difference that the form factor oscillations vanish with EtOH). This suggests that more and more fibrils are broken down into smaller aggregates with an increasing amount of EtOH. Note that, as can be inferred from the phase map in **Fig. VI.1**, it is still possible to form a gel at 25 wt% EtOH if the AGA content is increased to 4.6 wt%, i.e., it is possible to increase the length or number of the remaining fibrils by increasing the AGA concentration. This is no longer possible at 30 wt% EtOH.

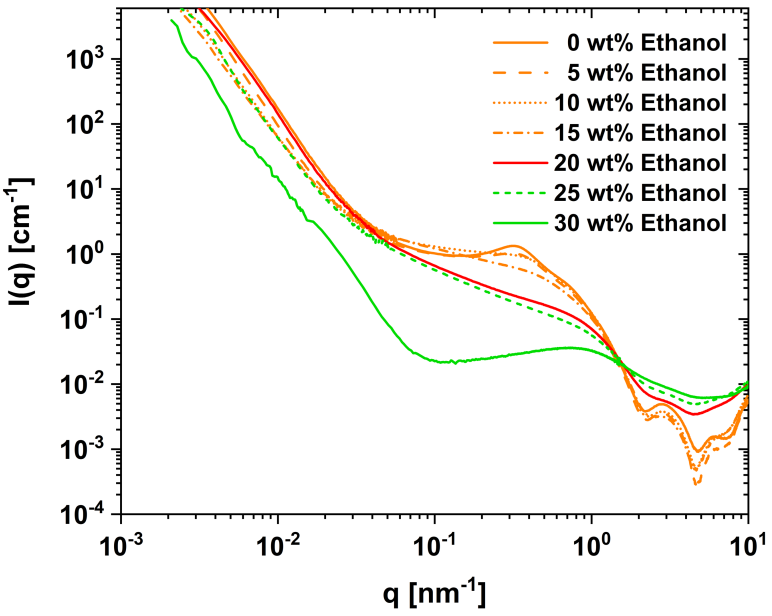

Fig. VI.5. SAXS spectra of ternary mixtures of AGA/EtOH/H_2O at a constant AGA content of 3 wt% and a varying EtOH content. The EtOH concentration is increased from 0 wt% to 30 wt% in steps of 5 wt%. Note that the spectrum at 0 wt% EtOH is identical to the spectrum of the binary mixture of 3 wt% AGA and H_2O, shown in **Figs. VI.3** and **VI.4**. An orange color indicates a turbid gel, a red color indicates a clear gel, and a green color indicates a liquid behavior. The q-range around the correlation peak is given in linear scale in **Fig. E.11**.

Before discussing the structure factor peak around q = 0.3 nm^{-1}, it is worth noting that the shear-induced anisotropy of the mid-q scattering data originating from capillary filling does influence the visibility of the structure factor peak (see **Section VI.4.2.** and **Fig. E.6**). However, the anisotropy, see **Fig. E.5**B, is consistent and quite reproducible, i.e., observed differences of the structure factor peak in the averaged spectra of different samples are not merely a result of random differences in anisotropy caused by capillary filling. Upon addition of EtOH in presence of 3 wt% AGA, the interaction peak around q = 0.3 nm^{-1} vanishes above 5 wt% EtOH, best seen in a linear scale in **Fig. E.11**. This observation would be in line with a reduced surface charge density of the fibrils, resulting in decreased electrostatic repulsion between fibrils. Surface charge density can be reduced by protonation of the

carboxylic acid moieties of AGA and/or penetration of EtOH in the fibrillar structure. It is suggested in the literature that the pK_a value of a carboxylic acid in aqueous solution increases with an increasing EtOH concentration, because the relative permittivity of the solvent decreases, leading to a decreasing degree of dissociation [34,35]. In this case, the pH should increase with increasing EtOH content. However, the pH is found to actually decrease from 4.63 at 0 wt% EtOH to 4.33 at 15 wt% EtOH, indicating a slightly higher degree of dissociation in presence of EtOH. Thus, it can be excluded that the effect of EtOH as a cosolvent on the acid dissociation constants of AGA is responsible for the vanishing of the repulsive interaction peak.

It is also known that EtOH decreases the surface charge density of surfactant micelles by increasing their surface by penetration of the micelles [36]. A similar effect could play a role here and would give an explanation for the counter-intuitive decrease of pH upon addition of EtOH. If incorporation of EtOH into the fibrils would slightly increase the stacking distance of AGA molecules parallel to the fibrillar axis, the increased spacing between the carboxylic acid moieties would enable a higher degree of dissociation according to the universal charge regulation model [37]. While some penetration of EtOH in the fibrils to a small extent cannot be excluded, the spacing of the carboxylic acid moieties certainly changes when fibrils break down into smaller aggregates containing EtOH. Thus, the structural changes could explain why the pH decreases with addition of EtOH.

Hence, EtOH has two opposing effects on the dissociation of the carboxylic acid moieties and therefore on the pH: (a) EtOH reduces the relative permittivity of the solvent and makes the solvent less favorable for dissociated ions, which results in an increasing pH, and (b) EtOH increases the distance between carboxylic acid moieties of neighboring AGA molecules, enabling a higher degree of dissociation and thus decreasing the pH. The latter is certainly achieved by the formation of smaller solvent-containing aggregates, i.e., by a change of the microstructuring, and possibly by incorporation of some EtOH into the fibrillar structure. Up to 30 wt% EtOH, the pH decreasing effects exceed the pH increasing co-solvent effect. Above 30 wt% EtOH, however, the pH increases with increasing EtOH content, because the structural change from AGA fibrils to smaller aggregates of AGA and EtOH is complete. Note that both the “infinite” fibrils and the shorter fibrils contribute to the interaction peak in the mid-q range. One can expect that fibrillar end caps similar to the smaller aggregates form in presence of EtOH, and that EtOH (at first) preferably breaks

down the shorter fibrils, while keeping most of the "infinite" fibrils intact, because the end points of the fibrils are energetically unfavorable. The conversion of some of the shorter fibrils to smaller aggregates and possibly a reduction of the average length of remaining smaller fibrils can also explain the vanishing of the interaction peak: If the distance between fibrils increases and the average length of the shorter fibrils becomes smaller than the distance between the fibrils, the shorter fibrils become free to rotate, which in turn leads to a broadening of the peak. This would also result in a vanishing of the local nematic order, which is in agreement with the significant decrease in anisotropy of the data seen above 5 wt% EtOH, see **Fig. E.5**B. As mentioned earlier, the low-q scattering is susceptible to influences of inhomogeneities on the micron-scale, but its intensity can give a hint towards the formation of micrometer sized aggregates ("infinite" fibrils). The low-q scattering at 30 wt% EtOH deviates from the solvent scattering by only about 1%, in line with the idea that all long fibrils are broken down into smaller aggregates. The liquid 25 wt% sample still exhibits a one order of magnitude larger low-q scattering intensity, indicating that there are still remaining "infinite" fibrils, and conforming to the hypotheses made above.

VI.4.4. Microstructuring at a Constant, Higher Ethanol Content

To further examine the small aggregates formed at 30 wt% EtOH, where samples are isotropic liquids no longer containing fibrils, SAXS of samples containing 30 wt% EtOH and 0.5 wt% to 6.0 wt% AGA in H_2O or D_2O was measured. The spectra are shown in a logarithmic scale in **Fig. VI.6**A and in a linear scale in **Fig. E.12**. Samples containing 0.5 wt% and 1.0 wt% AGA show virtually no scattering (same order of magnitude as the solvent), whereas samples containing more AGA exhibit an interaction peak at an almost constant position ($0.732\ nm^{-1} \leq q_{peak} \leq 0.755\ nm^{-1}$; $8.3\ nm \leq D^* \leq 8.6\ nm$). Only at 2.0 wt%, where the peak is less pronounced and the reading of q_{peak} therefore is more error-prone, q_{peak} is found at slightly lower q ($q_{peak} = 0.667\ nm^{-1}$; $D^* = 9.4\ nm$). This indicates that the CAC in presence of 30 wt% EtOH is between 1.0 wt% and 2.0 wt% AGA, compared to <0.1 wt% AGA in absence of EtOH. The significant increase of the CAC shows that the mixture of water and 30 wt% EtOH is a better solvent for AGA than pure water.

In solvent mixtures, it is frequently observed that the solvation layer around a solute is

enriched in one solvent component, which is known as preferential solvation [38–40]. To check whether there is an enrichment of ethanol inside the aggregates, i.e., preferential solvation of AGA, small-angle scattering data acquired with three different contrasts are compared in **Fig. E.13**. SAXS of a sample containing 3 wt% AGA and 30 wt% d0-EtOH in H_2O is mainly sensitive to the diglucuronic acid groups, while SANS of a sample containing 3 wt% AGA and 30 wt% d6-EtOD in D_2O is mainly sensitive to the aglycone groups, and SANS of a sample containing 3 wt% AGA and 30 wt% d0-EtOH in D_2O is sensitive to both the aglycone groups and d0-EtOH (see **Table VI.1** for the scattering length densities). The scattering intensities for the different contrasts suggest that there is a preferential solvation of the AGA molecules with ethanol inside the aggregates (see **Appendix E.4.** for the calculation). Thus, the aggregates are pervaded preferentially by ethanol. While the peak positions are the same for the two different contrasts in SANS, the peak position is shifted to slightly lower q in SAXS. This indicates a form factor contribution to the SAXS scattering. Consequently, the peak positions extracted from SAXS spectra are not equal to the structure factor peak positions.

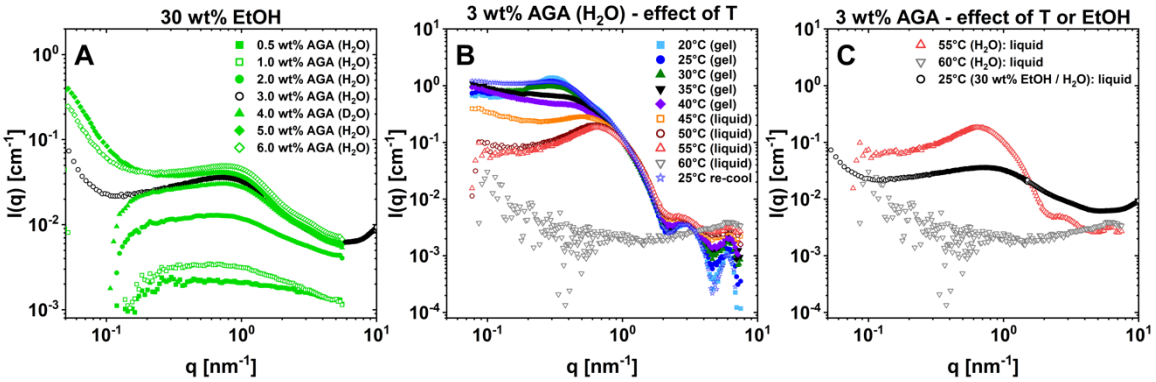

Fig. VI.6. (A) SAXS spectra of samples containing 0.5, 1.0, 2.0, 3.0, 5.0, or 6.0 wt% AGA and 30 wt% EtOH in H_2O and of a sample containing 4.0 wt% AGA and 30 wt% EtOH in D_2O. Corresponding solvent (30 wt% EtOH in H_2O or D_2O) backgrounds are subtracted. Note that the spectrum at 3.0 wt% was taken in a different series of measurements (see **Figs. VI.5** and **E.11**) and only H_2O is subtracted as background. The same spectra are given in a linear scale in **Fig. E.12**. (B) SAXS spectra of a sample containing 3.0 wt% AGA in H_2O at different temperatures. The sample is a gel at 20, 25, 30, 35, and 40°C and a liquid at 45, 50, 55, and 60°C. After re-cooling the sample from 60°C to 20°C, the gel is reformed. The solvent background (H_2O) is subtracted. (C) Comparison of the effect of temperature and the effect of EtOH on a sample containing 3.0 wt% AGA. SAXS spectra of 3.0 wt% AGA in H_2O at 55°C and 60°C are compared to the SAXS spectrum of a sample containing 3.0 wt % AGA and 30 wt% EtOH in H_2O. The data are identical to those in **Fig. VI.6**A and **VI.6**B.

Based on the fibrillar structuring of AGA in the binary system and the formation of end caps by EtOH reducing the length of (shorter) fibrils, a slightly spherocylindrical shape would be expected at 30 wt% EtOH. The spherocylindrical aggregate can be imagined as a fibril that was shrunken until more or less only the end caps remain, i.e., an ultrashort fibril

pervaded by the EtOH-enriched solvent. However, scattering shows that the aspect ratio, i.e., the ratio of the length and the diameter, of potential spherocylinders is too small (<2) for them to be distinguishable from spherical aggregates. Anyway, the aggregates are expected to be significantly pervaded by the solvent, preferentially by EtOH, which as a result do not have a well-defined shape but a rather open structure. Assuming globular aggregates with a local face-centered-cubic packing and using the decoupling approximation, the repeat distance D* obtained from the peak position can be used to approximate the aggregation number N_{agg} [41,42]. The obtained values for D* and N_{agg} are plotted as a function of the number of AGA molecules participating in aggregation per unit volume N(AGA) in **Fig. E.14**. N(AGA) is corrected for a monomer/dimer concentration of 1.0 wt% AGA. It should be noted that D* is only approximate because the structure factor S(q) was not extracted from the scattering. Since the peak position barely changes with increasing AGA concentration, it does not follow a simple dilution law of an immutable aggregate. Consequently, the aggregation number must increase with increasing AGA concentration, as in the case of short chain carboxylates [43]. The calculation suggests that N_{agg} increases from 8 at 2.0 wt% AGA to 27 at 6.0 wt% AGA.

A gel-to-sol transition is not only observed on increasing the EtOH content, but also on increasing temperature. SAXS spectra of a sample containing 3.0 wt% AGA in H_2O at different temperatures ranging from 20°C to 60°C are presented in **Fig. VI.6**B. The sample was heated in steps of 5°C. It remains a gel up to 40°C and is liquid at 45°C and above. At 60°C there is virtually no scattering, indicating that AGA is completely solubilized as monomers (or dimers) at temperatures ≥60°C. Hence, water is becoming a better solvent with increasing temperature. Analogously, the solvent mixture H_2O/EtOH is becoming a better solvent with increasing EtOH content. The latter is at least true up to about 30 wt% EtOH, as a further increase of the EtOH content leads to a decrease in AGA solubility, see **Fig. VI.1**. Nevertheless, there should be a certain threshold concentration of EtOH (>30 wt%), above which AGA molecules no longer aggregate, similar to what is known in the literature for the micellization of various surfactants [36]. From 20°C to 35°C, the intensity of the correlation peak at $q = 0.299\ nm^{-1}$ corresponding to the interaxial repeat distance of the fibrils continuously decreases, suggesting that the number of shorter fibrils that are longer than the interaxial distance decreases, i.e., that the average length of the shorter fibrils decreases. At 40°C, the sample is still a gel, which means that (most) “infinite” fibrils persist. However, the vanishing of the correlation peak suggests that shorter fibrils are free to rotate

and/or partially dissolved, driving towards a vanishing of the nematic order.

At that point, another correlation peak around q = 0.4 nm^{-1} emerges and is shifted to higher q with increasing temperature, accompanied by a gel-to-sol transition. The peak positions are q = 0.516 nm^{-1}, q = 0.631 nm^{-1}, and q = 0.645 nm^{-1}, at 45°C, 50°C, and 55°C, respectively. At the same time, there is no longer an indication of "infinite" fibrils. Since the high-q form factor oscillations, despite becoming less pronounced with increasing temperature, are still visible up to 55°C, suggesting that close-range ordering of the AGA molecules persists, the correlation peak is probably related to the repeat distance between cylindrical or spherocylindrical aggregates. Those aggregates may be understood as short bits of fibrils resulting from the destruction of longer fibrils due to thermal fluctuations and a decreased portion of aggregating AGA. Persistence of the form factor oscillations in the liquid state at higher temperatures marks a difference to the case of higher EtOH concentrations, where the form factor oscillations start to vanish at 20 wt% EtOH, despite the presence of fibrillar structures. This indicates that the solvent pervasion of the aggregates is less significant in heated pure water than in the mixed EtOH/H_2O solvent. **Fig. VI.6**C serves to directly compare the SAXS spectra of the liquid samples containing 3.0 wt% AGA in either pure water at 55°C and 60°C or in the solvent mixture 30 wt% EtOH/water at 25°C. The just mentioned form factor differences at high-q are clearly visible. Both the absence of the form factor oscillations in presence of 30 wt% EtOH and the reduced scattering intensity, suggesting reduced contrast, are hinting to significant solvent pervasion. Further, the correlation peak for the EtOH containing sample is shifted by about 0.1 nm^{-1} to higher q compared to the aqueous sample at 55°C, indicating that the aggregates are in average smaller in presence of EtOH. The similarity of the scattering patterns is expected to increase if temperature is increased above 55°C, closer to the transition to a completely dissolved state found at 60°C. In summary, the effects of EtOH addition and temperature are similar with respect to the increase in solvent quality and the triggering of a gel-to-sol transition, but the mechanisms behind the gel-to-sol transition differ. Since form factor oscillations persist even at 55°C, the pervasion of the aggregates by pure water is insignificant in a large temperature range up to temperatures close to complete dissolution of AGA as monomers (or dimers). While solvent pervasion should significantly increase at temperatures closer to the complete dissolution of the aggregates, the transition from defined aggregates to a monomer/dimer solution is quite sharp, which indicates that the Gibbs energy of transfer from the aggregate to the solvent pseudo-phase is larger than a few k_BT. The ethanolic solvent on the other

hand clearly pervades the structures and EtOH first breaks down shorter fibrils due to their energetically unfavorable end points and eventually also the “infinite” fibrils until only small, less defined structures containing a significant portion of solvent remain. Thus, the increase in solvent quality with increasing EtOH content is the cause of the gel-to-sol transition.

An increase in pH has a similar effect on the microstructuring as the addition of EtOH, which can be seen in the SAXS spectra of 3.0 wt% AGA in H_2O at pH 3.99, 4.65 (natural), 5.10, 6.00, and 6.99 shown in **Fig. E.15**. At pH 3.99 and 4.65, samples are gels and the scattering curves conform to those shown previously, whereas at pH 6.00 and 6.99, samples are isotropic liquids with scattering curves similar to those seen at 30 wt% EtOH. While the mixture is already an isotropic liquid at pH 5.10, scattering is intermediate between fibrils and small aggregates, suggesting a population of both types of self-assemblies. With increasing pH, the degree of dissociation of AGA increases (see **Fig. E.3**), rendering AGA more soluble in water. Hence, while addition of EtOH improves the quality of the solvent for AGA, an increase in pH improves the solubility of AGA in the solvent, resulting in similar small repulsive aggregates. Another effect destabilizing the fibrillar structures is that intermolecular repulsions between AGA molecules within the fibrils increase with increasing pH, as AGA molecules become more and more charged.

VI.4.5. The Effect of NaCl on the Microstructuring

Lastly, the effect of NaCl on the micro-structuring in both binary systems of AGA in water and ternary systems of AGA in water and EtOH is examined. SAXS spectra of samples containing 3.0 wt% AGA (≈35.7 mM) and 0, 1, 10, 30, or 100 mM NaCl in H_2O (empty symbols), as well as of samples containing 3.0 wt% AGA, 30 wt% EtOH, and 0, 1, 3, 10, 30, or 100 mM NaCl in H_2O (full symbols) are shown in a logarithmic scale in **Fig. VI.7**. The q-ranges covering the correlation peaks are also shown in a linear scale in **Fig. E.16**A and **E.16**B. Addition of NaCl to the binary system clearly proves that the mid-q correlation peak at $q = 0.326\ nm^{-1}$ is indeed originating from electrostatic repulsions between fibrils. Increasing the NaCl concentration leads to a vanishing of the correlation peak and a transition from repulsive to attractive interactions, which is typical of electrostatic screening. At NaCl concentrations ≥10 mM, electrostatics are sufficiently screened for the repulsive peak

to disappear. Electrostatic screening is also observed on addition of NaCl to the ternary system, where the peak starts to vanish at 30 mM NaCl, proving that the peak is indeed caused by electrostatic repulsion between charged aggregates, despite the high EtOH content. This is also in line with the discussion of the reduced pH in presence of EtOH (**Section VI.4.3.**). In both the binary and the ternary system, no structural change is induced by the addition of 100 mM NaCl.

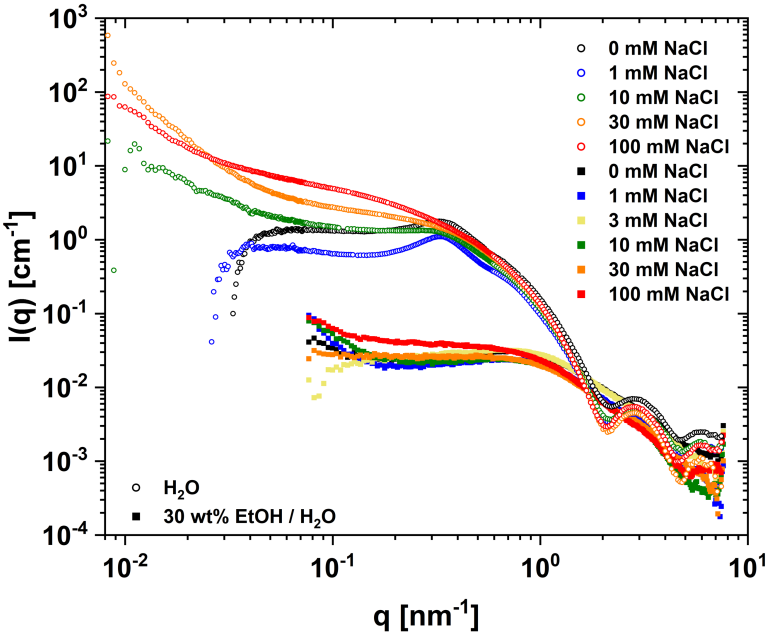

Fig. VI.7. SAXS spectra of samples containing 3.0 wt% AGA in H_2O and 30 wt% EtOH in H_2O with various NaCl concentrations: 0 (black), 1 (blue), 3 (yellow), 10 (green), 30 (orange), and 100 mM (red). Corresponding solvent backgrounds (including NaCl) were subtracted. The same spectra are given in a linear scale in **Fig. E.16**.

Macroscopically, gels of 3.0 wt% AGA in water seemingly become stiffer with increasing NaCl concentration, which could be explained by two effects. On the one hand, a reduction of interfibrillar electrostatic repulsions could reduce the interaxial distance between fibrils and favor the formation of a higher number of "infinite" fibrils, and on the other hand, screening of the negative charges of AGA's glycone part should decrease the intrafibrillar repulsion between stacks of AGA, which results in more stable fibrils. The latter effect can also explain the observed increase in the gel-to-sol transition temperature from 45°C at 0 mM NaCl to 68°C at 100 mM NaCl since it makes the fibrils harder to break. In addition to simply reducing intrafibrillar repulsion, Na^+ could even enable attractive bridging of carboxylate groups by the formation of ion triplets ($RCOO^-\cdots Na^+\cdots RCOO^-$), leading to a stronger binding than that known from carboxylic acid dimers [44,45]. The effect of NaCl may also be simplified as a salting-out effect on AGA, where the presence of NaCl makes

water a worse solvent for AGA. Consequently, a higher temperature is needed to render the solution a better solvent for AGA. This is also in agreement with the affinities of the cations to the carboxylate groups of AGA. Na^+ is known to have a significantly higher affinity to carboxylates than NH_4^+, forming significantly more ion pairs and reducing the solubility in water [46,47]. This is also a well-known counterion effect for soaps.

The spectrum of the sample containing 3.0 wt% AGA and 100 mM NaCl in water can be used to estimate the average length of the shorter fibrils by fitting I(q) = P(q)S(q) to a simple form factor of long cylindrical scatterers P(q) [48] with a fractal Gaussian cutoff structure factor S(q) [49], see **Fig. E.17**. The average observable length is estimated to be approximately 25 nm, which is, as expected, slightly longer than the interaxial distance between fibrils, which is in the order of magnitude of 20 nm. As mentioned in **Section VI.4.2.**, the interaxial distance at 3.0 wt% AGA in water is determined to be 17.1 nm. It is important to note that 100 mM NaCl could influence the average length and also the interaxial distance, but the fit allows the extraction of the order of magnitude of the average length of the shorter fibrils within the gel. In fact, a fit of SANS data obtained for a sample containing 5 mM AGA and 50 mM NaCl by Tucker *et al.* [13] suggests that the average fibrillar length is almost doubled compared to the same system in absence of NaCl. However, their samples were not gels and in their case the concentration of NaCl is ten times higher than that of AGA, whereas in our case it is only less than three times higher. Further, the shorter fibrils are probably not at all uniform in length, but rather polydisperse, as one main factor limiting the fibrillar growth is the limited space between "infinite" fibrils. Due to the lack of a suitable model for the proposed helical structure, fits remain rather qualitative.

An attempt to fit SANS data for samples containing 0.1 wt% to 3.0 wt% AGA in D_2O (**Fig. E.7**), where the scattering contribution comes mainly from the aglycone units, to a simple form factor of a uniform rectangular cuboid of sides 1.41 nm, 5.15 nm, and 28 nm is shown in **Fig. E.18**. Though this model is certainly an oversimplification of the structure, the length of 28 nm is in good agreement with the previously derived average fibrillar length of 25 nm and the length of 1.41 nm matches well the length of the side-by-side stacks of two AGA molecules. Further, the obtained length of 5.15 nm is, considering that the model is an oversimplification, reasonably close to the total diameter of the aglycone parts of the proposed helix (**Fig. VI.2**E), i.e., 7.70 nm – 2·0.72 nm = 6.26 nm, where 7.70 nm is the diameter of the helix including the glycone moieties and 0.72 nm is the thickness of a glycone

moiety. Note that the diameter of the helix was deduced from AFM data reported by Saha *et al.* [12] (see **Section VI.4.2.**). Further, the forward scattering obtained for these rectangular cuboids (≈2.3 cm^{-1} per 1 wt% of AGA) leads to a molecular weight estimate of the aggregate of 159000 $g \cdot mol^{-1}$, which corresponds to 189 AGA molecules. Given the proposed model of dimeric AGA stacks, 95 stacks form one aggregate of 28 nm length. One helical period of 9 nm length is therefore suggested to contain 30 stacks (see **Appendix E.4.** for the calculation).

VI.5. Conclusion and Outlook

In binary aqueous solutions of glycyrrhizic acid monoammonium salt (AGA), the basic structure of a helical fibril is confirmed. The formation of fibrils was previously suggested by Matsuoka *et al.* [11], Saha *et al.* [12], and Tucker *et al.* [13]. Saha *et al.* further observed a right-handed helical twist of the fibrils with a periodicity of 9 nm. In this work, it is found that in both gel and sol samples shorter fibrils (average length ≈25 nm) and long "infinite" fibrils with a diameter around 3 nm coexist. The interaxial distance between fibrils (≈20 nm) is in the order of magnitude of two times the helix periodicity (9 nm), and slightly smaller than the average length of the shorter fibrils (≈25 nm). Short and long fibrils are suggested to be structurally identical and are made of stacks of AGA molecules with two AGA molecules per stack and the hydrophilic diglucuronic acid moieties pointing outwards (exposed to water). Each stack is slightly rotated to give a core-shell-like helical structure with about 30 stacks per helical period of 9 nm. Thus, the only difference between shorter and longer fibrils is the total number of stacks. A network of "infinite" fibrils is responsible for the gelation observed for most samples and their orientation induces a local nematic ordering with shorter fibrils by electrostatic repulsion. The nematic phase is calamitic with a dilution exponent slightly higher than 2. Shorter fibrils form due to limited space between longer fibrils or by destruction of longer fibrils through shear forces. The latter is responsible for the shear-thinning behavior of the gel samples. Self-healing properties of the gels are observed at higher AGA concentrations, where more shorter fibrils are in close proximity to enable reformation of longer fibrils.

Gelation is found to be strongly influenced by heating and cooling. On heating to a certain temperature (60°C at 3 wt% AGA), a monomeric (or dimeric) solution of AGA is achieved,

which enables the growth of fewer but longer fibrils on slowly re-cooling samples. Addition of NaCl is found to increase the stability of the gels, both towards higher temperatures and, presumably, towards higher shear forces.

Addition of ethanol causes the formation of fibrillar end caps and reduces the average length of fibrils. At first, this effect is predominantly affecting the shorter fibrils, until the interaxial distance is larger than the average fibrillar length and the nematic ordering is lost, while the gel network of "infinite" fibrils can persist up to about 25 wt% ethanol, depending on the AGA concentration. At 30 wt% ethanol, only isotropic sols are observed. Fibrils are no longer formed and, consequently, a gel can no longer form. Instead, only an electrostatic repulsion peak between small aggregates is seen in small-angle scattering. The aggregates could be prolate ellipsoids, a similar peak was found in SANS for prolate ellipsoids of sodium dodecyl sulfate in presence of strongly hydrated cosmotropic counterions by Sheu *et al.* [50] almost 40 years ago, or short bits of fibrils. In any case, the aggregates are not well-defined but significantly pervaded by an ethanol-enriched solvent. Up to about 30 wt% of ethanol, ethanol acts as a co-solvent, enhancing the solubility of AGA in the mixed solvent. At even higher ethanol contents, ethanol acts as an anti-solvent, reducing the solubility of AGA in the mixed solvent. Since the structures and gels are resilient to the addition of a significant amount of ethanol, a combination of the solubilizing effects of AGA and ethanol (as a hydrotrope) is indeed feasible. An application of this combination will be presented in a paper currently in preparation by Kunz and co-workers [24].

Hopefully, the presented structural elucidation of AGA hydrogels with and without ethanol will allow for a deeper understanding of peculiar solubilization properties of such mixtures and a specific fine tuning of desired properties in formulation for potential applications such as drug delivery. Moreover, this work could help achieving a better understanding of hydrogel formation, not only by AGA, but also by similar compounds.

VI.6. References

[1] P. Denk, S. Prévost, L. Matthews, Q. Prasser, T. Zemb, W. Kunz, The effect of ethanol on fibrillar hydrogels formed by glycyrrhizic acid monoammonium salt, J Colloid Interface Sci 630 (2023) 762–775. https://doi.org/10.1016/j.jcis.2022.10.138.

[2] J.W. Conn, D.R. Rovner, E.L. Cohen, Licorice-Induced Pseudoaldosteronism, JAMA 205 (1968) 492. https://doi.org/10.1001/jama.1968.03140330034006.

[3] B.B. Hamidon, V. Jeyabalan, Exogenously-induced apparent hypermineralocorticoidism associated with ingestion of "asam boi," Singapore Med J 47 (2006) 156–158.

[4] M.N. Asl, H. Hosseinzadeh, Review of Pharmacological Effects ofGlycyrrhiza sp. and its Bioactive Compounds, Phytotherapy Research 22 (2008) 709–724. https://doi.org/10.1002/ptr.2362.

[5] Scientific Committee on Food, Opinion of the Scientific Committee on Food on Glycyrrhizinic Acid and its ammonium salt, 2003. https://ec.europa.eu/food/system/files/2020-12/sci-com_scf_out186_en.pdf.

[6] C.S. Graebin, The Pharmacological Activities of Glycyrrhizinic Acid ("Glycyrrhizin") and Glycyrrhetinic Acid, in: Reference Series in Phytochemistry, 2018: pp. 245–261. https://doi.org/10.1007/978-3-319-27027-2_15.

[7] J. Cinatl, B. Morgenstern, G. Bauer, P. Chandra, H. Rabenau, H. Doerr, Glycyrrhizin, an active component of liquorice roots, and replication of SARS-associated coronavirus, The Lancet 361 (2003) 2045–2046. https://doi.org/10.1016/S0140-6736(03)13615-X.

[8] L. van de Sand, M. Bormann, M. Alt, L. Schipper, C.S. Heilingloh, E. Steinmann, D. Todt, U. Dittmer, C. Elsner, O. Witzke, A. Krawczyk, Glycyrrhizin Effectively Inhibits SARS-CoV-2 Replication by Inhibiting the Viral Main Protease, Viruses 13 (2021) 609. https://doi.org/10.3390/v13040609.

[9] S. Saito, T. Furumoto, M. Ochiai, A. Hosono, H. Hoshino, U. Haraguchi, R. Ikeda, N. Shimada, Synthetic studies on the relationship between anti-HIV activities and micelle forming abilities of various alkylated glycyrrhetinate diglycoside sodium sulfates and related compounds, Eur J Med Chem 31 (1996) 365–381. https://doi.org/10.1016/0223-5234(96)89163-X.

[10] E. Touitou, R. Segal, S. Pisanty, I. Milogoldzweig, Glycyrrhizin gel as vehicle for idoxuridine topical preparation: skin permeation behaviour., Drug Des Deliv 3 (1988) 267–72. http://www.ncbi.nlm.nih.gov/pubmed/3255333.

[11] K. Matsuoka, R. Miyajima, Y. Ishida, S. Karasawa, T. Yoshimura, Aggregate formation of glycyrrhizic acid, Colloids Surf A Physicochem Eng Asp 500 (2016) 112–117. https://doi.org/10.1016/j.colsurfa.2016.04.032.

[12] A. Saha, J. Adamcik, S. Bolisetty, S. Handschin, R. Mezzenga, Fibrillar Networks of Glycyrrhizic Acid for Hybrid Nanomaterials with Catalytic Features, Angewandte Chemie 127 (2015) 5498–5502. https://doi.org/10.1002/ange.201411875.

[13] I.M. Tucker, A. Burley, R.E. Petkova, S.L. Hosking, J. Penfold, R.K. Thomas, P.X. Li, J.R.P. Webster, R. Welbourn, J. Doutch, Adsorption and self-assembly properties of the plant based biosurfactant, Glycyrrhizic acid, J Colloid Interface Sci 598 (2021) 444–454. https://doi.org/10.1016/j.jcis.2021.03.101.

[14] R.G. Weiss, P. Terech, eds., Molecular Gels, Springer Netherlands, Dordrecht, 2006. https://doi.org/10.1007/1-4020-3689-2.

[15] S. Banerjee, R.K. Das, U. Maitra, Supramolecular gels 'in action,' J Mater Chem 19 (2009) 6649. https://doi.org/10.1039/b819218a.

[16] M. de Loos, B.L. Feringa, J.H. van Esch, Design and Application of Self-Assembled Low Molecular Weight Hydrogels, European J Org Chem 2005 (2005) 3615–3631. https://doi.org/10.1002/ejoc.200400723.

[17] T. Kato, Self-Assembly of Phase-Segregated Liquid Crystal Structures, Science (1979) 295 (2002) 2414–2418. https://doi.org/10.1126/science.1070967-a.

[18] M.M. Piepenbrock, G.O. Lloyd, N. Clarke, J.W. Steed, Metal- and Anion-Binding Supramolecular Gels, Chem Rev 110 (2010) 1960–2004. https://doi.org/10.1021/cr9003067.

[19] R. V. Ulijn, A.M. Smith, Designing peptide based nanomaterials, Chem Soc Rev 37 (2008) 664. https://doi.org/10.1039/b609047h.

[20] E. Zaccarelli, Colloidal gels: equilibrium and non-equilibrium routes, Journal of Physics: Condensed Matter 19 (2007) 323101. https://doi.org/10.1088/0953-8984/19/32/323101.

[21] X. Du, J. Zhou, J. Shi, B. Xu, Supramolecular Hydrogelators and Hydrogels: From Soft Matter to Molecular Biomaterials, Chem Rev 115 (2015) 13165–13307. https://doi.org/10.1021/acs.chemrev.5b00299.

[22] X. Feng, Y. Luo, F. Li, X. Jian, Y. Liu, Development of Natural-Drugs-Based Low-Molecular-Weight Supramolecular Gels, Gels 7 (2021) 105. https://doi.org/10.3390/gels7030105.

[23] E. Tykarska, S. Sobiak, M. Gdaniec, Supramolecular Organization of Neutral and Ionic Forms of Pharmaceutically Relevant Glycyrrhizic Acid—Amphiphile Self-Assembly and Inclusion of Small Drug Molecules, Cryst Growth Des 12 (2012) 2133–2137. https://doi.org/10.1021/cg300160c.

[24] C.B. Jung, Q. Prasser, J. Mayr, M. Häring, V.O. Rodionov, E. Müller, D. Touraud, W. Kunz, D. Díaz Díaz, Glycyrrhizic Acid-based Hydrogels combined with Alcohols as Hydrotropes and their Potential as Nanocarriers, in preparation, (n.d.).

[25] T. Narayanan, M. Sztucki, P. Van Vaerenbergh, J. Léonardon, J. Gorini, L. Claustre, F. Sever, J. Morse, P. Boesecke, A multipurpose instrument for time-resolved ultra-small-angle and coherent X-ray scattering, J Appl Crystallogr 51 (2018) 1511–1524. https://doi.org/10.1107/S1600576718012748.

[26] T. Narayanan, M. Sztucki, T. Zinn, J. Kieffer, A. Homs-Puron, J. Gorini, P. Van Vaerenbergh, P. Boesecke, Performance of the time-resolved ultra-small-angle X-ray scattering beamline with the Extremely Brilliant Source, J Appl Crystallogr 55 (2022) 98–111. https://doi.org/10.1107/S1600576721012693.

[27] C.D. Dewhurst, I. Grillo, D. Honecker, M. Bonnaud, M. Jacques, C. Amrouni, A. Perillo-Marcone, G. Manzin, R. Cubitt, The small-angle neutron scattering instrument D33 at the Institut Laue–Langevin, J Appl Crystallogr 49 (2016) 1–14. https://doi.org/10.1107/S1600576715021792.

[28] P. Lindner, R. Schweins, The D11 Small-Angle Scattering Instrument: A New Benchmark for SANS, Neutron News 21 (2010) 15–18. https://doi.org/10.1080/10448631003697985.

[29] E.R. Draper, D.J. Adams, Low-Molecular-Weight Gels: The State of the Art, Chem 3 (2017) 390–410. https://doi.org/10.1016/j.chempr.2017.07.012.

[30] C.-X. Zeng, Q. Hu, Determination of the polyacid dissociation constants of glycyrrhizic acid, Indian Journal of Chemistry - Section A Inorganic, Physical, Theoretical and Analytical Chemistry 47 (2008) 71–74. http://nopr.niscair.res.in/handle/123456789/555.

[31] M. V. Zelikman, A. V. Kim, N.N. Medvedev, O.Y. Selyutina, N.E. Polyakov, Structure of dimers of glycyrrhizic acid in water and their complexes with cholesterol: Molecular dynamics simulation, Journal of Structural Chemistry 56 (2015) 67–76. https://doi.org/10.1134/S0022476615010102.

[32] A. Krężel, W. Bal, A formula for correlating pKa values determined in D2O and H2O, J Inorg Biochem 98 (2004) 161–166. https://doi.org/10.1016/j.jinorgbio.2003.10.001.

[33] S. Dieterich, F. Stemmler, N. Preisig, F. Giesselmann, Micellar Lyotropic Nematic Gels, Advanced Materials 33 (2021) 2007340. https://doi.org/10.1002/adma.202007340.

[34] E. Grunwald, B.J. Berkowitz, The Measurement and Correlation of Acid Dissociation Constants for Carboxylic Acids in the System Ethanol-Water. Activity Coefficients and Empirical Activity Functions 1a, J Am Chem Soc 73 (1951) 4939–4944. https://doi.org/10.1021/ja01154a139.

[35] M.A. Rahman, A.K. Ghosh, R.N. Bose, Dissociation constants of long chain fatty acids in methanol-water and ethanol-water mixtures, Journal of Chemical Technology and Biotechnology 29 (2007) 158–162. https://doi.org/10.1002/jctb.503290307.

[36] R. Zana, Aqueous surfactant-alcohol systems: A review, Adv Colloid Interface Sci 57 (1995) 1–64. https://doi.org/10.1016/0001-8686(95)00235-I.

[37] B.W. Ninham, V.A.A. Parsegian, Electrostatic potential between surfaces bearing ionizable groups in ionic equilibrium with physiologic saline solution, J Theor Biol 31 (1971) 405–428. https://doi.org/10.1016/0022-5193(71)90019-1.

[38] Y. Marcus, On the preferential solvation of drugs and PAHs in binary solvent mixtures, J Mol Liq 140 (2008) 61–67. https://doi.org/10.1016/j.molliq.2008.01.005.

[39] A. Jouyban, W.E. Acree, F. Martínez, Dissolution thermodynamics and preferential solvation of ketoconazole in some {ethanol (1) + water (2)} mixtures, J Mol Liq 313 (2020) 113579. https://doi.org/10.1016/j.molliq.2020.113579.

[40] S. Akay, B. Kayan, F. Martínez, Dissolution thermodynamics and preferential solvation of 2,4-dinitrotoluene in (ethanol + water) mixtures, J Mol Liq 330 (2021). https://doi.org/10.1016/j.molliq.2021.115675.

[41] S.H. Chen, E.Y. Sheu, J. Kalus, H. Hoffman, Small-angle neutron scattering investigation of correlations in charged macromolecular and supramolecular solutions, J Appl Crystallogr 21 (1988) 751–769. https://doi.org/10.1107/S0021889888008052.

[42] M. Kotlarchyk, S. Chen, Analysis of small angle neutron scattering spectra from polydisperse interacting colloids, J Chem Phys 79 (1983) 2461–2469. https://doi.org/10.1063/1.446055.

[43] J.B. Hayter, T. Zemb, Concentration-dependent structure of sodium octanoate micelles, Chem Phys Lett 93 (1982) 91–94. https://doi.org/10.1016/0009-2614(82)85062-8.

[44] P. Fromherz, The Surfactant-Block Structure of Micelles, Synthesis of the Droplet and of the Bilayer Concept, Berichte Der Bunsengesellschaft Für Physikalische Chemie 85 (1981) 891–899. https://doi.org/10.1002/bbpc.19810851015.

[45] J. Chen, C.L. Brooks, H.A. Scheraga, Revisiting the carboxylic acid dimers in aqueous solution: Interplay of hydrogen bonding, hydrophobic interactions and entropy, Journal of Physical Chemistry B 112 (2008) 242–249. https://doi.org/10.1021/jp074355h.

[46] N. Vlachy, B. Jagoda-Cwiklik, R. Vácha, D. Touraud, P. Jungwirth, W. Kunz, Hofmeister series and specific interactions of charged headgroups with aqueous ions, Adv Colloid Interface Sci 146 (2009) 42–47. https://doi.org/10.1016/j.cis.2008.09.010.

[47] T. Petit, K.M. Lange, G. Conrad, K. Yamamoto, C. Schwanke, K.F. Hodeck, M. Dantz, T. Brandenburg, E. Suljoti, E.F. Aziz, Probing ion-specific effects on aqueous acetate solutions: Ion pairing versus water structure modifications, Structural Dynamics 1 (2014) 034901. https://doi.org/10.1063/1.4884600.

[48] G. Porod, Die Abhängigkeit der Röntgenkleinwinkelstreuung von Form und Größe der Kolloiden Teilchen in verdünnten Systemen, IV., Acta Physica Austriaca 2 (1948) 255–292.

[49] C.M. Sorensen, J. Cai, N. Lu, Test of static structure factors for describing light scattering from fractal soot aggregates, Langmuir 8 (1992) 2064–2069. https://doi.org/10.1021/la00044a029.

[50] E.Y. Sheu, C.F. Wu, S.H. Chen, Effects of ion sizes on the aggregation and surface charge of ionic micelles in 1:1 electrolyte solutions, J Phys Chem 90 (1986) 4179–4187. https://doi.org/10.1021/j100408a068.

Chapter VII.

Summary and Outlook

In the last chapter of this thesis, first a brief summary of the most important results of the studies presented in **Chapters II.** to **VI.** will be given, followed by the description of an apparent paradox in the self-assembly of C_8E_j surfactants, the explanation of which may be supported by this thesis, and a short outlook on some open questions and possible applications. The summary is meant as a short overview of these results only. For more details, the reader is referred to the Conclusion and Outlook sections of the respective chapters.

VII.1. Summary

In **Chapter II.**, the aqueous phase behavior of octaoxyethylene octyl ether carboxylic acid ($C_8E_8CH_2COOH$) was studied. The large headgroup compared to the short hydrophobic chain is found to impose a significant steric packing constraint on micelle formation, resulting in the surfactant resisting the common sphere-to-rod shape transition. As a consequence, no liquid crystalline phases are formed, and only small direct globular micelles are found independent of surfactant concentration. Two different domains can be distinguished within the micellar domain, (a) the L_1 phase comprising classical core-shell micelles dispersed in water at lower surfactant concentrations, and (b) the L_1' phase at higher surfactant concentrations, where all water molecules are bound as hydration water to the headgroups, which interdigitate to produce a dispersion of hydrocarbon cores in a medium of more or less hydrated headgroups.

In the L_1 phase, a constant area per molecule of around 0.6 nm^2 and an aggregation number of around 30 is found. As headgroups start to interdigitate in the transition to the L_1' phase, the area per molecule increases, resulting in a lower aggregation number, reaching a minimum of 8 in the total absence of water, as the area per molecule approaches a value of almost 1 nm^2. The L_1' phase can be described as direct micelles without any "bulk" pseudo-phase. As a consequence, there are no monomers and the chemical potential is low: One expects a low water reactivity, a property sometimes useful if hydrolysis should be reduced.

As expected, due to the high degree of ethoxylation, the surfactant is found to be pseudo-nonionic, i.e., counterions have little effect on the phase behavior and the phase behavior closely resembles that of a nonionic surfactant.

However, as shown in **Chapter III.**, the carboxylic acid group allows for fine-tuning of the phase behavior. If electrostatics are not screened, sodium and calcium salts of the surfactant no longer exhibit a lower critical solution temperature (clouding) due to electrostatic repulsion between micelles. In the ionic forms, the micelles are slightly ellipsoidal, indicating that the area per molecule slightly decreases. This is due to charge regulation [1] and bridging between neighboring headgroups via counterions. A sphere-to-rod transition is still resisted throughout the whole concentration and temperature range, the only exception being a small hexagonal lyotropic liquid crystal present at lower temperatures around 60 wt% of surfactant. It is around this surfactant concentration, where the L_1 phase transitions into the

L_1' phase. Therefore, micelles are in close proximity to each other and intermicellar counterion bridging is sufficient to induce the otherwise sterically impossible sphere-to-rod transition. At even higher surfactant concentrations, headgroup interdigitation again increases the area per molecule, making a sphere-to-rod transition impossible. When increasing temperature, the hexagonal phase again "melts" into a micellar phase of small spheroidal micelles. As an intermediate phase, a previously unknown calamitic nematic phase of ion-bridged prolate micelles is identified. Due to the ethoxylation, as explained in **Section I.2.** of **Chapter I.**, even the neat metal salts of this surfactant are liquid at room temperature or slightly above room temperature, thus representing microstructured ionic liquids.

The high Gibbs free energy necessary to induce a shape transition for $C_8E_8CH_2COOH$ was used to induce intramicellar molecular segregation into a curved rim and a flat disc, when mixing $C_8E_8CH_2COOH$ with dioxyethylene oleyl ether carboxylic acid ($C_{18:1}E_2CH_2COOH$). The aqueous phase behavior of this system was studied in **Chapter IV.**, revealing the formation of a discotic nematic phase made of large (diameter ≈ 50 nm) disc-like bicelles if the two surfactants are mixed in adequate mole ratios. The diameter of the discs can be controlled and fine-tuned by the exact mole ratio of the two components as well as by temperature, making them similar to classical lipid bicelles used to orient membrane proteins for scattering or NMR. $C_{18:1}E_2CH_2COOH$ has a spontaneous packing parameter of around 1, thus favoring the flat, i.e., zero-curvature, part of the disc, whereas $C_8E_8CH_2COOH$ has a spontaneous packing parameter below or around 1/3, thus favoring the curved outer rim of the bicelle. The nematic phase has interesting properties. It is self-thickening, i.e. gel-like viscoelastic without additives, capable of entrapping air bubbles or other objects, while at the same time being strongly shear-thinning. Since it can be handled like a liquid due to the shear-thinning behavior, but does not exhibit noticeable thixotropic behavior, i.e., has quasi-instantaneous structural restoration, these nematic gels combine the benefits of gels at rest (zero-shear) with the benefits of easy-to-handle liquids.

In **Chapter V.**, the effects of three additives commonly used in industrial formulation for health- and home care on the nematic gel were examined. Propylene glycol was found to act predominantly as a co-solvent with a preference for one surfactant over the other, which can improve temperature stability of the nematic phase if used in adequate amounts. Glycerol on the other hand acts as an anti-solvent, progressively decreasing the temperatures required to induce microstructural transitions. Ethanol was found to be a good co-solvent

for both surfactants, which can be used in low quantities to influence the temperature stability of the nematic phase but leads to more and more molecular dissolution in an isotropic liquid phase.

The aim of **Chapter VI.** was to assess the influence of ethanol as an additive on the microstructures in fibrillar hydrogels formed by the amphiphilic natural sweetener glycyrrhizic acid, as ethanol could potentially be used to enhance drug loading of the hydrogels. To complement the already available data in the literature, the binary system of water and the monoammonium salt of glycyrrhizic acid (AGA) was also studied in detail by small-angle scattering. From the results reported in the literature and the data presented in this work, a model of the microstructure and its change on addition of ethanol could be constructed. "Infinitely" long negatively charged helical fibrils coexist with shorter fibrils with an average length of around 25 nm, both of which have an identical molecular arrangement. The fibrillar strand has a diameter of around 3 nm and 30 stacks of AGA molecules make up one helical period (≈9 nm) of the right-handed helix, each stack consisting of two AGA molecules. Ethanol reduces electrostatic repulsion and favors the formation of fibrillar end caps. As a result, the average fibrillar length decreases with increasing ethanol content, until only small, swollen aggregates remain. The "infinite" fibrils, which are responsible for the gel network, are found to be resilient to a significant amount of ethanol, i.e., ethanol first breaks down shorter fibrils before breaking down "infinite" fibrils. Above a certain threshold concentration of ethanol, however, all fibrils are dissolved into small aggregates and gel formation is no longer possible.

VII.2. Apparent Paradox in the Self-Assembly of C_8E_j Surfactants

An apparent paradox is found when comparing the phase behaviors of C_8E_4, C_8E_5, C_8E_6, and C_8E_8. C_8E_8 and homologues with even larger headgroups do not form any liquid crystalline phase [2] and resist a sphere-to-rod transition, as shown in this work for the similar $C_8E_8CH_2COOH$. C_8E_6 on the other hand forms a hexagonal phase around 60 wt% of surfactant below 14°C [3], therefore not resisting a sphere-to-rod transition. C_8E_5 too forms a hexagonal phase around 55 wt% of surfactant below 6°C [4]. C_8E_4, however, does not form

a hexagonal phase above the freezing temperature of water [2]. This seems paradoxical because the spontaneous packing parameter decreases with decreasing headgroup size from C_8E_8 to C_8E_6 to C_8E_5 to C_8E_4, and therefore a sphere-to-rod transition should be easier for C_8E_4 than for C_8E_5 than for C_8E_6. However, the opposite is found and C_8E_6 forms the largest hexagonal domain.

It is easy to rationalize that a sphere-to-rod transition is not possible for C_8E_8, because above a certain threshold number of ethylene oxide units the (hydrated) headgroup is too bulky and the area per molecule is just too large to adopt cylindrical packing. This was also demonstrated in this work for $C_8E_8CH_2COOH$. But why is the formation of a hexagonal phase, i.e., the formation of long cylindrical micelles easier for larger headgroups below this threshold size? To the knowledge of the author of this thesis, this question is not yet answered by current theory, but a tentative idea can be formulated after this thesis: There must be a favorable free energy contribution linked to the lateral, i.e., intramicellar, attractive interaction of ethylene oxide chains, which increases with increasing number of ethylene oxide units.

When looking at the crystallization of polyoxyethylene chains, one finds that a larger number of ethylene oxide groups favors crystallization. As the ethylene oxide chains prefer to crystallize in 7/2 helices [5], the increase in the melting temperature of polyethylene glycols (PEGs) with each additional ethylene oxide group is most significant for low numbers ($\leq$7) of ethylene oxide units, where one additional ethylene oxide unit can increase the melting temperature by more than 20°C, and is negligible for high numbers of ethylene oxide units. For crystallization to occur, the enthalpic gain in free energy by molecular interactions must exceed the loss in entropy due to higher order. Since the melting temperature increases with increasing number of ethylene oxide units, the gain in enthalpy of crystallization seems to dominate over the gain in conformational entropy due to increased chain flexibility. In parallel, interactions between neighboring ethylene oxide chains in micelles could increase with increasing ethylene oxide number.

A higher order of the ethylene oxide chains imposed by these interactions would result in an entropic penalty due to a decreased conformational entropy. The latter is already imposed to some degree by a shape-transition from spherical to cylindrical, as the available area per headgroup decreases. Zulauf *et al.* [4] reported that C_8E_5 does not undergo a sphere-to-rod transition preceding the hexagonal phase, indicating that the transition from

globular micelles to “infinite” rods is not continuous but sharp. The same was found for the sodium salt of $C_8E_8CH_2COOH$ in this work, where the only region in the phase diagram where rod-like micelles are formed is the hexagonal phase. Note that in this case the sodium counterions are necessary for additional attractive counterion bridging. As suggested by the relatively sharp Bragg-like peaks of the hexagonal phase, the headgroups are well-ordered, though not crystalline. Therefore, the free energy gain by the ordering of the ethylene oxide headgroups seems to be enough for E_5 and E_6, but not for E_4, to undergo a sphere-to-rod transition to form a well-ordered hexagonal phase at relatively high surfactant concentrations (≈60 wt%) and low temperatures, where the penalty of a loss in conformational entropy is sufficiently small. For E_8, the free energy gain of the headgroup interactions would be higher than for E_5 or E_6, the area per molecule, however, is too large for a sphere-to-rod transition to occur.

Further research is required to solve this apparent paradox, including the examination of the microstructures at temperatures above the hexagonal phases of C_8E_5 and C_8E_6 and in the range, where a hexagonal phase is “missing” for C_8E_4. If flexible worm-like cylinders were formed, but no hexagonal phase is found, an alternative explanation could be given: The smaller the headgroup is, the larger should be the flexibility of these worm-like micelles. The entropic penalty of forming a well-ordered hexagonal phase is higher if formed from more flexible cylinders than if formed from more rigid cylinders.

VII.3. Outlook – Open Questions and Possible Applications

In absence of water, metal salts of $C_8E_8CH_2COOH$ or similar compounds $C_iE_jCH_2COOH$ are ionic liquids. The anion and the cation are extremely asymmetric in volume, as in the case of antagonistic salts [6]. The possible applications of such ionic liquids are currently explored at our institute. Due to the self-assembly of the surfactant’s metal salts, two fields of application are of particular interest:

(a) Can the structure of the neat surfactant, comprising a continuous medium of ethoxylated headgroups with their metal counterions and confined hydrocarbon cores be used as a template for mineralization? In this case, the metal ion would be crystallized

by the introduction of a suitable counterion and the obtained solid would be porous due to holes arising from the hydrocarbon cores. Some preliminary tests trying to precipitate carbonates by storing the ionic liquid in a CO_2-rich atmosphere or by in-situ formation of CO_2 did not yield the desired porous material. However, different approaches could be explored. One of the main problems is the introduction of the anionic counterion into the ionic liquid. Due to the increased viscosity, another solution cannot be homogeneously mixed quickly, probably leading to diffusion effects resulting in crystal formation outside of the "template". In principle, one could imagine using two mixtures: i) A certain amount of an aqueous metal chloride solution is added to an ionic liquid containing the same metal as counterion. ii) An appropriate amount of an aqueous solution containing the desired anion for precipitation is added to a portion of the neat acidic surfactant. If mixtures i) and ii) are prepared in such a way that the water content in both mixtures is identical and low enough to preserve the interdigitated L_1' phase (≤30 wt% water, ideally ≤20 wt% water), the same microstructure is present in both mixtures. The problem of quick homogeneous mixing would remain, but possibly using the vortex tangential mixer [7,8] and/or working at temperatures below the chain melting could produce interesting materials or gels. It should also be noted that in the case of metal counterions such as Co^{2+}, which tend to form metal oxides if exposed to air, slow formation of metal oxide particles is observed when exposing the ionic liquid to air. A characterization of these particles was not conducted.

(b) Can the large internal interface between the continuous hydrophilic medium and the small, confined hydrocarbon cores be utilized for organic reactions? The counterion can be freely varied and since the headgroups are flexible, the counterions are not spatially confined but can move rather freely in the hydrophilic medium and thus could in principle act as phase-transfer catalysts. A drawback of such an ionic liquid is of course the high viscosity compared to classical organic solvents. However, some reactions may benefit from the small hydrocarbon "microreactors", which can be loaded with hydrophobic compounds without changing the microstructure. Key points are again the reduced activity of water associated to partially interdigitated headgroups, and the possibility to quick-start a reaction through water release by microwave heating bursts.

The latter statement in point (b) leads to a still unanswered question. As shown in **Chapter**

II. (**Section II.4.5.**), $C_8E_8CH_2COOH$ and its metal salts are not miscible with hydrocarbon oils even in the absence of water. Only a certain amount of oil can be solubilized and any excess oil phase separates. This suggests that the microstructure of interdigitated direct globular micelles persists even in presence of oil. However, experimental proof of the microstructure in presence of oil is missing, and therefore the question if the microstructure really remains unchanged upon saturation with oil is yet to be answered conclusively.

Another, somewhat related, conclusion that lacks final experimental proof is that there is no sphere-to-cylinder transition close to the cloud point. All data presented in this work suggest that there is no sphere-to-cylinder growth, but no direct measurements were performed close to the clouding temperature. A small-angle scattering study, probing the microstructures as a function of temperature approaching the cloud point, could be undertaken to give direct experimental proof.

The discotic nematic phase made of two cheap commercial surfactants examined in **Chapters IV.** and **V.** has interesting properties for encapsulation. It is easy to handle due to its strong shear-thinning behavior, but at rest it immediately relaxes into its viscoelastic gel state. Bubbles, droplets, or solid objects can be dispersed and entrapped in the nematic gel, as long as the dispersed material does not influence the phase behavior of the surfactant mixture. Since the nematic gel is made of disc-like bicelles in a continuous aqueous medium, and dispersed objects are not encapsuled in a closed microstructure such as a vesicle or a liquid crystalline droplet, this kind of "encapsulation" can be referred to as "capsule-free encapsulation". The gel is self-thickening, i.e., does not require polymers or hydrogelators, and is thus an alternative to classical formulations based on polymers. However, the potential applications are greatly limited by the sensitivity of the microstructure to solubilization of other compounds. In the case of a hydrophobic liquid droplet, the surfactant tends to solubilize a certain amount of the oily compound, which can induce shape-transition of the micelles and consequently destroy the nematic gel. So far, the only promising results were obtained dispersing silicone oils, but most compounds of interest for applications, such as perfume oils, cannot be dispersed as droplets as they participate in the self-assembly on a molecular level.

Glycyrrhizic acid and its salts are already widely used in food, health, and personal care products. With the knowledge of the microstructures with and without ethanol gained in **Chapter VI.**, an interesting goal for cosmetic and personal care products can be started to

be tackled: How to formulate four component gels made with glycyrrhizic acid salt with formulated cations such as choline or natural spermine or spermidine – water – ethanol or glycerol or other alcohols and natural lipids? Polymer-free encapsulation is a major goal that, to the best of the authors knowledge, has not yet been achieved in the cosmetics industry.

VII.4. References

[1] B.W. Ninham, V.A.A. Parsegian, Electrostatic potential between surfaces bearing ionizable groups in ionic equilibrium with physiologic saline solution, J Theor Biol 31 (1971) 405–428. https://doi.org/10.1016/0022-5193(71)90019-1.

[2] D.J. Mitchell, G.J.T. Tiddy, L. Waring, T. Bostock, M.P. McDonald, Phase behaviour of polyoxyethylene surfactants with water. Mesophase structures and partial miscibility (cloud points), Journal of the Chemical Society, Faraday Transactions 1: Physical Chemistry in Condensed Phases 79 (1983) 975. https://doi.org/10.1039/f19837900975.

[3] J.S. Marland, B.A. Mulley, A phase-rule study of multiple-phase formation in a model emulsion system containing water, n-octanol, n-dodecane and/a non-ionic surface-active agent at 10 and 25°, Journal of Pharmacy and Pharmacology 23 (1971) 561–572. https://doi.org/10.1111/j.2042-7158.1971.tb08718.x.

[4] M. Zulauf, K. Weckstrom, J.B. Hayter, V. Degiorgio, M. Corti, Neutron scattering study of micelle structure in isotropic aqueous solutions of poly(oxyethylene) amphiphiles, J Phys Chem 89 (1985) 3411–3417. https://doi.org/10.1021/j100261a051.

[5] Y. Takahashi, H. Tadokoro, Structural Studies of Polyethers, (-(CH2)m-O-)n . X. Crystal Structure of Poly(ethylene oxide), Macromolecules 6 (1973) 672–675. https://doi.org/10.1021/ma60035a005.

[6] A. Onuki, S. Yabunaka, T. Araki, R. Okamoto, Structure formation due to antagonistic salts, Curr Opin Colloid Interface Sci 22 (2016) 59–64. https://doi.org/10.1016/j.cocis.2016.02.007.

[7] Y. Liu, C. Cheng, Y. Liu, R.K. Prud'homme, R.O. Fox, Mixing in a multi-inlet vortex mixer (MIVM) for flash nano-precipitation, Chem Eng Sci 63 (2008) 2829–2842. https://doi.org/10.1016/j.ces.2007.10.020.

[8] K. Roger, N. El Amri, Controlling nanoparticle formation from the onset of nucleation through a multi-step continuous flow approach, J Colloid Interface Sci 608 (2022) 1750–1757. https://doi.org/10.1016/j.jcis.2021.10.071.

Appendix A.

Supplementary Material – Chapter II.

A.1. Supplementary Figures

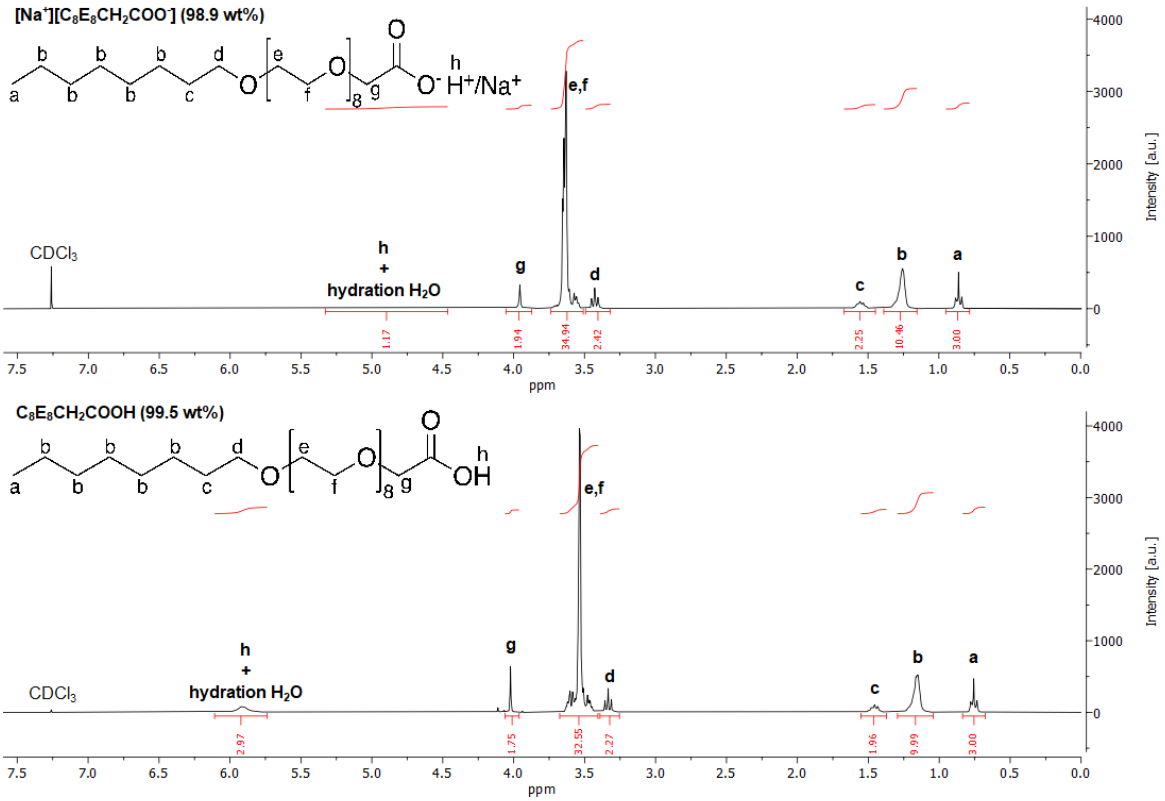

Fig. A.1. ^{1}H-NMR (300 MHz, 16 scans, $CDCl_3$) spectra of $[Na^+][C_8E_8CH_2COO^-]$ with a water content of 1.1 wt% (top) and $C_8E_8CH_2COOH$ with a water content of 0.5 wt% (bottom). Both spectra are similar, with the exception of the -OH-peak (h and hydration water), which is much more pronounced in the case of $C_8E_8CH_2COOH$, despite containing less water than $[Na^+][C_8E_8CH_2COO^-]$. This indicates that the majority of the carboxylate functions is indeed deprotonated and has Na^+ as their counterion.

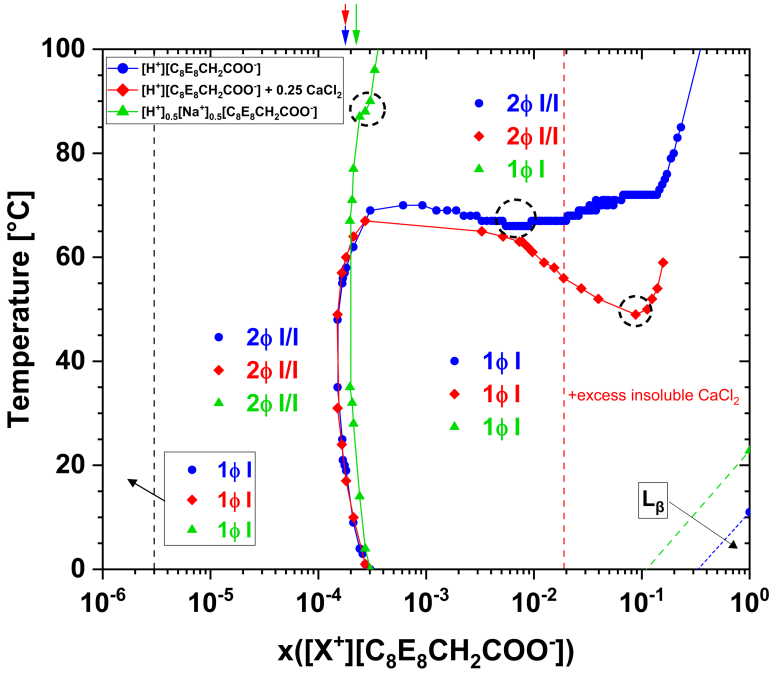

Fig. A.2. Binary phase diagrams of $C_8E_8CH_2COOH$ (here denoted as $[H^+][C_8E_8CH_2COO^-]$), $C_8E_8CH_2COOH$ with 0.25 $CaCl_2$ per $C_8E_8CH_2COOH$ molecule, and $[H^+]_{0.5}[Na^+]_{0.5}[C_8E_8CH_2COO^-]$ in water as a function of the mole fraction $x([X^+][C_8E_8CH_2COO^-])$ in a logarithmic scale. The precision of the phase boundaries in temperature is ±1°C. The red dashed line at a higher concentration indicates the solubility limit of $CaCl_2$, above which the mole ratio of $CaCl_2$ and surfactant in the examined liquid deviates from 0.25. Black dashed circles indicate the lower critical solution temperatures. The colored arrows at the top x-axis indicate the respective critical micelle concentrations at 25°C. 1ϕ I: Single isotropic phase. 2ϕ I/I: Two isotropic phases in equilibrium. L_β: Semi-crystalline lamellar phase. The same phase diagrams are shown as a function of the surfactant weight fraction in **Fig. II.1** and as a function of the surfactant concentration in mol·L^{-1} in **Fig. A.3**.

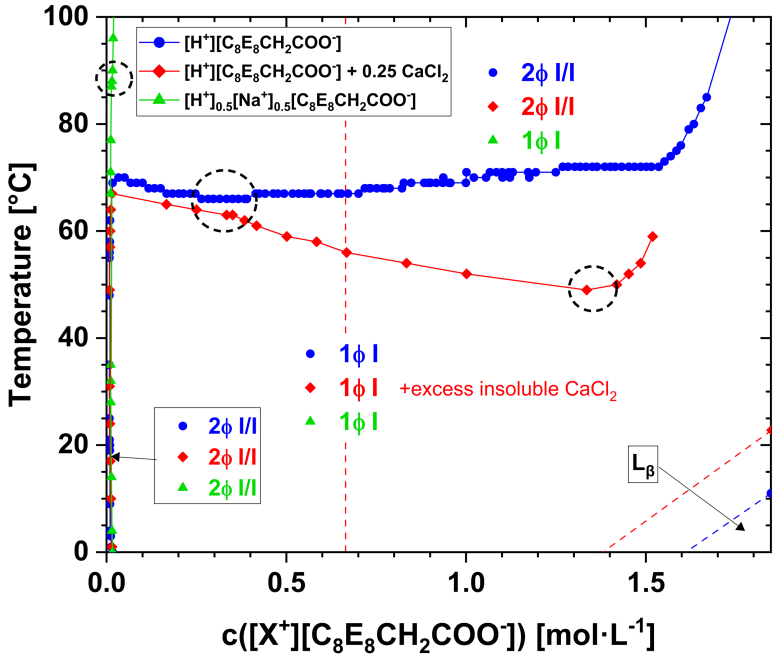

Fig. A.3. Binary phase diagrams of $C_8E_8CH_2COOH$ (here denoted as $[H^+][C_8E_8CH_2COO^-]$), $C_8E_8CH_2COOH$ with 0.25 $CaCl_2$ per $C_8E_8CH_2COOH$ molecule, and $[H^+]_{0.5}[Na^+]_{0.5}[C_8E_8CH_2COO^-]$ in water as a function of the molar surfactant concentration $c([X^+][C_8E_8CH_2COO^-])$ in linear scale. The precision of the phase boundaries in temperature is ±1°C. The red dashed line at a higher concentration indicates the solubility limit of $CaCl_2$, above which the mole ratio of $CaCl_2$ and surfactant in the examined liquid deviates from 0.25. Black dashed circles indicate the lower critical solution temperatures. 1ϕ I: Single isotropic phase. 2ϕ I/I: Two isotropic phases in equilibrium. L_β: Semi-crystalline lamellar phase. The same phase diagrams are shown as a function of the surfactant weight fraction in **Fig. II.1** and as a function of the surfactant mole fraction in **Fig. A.2**.

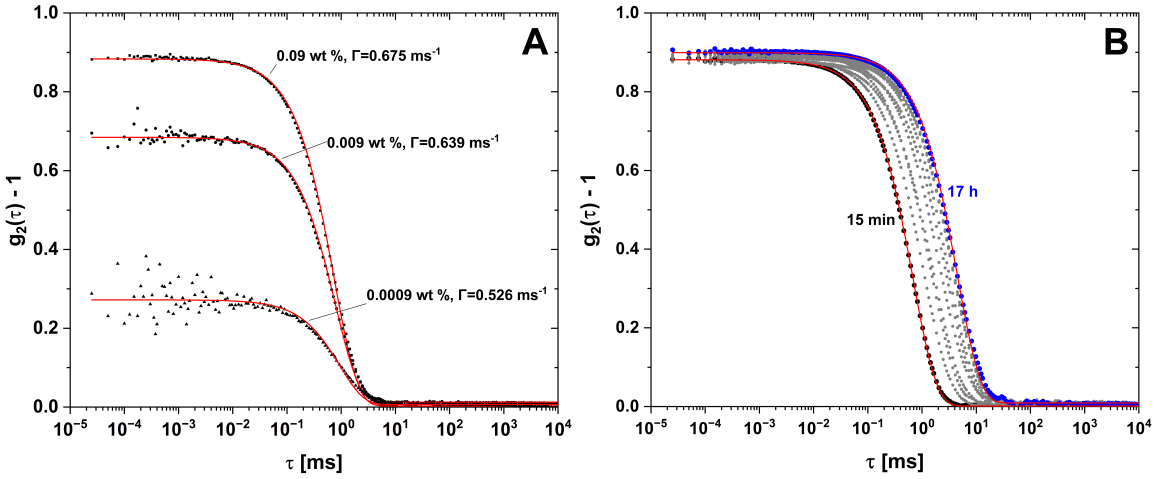

Fig. A.4. Correlation functions obtained by dynamic light scattering at 25°C at a scattering angle of 90° with a measuring time of 120 s. Solid red lines represent single exponential fits. (A) Three samples containing 0.09 wt%, 0.009 wt%, and 0.0009 wt% $C_8E_8CH_2COOH$ were measured after an equilibration time of 17 h. The exponential fits yield decay rates Γ of 0.675 ms^{-1} ($D = 1.93\ \mu m^2 \cdot s^{-1}$), 0.639 ms^{-1} ($D = 1.82\ \mu m^2 \cdot s^{-1}$), and 0.526 ms^{-1} ($D = 1.50\ \mu m^2 \cdot s^{-1}$), respectively. Using the Stokes-Einstein equation [1] and the viscosity of water, these diffusion coefficients correspond to hydrodynamic radii R_h of 127 nm, 135 nm, and 163 nm, respectively. (B) A sample containing 0.45 wt% $C_8E_8CH_2COOH$ was measured after different equilibration times between 15 min and 17 h. The exponential fits yield $\Gamma = 0.734\ ms^{-1}$ ($D = 2.09\ \mu m^2 \cdot s^{-1}$, $R_h = 117$ nm) after 15 min and $\Gamma = 0.113\ ms^{-1}$ ($D = 0.32\ \mu m^2 \cdot s^{-1}$, $R_h = 763$ nm) after 17 h.

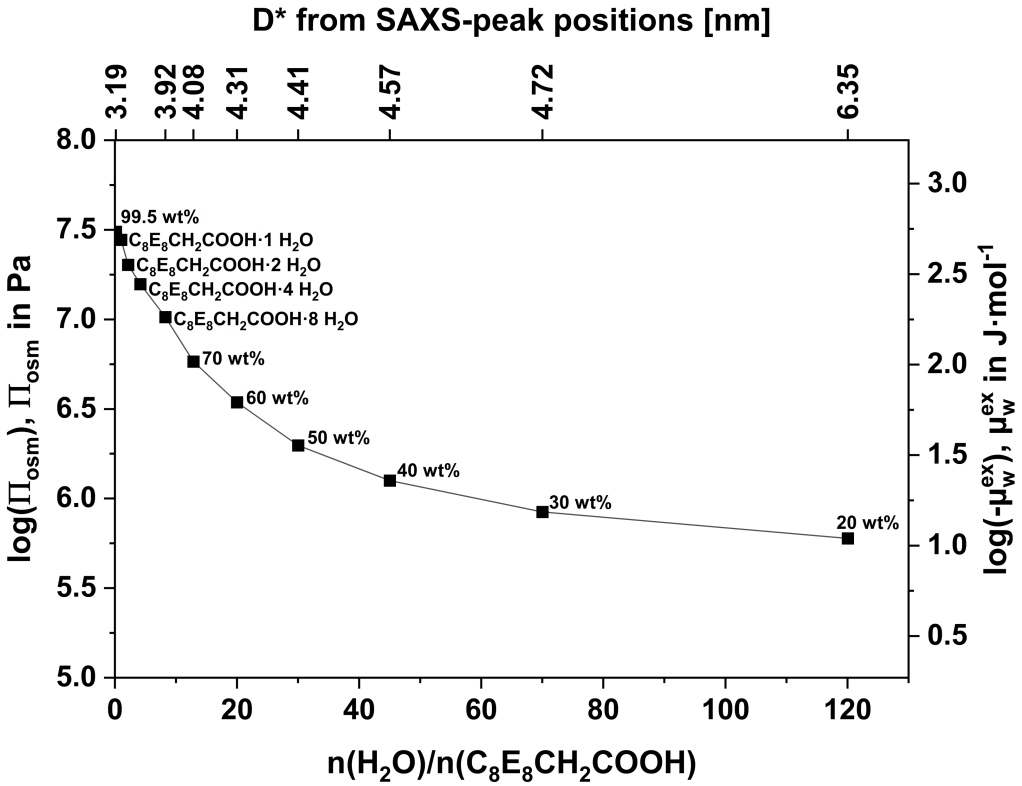

Fig. A.5. The decadic logarithm of the osmotic pressure Π_{osm} as well as the decadic logarithm of the negative excess chemical potential of water μ_w^{ex} are plotted as a function of the mole ratio of water and $C_8E_8CH_2COOH$ for several binary mixtures of $C_8E_8CH_2COOH$ and water. If known, the repeat distance $D^* = 2\pi \cdot q^{-1}$ for the sample calculated from the peak position in the respective SAXS spectrum is shown on the non-linear top-axis. Note that D* values for samples containing 20 wt% or 30 wt% surfactant were calculated from the structure factors S(q) obtained from model fits, see **Section II.4.4.**, because no pronounced structure factor peaks are visible in the spectra. Π_{osm} was calculated from the water activity a_w, obtained by vapor pressure osmometry, according to eq. (II.4). The excess chemical potential of water μ_w^{ex} is given by eq. (II.3).

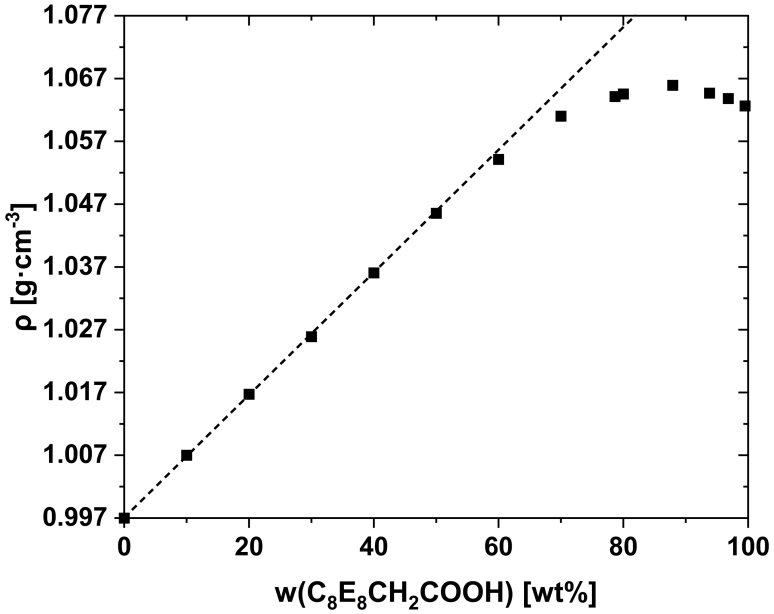

Fig. A.6. Physical densities of mixtures of $C_8E_8CH_2COOH$ and water at 25°C with $C_8E_8CH_2COOH$ contents ranging from 0 wt% to 99.5 wt% as a function of the $C_8E_8CH_2COOH$ content in wt%. The dashed line indicates the linear relation between density and concentration up to around 60 wt%. The corresponding data are given in **Table A.2**. Note that the used surfactant was only dried with subsequent removal of precipitated NaCl, without preceding cloud point extraction, in contrast to following chapters.

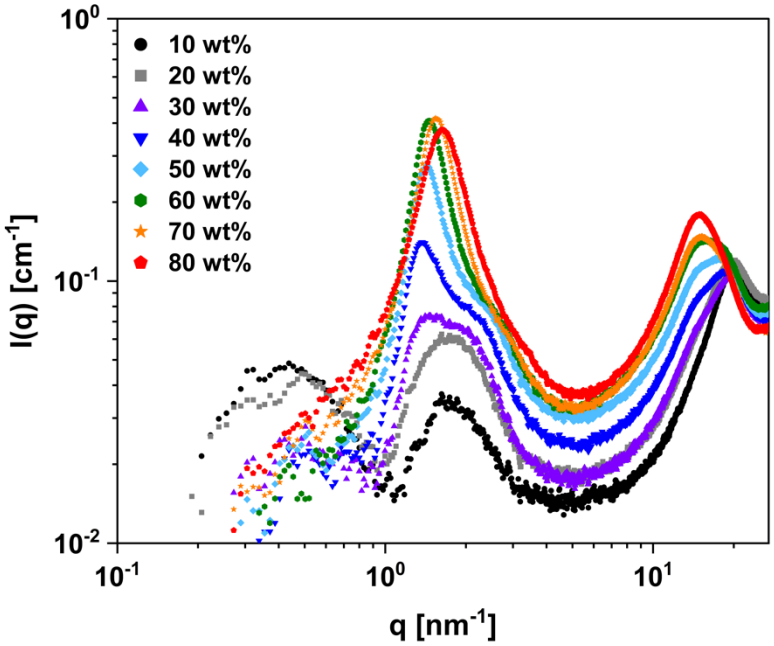

Fig. A.7. SWAXS data of binary mixtures of 10 wt% to 80 wt% $C_8E_8CH_2COOH$ and water in logarithmic scale. The same data are presented in linear scale in **Fig. II.5**.

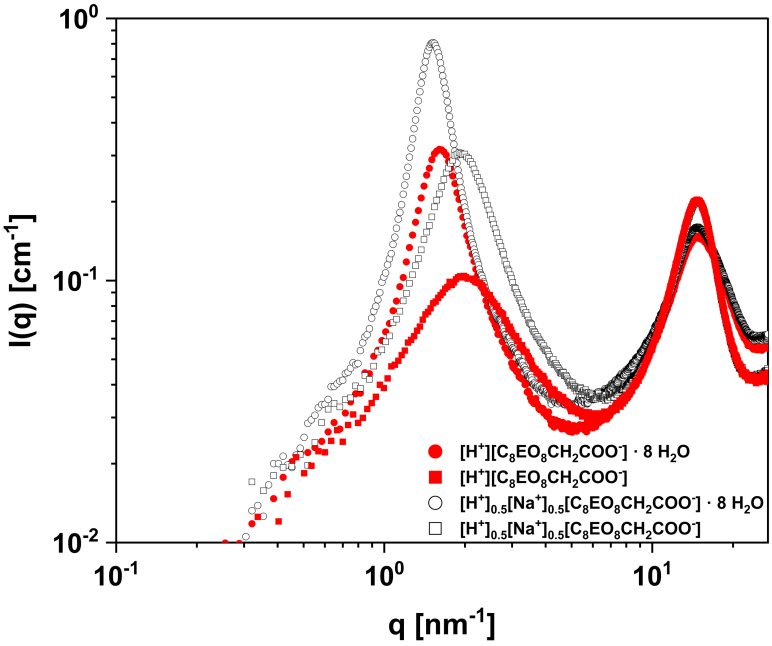

Fig. A.8. SWAXS data of the neat surfactants $C_8E_8CH_2COOH$ (≥99.5 wt%, ≤0.15 H_2O per surfactant molecule), here denoted as $[H^+][C_8E_8CH_2COO^-]$, and $[H^+]_{0.5}[Na^+]_{0.5}[C_8E_8CH_2COO^-]$ (≥99.2 wt%, ≤0.30 H_2O per surfactant molecule), as well as of both surfactants in presence of 8 H_2O molecules per surfactant molecule in linear scale. The same data are presented in linear scale in **Fig. II.6**.

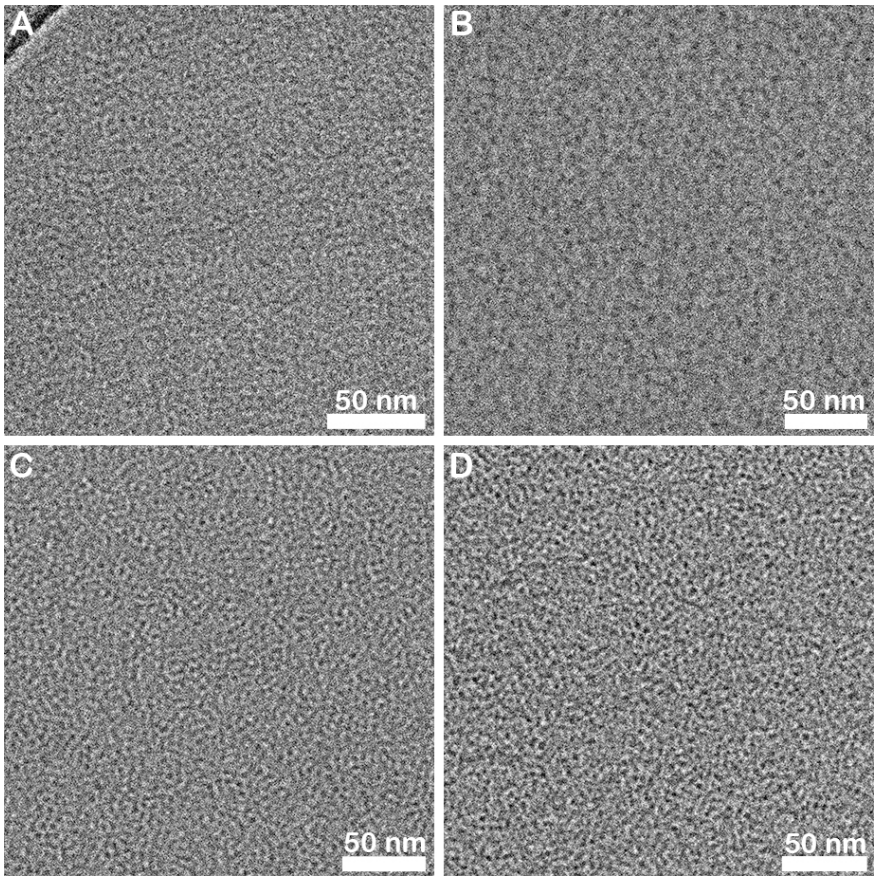

Fig. A.9. Cryo-TEM images of $C_8E_8CH_2COOH$ in water. Images (A) and (B) represent a concentration of 2 wt%, where the small spherical micelles are more scattered than in images (C) and (D), which represent a concentration of 20 wt%. The scale bars indicate a length of 50 nm.

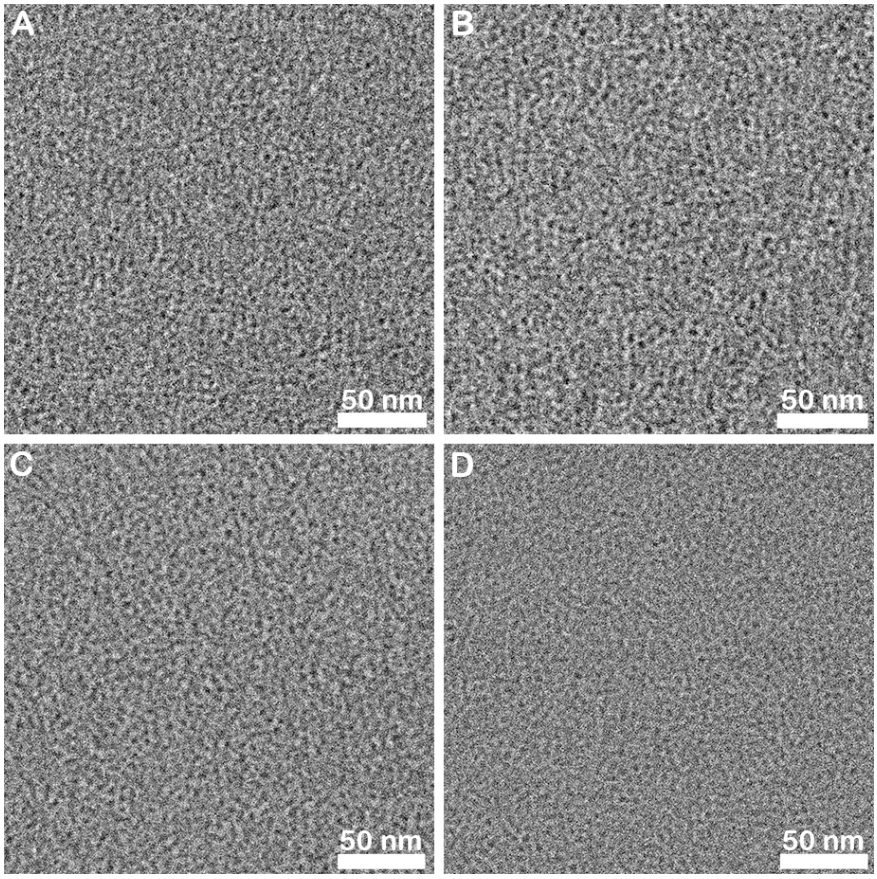

Fig. A.10. Cryo-TEM images of 20 wt% $[H^+]_{0.5}[Na^+]_{0.5}[C_8E_8CH_2COO^-]$ in water. Images (A) and (B) were recorded using the T12, while images (C) and (D) were recorded using the Talos. A high accumulation of small spherical micelles is seen in all of the images. The scale bars indicate a length of 50 nm.

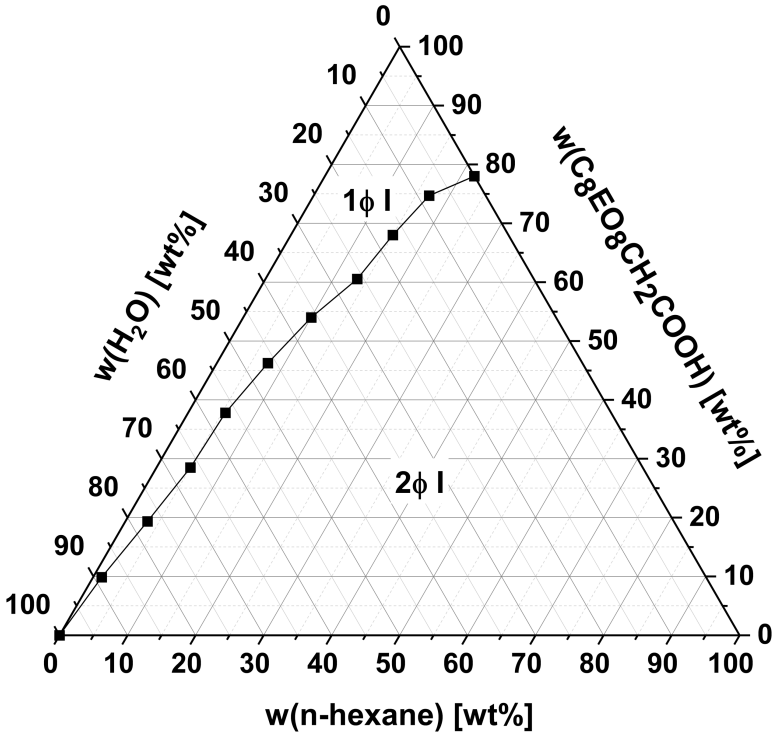

Fig. A.11. Ternary phase diagram of $H_2O/C_8E_8CH_2COOH$/n-hexane at a temperature of 23°C. The precision in w(n-hexane) is at least ±0.5 wt%. 1ϕ I: Single isotropic phase. 2ϕ I/I: Two isotropic phases in equilibrium.

A.2. Supplementary Tables

Table A.1. Analysis of the impurities contained in the Akypo® LF2 ($C_8E_8CH_2COOH$) batch received from Kao Chemicals. The analysis was provided by Kao Chemicals and the water content was checked by Karl Fischer titration.

substance	content [wt%]
water	9.0
NaCl	0.9
acetic acid	0
formic acid	0.0324
glycolic acid	0.0197
diglycolic acid	0.1349

Table A.2. Measured physical densities of various binary mixtures of $C_8E_8CH_2COOH$ and water at 25°C. Note that the used surfactant was only dried with subsequent filtration to remove precipitated salt, not cloud point extracted as typically done in following chapters. The precision of a single measurement is $1 \cdot 10^{-6}$ g·cm^{-3}. While only single measurements were performed, variations between different fillings of the oscillating tube with the same sample are typically only found in the last given digit, as can also be seen in the deviation of the measured value of pure water from the literature value of 0.99705 g·cm^{-3} [2].

w($C_8E_8CH_2COOH$) [wt%]	n(H_2O)/n($C_8E_8CH_2COOH$)	ρ [g·cm^{-3}]
99.5	0.15	1.06265
96.8	1	1.06383
93.8	2	1.06469
87.9	4	1.06594
80.0	7.5	1.06455
79.0	8	1.06413
70.0	13	1.06101
60.0	20	1.05414
50.0	30	1.04554
40.0	45	1.03606
30.0	70	1.02590
20.0	120	1.01671
10.0	270	1.00701
0	–	0.99700

Table A.3. Fitting parameters of the best fits obtained using a sphere form factor for spheres suspended in a fluid made of partially interdigitated headgroups and hydrating water and an effective Hayter-Penfold RMSA structure factor. The respective fits are shown in **Figs. II.7** and **II.8**A. The given values for the scattering length densities of the solvents, sld_solvent, are calculated based on the sample composition, using the measured physical densities given in **Table A.2**, and were not fitted as the amount of hydrating water is known and cannot vary. The scattering length density of the hydrocarbon cores, sld_core = $7.44 \cdot 10^{-4}$ nm^{-2}, is fixed and calculated using the molecular volume of a C_8 chain, V_{chain} = 0.247 nm^3, obtained by addition of group contributions, CH_3: 0.0548 nm^3 [3] and CH_2: 0.0274 nm^3 [4]. φ_{eff}: Effective volume fraction of the hydrocarbon cores. R_c: Radius of the spheres, i.e., of the hydrocarbon cores. q: Effective charge of the spheres, which in this case does not correspond to the actual surface charge. The scale factor was fixed at a value of 1. Additional quantities are derived from the fitting parameters. N_{agg}: Aggregation number, $N_{agg} = V/V_{chain}$. V: Volume of the hydrocarbon sphere, $V = 4\pi R_c^3/3$. A: Surface area of the hydrocarbon sphere, $A = 4\pi R_c^2$. a: Area per molecule, $a = A/N_{agg}$.

	w($C_8E_8CH_2COOH$) [wt%]						**w($[H^+]_{0.5}[Na^+]_{0.5}[C_8E_8CH_2COO^-]$) [wt%]**	
	50	**60**	**70**	**79**	**80**	**≥99.5**	**79.3**	**≥99.2**
n(H_2O)/n(surfactant)	30	20	13	8	7.5	≤0.15	8	≤0.30
sld_solvent [10^{-4} nm^{-2}]	10.2	10.4	10.5	10.6	10.6	10.8	10.7	10.7
φ_{eff}	$5.3 \cdot 10^{-2}$	$6.7 \cdot 10^{-2}$	$7.3 \cdot 10^{-2}$	$6.6 \cdot 10^{-2}$	$7.7 \cdot 10^{-2}$	$4.6 \cdot 10^{-2}$	$9.9 \cdot 10^{-2}$	$9.9 \cdot 10^{-2}$
R_c [nm]	1.13	1.19	1.16	1.10	1.12	0.77	1.31	1.00
q [e]	41.8	46.0	45.6	39.5	42.9	19.6	54.3	31.2
background [cm^{-1}]	$2.9 \cdot 10^{-2}$	$2.6 \cdot 10^{-2}$	$2.5 \cdot 10^{-2}$	$3.1 \cdot 10^{-2}$	$2.9 \cdot 10^{-2}$	$2.3 \cdot 10^{-2}$	$3.8 \cdot 10^{-2}$	$2.4 \cdot 10^{-2}$
N_{agg}	24	29	27	23	24	8	38	17
V [nm^3]	6.0	7.2	6.5	5.6	5.8	1.9	9.4	4.2
A [nm^2]	16	18	17	15	16	7.5	21	13
a [nm^2]	0.66	0.62	0.64	0.67	0.66	0.96	0.57	0.74

Table A.4. Fitting parameters of the best fits obtained using a core-shell sphere form factor and a Hayter-Penfold RMSA structure factor, as well as a Schulz polydispersity distribution for the radius and shell thickness. The respective fits are shown in **Fig. II.8**B. The scattering length density of the solvent (water), sld_solvent = $9.41 \cdot 10^{-4}$ nm^{-2}, is known. The scattering length density of the hydrocarbon cores, sld_core = $7.44 \cdot 10^{-4}$ nm^{-2}, is fixed and calculated using the molecular volume of a C_8 chain, V_{chain} = 0.247 nm^3, obtained by addition of group contributions, CH_3: 0.0548 nm^3 [3] and CH_2: 0.0274 nm^3 [4]. The volume fraction of surfactant φ is approximated using the physical densities of neat $C_8E_8CH_2COOH$ and water, assuming ideal mixing, and was fixed during fitting. R_c: Radius of the hydrocarbon core. t_s: Thickness of the shell. R_{eff}: Effective radius of the core-shell sphere. q: Effective charge of the spheres, which does not necessarily correspond to the actual surface charge. sld_shell: Fitted scattering length density of the shell. PD(R_c): Polydispersity of R_c. PD(t_s): Polydispersity of t_s. The scale factor was fixed at a value of 1. Additional quantities are derived from the fitting parameters. N_{agg}: Aggregation number, $N_{agg} = V_c/V_{chain}$. V_c: Volume of the hydrocarbon core, $V_c = 4\pi R_c^3/3$. A_c: Surface area of the hydrocarbon core, $A_c = 4\pi R_c^2$. a: Area per molecule, $a = A_c/N_{agg}$. V_s: Volume of the shell, $V_s = 4\pi R_{eff}^3/3 - V_c$. ν_{head}: Volume fraction of the headgroups in the shell, calculated with eq. (II.6). The scattering length density of the headgroup, sld_head was calculated using the physical density of the neat surfactant to obtain the molecular volume of the surfactant $V_{surfactant}$ = 0.848 nm^3 and subtracting V_{chain} to obtain the molecular volume of the headgroup V_{head} = 0.601 nm^3. r_{shell}: Number of water molecules per headgroup in the shell according to ν_{head}. L: Apparent length of the headgroup, $L = (V_{surfactant} + r_{shell} \cdot V_w)/a$, where V_w = 0.030 nm^3 is the molecular volume of water. Note that the extended length of EO_8CH_2COOH, approximated as EO_9, is 3.3 nm [5].

	w($C_8E_8CH_2COOH$) [wt%]							
	10	**20**	**30**	**40**	**50**	**60**	**70**	**80**
n(H_2O)/n(surfactant)	270	120	70	45	30	20	13	7.5
φ	$9.5 \cdot 10^{-2}$	$1.91 \cdot 10^{-1}$	$2.88 \cdot 10^{-1}$	$3.86 \cdot 10^{-1}$	$4.85 \cdot 10^{-1}$	$5.86 \cdot 10^{-1}$	$6.87 \cdot 10^{-1}$	$7.90 \cdot 10^{-1}$
R_c [nm]	1.23	1.24	1.19	1.20	1.22	1.25	1.21	1.21
t_s [nm]	1.21	1.18	1.17	1.24	1.16	1.08	1.04	1.04
R_{eff} [nm]	2.43	2.43	2.37	2.44	2.37	2.33	2.25	2.25
q [e]	2.5	2.7	2.9	8.9	6.4	7.1	6.7	6.7
sld_shell [10^{-4} nm^{-2}]	9.93	9.95	9.89	9.89	9.96	10.04	10.06	10.06
PD(R_c)	$2.63 \cdot 10^{-7}$	$9.52 \cdot 10^{-2}$	$1.58 \cdot 10^{-1}$	$2.03 \cdot 10^{-1}$	$2.76 \cdot 10^{-1}$	$3.38 \cdot 10^{-1}$	$3.75 \cdot 10^{-1}$	$3.75 \cdot 10^{-1}$
PD(t_s)	$4.09 \cdot 10^{-1}$	$2.63 \cdot 10^{-7}$	$1.48 \cdot 10^{-1}$	$7.26 \cdot 10^{-6}$	$2.89 \cdot 10^{-6}$	$2.30 \cdot 10^{-4}$	$6.95 \cdot 10^{-2}$	$6.95 \cdot 10^{-2}$
background [cm^{-1}]	$1.45 \cdot 10^{-2}$	$1.83 \cdot 10^{-2}$	$1.67 \cdot 10^{-2}$	$2.35 \cdot 10^{-2}$	$2.80 \cdot 10^{-2}$	$2.63 \cdot 10^{-2}$	$2.49 \cdot 10^{-2}$	$2.49 \cdot 10^{-2}$
N_{agg}	31	33	29	30	31	33	30	30
V_c [nm^3]	7.7	8.1	7.1	7.3	7.5	8.2	7.4	7.4
A_c [nm^2]	18.9	19.4	17.9	18.2	18.6	19.6	18.4	18.4
a [nm^2]	0.60	0.59	0.62	0.62	0.61	0.59	0.61	0.61
V_s [nm^3]	52.6	51.7	48.4	53.4	48.3	44.6	40.1	40.1
ν_{head}	$3.59 \cdot 10^{-1}$	$3.80 \cdot 10^{-1}$	$3.59 \cdot 10^{-1}$	$3.32 \cdot 10^{-1}$	$3.81 \cdot 10^{-1}$	$4.45 \cdot 10^{-1}$	$4.52 \cdot 10^{-1}$	$4.52 \cdot 10^{-1}$
r_{shell}	36	33	36	40	33	25	24	24
L [nm]	3.2	3.1	3.1	3.3	3.0	2.7	2.6	2.6

A.3. Different Packing Parameters Encountered in the Literature and the One Used in This Work

A theory attempting to predict the self-assembly of surfactants into different micellar shapes, taking into account thermodynamics, interaction free energies, and geometrical packing constraints, was presented by Israelachvili *et al.* in 1976 [6]. The "packing parameter" was originally used in a "packing equation", quantifying the sterical constraints induced by lateral packing in a molecular film. In the literature, there are now three different adjectives trying to sharpen the concept of the packing parameter and its quantification, the "spontaneous" packing parameter, the "effective" packing parameter, and the "critical" packing parameter.

The "spontaneous" packing parameter p_0 of a surfactant consisting of a hydrophobic chain and a hydrophilic headgroup is defined as

$$p_0 = \frac{\nu}{a_0 \cdot l_c} , \tag{A.3.1}$$

where ν is the partial molecular volume attributed to the hydrophobic chain, l_c is the critical length that the radius or thickness of the micellar hydrocarbon core cannot exceed, and a_0 is the equilibrium (or optimum) surface area per surfactant molecule at the hydrophobic-hydrophilic interface. Since the hydrocarbon core is a continuous liquid medium, there are no "holes" allowed, and the critical length l_c is given by the effective length of the hydrocarbon chain, averaged over all the conformations present. Typically, l_c is equal to 80–90% of the full extended length of the chain, which can be easily calculated for saturated hydrocarbon chains with n_c carbon atoms according to Tanford [7].

$$l_c \leq (0.15 + 0.1265 \cdot n_c)\ \text{nm} \tag{A.3.2}$$

In a similar way, the volume ν of the chain can be calculated from increment values derived from hundreds of known lipid densities. A general explicit expression was proposed by Tanford [7].

$$\nu = (27.4 + 26.9 \cdot n_c) \cdot 10^{-3}\ \text{nm}^3 \tag{A.3.3}$$

a_0 is obtained by minimizing the lateral equation of state for the surfactant molecules in the

surfactant film, i.e., if a surfactant occupies the surface area a_0, the Gibbs free energy is minimal. A review covering the lateral equation of state is given by Bauduin and Zemb [8]. For lipid bilayers, the first quantitative theory of the lateral equation of state was formulated by Marcelja and Wolfe in 1979 [9]. Since interaction free energies between surfactant molecules are considered in the calculation of the equilibrium surface area per molecule a_0, a_0 is not simply a geometrical parameter given by the molecular dimensions. A common error is also to use the area per molecule obtained from the crystal structure instead of a_0. The optimal area of contact of the headgroup with water a_0 is at least twice as large as the area per molecule in the crystalline state. Using the correct value for a_0, the "spontaneous" packing parameter p_0 is obtained according to eq. (A.3.1).

The value of p_0 allows for the prediction of the equilibrium micellar shape, for which the surfactants occupy a surface area equal to a_0. Among multiple shapes sharing the same a_0, the one with the lowest aggregation number is entropically favored. Spherical micelles are formed for $p_0 \leq 1/3$, cylindrical micelles for $p_0 \approx 1/2$, and bilayers for $p_0 \approx 1$. In a zero-order approximation, the packing parameter can be estimated comparing the molecular volumes of the headgroup and the hydrocarbon chain, similar to the hydrophilic-lipophilic balance (HLB) used in chemical engineering.

However, the value of a_0 is often not easily accessible. By small-angle scattering techniques a surface area per molecule for an average structure can be derived from a real sample. This experimentally accessible effective surface area per molecule, a, is often different from the equilibrium surface area a_0. In analogy to the "spontaneous" packing parameter p_0 with the equilibrium surface area per molecule a_0, an "effective" packing parameter p is then defined with the effective surface area per molecule a.

$$p = \frac{v}{a \cdot l_c} \tag{A.3.4}$$

The discrepancy between a_0 and a, and therefore also between p_0 and p, is a consequence of additional constraints imposed on the surfactant packing in a real sample. While the Gibbs free energy is minimal for one surfactant molecule in an interfacial layer surrounded by on average 5-7 neighbors, depending on the Gaussian curvature, if the area per molecule equals a_0, the Gibbs free energy of the whole system is minimal if the area per molecule equals a at a given point in the equilibrium phase diagram. It is also possible that the energetically favored structure with minimal interfacial energy, i.e., the one that fulfills $a = a_0$

for all molecules, is not the thermodynamically favored structure, because another structure with $a \neq a_0$ has a lower aggregation number and is therefore entropically favored in such a way that the total free energy is minimal for $a \neq a_0$ [10]. The deviation from a_0, i.e., from the preferred, spontaneous packing, results in a cost in bending free energy. The difference between p_0 and p is directly linked to the bending free energy

$$F = \frac{1}{2} \cdot k^* \cdot (p - p_0)^2 \,, \tag{A.3.5}$$

where k* is a generalized bending constant [11]. The bending free energy is taken as a harmonic expression coupled to the packing parameter and allows to define quantitatively the stiffness in $kJ \cdot mol^{-1}$ [12].

Though the term “critical packing parameter” is also used for example in a book by Israelachvili [13], the terminology of “spontaneous” and “effective” packing parameter should be used instead for clarity, as the “critical” packing parameter is ill-defined. It is regularly used in the literature either for the “spontaneous” or the “effective” packing parameter, leading to the confusion of the two different parameters [14]. The notation as “critical” usually suggests a critical value for which a transition is induced, e.g., a phase transition at a critical temperature. A critical value for the packing parameter is for example exactly 1/3, for which molecules can be packed into a perfect sphere. However, the calculated “effective” or “spontaneous” packing parameter is not a critical value, it can only be compared to the intrinsic critical values of the packing parameter. The notation of either the “spontaneous” or the “effective” packing parameter as the “critical” packing parameter is therefore in itself misleading. In the present work, the “critical” packing parameter is not used at all, and the used packing parameter is specified in each sentence.

A.4. References

[1] A. Einstein, Über die von der molekularkinetischen Theorie der Wärme geforderte Bewegung von in ruhenden Flüssigkeiten suspendierten Teilchen, Ann Phys 17 (1905) 549–560.

[2] W. Wagner, A. Pruß, The IAPWS Formulation 1995 for the Thermodynamic Properties of Ordinary Water Substance for General and Scientific Use, J Phys Chem Ref Data 31 (2002) 387–535. https://doi.org/10.1063/1.1461829.

[3] D. Hoshino, K. Nagahama, M. Hirata, Prediction of the liquid molar volume and the latent heat of vaporization for aliphatic hydrocarbons by the group contribution method., Journal of The Japan Petroleum Institute 22 (1979) 32–37. https://doi.org/10.1627/jpi1958.22.32.

[4] D.W. van Krevelen, K. te Nijenhuis, Properties of Polymers, 4th ed., Elsevier B.V., Amsterdam, 2009.

[5] P. Alexandridis, U. Olsson, B. Lindman, Self-Assembly of Amphiphilic Block Copolymers, Macromolecules 28 (1995) 7700–7710.

[6] J.N. Israelachvili, D.J. Mitchell, B.W. Ninham, Theory of self-assembly of hydrocarbon amphiphiles into micelles and bilayers, Journal of the Chemical Society, Faraday Transactions 2: Molecular and Chemical Physics 72 (1976) 1525–1568. https://doi.org/10.1039/F29767201525.

[7] C. Tanford, Micelle shape and size, Journal of Physical Chemistry 76 (1972) 3020–3024. https://doi.org/10.1021/j100665a018.

[8] P. Bauduin, T. Zemb, Perpendicular and lateral equations of state in layered systems of amphiphiles, Curr Opin Colloid Interface Sci 19 (2014) 9–16. https://doi.org/10.1016/j.cocis.2014.02.002.

[9] S. Marčelja, J. Wolfe, Properties of bilayer membranes in the phase transition or phase separation region, Biochimica et Biophysica Acta (BBA) - Biomembranes 557 (1979) 24–31. https://doi.org/10.1016/0005-2736(79)90086-5.

[10] J.N. Israelachvili, S. Marčelja, R.G. Horn, Physical principles of membrane organization, Q Rev Biophys 13 (1980) 121–200. https://doi.org/10.1017/S0033583500001645.

[11] W. Kunz, F. Testard, T. Zemb, Correspondence between Curvature, Packing Parameter, and Hydrophilic−Lipophilic Deviation Scales around the Phase-Inversion Temperature, Langmuir 25 (2009) 112–115. https://doi.org/10.1021/la8028879.

[12] S. Hyde, S. Andersson, K. Larsson, Z. Blum, T. Landh, S. Lidin, B.W. Ninham, The Language of Shape: The Role of Curvature in Condensed Matter: Physics, Chemistry and Biology, Elsevier, Amsterdam, 1997. https://doi.org/10.1016/B978-0-444-81538-5.X5000-X.

[13] J.N. Israelachvili, Intermolecular and Surface Forces, 3rd ed., Academic Press, Waltham, MA, 2011.

[14] J.-F. Dufrêche, T. Zemb, Bending: from thin interfaces to molecular films in microemulsions, Curr Opin Colloid Interface Sci (2020). https://doi.org/10.1016/j.cocis.2020.06.001.

Appendix B.

Supplementary Material – Chapter III.

B.1. Supplementary Figures

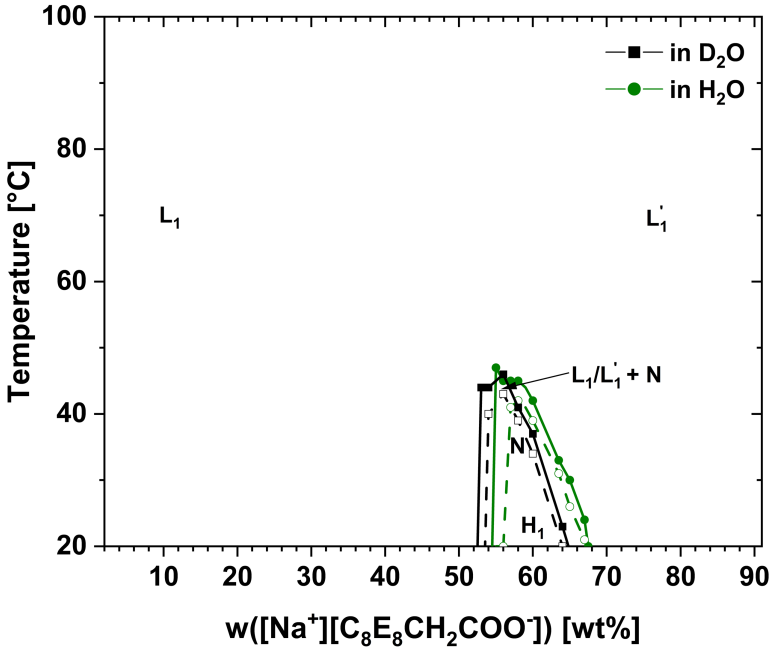

Fig. B.1. Comparison of phase boundaries in binary mixtures of [Na^+][$C_8E_8CH_2COO^-$] and H_2O or D_2O. The binary phase diagram of [Na^+][$C_8E_8CH_2COO^-$] in H_2O is the same as the one given in **Fig. III.2**A. Phase boundaries of the liquid crystalline regions in D_2O were determined by visual observation combined with polarized optical microscopy with an accuracy in temperature of ±1°C (in analogy to the one recorded with H_2O). Filled symbols mark the transition between a completely isotropic mixture and a mixture that exhibits birefringence. Empty symbols mark the transition between a fully birefringent liquid crystalline mixture and a mixture, in which birefringent and isotropic domains coexist. L1: Solution of core-shell micelles. L_1': Head-group-interdigitated micellar regime. L_1/L_1': Transition zone between L_1 and L_1'. H_1: Hexagonal phase. N: Nematic phase.

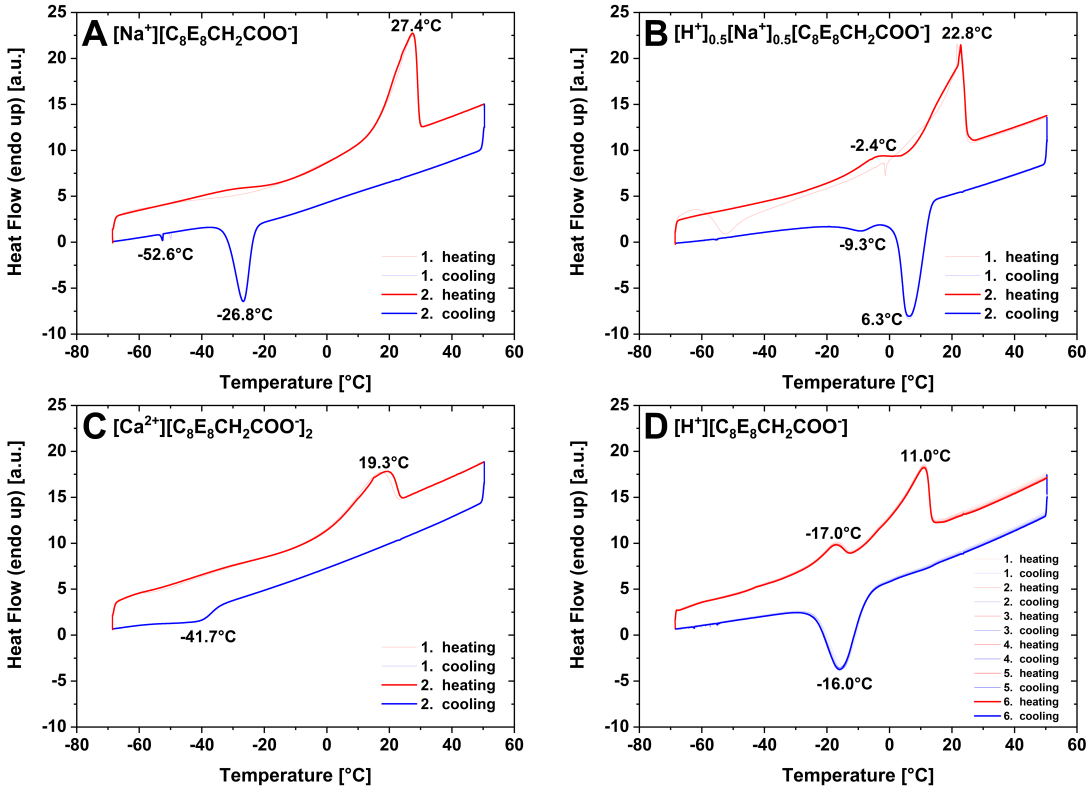

Fig. B.2. Heat flux differential scanning calorimetry (DSC) of $[X^+][C_8E_8CH_2COO^-]$. (A) Neat $[Na^+][C_8E_8CH_2COO^-]$ exhibits an endothermic peak on heating with a maximum at 27.4°C during the second heating and cooling cycle. (B) Neat $[H^+]_{0.5}[Na^+]_{0.5}[C_8E_8CH_2COO^-]$ shows a similar maximum at 22.8°C on heating during the second heating and cooling cycle. (C) For neat $[Ca^{2+}][C_8E_8CH_2COO^-]_2$, the peak maximum is found slightly below room temperature at 19.3°C during the second heating and cooling cycle. (D) The neat acid $[H^+][C_8E_8CH_2COO^-]$ also exhibits the same transition with its peak maximum being located at 11.0°C during the sixth heating and cooling cycle. DSC measurements were conducted in a temperature range from -70°C to 50°C. Prior to heating and cooling, samples were held for 60 min and 10 min at -70°C and 50°C, respectively. Heating and cooling rates were fixed at 3°C·min^{-1}. In all cases, only small differences can be observed between different heating and cooling cycles.

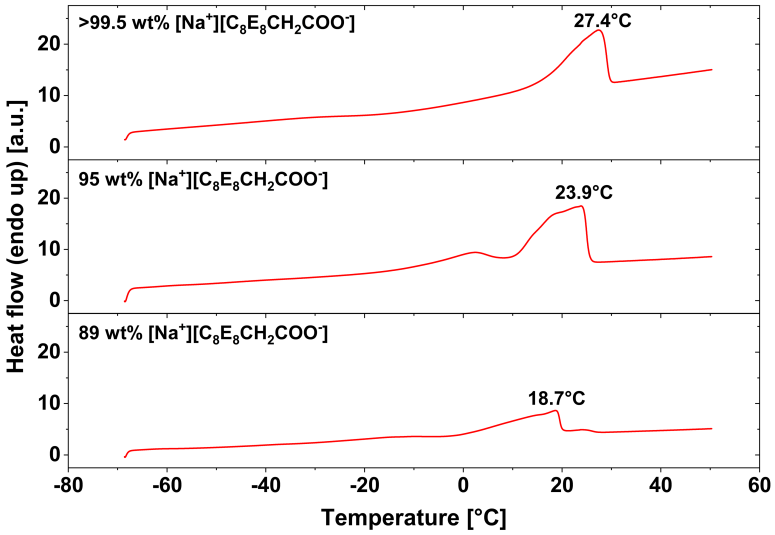

Fig. B.3. From top to bottom: Heating curves of the second heating and cooling cycle of neat $[Na^+][C_8E_8CH_2COO^-]$ (>99.5 wt%), 95 wt% $[Na^+][C_8E_8CH_2COO^-]$, and 89 wt% $[Na^+][C_8E_8CH_2COO^-]$ are given. A peak maximum is observed at 27.4°C, 23.9°C, and 18.7°C, respectively. DSC measurements were conducted in a temperature range from -70°C to 50°C. Prior to heating and cooling, samples were held for 60 min and 10 min at -70°C and 50°C, respectively. Heating and cooling rates were fixed at 3°C·min^{-1}.

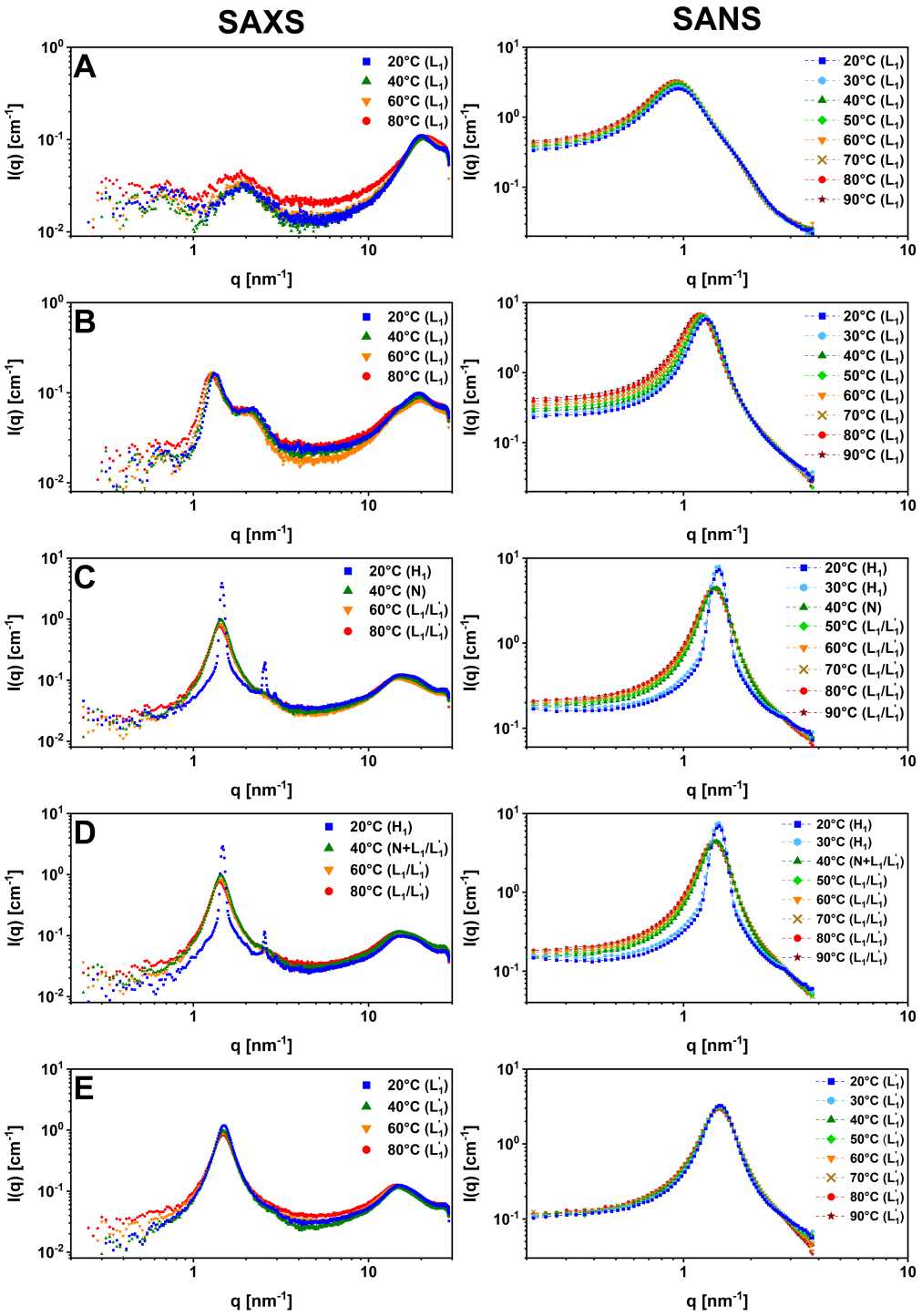

Fig. B.4. SAXS (left column) and SANS (right column) along a dilution line of $[Na^+][C_8E_8CH_2COO^-]$ at different temperatures in logarithmic scale. (A) 10 wt% of $[Na^+][C_8E_8CH_2COO^-]$ in water (H_2O for SAXS and D_2O for SANS). The L_1 core-shell microstructure is found at any temperature. (B) 30 wt% of $[Na^+][C_8E_8CH_2COO^-]$ in water (H_2O for SAXS and D_2O for SANS). The L_1 core-shell microstructure is found at any temperature. (C) 58 wt% of $[Na^+][C_8E_8CH_2COO^-]$ in water (H_2O for SAXS and D_2O for SANS). At 20°C and 30°C, the hexagonal phase (H_1) is observed. At 40°C the H_1 phase is molten into an optically birefringent nematic phase (N). For higher temperatures, the flocculated micellar regime (transition between L_1 and L_1') is observed. (D) 60 wt% of $[Na^+][C_8E_8CH_2COO^-]$ in water (H_2O for SAXS and D_2O for SANS). At 20°C and 30°C, the hexagonal phase (H_1) is observed. At 40°C the H_1 phase is molten into an optically birefringent nematic phase in equilibrium with a flocculated micellar phase (N+L_1/L_1'). For higher temperatures, the flocculated micellar regime is observed. (E) 70 wt% of $[Na^+][C_8E_8CH_2COO^-]$ in water (H_2O for SAXS and D_2O for SANS). The headgroup interdigitated micellar regime (L_1') is observed at any temperature. The same spectra in linear scale are given in **Fig. III.3**.

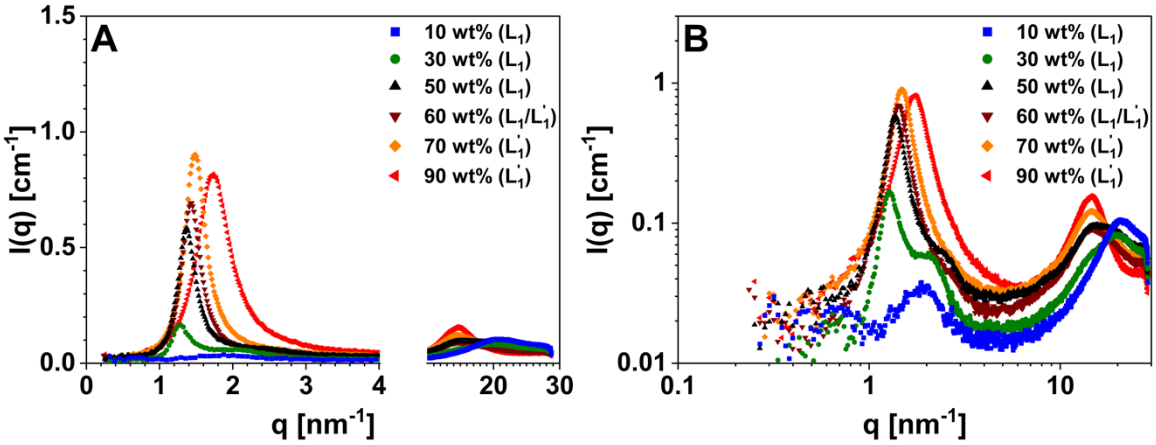

Fig. B.5. SAXS spectra of binary mixtures of 10, 30, 50, 60, 70, and 90 wt% $[Na^+][C_8E_8CH_2COO^-]$ and water in (A) linear scale and (B) logarithmic scale. Spectra at 10, 30, and 50 wt% represent classical core-shell micelles (L_1), while spectra at 70 wt% and 90 wt% represent the headgroup interdigitated micellar regime (L_1'). At 60 wt%, there is a transition state of flocculated micelles between L_1 and L_1' (L_1/L_1'). For a more detailed discussion regarding this transition (in the case of $[H^+][C_8E_8CH_2COO^-]$), the reader is referred to **Chapter II**.

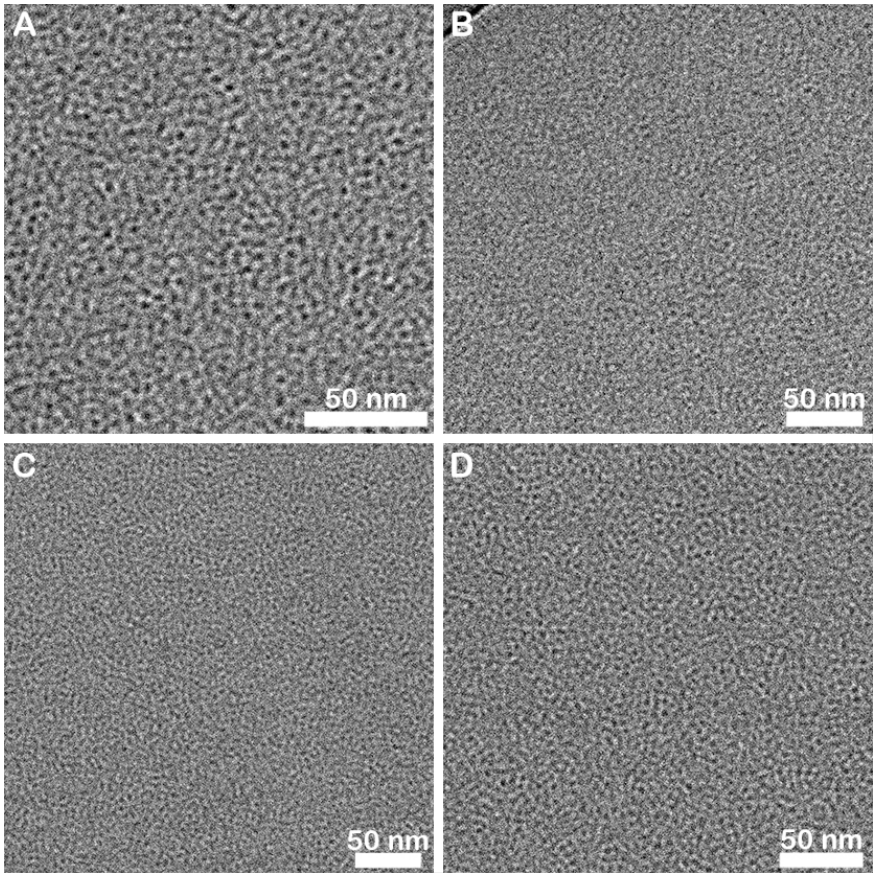

Fig. B.6. Cryo-TEM images of 20 wt% $[Na^+][C_8E_8CH_2COO^-]$ in water. Images (A) and (B) were recorded using the T12, while images (C) and (D) were recorded using the Talos. In (A), the structures are shown at high magnification. A high accumulation of aggregates near the supporting carbon film in the top left corner of the image is seen in (B). Closely packed small spherical micelles are seen in all of the images. The scale bars indicate a length of 50 nm.

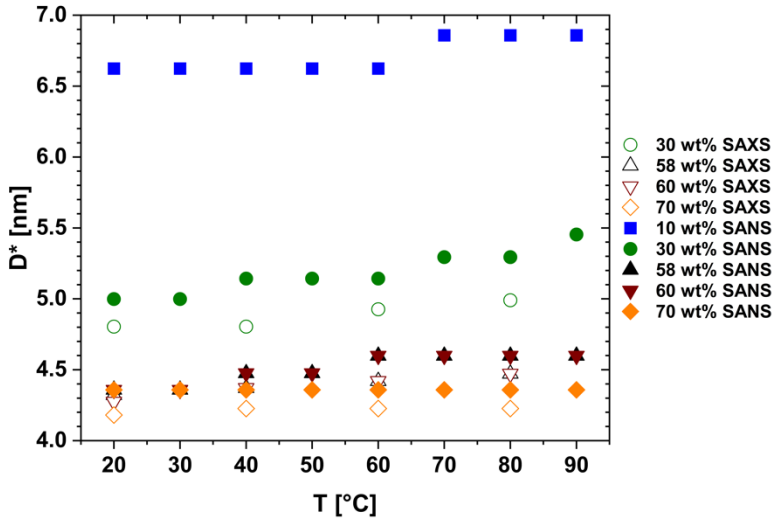

Fig. B.7. Temperature dependence of the repeat distance $D^* = 2\pi \cdot q^{-1}$, obtained from the structure factor peak position in SAXS (empty symbols) and SANS (full symbols) for different binary mixtures of $[Na^+][C_8E_8CH_2COO^-]$ and water (H_2O for SAXS and D_2O for SANS). The corresponding SAXS and SANS spectra are given in **Figs. III.3** and **B.4**.

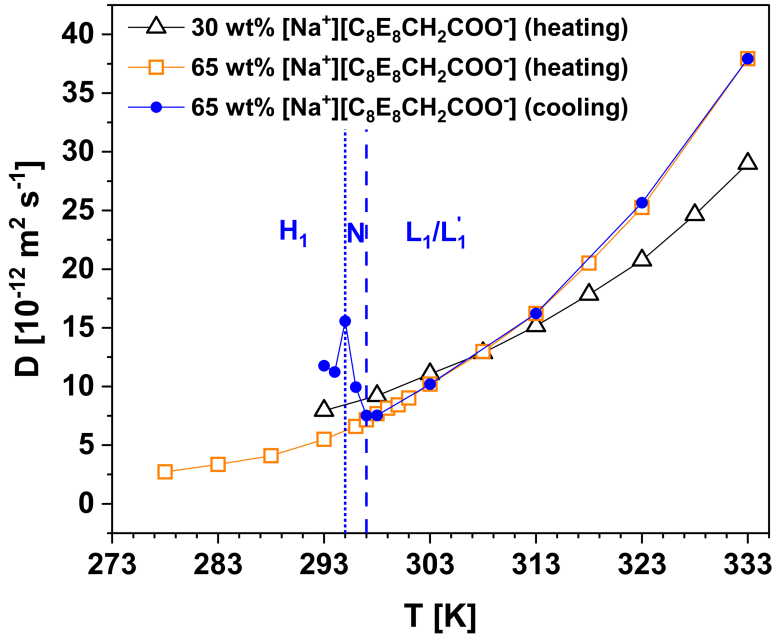

Fig. B.8. The self-diffusion coefficient of $[Na^+][C_8E_8CH_2COO^-]$ in binary mixtures of 30 wt% or 65 wt% $[Na^+][C_8E_8CH_2COO^-]$ and water is given as a function of temperature. The self-diffusion was measured by DOSY-NMR. The sample containing 65 wt% $[Na^+][C_8E_8CH_2COO^-]$ shows a phase transition from a hexagonal (H_1) phase, or rather from a nematic (N) phase, to an isotropic L_1/L_1' phase at a temperature of 297 K. The self-diffusion was measured both during heating and cooling of the sample. The dashed blue line indicates the phase transition of the 65 wt% sample, which corresponds to the nematic-to-L_1/L_1' transition. The dotted blue line indicates the temperature, at which the hexagonal-to-nematic transition is expected to be. The sample containing 30 wt% of surfactant exhibits no phase transition and is located in the core-shell micellar regime (L_1). The equilibration time at each temperature was 10 min. Above 35°C, the surfactant self-diffusion is higher at 65 wt% (L_1/L_1') than at 30 wt% (L_1), while it is lower below 35°C. The reason for this is probably an interplay between the viscosity of the sample and the presence or absence of bulk water hindering the surfactant self-diffusion. The presence of bulk-water at 30 wt% $[Na^+][C_8E_8CH_2COO^-]$ decreases the surfactant self-diffusion compared to the 65 wt% sample, where there is no longer bulk-water separating the micelles. On the other hand, the viscosity at 65 wt% is increased, especially at lower temperatures, compared to 30 wt%.

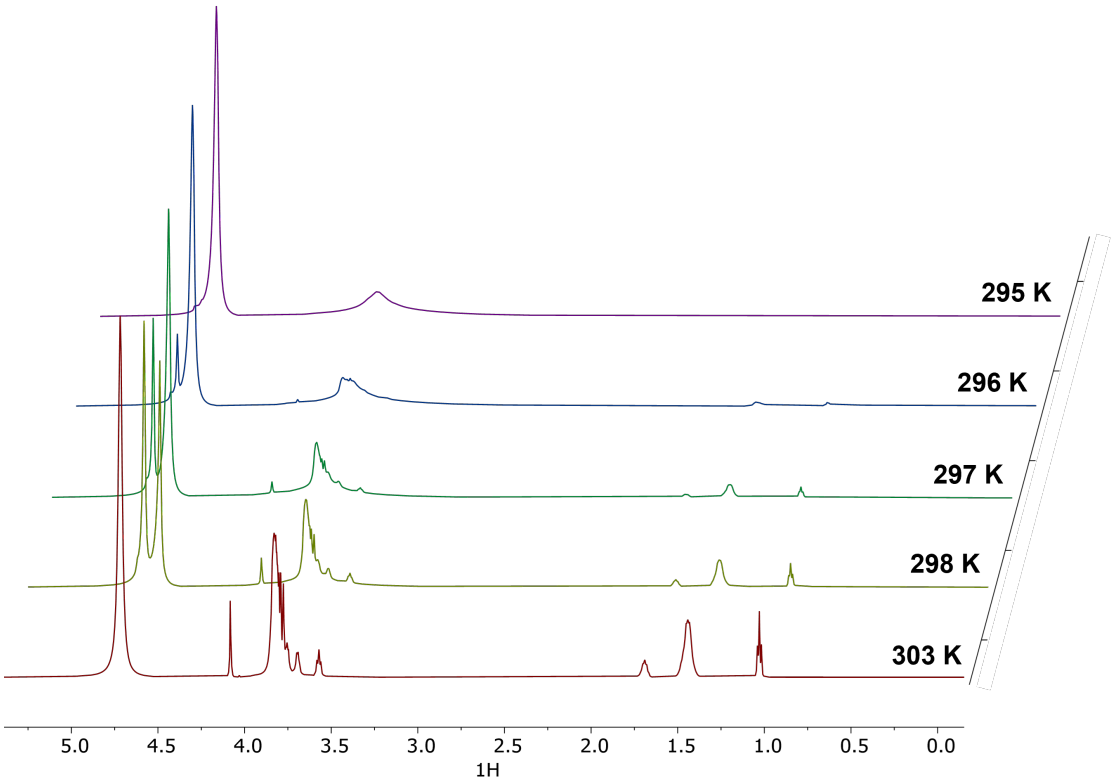

Fig. B.9. ^{1}H-NMR spectra (D1 2s, NS 8, DS 4, and TD 65k) at different temperatures obtained during cooling of a 65 wt% [Na^{+}][$C_8E_8CH_2COO^{-}$] sample. A phase transition is indicated at 297 K, where the typical broadening of the signals on gel formation (hexagonal or nematic phase) starts. At temperatures below the transition temperature, most signals are absent due to the low T_2 (spin-spin) relaxation times and the slow molecular mobility.

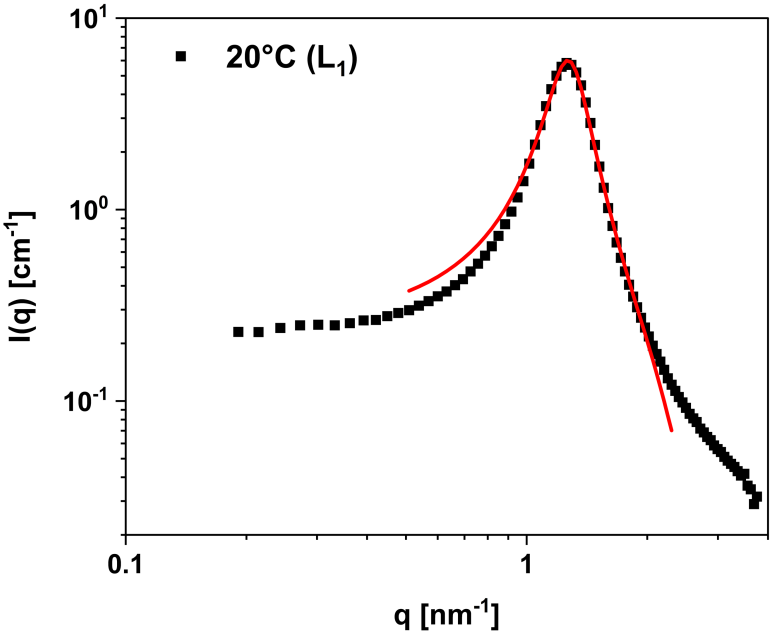

Fig. B.10. Best fit (solid red line) to the SANS spectrum on absolute scale of a mixture of 30 wt% $[Na^+][C_8E_8CH_2COO^-]$ and D_2O at 20°C (black squares) in logarithmic scale, using a prolate core-shell ellipsoid form factor and a Hayter-Penfold RMSA structure factor [1,2]. Fits were performed using the SasView package (version 5.0.4) [3]. The fit is constrained by keeping known parameters fixed (SLD of the core, SLD of the solvent, and volume fraction of the surfactant ($\varphi = 0.284$)), an approach initiated by Hayter and Penfold [4], and making sure that fitted parameters are self-consistent and make physical sense. For neutrons, the scattering length density (SLD) of the solvent D_2O is $6.39 \cdot 10^{-4}$ nm^{-2}. The SLD of the surfactant's neat hydrophilic headgroup ($C_{18}O_{11}H_{34}Na$, $V_{head} = 0.604$ nm^3) is $1.53 \cdot 10^{-4}$ nm^{-2} and the SLD of the hydrophobic hydrocarbon chain (C_8H_{17}, $V_{chain} = 0.247$ nm^3) is $-0.42 \cdot 10^{-4}$ nm^{-2}. The molecular volume of the hydrocarbon chain is calculated by the addition of group contributions (CH_3: 0.0548 nm^3 [5], CH_2: 0.0274 nm^3 [6]). From the density of neat $[Na^+][C_8E_8CH_2COO^-]$ at 25°C ($\rho = 1.099$ g·cm^{-3}) and the surfactant's molar mass of 563 g·mol^{-1}, a molecular volume of 0.850 nm^3 can be deduced for the whole surfactant (note that the neat $[Na^+][C_8E_8CH_2COO^-]$ at 25°C was in a subcooled state prior to forming a L_β phase). Since the SLD of the shell can vary depending on the volume fraction of D_2O (φ_{D2O}) in the shell, the SLD of the shell was fitted. However, the fitted SLD of the shell was compared to the SLD expected for the obtained volume fraction of water in the shell, i.e., the fitted SLD(shell) was compared to $SLD_{calc}(shell) = \varphi_{D2O} \cdot SLD(D_2O) + (1-\varphi_{D2O}) \cdot SLD(head)$. φ_{D2O} was obtained from the fitted aggregation number N_{agg} and shell volume V_s according to the equation $1-(N_{agg} \cdot V_{head}/V_s)$, where V_{head} is the molecular volume of the headgroup. In addition to the already mentioned ones, the following parameters were used: background = 0.031 cm^{-1}, equatorial core radius = 1.10 nm, core ellipticity = 1.27, shell thickness = 1.01 nm, SLD(shell) = $4.146 \cdot 10^{-4}$ nm^{-2}, and charge = 33 e. Further, the thickness of the shell was assumed to be uniform. The fitted values correspond to an aggregation number of 29 (obtained by dividing the core volume by the molecular volume of one chain) and an area per molecule of 0.627 nm^2. It is important to note that the same fit can be produced with different combinations of radius and ellipticity, as long as the volume is constant. Even a core-shell model can be used to produce the same fit with a core radius of 1.2 nm. Thus, it is not possible to deduce the ellipticity of the micelles.
Comment: In the concentrated L_1' regime, fits would not be very helpful, as the repulsive potential is no longer electrostatics plus some hard sphere potential. In the core-shell domain (L_1), on the other hand, constrained fits, as shown in **Fig. B.10**, are possible. Further fits are not shown in this chapter, as they not substantially benefit the discussion.

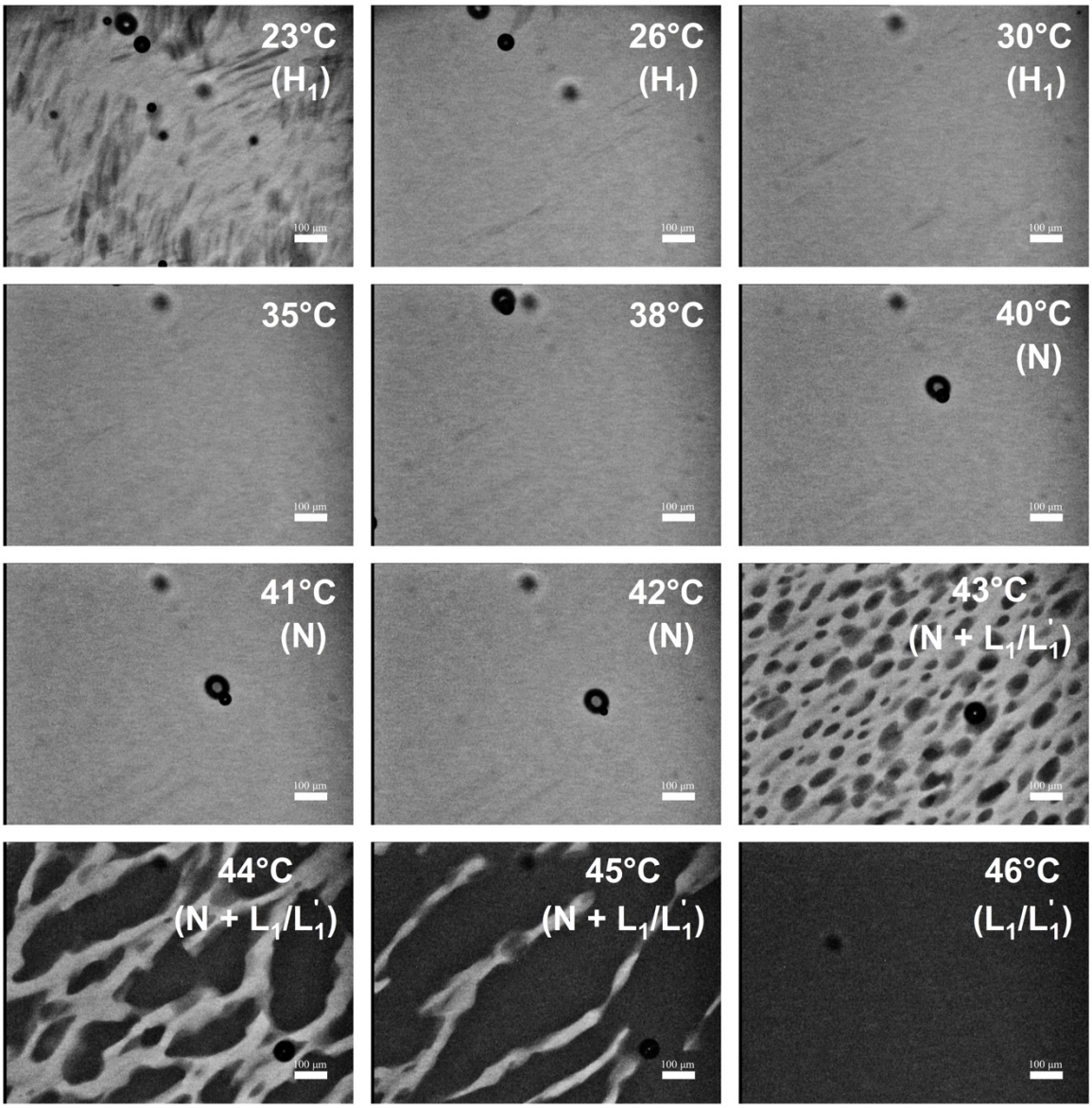

Fig. B.11. Transition from the H_1 phase to the L_1/L_1'phase as observed by polarized optical microscopy. Images of 58 wt% $[Na^+][C_8E_8CH_2COO^-]$ in water at different temperatures were taken through crossed polarizers with a 100x magnification. Scale bars indicate a length of 100 µm. Respective temperatures and phases, as deduced from SAXS and SANS, are indicated. H_1: Hexagonal phase. N: Nematic phase. $N+L_1/L_1$': Nematic phase and isotropic "flocculated" micellar phase (transition state between core-shell micellar L_1 phase and headgroup interdigitated L_1' phase) in equilibrium. L_1/L_1': "Flocculated" micellar phase.

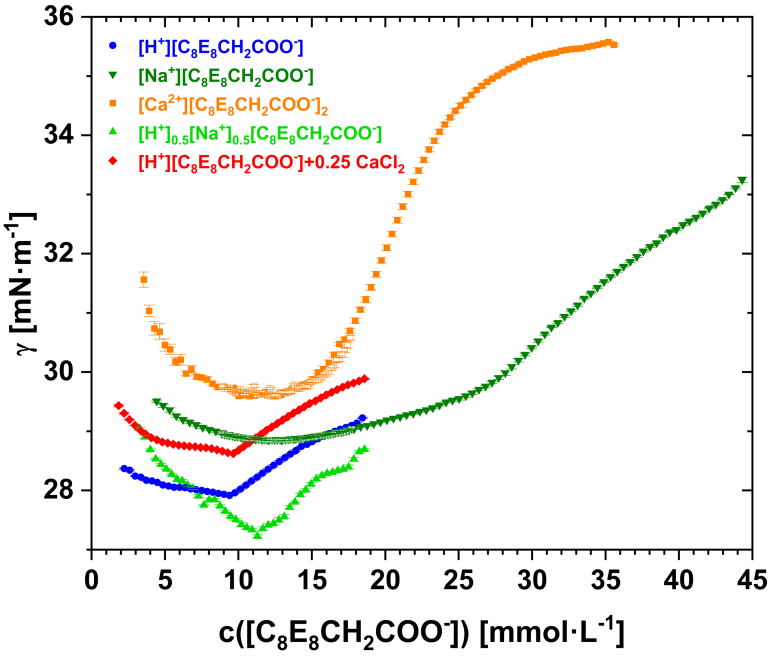

Fig. B.12. Equilibrium surface tension γ at 25°C for $[H^+][C_8E_8CH_2COO^-]$, $[Na^+][C_8E_8CH_2COO^-]$, $[Ca^{2+}][C_8E_8CH_2COO^-]_2$, $[H^+]_{0.5}[Na^+]_{0.5}[C_8E_8CH_2COO^-]$, and $[H^+][C_8E_8CH_2COO^-]$ in presence of 0.25 mol $CaCl_2$ per mol of surfactant in water as a function of the surfactant concentration. Note that the concentrations are related to the concentration of the surfactant anion $[C_8E_8CH_2COO^-]$, i.e., $[Ca^{2+}][C_8E_8CH_2COO^-]_2$ is not accounted for as one complex. A second measurement around the surface tension minimum is shown for $[Na^+][C_8E_8CH_2COO^-]$ and $[Ca^{2+}][C_8E_8CH_2COO^-]_2$ (empty symbols). The minimum in surface tension is given as the respective CMC. CMC: $c([H^+][C_8E_8CH_2COO^-]) = 9.4$ mmol·L^{-1} (0.51 wt%), $c([Na^+][C_8E_8CH_2COO^-]) = 12.5$ mmol·L^{-1} (0.71 wt%), $c([Ca^{2+}][C_8E_8CH_2COO^-]_2) = 12.0$–$12.7$ mmol·L^{-1} (0.67–0.71 wt%), $c([H^+]_{0.5}[Na^+]_{0.5}[C_8E_8CH_2COO^-]) = 11.3$ mmol·L^{-1} (0.62 wt%), and $c([H^+][C_8E_8CH_2COO^-]+0.25\ CaCl_2) = 9.7$ mmol·L^{-1} (0.52 wt%). CMC values also correspond to the respective upper limits of auto-coacervation. The increase in surface tension above the CMC is usually described by surface active impurities that are depleted from the surface above the CMC. A similar description may be feasible here, with the "impurities" being the proportion of the surfactant with a smaller number of EO-groups. Another effect may be the adsorption of micelles to the surfactant monolayer (interdigitating headgroups) at the water/air interface, forming an interphase which is thicker than the classical monolayer. Such effects have been reviewed by Thomas and Penfold (2015) [7].

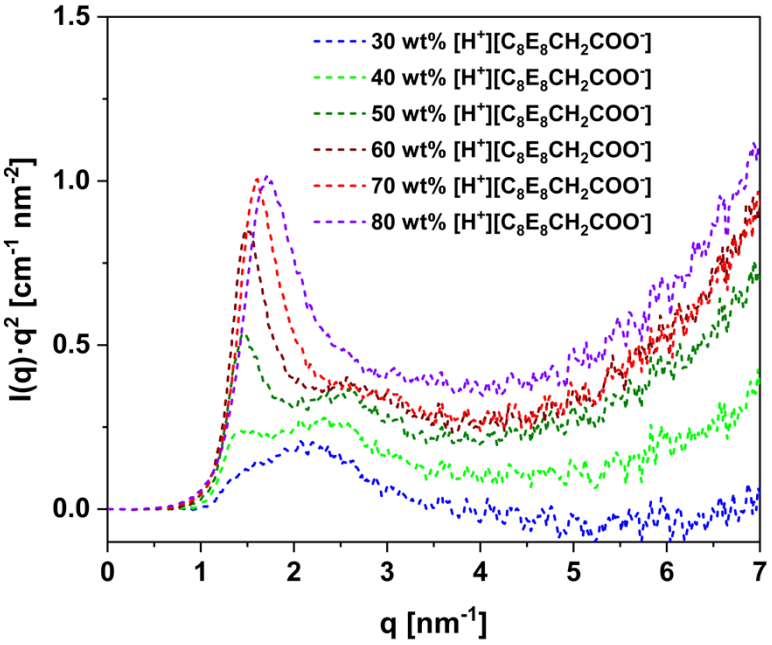

Fig. B.13. $I(q)\cdot q^2$ plotted as a function of q for $[H^+][C_8E_8CH_2COO^-]$ at different concentrations after background subtraction, as derived from the respective SAXS spectra (**Fig. III.8**). The invariant Q * is determined as the integral after defining the baseline. The invariants of the coacervate SAXS spectra are determined analogously.

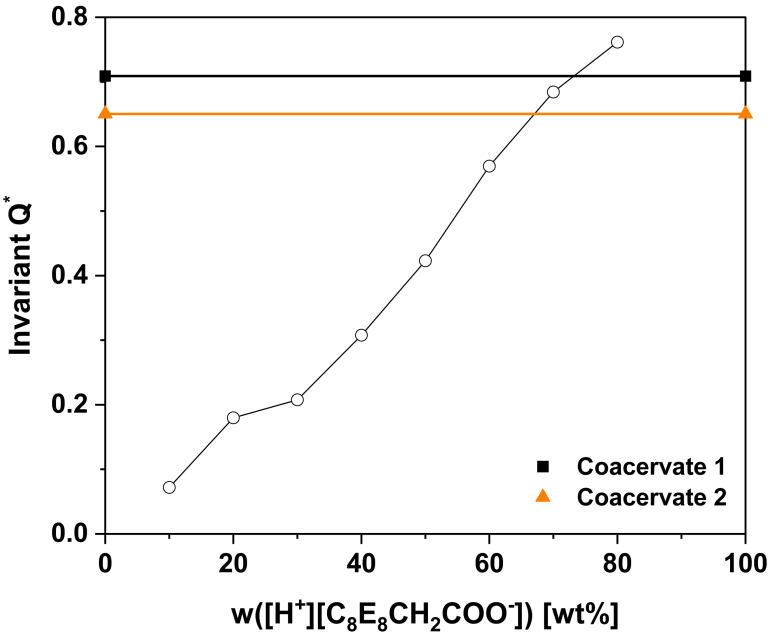

Fig. B.14. Concentration of $[H^+][C_8E_jCH_2COO^-]$ in the coacervate derived from the invariants. Invariants derived from coacervate SAXS spectra are compared to the invariants derived from $[H^+][C_8E_8CH_2COO^-]$ SAXS spectra at different concentrations (**Fig. III.8**). The coacervate was separated twice from two different 0.36 wt% $[H^+][C_8E_8CH_2COO^-]$ samples. Invariants suggest a surfactant concentration of 67 wt% and 74 wt%, respectively. However, since the coacervate is enriched in surfactants with shorter headgroups to give in average $[H^+][C_8E_5CH_2COO^-]$, the invariant has to be rescaled taking into account the increase in the volume fraction of the hydrocarbon core. At 60 wt% of surfactant, the hydrocarbon core volume fraction increases from 0.175 for $[H^+][C_8E_8CH_2COO^-]$ to 0.202 for $[H^+][C_8E_5CH_2COO^-]$. With the rescaled invariants, a surfactant concentration of 58 wt% to 64 wt% is obtained.

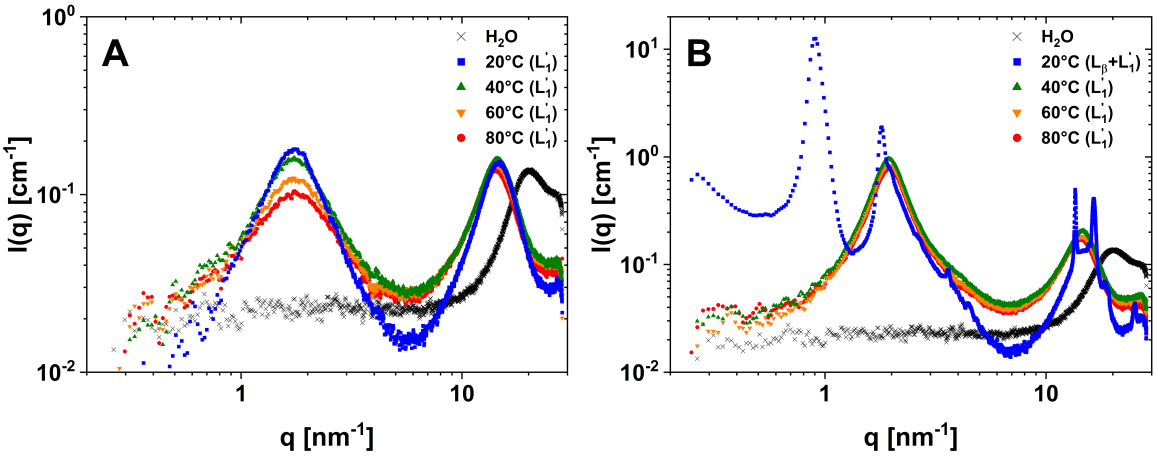

Fig. B.15. (A) SWAXS of neat $[H^+][C_8E_8CH_2COO^-]$ at 20, 40, 60, and 80°C. Only the headgroup interdigitated L_1' phase is observed. (B) SWAXS of neat $[Na^+][C_8E_8CH_2COO^-]$ at 20, 40, 60, and 80°C. At 20°C, a lamellar L_β phase with crystalline headgroups in equilibrium with some L_1' phase is observed. At 40°C and above, the headgroup interdigitated L_1' phase is observed.

B.2. Aggregation Number and Ellipticity of Prolate Micelles in the Isotropic Domain, and Theoretical SAXS/SANS Peak Position in the Hexagonal Phase if Hydrocarbon Cores Merged into Cylinders

B.2.1. Aggregation Number and Ellipticity of Prolate Micelles

In an isotropic micellar solution of spheroidal micelles, micelles are locally face-centered-cubic-like closed packed and D* is related to the number density of micelles per unit volume N_{mic} in the following way [8].

$$N_{mic} = \frac{\sqrt{2}}{(1.225 \cdot D^*)^3} \tag{B.2.1}$$

D* is obtained from the wavevector q_{max}, where the (structure factor) peak maximum is located.

$$D^* = \frac{2\pi}{q_{max}} \tag{B.2.2}$$

The number of surfactant molecules per unit volume (nm^3) in solution N_{mol} is given by

$$N_{mol} = \frac{\beta([Na^+][C_8E_8CH_2COO^-])\cdot N_A}{M([Na^+][C_8E_8CH_2COO^-])} \cdot \frac{1}{10^{24}\ [nm^3\cdot dm^{-3}]}\ , \qquad (B.2.3)$$

where N_A is Avogadro's constant, $\beta([Na^+][C_8E_8CH_2COO^-])$ is the surfactant concentration in $g\cdot L^{-1}$, and $M([Na^+][C_8E_8CH_2COO^-])$ is the surfactant's molar mass. The aggregation number N_{agg} is then given by

$$N_{agg} = \frac{N_{mol}}{N_{mic}}\ . \qquad (B.2.4)$$

The corresponding volume of the hydrocarbon core V_c is obtained by multiplying N_{agg} with the volume of one hydrocarbon chain V_{chain}, and is in the case of prolate ellipsoids also given by the volume of an ellipsoid with ellipticity e and equatorial hydrocarbon core radius R_c^{eq}, where the axial radius R_c^{ax} is given by $R_c^{ax} = e\cdot R_c^{eq}$.

$$V_c = V_{chain}\cdot N_{agg} = \frac{4}{3}\pi\cdot(R_c^{eq})^3\cdot e \qquad (B.2.5)$$

The surface area of the respective hydrocarbon core A_c is given by

$$A_c = 2\pi\cdot R_c^{eq}\cdot\left[R_c^{eq} + \frac{(e\cdot R_c^{eq})^2}{\sqrt{(R_c^{eq})^2\cdot(e^2\text{-}1)}}\cdot\arcsin\left(\frac{\sqrt{(R_c^{eq})^2\cdot(e^2\text{-}1)}}{e\cdot R_c^{eq}}\right)\right], \qquad (B.2.6)$$

and the area per molecule, a, is then given by

$$a = \frac{A_c}{N_{agg}}\ . \qquad (B.2.7)$$

In the present case, $M([Na^+][C_8E_8CH_2COO^-]) = 563\ g\cdot mol^{-1}$, D* = 4.80 nm (SAXS) at a concentration of 30 wt% $[Na^+][C_8E_8CH_2COO^-]$ at a temperature of 20°C, D* = 4.42 nm (SAXS) at a concentration of 58 wt% $[Na^+][C_8E_8CH_2COO^-]$ at a temperature of 60°C, and $V_{chain} = 0.247\ nm^3$ [5,9,10]. The surfactant concentrations in wt% are converted to $\beta([Na^+][C_8E_8CH_2COO^-])$ using the measured physical density of a 30 wt% $[Na^+][C_8E_8CH_2COO^-]$ solution at 25°C ($\rho = 1.041\ g\cdot cm^{-3}$) and the extrapolated physical density of a 58 wt% solution assuming a linear growth and neglecting the influence of temperature ($\rho = 1.086\ g\cdot cm^{-3}$). At 30 wt% and 20°C, eq. (B.2.1) to (B.2.4) yield $N_{agg} = 44$, and assuming the conformation-averaged length $l_0 = 1.16$ nm [9] as R_c^{eq}, eq. (B.2.5) yields

e = 1.675. The respective area per molecule obtained through eq. (B.2.6) and (B.2.7) is a = 0.588 nm^2. At 58 wt% and 60°C, N_{agg} = 76, and using l_0 = 1.16 nm as R_c^{eq} would yield e = 2.850 and a = 0.525 nm^2. An ellipticity of e = 2.850 is considered to be too high, since such an ellipticity should be visible in SAXS and SANS. Probably, the large aggregation number introduces stress on the area per molecule, extending the chain length beyond l_0 to the maximum extended all-*trans* chain length l_{max} = 1.4–1.5 nm. As mentioned in **Section III.4.2.**, such a constraint on the chain packing is also suggested by the sharp peaks produced by the hexagonal order, since the hexagonal phase is too well-ordered for a purely liquid state. With $R_c^{eq} = l_{max}$, e = 1.325–1.625 and a = 0.455–0.470 nm^2 are obtained.

B.2.2. Hexagonal Phase

The length D* in the hexagonal packing is derived from the first diffraction order of the equatorial in-plane hexagonal ordering in **Fig. III.4**. The volume fraction of the hydrocarbon cores φ_c is the fraction of the volume of hydrocarbon cores V_c in the volume of the hexagon V_{hex}.

$$\varphi_c = \frac{V_c}{V_{hex}} \tag{B.2.8}$$

The two possible states are: (a) A hexagonal packing of prolate micelles, and (b) a hexagonal packing of cylindrical micelles. If we assume a single layer of prolate micelles in (a), there are 3 hydrocarbon cores in a hexagon of height h and circumradius r. The hexagon's circumradius r is linked to D* in the following way.

$$r = \frac{2}{\sqrt{3}} D^* \tag{B.2.9}$$

Using the formulas for the volume of an ellipsoid and the volume of a hexagon, the volume fraction of the hydrocarbon cores φ_c in scenario (a) is given by

$$\varphi_c = \frac{3\frac{4}{3}\pi (R_c^{eq})^3 e}{2\sqrt{3}(D^*)^2 h} \,. \tag{B.2.10}$$

Eq. (B.2.10) allows for the calculation of h, if the ellipticity e and the equatorial radius R_c^{eq}

are assumed to remain constant upon cooling from 60°C (isotropic L_1/L_1' phase) to 20°C (wormlike hexagonal phase) at 58 wt%. The volume fraction at 58 wt% is known ($\varphi_c = 0.172$), using the same physical density as mentioned above ($\rho = 1.086\ g \cdot cm^{-3}$) and V_{chain}. If the prolate micelles merge into infinite cylinders, the same volume of hydrocarbon cores is given as a cylinder of height h and radius R_{cyl} within the same hexagon. The area per molecule, i.e., the surface area of the hydrocarbon core, must remain unchanged. Thus, the expected radius R_{cyl} of the hypothetical cylinder can be calculated according to eq. (B.2.11), using the lateral surface of the cylinder and the surface area of the prolate ellipsoid.

$$R_{cyl} = \frac{A_c}{2\pi h} \tag{B.2.11}$$

The expected D*(cylinder) in the case of infinite cylinders in a hexagonal packing is then given by

$$D^*(\text{cylinder}) = \sqrt{\frac{\sqrt{3}\pi (R_{cyl})^2}{2\varphi_c}}\ . \tag{B.2.12}$$

D* is given from the experiment and is 4.32 nm in the hexagonal phase of 58 wt% $[Na^+][C_8E_8CH_2COO^-]$ at 20°C. With the above mentioned equatorial radius ranging from 1.4 nm to 1.5 nm and the ellipticity e ranging from 1.325 to 1.625, h ranges from 5.03 nm to 5.05 nm, resulting in an expected R_{cyl} ranging from 1.09 nm to 1.12 nm and a D*(cylinder) ranging from 4.34 nm to 4.45 nm. The values obtained for D*(cylinder) are barely different from the measured D* value of 4.32 nm, not allowing the exclusion of one of the two possible states (cylinders or chains of prolate micelles) from small-angle scattering alone.

B.3. References

[1] J.B. Hayter, J. Penfold, An analytic structure factor for macroion solutions, Mol Phys 42 (1981) 109–118. https://doi.org/10.1080/00268978100100091.

[2] J. Hansen, J.B. Hayter, A rescaled MSA structure factor for dilute charged colloidal dispersions, Mol Phys 46 (1982) 651–656. https://doi.org/10.1080/00268978200101471.

[3] M. Doucet, J.H. Cho, G. Alina, Z. Attala, J. Bakker, W. Bouwman, P. Butler, K. Campbell, T. Cooper-Benun, C. Durniak, L. Forster, M. Gonzalez, R. Heenan, A. Jackson, S. King, P. Kienzle, J. Krzywon, R. Murphy, T. Nielsen, L. O'Driscoll, W. Potrzebowski, S. Prescott, R. Ferraz Leal, P. Rozyczko, T. Snow, A. Washington, SasView, (2021). https://doi.org/10.5281/zenodo.4467703.

[4] J.B. Hayter, J. Penfold, Self-consistent structural and dynamic study of concentrated micelle solutions, Journal of the Chemical Society, Faraday Transactions 1: Physical Chemistry in Condensed Phases 77 (1981) 1851–1863. https://doi.org/10.1039/F19817701851.

[5] D. Hoshino, K. Nagahama, M. Hirata, Prediction of the liquid molar volume and the latent heat of vaporization for aliphatic hydrocarbons by the group contribution method., Journal of The Japan Petroleum Institute 22 (1979) 32–37. https://doi.org/10.1627/jpi1958.22.32.

[6] D.W. van Krevelen, K. te Nijenhuis, Properties of Polymers, 4th ed., Elsevier B.V., Amsterdam, 2009.

[7] R.K. Thomas, J. Penfold, Multilayering of Surfactant Systems at the Air-Dilute Aqueous Solution Interface, Langmuir 31 (2015) 7440–7456. https://doi.org/10.1021/la504952k.

[8] S.H. Chen, E.Y. Sheu, J. Kalus, H. Hoffman, Small-angle neutron scattering investigation of correlations in charged macromolecular and supramolecular solutions, J Appl Crystallogr 21 (1988) 751–769. https://doi.org/10.1107/S0021889888008052.

[9] C. Tanford, Micelle shape and size, Journal of Physical Chemistry 76 (1972) 3020–3024. https://doi.org/10.1021/j100665a018.

[10] F. Reiss-Husson, V. Luzzati, The Structure of the Micellar Solutions of Some Amphiphilic Compounds in Pure Water as Determined by Absolute Small-Angle X-Ray Scattering Techniques, J Phys Chem 68 (1964) 3504–3511. https://doi.org/10.1021/j100794a011.

Appendix C.

Supplementary Material – Chapter IV.

C.1. Supplementary Figures, Tables, and Videos

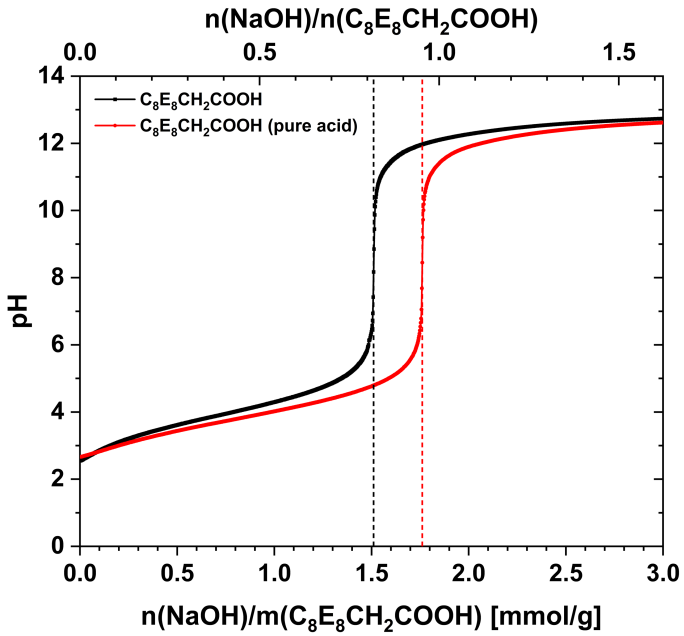

Fig. C.1. Potentiometric pH titration of aqueous solutions of $C_8E_8CH_2COOH$ purified by cloud point extraction (black) and $C_8E_8CH_2COOH$ purified by ion exchange and cloud point extraction (red) at room temperature. For each measurement, 10 g of a 5 wt% surfactant solution were titrated with 3 mL of a 1 M NaOH solution. The bottom x-axis gives the amount of added NaOH in mmol per 1 g of surfactant present in the mixture. The top x-axis gives the molar ratio of NaOH and $C_8E_8CH_2COOH$, assuming a surfactant molar mass of 541 g·mol^{-1} in both cases.

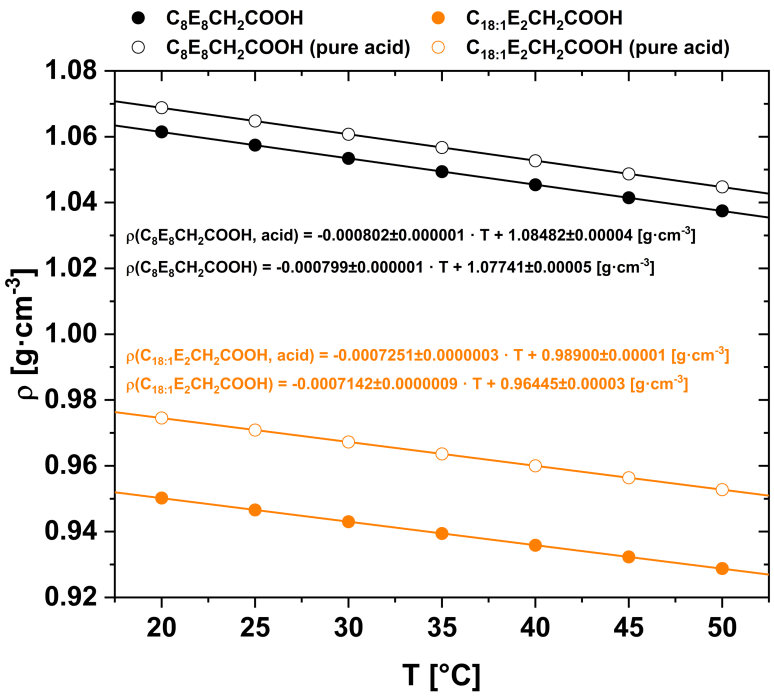

Fig. C.2. Measured physical densities of $C_8E_8CH_2COOH$ (after cloud point extraction), $C_{18:1}E_2CH_2COOH$ (vacuum dried), as well as $C_8E_8CH_2COOH$ (pure acid) and $C_{18:1}E_2CH_2COOH$ (pure acid) after purification by ion exchange and cloud point extraction as a function of temperature. The given equations represent the functions of linear fits, where T is in units of °C.

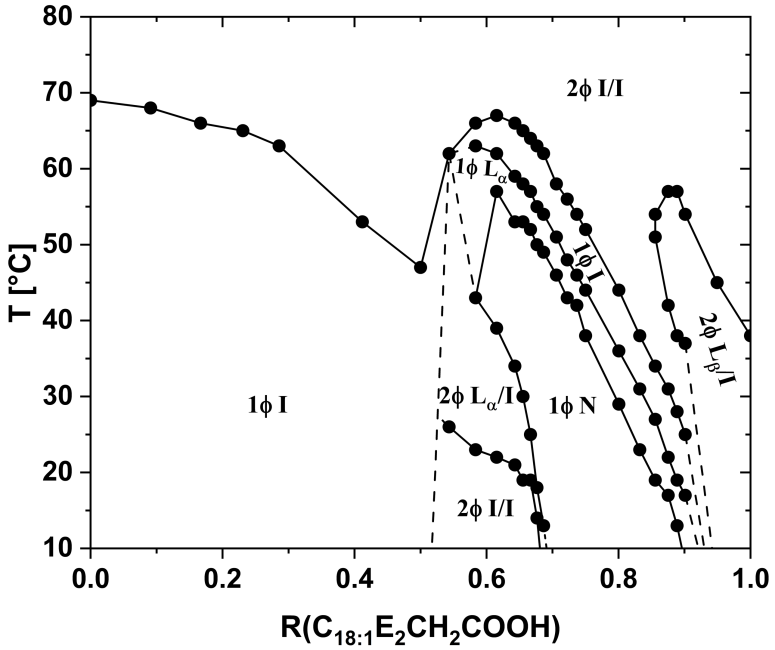

Fig. C.3. Phase diagram of the $C_8E_8CH_2COOH/C_{18:1}E_2CH_2COOH$ surfactant mixture in water, using surfactants purified by ion exchange. The total surfactant content is fixed at 20 wt%, while the mixing ratio of the two surfactants, given as $R(C_{18:1}E_2CH_2COOH)$, is varied. 1ϕ I: Monophasic isotropic liquid. 2ϕ I/I: Two isotropic liquids in equilibrium. In the notation 2ϕ I/I, the former "I" regards the top phase, whereas the latter "I" regards the bottom phase. L_α: Lyotropic lamellar phase. L_β: Semi-crystalline lamellar phase. N: Lyotropic nematic phase. Compared to the corresponding phase diagram using the unpurified surfactants, see **Fig. IV.2**, phase boundaries are generally shifted to higher temperatures and slightly higher values of $R(C_{18:1}E_2CH_2COOH)$. A small 2ϕ I/I region around $R(C_{18:1}E_2CH_2COOH) = 0.2$ and the 2ϕ I/N region at higher $R(C_{18:1}E_2CH_2COOH)$ within the nematic domain disappear in the absence of nonionic (ester) impurities. In absence of nonionic impurities, the formation of a L_β phase is facilitated, allowing its formation above $R(C_{18:1}E_2CH_2COOH) \approx 0.9$. Note that a different batch of purified $C_{18:1}E_2CH_2COOH$ was used compared to **Fig. IV.1**. The difference in melting temperature may be the result of a slightly different degree of purification, since the melting temperature is quite sensitive towards impurities.

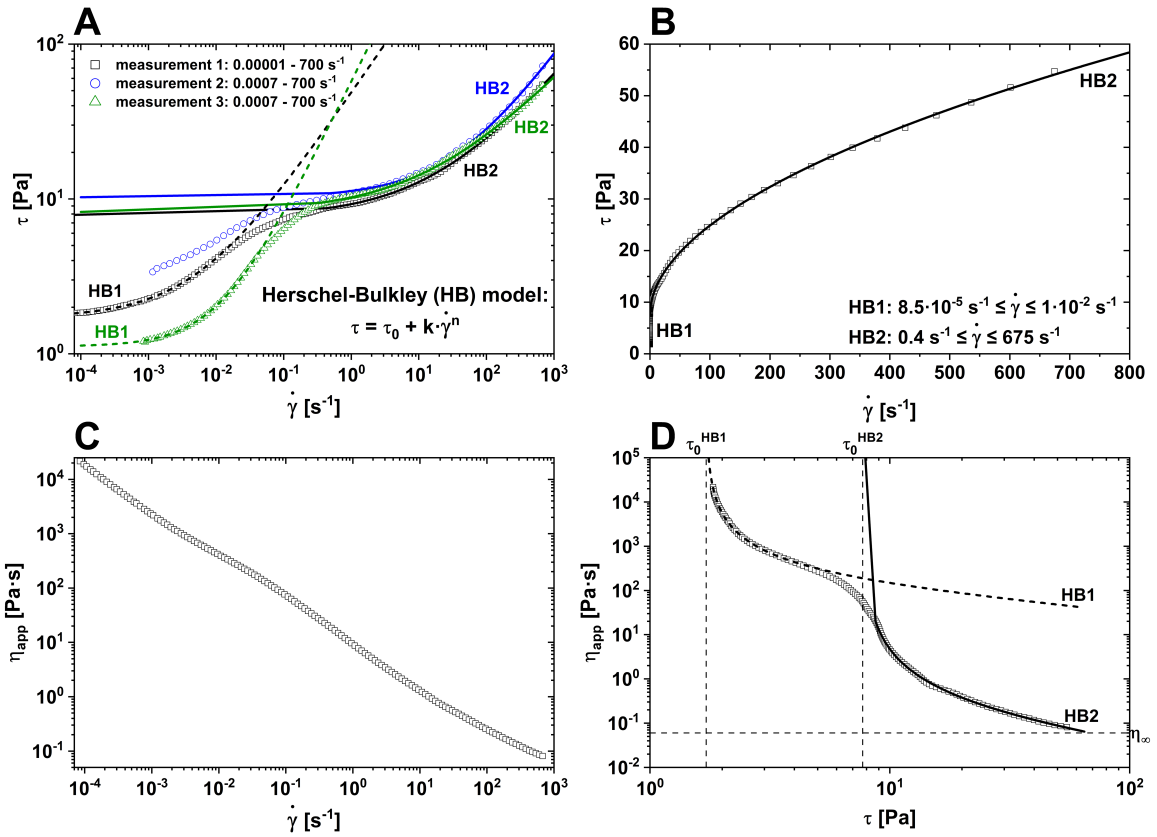

Fig. C.4. (A) Flow curves (shear stress τ versus shear rate $\dot{\gamma}$) obtained by measuring the same nematic gel containing 20 wt% surfactant mixture with R($C_{18:1}E_2CH_2COOH$) = 0.655 three times at 25°C, shown in log-log scale. Note that the mixture was placed between the cone and the plate of the rheometer three separate times. The basic shape of the flow curves is identical. Small deviations can arise from air bubbles entrapped in the mixture. The curves exhibit two shear thinning regions that can both be fitted with the Herschel-Bulkley (HB) fluid model [1]. At low shear rates (< 0.1 s^{-1}) the curves are fitted with a first HB model (HB1, dashed lines), and at higher shear rates (≥ 0.4 s^{-1}) a second HB model is applied (HB2, solid lines). The obtained parameters are given in **Table C.1**. As a result, two yield stresses τ_0^{HB1} (≈ 1–3 Pa) and τ_0^{HB2} (≈ 8–10 Pa) are obtained. The first region above τ_0^{HB1} may be assigned to the movement of large domains of the gel, while the second range above τ_0^{HB2} may be assigned to the movement of small nematic domains or individual discs, leading to microscopic shear alignment. (B) Flow curve τ($\dot{\gamma}$) of the first measurement, given in linear scale. (C) Apparent dynamic viscosity η_{app} as a function of the shear rate for the first measurement. (D) Apparent dynamic viscosity η_{app} as a function of the shear stress for the first measurement. η_{app} measured close to the first yield stress τ_0^{HB1} is above $1 \cdot 10^4$ Pa·s, while it is decreased to around 10 Pa·s close to the second yield stress τ_0^{HB2}. The viscosity at infinite shear η_∞ is well below 0.1 Pa·s.

Table C.1. Consistency k, flow index n, and yield stress τ_0 obtained for each fit of the flow curves to a Herschel-Bulkley (HB) model [1], see **Fig. C.4**. In **Fig. C.4**, measurement 1 is shown in black, measurement 2 in blue, and measurement 3 in green.

Herschel-Bulkley (HB) model: $\tau = \tau_0 + k \cdot \dot{\gamma}^n$						
	HB1 (low $\dot{\gamma}$)			**HB2 (higher $\dot{\gamma}$)**		
measurement (25°C)	**τ_0^{HB1} [Pa]**	**k^{HB1} [Pa·s^n]**	**n^{HB1}**	**τ_0^{HB2} [Pa]**	**k^{HB2} [Pa·s^n]**	**n^{HB2}**
1	1.716 ± 0.006	47 ± 1	0.644 ± 0.005	7.71 ± 0.06	1.56 ± 0.03	0.521 ± 0.003
2	not enough data points			10.3 ± 0.2	0.99 ± 0.06	0.63 ± 0.01
3	1.116 ± 0.003	56.3 ± 0.8	0.893 ± 0.004	8.2 ± 0.1	2.03 ± 0.06	0.472 ± 0.005

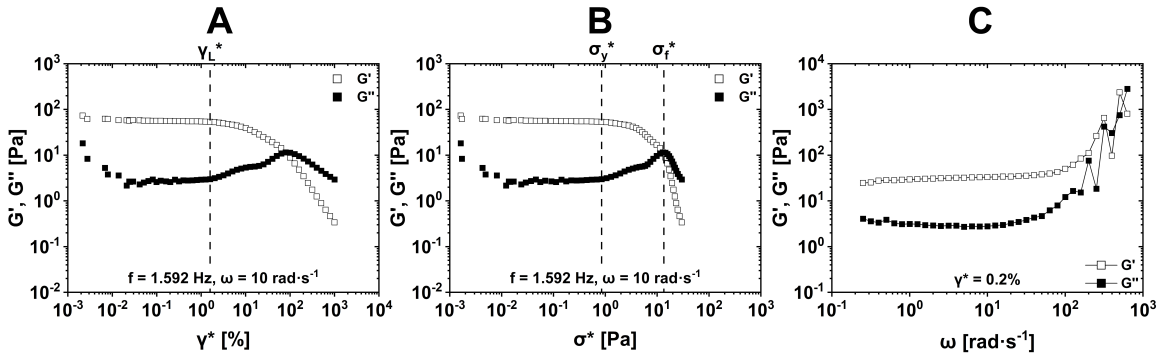

Fig. C.5. (A) Strain controlled amplitude sweep of a nematic gel containing 20 wt% of surfactant mixture with R($C_{18:1}E_2CH_2COOH$) = 0.655 at a constant angular frequency of 10 rad·s^{-1} (1.592 Hz) to determine the linear viscoelastic region, which in this case extends up to a complex shear strain γ* of around 2%. (B) The same amplitude sweep as a function of the complex shear stress σ*. The complex yield stress σ_y* = 0.85 Pa was determined as the point where the loss modulus G'' starts to increase. The complex flow-stress σ_f* = 13.5 Pa was determined as the crossover of G'' and the storage modulus G'. σ_y* is in the same order of magnitude as the yield stress τ_0^{HB1} obtained from the Herschel-Bulkley fits at low shear rates, while σ_f* is in the same order of magnitude as the yield stress τ_0^{HB2} obtained from the Herschel-Bulkley fits at higher shear rates, see **Fig. C.4** and **Table C.1**. This is in agreement with the idea of initially only large domains moving above τ_0^{HB1} (σ_y*), until small nematic domains or individual discs start to move above τ_0^{HB2} (σ_f*). Between σ_y* and σ_f*, the loss modulus G'' increases because additional force is required due to internal friction between the large domains, while the storage modulus G' still exceeds G''. (C) Frequency sweep at a constant complex shear strain of γ* = 0.2%. The nematic gel is clearly viscoelastic with a damping factor of G''/G' = 0.1. G'' and G' both behave mostly linearly, the upturn at high angular frequencies ω probably being an artifact of the measurement. Since there is no crossover from G''>G' to G'>G'', the structure relaxation time is longer than the measured time scale (>30 s).
Amplitude sweeps were also recorded at different frequencies ranging from 6.28 rad·s^{-1} ≤ ω ≤ 100 rad·s^{-1}, all giving similar values for σ_y* and σ_f*. Frequency sweeps were also performed at different complex shear strains, all giving similar results. The gap size used for the shown measurements is 500 µm. Note that the same measurements were also performed with a gap size of 1000 µm, giving similar results.

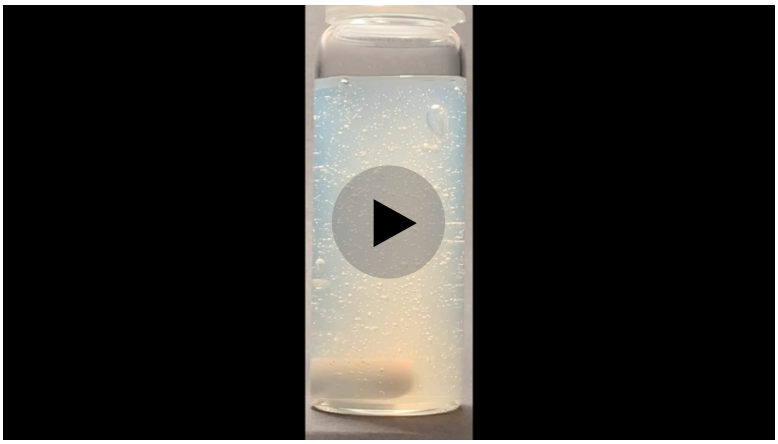

Video C.1. Viscoelastic behavior and air bubble entrapment of a shear thinning nematic gel containing 20 wt% of surfactant mixture with R($C_{18:1}E_2CH_2COOH$) = 0.655, visualized by stirring with a magnetic stirring bar. (Digital version: Click image. Printed version: Go to https://nbn-resolving.org/urn:nbn:de:bvb:355-epub-552006.)

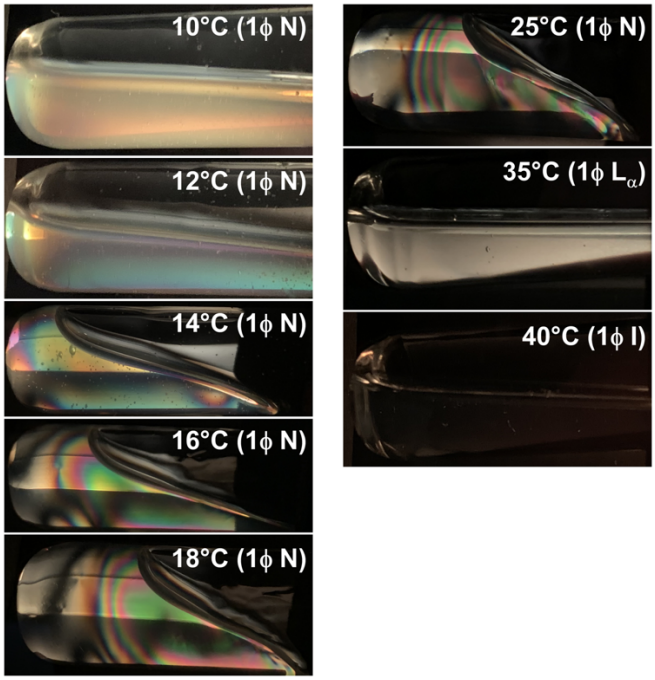

Fig. C.6. Images of sample 20M (20 wt% surfactant, R($C_{18:1}E_2CH_2COOH$) = 0.655) taken between crossed polarizers at 10°C to 25°C (1ϕ N), 35°C (1ϕ L_α), and 40°C (1ϕ I). Pictures were taken during heating of the sample from 10°C. After 30 min of equilibration at the respective temperature with occasional mixing using a vortex mixer, the cylindrical glass tube (diameter ≈ 1.6 cm) containing the sample was placed horizontally (perpendicular to the direction of gravity) between crossed polarizers.

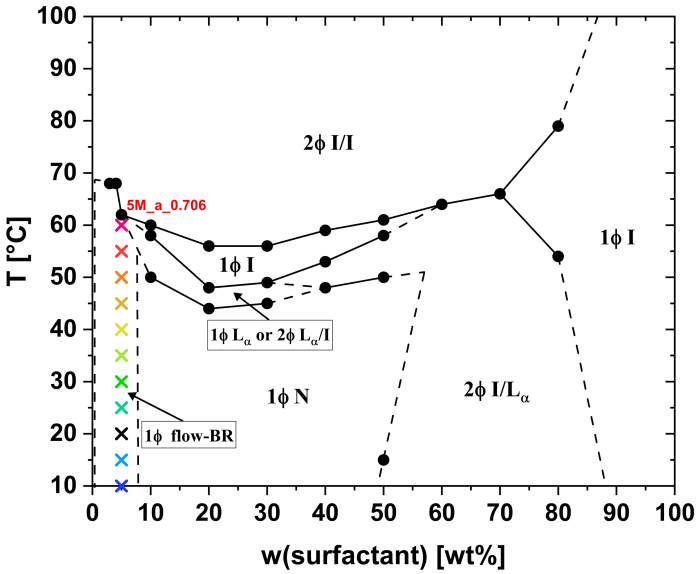

Fig. C.7. Pseudo-binary phase diagram of a $C_8E_8CH_2COOH$/$C_{18:1}E_2CH_2COOH$ surfactant mixture in water with a fixed surfactant composition of R($C_{18:1}E_2CH_2COOH$) = 0.706, using surfactants purified by ion exchange. 1ϕ I: Monophasic isotropic liquid. 2ϕ I/I: Two isotropic liquids in equilibrium. In the notation 2ϕ I/I, the former "I" regards the top phase, whereas the latter "I" regards the bottom phase. L_α: Lyotropic lamellar phase. N: Lyotropic nematic phase. Flow-BR denotes flow birefringence. The colored crosses indicate samples measured with SAXS. The phase diagram is similar to the phase diagram obtained with unpurified surfactants, see **Fig. IV.3**, the only noticeable difference being the flow birefringent phase at surfactant concentrations below 8 wt%, which is monophasic in absence of nonionic (ester) impurities but biphasic in their presence. Note that the surfactant ratio was adjusted from R($C_{18:1}E_2CH_2COOH$) = 0.655 using the unpurified surfactants to R($C_{18:1}E_2CH_2COOH$) = 0.706 using the purified surfactants to ensure the presence of a nematic phase from 10°C upwards. The shift of the nematic domain to higher R($C_{18:1}E_2CH_2COOH$) with purified surfactants can be seen comparing **Figs. IV.2** and **IV.3**.

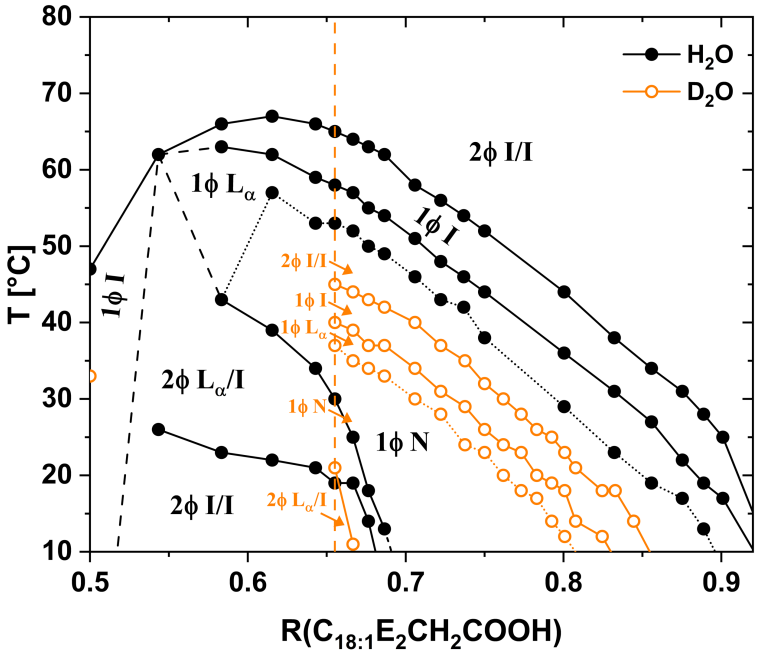

Fig. C.8. Partial phase diagrams of the $C_8E_8CH_2COOH/C_{18:1}E_2CH_2COOH$ surfactant mixture in H_2O (●) or D_2O (○), using surfactants purified by ion exchange. The total surfactant content is fixed at 20 vol% (20.0 wt% in H_2O, 18.4 wt% in D_2O), while the mixing ratio of the two surfactants, given as $R(C_{18:1}E_2CH_2COOH)$ is varied. 1ϕ I: Monophasic isotropic liquid. 2ϕ I/I: Two isotropic liquids in equilibrium. In the notation 2ϕ I/I, the former "I" regards the top phase, whereas the latter "I" regards the bottom phase. L_α: Lyotropic lamellar phase. L_β: Semi-crystalline lamellar phase. N: Lyotropic nematic phase. The whole phase diagram in H_2O, covering the whole range of $R(C_{18:1}E_2CH_2COOH)$, is given in **Fig. C.3**. In D_2O the same phase behavior is observed, but phase boundaries are all shifted to lower temperatures by up to 20°C.

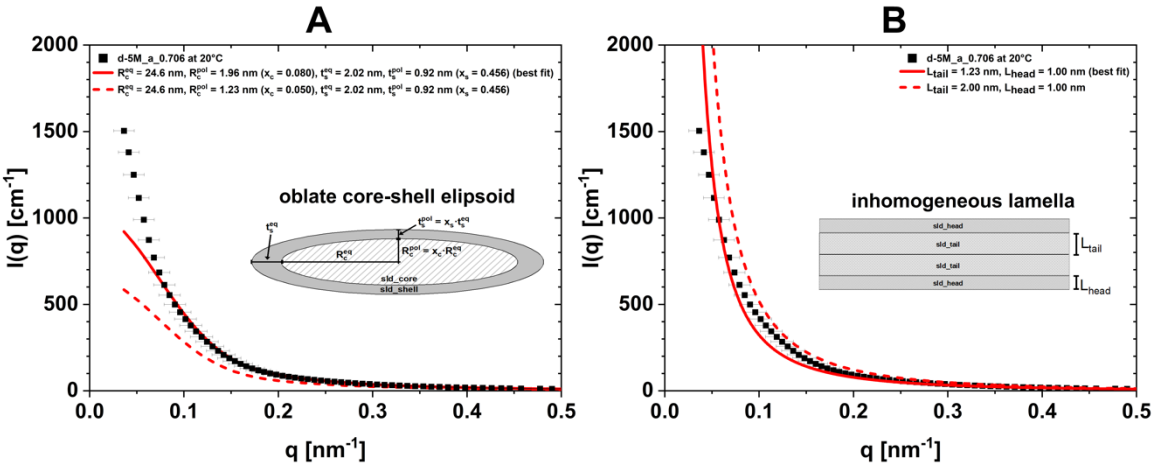

Fig. C.9. (A) SANS data (black squares) of sample d-5M_a_0.706 at 20°C, containing 5.0 vol% (4.5 wt%) surfactant mixture with $R(C_{18:1}E_2CH_2COOH) = 0.706$ in D_2O, fitted to the form factor of an oblate core-shell ellipsoid using the SasView package (version 5.0.4) [2]. (B) SANS data (black squares) of sample d-5M_a_0.706 at 20°C, fitted to an inhomogeneous lamellar form factor using the SasView package (version 5.0.4) [2].
The data and fits are shown in linear scale in a limited q range in the low-q region. The solid red lines represent the best fits, while the dashed red lines visualize the influence of a change in R_c^{pol} or L_{tail}, respectively. If R_c^{pol} or L_{tail} equal 2.0 nm, they correspond to the length of a $C_{18:1}$ chain. The lamellar model clearly suggests interdigitation of the hydrocarbon chains with $L_{tail} = 1.23$ nm and the oblate ellipsoidal model suggests an equatorial core radius close to 2 nm. The latter case is also in agreement with hydrocarbon chain interdigitation, as the cross-sectional polar radius decreases towards the equator of the oblate ellipsoid. Fitting parameters are given in detail in **Table C.2**. The whole recorded q range is given as a Kratky plot in **Fig. IV.5**.

Table C.2. Parameters of the fits and simulations of SANS data at 20°C given in **Figs. IV.4**C, **IV.5**, and **C.9**. The scattering patterns of all fitted samples are isotropic. Data were fitted either to a core-shell ellipsoid form factor ("core_shell_ellipsoid") or to an inhomogeneous lamella form factor ("lamellar_hg") using the SasView package (version 5.0.4) [2]. The scale factor was fixed to be equivalent to the surfactant volume fraction φ(surfactant) = 0.0494. The neutron scattering length densities were calculated based on the values given in **Appendix C.3**. Ideal mixing of the surfactants was assumed in the calculations. Though sld_core = sld_tail = $-0.354 \cdot 10^{-4}$ nm^{-2} is the obtained value for a surfactant mixture with R($C_{18:1}E_2CH_2COOH$) = 0.706, the value only changes insignificantly (by ≈$2 \cdot 10^{-7}$ nm^{-2}) for R($C_{18:1}E_2CH_2COOH$) = 0.677 or 0.750. Thus, the same value was used in all three cases. The scattering length density of the shell depends on the volume fraction of D_2O, φ(D_2O), in the shell. If hydration of the headgroups by three D_2O molecules per EO group is assumed, the theoretical sld_shell varies between $3.734 \cdot 10^{-4}$ nm^{-2} and $3.860 \cdot 10^{-4}$ nm^{-2} at φ(D_2O) ≈ 0.5 for the three different surfactant mixing ratios. The best fit at R($C_{18:1}E_2CH_2COOH$) = 0.706 suggested sld_shell = $3.802 \cdot 10^{-4}$ nm^{-2}, which was then used in all cases. The scattering length density of D_2O is given as sld_solvent = $6.361 \cdot 10^{-4}$ nm^{-2}. The background was fitted once for sample d-5M_a_0.706 and subsequently kept constant for the other samples. In the core-shell ellipsoid model, R_c^{eq} is the equatorial radius of the hydrophobic core, $R_c^{pol} = R_c^{eq} \cdot x_c$ is the polar radius of the hydrophobic core, t_s^{eq} is the thickness of the hydrophilic shell at the equatorial half-axis, and $t_s^{pol} = t_s^{eq} \cdot x_s$ is the shell thickness at the polar half-axis. In the lamellar model, L_{tail} is the half-thickness of the hydrophobic alkyl chain layer and L_{head} is the thickness of the hydrated headgroup layer. The form factors and respective parameters are depicted in **Figs. IV.5** and **C.9**. The core-shell ellipsoid form factor model was combined with a Hayter-Penfold RMSA structure factor [3,4] to fit SANS data at 33°C given in **Fig. C.11**. The scale factor was set to unity because the structure factor contains the volume fraction of surfactant φ(surfactant). The scattering length densities of the core and the shell were left unchanged, even though they were calculated separately from the measured physical densities at 33°C, because changes were negligible. R_{eff} is the effective radius used for the structure factor computation. The parameter c('salt') is used to compute the Debye length, and since no additional salt was added, the concentration of protons c(H^+) = 3.6 mM was used, as derived from the equivalent pH of 2.44 (H_2O-calibrated electrode reading pH^* = 2.17), since the dissociated acid can be treated as a 1:1 electrolyte. The relative permittivity of D_2O was taken from ref. [5]. Since the charge converges to zero, the structure factor is similar to that of a hard sphere, in agreement with an expected dissociation of less than 0.5% (apparent pKa of the mixture in H_2O is 4.6), rendering the surfactants effectively nonionic.

Form factor model: Core-shell ellipsoid

sample (20°C)	scale	background [cm^{-1}]	R_c^{eq} [nm]	R_c^{pol} [nm] (x_c)	t_s^{eq} [nm]	t_s^{pol} [nm] (x_s)	sld_core [10^{-4} nm^{-2}]	sld_shell [10^{-4} nm^{-2}]	sld_solvent [10^{-4} nm^{-2}]
d-5M_a_0.677 (fit)	0.0494	0.0359	23.8	1.9 (0.0806)	2.3	0.9 (0.3957)	-0.354	3.802	6.361
d-5M_a_0.706 (fit)	0.0494	0.0359	24.6	2.0 (0.0798)	2.0	0.9 (0.4560)	-0.354	3.802	6.361
d-5M_a_0.706 (simulation)	0.0494	0.0359	24.6	1.2 (0.0500)	2.0	0.9 (0.4560)	-0.354	3.802	6.361
d-5M_a_0.750 (fit)	0.0494	0.0359	27.1	2.0 (0.0738)	2.3	0.8 (0.3607)	-0.352	3.802	6.361

Form factor model: Inhomogeneous lamella

sample (20°C)	scale	background [cm^{-1}]	L_{tail} [nm]	L_{head} [nm]	sld_tail [10^{-4} nm^{-2}]	sld_head [10^{-4} nm^{-2}]	sld_solvent [10^{-4} nm^{-2}]
d-5M_a_0.706 (fit)	0.0494	0.0359	1.2	1.0	-0.354	3.802	6.361
d-5M_a_0.706 (simulation)	0.0494	0.0359	2.0	1.0	-0.354	3.802	6.361

Form factor model: Core-shell ellipsoid + Structure factor: Hayter-Penfold RMSA

sample (33°C)	scale	background [cm^{-1}]	R_c^{eq} [nm]	R_c^{pol} [nm] (x_c)	t_s^{eq} [nm]	t_s^{pol} [nm] (x_s)	sld_core [10^{-4} nm^{-2}]	sld_shell [10^{-4} nm^{-2}]	sld_solvent [10^{-4} nm^{-2}]
d-20M (fit)	1.0000	0.1700	11.8	2.2 (0.1829)	2.3	0.8 (0.3365)	-0.354	3.802	6.344

S(q): R_{eff} = 11.8 nm, φ(surfactant) = 0.2, charge = 0.013 e, ε_r = 75.11 (T = 306.15 K), c('salt') = c([H^+][surfactant$^-$]) = 3.6 mM

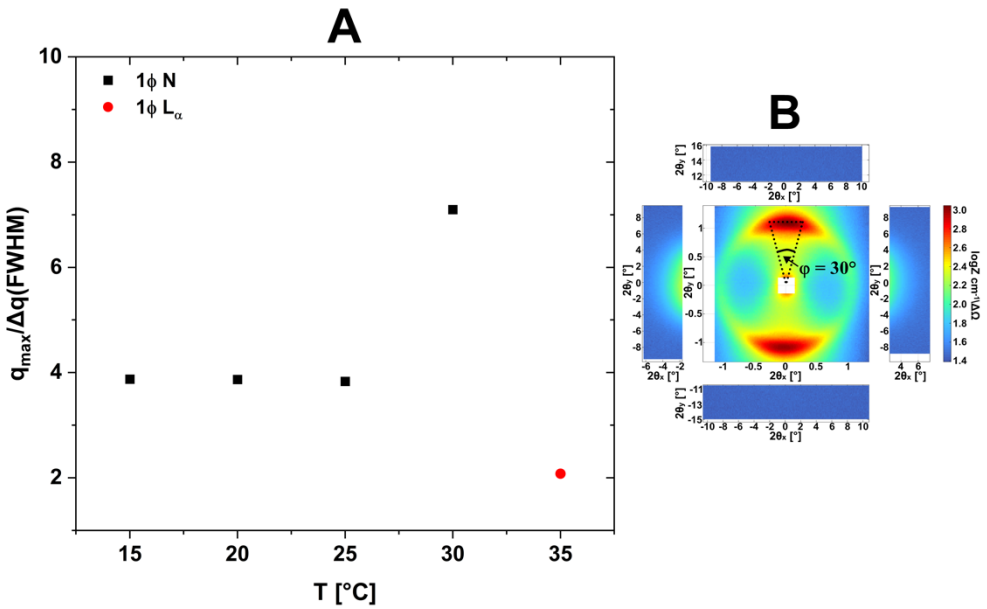

Fig. C.10. (A) The ratio of the position of the structure factor peak maximum, q_{max}, to the full width at half maximum (FWHM) of the peak is plotted for the SAXS data of sample 20M, given in **Fig. IV.6**, as a function of temperature. 1ϕ N denotes a nematic phase, whereas 1ϕ L_α denotes a (pseudo-)lamellar phase. (B) 2D SANS pattern of sample d-20M at 20°C. Scattering is anisotropic with the highest intensity found in a sector of φ ≈ 30°. Anisotropy originates from the shear-induced alignment of bicelles (discs) on cuvette filling, leaving most of the bicelles oriented along the direction of shear with a tilt ≤15° relative to the shear axis.

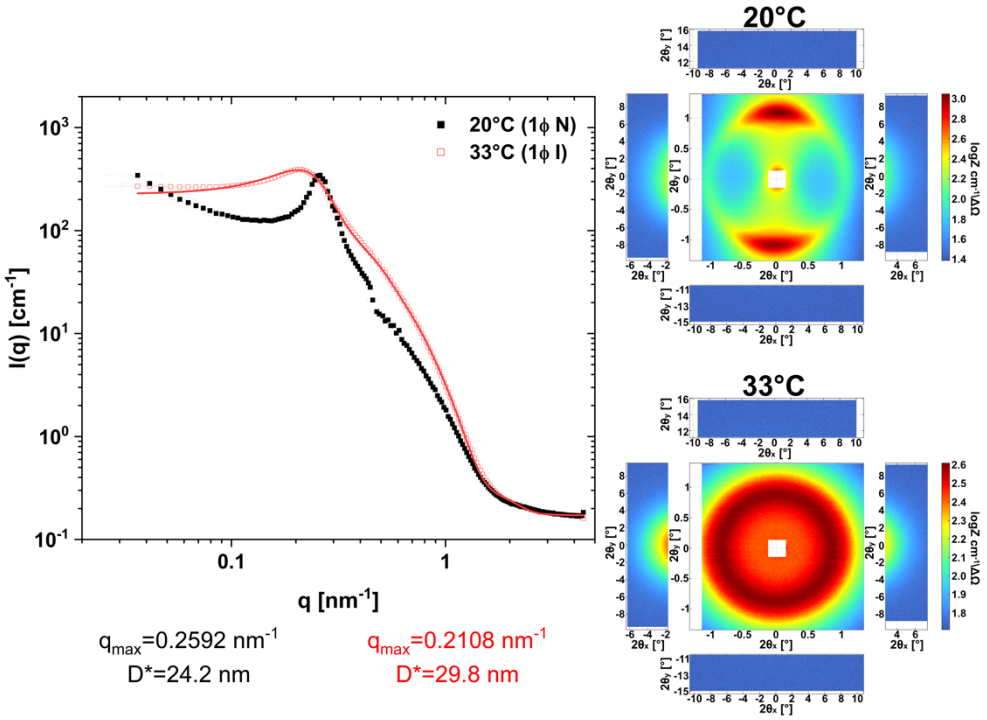

Fig. C.11. Radially averaged SANS data of sample d-20M at 20°C (black) and 33°C (red). The solid red line is a fit of the 33°C scattering data to a core-shell ellipsoid form factor and an applied Hayter-Penfold RMSA structure factor [3,4] using the SasView package (version 5.0.4) [2]. Detailed parameters are given in **Table C.2**. The sample contains 20 vol% of surfactant mixture in D_2O and is a nematic gel (1ϕ N) at 20°C and an isotropic liquid (1ϕ I) at 33°C. The respective 2D scattering patterns are shown. Due to the five-detector setup and anisotropy in scattering at 20°C, radial averaging leads to a slight mismatch between the different q-ranges, mainly visible around q = 0.5 nm^{-1}.

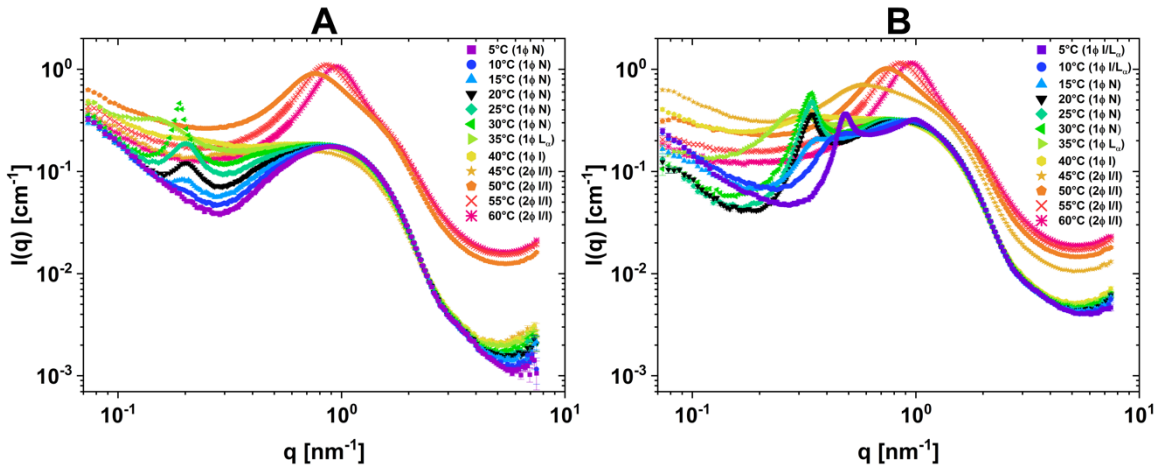

Fig. C.12. (A) SAXS data of sample 15M, containing 15 vol% (= 15 wt%) surfactant mixture with R($C_{18:1}E_2CH_2COOH$) = 0.655 in H_2O, at various temperatures, taken during heating from 5°C to 60°C. At 5°C to 30°C, the sample is a nematic phase (1ϕ N), where birefringence and viscosity increase with increasing temperature. At 35°C, a pseudo-lamellar phase (1ϕ L_α) is formed, which transitions into an isotropic phase (1ϕ I) at 40°C. At 45°C and above, phase separation into a dilute bottom phase and a surfactant-rich top phase occurs. (B) SAXS data of sample 25M, containing 25 vol% (= 25 wt%) surfactant mixture with R($C_{18:1}E_2CH_2COOH$) = 0.655 in H_2O, at various temperatures, taken during heating from 5°C to 60°C. At 5°C and 10°C, an isotropic phase is in equilibrium with a lamellar L_α phase, resulting in a turbid mixture. At 15°C to 30°C, the sample is a nematic phase (1ϕ N), where birefringence and viscosity increase with increasing temperature. At 35°C, a pseudo-lamellar phase (1ϕ L_α) is formed, which transitions into an isotropic phase (1ϕ I) at 40°C. At 45°C and above, phase separation into a dilute bottom phase and a surfactant-rich top phase occurs.
The measured points are indicated in the phase diagram in **Fig. IV.3**. SAXS data of sample 20M of the same dilution series are shown in **Fig. IV.6**.

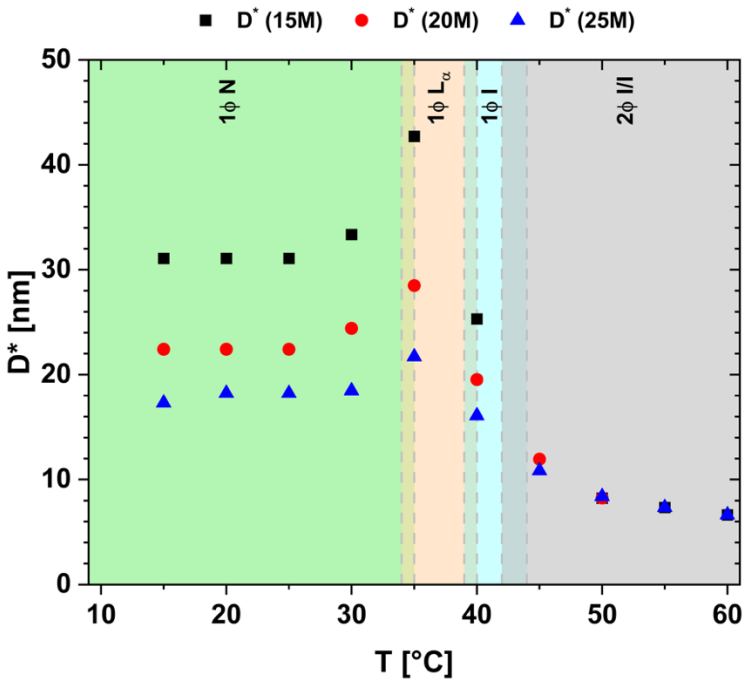

Fig. C.13. Repeat distance $D^* = 2\pi \cdot q_{max}^{-1}$ as a function of temperature, calculated from the peak positions of the SAXS data of samples 15M, 20M, and 25M, containing, respectively, 15, 20, and 25 vol% of surfactant, R($C_{18:1}E_2CH_2COOH$) = 0.655, in H_2O. The data are shown in **Figs. IV.6** and **C.12**. The respective phases at the different temperatures are indicated, and can be inferred from the phase diagram in **Fig. IV.3**. 1ϕ N: Nematic phase. 1ϕ L_α: Pseudo-lamellar phase. 1ϕ I: Isotropic phase. 2ϕ I/I: Two isotropic phases in equilibrium.

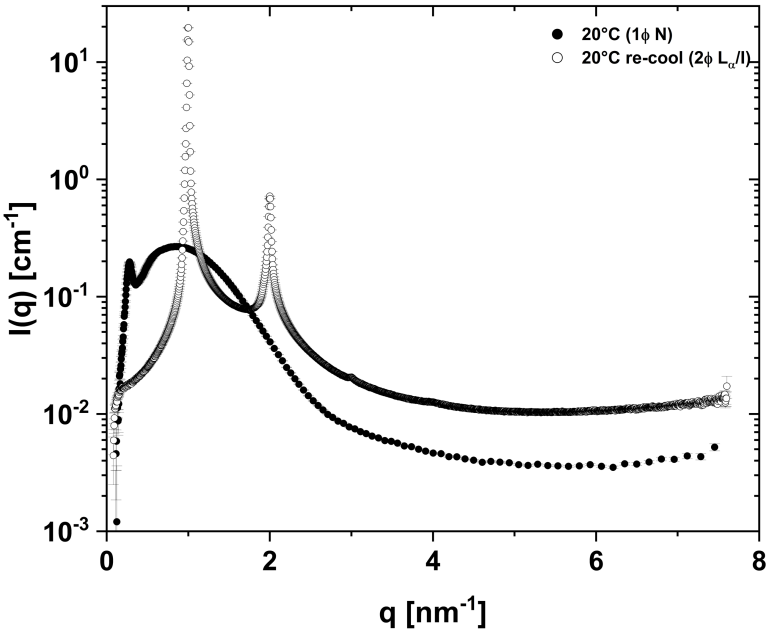

Fig. C.14. Semi-logarithmic representation of SAXS data of sample 20M, containing 20 vol% (= 20 wt%) surfactant mixture with R($C_{18:1}E_2CH_2COOH$) = 0.655 in H_2O, at 20°C (full symbols) and after re-cooling from 60°C to 20°C (empty symbols). As can be seen in **Fig. IV.3**, heating the nematic sample 20M to 60°C eventually leads to phase separation into an isotropic surfactant-rich and an isotropic dilute aqueous phase. On re-cooling the two separated phases, the surfactant-rich phase forms a lyotropic lamellar L_α phase, which is seen in the scattering curve. Note that the same data are shown in **Fig. IV.6**.

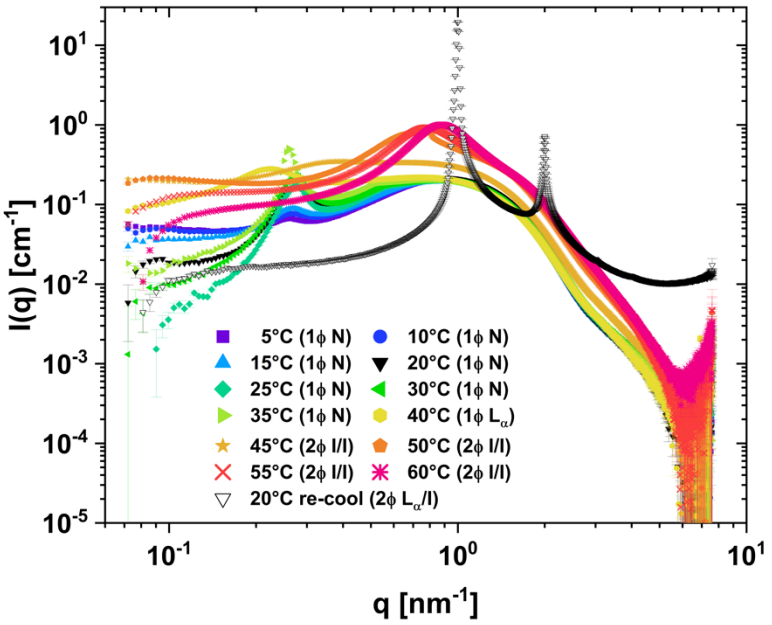

Fig. C.15. SAXS data of sample 20M* similar to sample 20M, also containing 20 vol% surfactant mixture with R($C_{18:1}E_2CH_2COOH$) = 0.655 in H_2O, at various temperatures, taken during heating from 5°C to 60°C and after re-cooling to 20°C. The difference to sample 20M is that the surfactant $C_{18:1}E_2CH_2COOH$ was used after vacuum drying, which leads to the slow formation of esters between carboxylic acids and nonionic impurities as a consequence of a shift in equilibrium due to water removal. The increased ester content leads to a small shift of the phase boundaries compared to those shown in **Figs. IV.2** and **IV.3**. At 5°C to 35°C, the sample is a nematic phase (1ϕ N), where birefringence and viscosity increase with increasing temperature. At 40°C, a pseudo-lamellar phase (1ϕ L_α) is formed. At 45°C and above, phase separation into a dilute bottom phase and a surfactant-rich top phase occurs. Scattering at 45°C, around the phase transition 1ϕ I → 2ϕ I/I, closely resembles that of the monophasic isotropic phase (1ϕ I) obtained for samples 15M, 20M, and 25M, see **Figs. IV.6** and **C.12**.

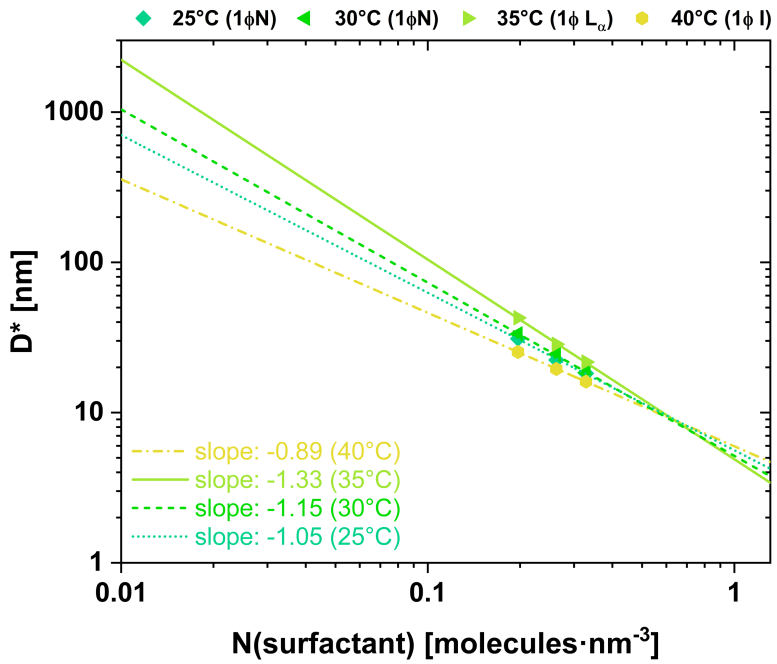

Fig. C.16. Repeat distance $D^* = 2\pi/q_{max}$, obtained from the SAXS peak maxima in **Figs. IV.6** and **C.12**, as a function of the number of surfactant molecules per unit volume N(surfactant). The lines represent linear fits.

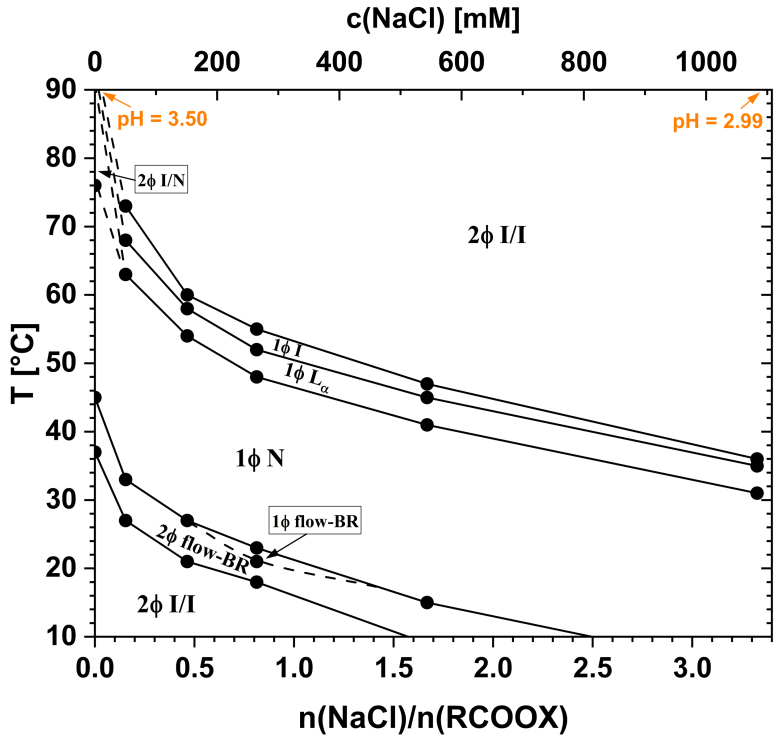

Fig. C.17. Phase diagram recorded by addition of NaCl to a mixture with an initial surfactant concentration of 20 wt% with $R(C_{18:1}E_2CH_2COOH) = 0.655$ and an initial $f(RCOO^- Na^+) = n(RCOO^- Na^+)/[n(ROOH)+n(RCOO^- Na^+)] = 0.1$, corrected for an apparent acid fraction of 74.7 mol% (see **Fig. IV.8**A), as a function of the NaCl concentration. The bottom x-axis gives the mole ratio of NaCl and carboxylate surfactants ($RCOOX = RCOOH + RCOO^- Na^+$), considering an apparent acid fraction of 74.7 mol%, while the top x-axis gives the molar concentration of NaCl.

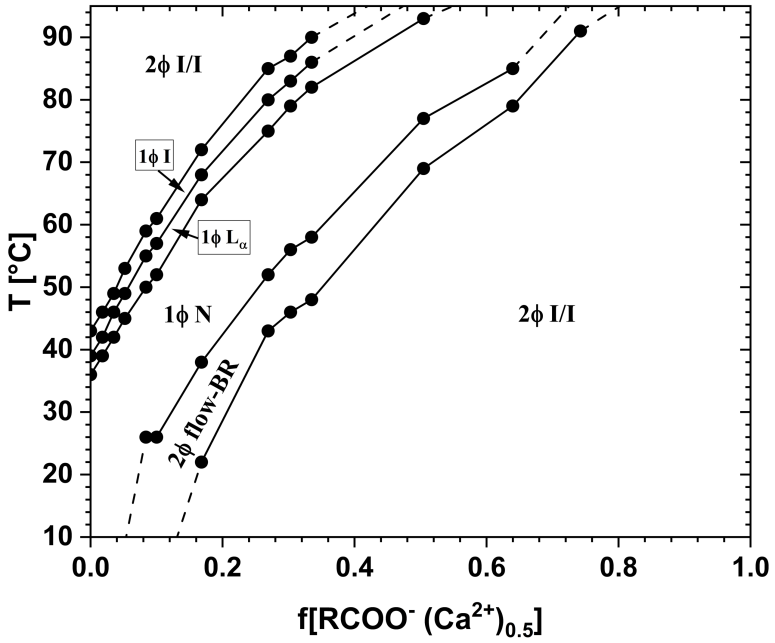

Fig. C.18. Phase diagram at a constant surfactant concentration of 20 wt% with R($C_{18:1}E_2CH_2COOH$) = 0.655 as a function of the degree of surfactant ionization, varied by addition of $Ca(OH)_2$. f[$RCOO^-$ $(Ca^{2+})_{0.5}$] = n($RCOO^-$ $(Ca^{2+})_{0.5}$)/[n(ROOH)+n($RCOO^-$ $(Ca^{2+})_{0.5}$)] is corrected for an apparent acid fraction of 74.7 mol% (see **Fig. IV.8**A).

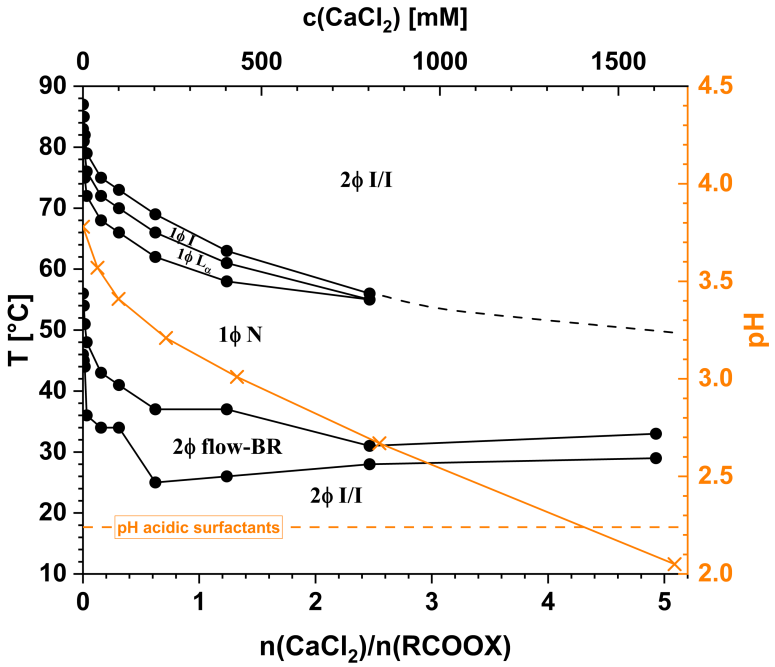

Fig. C.19. Phase diagram recorded by addition of $CaCl_2$ to a mixture with an initial surfactant concentration of 20 wt% with R($C_{18:1}E_2CH_2COOH$) = 0.655 and an initial f[$RCOO^-$ $(Ca^{2+})_{0.5}$] = n($RCOO^-$ $(Ca^{2+})_{0.5}$) / [n(ROOH)+n($RCOO^-$ $(Ca^{2+})_{0.5}$)] = 0.3, corrected for an acid fraction of 74.7 mol% (see **Fig. IV.8**A), as a function of the $CaCl_2$ concentration. The bottom x-axis gives the mole ratio of $CaCl_2$ and carboxylate surfactants (RCOOX = RCOOH + $RCOO^-$ $(Ca^{2+})_{0.5}$), considering an apparent acid fraction of 74.7%, while the top x-axis gives the molar concentration of $CaCl_2$. The right y-axis gives the measured pH (orange crosses). The horizontal orange dashed line indicates the pH of a respective mixture of the two acidic surfactants, i.e., at f[$RCOO^-$ $(Ca^{2+})_{0.5}$] = 0, in absence of salt.

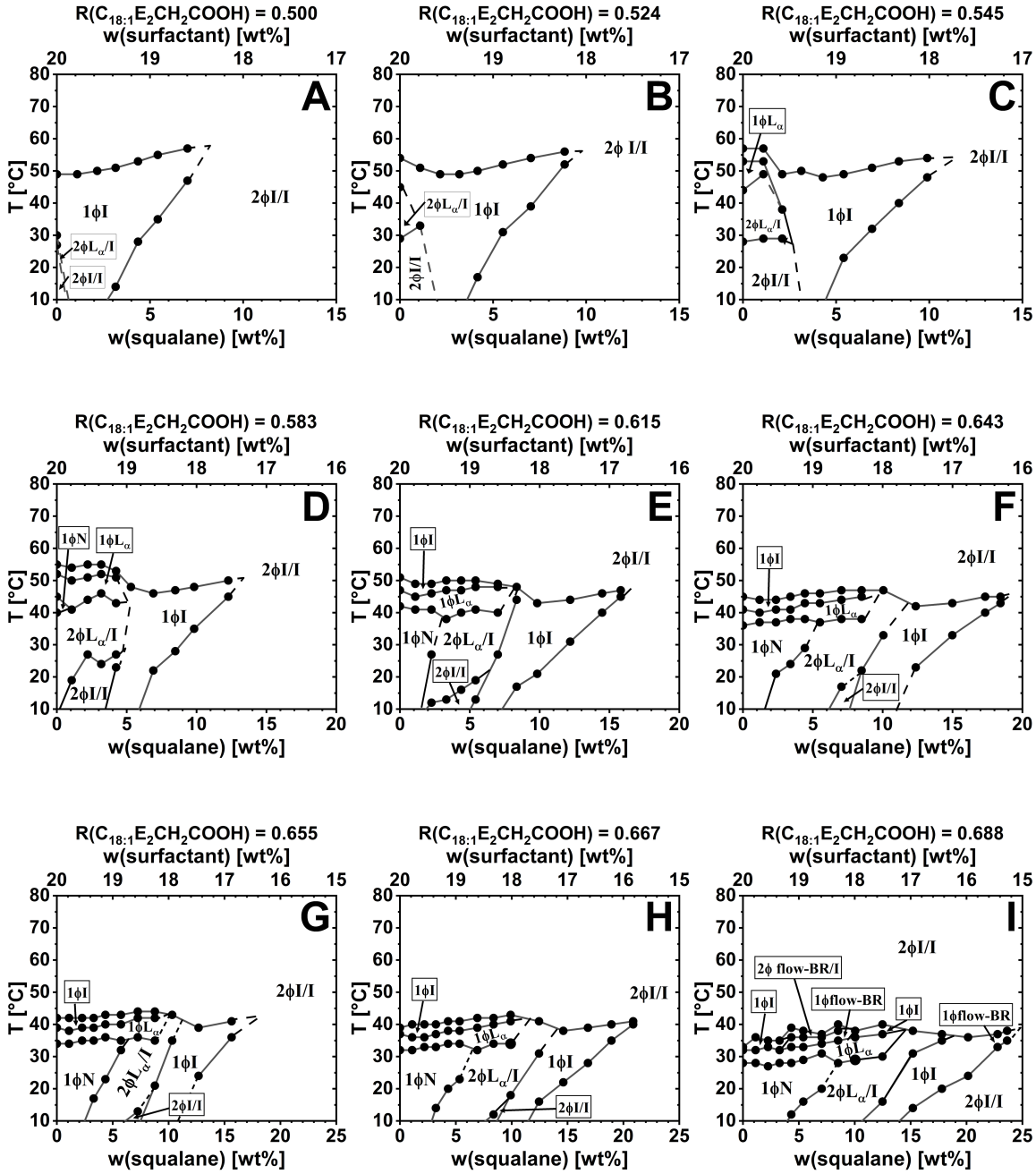

Fig. C.20. Phase maps obtained by successive addition of squalene to nematic gels containing 20 wt% of surfactant with (A) $R(C_{18:1}E_2CH_2COOH) = 0.500$, (B) $R(C_{18:1}E_2CH_2COOH) = 0.524$, (C) $R(C_{18:1}E_2CH_2COOH) = 0.545$, (D) $R(C_{18:1}E_2CH_2COOH) = 0.583$, (E) $R(C_{18:1}E_2CH_2COOH) = 0.615$, (F) $R(C_{18:1}E_2CH_2COOH) = 0.643$, (G) $R(C_{18:1}E_2CH_2COOH) = 0.655$, (H) $R(C_{18:1}E_2CH_2COOH) = 0.667$, or (I) $R(C_{18:1}E_2CH_2COOH) = 0.688$. 1ϕ N: Nematic phase. 1ϕ L_α: Pseudo-lamellar phase. 1ϕ I: Isotropic phase. 2ϕ I/I: Two isotropic phases in equilibrium. 2ϕ L_α/I: Lamellar phase in equilibrium with an isotropic phase. "Flow-BR" indicates flow birefringence. The flow birefringent phases could be L_3 sponge phases. At low oil contents and higher temperatures above the nematic phase, the size of the disc-like micelles in the isotropic phase could be increased by oil loading and in turn lead to sufficient alignment under shear. The phase behavior in absence of oil as a function of $R(C_{18:1}E_2CH_2COOH)$ can be inferred from **Fig. IV.2**.

C.2. Surfactant Purification by Cloud Point Extraction and Ion Exchange

For the removal of hydrophilic non-surfactant impurities by cloud point extraction, the surfactant was thoroughly mixed with around 70 vol% water, and phase separation was induced by equilibration at 90°C. After the aqueous phase was removed, the process was repeated two additional times, before the surfactant-rich phase was vacuum dried. It was observed that the phase behavior of surfactant mixtures of $C_{18:1}E_2CH_2COOH$ and $C_8E_8CH_2COOH$ is influenced by vacuum drying of $C_{18:1}E_2CH_2COOH$, depending on the resting time of the water-free $C_{18:1}E_2CH_2COOH$. This was not observed for $C_8E_8CH_2COOH$. The reason for the change is most likely a shift of the equilibrium of ester formation between the carboxylic acid surfactant and nonionic surfactant impurities due to the removal of water. Since $C_{18:1}E_2CH_2COOH$ contains a higher fraction of nonionic impurities and has a lower degree of ethoxylation than $C_8E_8CH_2COOH$, the effect is more pronounced for $C_{18:1}E_2CH_2COOH$.

Nonionic surfactant impurities that cannot be removed by cloud point extraction were removed by ion exchange. A chromatographic column with frit was packed with the anion exchange resin Amberlyst® A26(OH), purchased from Sigma-Aldrich (St. Louis, Missouri, USA), and wetted with 2-propanol. The column was loaded with one column volume (CV) of a surfactant/2-propanol (40/60 vol%) mixture and the nonionic fraction was further eluted with 1 CV of 2-propanol. Subsequently, the column was loaded with the eluate, and the nonionic fraction was eluted with at least 1 CV of 2-propanol. This step was performed at least twice. To release the carboxylic acid fraction bound to the resin, the column was rinsed with 2 CV of a 1.5 M solution of KOH in 2-propanol. To remove 2-propanol, the obtained mixture was vacuum dried. After subsequent addition of 1 M aqueous HCl-solution to the mixture until a pH < 2 was reached, cloud point extraction was performed three times to remove hydrophilic non-surfactant impurities and KCl. In a last step, the surfactant-rich phase was thoroughly vacuum dried at 90°C to obtain the neat surfactant.

C.3. Molecular Volumes and Scattering Length Densities of the Used Compounds

The average molecular volumes of the surfactants $C_8E_8CH_2COOH$ after cloud point extraction, $C_{18:1}E_2CH_2COOH$, and $C_8E_8CH_2COOH$ and $C_{18:1}E_2CH_2COOH$ after purification by ion exchange and cloud point extraction are calculated from the measured physical densities and the respective molar masses. The molecular volume of each surfactant can be split into a hydrophobic part, consisting of its alkyl chain, and a hydrophilic part, consisting of the EO groups and the carboxylic acid moiety. The molecular volumes of the hydrophobic parts were estimated using incremental values of $V(-CH_3) = 0.0536\ nm^3$ [6], $V(-CH_2-) = 0.0269\ nm^3$ [6], and $V(-CH=) = 0.0221\ nm^3$ [7] at 20°C. Typically, the available literature data at various temperatures were linearly extrapolated to the desired temperature. The calculated molecular volumes as well as the scattering length densities (SLDs) for the pure surfactants and the solvents H_2O and D_2O at 20°C are given in **Table C.3.1**. Note that neat $C_{18:1}E_2CH_2COOH$ was used for the density measurements right after vacuum drying, while $C_{18:1}E_2CH_2COOH$ was used as received (containing 4.1 wt% water) in all other experiments. It should also be noted that constant average molar masses were assumed, 541 $g \cdot mol^{-1}$ for $C_8E_8CH_2COOH$ and 415 $g \cdot mol^{-1}$ for $C_{18:1}E_2CH_2COOH$. Average molecular volumes and scattering length densities of mixtures of the two surfactants can be calculated from the data of the pure surfactants assuming ideal mixing. If headgroup hydration with three water molecules per EO-group is assumed, the SLDs of the hydrated headgroup shells with a resulting volume fraction of water close to 50 vol% further approach the SLD of water (H_2O or D_2O), thus reducing the scattering contrast between solvent and shell.

Table C.3.1. Scattering length densities for X-rays (SLD_X) and neutrons (SLD_N), molecular volumes V, physical densities, and molar masses of the used surfactants and solvents at 20°C. The physical densities of neat $C_8E_8CH_2COOH$ (after cloud point extraction) and $C_{18:1}E_2CH_2COOH$ (after vacuum drying) were measured, see **Section IV.3.5**. "Pure acid" indicates the obtained values for the surfactants after purification by ion exchange and subsequent cloud point extraction.

compound	formula	M [g·mol^{-1}]	ρ [g·cm^{-3}]	V [nm^{-3}]	SLD_X [10^{-4} nm^{-2}]	SLD_N [10^{-4} nm^{-2}]
Water	H_2O	18.015	0.998	0.030	9.40	-0.56
Heavy water	D_2O	20.028	1.105	0.030	9.37	6.36
$C_8E_8CH_2COOH$	$C_{26}H_{52}O_{11}$	541	1.061 pure acid: 1.069	0.846 pure acid: 0.841	9.86 pure acid: 9.92	0.50 pure acid: 0.50
$C_8E_8CH_2COOH$ hydrophobic	C_8H_{17}	113	0.777 pure acid: 0.777	0.242 pure acid: 0.242	7.57 pure acid: 7.57	-0.43 pure acid: -0.43
$C_8E_8CH_2COOH$ hydrophilic	$C_{18}H_{35}O_{11}$	427	1.174 pure acid: 1.186	0.604 pure acid: 0.599	10.77 pure acid: 10.87	0.87 pure acid: 0.88
$C_{18:1}E_2CH_2COOH$	$C_{24}H_{46}O_5$	415	0.950 pure acid: 0.975	0.725 pure acid: 0.707	8.9 pure acid: 9.17	0.23 pure acid: 0.23
$C_{18:1}E_2CH_2COOH$ hydrophobic	$C_{18}H_{35}$	251	0.833 pure acid: 0.833	0.501 pure acid: 0.501	8.04 pure acid: 8.04	-0.34 pure acid: -0.34
$C_{18:1}E_2CH_2COOH$ hydrophilic	$C_6H_{11}O_5$	163	1.210 pure acid: 1.317	0.224 pure acid: 0.206	10.95 pure acid: 11.92	1.50 pure acid: 1.63

C.4. Evaluation of the Threshold of Bubble Rising in the Nematic Gel

The used swing-out rotor geometry results in a horizontal orientation of the centrifuge tubes with the bottom of the tubes being on the outside during centrifugation. The distance between the bottom of the tube and the center of the rotor is then R_r = 172 mm. In the tubes filled with 10 mL of nematic gel, the cylindrical area between approximately 2 mL and 9.5 mL of filling is monitored. The resulting minimal effective rotor radius is $R_{r,min}$ = 75 mm, while the maximal effective rotor radius is $R_{r,max}$ = 135 mm. A ruler placed

next to the tubes when taking the image allows to determine the effective R_r for any given bubble position. A series of images taken for a sample after each step of centrifugation is given in **Fig. C.4.1**. Affinity Photo 2 (version 2.1.1) was used to determine the bubble positions and bubble diameters by measuring pixels. The distance between $R_{r,min}$ and $R_{r,max}$ was used as reference length. An error of ±4 pixels was estimated for the determination of the bubble position (R_r), while an error of ±2 pixels was estimated for the determination of the bubble diameter. An error that was not accounted for is that bubbles appear slightly smaller or lager, depending on their position in the liquid.

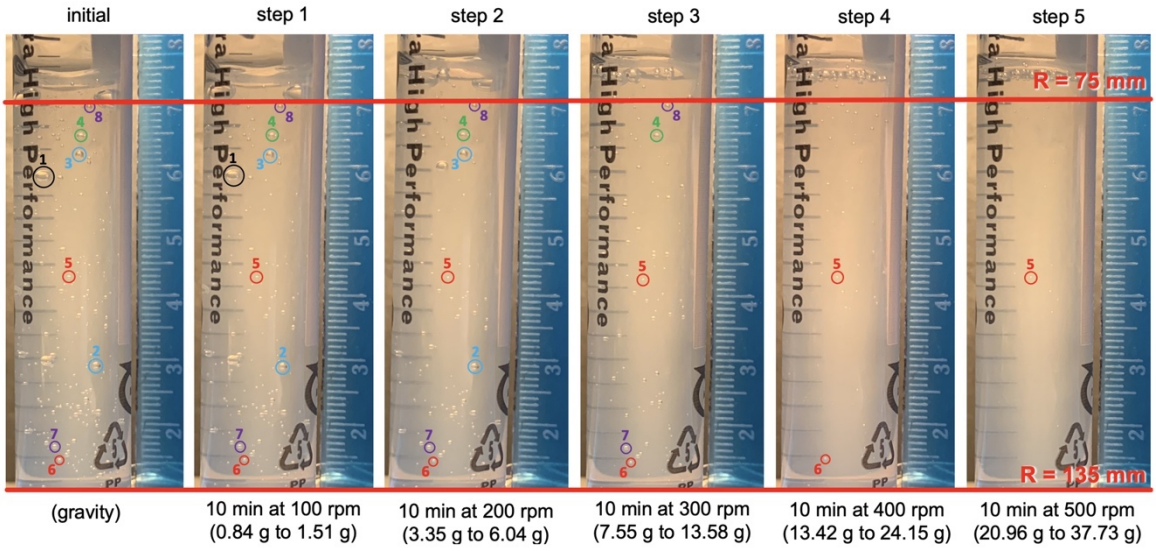

Fig. C.4.1. Photographs of a 15 mL centrifuge tube containing 10 mL of a nematic gel before centrifugation and after each step of centrifugation at 25°C. Tracked bubbles are marked with colored circles.

At a given position of the bubble in the mixture, i.e., at a given R_r, and a given number of revolutions per minute (RPM) the relative centrifugal force $F_{CF,rel}$ is given by

$$F_{CF,rel} = \frac{\left(\frac{2\pi}{60}\cdot RPM\right)^2 \cdot R_r}{g}\ , \qquad (C.4.1)$$

where g is the gravitational acceleration. The buoyant force F_a acting on a bubble of volume V_{bubble} is then given by

$$F_a = \rho_{mixture} \cdot V_{bubble} \cdot g \cdot F_{CF,rel}\ , \qquad (C.4.2)$$

where $\rho_{mixture} = 999\ kg \cdot m^{-3}$ is the physical density of the nematic gel mixture at 25°C. V_{bubble} is given by the following equation.

$$V_{bubble} = \frac{4}{3}\pi \cdot R_{bubble}^{3} \tag{C.4.3}$$

Counteracting forces are the centrifugal force F_{CF}

$$F_{CF} = \rho_{bubble} \cdot V_{bubble} \cdot g \cdot F_{CF,rel} \, , \tag{C.4.4}$$

where $\rho_{bubble} \approx 1.2 \text{ kg} \cdot \text{m}^{-3}$ is the physical density of air, and the force F_{nem} exerted by the nematic gel on the bubble, as indicated in the schematic drawing in **Fig. C.4.2**. The balance of forces at the threshold, at which the bubble is just held in its spot, is given as

$$F_{CF}^{threshold} + F_{a}^{threshold} + F_{nem} = 0 \, . \tag{C.4.5}$$

Therefore, F_{nem} can be calculated by determining the threshold centrifugal and buoyancy forces required to make a bubble float. Since a bubble of radius R_{bubble} has to move through an area A (see **Fig. C.4.2**) given by

$$A = \pi \cdot R_{bubble}^{2} \, , \tag{C.4.6}$$

the pressure P that has to be exerted by the nematic gel on the bubble to prevent its movement at a given relative centrifugal force is given by

$$P = \frac{F_{CF} + F_{a}}{A} \, . \tag{C.4.7}$$

The actual pressure P_{nem} exerted by the nematic gel equals the pressure $P_{threshold}$ required at the threshold.

$$P_{nem} = P_{threshold} = \frac{F_{nem}}{A} \tag{C.4.8}$$

Note that the gravitational force is acting on the air bubble perpendicular to the given forces during centrifugation. However, the gravitational force is neglected, as the calculation is only an approximation and the bubbles clearly resist the buoyancy induced by the gravitational force.

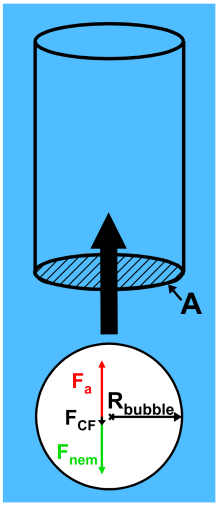

Fig. C.4.2. Schematic drawing of a bubble entrapped in the nematic gel. The area A, see eq. (C.4.6), a bubble has to move through and the forces acting on the bubble are indicated.

C.5. Calculation of Bicellar Size as a Function of Intramicellar Segregation

The cross-section of the bicellar model used for the calculations is given in **Fig. C.5.1**. For the calculations, only the solvent-free hydrophobic core is considered. A bicelle consists of a disc (orange), described by a flat cylinder of radius r and height 2h, and a rim (green), described as a half-toroid of radius r with an elliptical cross-section with half-axes a and h. The total core radius R_{core} is then given by $R_{core} = r + a$. a = 1.17 nm is given by the length of the C_8 chain of $C_8E_8CH_2COOH$ [8]. As suggested by model fits of SANS data, see **Figs. IV.5** and **C.9**, h does not equal the length of the $C_{18:1}$ chain of $C_{18:1}E_2CH_2COOH$, which is around 2 nm, as the chains are interdigitated. The effective half thickness of the disc core is around h = 1.2 nm, see **Figs. IV.5**B and **C.9**B. Consequently, the only geometrical variable is the disc radius r. In the following equations, $C_{18:1}E_2CH_2COOH$ will be abbreviated as RO 20, while $C_8E_8CH_2COOH$ will be abbreviated as LF2.

Only considering the surfactant mixture, one can define separate mole fractions for the disc, x_{disc}(RO 20) and x_{disc}(LF2), and the rim, x_{rim}(RO 20) and x_{rim}(LF2). The two pairs of mole fractions fulfill the conditions x_{disc}(RO 20) + x_{disc}(LF2) = 1 and x_{rim}(RO 20) + x_{rim}(LF2) = 1 and are not directly linked to the given mole fraction of the total surfactant mixture R(RO 20). However, a combination of disc and rim mole fractions

and disc radius r is only valid, if the total mole fraction of the resulting bicelle equals R(RO 20).

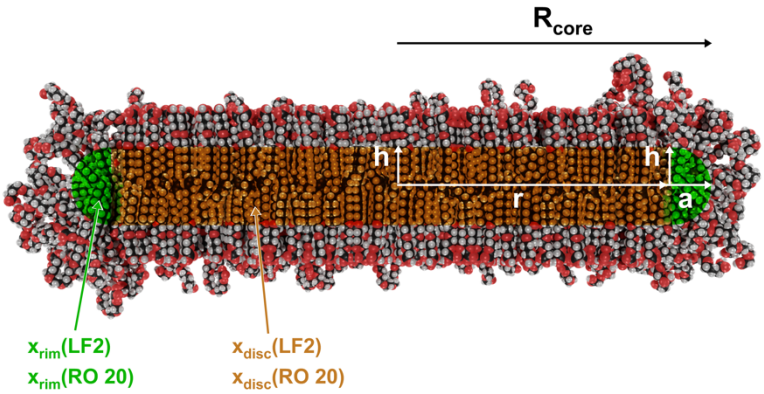

Fig. C.5.1. Cross-section of the bicellar model.

The volumes of the cylindrical disc, V_{disc}, and the half-toroidal rim, V_{rim} are given by

$$V_{disc} = r^2 \cdot \pi \cdot 2h \tag{C.5.1}$$

and

$$V_{rim} = \frac{1}{2}(2 \cdot r \cdot \pi)(a \cdot h \cdot \pi) \, . \tag{C.5.2}$$

Using the molecular volumes of the hydrophobic alkyl chains, $v_{tail}(RO\ 20) = 0.501\ nm^3$ and $v_{tail}(RO\ 20) = 0.242\ nm^3$ (see **Appendix C.3.**), a hydrophobic molecular volume of a hypothetical average surfactant molecule can be defined. For the disc, we define $v_{disc}(avg)$, and for the rim, we define $v_{rim}(avg)$, where

$$v_{disc}(avg) = x_{disc}(RO\ 20) \cdot v_{tail}(RO\ 20) + (1 - x_{disc}(RO\ 20)) \cdot v_{tail}(LF2) \tag{C.5.3}$$

and

$$v_{rim}(avg) = x_{rim}(RO\ 20) \cdot v_{tail}(RO\ 20) + (1 - x_{rim}(RO\ 20)) \cdot v_{tail}(LF2) \, . \tag{C.5.4}$$

The aggregation numbers of the hypothetical average surfactant in the disc, N_{disc}, and in the rim, N_{rim}, are then given by

$$N_{disc} = \frac{V_{disc}}{v_{disc}(avg)} \tag{C.5.5}$$

and

$$N_{rim} = \frac{V_{rim}}{v_{rim}(avg)} \ . \qquad (C.5.6)$$

The mole fractions x_{disc}(RO 20) and x_{rim}(RO 20) are linked to the given R(RO 20) by the following relation.

$$R(RO\ 20) = \frac{N_{disc} \cdot x_{disc}(RO\ 20) + N_{rim} \cdot x_{rim}(RO\ 20)}{N_{disc} + N_{rim}} \qquad (C.5.7)$$

Combining eq. (C.5.7) with eqs. (C.5.1)–(C.5.6), a relation between the disc radius r and the mole fractions is obtained.

$$r = -\frac{\pi \cdot a \cdot v_{disc}(avg)}{2 v_{rim}(avg)} \cdot \frac{R(RO\ 20) - x_{rim}(RO\ 20)}{R(RO\ 20) - x_{disc}(RO\ 20)} \qquad (C.5.8)$$

Thus, for a given combination of x_{rim}(RO 20) and x_{disc}(RO 20), only one disc radius r is possible. Consequently, the disc size is controlled by intramicellar segregation. Approaching full intramicellar mixing, i.e., no segregation, the calculation diverges. For full intramicellar mixing, i.e., for x_{rim}(RO 20) = R(RO 20) and x_{disc}(RO 20) = R(RO 20), the calculation does not work. In case of full intramicellar mixing, either an 'infinite' lamellar phase or small spheroidal micelles would be expected, the former being more probable due to the significantly higher fraction of $C_{18:1}E_2CH_2COOH$. For a given combination of x_{rim}(RO 20) and x_{disc}(RO 20), the number of surfactant molecules in the rim and the disc can be easily calculated from the aggregation numbers N_{disc} and N_{rim}.

Note that not every combination of x_{rim}(RO 20) and x_{disc}(LF2) is physically possible. For an impossible combination, eq. (C.5.8) yields a negative r. For full intramicellar segregation, i.e., for x_{rim}(RO 20) = 0 and x_{disc}(RO 20) = 1, r = 9.1 nm and R_{core} = 10.3 nm, corresponding to an outer radius of 12–13 nm including the hydrophilic shell. However, complete intramicellar segregation is not realistic. Not only is a certain degree of intramicellar mixing to be expected, but since $C_{18:1}E_2CH_2COOH$ is insoluble in water and forms a L_β phase in absence of $C_8E_8CH_2COOH$, some $C_8E_8CH_2COOH$ must be mixed into the bilayer to alter this behavior.

It should also be noted that with a certain degree of intramicellar mixing, an oblate ellipsoidal shape would be feasible. The model of a "perfect" bicelle is an idealized model.

C.6. Dispersion of Oils in the Nematic Gel

The possibility of dispersing oil droplets in the nematic phase without destroying the nematic phase, i.e., without inducing a phase transition, was tested using various different oils, primarily squalane, n-dodecane, (R)-(+)-Limonene, olive oil, and silicon oil M20 (linear polydimethylsiloxane). None of the hydrocarbon oils could be dispersed in the nematic gel, the oils influence phase behavior and are either solubilized in the bicellar cores or induce a phase transition. The only oil that could be dispersed in the nematic gel leaving the viscoelasticity intact is the silicon oil. The emulsions with significant oil loading were stable for at least several weeks. An image of an obtained viscoelastic emulsion containing 53 wt% silicon oil and 9.4 wt% surfactant (R($C_{18:1}E_2CH_2COOH$) = 0.655) is shown in **Fig. C.6.1**.

Fig. C.6.1. Viscoelastic emulsion of silicon oil M20 in a nematic gel, initially containing 20 wt% surfactant with R($C_{18:1}E_2CH_2COOH$) = 0.655. The emulsion contains 53 wt% silicon oil, 9.4 wt% surfactant, and 37.6 wt% water. The emulsion was prepared by adding silicon oil and thoroughly mixing by shaking by hand and vortex mixing. Birefringence could not be checked due to strong turbidity, but the viscoelastic gel-like behavior suggests that the nematic phase stayed intact.

Squalane, see **Fig. C.20**, and n-dodecane, see **Fig. C.6.2**, have similar effects on phase behavior. The phase behavior with limonene as the oil was not examined in detail, but the general phase sequence is also similar. Even though the microstructures were not investigated, a general mechanism of the destruction of the nematic phase by hydrocarbon oils can be proposed: With increasing incorporation of oil into the bicellar hydrocarbon core, the interdigitation of the surfactants' alkyl chains decreases, resulting in higher bilayer flexibility and facilitating a transition to a lamellar phase. As a result, only a certain amount of oil can be incorporated into the bicellar hydrocarbon core, before the transition into a lamellar phase, and eventually into a microemulsion, occurs. The threshold concentration of

oil increases with R($C_{18:1}E_2CH_2COOH$), as the hydrophobic core volume increases with R($C_{18:1}E_2CH_2COOH$).

A difference between the effects of n-dodecane and squalane arises from the significant difference in their molecular dimensions. While squalane has an extended length of around 3.6 nm [8], which is larger than the core thickness of a bicelle of around 2.4 nm, n-dodecane has an extended length of only around 1.8 nm [8], which is smaller than the bicellar core thickness. Whereas squalane only has the effect described above, n-dodecane also influences the phase behavior by increasing the apparent value of R($C_{18:1}E_2CH_2COOH$), i.e., the addition of n-dodecane is to a certain extent equivalent to the addition of more long-chain surfactant. This is best seen in **Figs. C.6.2** C and D, where the addition of n-dodecane induces the formation of the nematic phase, which is usually not formed at the respective surfactant compositions, as the value of R($C_{18:1}E_2CH_2COOH$) is too low.

Olive oil consists mainly of triglycerides, oleic acid being the main fatty acid group. Since the hydrocarbon chain of the hydrophobic surfactant is also an oleyl chain, olive oil and $C_{18:1}E_2CH_2COOH$ are fully miscible. The addition of olive oil to a nematic phase eventually leads to the separation of an isotropic concentrated O/W emulsion (very high volume fraction of oil) from an isotropic micellar phase. The reason for the destruction of the nematic phase is most likely a significant decrease of R($C_{18:1}E_2CH_2COOH$), resulting from the extraction of the long-chain surfactant from the micellar phase into the oil phase. Therefore, the replacement of $C_{18:1}E_2CH_2COOH$ with similar surfactants $C_{18:1}E_jCH_2COOH$ with $j > 2$ was tested. $C_{18:1}E_9CH_2COOH$ (Akypo® RO 90 VG) for example is still not sufficiently hydrophilic to not be fully miscible with olive oil. However, $C_{18:1}E_9CH_2COOH$ is already too hydrophilic, i.e., has a too low spontaneous packing parameter, to form the bicelles with $C_8E_8CH_2COOH$. No combination of surfactants was found that allowed for the dispersion of olive oil droplets in a nematic phase. Further tests involved the change of salinity by NaCl addition, the variation of f[$RCOO^-$ $(Ca^{2+})_{0.5}$] or f($RCOO^-$ Na^+), and the partial replacement of $C_{18:1}E_2CH_2COOH$ by lauric acid, none of which were successful. In the latter case, up to around 60% of $C_{18:1}E_2CH_2COOH$ can be replaced by lauric acid ($C_{11}COOH$) in the absence of oil without changing the phase sequence, but decreasing the phase transition temperatures by about 10°C, see **Fig. C.6.3**. If more than 60% of $C_{18:1}E_2CH_2COOH$ are replaced by lauric acid, lauric acid can crystallize.

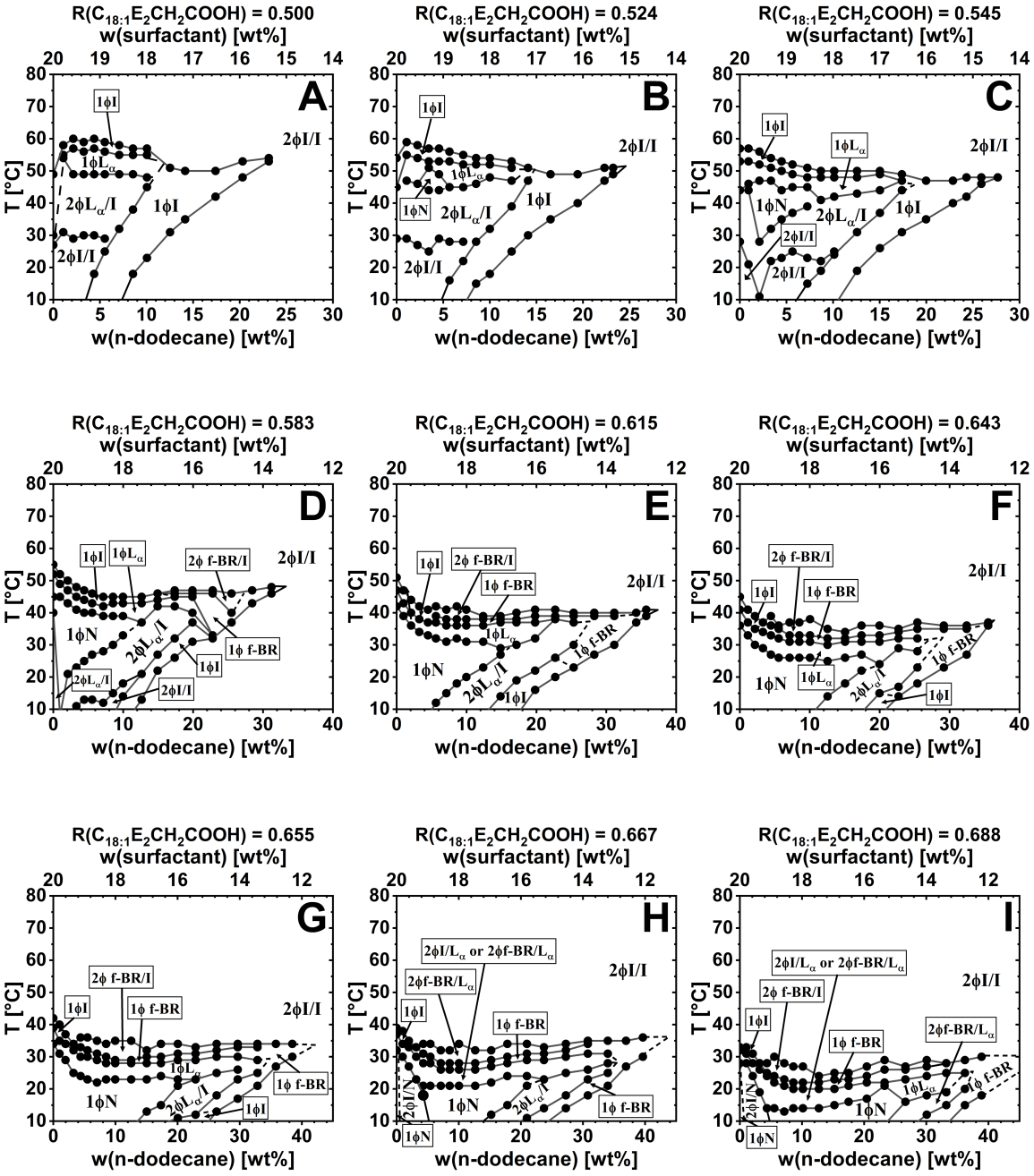

Fig. C.6.2. Phase maps obtained by successive addition of n-dodecane to nematic gels containing 20 wt% of surfactant with (A) $R(C_{18:1}E_2CH_2COOH) = 0.500$, (B) $R(C_{18:1}E_2CH_2COOH) = 0.524$, (C) $R(C_{18:1}E_2CH_2COOH) = 0.545$, (D) $R(C_{18:1}E_2CH_2COOH) = 0.583$, (E) $R(C_{18:1}E_2CH_2COOH) = 0.615$, (F) $R(C_{18:1}E_2CH_2COOH) = 0.643$, (G) $R(C_{18:1}E_2CH_2COOH) = 0.655$, (H) $R(C_{18:1}E_2CH_2COOH) = 0.667$, or (I) $R(C_{18:1}E_2CH_2COOH) = 0.688$. 1ϕ N: Nematic phase. 1ϕ L_α: Pseudo-lamellar phase. 1ϕ I: Isotropic phase. 2ϕ I/I: Two isotropic phases in equilibrium. 2ϕ L_α/I: Lamellar phase in equilibrium with an isotropic phase. "Flow-BR" indicates flow birefringence. The flow birefringent phases could be L_3 sponge phases. At low oil contents and higher temperatures above the nematic phase, the size of the disc-like micelles in the isotropic phase could be increased by oil loading and in turn lead to sufficient alignment under shear. The phase behavior in absence of oil as a function of $R(C_{18:1}E_2CH_2COOH)$ can be inferred from **Fig. IV.2**.

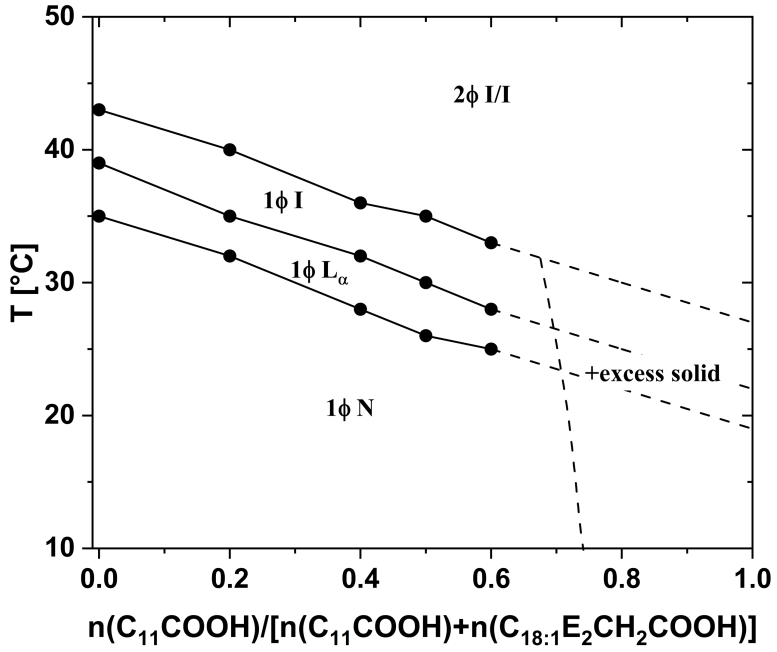

Fig. C.6.3. Phase diagram at a constant surfactant concentration of 20 wt% with $R(C_{18:1}E_2CH_2COOH + C_{11}COOH) = 0.655$, as a function of the lauric acid ($C_{11}COOH$) fraction. The surfactant mixture contains $C_{18:1}E_2CH_2COOH$, $C_8E_8CH_2COOH$, and $C_{11}COOH$. The lauric acid content is plotted as the fraction of $C_{18:1}E_2CH_2COOH$ replaced by lauric acid, i.e., $n(C_{11}COOH)/[n(C_{11}COOH) + n(C_{18:1}E_2CH_2COOH)]$. 1ϕ N: Nematic phase. 1ϕ L_α: Pseudo-lamellar phase. 1ϕ I: Isotropic phase. 2ϕ I/I: Two isotropic phases in equilibrium.

C.7. A Dilute Biaxial Calamitic Nematic Phase

Tchakalova *et al.* [9] reported on a nematic phase with similar macroscopic properties as the discotic nematic phase described in this work. The system comprises lauric acid ($C_{11}COOH$), Neodol 91-8 ($C_{9\text{-}11}E_8$), and a fragrance oil such as dihydromyrcenol (2,6-dimethyl-7-octen-2-ol; DHM) in water with some propylene glycol as additive. Tchakalova *et al.* suggested that small prolate micelles with an ellipticity of around 2 are formed, which then align to form large planar sheets that are electrostatically swollen. Swelling is found to be two-dimensional, as expected for layered structures.

Since $C_{11}COOH$ has a high spontaneous packing parameter p_0, thus favoring low or zero curvature, whereas $C_{9\text{–}11}E_8$ has a low p_0, thus favoring high curvature, intramicellar molecular segregation can be expected. DHM acts as a co-surfactant, which hinders crystallization of $C_{11}COOH$. $C_{9\text{–}11}E_8$ is expected to prefer the axial positions of the prolate ellipsoids, while $C_{11}COOH$ and DHM are expected to prefer the equatorial positions of lower curvature. It should be noted that the authors did not exclude small oblate micelles, which would

offer regions of lower curvature for $C_{11}COOH$ than prolate micelles.

The SAXS data presented in Figure 4 of ref. [9] are replotted in **Fig. C.7.1**A. The compositions of the samples are given in **Table C.7.1**, where also the mole ratio of $C_{11}COOH$ and DHM as well as $R(C_{11}COOH+DHM)$ are given. $R(C_{11}COOH+DHM)$ is the mole fraction of the components favoring low curvature in the surfactant – fragrance mixture.

$$R(C_{11}COOH+DHM) = \frac{n(C_{11}COOH)+n(DHM)}{n(C_{11}COOH)+n(DHM)+n(C_{9-11}E_8)} \qquad (C.7.1)$$

The spectra follow a slope of q^{-1} in the mid-q range, usually typical for "one-dimensional", i.e., rod-like, structures. However, as shown in Figure 10B of ref. [9], see **Fig. C.7.2**, the swelling of the structures, i.e., the repeat distance of the planar sheets taken from the structure factor peak maximum, is clearly one-dimensional, which also holds for the here shown samples "1.6 wt% $C_{11}COOH$", "1.9 wt% $C_{11}COOH$", and "2.5 wt% $C_{11}COOH$". One-dimensional swelling is only possible for (locally) layered structures. Thus, the slope of the spectra and the swelling appear to be paradoxical, and a satisfactory explanation is still missing, as the individual prolate micelles are too small to produce a slope of -1.

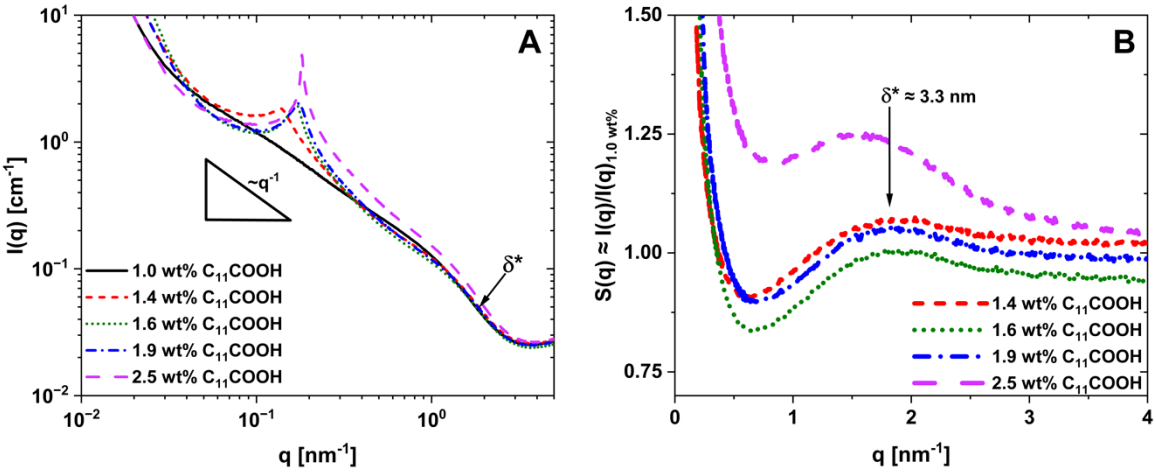

Fig. C.7.1. (A) SAXS data of various samples with fixed weight fractions of DHM and $C_{9-11}E_8$ and varying concentrations of $C_{11}COOH$. Exact compositions can be inferred from **Table C.7.1**. The position of a weak second peak of the apparent structure factor, δ*, shown in (B) is also indicated. (B) Apparent structure factor S(q) as obtained by dividing the SAXS curves given in (A) by the SAXS data of the 1.0 wt% $C_{11}COOH$ sample. $\delta^* = 2\pi \cdot q_{max}^{-1}$. Note that the low-q region including the pronounced structure factor peak of the plane-plane-spacing is cut-off.

When extracting the apparent structure factor S(q) from the spectra of samples "1.4 wt% $C_{11}COOH$, "1.6 wt% $C_{11}COOH$", "1.9 wt% $C_{11}COOH$", and "2.5 wt% $C_{11}COOH$" by dividing the data by the data obtained for the sample "1.0 wt% $C_{11}COOH$", where no

structure factor peak is observed, see **Fig. C.7.1**B, a broad second peak is evidenced around q = 1.90 nm^{-1} (δ* = 3.3 nm). No higher order peaks of the planar spacing are observed due to the lack of long-range order in the nematic phase. Note that the peak is either a peak of the structure factor, or an "artifact" of the form factor, arising from the variation of the surfactant composition on increasing the C_{11}COOH content (see **Table C.7.1**).

Table C.7.1. Compositions of the samples for which SAXS data are shown in **Fig. C.7.1**.The mole ratio of C_{11}COOH and DHM is given to show that the composition of the low curvature favoring fraction changes significantly. R(C_{11}COOH+DHM) is the mole fraction of low curvature favoring components in the surfactant – fragrance mixture. Note that the solvent contains propylene glycol. The weight fraction of propylene glycol is around 16 wt% in these samples.

sample	w(C_{11}COOH) [wt%]	w(DHM) [wt%]	w($C_{9-11}E_8$) [wt%]	$\frac{n(C_{11}COOH)}{n(DHM)}$	R(C_{11}COOH+DHM)
"1.0 wt% C_{11}COOH"	1.0	1.9	6.0	0.405	0.602
"1.4 wt% C_{11}COOH"	1.4	1.9	6.0	0.567	0.628
"1.6 wt% C_{11}COOH"	1.6	1.9	6.0	0.648	0.640
"1.9 wt% C_{11}COOH"	1.9	1.9	6.0	0.770	0.656
"2.5 wt% C_{11}COOH"	2.5	1.9	6.0	1.013	0.684

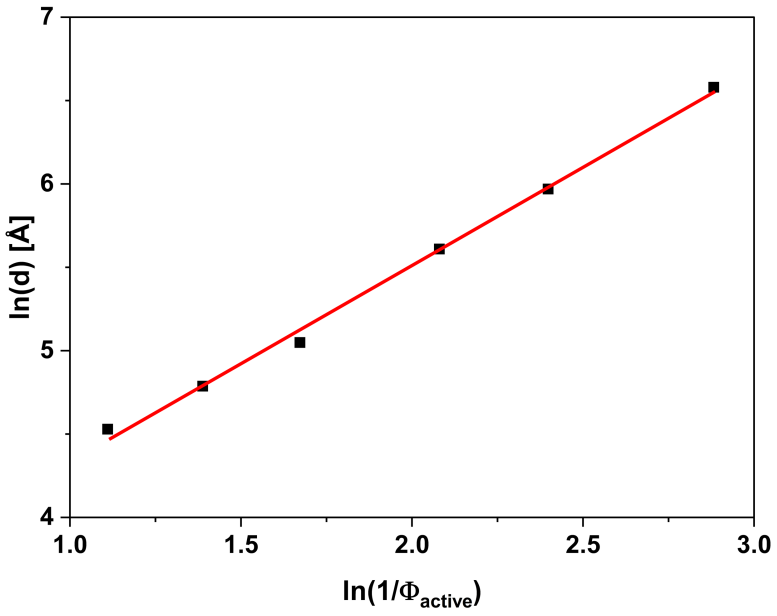

Fig. C.7.2. One-dimensional swelling of the repeat distance of the planar sheets, d, as shown by Tchakalova *et al.* [9]. The red line is a linear fit with a slope of 1.18 and an intercept at d = 24 Å. Φ_{active} is the volume fraction of active material (C_{11}COOH, DHM, and $C_{9-11}E_8$). Reproduced from [9] (Copyright © The authors of [9]).

In principle, one could expect a similar situation as in the present work: The C_{11}COOH and DHM molecules favor bilayer formation, whereas $C_{9-11}E_8$ favors spherical packing. As a result, there is some degree of intramicellar molecular segregation and a large bicelle with a flat disc part and a curved spherical rim is formed. As can be inferred from **Table C.7.1**,

the fraction of surfactants favoring low curvature, R(C_{11}COOH+DHM), is in a similar range as R($C_{18:1}E_2CH_2COOH$) in this work. Given the fact that the macroscopic properties of both systems are also similar, one could imagine that in this case also large discs are formed, which, however, would produce a q^{-2} slope and not a q^{-1} slope. The peak seen in **Fig. C.7.1**B would then be a form factor peak reflecting the spacing of the two COOH layers within the disc, i.e., the thickness of the disc. Interestingly, the spacing of $\delta^* = 3.3$ nm is in perfect agreement with the expected thickness of a C_{11}COOH bilayer, given the length of 1.67 nm for a C_{12} chain [8].

If the peak seen in **Fig. C.7.1**B is indeed a structure factor peak, it would reflect the average in-plane spacing of the nematically ordered prolate micelles, i.e., the center-to-center distance of the prolate micelles averaged over all orientations. The maximum equatorial radius is also 3.3 nm, and the axial radius is around twice as large for an ellipticity of around 2. In this case, the value of δ^* would be expected to be larger than 3.3 nm. The spacing of 3.3 nm is reasonable for the smaller equatorial diameter of 2.4 nm suggested by Tchakalova *et al*. An equatorial radius of 1.2 nm is intermediate between the length of C_{11}COOH and the length of DHM (≈ 1 nm). It is important to note, however, that the sketches presented by Tchakalova *et al.* (graphical abstract and figure 5 of ref. [9]), suggesting that the prolate micelles forming a two-dimensional sheet are separated by solvent, are not compatible with the data. The in-plane spatial separation would only be possible if the forces responsible for the arrangement would be repulsive: With a repulsive in-plane interaction, the micelles would have no reason to stay in the plane to minimize electrostatic interactions. This situation would also produce a pronounced peak with a spacing larger than the micellar dimension, which is clearly not observed. Notably, the authors also suspected attractive hydrogen bonding to be responsible for the connection of the prolate micelles. The small micelles must be connected and not separated by "bulk" solvent. Since the line tension is probably very low, it is further unlikely that the micelles connect to form rectangular sheets, and a disc-like shape would be energetically preferable due to minimization of the interfacial area. The disc may be of irregular shape as in the case of liquid expanded phases of lipids. Only large line-tensions would drive to a regular disc-like shape.

Two attractive intermicellar contributions can be imagined: The hydrogen bonding, specifically the COOH-COOH interactions [10] in the equatorial regions of the micelles, on the one hand, and the interdigitation of the polyoxyethylene headgroups, predominantly

populating the axial region of the micelle, on the other hand. Therefore, the schematic drawing given in **Fig. C.7.3**B is a more likely representation of the microstructure. This is, however, only possible if there is electrostatic repulsion between the sheets as negative charges accumulate at the planar surfaces. Otherwise, there would be no reason for a sheet-like organization, as the micelles could attractively interact in all directions. If the sheets become large enough by connection of sheets at higher surfactant concentrations or if an increased fraction of C_{11}COOH leads to more intermicellar attraction, a smectic phase is formed, see **Fig. C.7.3**C. If the C_{11}COOH content is too low, a nematic or smectic phase cannot be formed due to a lack of intermicellar attraction at equatorial micellar positions, and an isotropic phase is formed, see **Fig. C.7.3**A.

Since the small prolate micelles can connect at the axial positions via headgroup interdigitation, they form longer chains of connected micelles in the in-plane nematic direction, which could produce the slope of -1. While it may still be questionable if a close packing of these chains into a planar sheet would produce a slope of -1 due to the chains rather than -2 due to the overall planar structure, such chains could explain the q^{-1} behavior at least in the isotropic phase. The individual prolate micelles with an ellipticity around 2 are too small to produce a clear slope of -1 in the mid-q range.

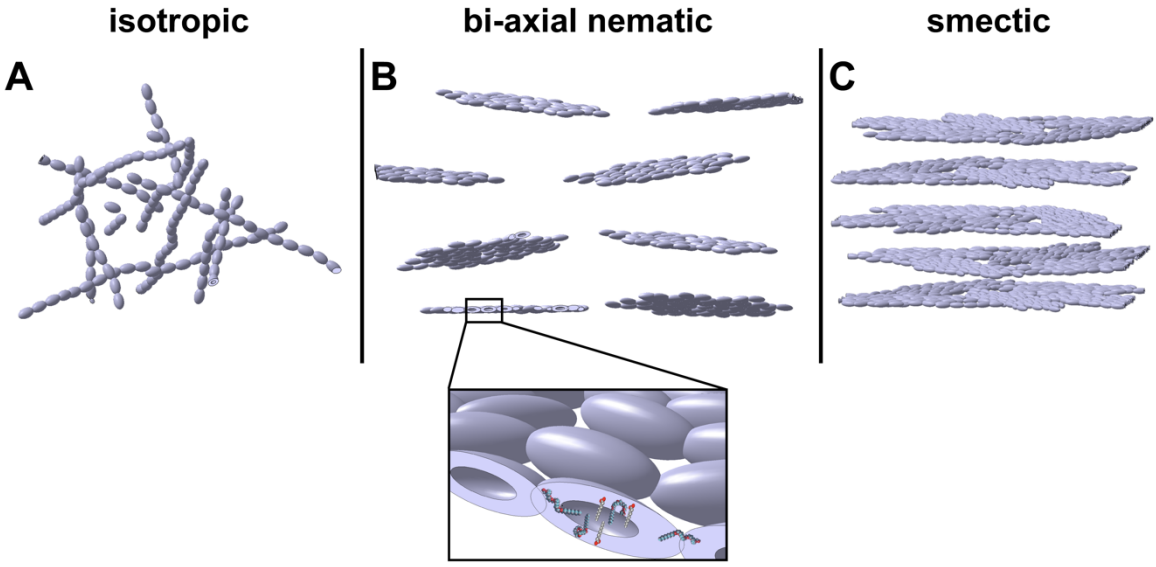

Fig. C.7.3. Schematic drawings of the formed microstructures. (A) Isotropic phase of small prolate micelles. $C_{9–11}E_8$ headgroups at the axial positions of the micelles interdigitate, leading to the formation of chains of connected prolate micelles. (B) Bi-axial nematic phase formed if enough C_{11}COOH is present. COOH-COOH interactions connect the micelles at their equatorial positions and disc-like sheets of small, cross-linked micelles are formed. The sheets are nematically ordered and responsible for the one-dimensional swelling. The enlargement indicates the intramicellar molecular segregation responsible for the structure. (C) Smectic phase of higher order at higher surfactant concentrations and/or higher C_{11}COOH contents. The drawings used in this image were created by Baptiste Ribéreau-Gayon based on ideas of Prof. Dr. Thomas Zemb.

It should be noted that a degree of $C_{11}COOH$ dissociation of around 15%, as stated by Tchakalova *et al.* [9], would be sufficient for electrostatic swelling. However, using the same apparent $pK_a = 6.7$ and the reported pH of 4.9, a degree of dissociation of only around 1.5% would be expected. The surface charge density is unknown, but large enough to produce swelling up to 60 nm between the planar sheets, see **Fig. C.7.2**. The swelling curve shown in **Fig. C.7.2** reveals an intercept at 2.4 nm: The layers must be compact, as shown in **Fig. C.7.3**C. In the schematic drawings in the original work, the plane is made of repulsive micelles: If this would be the case, the swelling curve would have the same slope, but a five to ten times larger intercept. Moreover, a peak at the in-plane average intermicellar distance would be seen, which is not observed. Therefore, the nematic phase has two axes: One for the swelling and one for the preferred in-plane distance, as shown to scale in **Fig. C.7.3**.

As a concluding remark, it must be emphasized that the apparent structure factor given in **Fig. C.7.2**B must be cross-checked, as the "1.0 wt% $C_{11}COOH$" spectrum cannot be safely taken as the form factor for the other samples, which is subject to slight variations when increasing the molecular composition.

The $C_{11}COOH$ carboxylic acid is used as a linker [10] in the system studied by Tchakalova *et al.* [9]. The ratio between bulky ethoxylated headgroups and carboxylic acid linkers can be varied by formulation. In the nematic phase presented in this work, made from mixed ethoxylated carboxylic acid surfactants, there is one potential linker per surfactant molecule and this ratio cannot be varied, and it was also shown in this work that the carboxylic acid groups are not necessary for the formation of the discotic nematic phase.

Acknowledgement

Dr. Daniel Benczedi and Dr. Vera Tchakalova are gratefully acknowledged for granting access to published data in numeric form, allowing the comparison of structure factors in the biaxial nematic phases patented at Firmenich (EP3528902A1 and EP3528902B1) and uniaxial nematic phases studied in this thesis.

C.8. References

[1] W.H. Herschel, R. Bulkley, Konsistenzmessungen von Gummi-Benzollösungen, Kolloid-Zeitschrift. 39 (1926) 291–300. https://doi.org/10.1007/BF01432034.

[2] M. Doucet, J.H. Cho, G. Alina, Z. Attala, J. Bakker, W. Bouwman, P. Butler, K. Campbell, T. Cooper-Benun, C. Durniak, L. Forster, M. Gonzalez, R. Heenan, A. Jackson, S. King, P. Kienzle, J. Krzywon, R. Murphy, T. Nielsen, L. O'Driscoll, W. Potrzebowski, S. Prescott, R. Ferraz Leal, P. Rozyczko, T. Snow, A. Washington, SasView, (2021). https://doi.org/10.5281/zenodo.4467703.

[3] J. Hansen, J.B. Hayter, A rescaled MSA structure factor for dilute charged colloidal dispersions, Mol Phys. 46 (1982) 651–656. https://doi.org/10.1080/00268978200101471.

[4] J.B. Hayter, J. Penfold, An analytic structure factor for macroion solutions, Mol Phys. 42 (1981) 109–118. https://doi.org/10.1080/00268978100100091.

[5] C.G. Malmberg, Dielectric Constant of Deuterium Oxide, J Res Natl Bur Stand (1934). 60 (1958) 609–612.

[6] F. Reiss-Husson, V. Luzzati, The Structure of the Micellar Solutions of Some Amphiphilic Compounds in Pure Water as Determined by Absolute Small-Angle X-Ray Scattering Techniques, J Phys Chem. 68 (1964) 3504–3511. https://doi.org/10.1021/j100794a011.

[7] D. Uhríková, P. Rybár, T. Hianik, P. Balgavý, Component volumes of unsaturated phosphatidylcholines in fluid bilayers: a densitometric study, Chem Phys Lipids. 145 (2007) 97–105. https://doi.org/10.1016/j.chemphyslip.2006.11.004.

[8] C. Tanford, Micelle shape and size, Journal of Physical Chemistry. 76 (1972) 3020–3024. https://doi.org/10.1021/j100665a018.

[9] V. Tchakalova, C.L.P. Oliveira, A.M. Figueiredo Neto, New Lyotropic Complex Fluid Structured in Sheets of Ellipsoidal Micelles Solubilizing Fragrance Oils, ACS Omega (2023). https://doi.org/10.1021/acsomega.3c03500.

[10] J. Chen, C.L. Brooks, H.A. Scheraga, Revisiting the carboxylic acid dimers in aqueous solution: Interplay of hydrogen bonding, hydrophobic interactions and entropy, Journal of Physical Chemistry B 112 (2008) 242–249. https://doi.org/10.1021/jp074355h.

Appendix D.

Supplementary Material – Chapter V.

D.1. Supplementary Figures

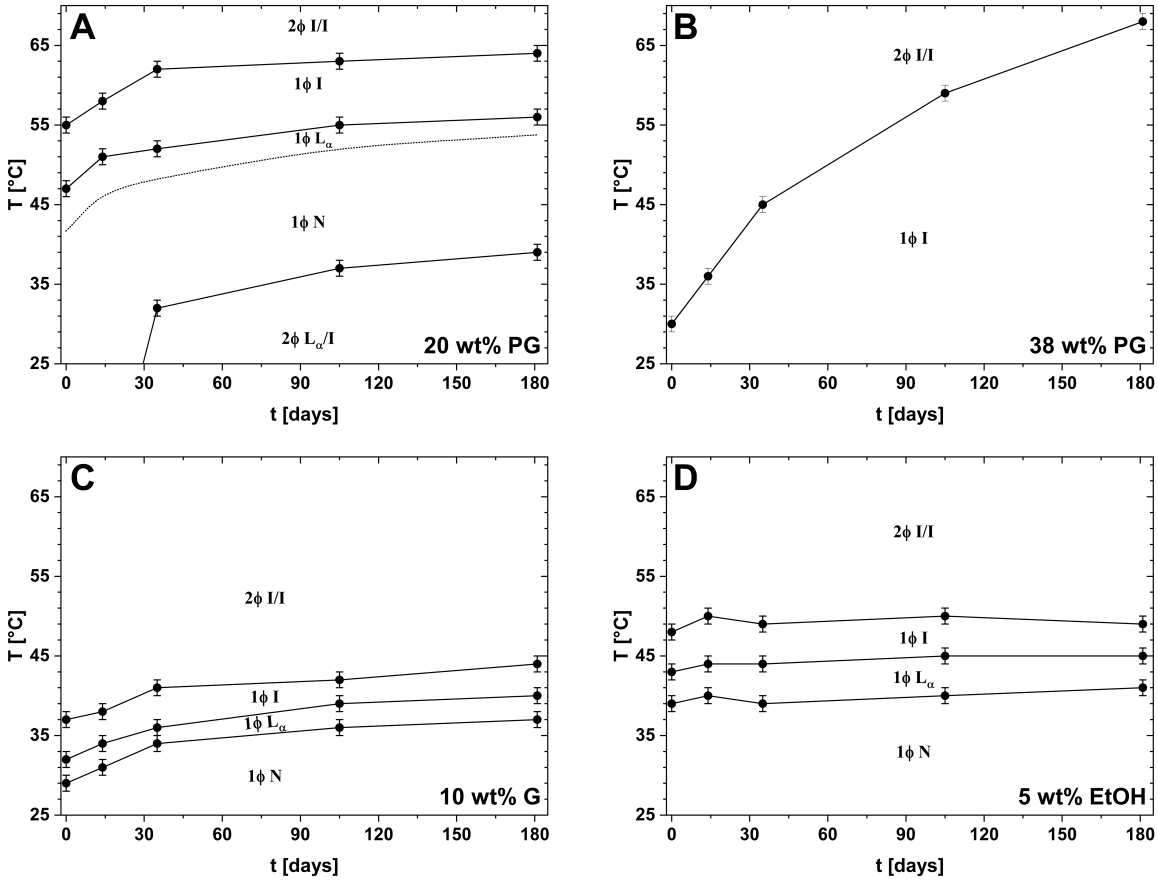

Fig. D.1. Phase boundaries of samples containing 20 wt% of surfactant, R($C_{18:1}E_2CH_2COOH$) = 0.655, in water and (A) 20 wt% PG, (B) 38 wt% PG, (C) 10 wt% G, or (D) 5 wt% EtOH as a function of time since sample preparation (t = 0 days). For each determination of the phase transition temperatures, the samples were heated in steps of 1°C up to above 80°C. The same sample was examined every time, i.e., the change in phase boundaries does not reflect only the change during storage at room temperature but also the change induced by heating of the samples. The change at room temperature was not quantified but seems to be rather insignificant within at least one month of storage. 1ϕ N: Nematic phase. 1ϕ L_α: Pseudo-lamellar phase. 1ϕ I: Isotropic phase. 2ϕ I/I: Two isotropic phases in equilibrium. 2ϕ L_α/I: Lamellar phase in equilibrium with an isotropic phase.

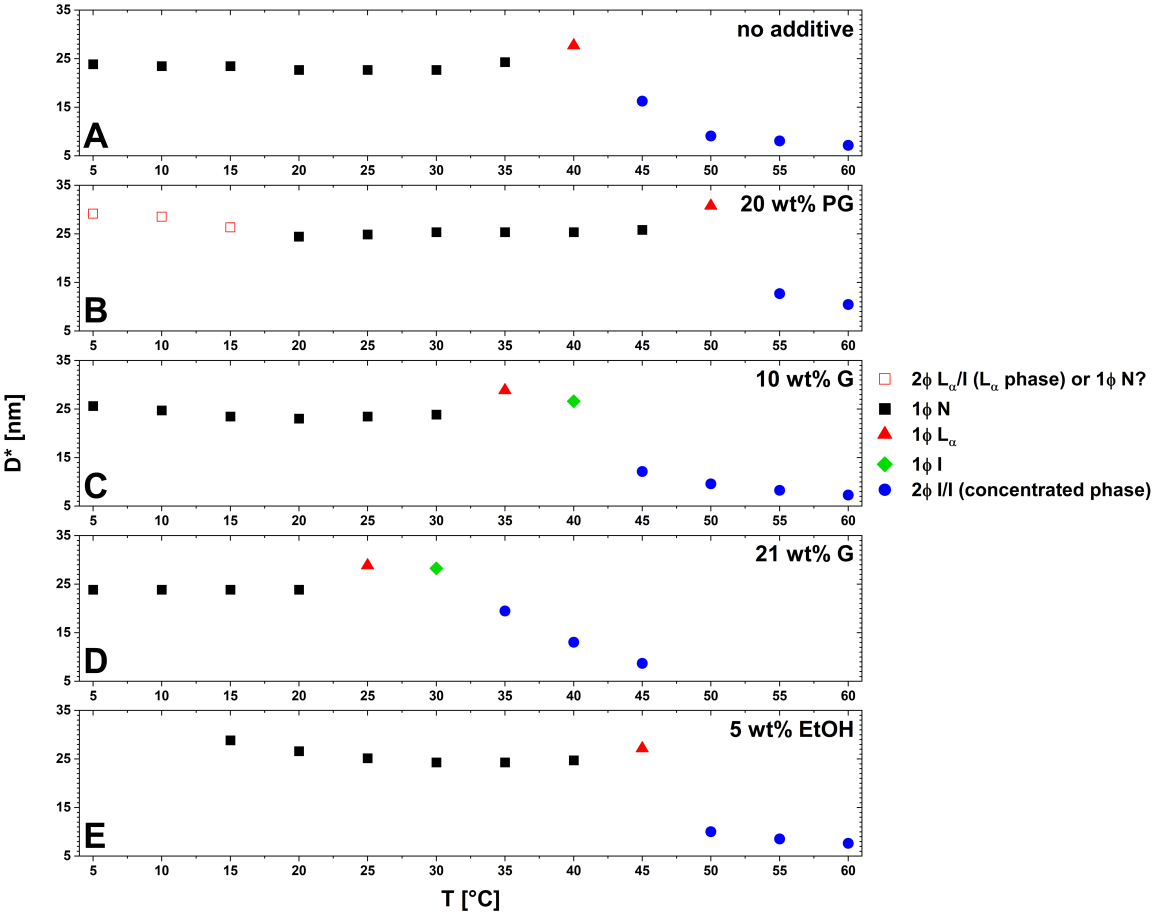

Fig. D.2. Repeat distance $D^* = 2\pi \cdot q_{max}^{-1}$ obtained from the SAXS correlation peaks at different temperatures of samples (A) "M", identical to sample "20M*" in **Chapter IV.**, containing no additive, (B) "M-20PG", containing 20 wt% of PG, (C) "M-10G", containing 10 wt% of G, (D) "M-21G", containing 21 wt% of G, and (E) "M-5E", containing 5 wt% of EtOH. All samples contain 20 wt% of a surfactant mixture with $R(C_{18:1}E_2CH_2COOH) = 0.655$. The SAXS data for (B) to (E) are given in **Figs. V.2**A, **V.4**A, **V.4**B, and **V.6**A. The data of sample "M" are given in **Fig. C.15**.

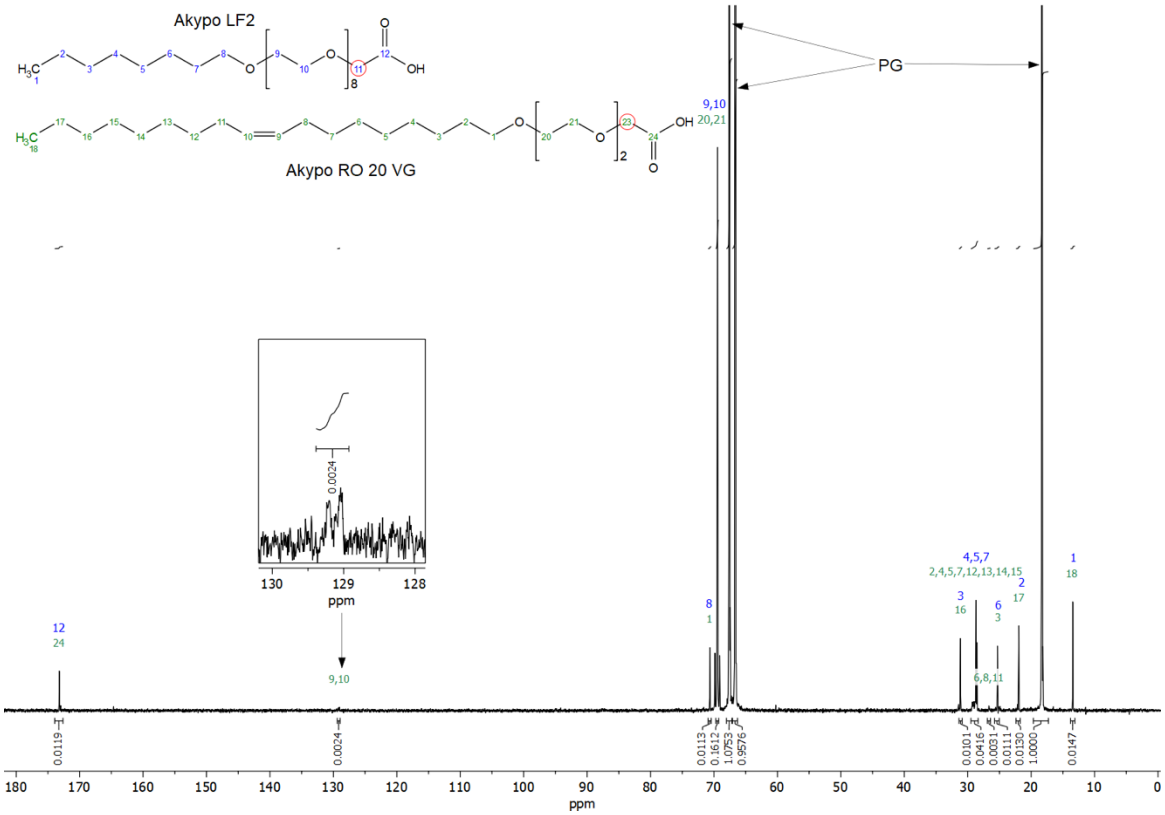

Fig. D.3. Quantitative ^{13}C-NMR (150.94 MHz, 128 scans, D_2O without solvent lock) spectrum of the bottom phase of sample "M-55PG" separated at 25°C. No actual solvent was used and the H_2O content is around 30 wt%. Since the surfactant content is low compared to the propylene glycol (PG) content, the relevant peaks for the surfactants have small integrals compared to those obtained from PG. The structures of the two surfactants, $C_8E_8CH_2COOH$ and $C_{18:1}E_2CH_2COOH$, are shown in the figure. The respective atom numbers correspond to those in the image. The signals of C-11 for $C_8E_8CH_2COOH$ and C-23 for $C_{18:1}E_2CH_2COOH$ are overlapping with signals of PG.
PG: δ_C [ppm] 18.3 (1 C, s, -CH_3, integral 1.0000), 66.6 (1 C, s, -CH_2OH, integral 0.9576), 67.6 (1 C, s, >CHOH, integral 1.0753).
$C_8E_8CH_2COOH$ (LF2)/$C_{18:1}E_2CH_2COOH$ (RO 20): δ_C [ppm] 13.4 (LF2: C-1 and RO 20: C-18, s, integral 0.0147), 22.0 (LF2: C-2 and RO 20: C-17, s, integral 0.0130), 25.3 (LF2: C-6 and RO 20: C-3, s, integral 0.0111), 26.4–26.9 (RO 20: C-6,8,11, m, integral 0.0031), 28.5–29.5 (LF2: C-4,5,7 and RO 20: C-2,4,5,7,12,13,14,15, m, integral 0.0416), 31.1 (LF2: C-3 and RO 20: C-16, s, integral 0.0101), 69.4 (LF2: C-9,10 and RO 20: C-20,21, s, integral 0.1612), 70.7 (LF2: C-8 and RO 20: C-1, s, integral 0.0113), 129.0–129.3 (RO 20: C-9,10, m, integral 0.0024), 173.2 (LF2: C-12 and RO 20: C-24, s, integral 0.0119).
The signals with a different atom number for the two surfactants at 26.4–26.9, 28.5–29.5, 69.4, and 129.0–129.3 ppm were used to calculate the surfactant ratio $R(C_{18:1}E_2CH_2COOH) = n(C_{18:1}E_2CH_2COOH)/[n(C_{18:1}E_2CH_2COOH)+n(C_8E_8CH_2COOH)]$. The obtained average value is $R(C_{18:1}E_2CH_2COOH) \approx 0.13$. Note that for the calculation the two surfactants were assumed to produce signals corresponding exactly to their theoretical structure, i.e., even "average" atom numbers. The peak of PG at 18.3 ppm and all other signals of the surfactants involving equal atom numbers for both surfactants were used to calculate and average the mole fraction of PG and surfactant in the PG/surfactant mixture. Since the water content is known, the respective masses can be calculated using the molar masses $M(PG) = 76.09\ g \cdot mol^{-1}$, $M(C_{18:1}E_2CH_2COOH) = 415\ g \cdot mol^{-1}$, and $M(C_8E_8CH_2COOH) = 541\ g \cdot mol^{-1}$.

D.2. Supplementary Tables

Table D.1. Determined contents of H_2O, propylene glycol (PG), $C_{18:1}E_2CH_2COOH$, and $C_8E_8CH_2COOH$ in the two phases of sample "M-55PG" at 25°C. The mixture contains 20 wt% of $C_8E_8CH_2COOH/C_{18:1}E_2CH_2COOH$ surfactant mixture with $R(C_{18:1}E_2CH_2COOH)$ = 0.655, 55 wt% PG, and 25 wt% H_2O. Complete phase separation was ensured by centrifugation at 14,000 g for 30 min at 25°C. 15 g (14.6 mL) of the mixture separated into 8.7 mL bottom phase (ρ = 1.0401 g·cm^{-3}) and 5.9 mL top phase (ρ = 1.0119 g·cm^{-3}). Water contents were measured using volumetric Karl-Fischer titration. The mole fractions of PG, $C_{18:1}E_2CH_2COOH$ and $C_8E_8CH_2COOH$ in the bottom phase were determined by quantitative ^{13}C-NMR, see **Fig. D.3**. To obtain the weight fraction w, the respective molar mass was used, where M(PG) = 76.09 g·mol^{-1}, $M(C_{18:1}E_2CH_2COOH)$ = 415 g·mol^{-1}, and $M(C_8E_8CH_2COOH)$ = 541 g·mol^{-1}. The contents of PG, $C_{18:1}E_2CH_2COOH$, and $C_8E_8CH_2COOH$ in the top phase could be calculated from the data of the bottom phase, the phase volumes, and densities due to conservation of mass. $f_{initial}$ is the percentage of the initial amount of the respective component in the respective phase. Note that $f_{initial}(H_2O)$ and the combined weight fractions in the top phase exceed 100% because $w(H_2O)$ in the top phase was measured and not calculated based on the measured value in the bottom phase. The deviation is mainly a result of errors involved in the water content measurements and especially in the determination of the phase volumes. The error in the measured density is negligible in comparison (typical error in the order of magnitude of 10^{-5} g·cm^{-3}).

	H_2O		**PG**		**$C_{18:1}E_2CH_2COOH$**		**$C_8E_8CH_2COOH$**		**$C_{18:1}E_2CH_2COOH$ / $C_8E_8CH_2COOH$**
M-55PG	**w [wt%]**	**$f_{initial}$ [%]**	**w [wt%]**	**$f_{initial}$ [%]**	**w [wt%]**	**$f_{initial}$ [%]**	**w [wt%]**	**$f_{initial}$ [%]**	**$R(C_{18:1}E_2CH_2COOH)$**
top phase	19.0	30.2	40.2	29.1	29.0	97.4	13.2	64.4	0.74
bottom phase	30.0	72.4	64.6	70.9	0.5	2.7	4.8	35.6	0.13

Appendix E.

Supplementary Material – Chapter VI.

E.1. Supplementary Figures and Tables

Table E.1. Measured physical densities of two solutions ρ(solution) and their corresponding solvents ρ(solvent) at 25°C. The density of water at 25°C was taken from Tanaka *et al.* [1]. For each measurement, the apparent density of AGA ρ_{app}(AGA) is extrapolated from ρ(solution), with a given mass fraction β(AGA), and ρ(solvent), where β(AGA) = 0, assuming a linear dependence of the reciprocal density on the mass fraction. Since the obtained mean value for ρ_{app}(AGA) in pure water of 1.349 ± 0.016 g·cm^{-3} and the obtained mean value for ρ_{app}(AGA) in the mixed solvent of 1.329 ± 0.008 g·cm^{-3} are similar, a mean value of both results as ρ_{app}(AGA) = 1.339 ± 0.009 g·cm^{-3} in this work. The similarity of the results is also an indication that the apparent physical density of AGA is approximately constant throughout the studied range of compositions. The resulting mean value and its standard deviation are also given at the end of the table.

solution	measurement (number)	ρ(solution) [g·cm^{-3}]	ρ(solvent) [g·cm^{-3}]	ρ_{app}(AGA) [g·cm^{-3}]
0.5 wt% AGA in H_2O (solvent: H_2O [1])	1	0.99836	0.99705	1.35254
	2	0.99835	0.99705	1.34961
	3	0.99837	0.99705	1.35659
	4	0.99827	0.99705	1.31924
	5	0.99827	0.99705	1.31889
	6	0.99838	0.99705	1.35880
	7	0.99838	0.99705	1.35992
	8	0.99836	0.99705	1.35364
	9	0.99838	0.99705	1.36029
	10	0.99838	0.99705	1.35992
1.0 wt% AGA + 30 wt% ethanol in H_2O (solvent: 30.3 wt% ethanol in H_2O)	1	0.95292	0.95022	1.32493
	2	0.95291	0.95020	1.32744
	3	0.95290	0.95022	1.32204
	4	0.95290	0.95022	1.32165
	5	0.95294	0.95021	1.33192
	6	0.95300	0.95021	1.34375
average ρ_{app}(AGA) = 1.339 ± 0.009 g·cm^{-3}				

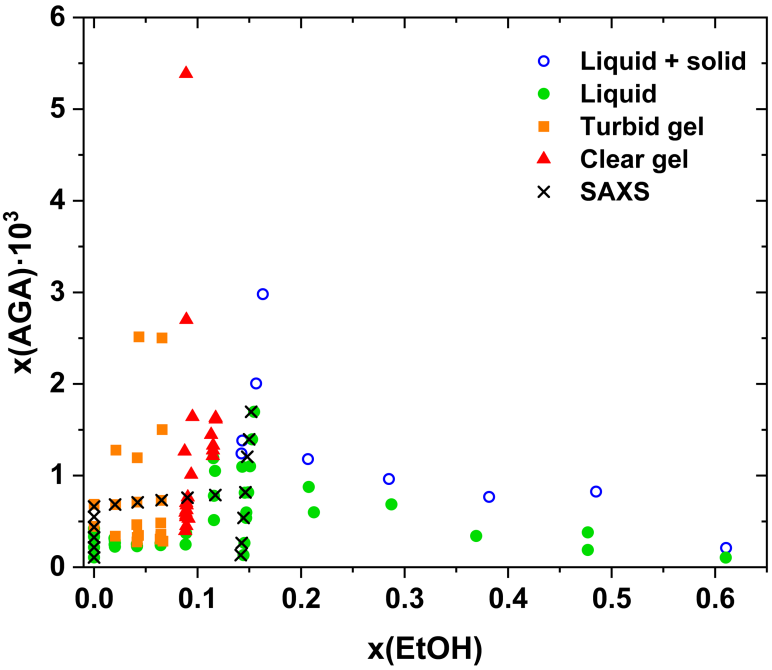

Fig. E.1. Phase map of the ternary AGA/EtOH/H_2O system at room temperature (T ≈ 23°C) in a rectangular representation. The mole fraction of AGA is plotted against the mole fraction of ethanol. Empty blue points indicate a saturated solution of AGA in equilibrium with excess solid AGA, green points indicate a monophasic sol, orange squares a turbid gel, and red triangles a clear gel. Black crosses mark the compositions of samples used for small-angle X-ray scattering. The same phase map is given in wt% in **Fig. VI.1**.

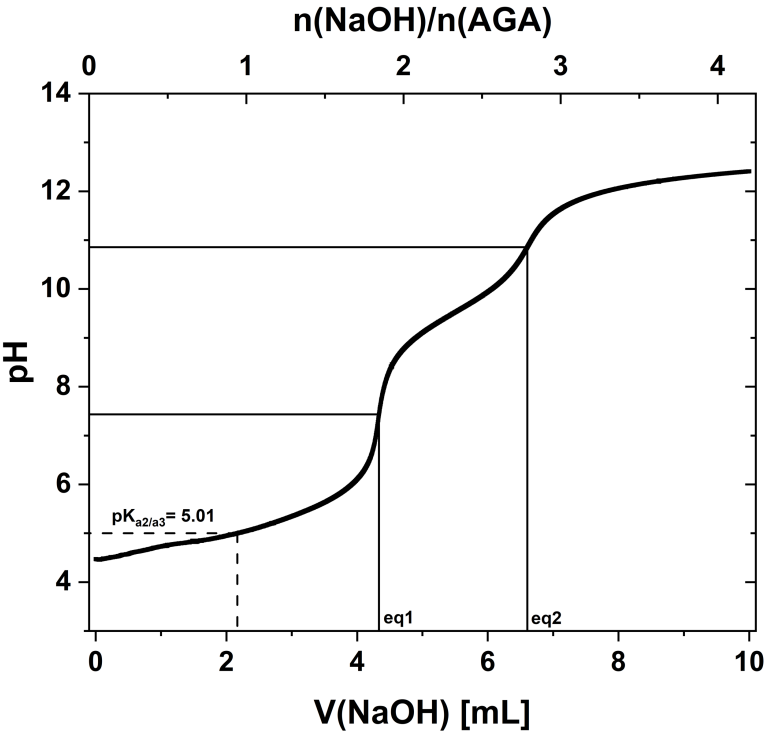

Fig. E.2. Potentiometric pH titration of 25 mL of an aqueous solution containing 30 g·L^{-1} AGA with a 0.375 mol·L^{-1} NaOH solution at room temperature (≈23°C). The mole ratio of NaOH and AGA shown on the top axis is calculated assuming pure AGA, i.e., without taking into account the water content of AGA. Two equivalence points are observed. Approximately two equivalents of NaOH are required to reach the first equivalence point, while the second one only requires one equivalent. The first equivalence point can be assigned to the two remaining carboxylic acid moieties of AGA with ap$K_{a2/a3}$ = 5.01, while the second one can be assigned to the ammonium ion with a pK_a of 9.50 (Bates and Pinching [2]: 9.24 at 25°C).

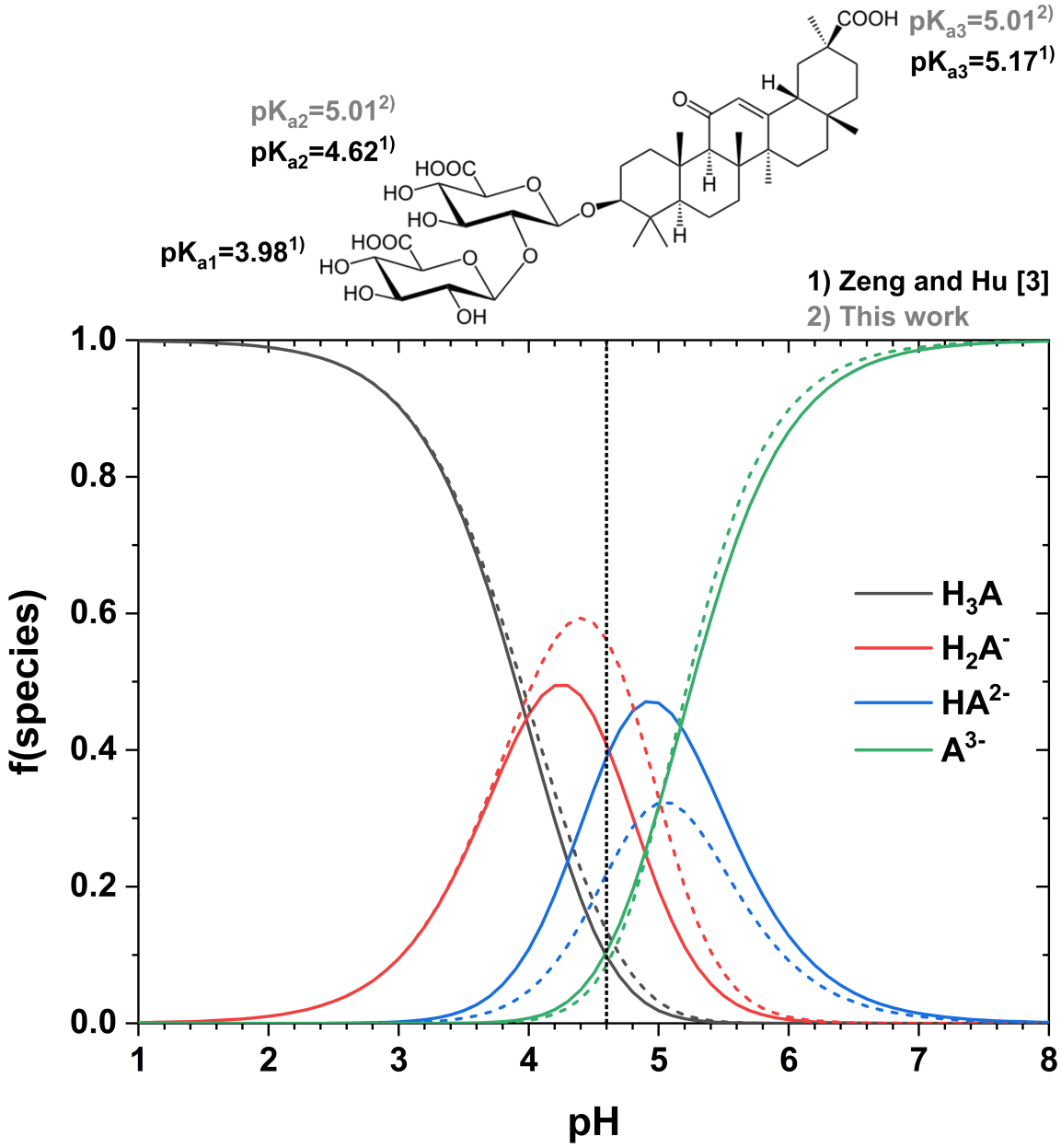

Fig. E.3. Computation of the species distribution in a solution of glycyrrhizic acid (GA) as a function of pH. The fully protonated form is denoted as H_3A (black), the singly deprotonated form as H_2A^- (red), the di-deprotonated form as HA^{2-} (blue), and the fully deprotonated form is denoted as A^{3-} (green). The fraction of the respective species f(species) is calculated as $f(H_3A) = [H^+]^3/D$, $f(H_2A^-) = K_{a1}[H^+]^2/D$, $f(HA^{2-}) = K_{a1}K_{a2}[H^+]/D$, and $f(A^{3-}) = K_{a1}K_{a2}K_{a3}/D$, where $[H^+]$ is the molar concentration of protons and $D = [H^+]^3+K_{a1}[H^+]^2+K_{a1}K_{a2}[H^+]+K_{a1}K_{a2}K_{a3}$. For the solid lines (—), $K_{a1} = 10^{-3.98}$, $K_{a2} = 10^{-4.62}$, and $K_{a3} = 10^{-5.17}$ are taken from the study of Zeng and Hu [3]. For the dashed lines (---), $K_{a1} = 10^{-3.98}$ is taken from the study of Zeng and Hu [3], whereas the apparent $aK_{a2} = aK_{a3} = 10^{-5.01}$ are inferred from the titration curve in **Fig. E.2**. The vertical dotted line indicates a pH of 4.6, typically measured for a binary mixture of 3.0 wt% AGA and water. The GA molecule and the assignment of the respective pK_a values is shown in the top.

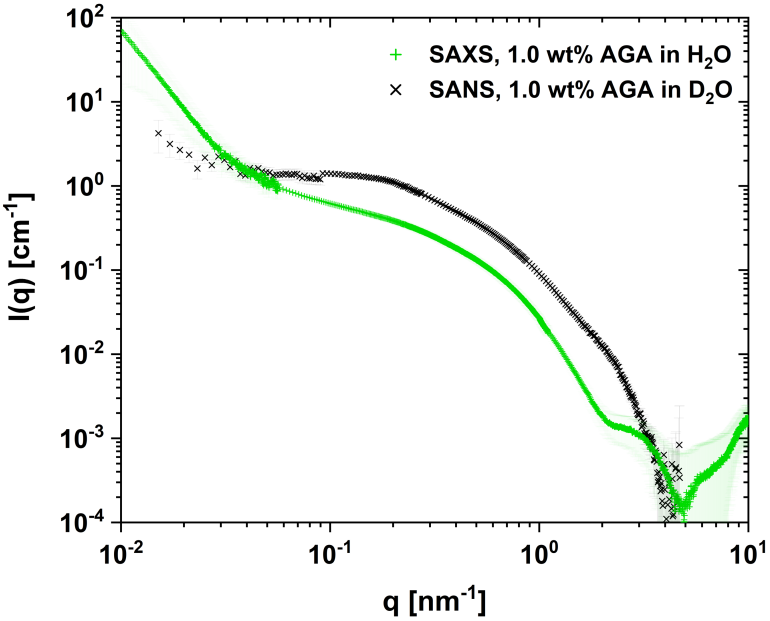

Fig. E.4. Comparison of the SAXS data of a binary mixture of 1 wt% AGA and H_2O and the SANS data of a binary mixture of 1 wt% AGA and D_2O.

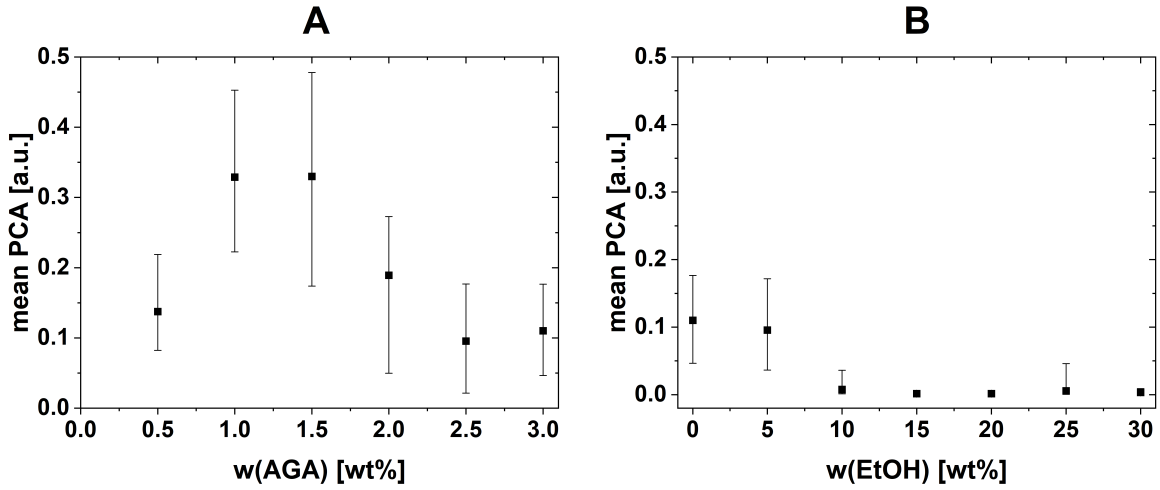

Fig. E.5. Anisotropy of SAXS data of mixtures of (A) 0.5 wt% to 3.0 wt% AGA in water and (B) 3 wt% AGA and 0 wt% to 30 wt% EtOH in water is given as the mean PCA, calculated via Principal Component Analysis using SASET [4]. For each sample, eleven scattering data at different positions in the capillary were recorded. Anisotropy (PCA) was calculated for each measurement at a sample-to-detector distance of 5 m (mid-q range). The respective mean values of the eleven measurements (mean PCA) are given and the error bars indicate the lowest and the highest PCA values calculated for each sample, i.e., the error bars indicate the range of the obtained PCA values for the eleven measurements.

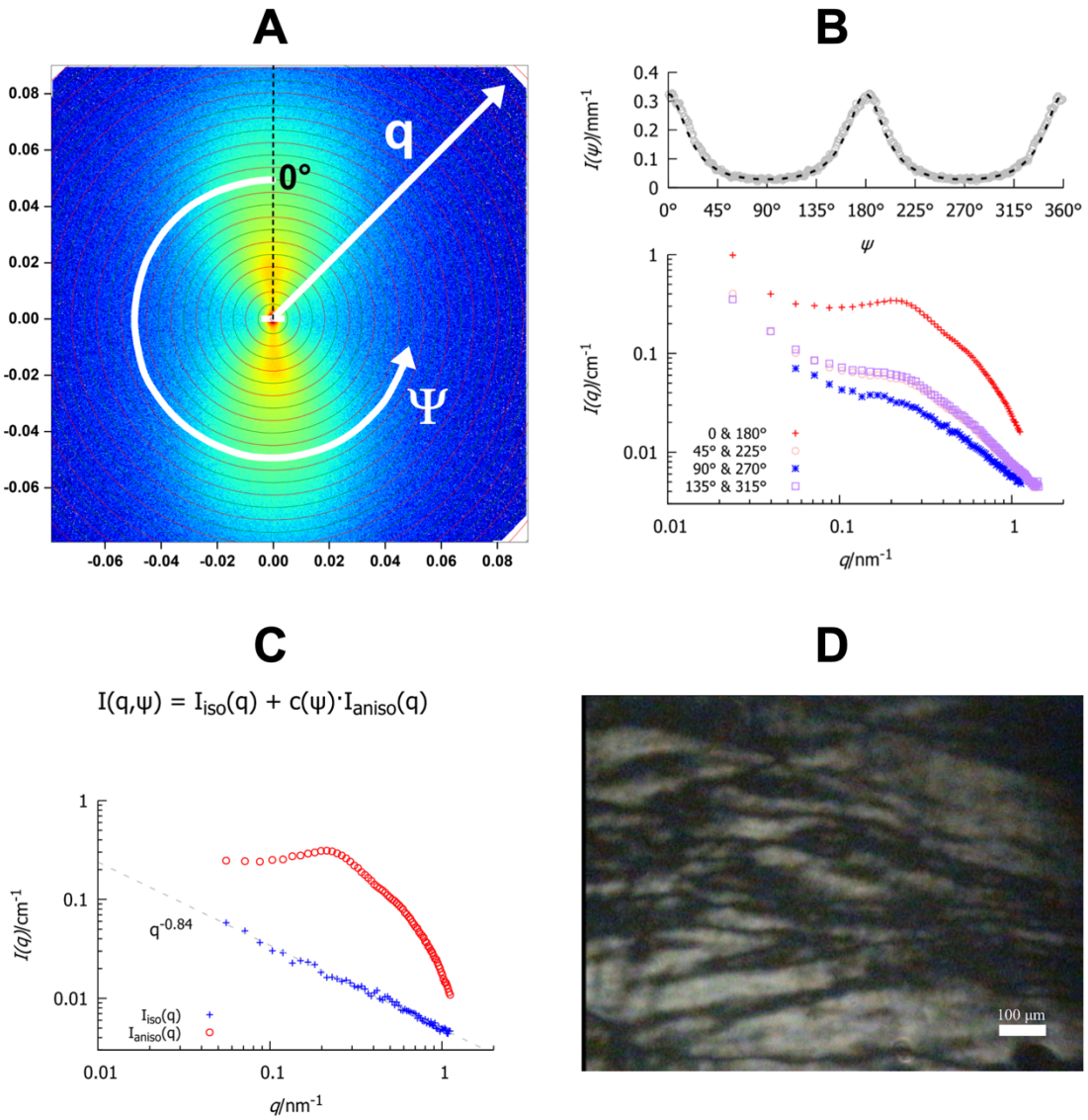

Fig. E.6. (A) Corrected 2D SAXS pattern (ID02, ESRF) for 1.5 wt% AGA in water. The q_x and q_y scale is given in nm^{-1}; the straight arrow indicates the direction of the magnitude of the wavevector q (i.e., the scattering angle theta); the circular arrow indicates the direction of the azimuthal angle Ψ, with a value fixed at 0° for the main direction of anisotropy (as obtained by Principal Component Analysis, PCA), which on this figure corresponds coincidentally to the upper direction (for all samples, the anisotropy tends to be perpendicular to the direction of the capillaries, which are horizontal, but the alignment moves around this direction). (B) 1D spectra obtained from the 2D pattern given in (A), with 4 sectors of 22.5° width centered at azimuthal angles of 0°, 45°, 90° and 135°, averaged with their opposite sectors (at 180°), and intensity as a function of the azimuthal angle taken in a small circle at q = 0.2 nm^{-1}. (C) Applying PCA to the spectra obtained at several azimuthal angles, one obtains visually that there are two main components, which are in turn calculated using the Non-Negative Matrix Factorization (NNMF) built-in function in Matlab. All azimuthal data can be reconstructed by combining linearly two q-dependent (Ψ-independent) intensity spectra (a simple decaying power-law and a curve with a peak), and one Ψ-dependent (q-independent) anisotropy distribution: $I(q,\Psi) = I_{iso}(q)+c(\Psi)\cdot I_{aniso}(q)$. (D) Birefringence of a sample containing 3.0 wt% AGA in H_2O observed at room temperature between crossed polarizers using a Leitz Orthoplan polarizing microscope (Wetzlar, Germany) equipped with a JVC (Yokohama, Japan) digital camera (TK-C1380) at 100x magnification and 120 µm sample thickness. The scale bar indicates a length of 100 µm.

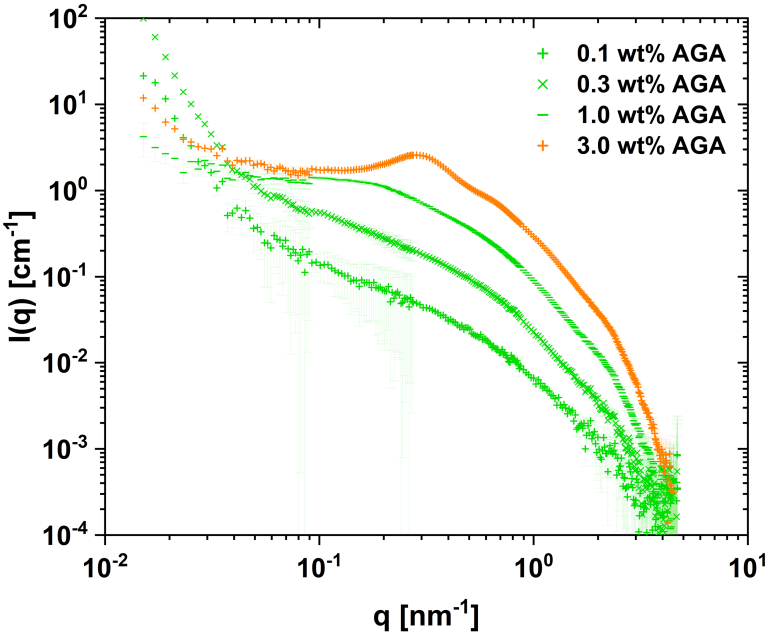

Fig. E.7. SANS spectra of binary mixtures of AGA and D_2O in a logarithmic scale. The AGA concentration ranges from 0.1 wt% to 3.0 wt%. A green color indicates a sol sample, while an orange color indicates a turbid gel.

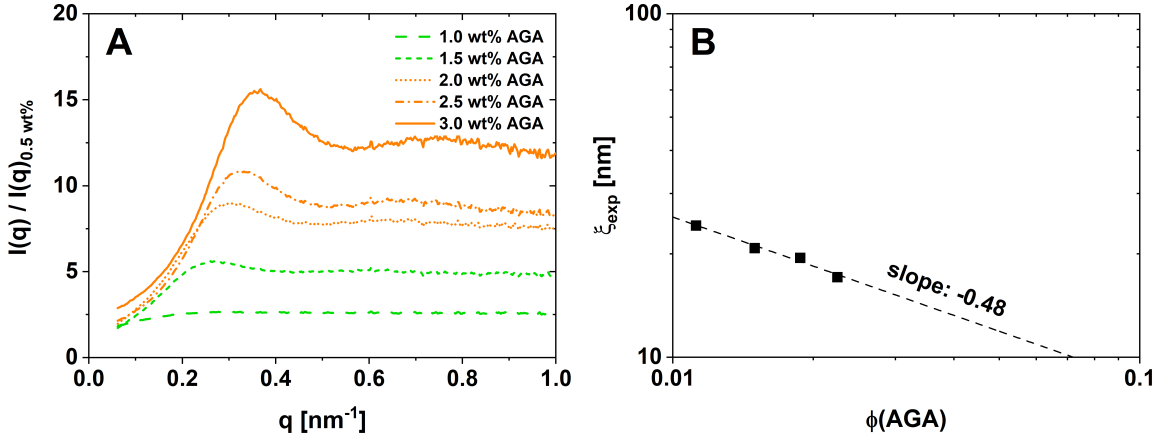

Fig. E.8. (A) Approximate structure factor S(q) of the data given in **Fig. VI.4**, as obtained by dividing the intensity I(q) by the intensity $I(q)_{0.5\ wt\%}$ of the sample containing 0.5 wt% AGA. (B) Experimental interaxial distance $\xi_{exp} = 2\pi/q_{max}$, as derived from the apparent structure factor (**Fig. E.8**A), as a function of the volume fraction of AGA. The dashed line indicates a slope of -0.48.

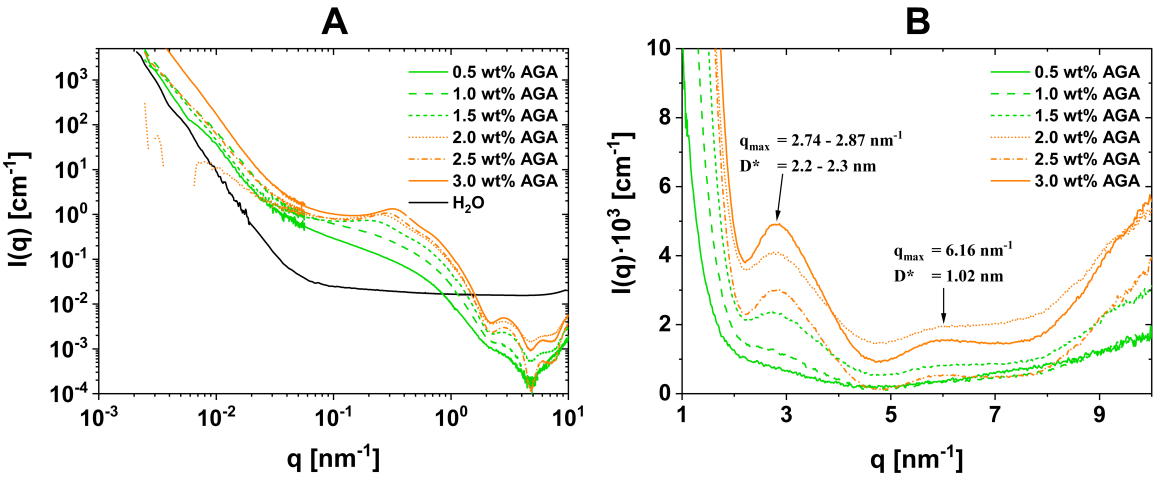

Fig. E.9. (A) SAXS spectra of binary mixtures of AGA and water with AGA concentrations ranging from 0.5 wt% to 3.0 wt% in logarithmic scale. Sol samples are shown in green, while samples that formed a turbid gel are shown in orange. The black curve represents the scattering of pure water. Solvent scattering (H_2O) is already subtracted from the scattering of the samples. (B) The form factor oscillations seen in the higher q-range are given in a linear scale. The maxima of the form factor oscillations are indicated.

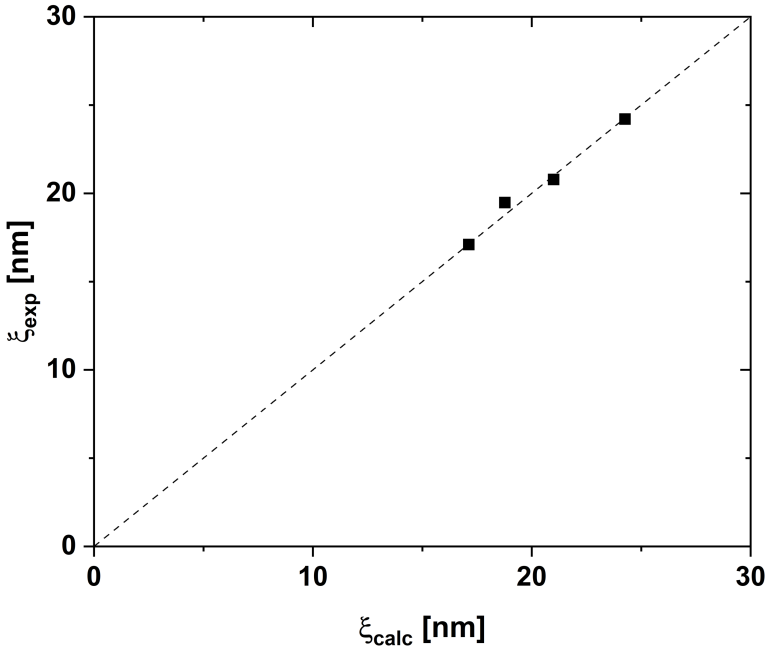

Fig. E.10. Experimental interaxial distance $\xi_{exp} = 2\pi/q_{max}$, as derived from the apparent structure factor of the SAXS spectra of binary mixtures of 1.5, 2.0, 2.5, and 3.0 wt% AGA and water (**Figs. VI.4**A and **E.8**A), plotted against the theoretical mesh size ξ_{calc}, calculated based on a hexagonal ordering of "infinite" fibrils. The fibrils were assumed to consist of stacks of AGA-dimers, as illustrated in **Fig. VI.2**E. ξ_{calc} matches ξ_{exp} for two borderline cases: Either (a) (almost) all available AGA molecules form fibrils longer than the interaxial distance and the fibrils form some superhelices (double or triple helices) so that in average 1.1 fibrils form one superhelix, or (b) only 90% of the AGA molecules form long fibrils and the fibrils do not form superhelices with one another at all. The calculation of ξ_{calc} is given in **Appendix E.3**. Note that ξ_{calc} matches ξ_{exp} for any intermediate case between (a) and (b), as long as the ratio of the fraction of AGA molecules participating in aggregation and the helicity is the same.

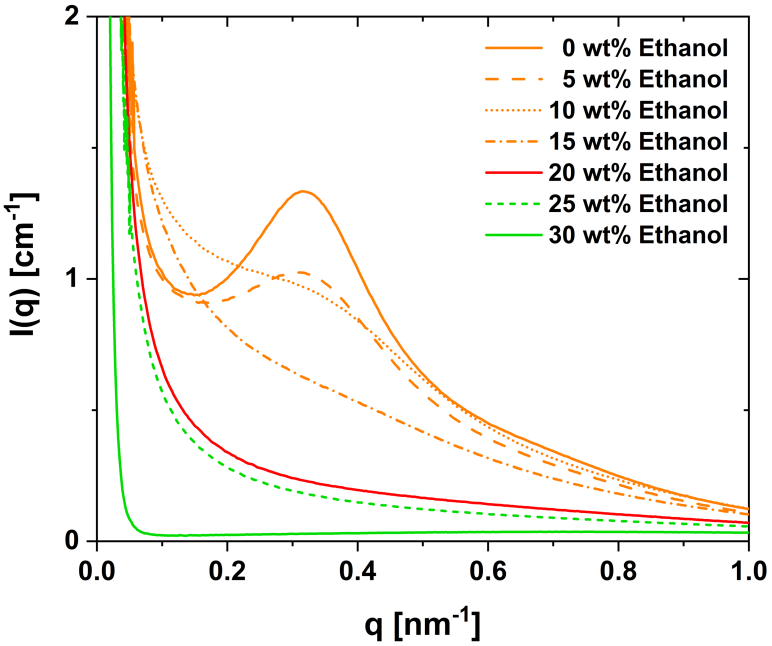

Fig. E.11. SAXS spectra in linear scale of ternary mixtures of AGA/EtOH/H_2O at a constant AGA content of 3 wt% and a varying EtOH content ranging from 0 wt% to 30 wt% in the q-range of the correlation peak. Note that the spectrum at 0 wt% EtOH is identical to the spectrum of the binary mixture of 3 wt% AGA and H_2O in **Figs. VI.3** and **VI.4**. The full spectra are given in logarithmic scale in **Fig. VI.5**.

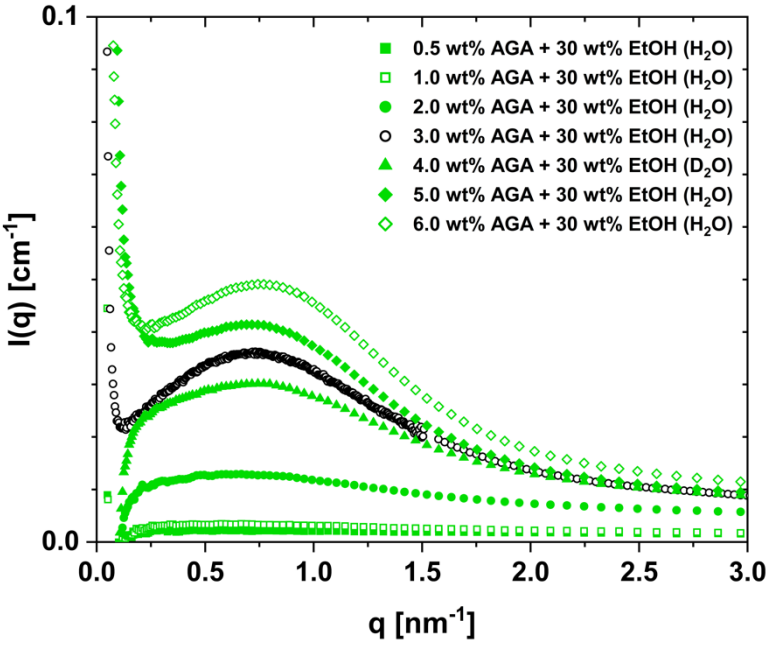

Fig. E.12. SAXS spectra in linear scale of samples containing 0.5, 1.0, 2.0, 3.0, 5.0, or 6.0 wt% AGA and 30 wt% EtOH in H_2O and of a sample containing 4.0 wt% AGA and 30 wt% EtOH in D_2O in the q-range of the correlation peak. Corresponding solvent (30 wt% EtOH in H_2O or D_2O) backgrounds are subtracted. Note that the spectrum at 3.0 wt% was taken in a different series of measurements (see **Figs. VI.5** and **E.11**) and only H_2O was subtracted as background. The full spectra are given in a logarithmic scale in **Fig. VI.6**A.

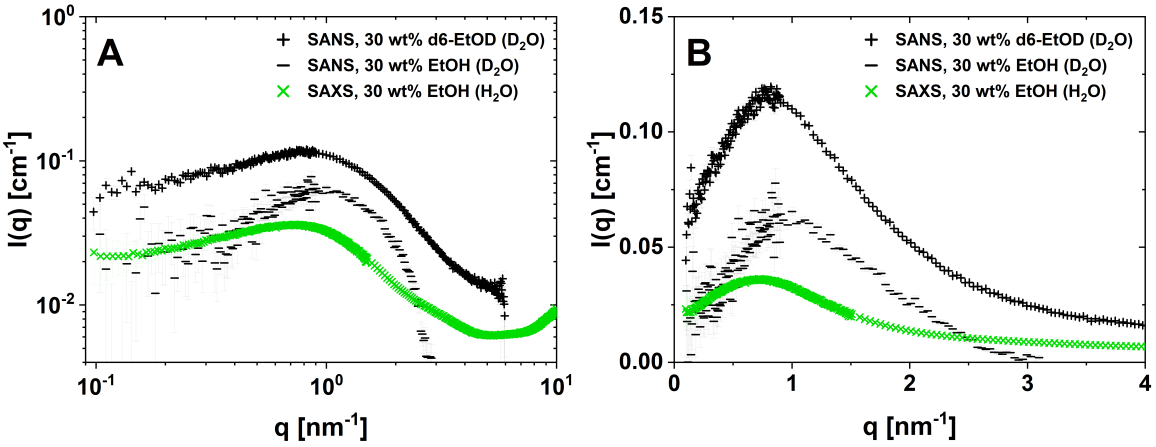

Fig. E.13. Comparison of SAXS data of a sample containing 3 wt% AGA and 30 wt% EtOH in H_2O with SANS data of samples containing 3 wt% AGA and 30 wt% EtOH or 30 wt% d6-EtOD in D_2O in a logarithmic scale (A) and a linear scale (B). Error bars indicate the standard deviations obtained from the averaging of ten successive measurements at different positions in the capillary. Solvent (D_2O or H_2O) backgrounds are subtracted.

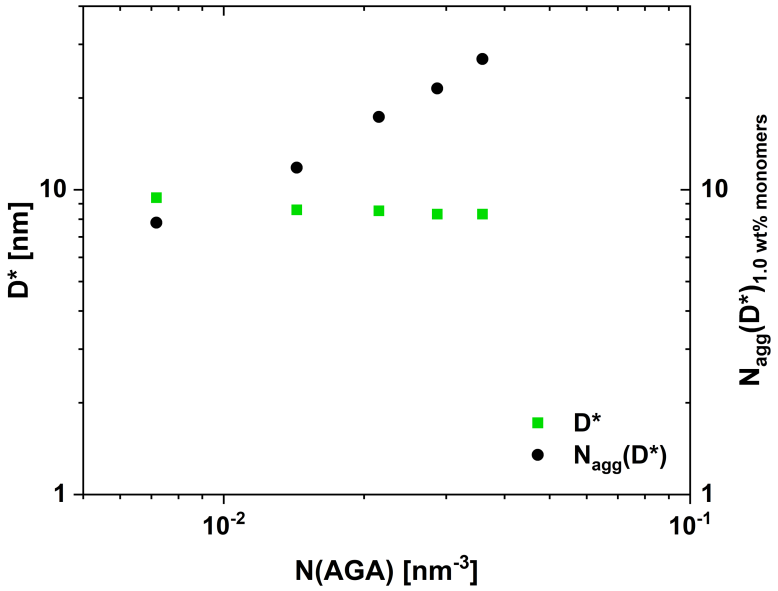

Fig. E.14. D* values obtained as $D^* = 2\pi/q_{max}$ from the SAXS spectra of samples containing 2 wt% to 6 wt% AGA (shown in **Figs. VI.6** and **E.12**) are plotted as a function of the number of AGA molecules per unit volume N(AGA). N(AGA) is the number of AGA molecules per unit volume that form aggregates. Thus, 1.0 wt% AGA are subtracted, as there is virtually no scattering at 1.0 wt% AGA, which suggests that this amount of AGA molecules is dissolved as monomers (or dimers). The right axis gives the corresponding aggregation number, which is calculated assuming a local face-centered-cubic ordering of spherical aggregates.

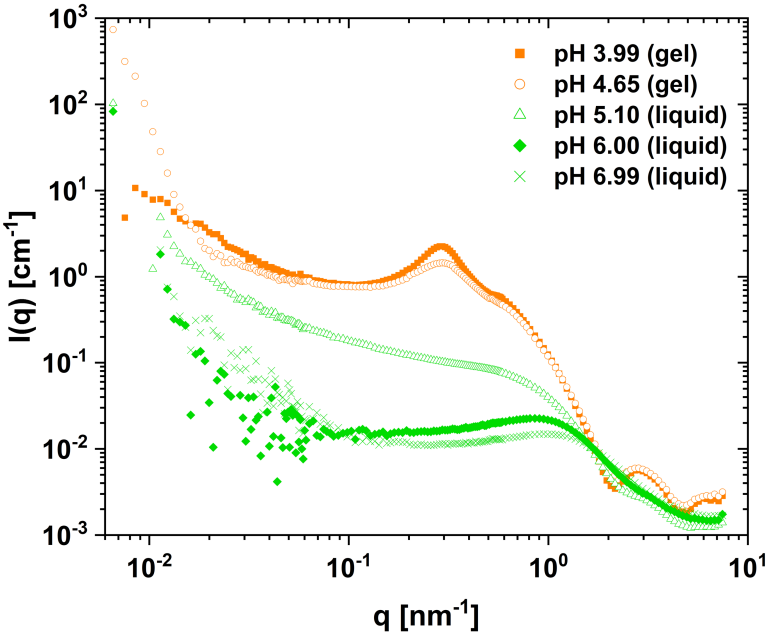

Fig. E.15. SAXS spectra of samples containing 3.0 wt% AGA in H_2O at pH 3.99 (HCl), 4.65 (natural), 5.10 (NaOH), 6.00 (NaOH), and 6.99 (NaOH) in a logarithmic scale. Scattering of water was subtracted as solvent background.

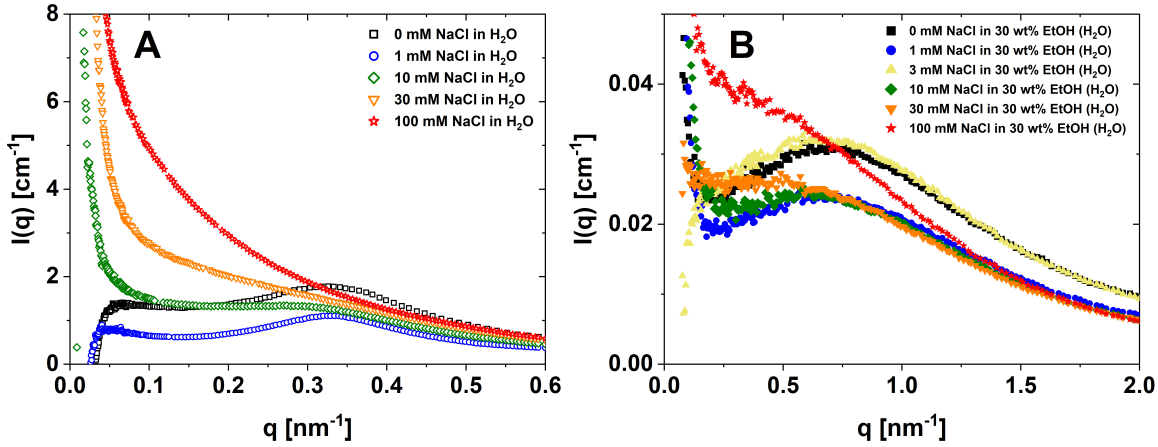

Fig. E.16. (A) SAXS spectra of samples containing 3.0 wt% AGA in H_2O (empty symbols) and (B) 30 wt% EtOH in H_2O (full symbols) with various NaCl concentrations: 0 (black), 1 (blue), 3 (yellow), 10 (green), 30 (orange), and 100 mM (red). Corresponding solvent backgrounds (including NaCl and EtOH) were subtracted. The same spectra are given in a logarithmic scale in **Fig. VI.7**.

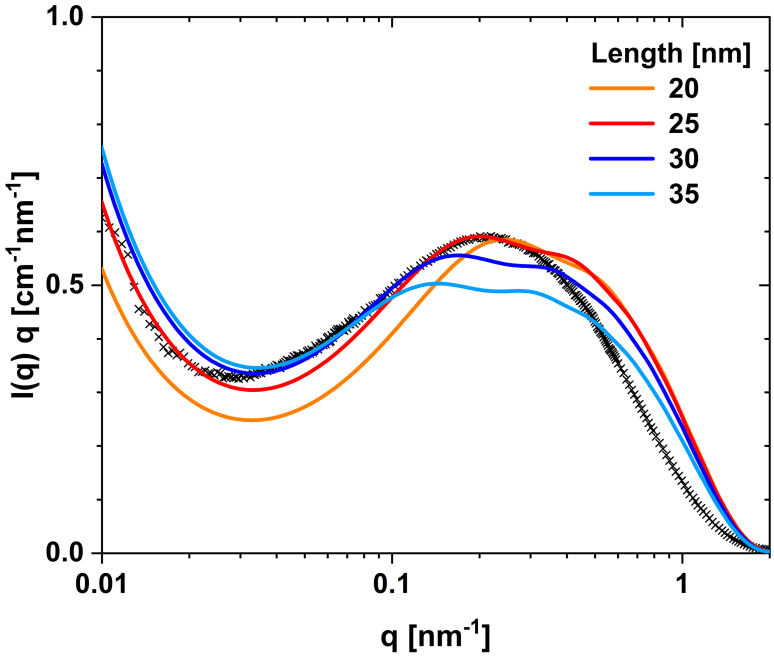

Fig. E.17. SAXS spectrum (I(q)·q versus q) of the sample containing 3.0 wt% AGA and 100 mM NaCl in H_2O (see **Figs. VI.7** and **E.16**). The simulations (continuous lines) use a form factor for a long cylinder with homogeneous circular cross-section and a structure factor for fractal clusters with a Gaussian cut-off (to account for the low-q upturn; fractal dimension 2.2). Simulations were obtained for a fixed cylinder radius of 1.9 nm – in agreement with our geometric model –, for different cylinder lengths: 20 nm (orange), 25 nm (red), 30 nm (blue), and 35 nm (light blue). The mid-q data are best reproduced for a length close to 25 nm (although the actual length is certainly not uniform). Note that the high-q cannot be reproduced by a simple cylinder with homogeneous circular cross-section, as AGA forms helices and the aglycone/diglucuronate groups have significantly different X-ray contrasts; the simulations only aim at determining the most probable length of these helices.

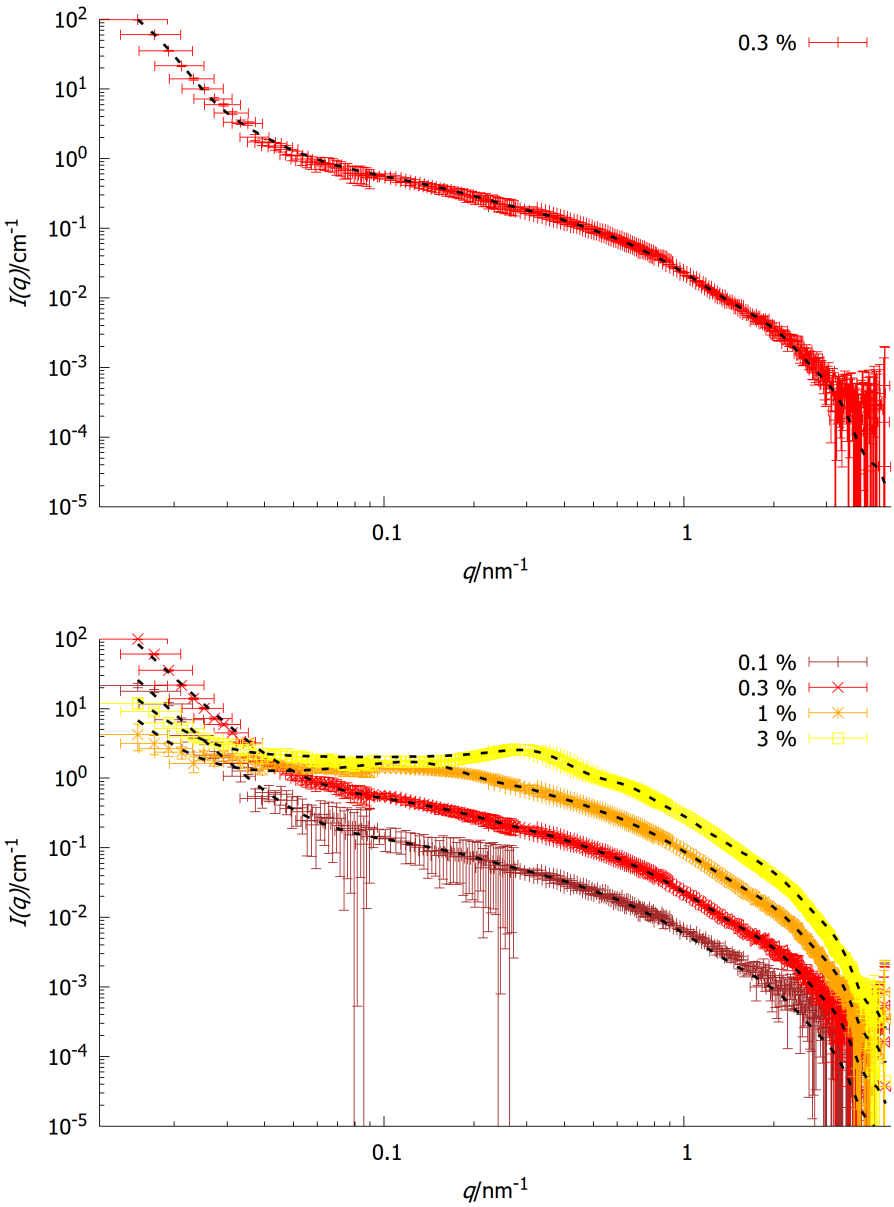

Fig. E.18. Fits of SANS data of 0.1 wt% to 3.0 wt% AGA in D_2O (**Fig. E.7**) to a form factor of rectangular cuboids [5] of sides 1.41 nm, 5.15 nm, and 28 nm. Top: Fit of the 0.3 wt% AGA solution with rectangular cuboids plus a Porod contribution (q^{-4}) [6,7] to account for the low-q upturn. Bottom: Fits of the four concentrations with the same model, plus an ad hoc hard sphere structure factor [8] to produce a correlation peak for the two highest concentrations.
For neutrons, the scattering contribution from AGA in D_2O comes primarily from the aglycone moieties, due to the small amount of non-exchangeable protons in the glycone moieties. To test the hypothesized geometrical model, given the lack of a form factor for helicoidal structures of the kind proposed, with two contrasts, the experimental data are compared to a simple form factor for rectangular cuboids, uniform in size (no polydispersity) and in scattering length density (single contrast towards the solvent). Note that the data for 0.3 wt% AGA show no clear evidence of a structure factor due to strong interactions, as for data at 1 wt% and 3 wt% AGA. Thus, the data for 0.3 wt% can be fitted to the form factor. Data for 0.3 wt% were chosen over data at 0.1 wt%, because those at 0.3 wt% have better statistics. With the addition of a structure factor for higher concentrations, the same model works well with the entire data set.

E.2. Calculation of the Overlap Volume Fraction of the Fibrils

To calculate the overlap volume fraction φ*, we use the observed average fibrillar length of about 25 nm. We approximate the volume occupied per AGA fibril as the volume of a sphere with a diameter of 25 nm, i.e., $V = (12.5\ \text{nm})^3 \cdot \pi \cdot 4/3$. Assuming that all AGA molecules are available to form fibrils, the overlap volume fraction φ* is then obtained by multiplying V with the number of fibrils per unit volume (nm^3) n_F^*.

$$\varphi^* = V \cdot n_F^* \tag{E.2.1}$$

n_F^* is calculated by dividing the total available length of fibrils per unit volume (nm^3) l_T^* by the average length of one fibril (25 nm). For a dimeric stacking of AGA molecules, see **Fig. VI.2**E, l_T^* is calculated as

$$l_T^* = \frac{\frac{\beta(AGA)}{M(AGA)} \cdot N_A}{\frac{\beta(AGA)}{\rho(AGA)} + \frac{1\text{-}\beta(AGA)}{\rho(H_2O)}} \cdot \frac{1}{2} \cdot d\,, \tag{E.2.2}$$

where β(AGA) is the mass fraction of AGA, $M(AGA) = 839.96\ g \cdot mol^{-1}$ is the molar mass of AGA, N_A is the Avogadro constant, $\rho(AGA) = 1.339\ g \cdot cm^{-3} = 1.339 \cdot 10^{-21}\ g \cdot nm^{-3}$ is the physical density of AGA at 25°C, $\rho(H_2O)$ is the physical density of water at 25°C, and d is the fibrillar length (along the helical axis) per individual (dimeric) stack of AGA. The fibrillar length per stack is not equal to the stacking distance of 0.61 nm, as derived by Saha *et al.* [9], but 0.30 nm, which is obtained by dividing the helical period of 9 nm by the number of AGA stacks in one period (≈30).

E.3. 2D Mesh Size Expected for a Gel Made of "Infinite" Fibrils Aligned in a Hexagonal Cell

In the case of only "infinite" fibrils forming the birefringent gel, we model the gel as fibrils aligned in a hexagonal cell. We consider one unit hexagon of volume V that is linked to the mesh size ξ (experimental ξ_{exp} or calculated ξ_{calc}) in the following way.

$$V = \frac{3\sqrt{3}}{2} \cdot \xi^2 \cdot h \tag{E.3.1}$$

The hexagon's height h is linked to the length of fibrils l_T^* "consumed" by one unit hexagon, i.e., the total available length of fibrils per unit volume l_T^*.

$$l_T^* = \frac{1}{0.9} \cdot 2 \cdot h \tag{E.3.2}$$

Combination of eq. (E.3.1) and (E.3.2) yields the relation between l_T^* and ξ.

$$l_T^* = \frac{2}{3\sqrt{3}} \cdot \frac{2}{0.9 \cdot \xi^2} \tag{E.3.3}$$

l_T^* is also given by the mass fraction of AGA, β(AGA), if the fibrillar structure is known. We assume a dimeric stacking of AGA molecules, as shown in **Fig. VI.2**E, with a fibrillar length per AGA stack of d = 0.30 nm. Further, we introduce the parameter of helicity H ($H \geq 1$) and the fraction of AGA molecules available for the formation of fibrils α ($0 \leq \alpha \leq 1$). H is the average number of individual helical AGA fibrils ("strands") forming one superhelical fibril. E.g., H = 1 means that the individual fibrils do not form superhelices, whereas H = 2 means that two fibrils combine to one double helical fibril. l_T^* is then given by

$$l_T^* = \frac{\frac{\beta(AGA)}{M(AGA)} \cdot N_A}{\frac{\beta(AGA)}{\rho(AGA)} + \frac{1-\beta(AGA)}{\rho(H_2O)}} \cdot \frac{1}{2} \cdot d \cdot \frac{\alpha}{H}\,, \tag{E.3.4}$$

where M(AGA) = 839.96 $g \cdot mol^{-1}$ is the molar mass of AGA, N_A is the Avogadro constant, ρ(AGA) = 1.339 $g \cdot cm^{-3}$ = $1.339 \cdot 10^{-21}$ $g \cdot nm^{-3}$ is the physical density of AGA at 25°C, and $\rho(H_2O)$ is the physical density of water at 25°C.

By adjusting H and α, we can now calculate different values for ξ_{calc} for the different concentrations of AGA using eqs. (E.3.3) and (E.3.4) and compare them to the experimental values ξ_{exp} to find the matching values for H and α. Since only the ratio of α and H is decisive for the result, a multitude of combinations of H and α lead to the same result. Nevertheless, two borderline cases can be deduced by either minimizing H or maximizing α. Note that this calculation is no longer valid if a larger portion of shorter fibrils is present, even if the short fibrils are also perfectly aligned in the same hexagonal cell, because there

are gaps between the fibrils parallel to the fibrillar axis. However, if the gaps are small, the error made by assuming only "infinite" fibrils is also small.

E.4. Inference of Preferential Solvation from the Forward Scattering Intensity

The scattering intensity of a population of discrete scatterers is written as

$$I(q) = \frac{N_P}{V_{tot}} \cdot \langle V \cdot \Delta SLD \rangle^2 \cdot P(q) \cdot S^{eff}(q) \,, \tag{E.4.1}$$

where N_P is the total number of particles in the volume V_{tot} (N_P/V_{tot} is the concentration of particles, called the number density), V the particle's volume, ΔSLD the overall contrast (difference in Scattering Length Densities) between the particle of volume V and the medium, P(q) the normalized form factor (P(0) = 1) describing the particles shape(s) and size(s), and $S^{eff}(q)$ the effective structure factor accounting for interactions between particles. The brackets ⟨ ⟩ signify an average over all particles.

If there are no interactions, which only happens for well dispersed (no aggregation) dilute (<1%) particles with no electrostatic repulsions (uncharged particles, or medium with low relative permittivity, or high ionic strength screening charges), then $S^{eff}(q) = 1$. The forward scattering is then

$$I(0) = \frac{N_P}{V_{tot}} \cdot \langle V \cdot \Delta SLD \rangle^2 \,. \tag{E.4.2}$$

I(0) can be re-written as a function of the concentration c (in units of $g \cdot cm^{-3}$) and the molar mass M:

$$I(0) = c \cdot \frac{M}{\rho^2} \cdot \frac{(\Delta SLD)^2}{N_A} \tag{E.4.3}$$

with the apparent physical density ρ and the Avogadro number N_A. We then get

$$M = \frac{I(0)\rho^2 N_A}{c \cdot \Delta SLD^2} \ . \qquad (E.4.4)$$

Another useful re-writing of the forward scattering is to express it as a function of the volume fraction of scatterers ϕ (given that $\phi = \langle V \rangle \cdot N_P / V_{tot}$).

$$I(0) = \phi \cdot V \cdot \Delta SLD^2 \qquad (E.4.5)$$

The forward scattering is insensitive to solvation of the particle insofar as the solvent density remains the same as in the bulk, i.e., neglecting the solvation layer surrounding dissolved scatterers, and if the composition of the solvent remains the same as in the bulk for buffers and mixed solvents. This is because solvation increases the volume of the particle, but decreases the contrast, and these two effects cancel out.

Binary mixtures of alcohols and water are non-ideal. However, the linear approximation holds within about 2% (see e.g., González *et al.* [10]), so we consider that apparent densities and molecular volumes are constant for our multi-component system (see **Table VI.1**). To simplify, we also consider that the counterions of AGA are condensed and not exchanged with other ions from the solution.

In the case of SANS data for binary mixtures at 0.1, 0.3, 1.0, and 3.0 wt% (approximately 1, 3, 10, and 30 $mg \cdot mL^{-1}$) in D_2O, the fits proposed in **Fig. E.18** give forward scattering intensities that increase linearly with the concentration of AGA: $I(0) = 241.39 \cdot c - 0.131$, where I(0) is in units of cm^{-1} and the concentration c is in units of $g \cdot cm^{-3}$. The linear relation suggests a CAC of 0.54 $mg \cdot mL^{-1}$ (≈0.054 wt%). For neutrons, the contrast between D_2O and AGA is $4.05 \cdot 10^{10}$ cm^{-2} (see **Table VI.1**, with d = 1 for AGA). According to eq. (E.4.4), the molar mass of the self-assembled structure is therefore $M_{agg} \approx 159000$ $g \cdot mol^{-1}$, using the physical density $\rho_{AGA} = 1.339$ $g \cdot cm^{-3}$. An aggregation number of 189 is then obtained by dividing M_{agg} by $M_{AGA} = 839.96$ $g \cdot mol^{-1}$. Different simplified fits, see **Sections VI.4.2.** and **VI.4.5.**, suggest an average fibrillar length of around 25 nm, corresponding to around 3 helical periods per fibril. Thus, a number of around 30 dimeric AGA stacks per helical period can be derived from simple model fits and forward scattering.

As the X-ray contrast between AGA and H_2O (see **Table VI.1**) is $2.83 \cdot 10^{10}$ cm^{-2}, a forward scattering for SAXS of $I(0) = c \cdot 118$ $cm^2 \cdot g^{-1}$, where c is in units of $g \cdot cm^{-3}$ and I(0) is in units of cm^{-1}, is expected for $M_{agg} \approx 159000$ $g \cdot mol^{-1}$. E.g., for a 1 wt% (≈10 $mg \cdot mL^{-1}$) AGA

solution, I(0) is expected to be around 1 cm^{-1}, which is in line with the experimental results.

In the case of ternary mixtures, we must consider the possibility that water and/or ethanol partition towards the self-assembled scatterer. Let ξ_w and ξ_a be the ratios of water and alcohol molecules per AGA molecule involved in the aggregate.

$$M_{agg} = N_{agg}\left(M_{AGA}+\xi_w M_w+\xi_a M_a\right) \tag{E.4.6}$$

$$SLD_{agg} = \frac{v_{AGA}SLD_{AGA}+\xi_w v_w SLD_w+\xi_a v_a SLD_a}{v_{AGA}+\xi_w v_w+\xi_a v_a} \tag{E.4.7}$$

Neglecting the consumption of water and ethanol by the scatterer, the solvent's SLD can be expressed as a function of the mass fraction of water β_w in the water/alcohol binary mixture.

$$SLD_{solvent} = \phi_{w,solvent}SLD_w+\phi_{a,solvent}SLD_a = \frac{SLD_a\rho_w\left(1-\beta_w\right)+SLD_w\rho_a\beta_w}{\rho_w\left(1-\beta_w\right)+\rho_a\beta_w} \tag{E.4.8}$$

The scattering curves obtained at 3 wt% AGA in a binary solvent at 30 wt% of ethanol (see **Fig. E.13**) can be rescaled to match approximately in scattering intensity. We deduce that the contrasts (which contribute to the square to the intensity) are $\sqrt{1.4}$ times smaller with h-ethanol than with d6-ethanol, and $\sqrt{3.5}$ times smaller for SAXS than for SANS (D_2O/h-ethanol). We therefore have two equations and two unknowns (ξ_w and ξ_a), from which we deduce $\xi_w \approx 0$ and $\xi_a \approx 5.3$.

E.5. References

[1] M. Tanaka, G. Girard, R. Davis, A. Peuto, N. Bignell, Recommended table for the density of water between 0 °C and 40 °C based on recent experimental reports, Metrologia. 38 (2001) 301–309. https://doi.org/10.1088/0026-1394/38/4/3.

[2] R.G. Bates, G.D. Pinching, Acidic dissociation constant of ammonium ion at 0 to 50 C, and the base strength of ammonia, J. Res. Natl. Bur. Stand. (1934). 42 (1949) 419. https://doi.org/10.6028/jres.042.037.

[3] C.-X. Zeng, Q. Hu, Determination of the polyacid dissociation constants of glycyrrhizic acid, Indian J. Chem. - Sect. A Inorganic, Phys. Theor. Anal. Chem. 47 (2008) 71–74. http://nopr.niscair.res.in/handle/123456789/555.

[4] M. Muthig, S. Prévost, R. Orglmeister, M. Gradzielski, SASET : a program for series analysis of small-angle scattering data, J. Appl. Crystallogr. 46 (2013) 1187–1195. https://doi.org/10.1107/S0021889813016658.

[5] P. Mittelbach, G. Porod, Zur Röntgenkleinwinkelstreuung verdünnter kolloider Systeme. Die Berechnung der Streukurven von Parallelepipeden, Acta Phys. Austriaca. 14 (1961) 185–211.

[6] G. Porod, Die Röntgenkleinwinkelstreuung von dichtgepackten kolloiden Systemen, Kolloid-Zeitschrift. 124 (1951) 83–114. https://doi.org/10.1007/BF01512792.

[7] G. Porod, Die Röntgenkleinwinkelstreuung von dichtgepackten kolloiden Systemen, Kolloid-Zeitschrift. 125 (1952) 51–57. https://doi.org/10.1007/BF01519615.

[8] J.K. Percus, G.J. Yevick, Analysis of Classical Statistical Mechanics by Means of Collective Coordinates, Phys. Rev. 110 (1958) 1–13. https://doi.org/10.1103/PhysRev.110.1.

[9] A. Saha, J. Adamcik, S. Bolisetty, S. Handschin, R. Mezzenga, Fibrillar Networks of Glycyrrhizic Acid for Hybrid Nanomaterials with Catalytic Features, Angew. Chemie. 127 (2015) 5498–5502. https://doi.org/10.1002/ange.201411875.

[10] B. González, N. Calvar, E. Gómez, Á. Domínguez, Density, dynamic viscosity, and derived properties of binary mixtures of methanol or ethanol with water, ethyl acetate, and methyl acetate at T=(293.15, 298.15, and 303.15)K, J. Chem. Thermodyn. 39 (2007) 1578–1588. https://doi.org/10.1016/j.jct.2007.05.004.

List of Figures

List of Tables

List of Publications

(1) Patrick Denk, Asmae El Maangar, Jyotsana Lal, David Kleber, Thomas Zemb, Werner Kunz

"Phase diagrams and microstructures of aqueous short alkyl chain polyethylene glycol ether carboxylate and carboxylic acid triblock surfactant solutions"

Journal of Colloid and Interface Science 590 (2021) 375–386. (Chapter II.)

(2) Manuel Rothe, Eva Müller, Patrick Denk, Werner Kunz

"Ionic Liquids Based on the Concept of Melting Point Lowering Due to Ethoxylation"

Molecules 26 (2021) 4034. (Chapter II.)

(3) Jonas Blahnik, Eva Müller, Lydia Braun, Patrick Denk, Werner Kunz

"Nanoscopic microheterogeneities or pseudo-phase separations in non-conventional liquids"

Current Opinion in Colloid and Interface Science 57 (2022) 101535. (Chapter II.)

(4) Patrick Denk, Asmae El Maangar, Sylvain Prévost, Wagner Silva, Ruth Gschwind, Thomas Zemb, Werner Kunz

"Cloud point, auto-coacervation, and nematic ordering of micelles formed by ethylene oxide containing carboxylate surfactants"

Journal of Colloid and Interface Science 621 (2022) 470–488. (Chapter III.)

(5) Patrick Denk, Sylvain Prévost, Lauren Matthews, Quirin Prasser, Thomas Zemb, Werner Kunz

"The effect of ethanol on fibrillar hydrogels formed by glycyrrhizic acid monoammonium salt"

Journal of Colloid and Interface Science 630 (2023) 762–775. (Chapter VI.)

(6) Patrick Denk, Lauren Matthews, Sylvain Prévost, Thomas Zemb, Werner Kunz

"A dilute nematic gel produced by intramicellar segregation of two polyoxyethylene alkyl ether carboxylic acids"

Journal of Colloid and Interface Science 659 (2024) 833–848. (Chapter IV.)

(7) Patrick Denk, Lauren Matthews, Thomas Zemb, Werner Kunz

"Formulating additives in thermoresponsive surfactant-based nematic liquid crystals"

Tenside Surfactants Detergents 61 (2024) 228–239. (Chapter V.)

List of Poster Presentations

09/2021 35th Conference of the European Colloid and Interface Society (ECIS), Athens, Greece
"Aqueous Phase Behavior and Microstructuring of Octyl Octaethylene Glycol Ether ($C_8E_8CH_2COOH$)"

04/2022 17th Zsigmondy Colloquium of the German Colloid Society, Aachen, Germany
"Phase Behavior and Microstructuring of a Short-Chain Alcohol Ethoxycarboxylate"

Eidesstattliche Erklärung

(1) Ich erkläre hiermit an Eides statt, dass ich die vorliegende Arbeit ohne unzulässige Hilfe Dritter und ohne Benutzung anderer als der angegebenen Hilfsmittel angefertigt habe; die aus anderen Quellen direkt oder indirekt übernommenen Daten und Konzepte sind unter Angabe des Literaturzitats gekennzeichnet.

(2) Die zu Beginn eines Kapitels aufgeführten Personen haben meine Arbeit in der beschriebenen Weise unentgeltlich unterstützt.

(3) Weitere Personen waren an der inhaltlich-materiellen Herstellung der vorliegenden Arbeit nicht beteiligt. Insbesondere habe ich hierfür nicht die entgeltliche Hilfe eines Promotionsberaters oder anderer Personen in Anspruch genommen. Niemand hat von mir weder unmittelbar noch mittelbar geldwerte Leistungen für Arbeiten erhalten, die im Zusammenhang mit dem Inhalt der vorgelegten Dissertation stehen.

(4) Die Arbeit wurde bisher weder im In- noch im Ausland in gleicher oder ähnlicher Form einer anderen Prüfungsbehörde vorgelegt.

Ort, Datum	Patrick Denk